Uncertainties in Space-Based Estimates of Clouds and Precipitation: Implications for Deriving Global Diabetic Heating

By
Tristan S. L'Ecuyer and Graeme L. Stephens

Department of Atmospheric Science
Colorado State University
Fort Collins, Colorado

Research supported by NASA TRMM research grant NAG5-7719 and grant NAS5-99237.
PI: G. Stephens

Colorado State University

Department of Atmospheric Science

Paper No. 721

UNCERTAINTIES IN SPACE-BASED ESTIMATES OF CLOUDS AND PRECIPITATION: IMPLICATIONS FOR DERIVING GLOBAL DIABATIC HEATING

Tristan S. L'Ecuyer and G. L. Stephens

Supported by NASA TRMM Research Grant NAG5-7719
and by NASA Research Grant NAS5-99237.

Principal Investigator: Graeme L. Stephens

Department of Atmospheric Science
Colorado State University
Fort Collins, Colorado

August, 2001

Atmospheric Science Paper No. 721

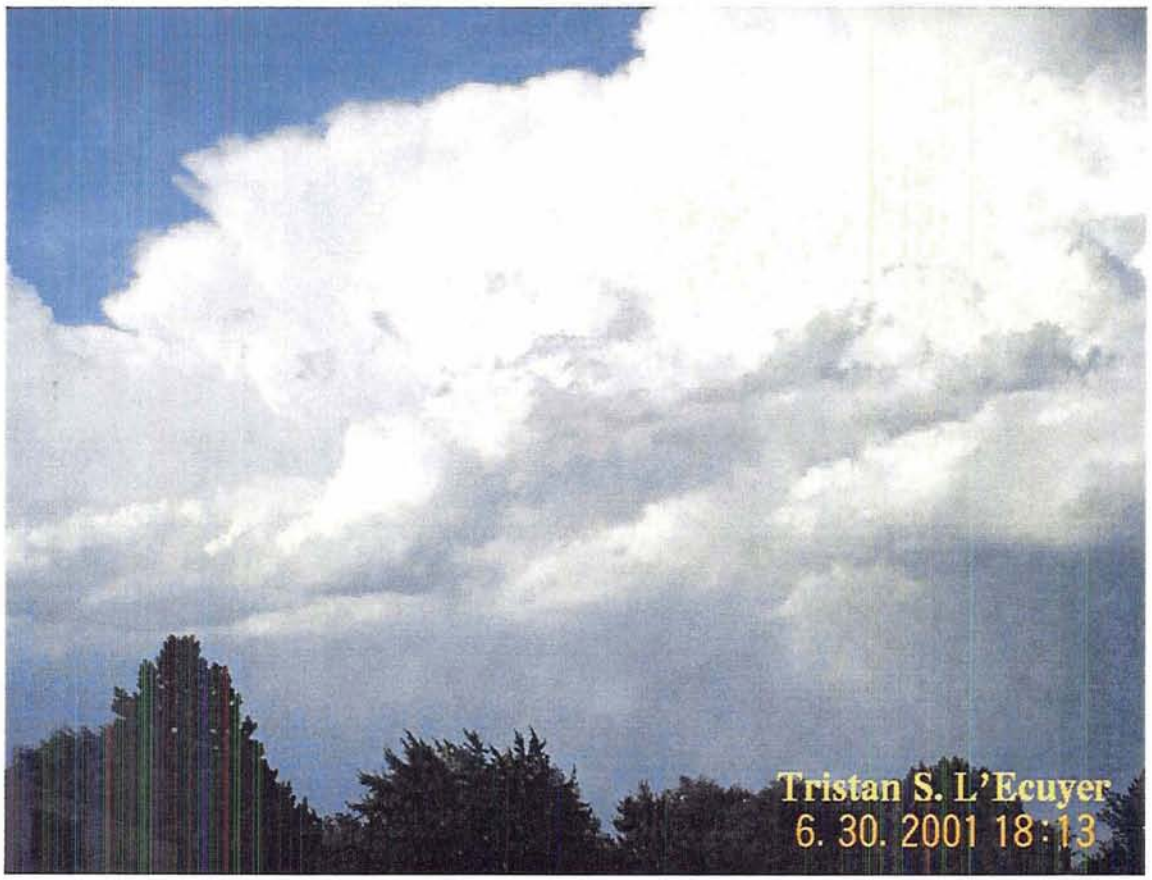

"Truths are first clouds; then rain, then harvest and food.",

—- Henry Ward Beecher ("Life Thoughts," 1858)

ABSTRACT

UNCERTAINTIES IN SPACE-BASED ESTIMATES OF CLOUDS AND PRECIPITATION: IMPLICATIONS FOR DERIVING GLOBAL DIABATIC HEATING

The Earth's weather and climate is driven by the exchange of energy between the sun, atmosphere, surface, and space and energy transport required to establish a global balance. Clouds and precipitation play an integral role in this exchange, enhancing reflection of solar radiation to space, trapping thermal emission from the surface, and providing a mechanism for the direct transfer of energy to the atmosphere through the release of latent heat in precipitation. As a result, there is an intimate coupling between the climate, energy budget, and global hydrologic cycle. The problem of establishing observational evidence for these connections and climate change in general, poses a significant challenge to the observational community. This dissertation seeks to address the components of this problem related to observing the hydrologic cycle and its role in modulating the tropical energy budget, from space-based measurements.

This work reports on a new technique which makes use of cloud and precipitation information from the Tropical Rainfall Measuring Mission to estimate the principal components of the tropical energy budget and to examine the mechanisms by which clouds and precipitation modify it. First, three distinct retrieval algorithms are employed to determine the three-dimensional structure of cloud and precipitation in the tropical atmosphere. The first retrieves cloud and precipitation profiles from passive microwave observations from the TRMM Microwave Imager while the second applies a different technique to the same observations in an effort to derive estimates of non-precipitating liquid cloud. Finally, the third algorithm makes use of infrared radiances from the Visible and Infrared Scanner to infer ice cloud optical properties in non-precipitating regions. The resulting representation of the three-dimensional strucure of cloud and precipitation in the tropical atmosphere is then used as input to a broadband radiative transfer model to derive profiles of short- and longwave fluxes. These flux profiles are composited to present a TRMM-based estimate of the short-term tropical energy budget for oceanic regions over the month of February 1998.

On average, over this period, the tropical atmosphere absorbs 51 Wm^{-2} or 13 % of the 393 Wm^{-2} of solar radiation it receives. A further 112 Wm^{-2} is reflected by atmospheric particles, clouds, and the surface, leaving 230 Wm^{-2} to be absorbed by the ocean. At thermal wavelengths, it is found that the ocean emits 436 Wm^{-2} of energy to the atmosphere while the atmosphere emits a total of 639 Wm^{-2} units, 407 Wm^{-2} downward toward the surface and 231 Wm^{-2} to space. Accounting for latent heat release which amounts to an exchange of 82 Wm^{-2} of energy between the surface and atmosphere, the results imply a deficit of 70 Wm^{-2} of energy in the atmosphere and a surplus of 121 Wm^{-2} at the Earth's surface. The implied net gain of 51 Wm^{-2} in the Earth-atmosphere system is consistent

with a difference between the incoming solar radiation and emitted thermal radiation at the top of the atmosphere. It is speculated that these imbalances are largely accounted for by sensible heating, meridional energy transport, and absorption and transport of energy in the ocean. Finally, on average for the month of February 1998, the tropical atmosphere cools at -1 $Kday^{-1}$ and experiences a net cloud forcing of -10 Wm^{-2} at TOA and -22 Wm^{-2} at the surface.

A concerted effort has been made to rigorously characterize the uncertainties in all aspects of the approach. In the absence of additional tuning or constraints, the procedure described in the present work provides monthly-mean estimates of column radiative heating accurate to $\sim$ 30 % and cloud radiative forcing with accuracies ranging from approximately 40 % for raining pixels to 75 % in non-precipitating clouds. It is shown that the dominant source of uncertainty in both the retrieval and radiative transfer models is a lack of vertical cloud boundary information inherent in the passive measurements. These results highlight the need for future algorithms to look toward making use of synergies between active and passive observations to simultaneously retrieve cloud and precipitation optical properties and their vertical distribution and ensure consistency between a wider variety of information sources. As a first step towards this undertaking, a new method for retrieving profiles of rainfall from spaceborne radars based on an optimal estimation technique is also introduced. The method is readily adapted to include information from a variety of sources and provides a suite of diagnostic tools with which to assess its performance. Preliminary results from synthetic retrievals highlight the utility of the algorithm for estimating profiles of precipitation up to 60 mmh^{-1} at 14 GHz and up to 8 mmh^{-1} at 94 GHz, provided some form of attenuation constraint is implemented.

The technique described herein provides a complete approach for generating tropic-wide (and ultimately global) estimates of the components of the energy budget using explicit cloud and precipitation information from spaceborne observations. The results can, in principle, be applied to study short term climate variability through investigations of perturbations to the radiation balance induced by changes in the distributions of water vapor, cloud, and precipitation on short to moderate timescales affording us the opportunity to quantify important relationships between the hydrologic cycle and the Earth's energy budget.

Tristan S. L'Ecuyer
Department of Atmospheric Science
Colorado State University
Fort Collins, CO 80523
Fall 2001

ACKNOWLEDGEMENTS

Financial support for this research was provided, in part, by NASA TRMM Research Grant NAG5-7719 and by NASA Research Grant NAS5-99237. The Goddard Profiling Algorithm source code and cloud databases were obtained courtesy of Dr. Chris Kummerow and his research group at Colorado State University. TRMM data was acquired through the Goddard DAAC at the Goddard Space Flight Center. Water vapor, SST, and surface wind speed data used in the estimation of covariance matrices and radiative transfer calculations are produced by Remote Sensing Systems and sponsored, in part, by NASA's Earth Science Information Partnerships (ESIP): a federation of information sites for Earth science; and by the NOAA/NASA Pathfinder Program for early EOS products; principal investigator: Frank Wentz. Interpolated OLR data were provided by the NOAA-CIRES Climate Diagnostics Center, Boulder, Colorado, USA, from their Web site at http://www.cdc.noaa.gov and CERES data were obtained from the NASA Langley Research Center Atmospheric Sciences Data Center. Finally, I would like to acknowledge Dr. Chris Kummerow, Dr. Viswanathan Bringi, Dr. Steven Rutledge and the members of the Stephens reasearch group for their insights, advice and critique in editing this dissertation.

Contents

List of Figures

List of Tables

Chapter 1

Introduction

Recent advances in satellite technology have afforded us the opportunity to view the atmosphere in new and exciting ways. The Tropical Rainfall Measuring Mission (TRMM), for example, has broken new ground, providing concurrent observations of radar reflectivity, microwave brightness temperatures, visible and infrared radiances, longwave and shortwave radiative fluxes, and lightening around the globe from approximately 40°S to 40°N. For the first time, we are in a position to simultaneously observe three key elements of the hydrological cycle; water vapor, clouds, and precipitation, and their bulk radiative and electrical properties over a vast area encompassing much of the tropics and sub-tropics. In addition, through the use of physical models, we are able to infer vertical profiles of cloud and rainfall and, from them, derive estimates of radiative and latent heating profiles on a near-global scale. This dissertation provides a framework for estimating profiles of radiative and latent heating using the TRMM observations, thus laying the foundation for long-term analyses of the principal components giving rise to energy balance in the tropics.

1.1 Motivation: The "Big Picture"

The Earth's weather and climate is driven by the exchange of energy between the sun, atmosphere, surface, and space and the transport of this energy between tropical and polar regions required to establish a global balance between that which enters the earth-atmosphere system and that which leaves it. At the most fundamental level, the incoming radiation from the sun must be balanced by a combination of reflection and emission from the Earth-atmosphere system. Small perturbations in any of the factors which govern this balance can

lead to significant responses in the distribution and intensity of weather systems around the globe and can have important implications for life on Earth. The tumultuous history of our planet is filled with numerous examples ranging from the catastrophic climate changes which accompanied the extinction of the dinosaurs millions of years ago to the so-called "Little Ice Age" between approximately 1550 and 1800 which impacted both agriculture and population growth in the northern hemisphere (Grove, 1988). There is little doubt that the climate will continue to evolve, not only through natural variability but also through the influence of human activities on the planet. If we are to adapt to such events in the future, it is critical that we have the ability to both predict and observe small changes in the global climate system. This can be accomplished through accurate global observations of the components which comprise the Earth's energy budget both to establish the equilibrium state and to refine models used to simulate climate change.

1.1.1 The Earth's Energy Budget

At this time, the basic components of the Earth's energy budget shown in Figure 1.1 are understood, but their precise magnitudes and their temporal, spatial and vertical distributions have yet to be quantified globally through observations to the accuracy required for early evidence of climate change. On average, the Earth intercepts $\sim$ 340 Wm^{-2} of solar energy in the form of photons mostly between the wavelengths from 0.4 to 4.0 μm. About thirty percent of this energy is reflected back to space, twenty five percent by clouds and the remaining five percent by the Earth's surface. The remainder is either absorbed by gases, clouds and aerosol particles in the atmosphere ($\sim$ 25 %) or the Earth's surface ($\sim$ 45 %). At the same time the Earth emits $\sim$ 350 Wm^{-2} of radiation at infrared wavelengths between 4.0 and 100.0 μm. Ninety five percent of this radiation is absorbed by the atmosphere and re-emitted both to space (outgoing longwave radiation (OLR)) or back to the surface (the "greenhouse effect"). Consequently, the atmosphere loses an average of $\sim$ 100

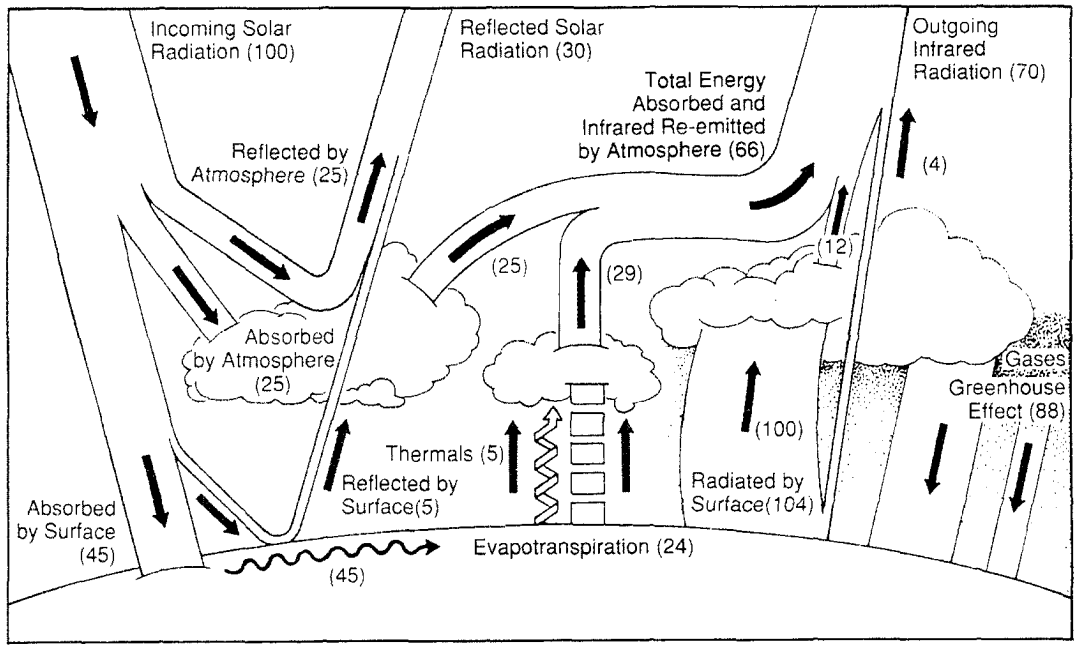

Figure 1.1: Principal components of the Earth's energy budget (adapted from Trenberth, 1992).

Wm^{-2} which is absorbed at the Earth's surface. This imbalance is largely offset by latent heat released in precipitation ($\sim$ 90 Wm^{-2}) (Schneider, 1992).

Clouds and precipitation play an integral role in the exchange of radiation between the Earth's surface, the atmosphere and space. As a result, there is a strong coupling between the energy budget and the global hydrological cycle and changes in the temporal, spatial, and vertical distributions of water vapor, cloud and precipitation, whether from natural climatic fluctuations or anthropogenic impacts, induce corresponding changes in the energy budget. Accurate observations of vertical profiles of clouds and precipitation are crucial in determining the distribution of atmospheric heating. Due to their high spatial and temporal variability, however, no other component influencing the energy budget poses a greater challenge to the observational community.

Ultimately profiles of radiative and latent heating from clouds and precipitation play a

key role in weather patterns on all scales from long-term global circulations to daily regional weather patterns. The importance of diabatic heating within deep cumulus cloud complexes in the tropical energy budget was demonstrated in the pioneering work of Riehl and Malkus (1958). Since then, numerous studies using General Circulation Models (GCMs), cloud models, and observations, have lead to similar conclusions regarding the importance of profiles of radiative and latent heating in driving local and large-scale tropical and extratropical circulations. Diabatic heating establishes a link between regional and planetary scale weather systems and provides a proxy for observing the strength of the coupling between the atmosphere and ocean such as hydrological exchanges through evaporation and precipitation processes or regulation of the sea-surface temperature (SST) by cloud radiative effects.

In the years since Riehl and Malkus (1958), numerous studies have demonstrated the significant role that radiative and latent heating profiles play in the global climate and hydrological cycle. Regional and global circulations have been investigated using GCMs, the impact of diabatic heating initialization in numerical weather prediction models has been studied, and a number of hypotheses regarding the role of latent and radiative heating in regulating the climate have been proposed. Accurate, long-term, global-scale estimates of radiative and latent heating will provide useful evidence to verify the various results. The goal of this dissertation will not be to address each of these areas directly but to develop a method which, once refined, will be well-suited to such studies in the future.

1.1.2 Heating in Cloud Models and GCMs

The importance of diabatic heating in the generation and maintenance of regional and global weather systems cannot be overstated. Early results from Palmén and Riehl (1957), Riehl and Malkus (1961), Yanai (1961), and Miller (1962) suggested that the latent heat released in penetrative cumulus towers provides the dominant source of energy in tropi-

cal cyclones. On a larger scale, Gill (1980) demonstrated the connection between diabatic heating and the tropical circulation using a linearized model of the tropical atmosphere. Slingo and Slingo (1988, 1991) investigated the impact of longwave radiative forcing by tropical clouds on global circulations using the National Center for Atmospheric Research (NCAR) Community Climate Model (CCM1). They found that the magnitude and vertical distribution of this forcing plays an integral role in the location and intensity of tropical precipitation, the tropical upper tropospheric and Walker circulations, and extratropical flow patterns.

The effects of the vertical structure of heating on the Walker Circulation were examined by Hartmann et al. (1984). They demonstrated that an idealized heating profile for mature convective cloud clusters (MC) proposed by Houze (1982) significantly improved the structure of the circulation relative to that produced using a conventional profile (CP). In both simulations the total atmospheric heating was held constant suggesting their findings were solely a result of the fact that the heating rate maximum was higher in the MC profile. Similar results have been documented regarding the sensitivity of the Madden-Julian Oscillation (MJO) to the vertical distribution of heating (Madden and Julian (1972), Lau and Peng (1987), Takahashi (1987), Miyahara (1987), and Chen and Yen (1991)). Lau and Peng (1987), for example, found that the phase speed of the waves that determine the amplitude and duration of the MJO critically depends on the vertical placement of the diabatic heating maximum. The vertical distribution of heating is also expected to play a crucial role in teleconnections between tropical and mid-latitude circulations from which 30-50 day oscillations are observed to manifest themselves in global phenomena such as those observed by Weickmann et al. (1985) and Knutson et al. (1986).

The results from these studies demonstrate the key role that the vertical profile of diabatic heating plays in driving tropical circulations. Accurate estimates of radiative and latent heating will be invaluable in verifying these assertions. Also, provided adequate

continuity can be maintained in the data, longterm trends in the global distribution of radiative and latent heating may be well-suited for monitoring global climate change.

1.1.3 GCM Validation

Given their strong sensitivity to the vertical distribution of heating within the atmospheric column, it is reasonable to conjecture that GCMs may incur large errors due to inexact parameterizations of the elements of this heating. Evidence for this can be found in Cess et al. (1997) who compared intraseasonal variability of longwave (LW) and shortwave (SW) forcing from 18 GCMs with observations from the Earth Radiation Budget Experiment (ERBE). They found that many of the GCMs are unable to reproduce the intraseasonal variations observed in the ERBE data and that the GCMs exhibit significant variability among themselves. This suggests that seasonal variations in high and low cloud amounts are incorrectly represented in some models pointing to inconsistencies in the hydrological cycles and energy budgets for the ensemble of models.

Additional evidence for the possible misrepresentation of physical processes in some GCMs is seen in the results of Soden (2000) who compared predicted variability in a number of atmospheric variables from the 30 Atmospheric Modeling Intercomparison Project (AMIP) GCMs with observations. The time series illustrated in Figure 4 of that paper indicate that, although the GCMs capture interannual variations in precipitable water, 200 mb temperature, and OLR, variability in precipitation and surface LW radiation observations are not evident in the corresponding GCM fields. While these results are not conclusive since the observational data itself may be in error, they highlight the importance of taking a closer look at the parameterizations currently used in climate models.

One way to improve the agreement between different models and to more accurately represent the observations, is to systematically test all possible parameterizations for the major physical processes in the GCMs to determine which ones best represent the obser-

vations. Through such a "physical validation" approach, estimates of radiative and latent heating may help isolate possible weaknesses in the physical parameterizations and even select a subset of the ensemble which perform better than the others. Clearly, such a method will be of no use unless the accuracy of the heating profiles is known.

1.1.4 Data Assimilation in Numerical Weather Prediction Models

The subset of GCMs used in numerical weather prediction (NWP) exhibit equally varied diabatic heating profiles as is apparent in the study of Mizzi and Kasahara (1989), who compared diabatic heating rates in forecasts from the European Centre for Medium-Range Weather Forecasts (ECMWF), the Geophysical Fluid Dynamics Laboratory (GFDL) and Goddard Laboratory for Atmospheres (GLA) during the First GARP Global Experiment (FGGE). As with GCMs in general, heating information can be used to test the physical assumptions in the NWP models to isolate those which perform the best. Alternatively, the information can be assimilated directly into the models through diabatic initialization (DI). The results of Heckley et al. (1990), Puri and Davidson (1992) and Kasahara and Mizzi (1996) demonstrated that forecasts change significantly and model spin-up time is reduced when diabatic heating information is included in this way. Kasahara and Mizzi (1996) showed that DI and subsequent diabatic forcing (DF) using latent heating profiles derived from Special Sensor Microwave/Imager (SSM/I) precipitation estimates are required to simulate the development of hurricane Emily (1987) in their version of the Cooperative Institute for Meteorological Satellite Studies (CIMSS) Regional Assimilation System (CRAS) forecast model.

Given the importance of diabatic heating suggested by these studies, we can conclude that physical validation and diabatic initialization using accurate global diabatic heating rate profiles offers great potential for the improvement of medium to long-range weather forecasts. Once again, however, the value of these profiles can only be realized provided

reasonable estimates of the associated uncertainties can be made.

1.1.5 Climate Regulation Hypotheses

In addition to model results, numerous hypotheses that may have substantial implications for global climate change have been made based on observational data. A good example is the well-known thermostat hypothesis of Ramanathan and Collins (1991) who conjecture that the ocean temperature is regulated by highly reflective cirrus clouds which form in response to increasing SST. Pierrehumbert (1995) strongly opposed this viewpoint arguing that since observations demonstrate that the cloud greenhouse and albedo effects are more or less in balance, water vapor in clear-sky regions is the dominant source of fluctuations the tropical climate. Instead of a cirrus cloud thermostat, he proposes that an increase in the spatial extent of dry "radiator fins" in regions of large-scale subsidence represents a more plausible mechanism for regulating SST.

Based on observations of LW and SW cloud radiative forcing (CRF) from ERBE and the Clouds and the Earth's Radiant Energy System (CERES), Cess et al. (2001) found that the ratio of SW to LW CRF increases substantially during the 1998 El Niño relative to other years. Since tropical tropopause temperatures did not increase substantially in 1998, the authors concluded that the increase was due to lower mean cloud heights resulting from a reduction in the SST gradient across the Tropical Pacific and Indian Oceans during the 1998 El Niño event. The resulting negative net CRF would result in a net loss of energy in the atmosphere-ocean system relative to average conditions and act to return the climate to its mean state.

Lindzen et al. (2001) used cloud data from the Japanese Geostationary Meteorological Satellite-5 (GMS-5) and National Center for Environmental Prediction (NCEP) SST data (Reynolds and Smith, 1994) to conclude that, on average, a 1 K increase in tropical SSTs leads to a 15 % reduction in the areal coverage of cloudy/moist regions. This would in-

crease outgoing longwave radiation (OLR) in regions of high SST cooling the planet as a result. The authors go on to suggest that this negative feedback might resist global warming due to increasing carbon dioxide concentrations in the atmosphere.

These studies are just three examples from a long list of cloud-climate regulation hypotheses, many of which have lead to vigorous debates throughout the climate community (Hartmann and Michelsen (1993), Clement et al. (1996), Lau and Sui (1997), Seager and Murtugudde (1997), and Lagerloef et al. (1998) provide some other examples). The conclusions drawn from each of these studies rely heavily on the use of simple conceptual models focusing primarily on the radiative component of the atmosphere-ocean interaction and employing crude parameterizations of the exchanges in water vapor between at the air-sea interface in the Warm Pool region of the Tropical Pacific Ocean. Large-scale dynamics have largely been parameterized in *ad hoc* ways leading to conflicting results from apparently similar studies (Chou and Neelin (1999), for example, state that the areal coverage of cirrus increases with increasing SST, contradicting the foundation of the argument of Lindzen et al. (2001)). The findings in many of these studies can be partially addressed through the use of direct inferences of radiative and latent heating profiles on the global scale. The use of radiative and latent heating information over larger spatial and temporal scales provides a means for more rigorous testing of the models used and the conclusions drawn as a result.

1.2 The "State-of-the-Art"

There is little doubt that satellite platforms represent the best opportunity to obtain global observations of most atmospheric parameters particularly those relating to latent and radiative heating, namely precipitation and clouds. Figure 1.2, for example, presents a summary of all rainfall monitoring stations which participated in producing the Global Precipitation Climatology Centre (GPCC) total monthly precipitation product for February, 1998.

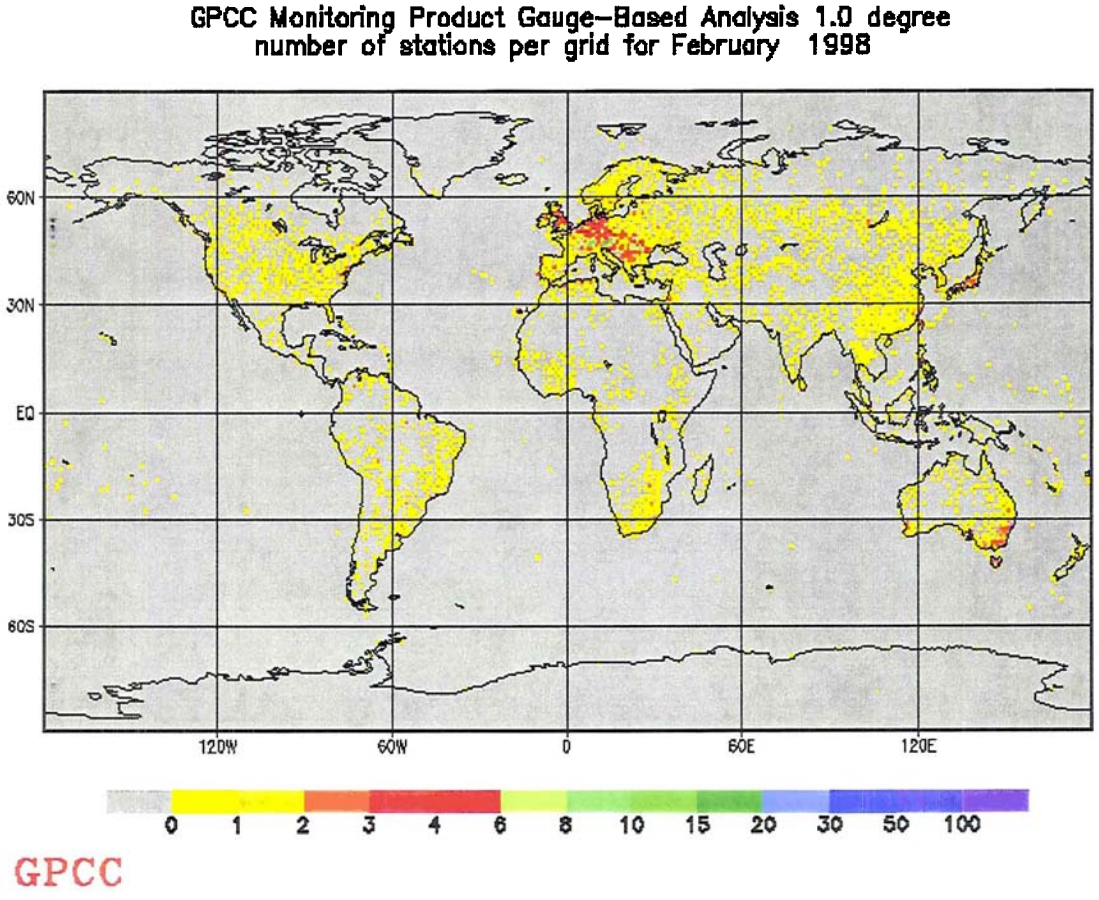

Figure 1.2: Global distribution of rainfall monitoring stations supplying data for the Global Precipitation Climatology Centre's gridded monthly total precipitation product (courtesy of The Global Precipitation Climatology Centre. HTTP://www.dwd.de/research/gpcc).

The observations are clearly biased toward densely populated, technologically advanced, land areas. Observations are sparse over oceanic, dessert, jungle, and mountainous regions since they are much less accessible to researchers than the more developed regions such as Europe and the United States.

Satellites, on the other hand, provide uniform measurements around the globe and have been developed for a wide range of observations over the past four decades. The world's first weather satellite, TIROS-1, was launched in 1960 providing the atmospheric science community with the first ever images of synoptic-scale cloud patterns from space (Rao

et al., 1990). In the years which followed, a continuously evolving series of Polar Orbiting Environmental Satellites (POES) originally operated by the Environmental Science Services Administration (ESSA) and currently by the National Oceanic and Atmospheric Administration (NOAA) were put into orbit and have been providing global images of cloud, atmospheric dust, land/ocean/sea ice boundaries, and water vapor for nearly four decades.

In 1966, the National Aeronautics and Space Administration (NASA) launched the first in a series of geostationary satellites, whose orbits are chosen such that the angular velocity of the satellite exactly matches that of the Earth's rotation to provide repetitive observations of the atmosphere over the same location at high temporal resolution in order to track synoptic and mesoscale weather systems. The Geostationary Operational Environmental Satellites (GOES), derivatives of these early geostationary satellites, have been in operation since 1974. Today, the combination of NOAA's GOES-E and GOES-W, the Japanese GMS, Russian Geosynchronous Meteorological Satellite (GOMS) and European Meteosat provides global imaging with a temporal resolution of better than three hours.

The undeniable success of these early missions has not only lead to their continuation and refinement but also fueled development of many new and unique satellite missions. Today, many instruments that have traditionally been operated in ground-based applications are being modified for use on satellites including a variety of radiometers operating in all regions of the electromagnetic spectrum, lidars in the ultraviolet (UV), lightening sensors in the visible (VIS), and radars in the microwave. Selected examples of this diverse array of satellite-based atmospheric measurements are summarized in Table 1.1 along with their primary scientific functions.

While other factors such as temperature, atmospheric gases, and aerosol impact the ERB, clouds, precipitation and water vapor comprise its most significant and highly variable components. Of those satellites which are currently in operation, TRMM represents

Table 1.1: Examples of the diverse array of current and future satellite-based observations of the atmosphere and their applications. Instruments are grouped according to whether they are passive (upper group) or active (lower group) and ordered by increasing wavelength. See Appendix G for a complete explanation of all acronyms.

Satellite	Instrument	Type of Measurement	Primary Scientific Function
EOS CHEM	OMI	740 VIS/UV Bands 0.27-0.5 μm	Global Ozone
Terra	MISR	Multi-angle VIS/NIR 0.4-0.87 μm	SFC, Aerosol, Vegetation,
ADEOS	POLDER[1]	WFOV VIS/NIR 0.4-0.9 μm	Aerosols, Clouds, Vegetation and Cloud Reflection Functions
Meteor 3M-1	SAGE III[2]	VIS/NIR Limb Measurements	Stratospheric and Upper Tropospheric Aerosol, O_3, H_2O, NO_2, NO_3
ACRIMSAT	ACRIM III	Active Cavity Radiometer	Total Solar Irradiance (TSI)
GOES	Imager	VIS/IR 0.55-12.5 μm	Cloud, Pollution, Dust, Moisture
GOES	Sounder	VIS/IR 0.7-14.7 μm	Temperature, Moisture, O_3, Cloud
POES	AVHRR	VIS/IR 0.58-12.5 μm	Cloud and SFC Properties
TRMM	VIRS	VIS/IR 0.6-12 μm	Clouds and Aerosol
Terra	MODIS[3]	36 VIS/IR Bands 0.4-14 μm	Clouds, Radiative Fluxes, Aerosol, SFC Properties, Temperature, H_2O
Aqua	AIRS	2300 VIS/IR Bands 0.4-15.4 μm	Temperature, H_2O, Clouds
TRMM	CERES[4]	Broadband Flux Measurements	Earth's Radiation Budget
TRMM	TMI	Microwave 10.6-85.5 GHz	H_2O, SST, SFC Winds, Precipitation
Aqua	AMSR-E	Microwave 6.9-89 GHz	Clouds, Precipitation, SFC Moisture, SFC Winds, Sea Ice, Snow Cover
POES	AMSU	Microwave 23.8-183.3 GHz	Atmospheric Temperature and H_2O
EOS CHEM	MLS	Microwave Limb Measurements	Temperature and Atmospheric Gases
Aqua	HSB	VHF Sounder 150-183 MHz	Atmospheric H_2O
ESSP 3-CENA	Lidar	Backscatter 0.532 & 1.064 μm	Aerosol and Cloud Boundaries
ICESat	GLAS	Backscatter 0.532 & 1.064 μm	Ice Topography, Clouds, Aerosol
TRMM	LIS	Lightening Detector	Lightening Location, Rate and Energy
QuikScat	SeaWinds[2]	SFC Backscatter at 13.4 GHz	SFC Winds
TRMM	PR	Reflectivities at 14 GHz	Precipitation
CloudSat	CPR	Reflectivities at 94 GHz	Cloud, Aerosol and Precipitation

the state-of-the art in rainfall and latent heating observations from space while providing limited yet useful cloud information.

There have been numerous studies of the radiative components of the Earth's energy budget from satellites. An annual mean estimate of the Earth's radiation budget (ERB) and its variability deduced from satellite data was made by Stephens et al. (1981) who pointed out the importance of interannual and regional variability. The importance of regional

[1] Also to be flown aboard ADEOS-II.

[2] Also to be placed on the International Space Station.

[3] Also aboard Aqua.

[4] Also aboard Terra and Aqua.

variations in cloudiness on the ERB and their feedback on the general circulation was also investigated in Hartmann and Short (1980). Results of these and a later study by Liebmann and Hartmann (1982) demonstrated a strong correlation between features in the seasonal maps of outgoing radiation and convective cloud patterns. Arking (1991) presents an overview of highlighting key findings from numerous ERB studies prior to 1990. Since then, Randel and Vonder Haar (1990), and Sohn and Smith (1992a,b,c) have explored the interannual variability of the top of the atmosphere radiation budget using Nimbus-7 data while Hartmann et al. (1992), Gupta et al. (1993), Ringer and Shine (1997), and Moore and Vonder Haar (2001) have combined data from the International Satellite Cloud Climatology Project (ISCCP) and ERBE to derive relationships between cloud types and their impact on the ERB.

Until recently, a lack of accurate global cloud, ice, and rainfall data has limited simultaneous observations of radiative and latent heating profiles to analyses from regional experiments such as the Tropical Ocean Global Atmosphere (TOGA) Coupled Ocean Atmosphere Response Experiment (COARE) (eg. Frank et al. (1996), Chou et al. (1998), Mather et al. (1998), and Johnson and Ciesielski (2000)). For this reason, quantitative estimates of latent heating profiles and their spatial and temporal variations throughout tropics, were among the principle scientific goals of the Tropical Rainfall Measuring Mission (TRMM) (Simpson et al. (1988, 1996)). Among the most complete methodologies proposed for computing latent heating from satellite observations are those of Yang and Smith (1999a, 2000) who adapt aspects of Yanai et al. (1973) to derive latent heating profiles using SSM/I measurements and high-resolution upper-air soundings. Yang and Smith (1999b) use a similar procedure to derive global-scale monthly mean latent heating estimates of from SSM/I measurements. Olson et al. (1999) proposed an alternative technique in which latent heating is retrieved quasi-directly from passive microwave measurements through the use of a Bayesian Monte Carlo integration technique and a database of cloud

profiles and associated latent heating derived from cloud resolving model simulations. A recent paper by Tao et al. (2001) overviews and compares both techniques and introduces a third technique based on surface rainfall rate and climatological mean profiles of latent heating for convective and stratiform rainfall.

The majority of atmospheric heating studies in the past have suffered from at least one of the following limitations:

- Budget studies only provide data on regional scales.
- A lack of simultaneous estimates of radiative and latent heating from a single platform.
- Difficulty in assessing the relative contributions of individual cloud types and precipitation to total atmospheric heating.
- The inability to provide information regarding both surface and top of the atmosphere energy budgets.
- A lack of rigorous uncertainty estimates.

By virtue of their diverse applications, the instrument complement on the TRMM satellite represents the most complete source of diabatic heating information in light of these three points. While the TRMM observations are restricted to the tropics and sub-tropics, they provide an opportunity to develop methods for deriving profiles of diabatic heating which can be readily applied to global data sets, such as that which is anticipated from the Global Precipitation Mission (GPM), when they become available.

1.3 Scientific Objectives

In the present work, the TRMM data will be used to examine some aspects governing our present capabilities for making quantitative observations of the ERB and its response

to changing environmental conditions. This research will concentrate on the cloud and precipitation components of Figure 1.1, seeking to develop a method for simultaneously estimating profiles of radiative and latent heating in the atmosphere using observations from the TRMM satellite. A preliminary comparison of the relative magnitudes of tropical radiative and latent heating will then be made through an estimate of the short-term tropical energy budget. In addition, we strive to determine error bounds which reflect our ability to measure profiles of diabatic heating globally and to suggest a direction to adopt for future satellite missions to meet our observational goals. To this end, an uncertainty analysis framework which can be applied as a whole or in part by future investigators to develop new, improved observing platforms and retrieval algorithms will be presented.

The focus here will be primarily directed at determining the diabatic heating information that can be gleaned from space-based measurements of microwave emission from the earth and atmosphere but some consideration will be given to supplemental information provided by satellite-based radar and visible and infrared observations. This approach is adopted for a variety of reasons. First, spaceborne platforms offer the best opportunity to make observations on the global scale which are required to make inferences regarding the radiation budget, hydrologic cycle, and climate system as a whole. From the list of current space-based observations (Table 1.1), the subset of microwave measurements (both active and passive) represent the most complete source of rainfall profile information presently available. Techniques for retrieving rainfall and cloud profiles based on passive microwave observations have been operational since the 1970's and, as a result, have been studied and refined in greater depth than spaceborne radar techniques which were first implemented operationally after the comparatively recent launch of the TRMM Precipitation Radar (PR). In addition, the swath of the TRMM Microwave Imager (TMI) is substantially broader than that of the PR providing a greater volume of data with greater spatial coverage resulting in better sampling of cloud, rainfall and resulting radiative and latent heating components of

the ERB.

The problem of developing a method for simultaneous global estimates of radiative and latent heating and the task of assessing the most complete sources of such information en route to determining an optimal satellite instrument complement for this purpose is large in scope and can not be exhaustively investigated by a single researcher in a single piece of work. Rather by touching on a number of areas of relevance, I hope to provide starting points for further study and open avenues for future work while furnishing the atmospheric science community with useful baseline estimates of radiative and latent heating in the tropics and the uncertainties associated with each. Preliminary results from a number of somewhat diverse aspects of the problem are presented in the hopes of detailing a complete course of action for resolving the problem as a whole, leaving much needed refinements as an exercise for the future. It is with these goals in mind that I present the remainder of this work.

1.4 Dissertation Blueprint

Prior to presenting the body of a work it is customary for the author(s) to provide a road-map outlining the structure of the remaining sections. Before offering a description of what is to follow, it is appropriate to diagram the master plan from the eyes of my supervisor. An outline developed in an early research meeting is presented in Figure 1.3. They say a picture says a thousand words and Figure 1.3 only serves to advance this notion but allow me to do my best to briefly summarize the details for those who are less accustomed to deciphering Dr. Stephens' insightful yet perhaps somewhat haphazard graffiti.

A semi-quantitative assessment of the information contained in the TMI measurements as a whole will be presented in Chapter 2 in an effort to establish a basic understanding of the physics which give rise to microwave radiances at the top of the atmosphere. Then, in Chapter 3, it will be demonstrated how this information and a degree of non-uniqueness

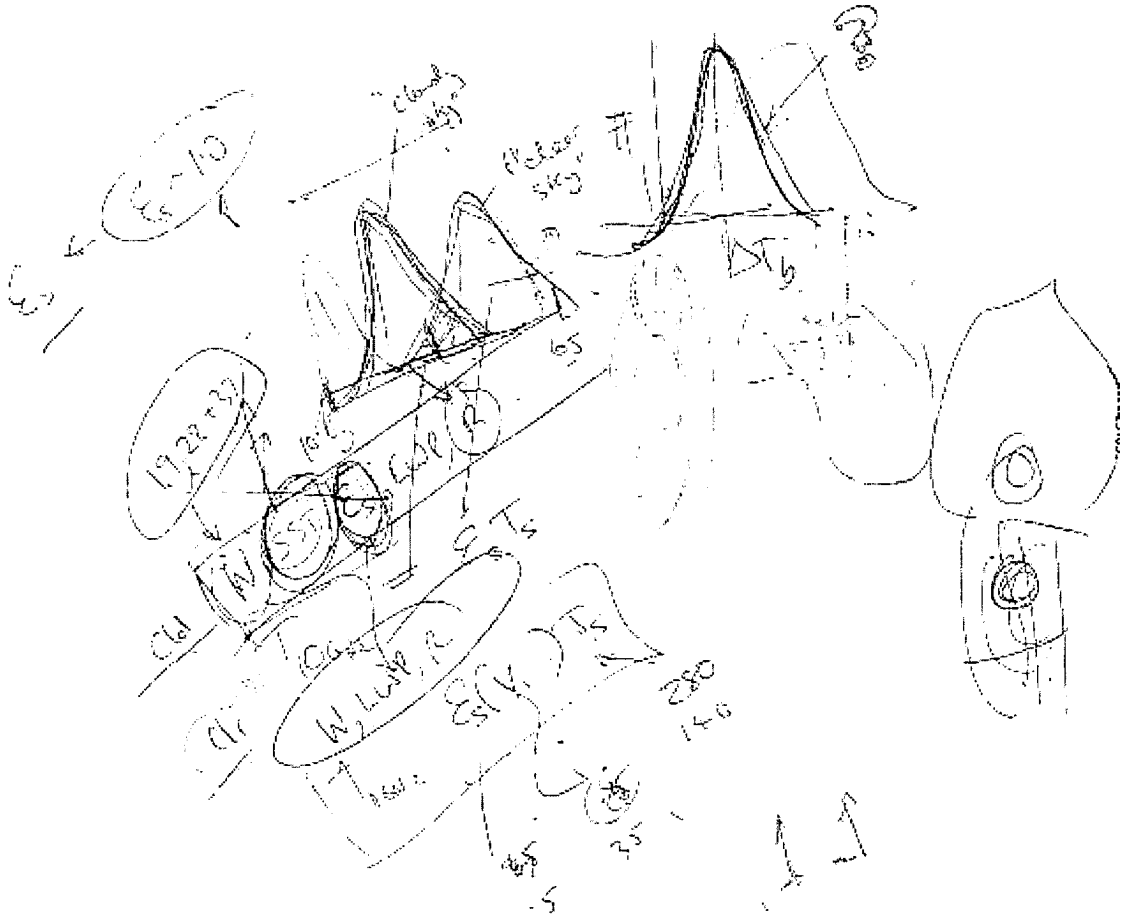

Figure 1.3: Schematic outline of the dissertation (from a personal communication with Dr. Graeme Stephens, early 1998).

inherent in all passive microwave-based rainfall retrievals lead to uncertainties in the TMI-based GPROF cloud and precipitation retrieval algorithm. A sophisticated new approach to determining the uncertainties in Bayesian Monte Carlo retrieval algorithms is introduced and applied to GPROF. For the first time, rigorous estimates of the uncertainties in all hydrometeor classes at each model level are determined, providing information desperately needed in data assimilation and model validation exercises (Hou et al. (2000a,b) and Marécal and Mahfouf (2000)). This information is also critical for evaluating uncertainties in estimates of radiative and latent heating in Chapter 5.

Since the GPROF algorithm only provides meaningful results in rainfall, supplemental cloud information from a VIRS-based retrieval of ice cloud optical properties and a TMI-based retrieval of liquid water path in low-level clouds is introduced in Chapter 4. While neither method is particularly accurate, each provides critical information needed in the radiative heating calculations which follow. The combination of these three retrievals represents the first attempt to quantify the complete three-dimensional structure of clouds and precipitation over the tropical region from TRMM. The results not only provide information necessary to derive flux and heating rate profiles in the present study but also furnish the community with the first crude breakdown of the spatial and temporal distributions of liquid cloud, thick and thin ice clouds, and precipitation over the complete region sampled by TRMM.

Results from Chapters 2-4 are then combined and used as input to a broadband radiative transfer model to derive profiles of radiative heating in the tropics for one month of TRMM data in Chapter 5. Concurrent estimates of latent heating profiles estimated using the GPROF algorithm are also presented and the results used to derive a short-term energy budget for the tropics as a whole. Uncertainty estimates are assigned to both forms of heating based on the accuracies of the component cloud and precipitation fields. In combination with the retrieval methodology outlined in the preceding chapter, the methods presented in Chapter 5 form a multi-sensor "algorithm" for determining atmospheric diabatic heating from the TRMM observations. With additional processing of data from the complete TRMM period, this novel approach provide benchmark tropical ERB estimates and associated uncertainties by which future refinements and improvements to the model can be judged. Although uncertainties estimated in Chapter 5 are understandably large considering the difficulties incurred in deriving cloud and precipitation profile information from passive sensors, the radiative flux estimates which emerge provide one of the most complete sets of such data available to date including TOA and SFC fluxes and cloud

forcing, column heating rates, and a breakdown of each into components owing to cloudy, precipitating, and clear skies.

Finally, the uncertainty estimates highlight key areas of deficiency in the method and an effort is made to suggest means for improving these estimates in the future. Appendix D investigates one possible improvement: the idea of utilizing the complementary information provided by spaceborne radars to improve both cloud and precipitation profile information required to make useful estimates of diabatic heating. A powerful new technique for estimating profiles of precipitation from spaceborne radars is presented and used to examine their capacity to profile rainfall through the use of synthetic retrievals from a large database of tropical cloud profiles. Here we take the somewhat novel point of view that such measurements provide complementary rather than alternative information to those from passive instruments.

Chapter 6 highlights relevant findings from this study and provides a detailed list of studies that are expected to evolve from this research in the near future. In many ways the conclusions drawn from this work should be viewed as a beginning rather than a termination as we now enter an age where the solutions to many problems which have plagued the climate community as a whole, are slowly materializing through the advent of new advances in satellite technology. As is the nature of science, with every solution, a multitude of new doors are opened offering numerous opportunities for future exploration.

Chapter 2

Information Content of the TMI

To address the issue of retrieval accuracy and its impact in climate study, it is important to understand the underlying principles of the remote sensing problem. In many regards, atmospheric remote sensing is analogous to the problem faced by a detective trying to solve a crime. The detective is presented with a crime scene containing various clues which provide varying degrees information concerning the perpetrator of the crime. His job is to compile as much relevent information as possible from the evidence to formulate a short list of suspects from which the perpetrator must ultimately be determined. Two factors are required to successfully solve the crime: the evidence must be related in some way to the perpetrator and enough evidence must be available to narrow the list of suspects to a single person by ruling out all other possibilities.

The same principles apply to the problem of retrieving cloud and precipitation profiles from passive microwave radiances. In this case, the atmosphere may be regarded as the "crime scene", observed radiances provide the "evidence", and the cloud and precipitation profiles are the "perpetrators". Once again, two factors are required to obtain reasonable results from the retrieval: the observations must reflect the hydrometeor profiles being inferred and a sufficient number of measurements must be available to constrain the problem. Our first objective will be to characterize the cloud and rainfall information available from passive microwave radiance measurements. In particular we will focus on the TMI since data derived from its measurements will be employed in subsequent chapters.

Many algorithms have been developed and are currently being employed which use passive microwave measurements from the TMI to estimate rainfall and retrieve vertical

profiles of liquid and frozen hydrometeors. The Goddard Profiling Algorithm (GPROF) (Kummerow et al., 1996), for example, uses products derived from the TMI observations to retrieve the TRMM instantaneous surface rainrate, windspeed and cloud hydrometeor profile product (2a12). All passive microwave algorithms, including GPROF, rely on the sensitivity of observed radiances to changes in the atmospheric properties they seek to retrieve. Furthermore, instruments are designed with a number of different channels spanning the range of frequencies between 5 and 100 GHz or higher, such that the optical thickness of the atmosphere is different for each channel. Passive microwave algorithms make use of the fact that the height from which any measurement originates increases with increasing atmospheric optical depth to estimate vertical structure in the atmosphere. It is, therefore, of utmost importance to determine the range of observable scenes to which the TMI measurements are sensitive and to determine the degree to which the altitude sensed by each channel is independent of the others. Retrievals over scenes to which the TMI measurements are largely insensitive or excessively redundant have poor accuracy and are of limited value in other applications.

The method adopted here is to quantify the information in the TMI measurements through a principal component analysis (PCA) described in Twomey (1977) and a later study by Engelen and Stephens (2000). Details of the theory are described in Section 2.1. A brief description of the TMI instrument and products derived from its measurements is provided in Section 2.2. In Section 2.3 a simplified model of a precipitating cloud is constructed. An estimate of the minimum rainrate detectable by each TMI channel individually is made in Section 2.4 prior to discussing the results of the application of the PCA method which are presented in Section 2.5. Finally a short discussion of non-uniqueness issues is presented in Section 2.6 and relevant conclusions are highlighted in Section 2.7. This exercise not only introduces the Twomey method to the problem of passive microwave rainfall retrievals, but also provides a forum to overview the principles behind passive microwave

techniques which are well-known to the passive microwave remote sensing community but may be less intuitive to the casual reader. Excerpts from this chapter have been submitted to *The Journal of Applied Meteorology* in a paper entitled "A Characterization of the Information Content of the TMI for Rainfall and Cloud Profile Retrievals".

2.1 Theory

In general the interaction of electromagnetic radiation with the Earth's atmosphere can be posed in the following way: the outgoing radiation at the top of the atmosphere, I, depends on the properties of the atmosphere, represented by the state vector, $\mathbf{x}$, through some physical model, F

$$I = F(\mathbf{x}) \tag{2.1}$$

Without specifying the details of F Equation (2.1) can be expanded in a Taylor series

$$I = F(\mathbf{x}_a) + \left.\frac{\partial F}{\partial \mathbf{x}}\right|_{\mathbf{x}=\mathbf{x}_a} (\mathbf{x} - \mathbf{x}_a) + O(\mathbf{x} - \mathbf{x}_a)^2 \tag{2.2}$$

Second and higher order terms can be neglected provided the reference state, $\mathbf{x}_a$, is close to the true state of the atmosphere, $\mathbf{x}$. Here 'close' requires that the model be approximately linear in the region between $\mathbf{x}$ and $\mathbf{x}_a$. Following Twomey (1977), Equation (2.2) can be rewritten as

$$I = \int_a^b K(\mathbf{x}) f(\mathbf{x}) d\mathbf{x} \tag{2.3}$$

defining the kernel or weighting function, $K = \frac{\partial \mathrm{F}}{\partial \mathbf{x}}$, which represents the sensitivity of the radiance measurement to the atmospheric state, $\mathbf{x}$. $f(\mathbf{x})$ represents the distibution of atmospheric parameters being sought. Cast in this form, it is clear that any two measurements, I_i and I_j, will be identical if their weighting functions, K_i and K_j, are equal. Furthermore, any measurement for which the weighting function can be expressed as a linear combina-

tion of the weighting functions of the other measurements in an observing system, i.e.

$$K_l(\mathbf{x}) = \sum_{j \neq l} a_j K_j(\mathbf{x}) \tag{2.4}$$

provides only redundant information. In reality this relation is seldom exactly satisfied but, since all measurements have some uncertainty, the measurement I_l can be "lost in the noise" of the other measurements when the difference

$$\delta_j = I_l - \sum_{j \neq l} a_j I_j \tag{2.5}$$

is less than the accuracy to which the observations can be made.

Assuming at least one measurement in the system can be written as a linear combination of the others, it is possible to determine an expression for the a_j in Equation (2.4). To avoid the trivial solution in which all $a_j = 0$ we further impose the constraint $\sum_i a_i^2 = 1$ and minimize the square norm $\int \left[\sum_i a_i K_i(\mathbf{x})\right]^2 dx$ subject to this constraint. Using the method of Lagrange multipliers a minimum must satisfy

$$\frac{\partial}{\partial a_i}\left(\mathbf{a}^{\mathrm{T}}\mathbf{C}\mathbf{a} - \lambda \mathbf{a}^{\mathrm{T}}\mathbf{a}\right) = 0 \tag{2.6}$$

where $\mathbf{a}$ is a vector consisting of the weights a_i, the matrix $\mathbf{C} = \mathbf{K}(\mathbf{x})^{\mathrm{T}}\mathbf{K}(\mathbf{x})$ is the covariance matrix of the weighting functions and λ is a Lagrange multiplier also to be determined. Rearranging terms and differentiating yeilds the eigenvalue problem

$$\mathbf{C}\mathbf{a} = \lambda \mathbf{a} \tag{2.7}$$

Vanishing eigenvalues represent weighting functions which can completely be expressed as a linear combination of the others.

Most useful is the case where one weighting function can be expressed in terms of the

others to within some small error $\delta(\mathbf{x})$ given by

$$\begin{aligned} \delta(\mathbf{x}) &= K_l(\mathbf{x}) - \sum_{j \neq l} \left(\frac{-a_j}{a_l} \right) K_j(\mathbf{x}) \\ &= a_l^{-1} \sum_{j=1}^{N} a_j K_j(\mathbf{x}) \end{aligned} \tag{2.8}$$

Returning to Equation (2.3) and assuming a measurement uncertainty of ϵ_l we have

$$\begin{aligned} I_l + \epsilon_l &= \int K_l(\mathbf{x}) f(\mathbf{x}) d\mathbf{x} \\ &= \int \left(\delta(\mathbf{x}) - \sum_{j \neq l} \frac{a_j}{a_l} K_j(\mathbf{x}) \right) f(\mathbf{x}) d\mathbf{x} \end{aligned} \tag{2.9}$$

So,

$$\begin{aligned} I_l &= -\sum_{j \neq l} \frac{a_j}{a_l} \int K_j(\mathbf{x}) f(\mathbf{x}) d\mathbf{x} + \int \delta(\mathbf{x}) f(\mathbf{x}) d\mathbf{x} - \epsilon_l \\ &= -\sum_{j \neq l} \frac{a_j}{a_l} I_j + \int \delta(\mathbf{x}) f(\mathbf{x}) d\mathbf{x} + \sum_{j \neq l} \frac{a_j}{a_l} \epsilon_j \end{aligned} \tag{2.10}$$

Any measurement, I_l, can be written in this form. The first term represents the portion of the l^{th} measurement that can be reconstructed from the other observations, the second is the portion of I_l which constitutes new information not present in the other measurements, and the third accounts for the combined error resulting from uncertainties in the measuring system as a whole including errors in the kernels themselves. New information is obtained from I_l only if the second term is larger than the third term, i.e. if the new information brought into the system by the l^{th} measurement exceeds the collective noise in the other observations. Making use of the mean value theorem the magnitude of the second term in

Eqn. (2.10) can be approximated as

$$\left|\int \delta(\mathbf{x}) f(\mathbf{x}) d\mathbf{x}\right|^2 = f_m^2 \left|\int \delta(\mathbf{x}) d\mathbf{x}\right| \leq f_m^2 \int [\delta(\mathbf{x})]^2 \, d\mathbf{x} \tag{2.11}$$

where f_m represents the mean value of $f(\mathbf{x})$ over the interval of integration. Combining Eqns. (2.7) and (2.8) we obtain

$$|\delta(\mathbf{x})| = |a_l^{-1}| \left|\sum_{j=1}^{N} a_j K_j(\mathbf{x})\right| = |a_l^{-1}| \lambda^{\frac{1}{2}} \tag{2.12}$$

Substituting this result into the preceeding equation and noting that, for most practical applications, a_l is on the order of unity yields

$$\left|\int \delta(\mathbf{x}) f(\mathbf{x}) d\mathbf{x}\right|^2 \leq f_m^2 \lambda \tag{2.13}$$

for the new information contained in the l^{th} measurement.

In estimating the magnitude of the error term, note that $\left|\sum a_j \epsilon_j\right|^2$ is the length of the projection of the random error vector ϵ onto the unit vector $\mathbf{a}$. Provided these vectors are uncorrelated, the resultant projection has length equal to the mean square error in the measurements, $|\epsilon|^2$. A new radiance measurement, I_l, therefore, will contribute distinct new information to the existing set of measurements provided

$$f_m^2 \lambda > |\epsilon|^2 \tag{2.14}$$

By virtue of the inherent ambiguities in the quantities in this equation, we conclude that a measurement brings new information into a system provided eigenvalues are *much greater* in magnitude than the average squared relative error in the measurements.

In addition to determining the number of independent pieces of information in the measurement set, it is also possible to determine which atmospheric levels dominate the TMI

signal as a whole. Making use of the fact that the weighting functions measure the sensitivity of a given measurement to the various parameters in the atmospheric state vector we define the following orthonormal set of functions as linear combinations of the original weighting functions

$$\phi_i(\mathbf{x}) = \lambda_i^{-\frac{1}{2}} \left(\sum_j b_{i_j} K_j(\mathbf{x}) \right) \tag{2.15}$$

where the $\mathbf{b}_i$ are the eigenvectors of the covariance matrix $\mathbf{C}$. Any atmospheric parameter retrieved via inversion of Equation (2.3) must result from a linear combination of these orthonormal functions. Peaks in the numerically significant ϕ_i directly correspond to altitudes of the primary atmospheric components influencing the set of measurements. Thus we can immediately determine which levels in the atmosphere are sampled by the data and which are not.

2.2 The TMI Instrument

The TMI has been operational aboard the TRMM satellite for more than three and a half years. For a detailed description of the characteristics of the TMI instrument, the reader is directed to Kummerow et al. (1998) but a brief overview of its salient features will be given here for completeness. Similar to the SSM/I which has been flying on Defense Meteorological Satellite Program (DMSP) satellites for more than a decade, the TMI possesses dual-polarization channels at 19.35, 37.0, and 85.5 GHz as well as a vertically polarized channel in the low frequency water vapor absorption band. As opposed to the SSM/I, however, the water vapor absorption channel has been set slightly off the peak of the center of this band at 21.3 as opposed to 22.3 GHz to accomodate extremely moist regions in the tropical atmosphere. Also, the TMI features a dual-polarized, low frequency channel at 10.65 GHz to provide better estimates of liquid water path in heavy rainfall. Finally, due to TRMM's lower orbit relative to the DMSP satellites, the TMI channels exhibit superior spatial resolution to those of the SSM/I.

The TMI antenna scans at 49° off nadir making one complete (i.e. 360°) rotation every 1.9 seconds. By virtue of this geometry, the TMI views the surface with an incident angle of 52.8° resulting in elliptical footprints (see Fig. 1 of Kummerow et al. (1998)). The cross-track effective field of view (EFOV) is 9.1 km for all channels except 85.5 GHz where it is a factor of two smaller. In the along-track direction, the EFOV ranges from 63 km at 10.6 GHz to 7.2 km at 85.5 GHz. TMI data is is taken in the $\pm 65°$ region about the ground track direction resulting in a swath width of 758.5 km. The remainder of the scan is used for onboard calibration which is conducted in every scan to provide instantaneous calibration for all TMI data in an effort to avoid potential biases due to antenna gain fluctuations.

At these frequencies the TMI channels are sensitive to absorption by atmospheric gases and absorption and scattering due to cloud and precipitation hydrometeors. Atmospheric absorption at microwave frequencies is dominated by molecular oxygen, O_2, and water vapor, H_2O as illustrated in Figure 2.1. The TMI is sensitive to the H_2O absorption band at 22.235 GHz and to the complex series of O_2 absorption lines around 60 GHz.

Absorption, scattering and extinction coefficients for monodispersed distributions of liquid and ice spheres are presented in Figures 2.2 and 2.3. Liquid water contents were all fixed at 1 gm^{-1} and radii of 50, 250, 500, and 1000 μm are shown to illustrate the differences between typical cloud and precipitation particles, represented by the two extremes, respectively, as well as some intermediate particles. At all frequencies, extinction by liquid hydrometeors is primarily due to absorption. Scattering by liquid hydrometeors becomes important only for large particles at high frequency. For frozen particles the opposite is true. Scattering dominates at all frequencies except 10 GHz. Total extinction due to ice particles is negligible at 10, 19, and 21 GHz compared to liquid droplets. Significant scattering by ice particles greater than 500 μm, on the other hand, results in total extinction comparable in magnitude to that of liquid droplets at 37 and 85 GHz. These results merely reflect the dependence of scattering and absorption efficiency on size parameter, $\chi = \frac{2\pi r}{\lambda}$

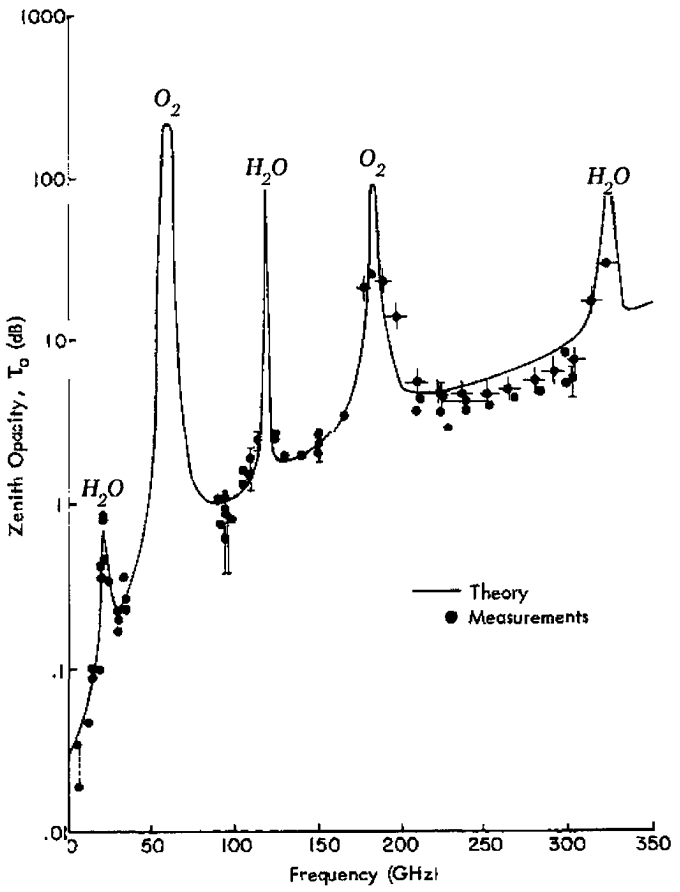

Figure 2.1: Microwave absorption of water vapor and Oxygen (adapted from Ulaby et al. (1981)).

in the Rayliegh regime

$$Q_{abs} \propto \chi \tag{2.16a}$$

$$Q_{sca} \propto \chi^4 \tag{2.16b}$$

In addition, they illustrate the physical processes essential to any passive microwave precipitation retrieval algorithm, namely the combination of strong ice scattering signals in high

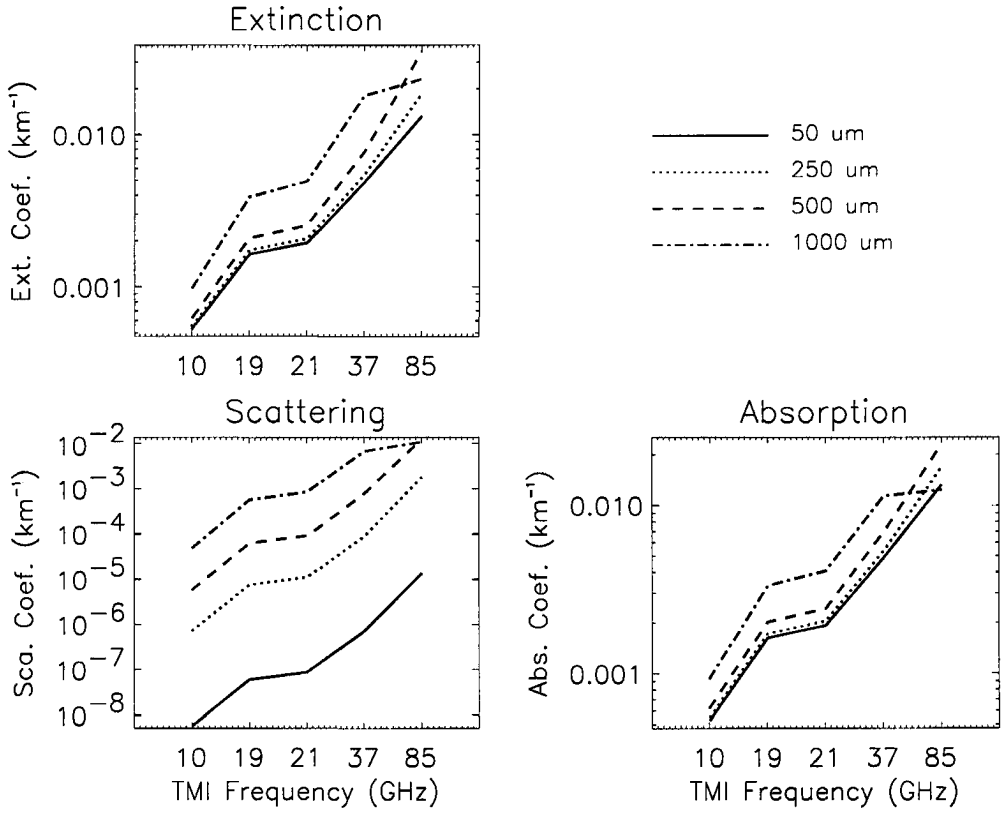

Figure 2.2: Extinction, scattering and absorption coefficients for liquid spheres at each TMI channel.

frequency channels and strong liquid water emission signals in low frequency channels.

2.3 "Cloud" Model

The primary objective of this chapter is to establish how much information the TMI radiances, or, equivalent blackbody brightness temperatures, T_B, yield in rainfall and cloud profile estimation as a function of near-surface rainrate. Furthermore, we wish to determine how this information is distributed in the atmosphere. To this end a simple cloud model is adopted in which the rainrate at the surface is used to prescribe ice and liquid water con-

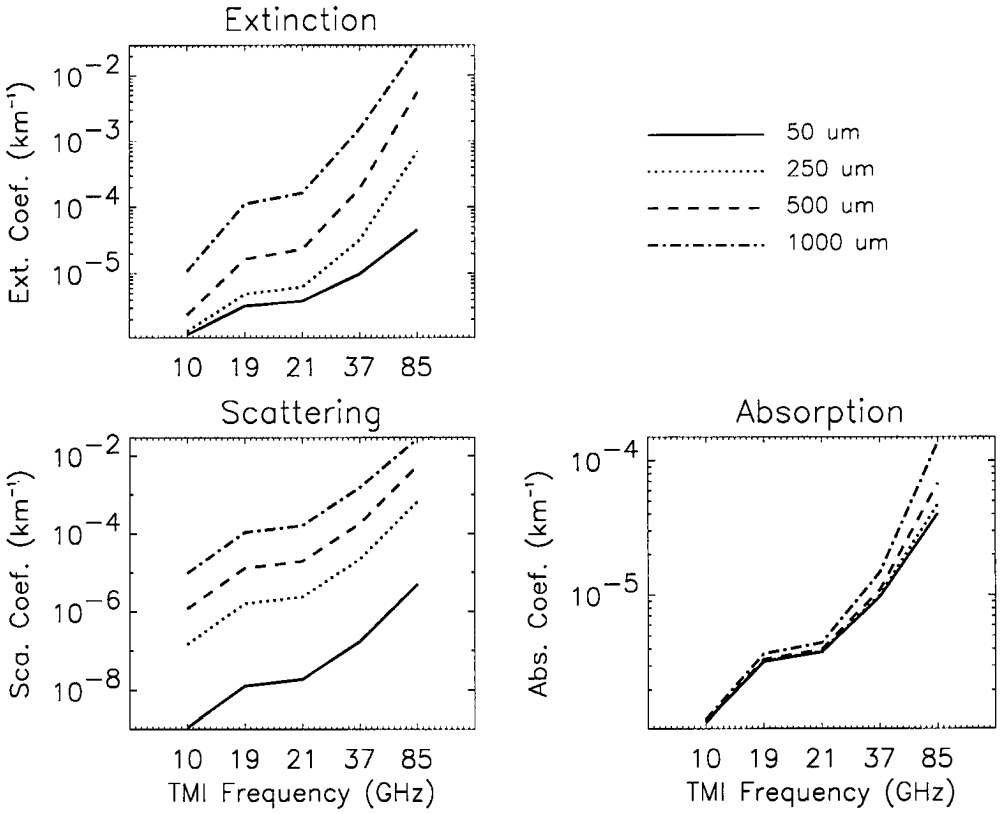

Figure 2.3: As in Figure 2.2 but for ice spheres.

tents at all atmospheric levels in a conceptually similar manner to the models employed in earlier studies by Wilheit et al. (1977) and Petty (1994a). A Marshall-Palmer distribution (Marshall and Palmer (1948), hereafter denoted MP) of spherical hydrometeors is assumed in which the liquid water content (LWC) is related to the rainrate at the surface, R, through

$$LWC = \frac{4\pi N_0 \Gamma(4)}{3b^4}\rho \tag{2.17}$$

where the number density $N_0 = 8\text{x}10^6\text{m}^{-4}$ and $b = 8200R^{-0.21}\text{m}^{-1}$. ρ is the mean density of the hydrometeors taken to be $1.0\text{x}10^6\text{gm}^{-3}$ for liquid and reduced to $0.1\text{x}10^6\text{gm}^{-3}$ for ice to avoid unreasonably large brightness temperature depressions at 85 GHz in accordance

with Petty (1994a). Only precipitating particles are considered explicitly although the small particle region of the MP distribution (i.e. less than 20 μm or so) behave like cloud particles by virtue of their low fall velocities. This is the reason for the quotation marks around the word cloud in the heading for this section. In what follows, the term "cloud" should be taken to represent the full range of particles described by the MP size distribution.

The model is depicted in Figure 2.4. The atmosphere is divided into 28 layers from the

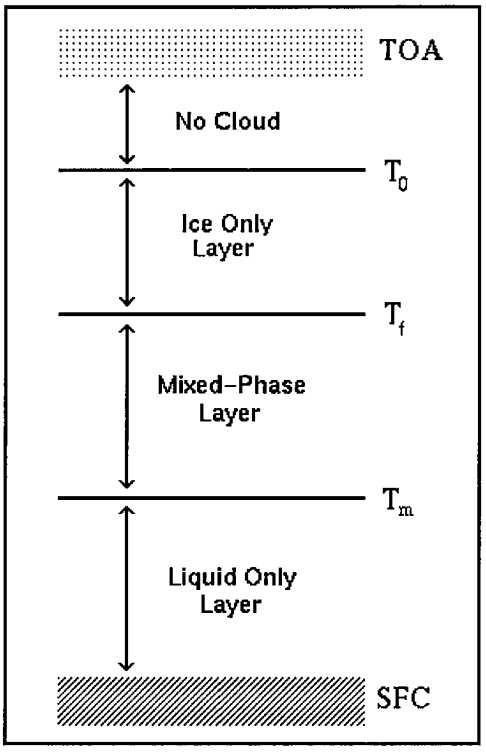

Figure 2.4: Schematic diagram of the cloud model.

surface to 18km. Below the melting layer, $T_m = 273.16$K, all hydrometeors are assumed to be liquid with constant LWC defined as in Equation (2.17). Above the freezing level, $T_f = 250.16$K, all hydrometeors are assumed to be frozen with ice water content (IWC) given by Equation (2.17). Between these levels we allow for a mixed-phase layer following

Tiedke (1993) in which the water content is defined in terms of the LWC and IWC as

$$WC = f * LWC + (1 - f) * IWC \tag{2.18}$$

where f is the liquid water fraction in the layer given by

$$f = \left[\frac{T - T_f}{T_m - T_f}\right]^2 \tag{2.19}$$

The atmosphere above $T_0 = 225.0$K is assumed cloud free. All other parameters such as temperature and relative humidity profiles, layer heights, freezing level and melting level are held constant. Profiles of temperature, humidity, and liquid and ice water using this model are displayed for three rainrates in Figure 2.5.

Both land and ocean background conditions are modeled. The ocean is modeled as a Fresnel surface with a temperature of 296K and overlying wind speed of $v = 0\text{ms}^{-1}$ to avoid the unnecessary complications introduced by ocean surface roughening which merely introduce an additional source of uncertainty in the results. The land surface is assumed to be Lambertian with a uniform emissivity of 0.9 and a temperature of 296K. Again, no topographical, vegetation or soil moisture effects are included to avoid introducing unnecessary uncertainties in the results.

Despite being a somewhat crude representation of real-world precipitating clouds, this simple model provides a great deal of insight into the physical processes within the atmosphere which give rise to the radiances observed at the TRMM satellite. Specifically the two dominant processes, absorption and re-emission of low frequency microwave radiation by liquid hydrometeors and scattering of higher frequency microwave radiation by ice hydrometeors, have been modeled. In principle it is possible to use more realistic clouds obtained from CRM simulations or observations but in practice the weighting functions obtained using such clouds are extremely complex and obscure the physical interpretation

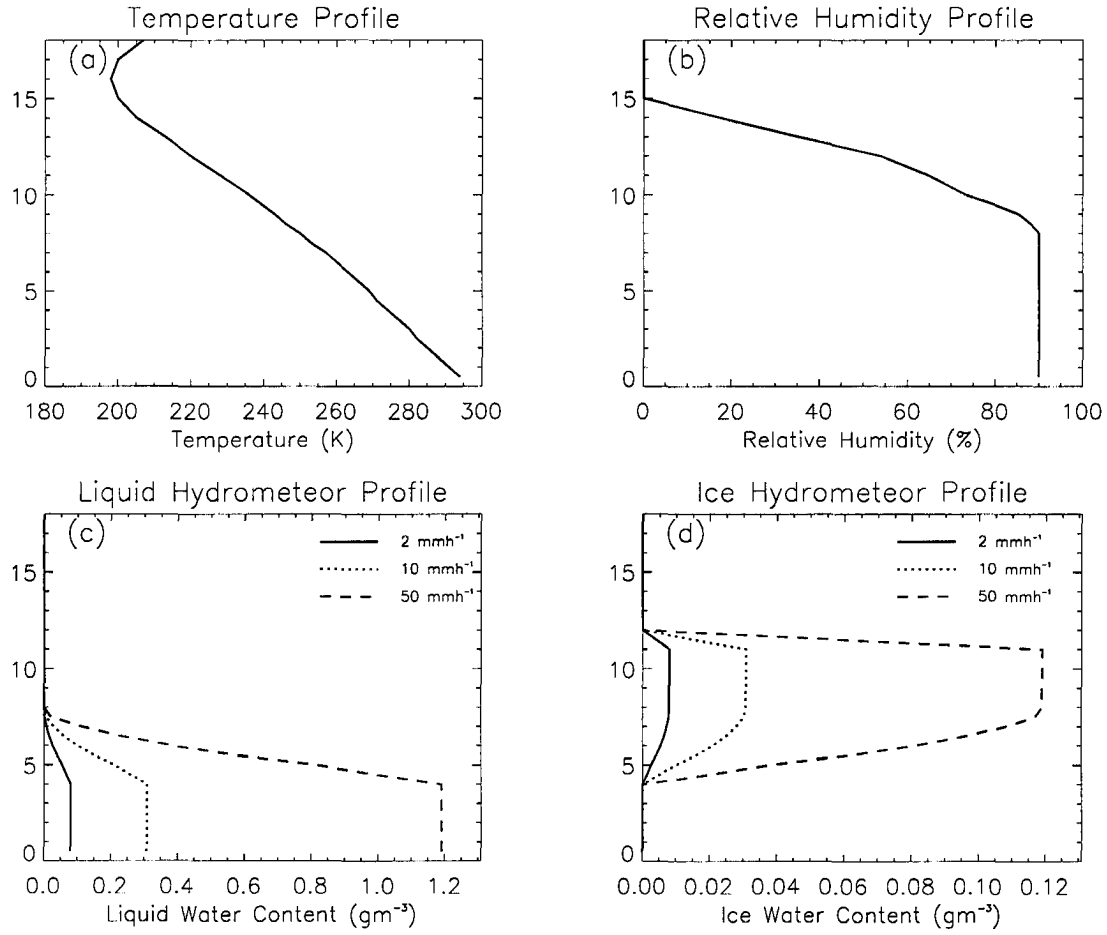

Figure 2.5: Profiles of (a) temperature, (b) relative humidity, (c) cloud liquid water, and (d) cloud ice water for selected rainrates.

of the results. It is encouraging to note that this model yields brightness temperature depressions at 85 GHz which increase by approximately 4K per mmh^{-1} increase in rainrate in good agreement with current theoretical and empirical evidence (Adler et al., 1991). This suggests that model sensitivities to changes in rainrate are of the right order of magnitude.

2.4 TMI Sensitivity to Rainfall Rate

Liquid water associated with rainfall is one of the more basic parameters to retrieve using passive microwave radiances. Numerous algorithms of varying complexity exist for this

purpose (eg. Wilheit et al. (1977), Spencer et al. (1989), Liu and Curry (1992), Smith et al. (1994b), and Sheu et al. (1996) to name but a few). It is instructive to determine the minimum rainrate required to give rise to a detectable difference in brightness temperature from clear conditions relative to the sensitivity of the TMI instrument, prior to conducting a more detailed study of its information content. Furthermore, this analysis serves as a test of the physical assumptions made in the cloud model.

Since numerous radiative transfer calculations were required throughout this analysis, we used an implementation of the Eddington approximation to the radiative transfer equation described in Kummerow (1993). Uncertainties in this approximation are likely to be small and the increase in speed afforded by using this model far outweighs the uncertainties it introduces in the analysis.

Brightness temperature signatures characteristic of scenes with rainrates varying from 0 to 100 mmh^{-1} are presented in Figure 2.6. Over ocean, the T_Bs exhibit the characteristic sharp increase with increasing rainrate due to emission from liquid water followed by a slow decrease at very high rainrate due to ice scattering in accord with theory. The 19.3 GHz T_Bs, for example, are in excellent agreement with those presented in Wilheit et al. (1977). Conversely, the warm land background masks emission from the rain and the T_B remains approximately constant with increasing rainrate until scattering effects become significant at which point they begin to decrease at a similar rate to those over ocean. It is interesting to note that at every frequency there is a rainrate at which the T_B over the land and ocean backgrounds converge. Physically this is the rainrate where the atmosphere becomes so opaque that it effectively masks the surface and the radiance measurement originates from some level within the rain column itself. Above this rainrate any rainfall retrieval, regardless of the specific method used, will no longer be sensitive to surface properties.

Figure 2.7 shows corresponding cloudy minus clear-sky T_B differences as a function of

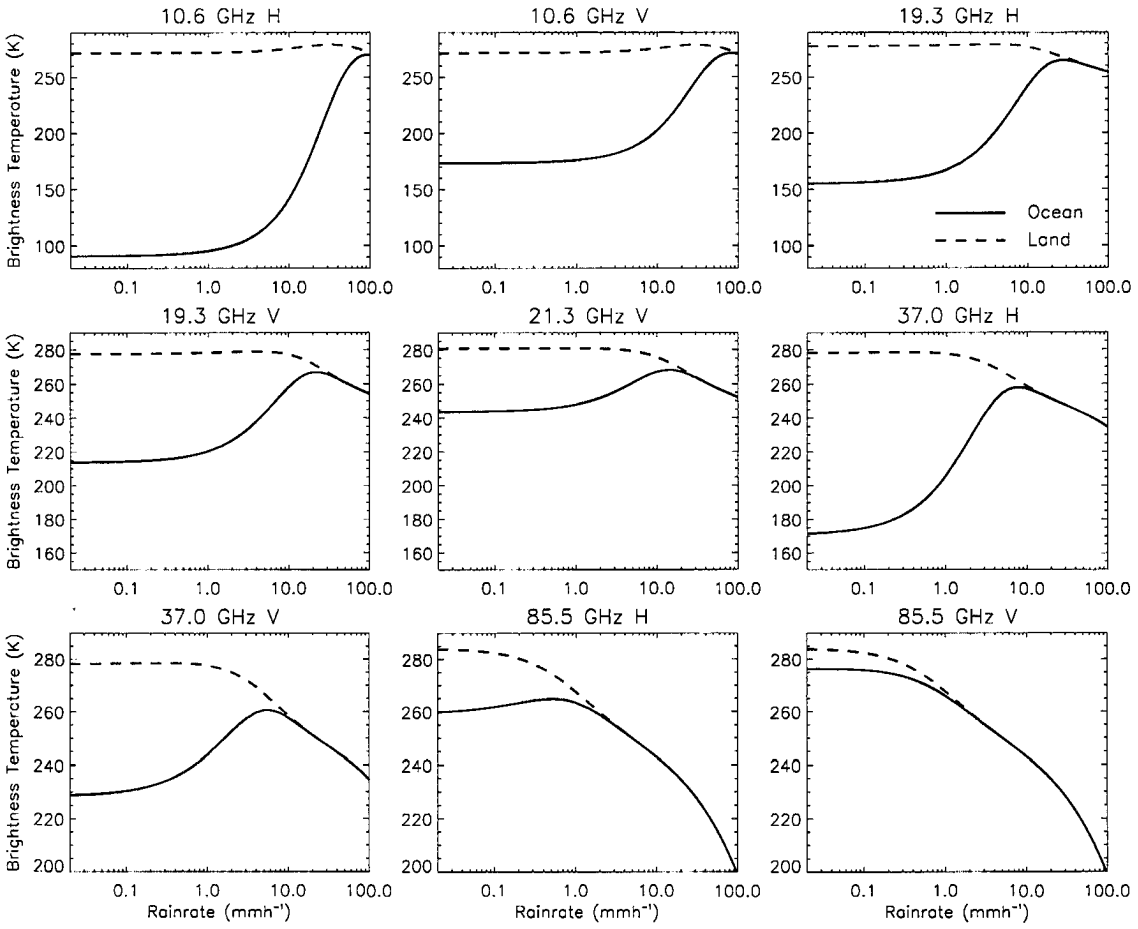

Figure 2.6: T_B as a function of rainrate for each TMI channel over both ocean and land backgrounds.

rainrate. A rainrate is considered detectable at frequency i only if

$$|T_{B_{i,raining}} - T_{B_{i,clear}}| > \sigma_i \tag{2.20}$$

where σ_i is the sensitivity of the i^{th} TMI channel. The values assumed for the σ_i, represented by the dot-dashed lines on Figure 2.7, correspond to TMI instrument specifications given in Kummerow et al. (1998) and are summarized in column 2 of Table 2.1. Minimum detectable rainrates for all channels, summarized in columns 3 and 4 of this table, emphasize the greater sensitivity of the TMI over ocean than over land.

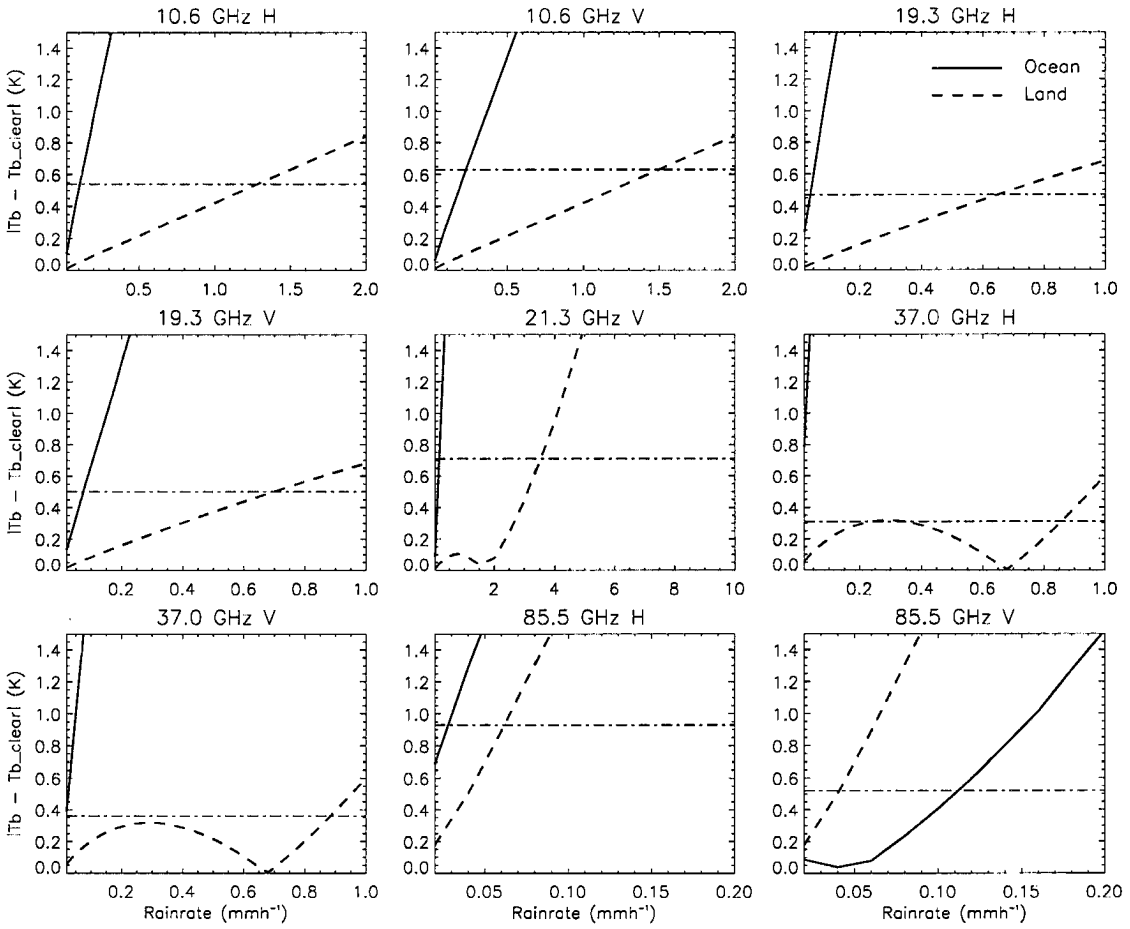

Figure 2.7: T_B difference between raining and clear sky scenes as a function of rainrate for each TMI channel. The horizontal dashed lines indicate the corresponding instrument sensitivity from Table 2.1.

According to Table 2.1 and under the simplifying assumptions imposed by the cloud model, rainfall less than about 1.0 mmh^{-1} is not detected over land, except for the weak ice scattering signature at 85.5 GHz. At 35 GHz, emission from warm rainfall near the surface increases brightness temperatures in very light rainfall while brightness temperatures are reduced at rainrates exceeding 0.5 mmh^{-1}. This feature, which appears as the bump at low rainrates in Figure 2.7, is extremely weak, however, and cannot be distinguished from measurement noise. In addition, due to the more Lambertian nature of dry land surfaces relative to ocean over the large field of view (FOV) the TMI (Ulaby et al., 1986), there

Table 2.1: T_B sensitivities and minimum detectable rainrates for each TMI channel.

Channel	σ (K)	Ocean R_{min} (mmh^{-1})	Land R_{min} (mmh^{-1})
10.6 GHz H	0.54	0.12	1.30
10.6 GHz V	0.63	0.24	1.50
19.3 GHz H	0.47	0.04	0.64
19.3 GHz V	0.50	0.08	0.70
21.3 GHz V	0.71	0.18	3.50
37.0 GHz H	0.31	0.02	0.86
37.0 GHz V	0.36	0.02	0.90
85.5 GHz H	0.93	0.03	0.06
85.5 GHz V	0.52	0.12	0.04

is very little difference between vertically and horizontally polarized T_Bs over land. This effectively reduces the number of available pieces of distinct information from 9 to 5. By contrast, the results are more encouraging for rainfall over the ocean. Table 2.1 suggests that rainrates exceeding 0.25 mmh^{-1} exhibit discernable signals in all the TMI channels.

Recall that these results have been obtained using a very simple model which does not account for differences between convective and stratiform rainfall or in the microphysical processes governing rainfall development over land and oceanic backgrounds. Furthermore, no effort has been made to simulate non-precipitating clouds which can also be distinguished from clear-sky conditions but are indistinguishable from extremely light precipitation. Instead of rigorous estimates of minimum detectable rainrates, the results represent ball-park estimates which primarily provide initial evidence for differences between land and ocean based retrievals. From this preliminary observation we launch into a more quantitative analysis of the different information used in TMI rainfall retrievals over land and ocean.

2.5 Information Content of the TMI Measurements

2.5.1 TMI Weighting Functions

The results of the preceeding section suggest a rainrate threshold exists below which the TMI T_Bs cannot be distinguished from instrument noise even if its value remains uncertain. We now apply the PCA described in Section 2 to estimate the information content of the TMI measurements over the range of $0 - 100\text{mmh}^{-1}$, typical of rainrates observed by the TRMM satellite in the tropics. The weighting functions defined in Eqn. (2.3) were constructed for each cloud profile by first computing the upwelling T_Bs at the top of the atmosphere (TOA) for the nine TMI channels for the unperturbed cloud and then perturbing each parameter at every level in the atmosphere and computing the change in TOA brightess temperatures corresponding to each perturbation. The value of the channel i weighting function for parameter x_j at level z_k is approximated as

$$\begin{aligned} K_j^i(z_k) &= \frac{\partial T_{B_i}}{\partial x_j(z_k)} \\ &\approx \frac{T_{B_i}(x_j+\delta) - T_{B_i}(x_j-\delta)}{2\delta} \end{aligned} \tag{2.21}$$

where T_{B_i} is the brightness temperature in channel i and δ is the magnitude of the perturbation taken to be $\sim 1\%$ in these simulations.

In the microwave region of the electromagnetic spectrum the strongest contributions to the observed TOA T_Bs are liquid and ice water, temperature, and, to a lesser degree, relative humidity. As a result the analysis focuses exclusively on these parameters. Figures 2.8 and 2.9 compare the temperature weighting functions for each vertically polarized channel of the TMI at a variety of near-surface rainrates. Low frequency microwave radiation penetrates the cloudy atmosphere even under moderately intense rain as indicated by the weighting functions at 10, 19, and 21 GHz which all peak at the surface for rainrates

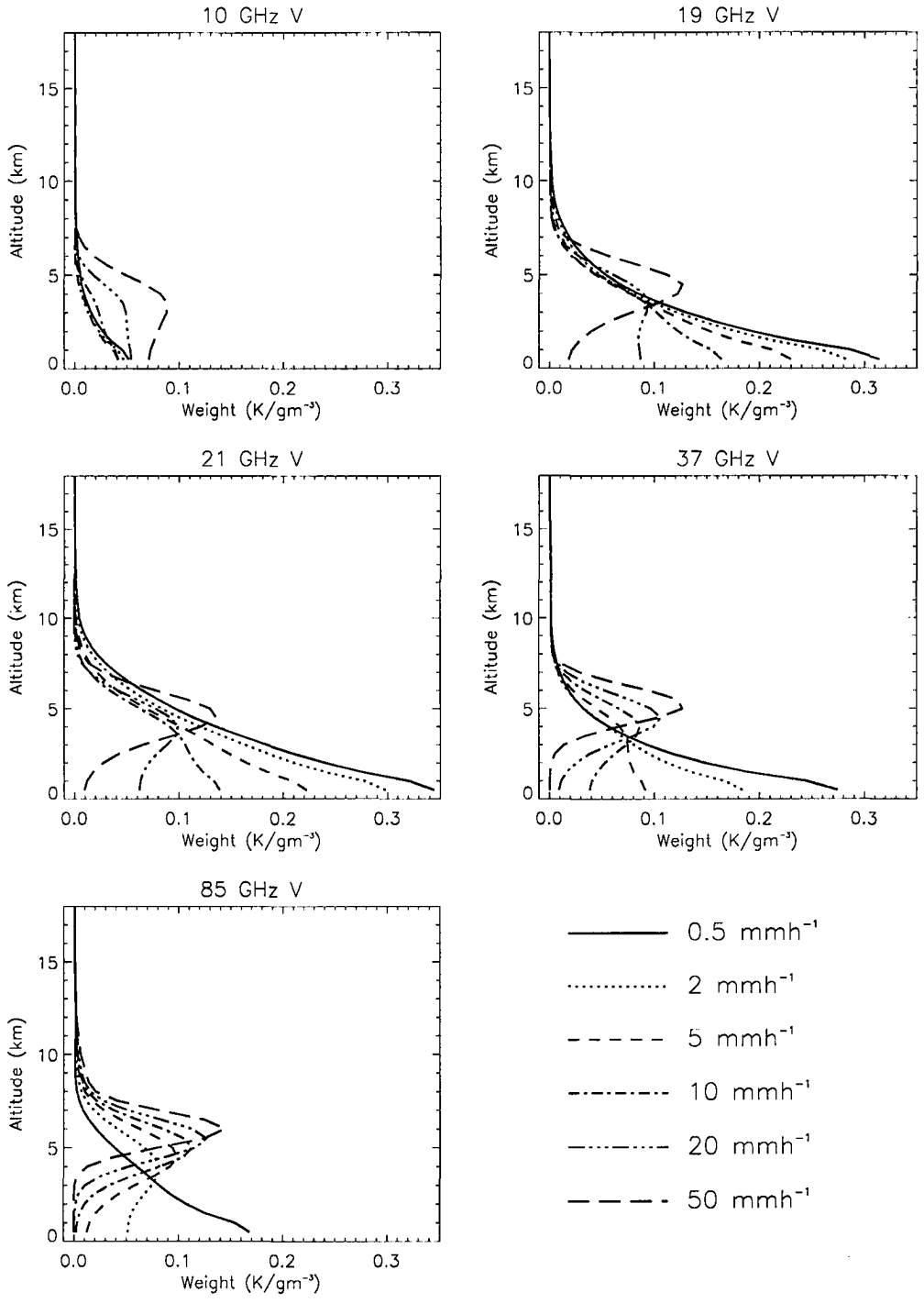

Figure 2.8: Temperature weighting functions for each vertically polarized TMI channel as a function of rainrate over an ocean background.

Table 2.2: Optical depths at each TMI frequency for selected rainrates.

Rainrate	10.6 GHz	19.3 GHz	21.3 GHz	37.0 GHz	85.5 GHz
0.5 mmh^{-1}	0.0238	0.1494	0.3179	0.2242	0.9204
2.0 mmh^{-1}	0.0356	0.2024	0.3840	0.4517	1.8742
5.0 mmh^{-1}	0.0634	0.3243	0.5348	0.9417	3.4550
10.0 mmh^{-1}	0.1175	0.5481	0.8094	1.7811	5.6845
20.0 mmh^{-1}	0.2442	1.0291	1.3947	3.4360	9.3870
50.0 mmh^{-1}	0.6927	2.5611	3.2378	8.0811	18.0769

less than 10 mmh^{-1}. At higher frequency, however, attenuation within the rain/ice column causes the surface signal to vanish at much lower rainrates. In all cases as rainrate increases the sensitivity to temperature near the surface decreases at the expense of enhanced sensitivity within the rain column itself.

Temperature weighting functions over a land background exhibit very similar trends to those over ocean. Weighting functions which peak above the surface are nearly identical regardless of the surface properties. Those which peak at the surface, however, exhibit dramatically reduced absolute sensitivities to temperature over the land background.

These results demonstrate the principle reason for selecting the channels used on the TMI and are consistent with those expected for an optically thin medium (Stephens, 1994). To illustrate this, total column optical depths, derived using the simple cloud model, are plotted as a function of rainrate in Figure 2.10 for the five TMI frequencies. To facilitate comparisons, optical depths at selected rainrates for each TMI frequency are summarized in Table 2.2. Regardless of rainfall rate the atmosphere appears much "thicker" to high frequency microwave radiation than to that at lower frequencies.

The effective level of emission, defined as the altitude at which the temperature weighting function peaks, emphasizes this point. Figures 2.11 and 2.12 show the effective level of emission over ocean and land backgrounds, respectively. At all rainrates below 1 mmh^{-1} all TMI channels are primarily sensitive to the surface and beyond 18 mmh^{-1} over land and 25 mmh^{-1} ocean, the surface signal is completely obscured. At intermediate rainrates low

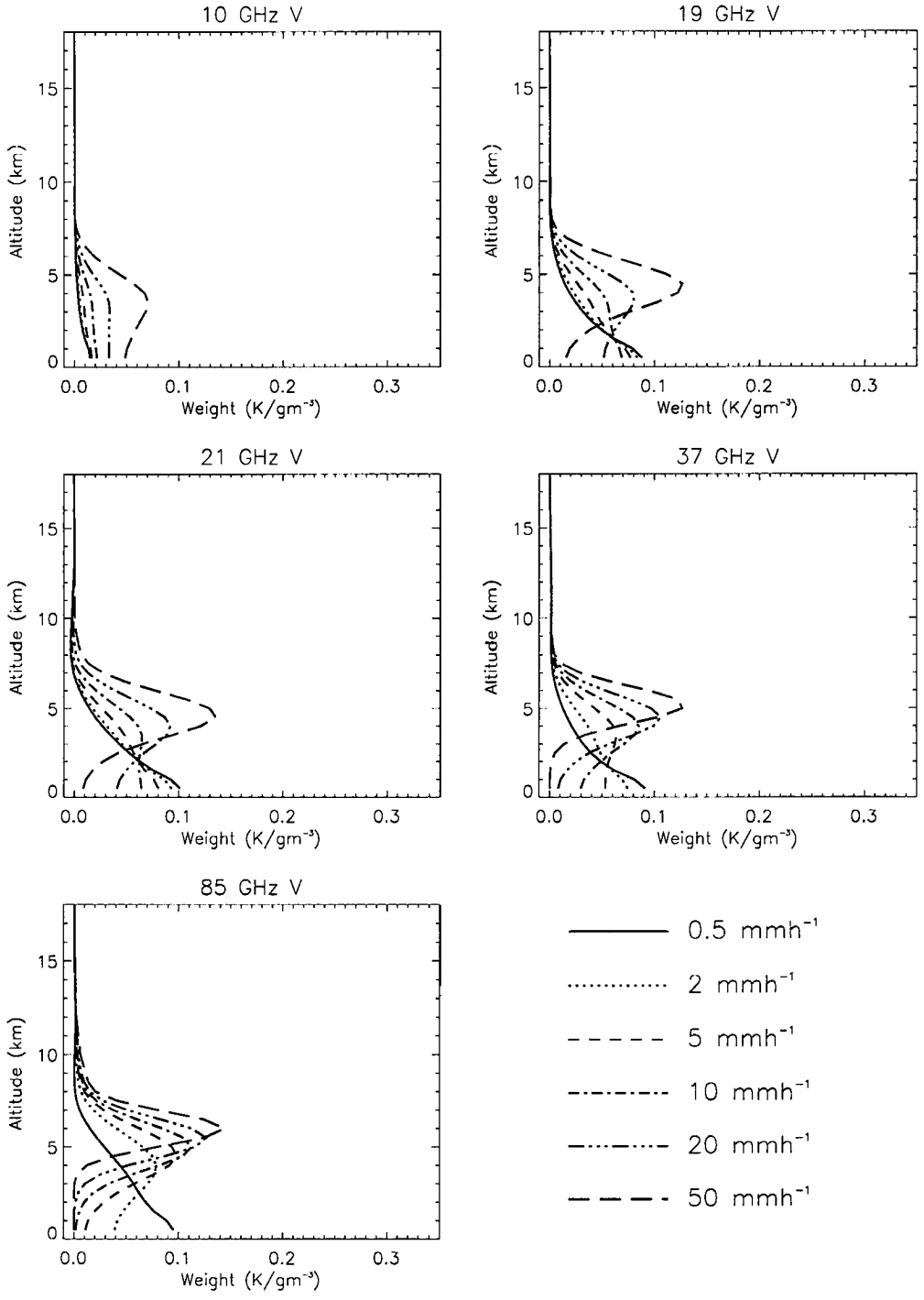

Figure 2.9: Temperature weighting functions for each vertically polarized TMI channel as a function of rainrate over a land background.

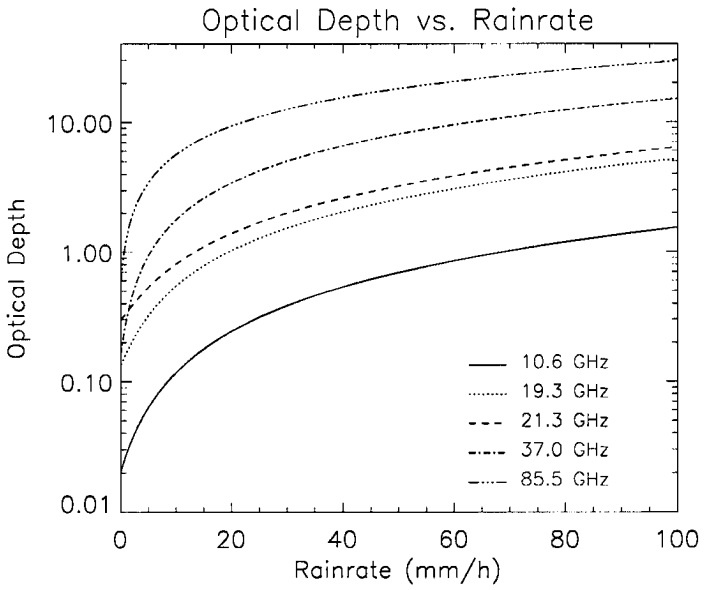

Figure 2.10: Optical depth as a function of rainrate at each TMI frequency.

frequency channels sample the surface while high frequency channels sample levels higher up in the atmosphere. Based on these results, we conclude that the ideal range of rainrates for both surface rainfall estimation and some degree of cloud profiling is 4.5 to 18 mmh^{-1} over land and 6 to 25 mmh^{-1} over ocean since the TMI provides information from a wide range of different levels in the rain column in this range.

Figures 2.13-2.16 focus on the sensitivity of each TMI channel to liquid and ice water in the atmospheric column. While the temperature weighting functions indicate the levels in the atmosphere at which the TMI provides the best sampling, these figures quantify the instrument's sensitivity to the specific parameters we wish to retrieve. The liquid water weighting functions demonstrate the fact that entirely different physical processes give rise to the TMI rainfall signature over land and oceand backgrounds. Over ocean, positive perturbations in the liquid water content give rise to increases in all but the 85 GHz T_B, a direct result of the higher emissivity of raindrops relative to ocean backgrounds, particularly in the warm layers near the surface. This effect increases with increasing rainrate until the amount of ice at upper levels increases to a point where scattering becomes important.

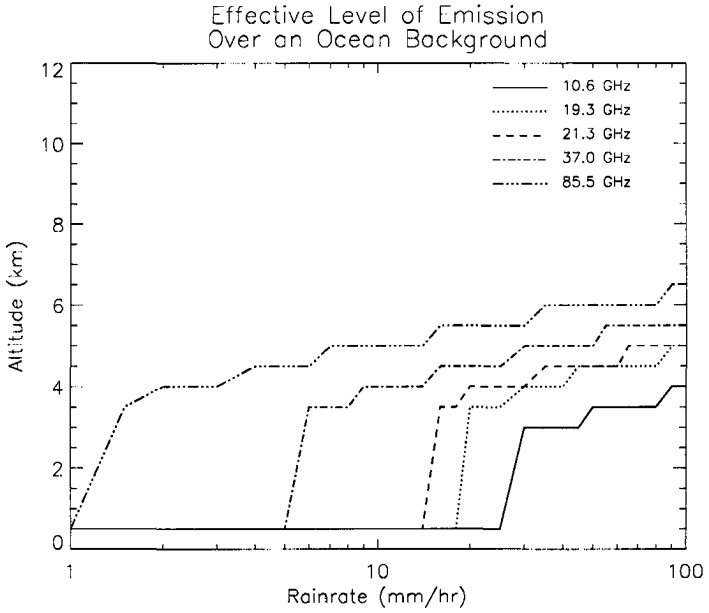

Figure 2.11: TMI effective levels of emission as a function of rainrate over an ocean background.

At this point the effects of enhanced emission diminish and eventually increasing rainrate results in a decrease in T_B. This is particularly evident at 85 GHz. Note that scattering effects are most prominent near the top of the rain column as opposed to emission effects which are always greatest near the surface where raindrops are the warmest.

The comparitively warm land background masks emission from raindrops and only the much weaker scattering signal of the larger raindrops remains in the T_B signature. As a result sensitivities to liquid water at 10, 19 and 21 GHz channels are much weaker over land than over ocean. These results emphasize the difficulties incurred when trying to retrieve atmospheric properties near the surface over land. For moderate rainrates at 19 GHz, for example, the T_B is nearly an order of magnitude more sensitive to perturbations in liquid water near the surface over ocean than land.

At all microwave frequencies ice water signatures are dominated by the scattering process. As a result the ice water weighting functions show no sensitivity to surface properties. At 10 GHz the scattering signature is negligible due to the long wavelength relative to the

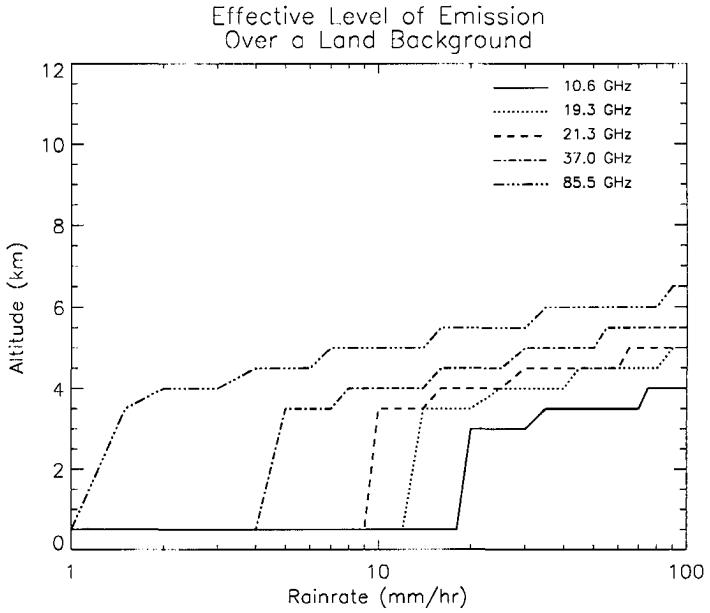

Figure 2.12: TMI effective levels of emission as a function of rainrate over a land background.

size of the ice particles. Sensitivity to scattering increases with increasing frequency, however, and the weighting functions show pronounced negative peaks at 37 and especially 85 GHz at high rainrate.

2.5.2 Eigenvalue Analysis

Using these weighting functions, principal component analyses have been conducted for each variable at each rainrate. An estimate of the mean uncertainty in the TMI measurements was obtained by averaging the sensitivities of each TMI channel. We find $\bar{\sigma} = 0.55K$ provides a suitable order-of-magnitude estimate for the mean error in the measurements.

Results of the eigenvalue analysis are summarized in Figure 2.17 which shows the number of independent pieces of information as a function of rainrate for each atmospheric parameter. Under cloud-free conditions, the TMI channels provide three independent pieces of temperature information, two regarding relative humidity profiles, and no information

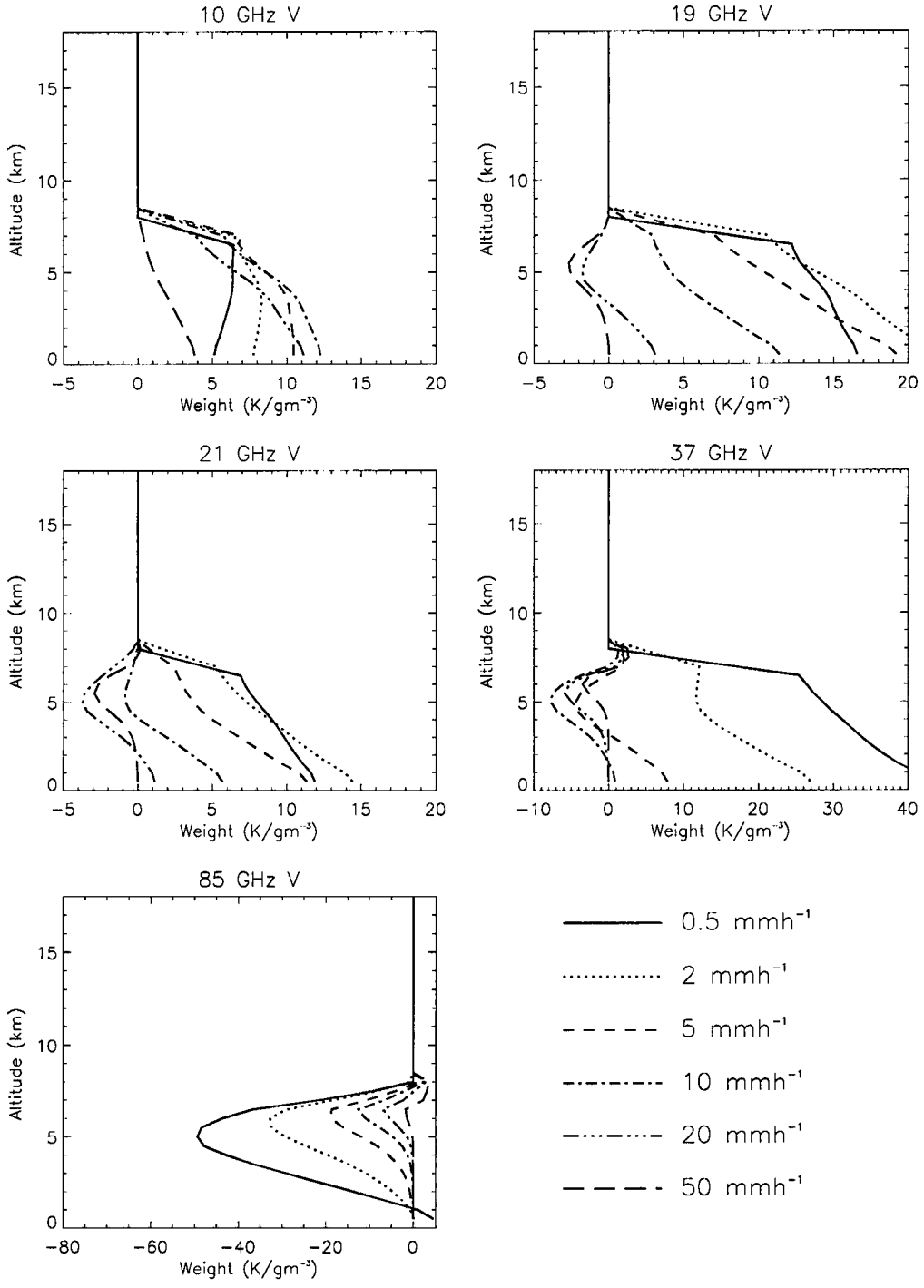

Figure 2.13: Liquid water weighting functions for each vertically polarized TMI channel as a function of rainrate over an ocean background.

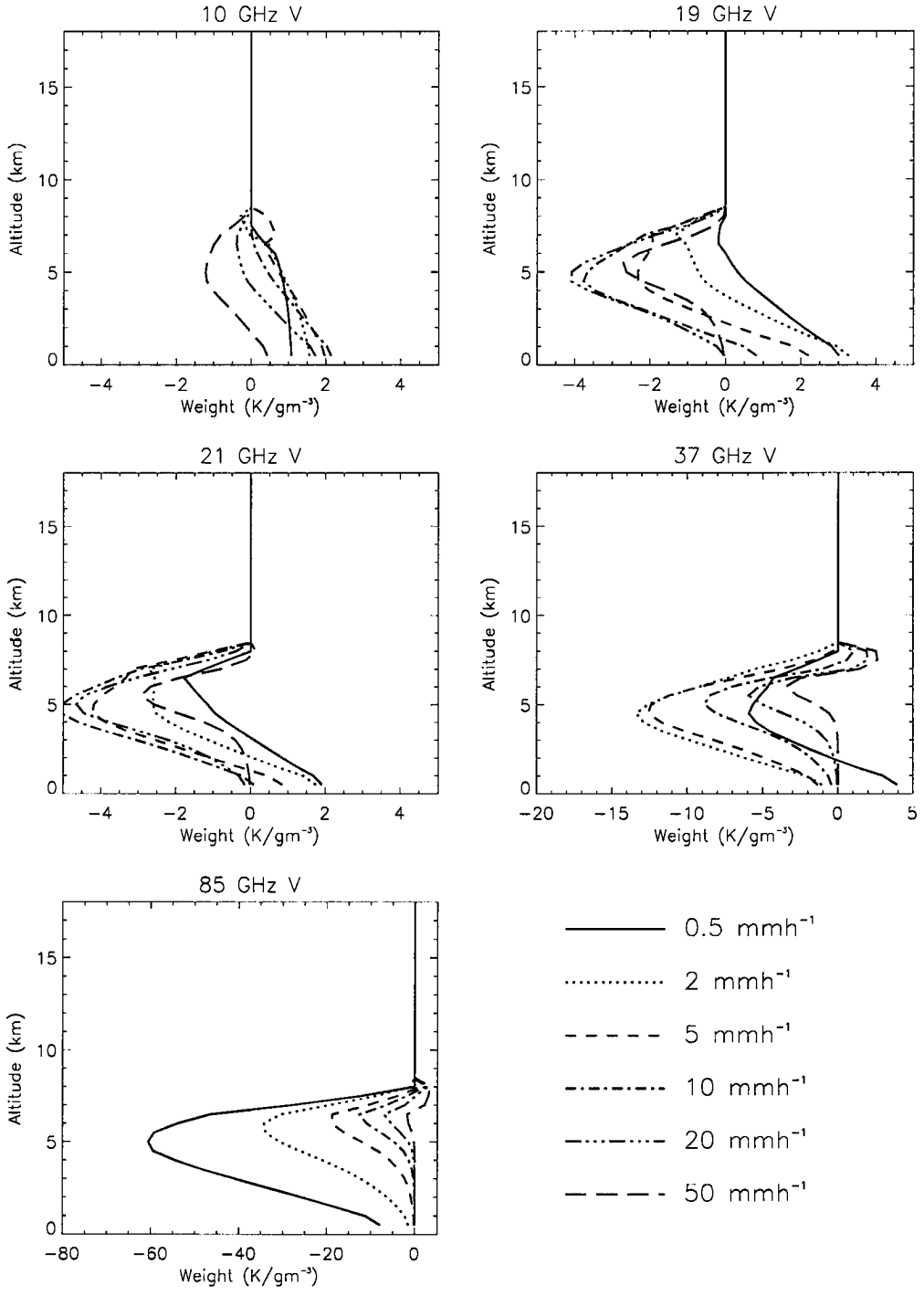

Figure 2.14: Liquid water weighting functions for each vertically polarized TMI channel as a function of rainrate over a land background.

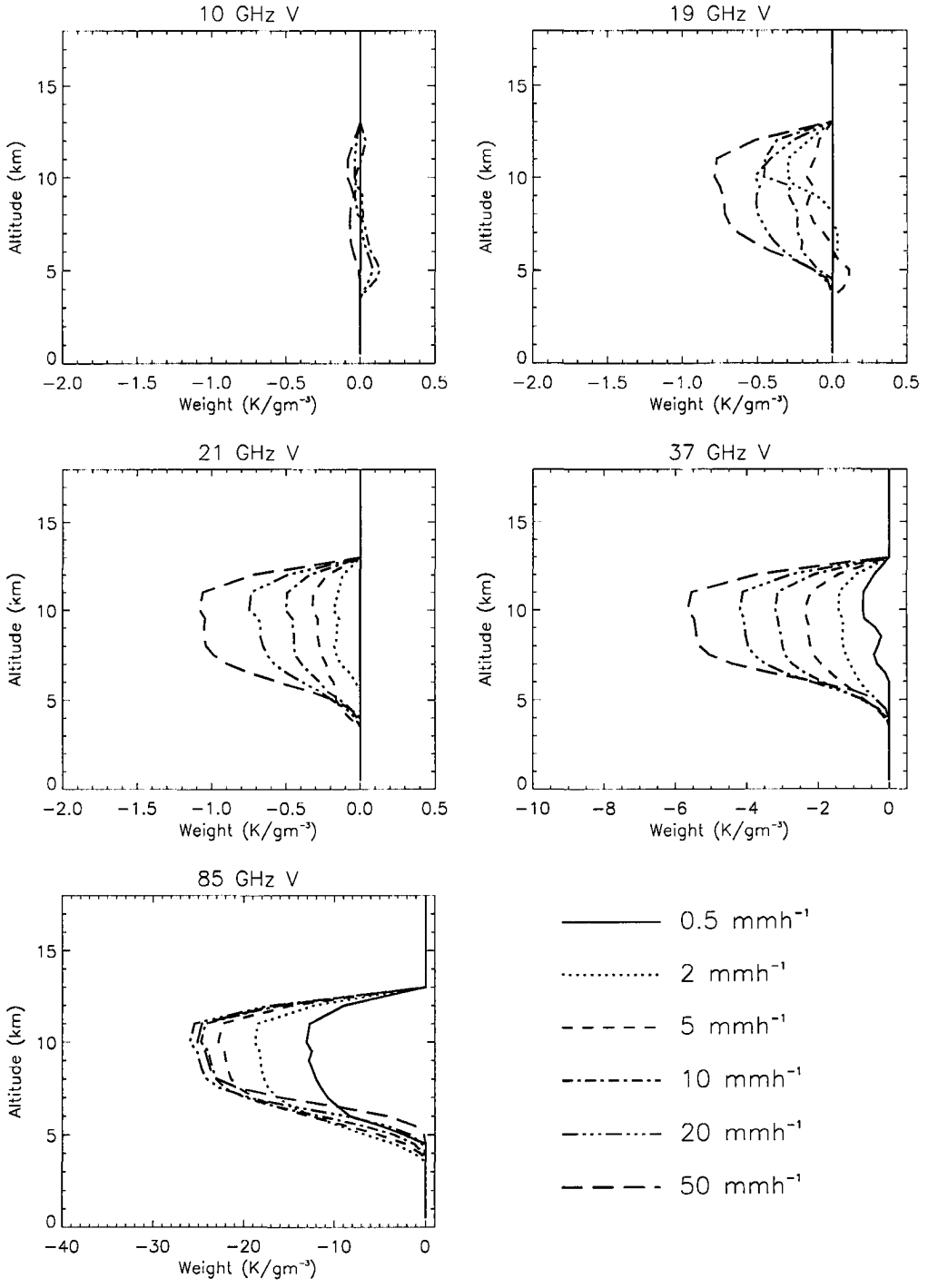

Figure 2.15: Ice water weighting functions for each vertically polarized TMI channel as a function of rainrate over an ocean background.

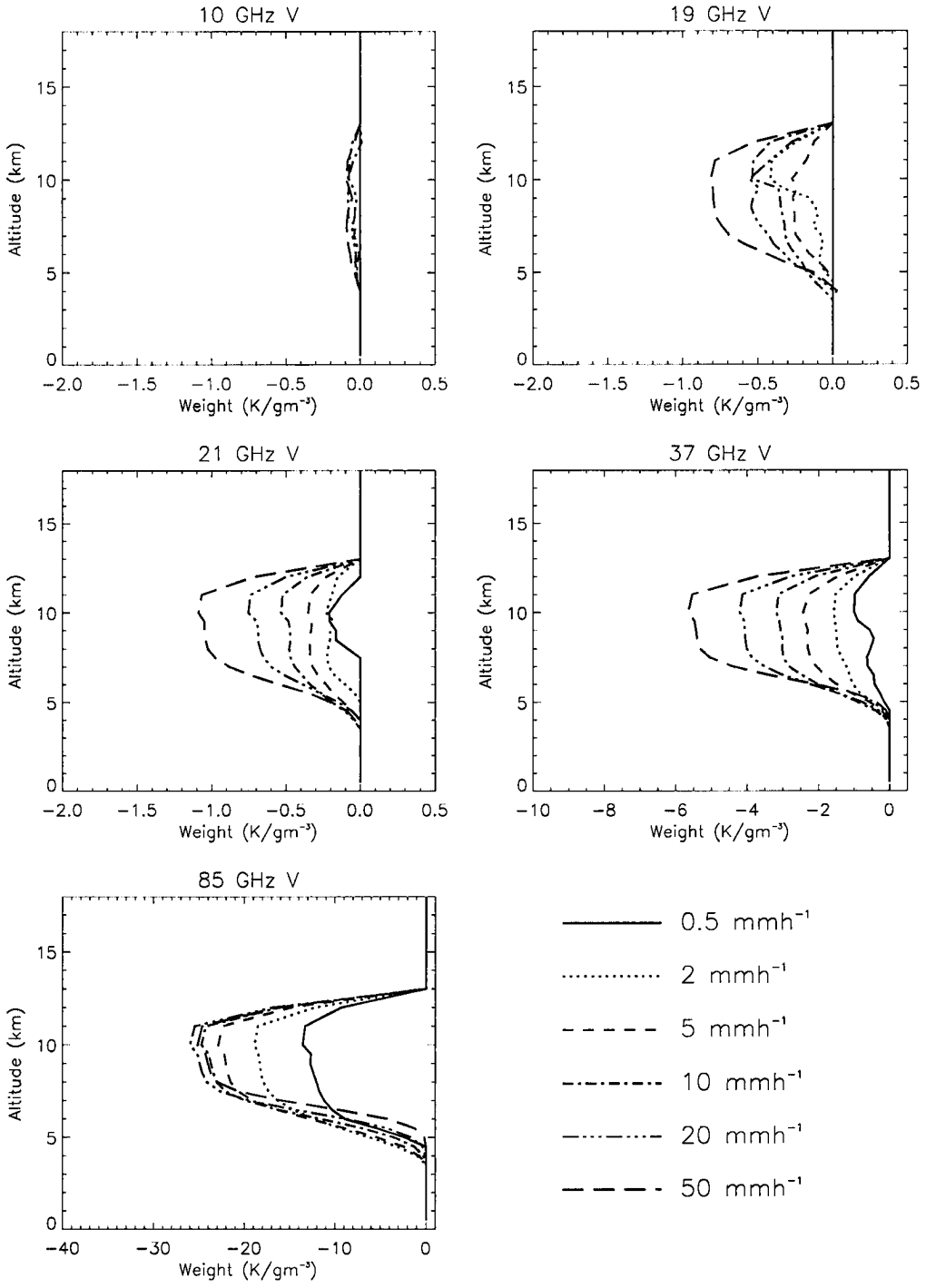

Figure 2.16: Ice water weighting functions for each vertically polarized TMI channel as a function of rainrate over a land background.

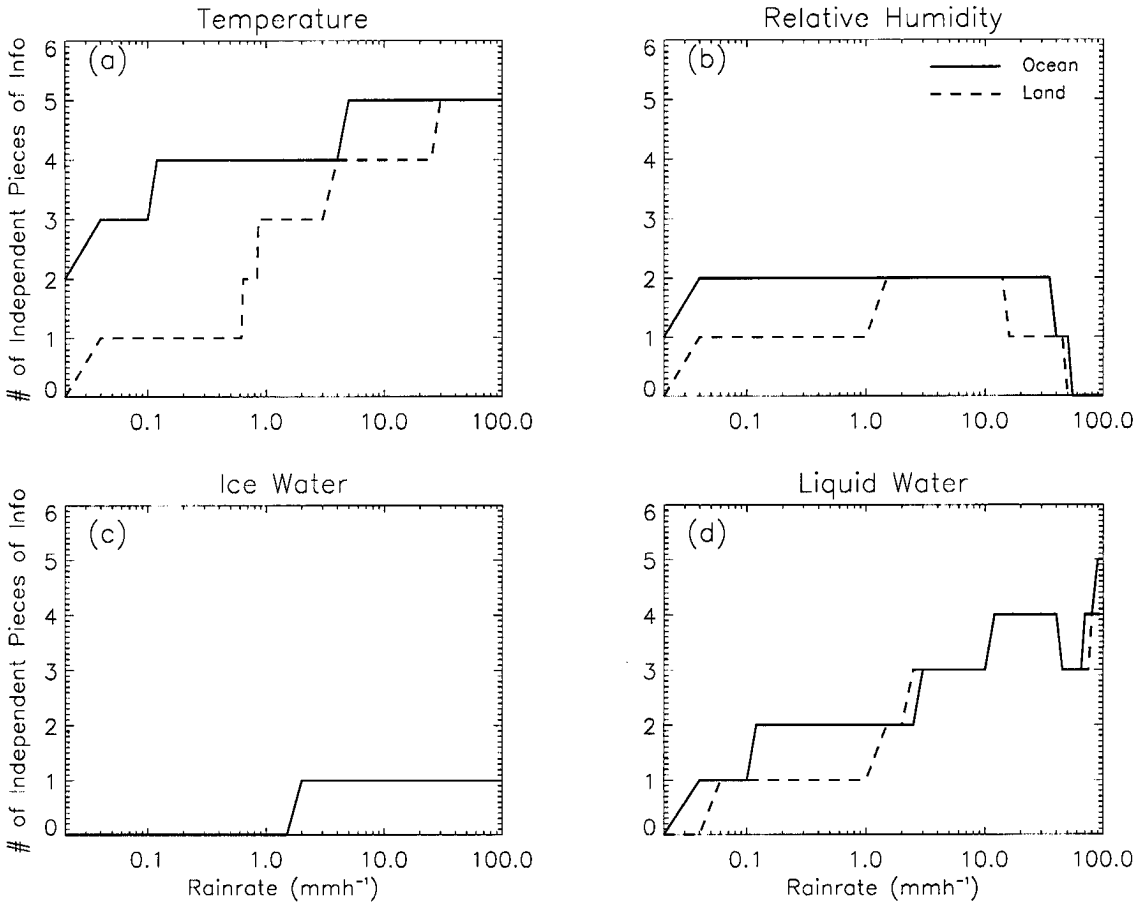

Figure 2.17: TMI information content as a function of rainrate for retrieving (a) temperature, (b) relative humidity, (c) liquid water and (d) ice water profiles over both ocean and land backgrounds.

regarding ice and liquid water content. As rainrate increases the effective levels of emission at each frequency spread in altitude reducing the redundancy of information between the channels. Over an ocean background the number of independent pieces of temperature information increases to five for rainrates above 40 mmh^{-1}. The warm land background, however, masks perturbations in temperature and the TMI provides far fewer independent pieces of temperature profile information over land than ocean in light rainfall. As rainrate increases T_Bs become less sensitive to the surface properties and more sensitive to the atmosphere yielding similar information contents over both land and ocean.

Water vapor is relatively transparent to microwave radiation compared with the effects of cloud liquid water. Only the 19 and 21 GHz channels are sensitive to perturbations in relative humidity by virtue of their proximity to the 22.3 GHz water vapor absorption line. At moderate rainrates the effective level of emission for these two channels differs enough to provide two independent pieces of water vapor information.

At rainrates below 1.5 mmh^{-1} cloud ice fails to change the T_B in any channel above the numerical accuracy of the radiative transfer model. Above 2 mmh^{-1}, the ice signature at 85.5 GHz is strong enough to provide a single piece of information. The weighting functions eventually show weak ice signatures at all frequencies except 10 GHz but all weighting functions overlap and therefore do not add any independent information to the measurements. It is clear from the width of the weighting functions in Figures 2.15 and 2.16 that this information originates almost equally from the entire ice column indicating the possibility for retrieving column-integrated ice water path (IWP) but very little information regarding its vertical distribution.

Liquid water weighting functions show distinct differences among the TMI channels and this is reflected in the information they provide. As rainrate increases and the effective levels of emission at different TMI frequencies become more disparate, the number of independent pieces of information increases. The information content over land differs from that over ocean at very low rainrates where the effective level of emission is near the surface and the rainfall emission signature is negligible compared with the warm land background. At rainrates greater than 2.5 mmh^{-1}, the TMI T_Bs contain information from three or more independent levels within the rain column regardless of the underlying surface. Consequently, the TMI is both well-suited for cloud profile estimation over this range of rainrate but also susceptible to erroneous cloud profile assumptions in less sophisticated surface rainrate retrievals.

These results are put into perspective in Figure 2.18 which provides the probability

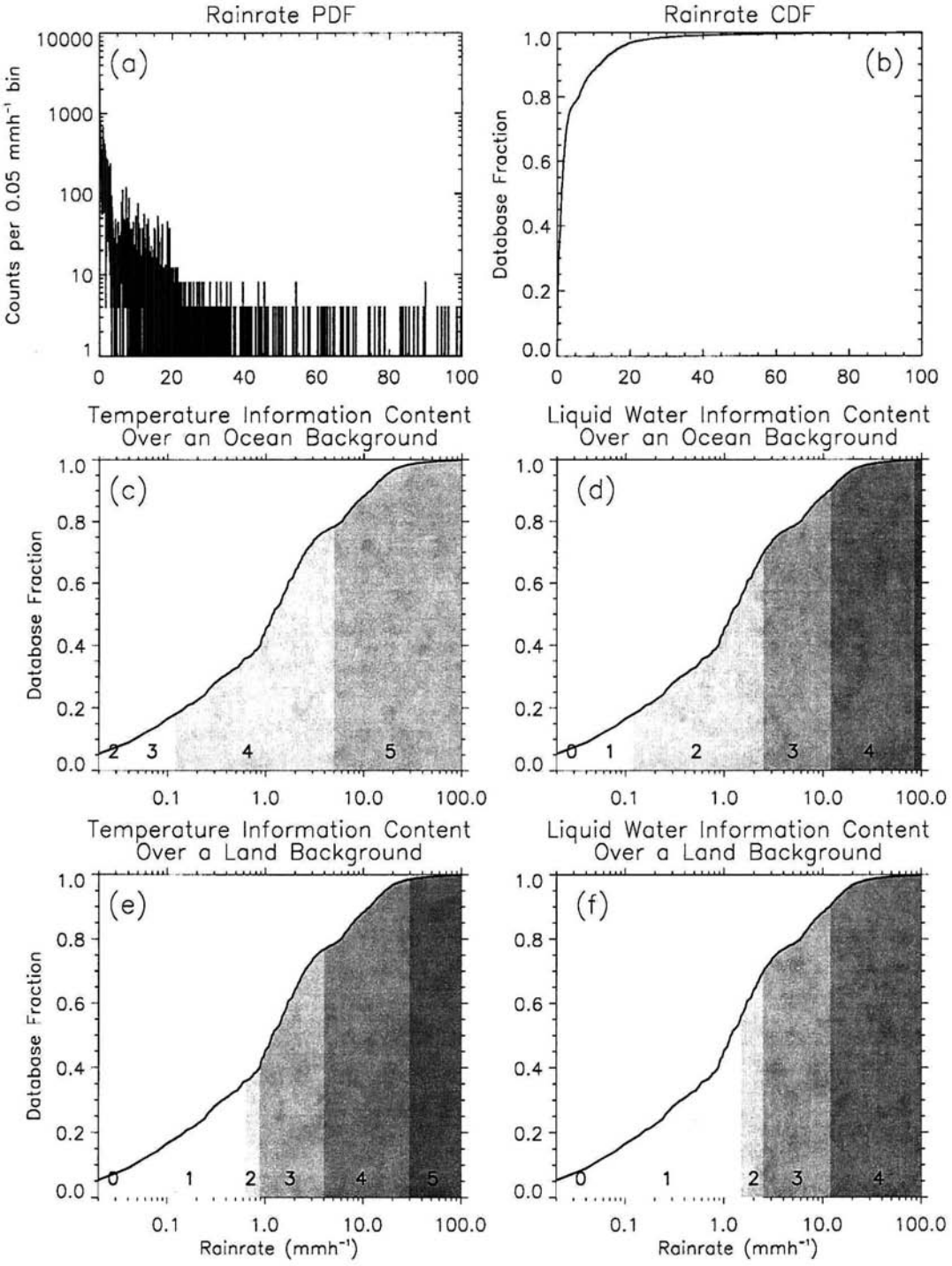

Figure 2.18: (a) and (b) PDF and normalized CDF of rainrate from the GPROF algorithm. (c) and (d) Shaded CDF indicating the number of independent pieces of information the TMI measurements contribute to temperature and ice water retrievals over an ocean background, respectively. Similar results over a land background are presented in (e) and (f).

density function (PDF) of surface rainrate from the cloud database used in the GPROF algorithm, highlighting the regions where the TMI observations contain the most information. The database consists of an amalgamation of a number of distinct cloud resolving model simulations of a wide range of tropical systems using the Goddard Cumulus Ensemble (GCE) model. Details of the specific cloud cases can be found in Olson et al. (1996) and Tao and Simpson (1993) provide an overview of the GCE model.

Figure 2.18 indicates that approximately half of the cloud profiles in the database have surface rainrates less than about 1.5 mmh^{-1}. This region corresponds to rainrates for which the TMI observations contain very little to no ice water profile information and at most two independent pieces of liquid water profile information. Most of the TMI information for retrieving both liquid water profiles lies in the region greater than 2.5 mmh^{-1} which accounts for only about 30 percent of the profiles in the database. This points to a potential inadequacy of TMI measurements alone when used to retrieve cloud profiles in the tropics in that they will be bereft of information in the significant number very light rain scenes which the TRMM satellite encounters. Recalling the results of Section 2.4, it should also be pointed out that surface rainfall detection may be difficult for about 40 percent of the cloud profiles in the database over a land background by virtue of the lack of a significant T_B deviation from clear-sky conditions. At mid-latitudes light rain may be even more prevelant. Thus in order to capture a complete spectrum of global rainfall in the future, it will be necessary to combine information from other sensors to account accurately for light rain.

2.5.3 Orthonormal Weighting Function Analysis

Eigenvectors corresponding to the principal eigenvalues have been used to construct a set of orthonormal weighting functions following Equation (2.15). As opposed to the weighting functions which indicate the levels from which the T_Bs of individual channels originate, the

orthonormal weighting functions show where the information from the entire measurement system as a whole originates. They represent weighting functions for the TMI instrument as a whole rather than each individual channel.

Orthonormal liquid water weighting functions over an oceanic background are plotted for three different rainrates in Figures 2.19-2.21. At low rainrate there are two domi-

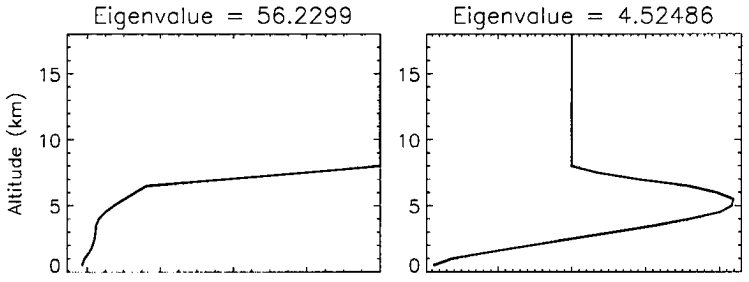

Figure 2.19: Statistically significant orthonormal weighting functions for retrieving liquid water profiles at a rainrate of 0.5 mmh^{-1} over an ocean background.

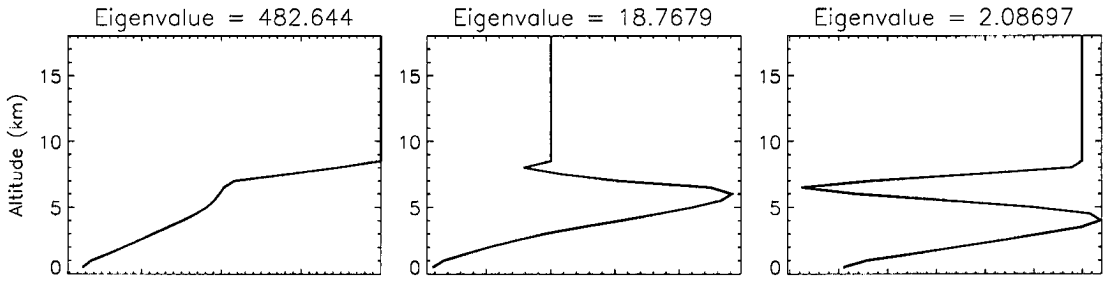

Figure 2.20: As in Figure 2.19 but at a rainrate of 5 mmh^{-1}.

nant orthonormal weighting functions. The first has a broad peak between 4 km and the surface while the second has a peak at 5 km. The structure of these weighting functions suggests that all liquid water below 5 km has some influence on the radiation measured by the TMI. As rainrate increases the number of significant orthonormal weighting functions increases and the individual peaks in the weighting functions become sharper indicative of the increased sensitivity of specific channels to specific levels in the atmosphere. In general, more levels contribute to the overall TMI T_B signature and the levels with the most

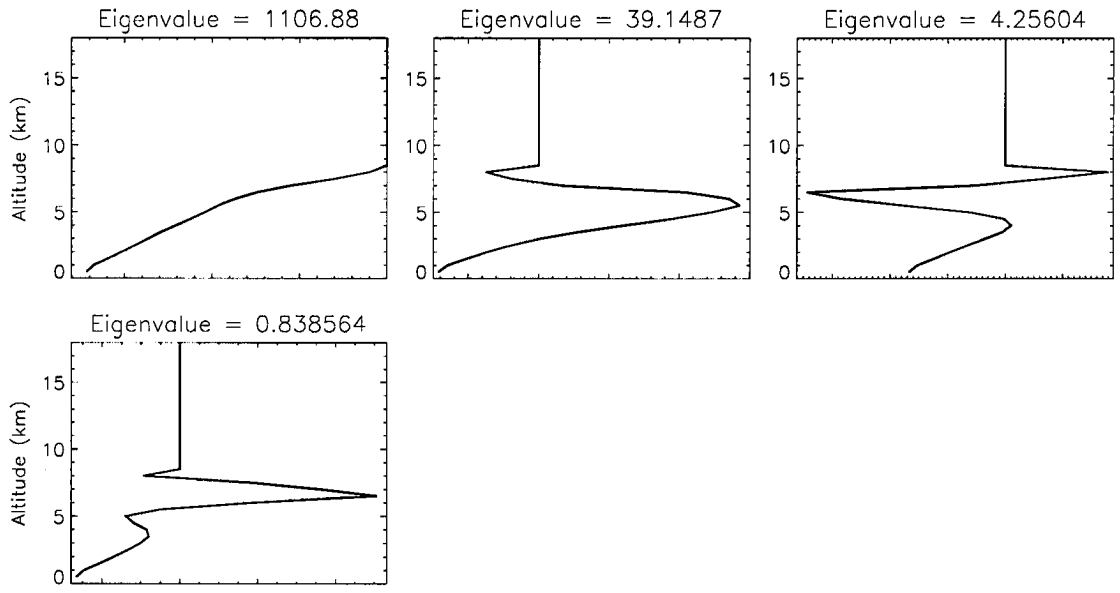

Figure 2.21: As in Figure 2.19 but at a rainrate of 20 mmh^{-1}.

influence rise in the atmosphere as rainrate increases consistent with the trends in both the information content, Figure 2.17, and the effective level of emission, Figure 2.11.

Corresponding weighting functions over a land background are plotted in Figures 2.22-2.24. At all rainrates the dominant weighting function exhibits a negative sensitivity to the

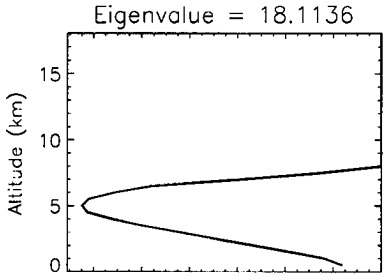

Figure 2.22: Significant orthonormal weighting functions for retrieving liquid water profiles at a rainrate of 0.5 mmh^{-1} over a land background.

liquid water content which sharpens and shifts slightly towards cloud top with increasing rainrate highlighting the fact that scattering is the dominant mechanism influencing the TMI T_B signature over land. At very low rainrate scattering uniquely provides the entire

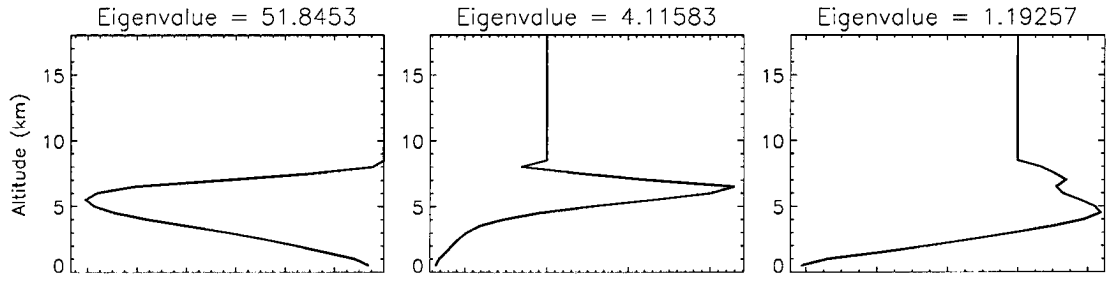

Figure 2.23: As in Figure 2.22 but at a rainrate of 5 mmh^{-1}.

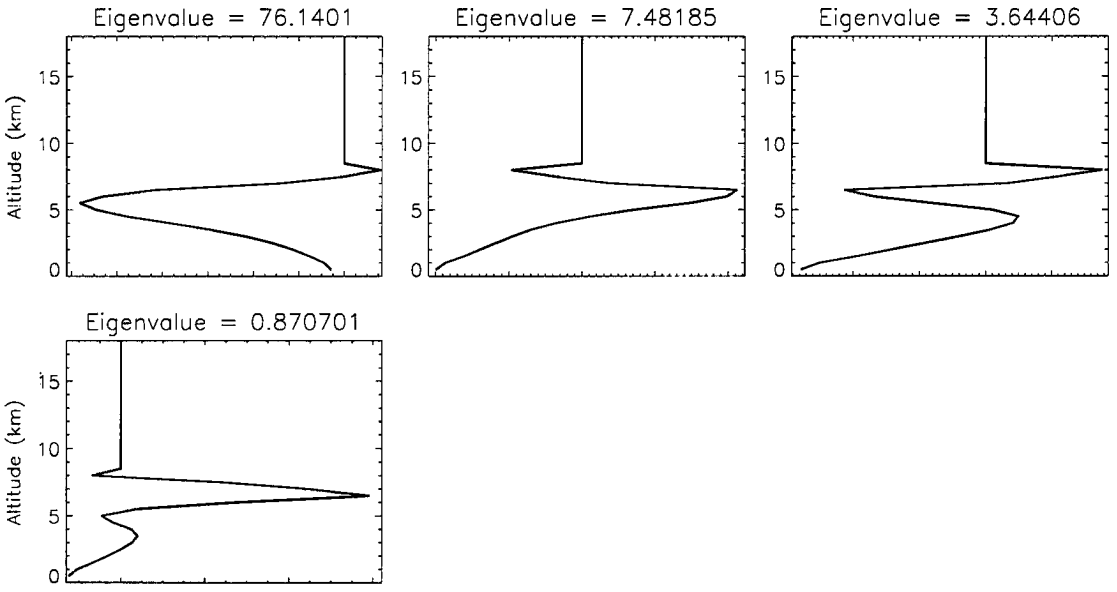

Figure 2.24: As in Figure 2.22 but at a rainrate of 20 mmh^{-1}.

signal but at higher rainrates positive sensitivity peaks are evident resulting from saturation of the higher frequency channels. At very high rainrate all TMI channels are primarily sensitive to the cloud column itself masking surface characteristics as is evidenced by the fact that the orthonormal weighting functions over land and ocean backgrounds are more or less identical at a rainrate of 20 mmh^{-1}.

Conclusions can also be made regarding ice water retrievals based on orthonormal weighting functions presented in Figures 2.25 and 2.26. Regardless of the surface rainfall rate, the ice information in the TMI comes from a broad layer between 5 and 11km with

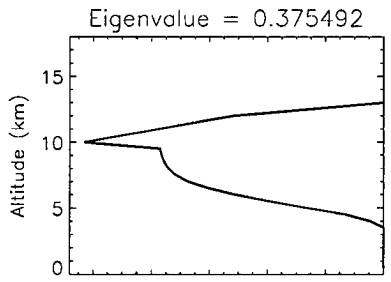

Figure 2.25: Statistically significant orthonormal weighting functions for retrieving ice water profiles at a rainrate of 2.0 mmh^{-1} over an ocean background.

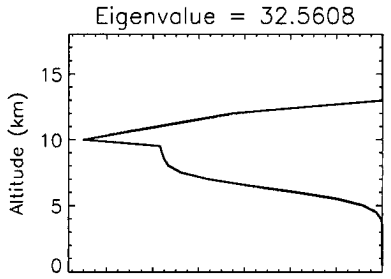

Figure 2.26: As in Figure 2.25 but at a rainrate of 20 mmh^{-1}.

a peak at 10km. The only exception is below 1.5 mmh^{-1} where there the TMI contributes no statistically significant ice water content information to the retrieval. The shape of the weighting function is independent of surface rainrate, confirming the fact that the TMI primarily provides a single piece of ice information related to the ice water path through the cloud.

These results highlight the important fact that, at most rainrates, the TMI exhibits some sensitivity to cloud water throughout the atmospheric column rather than just the rainfall near the surface. For rainrates less than 1 mmh^{-1} the TMI channels are strongly influenced by the emission properties of the surface. At higher rainrates, however, the cloud at higher levels of the atmosphere significantly impacts observed T_Bs emphasizing the need for explicit cloud profile information in passive microwave rainfall retrievals, a fact which is overlooked in many empirical algorithms.

2.6 The Issue of Non-uniqueness

Many retrievals are predicated on a quasi-unique relationship between measured T_Bs and the quantities to be retrieved. This is true of most rainfall and cloud/ice water content retrievals and is one of the key assumptions made in the preceeding sections. Unlike quantitative retrievals, the results of this chapter are primarily of a qualitative nature and we believe are still useful but we would be remiss if we didn't acknowledge the potentially far-reaching consequences of this assumption.

Figure 2.27 presents a scatter plot of TMI T_Bs as a function of rainrate for all cloud profiles in the database used in the GPROF surface rainrate and cloud profile retrieval for the TRMM mission. A cursory glance at this figure immediately reveals that, although the points exhibit the same general trend with increasing rainrate, the smooth T_B-rainrate relationship implied by Figure 2.6 is a highly idealized assumption. In reality TMI T_Bs result from the interaction of radiation with extremely complex and diverse cloud structures which depend on the specific atmospheric conditions under which the cloud was formed and evolved. This diversity results in a non-unique relationship between T_B signatures and near-surface rainrate, a problem inherent in all rainrate retrievals regardless of their level of sophistication.

The results presented here represent an idealized scenario and provide an upper bound on the information provided by the TMI instrument. Some rainfall systems, for example, are dominated by warm-rain microphysics in which rainfall is primarily created through collision and coalescence of liquid droplets rather than through the melting of ice. In this case information from ice scattering is lost reducing the number of independent pieces of information in the retrieval. Also, by virtue of its large footprint, the TMI instrument is susceptible to the effects of non-uniform beamfilling (NUBF) (Kummerow, 1998). The different cloud structures implied in Figure 2.6 will introduce similar scatter in the weighting functions of each TMI channel. Operationally, the TMI weighting functions will be

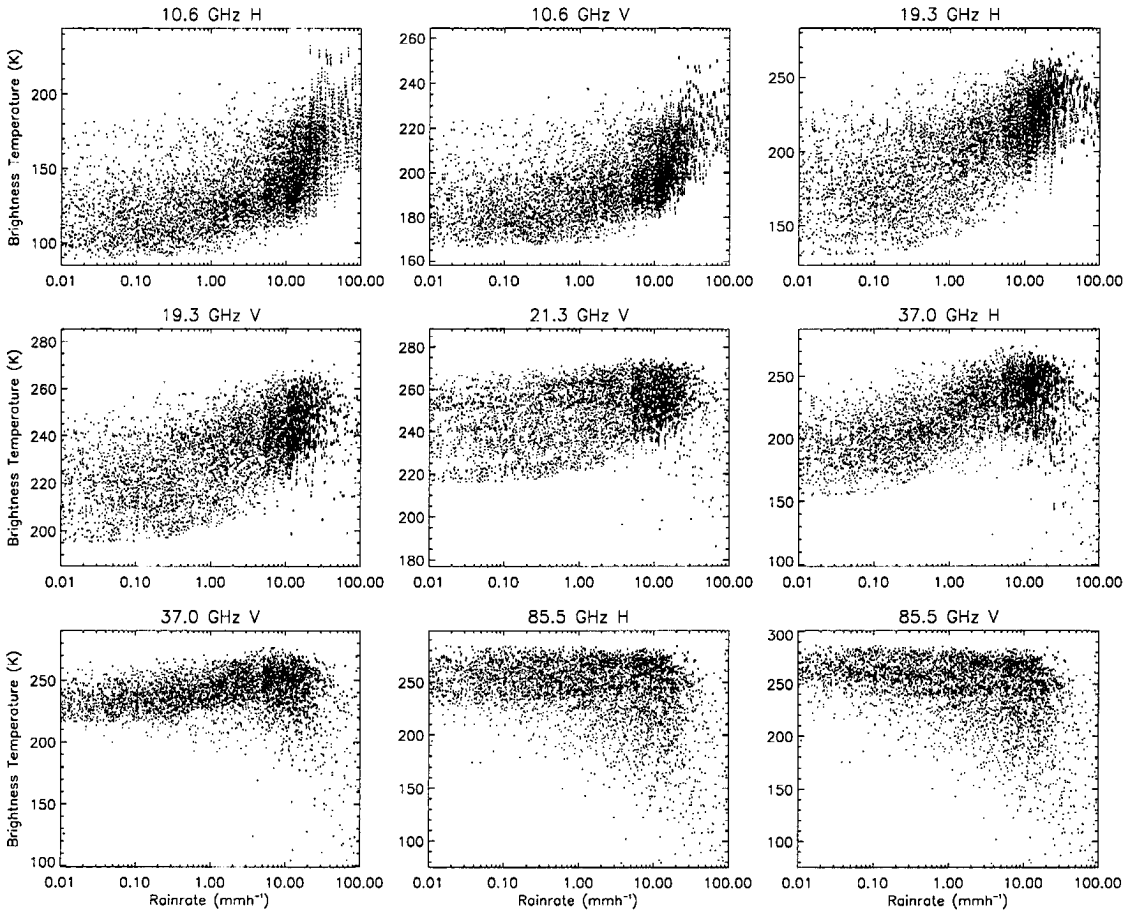

Figure 2.27: Scatter plots of TMI T_Bs as a function of rainrate for the entire GPROF database.

broader and weaker than those used in this chapter due to spatial averaging over the footprints in each channel. The increased overlap which results further reduces the amount of independent information contained in the TMI measurements.

The approach that has been adopted by Kummerow et al. (1996) in the GPROF algorithm to resolve this problem is to perform a weighted average of all cloud profiles in the database whose T_B signatures resemble those observed. While recognizing and attempting to account for indistinguishability between cloud profiles, this approach runs the risk of incurring large uncertainties resulting from the averaging process as we will see in the next chapter. We suggest that a more direct approach to resolving the non-uniqueness is-

sue might be to use radar reflectivities from the PR or a cloud profiling radar such as that which will be launched on CloudSat in the future to constrain the cloud profile. Since the TMI channels are quite sensitive to the cloud constituents at a variety of atmospheric levels over a wide range of surface rainrates, it is reasonable to conjecture that cloud profile information represents a strong candidate for significantly reducing indistinguishability.

2.7 Discussion

Through the use of a conceptually simple analysis of the principal components of the TMI measurements, the number of independent pieces of information contained in the data has been determined as a function of rainrate. The retrievable range of rainrates can be broken down into three regions:

- Low rainrates between 0.25 and 6 mmh^{-1} (1.5 and 4.5 mmh^{-1} over land). Here the instrument is most sensitive to the rain nearest the surface but exhibits slight sensitivity to the cloud above it.

- Moderate rainrates between 6 and 25 mmh^{-1} (4.5 and 18 mmh^{-1} over land). This is the ideal range of rainfall for algorithms which estimate surface rainfall and cloud profiles simultaneously since the instrument is sensitive to both the surface as well as a number of layers within the cloud.

- High rainrates above 25 mmh^{-1} (18 mmh^{-1} over land). Intense rainfall and the copious amount of ice which often overly it prevent all TMI channels from viewing the surface. At these rainrates, limited cloud profiling is possible but the surface rainrate must be inferred from the liquid and ice water at upper levels.

In the low rainrate region, cloud profiles impact the retrieval but the TMI instrument is likely not sensitive enough to retrieve profiles of cloud-sized liquid and ice particles without the aid of additional information. This is the region in which all TMI-only rainfall

retrieval algorithms will suffer the largest uncertainties due to cloud profile effects regardless of whether or not they attempt to retrieve cloud structure. At moderate rainrates more sophisticated algorithms should perform more accurately since the TMI channels carry information necessary to retrieve a full rainfall profile as well as an estimate of the column ice water content in addition to the surface rainrate. Finally, in heavy rain, the TMI does not directly sense the lowest levels of the atmosphere or surface at all. Surface rainfall estimates under such conditions require an explicit relationship between hydrometeor concentration and size within the cloud and rainfall at the surface.

It is important to note that in addition to the TMI, the TRMM satellite carries both the PR and the visible/infrared sounder (VIRS). Both instruments offer additional, possibly complementary information to the TMI. It may be possible, for example, to use the VIRS measurements to help overcome some of the difficulties encountered when using TMI measurements alone at low rainrates. At higher rainrates the PR will undoubtedly add additional information regarding near-surface rainrates and hydrometeor profiles but exactly how much information remains a topic for future study. Also, in the near future the combination of the Advanced Microwave Scanning Radiometer (AMSR-E) onboard the Earth Observing System (EOS) Aqua satellite and the 94 GHz Cloud Profiling Radar (CPR) flown on the CloudSat satellite will provide an opportunity to examine the possibility of constraining passive microwave retrievals with explicit cloud profile information. The method described here provides a useful diagnostic tool to study these and alternate combinations of instruments and channels to assess the best possible set for future rainfall estimation applications.

While we have determined the extent to which the TMI measurements provide liquid and ice profile information, it is still unclear exactly how this information (or lack-thereof) impacts uncertainties in retrievals and, in turn, applications which make use of their products. The next chapter seeks to address these questions through detailed analy-

sis of quantitative estimates of the uncertainty in GPROF cloud and precipitation profiles. Once established, these uncertainties provide a foundation to scrutinize the capability of current passive microwave observing systems for determining atmospheric heating as well as infering alternative sources of information to improve upon them.

Chapter 3

Uncertainties in the GPROF Precipitation and Cloud Profile Retrieval Algorithm

In principle one can infer any physical parameter(s) from any observation(s) as long as a model exists which describes the "mapping" of the parameter space into the observation space. Provided the model can be "inverted" to describe the reverse mapping from the observation space to the parameter space, it is possible to estimate the parameter(s) which gave rise to any given set of observation(s). The quality of the estimate depends on a number of factors including the quality of both the model and the method used to invert it. In a good retrieval the observations should be strongly dependent on the parameters being retrieved, should contain sufficient information to unambiguously categorize them, and must be suitably mapped into the retrieval parameter space by the model.

As an example, consider two techniques for determining the mass of an automobile. The first uses a spring scale and is based on a relation between the car's mass and the compression of four springs, δx. If the springs are characterized by spring constant k the mass can be determined through direct inversion of $mg = 4k\delta x$. The second uses a model based on a detailed compilation of statistics relating a car's mass to the color of the fuzzy dice hanging from its mirror. While there may be some evidence from a long-lost psychological experiment that the owners of smaller cars are in some way predisposed to hang blue dice, one would probably be more inclined to trust the result obtained by the first method than that of the second.

Our simple example illustrates the following crucial yet frequently overlooked fact: often the result is not as difficult to obtain as a complete understanding of its significance

since a detailed knowledge of all sources of uncertainty are required for the latter. In this case, the uncertainty in the first method can be directly estimated as it depends only upon the accuracy with which we can determine the spring constant, the compression distance of the springs, and the acceleration due to gravity, g. Besides our common sense, however, we have no way of determining the validity of the estimate produced using the second method without additional information such as the size of the sample used in deriving the model and the variance of its distribution about the mean.

Passive microwave retrievals of rainfall fall somewhere between these two extremes. Microwave brightness temperatures are more sensitive to the profiles of rainfall than the color of fuzzy dice is to the mass of a car but the relationship is not as well defined as that between the compression of a spring and the force that was exerted upon it. While sensitivity to the profile of liquid and frozen hydrometeors throughout the atmospheric column is useful in profiling applications, the complex physical processes involved in the exchange of radiation between its various levels invariably leads to a high degree of non-uniqueness in retrieval algorithms since, in principle, an infinite number of different combinations of rain, cloud liquid, cloud ice, hail, graupel and snow hydrometeors can give rise to very similar brightness temperature signatures. In this chapter our goal will be to quantify the uncertainty of passive microwave precipitation and cloud profile retrievals, explicitly accounting for the effects of non-uniqueness, through a detailed analysis of the TMI-based GPROF algorithm. The preceding chapter has furnished us with an understanding of the information contained in the TMI radiances, the next step is to determine how well the GPROF algorithm makes use of this information in estimating rainfall. An abridged version of this chapter has been summarized in a paper entitled "An Uncertainty Model for Bayesian Monte Carlo Retrieval Algorithms: Application to the TRMM Observing System" submitted to *The Quarterly Journal of the Royal Meteorological Society.*

3.1 Why GPROF?

Numerous algorithms for retrieving rainfall from passive microwave radiances have been introduced and employed with varying degrees of success in the past 25 years. Early results from Wilheit et al. (1977), Wilheit and Chang (1980), Spencer et al. (1983), and Wilheit (1986), for example, provided clear evidence for the existence of a rainfall signature in passive microwave radiances. Since then a variety of algorithms of varying complexity have been proposed to make use of this signature to estimate rainfall. All of these techniques are based on the same physical principles and all suffer from some degree of non-uniqueness even though very distinct models employing different information are used by each.

Researchers have classified these algorithms according to a variety of criteria such as one proposed by Petty (1994b) which defines all algorithms as statistical, empirical, or physically-based. For our purposes it is instructive to classify all algorithms into two categories depending on whether they implicitly or explicitly account for cloud profile information. Statistical and empirical algorithms such as those proposed by Spencer (1986), Spencer et al. (1989), Petty and Katsaros (1990), Grody (1991), Prabhakara et al. (1992), Liu and Curry (1992), Ferriday and Avery (1994), Li et al. (1996), Kidd (1998), and Prabhakara et al. (1998) fall into the first category. Despite being diverse in their approaches, each is fundamentally based on a relationship between surface rainfall and one or more microwave brightness temperatures or parameters derived from them. Implicit in these algorithms is some assumption of the vertical profiles of scattering and emission from liquid and ice hydrometeors above the surface. While they provide computationally simple methods for determining surface rainfall rate which can be quite useful on regional scales, these algorithms can seldom be applied globally without modifications to the coefficients to reflect regional changes in the microphysical processes responsible for the rainfall.

Despite using a more sophisticated iterative inversion scheme, the algorithm presented in the afore mentioned paper by Petty (1994b) is classified the same way as the statistical

and empirical algorithms. It relies on simple analytical relations involving total cloud optical depth which are computationally efficient but lack the rigor of full radiative transfer calculations and are still, therefore, susceptible to biases incurred as a result of incorrect microphysics. Through the use of polarization and scattering indices (described below), however, Petty's algorithm significantly reduces errors associated with modeling surface emission and, as such, should be considered as an improvement over the other algorithms.

To overcome the difficulties faced by the first class of algorithms, there has been a shift towards more sophisticated algorithms which explicitly account for the effects of different microphysics in the last decade or so. Algorithms such as those by Kummerow and Giglio (1994a,b), Smith et al. (1994a,b) and Aonashi et al. (1996), for example, perform radiative transfer calculations through explicitly defined profiles of cloud and precipitation to develop more complete ensembles of passive microwave brightness temperatures to better represent the variety of microphysical processes present on global scales. As we found in the previous chapter all passive microwave sensors are limited in the number of independent pieces of information they provide with regards to cloud and precipitation profiles so these algorithms only partially resolve the problems inherent in the simpler ones, still suffering from non-uniqueness caused by the inability to adequately distinguish all profiles using passive microwave radiances alone.

Since our focus has been the TRMM platform, it is logical to examine the GPROF algorithm. Furthermore, as stated above, GPROF and similar algorithms by Smith et al. (1994b) and Haddad et al. (1997)[1], use a Bayesian Monte Carlo (BMC) retrieval technique which explicitly accounts for the physical interactions between microwave radiation and realistic profiles of cloud and precipitation generated using a CRM. These algorithms are representative of the current "state-of-the-art" in passive microwave retrievals and will likely be used in future missions such as the EOS Aqua satellite or the proposed GPM. Also, its

[1]The algorithm of Haddad et al. (1997) makes use of a combination of radar and passive microwave data and is not, therefore, strictly a passive microwave algorithm but it employs a very similar technique for inversion and deserves to be acknowledged in this class of retrieval.

Bayesian formulation allows for rigorous uncertainty analyses of all retrieved parameters.

Finally, the TRMM data provide the most comprehensive set of tropical cloud and precipitation information available to date. As a result they have been used in a number of preliminary data assimilation studies (eg. Hou et al. (2000a,b) and Marécal and Mahfouf (2000)) and will be used in estimating profiles of radiative and latent heating in Chapter 5. Rigorous uncertainty estimates in the GPROF products are, therefore, of critical importance to the data assimilation community as well as in establishing error bounds on estimates of radiative and latent heating profiles.

Below, the underlying theoretical and practical considerations which form the basis of a comprehensive yet conceptually lucid technique for evaluating the overall uncertainty in the GPROF precipitation/cloud profile retrieval algorithm are presented. From these arguments, a method will be constructed to assess the accuracy of the GPROF retrieval scheme. Uncertainties associated with the individual elements of the retrieval process will be examined in detail as well as the way in which these components mix, through the retrieval process, to produce errors in the resulting precipitation and cloud profile estimates.

3.2 The Goddard Profiling Algorithm

The Goddard Profiling Algorithm (GPROF), outlined in Kummerow and Giglio (1994a) is performed in three steps. First, a large number of cloud profiles are simulated using the GCE CRM (for a description of the GCE model see Tao and Simpson (1993); Simpson and Tao (1993)). These profiles are then used as input to a radiative transfer model and a set of simulated observations are computed for each TMI channel.

All profiles and their corresponding simulated observations are then combined to form a very large database of scenes which the TRMM satellite may observe as it orbits the globe. The retrieval proceeds by assigning a weight to each profile in the database depending on how closely the modeled or simulated measurements match those observed by the satellite

at a given location. The final retrieved profile is a weighted sum of all the profiles in the database. This procedure is illustrated in the flow-chart in Figure 3.1.

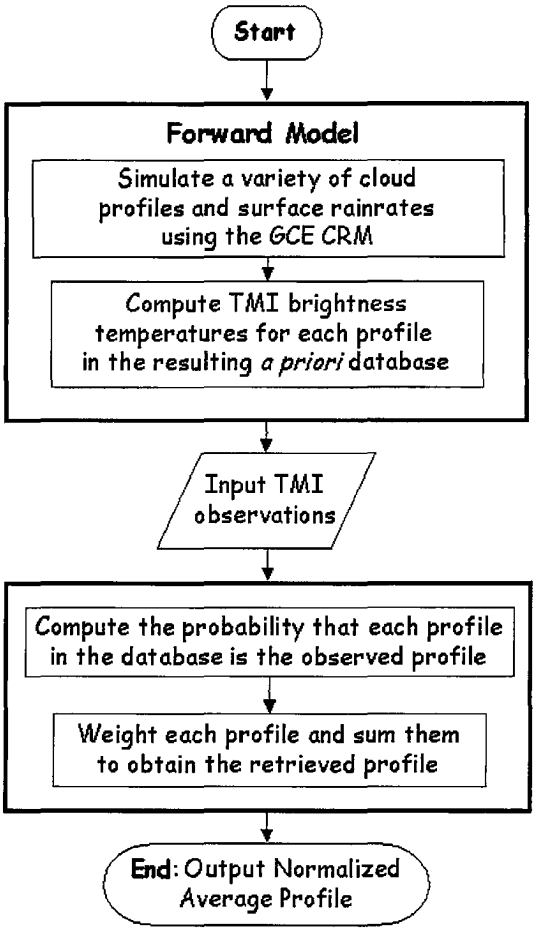

Figure 3.1: Flow chart representation of the 2A12 retrieval algorithm.

Let $\mathbf{x}$ be a vector of all physical quantities to be retrieved including vertical profiles of cloud particles and precipitation and let $\mathbf{y}_o$ be a vector of satellite observations. The 'best estimate' of $\mathbf{x}$ for a given set of measurements is found by evaluating

$$\hat{E}(\mathbf{x}) = \int \int \cdots \int \mathbf{x}\, pdf(\mathbf{x}) d\mathbf{x} \tag{3.1}$$

Following Olson et al. (1996), the probability density function, $pdf(\mathbf{x})$, is proportional to

the probability that $\mathbf{x}$ is the true profile, $\mathbf{x}_{true}$, given that $\mathbf{y}$, the simulated observation vector corresponding to profile $\mathbf{x}$, is equal to the observed $\mathbf{y}_o$,

$$pdf(\mathbf{x}) \propto P\left(\mathbf{x} = \mathbf{x}_{true} \mid \mathbf{y} = \mathbf{y}_o\right) \tag{3.2}$$

Employing Bayes' theorem, the probability $P(\mathbf{x} = \mathbf{x}_{true} \mid \mathbf{y} = \mathbf{y}_o)$ can be re-cast as a product of the probability that the set of simulated observations, $\mathbf{y}_s$, deviate from the TMI observations, $\mathbf{y}_o$, by a given amount, $P_{OS}(\mathbf{y} - \mathbf{y}_s)$, and the *a priori* probability that $\mathbf{x}$ is the true cloud profile, $P_a(\mathbf{x}) = P(\mathbf{x} = \mathbf{x}_{true})$. Provided the uncertainties in the observed and simulated measurements are Gaussian and uncorrelated, then

$$P_{OS}(\mathbf{y} - \mathbf{y}_s) \propto e^{-\frac{1}{2}[\mathbf{y}_o - \mathbf{y}_s(\mathbf{x}_j)]^T (\mathbf{O}+\mathbf{S})^{-1} [\mathbf{y}_o - \mathbf{y}_s(\mathbf{x}_j)]} \tag{3.3}$$

where $\mathbf{O}$ is the error covariance matrix of the observations and $\mathbf{S}$ is the error covariance matrix of the simulated observations which includes uncertainties due to both the cloud model and the radiative transfer model. The representation for the simulated observations, $\mathbf{y}_s(\mathbf{x})$, denotes all model calculations necessary to "map" a realization into the vector space of the observations. Substitution of Eqn. (3.3) into Eqn. (3.1) yields the following equation for the expected value of $\mathbf{x}$

$$\hat{E}(\mathbf{x}) = \frac{1}{A} \int \int \cdots \int \mathbf{x}\, e^{-\frac{1}{2}[\mathbf{y}_o - \mathbf{y}_s(\mathbf{x}_j)]^T (\mathbf{O}+\mathbf{S})^{-1} [\mathbf{y}_o - \mathbf{y}_s(\mathbf{x}_j)]} P_a(\mathbf{x}) d\mathbf{x} \tag{3.4}$$

where A is a normalization factor given by

$$A = \int \int \cdots \int e^{-\frac{1}{2}[\mathbf{y}_o - \mathbf{y}_s(\mathbf{x}_j)]^T (\mathbf{O}+\mathbf{S})^{-1} [\mathbf{y}_o - \mathbf{y}_s(\mathbf{x}_j)]} d\mathbf{x} \tag{3.5}$$

In general, all retrieval algorithms which derive from the application of Bayes' theorem in this way can be referred to as "Bayesian".

One method of evaluating Eqn. (3.4) is that of Rodgers (1976,1990) in which P_a is re-expressed in terms of the probability that $\mathbf{x}$ deviates from some initial guess $\mathbf{x}_i$, $P_i(\mathbf{x} - \mathbf{x}_i)$. One can then show that, provided $P_i(\mathbf{x} - \mathbf{x}_i)$ is Gaussian, the maximum likelihood and minimum variance solutions are identically given by the profile, $\mathbf{x}$, which minimizes the cost function

$$J(\mathbf{x}) = [\mathbf{y}_o - \mathbf{y}_s(\mathbf{x}_j)]^T (\mathbf{O} + \mathbf{S})^{-1} [\mathbf{y}_o - \mathbf{y}_s(\mathbf{x}_j)] + (\mathbf{x} - \mathbf{x}_i)^T \mathbf{I}^{-1} (\mathbf{x} - \mathbf{x}_i) \qquad (3.6)$$

where $[\mathbf{I}]$ is the error covariance matrix of the initial guess $\mathbf{x}_i$ (Daley, 1991). The minimum is then found using an iterative minimization approach such as the steepest descent method. This method is often referred to as "optimal estimation".

In atmospheric applications, the vector of retrieved parameters can be extremely large (in cloud and rainfall profile retrievals, for example, a hundred or more variables is not uncommon and in operational data assimilation the vector can approach 10^7 variables). Under these circumstances, methods which solve Eqn. (3.4) through the minimization of a cost function can be impractical since they require an enormous amount of computation and suffer from the fact that numerous minima exist due to non-linearities in the problem. Finally, the assumption that $P_i(\mathbf{x} - \mathbf{x}_i)$ is Gaussian may be suspect since the vector $\mathbf{x}$ is composed of hydrometeor water contents which generally follow a log-normal distribution Kedem et al. (1994).

As a result a significantly different approach to the problem of determining the best-estimate profile is adopted for the GPROF retrieval. This approach, still rooted in Bayes Theorem, utilizes a Monte Carlo integration scheme in which the integral in Eqn. (3.4) is approximated by a weighted summation over a large number of cloud profiles computed in advance using the GCE model. The surface precipitation rate, vertical cloud hydrometeor

profiles, surface wind speed, etc. are estimated by evaluating

$$\hat{E}(\mathbf{x}) = \frac{1}{\hat{A}} \sum_j \mathbf{x}_j e^{-\frac{1}{2}[\mathbf{y}_o - \mathbf{y}_s(\mathbf{x}_j)]^T (\mathbf{O}+\mathbf{S})^{-1} [\mathbf{y}_o - \mathbf{y}_s(\mathbf{x}_j)]} \tag{3.7}$$

where

$$\hat{A} = \sum_j e^{-\frac{1}{2}[\mathbf{y}_o - \mathbf{y}_s(\mathbf{x}_j)]^T (\mathbf{O}+\mathbf{S})^{-1} [\mathbf{y}_o - \mathbf{y}_s(\mathbf{x}_j)]} \tag{3.8}$$

is a normalization constant. Eqn. (3.7) represents a series of equations for each parameter in $\mathbf{x}$. After appropriate weights have been determined for each profile, all desired cloud parameters are estimated by computing the weighted sum. We refer to this approach as the Bayesian Monte Carlo (BMC) approach to the retrieval problem.

Implicit in this method of inversion is the assumption that the cloud profile database represents, with some accuracy, the actual probability density function of clouds in nature. Under this assumption the *a priori* probability, P_a, is replaced by the number of occurances of the given cloud profile in the database. Determining the validity of this assumption is a complicated issue but clearly extremely important since it is the foundation upon which the retrieval is based.

Until now no requirements have been made regarding the vector of observations, $\mathbf{y}$. The output from the forward radiative transfer model and the instruments on the satellite is generally cast in the form of upwelling radiances or brightness temperatures at the top of the atmosphere. It is possible to use these T_Bs directly in the retrieval but such an approach suffers from the fact that T_Bs do not vary monotonically with rainrate and are complicated by the effects of surface emission and water vapor emission within the atmospheric column. In an effort to reduce these problems, the GPROF algorithm adopts the emission and scattering indices introduced by Petty and Katsaros (1990) and Petty (1994a)

$$P = \frac{T_{B_V} - T_{B_H}}{T_{B_{V,0}} - T_{B_{H,0}}} \tag{3.9}$$

$$S = PT_{B_{V,0}} + (1 - P)T_c - T_{B_V} \tag{3.10}$$

where $T_c = 273$K. T_{B_V} and T_{B_H} are the horizontally and vertically polarized brightness temperatures and $T_{B_{V,0}}$ and $T_{B_{H,0}}$ are the corresponding brightness temperatures in the absence of cloud or precipitation. In addition to effectively separating out the effects of emission, which dominates P, and scattering, which dominates S, P monotonically decreases from 1 to 0 as rainrate increases and the influence of surface emission and column water vapor are significantly reduced by the presence of the ratio. In determining the weights, GPROF uses emission indices for all four dual polarization TMI channels and scattering indices at 37 and 85 GHz since the effects of scattering are generally small at low frequency. The uncertainty analysis which follows will assume this basis and the results will be compared to those obtained using raw T_Bs to quantify the differences in accuracy in using each method.

3.3 Overall Uncertainty

Rodgers (1976, 1990) and Marks and Rodgers (1993) have presented an elegant approach to the analysis of uncertainty associated with optimal estimation retrievals. As noted in the previous section, however, the method used here deviates substantially from that outlined by Rodgers and, as a result, an entirely different approach to the error analysis problem must be adopted to estimate the uncertainty associated with the GPROF product. Thacker (1989) demonstrates how the inverse of the Hessian matrix can be viewed as the covariance matrix provided a least-squares approach is used in the retrieval and Gaussian statistics have been assumed. The BMC algorithm, however, does not involve minimizing a cost function and does not assume Gaussian statistics so the Hessian does not provide a complete representation of the uncertainty in the retrieved quantities. The complete forward model in a

BMC approach must be thought of as consisting of both the radiative transfer model and the cloud database itself. To characterize the overall uncertainty in the retrieved quantities one must consider the impact of uncertainties in both of these elements as well as the observations themselves. In this section we seek to develop such a characterization by returning to the definition of the solution $\hat{E}(\mathbf{x})$.

Consider Eqn. (3.7) in the form

$$\hat{E}(\mathbf{x}) = \frac{\sum_j \mathbf{x}_j W_j}{\sum_j W_j} \tag{3.11}$$

Ignoring the specific elements which go into the computation of the W_j, $\hat{E}(\mathbf{x})$ is composed of two distinct quantities, the profile vectors $\mathbf{x}_j$ and their weights, W_j. Assuming the uncertainties associated with these quantities can be estimated, standard error combination theory[2] can be used to show that the uncertainty in the product of profile $\mathbf{x}_j$ with it's weight W_j is

$$\delta\left(\mathbf{x}_j W_j\right) = \sqrt{\left(W_j \delta \mathbf{x}_j\right)^2 + \left(\mathbf{x}_j \delta W_j\right)^2 + \mathbf{x}_j W_j \delta_{\mathbf{x}_j W_j}} \tag{3.12}$$

where $\delta_{\mathbf{x}_j W_j}$ is the estimated error covariance of the 'measurements' $\mathbf{x}_j$ and W_j. Similarly, following Section A.1, the uncertainty associated with the summation of j such products is

$$\delta\left(\sum_j \mathbf{x}_j W_j\right) = \sqrt{\sum_j \left[\left(W_j \delta \mathbf{x}_j\right)^2 + \left(\mathbf{x}_j \delta W_j\right)^2 + \mathbf{x}_j W_j \delta_{\mathbf{x}_j W_j}\right] + \sum_j^{j_{max}-1} \sum_{k=j+1}^{j_{max}} \delta_{jk}} \tag{3.13}$$

where δ_{jk} represents the error covariance of $(\mathbf{x}_j W_j)$ and $(\mathbf{x}_k W_k)$ and j_{max} is the total number of profiles in the summations of Eqn. (3.11). Finally, the uncertainty associated with

[2]Appendix A discusses standard methods for the estimation of the combined uncertainty associated with various combinations of variables.

the denominator of Eqn. (3.11) is

$$\delta\left(\sum_j W_j\right) = \sqrt{\sum_j (\delta W_j)^2 + \sum_j^{j_{max}-1} \sum_{k=j+1}^{j_{max}} \delta_{W_j W_k}} \tag{3.14}$$

where $\delta_{W_j W_k}$ is the error covariance of the weights W_j and W_k.

Making use of the uncertainty in a quotient evaluated in Section A.3, the overall uncertainty in $\hat{E}(\mathbf{x})$ is

$$\frac{\delta\hat{E}(\mathbf{x})}{\hat{E}(\mathbf{x})} = \sqrt{\frac{\sum_j \left[(W_j\delta\mathbf{x}_j)^2 + (\mathbf{x}_j\delta W_j)^2 + \mathbf{x}_j W_j \delta_{\mathbf{x}_j W_j}\right] + \sum_j^{j_{max}-1}\sum_{k=j+1}^{j_{max}} \delta_{jk}}{\left(\sum_j \mathbf{x}_j W_j\right)^2}}$$
$$+ \sqrt{\frac{\sum_j (\delta W_j)^2 + \sum_j^{j_{max}-1}\sum_{k=j+1}^{j_{max}} \delta_{W_j W_k}}{\left(\sum_j W_j\right)^2} - \frac{\delta_{nd}}{\left(\sum_j \mathbf{x}_j W_j\right)\left(\sum_j W_j\right)}} \tag{3.15}$$

where the correlation in errors between the numerator and denominator is represented by δ_{nd}.

Although, Equation (3.15) is the most general expression of the uncertainty in $\hat{E}(\mathbf{x})$, it is complicated and difficult to apply in practice. In fact it is rendered completely useless if one is unable to estimate the somewhat abstract covariances needed. In light of these problems it is instructive to look at a special case of Eqn. (3.15) in which all uncertainties are assumed uncorrelated. In this case δ_{nd}, $\delta_{\mathbf{x}_j W_j}$, $\delta_{W_j W_k}$, and δ_{jk} vanish yielding:

$$\frac{\delta\hat{E}(\mathbf{x})}{\hat{E}(\mathbf{x})} = \sqrt{\frac{\sum_j \left[(W_j\delta\mathbf{x}_j)^2 + (\mathbf{x}_j\delta W_j)^2\right]}{\left(\sum_j \mathbf{x}_j W_j\right)^2} + \frac{\sum_j (\delta W_j)^2}{\left(\sum_j W_j\right)^2}} \tag{3.16}$$

This result represents a first-order approximation to the overall uncertainty in $\hat{E}(\mathbf{x})$.

Equation (3.16) demonstrates that the overall uncertainty in a BMC retrieval consists

of two factors. The first component,

$$\frac{\sum_j \left(\mathbf{x}_j \delta W_j\right)^2}{\left(\sum_j \mathbf{x}_j W_j\right)^2} + \frac{\sum_j \left(\delta W_j\right)^2}{\left(\sum_j W_j\right)^2} \tag{3.17}$$

derives from uncertainty in computing the weights assigned to each realization while the second

$$\frac{\sum_j \left(W_j \delta \mathbf{x}_j\right)^2}{\left(\sum_j \mathbf{x}_j W_j\right)^2} \tag{3.18}$$

accounts for the impact of the finite cloud database and the non-uniqueness of the constituent realizations on the retrieval error. Eqn. (3.16), therefore, establishes a means of determining the dominant source of uncertainty in the retrieval as well as the value of the uncertainty itself. This error breakdown is depicted graphically in Figure 3.2.

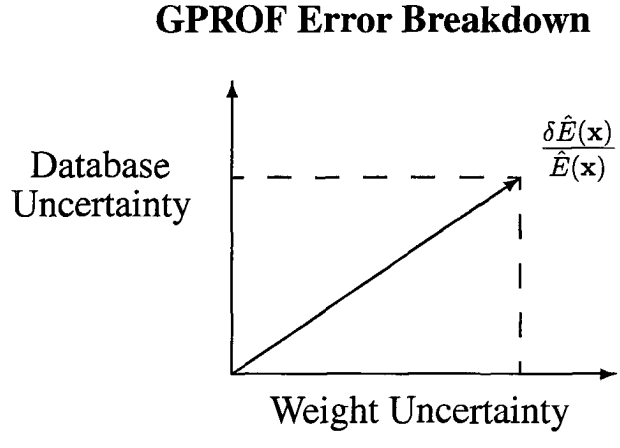

Figure 3.2: Reconstruction of the retrieval error from it's two components, the uncertainty associated with calculating the weights and that due to the cloud database.

Whether or not Eqn. (3.16) provides a reasonable estimate of the uncertainty in the retrieved profile is a point which requires careful consideration. Omitted from the math-

ematical details above is the physics behind the creation of the cloud profiles themselves. It turns out that all profiles originate from results of only a handful of separate runs of the GCE model. Three dimensional cloud profiles are extracted at different times during each run. This inevitably results in the errors introduced within the cloud model being propagated along in time from one profile to the next therefore introducing a correlation between the uncertainties in profiles taken from different times in the simulation. Also, since the profiles are spatially linked, i.e. the profile at horizontal grid point (x, y) shares boundaries with eight neighboring profiles, we expect correlations amongst the uncertainties of all neighboring cloud profiles extracted at a given time. In addition, for each profile a number of T_B profiles are generated by varying the properties of the underlying surface. The uncertainties in these T_B profiles must, therefore, also be correlated.

At first these considerations seem somewhat discouraging. As we will see shortly, however, due to the nature of the retrieval itself, uncertainties associated with the cloud model are actually not really important to the accuracy of the retrieval. In preparing a cloud database, the issue of primary importance concerns how well the database represents the distribution of clouds in nature. Whether or not the cloud model accurately reproduces the cloud profiles for the case being simulated is actually quite irrelevant as far as the retrieval is concerned. We merely require that it produce a variety of physically reasonable cloud structures, the distribution of which resembles the observed distribution of clouds in nature. As a result, it seems reasonable to neglect the uncertainty associated with the cloud model itself and assume that the covariance matrix $\mathbf{S}$ arises solely from errors associated with the radiative transfer model. Biases introduced as a result of incorrect representations of microphysics in the CRM may still exist, however, and such errors are accounted for in the formulation which is developed below.

In summary, will assume that the uncertainties associated with the cloud profiles, $\mathbf{x}_j$, are solely due to inadequacies in the database as a whole and neglect cloud model uncer-

tainties. Similarly, we will assume that the uncertainties in the weights, W_j, are due to a combination of errors introduced in the simulated T_Bs by the radiative transfer model and errors introduced in the observations by the instrument itself. No uncertainty is introduced due to the cloud model itself at any point in the analyses which follow.

3.4 Weight Uncertainty

The preceding analysis was predicated on the assumption that we know, or at least have a means of estimating, the uncertainties in the $\mathbf{x}_j$ and their weights, the W_j. Through comparison of Eqns. (3.7) and (3.11) we deduce that the weights, W_j, are given by

$$W_j = e^{-\frac{1}{2}[\mathbf{y}_o - \mathbf{y}_s(\mathbf{x}_j)]^T (\mathbf{O}+\mathbf{S})^{-1} [\mathbf{y}_o - \mathbf{y}_s(\mathbf{x}_j)]} \tag{3.19}$$

When expanded, it is clear that the term $[\mathbf{y}_o - \mathbf{y}_s(\mathbf{x}_j)]^T (\mathbf{O} + \mathbf{S})^{-1} [\mathbf{y}_o - \mathbf{y}_s(\mathbf{x}_j)]$ results in the coupling of all observed and simulated 'measurements' (i.e. all elements of both $\mathbf{y}_o$ and $\mathbf{y}_s(\mathbf{x}_j)$) through products and sums so that the uncertainties in all quantities inevitably combine to yield an uncertainty in W_j. Also, if correlations exist amongst the uncertainties in these quantities, they must be taken into account when determining the overall uncertainty in the W_j. Thus we again return to Appendix A and apply Eqn. (A.1) in its most general form.

There are no uncertainties associated with the error covariance matrices, $\mathbf{O}$ and $\mathbf{S}$, as they are themselves error estimates, but we expect uncertainties in all other variables in Eqn. (3.19). To apply Equation (A.1) we evaluate the derivatives of W_j with respect to each of these variables. Consider the first element of $\mathbf{y}_o$,

$$\frac{\partial W_j}{\partial y_{0_1}} = W_j \times \left(-\frac{1}{2} [\mathbf{y}_o - \mathbf{y}_s(\mathbf{x}_j)]^T (\mathbf{O} + \mathbf{S})^{-1} \frac{\partial}{\partial y_{0_1}} ([\mathbf{y}_o - \mathbf{y}_s(\mathbf{x}_j)]) \right.$$

$$-\frac{1}{2}\frac{\partial}{\partial y_{0_1}}\left(\left[\mathbf{y}_o-\mathbf{y}_s(\mathbf{x}_j)\right]^T\right)\left(\mathbf{O}+\mathbf{S}\right)^{-1}\left[\mathbf{y}_o-\mathbf{y}_s(\mathbf{x}_j)\right]\Bigg) \tag{3.20}$$

Now, noting that,

$$\left[\mathbf{y}_o-\mathbf{y}_s(\mathbf{x}_j)\right]=\begin{bmatrix} y_{0_1}-y_{s_1}(\mathbf{x}_j) \\ y_{0_2}-y_{s_2}(\mathbf{x}_j) \\ \vdots \\ y_{0_N}-y_{s_N}(\mathbf{x}_j) \end{bmatrix} \tag{3.21}$$

where N is the total number of measurements, it is clear that,

$$\frac{\partial}{\partial y_{0_1}}\left(\left[\mathbf{y}_o-\mathbf{y}_s(\mathbf{x}_j)\right]\right)=\begin{bmatrix} 1 \\ 0 \\ \vdots \\ 0 \end{bmatrix} \tag{3.22}$$

Note also that in general $\frac{\partial \mathbf{p}^T}{\partial q}=\left(\frac{\partial \mathbf{p}}{\partial q}\right)^T$ so that we have

$$\begin{aligned}\frac{\partial W_j}{\partial y_{0_1}} \;=\; W_j\times\Bigg(&-\frac{1}{2}\left[\mathbf{y}_o-\mathbf{y}_s(\mathbf{x}_j)\right]^T\left(\mathbf{O}+\mathbf{S}\right)^{-1}\begin{bmatrix} 1 \\ 0 \\ \vdots \\ 0 \end{bmatrix} \\ &-\frac{1}{2}\begin{bmatrix} 1 \\ 0 \\ \vdots \\ 0 \end{bmatrix}^T\left(\mathbf{O}+\mathbf{S}\right)^{-1}\left[\mathbf{y}_o-\mathbf{y}_s(\mathbf{x}_j)\right]\Bigg)\end{aligned} \tag{3.23}$$

Following similar arguments all derivatives of W_j can be evaluated. Defining $\mathbf{U}_i$ as

$$\mathbf{U}_i = \begin{bmatrix} 0 \\ 0 \\ \vdots \\ U_{i_i} = 1 \\ \vdots \\ 0 \end{bmatrix} \tag{3.24}$$

i.e. a unit vector in the i^{th} direction, all required derivatives can be summarized by:

$$\begin{aligned} \frac{\partial W_j}{\partial y_{0_i}} &= W_j \times \left(-\frac{1}{2} \left[\mathbf{y}_o - \mathbf{y}_s(\mathbf{x}_j) \right]^T (\mathbf{O} + \mathbf{S})^{-1} \mathbf{U}_i \right. \\ &\quad \left. -\frac{1}{2} \mathbf{U}_i^T (\mathbf{O} + \mathbf{S})^{-1} \left[\mathbf{y}_o - \mathbf{y}_s(\mathbf{x}_j) \right] \right) \end{aligned} \tag{3.25}$$

$$\begin{aligned} \frac{\partial W_j}{\partial y_{s_i}} &= W_j \times \left(\frac{1}{2} \left[\mathbf{y}_o - \mathbf{y}_s(\mathbf{x}_j) \right]^T (\mathbf{O} + \mathbf{S})^{-1} \mathbf{U}_i \right. \\ &\quad \left. +\frac{1}{2} \mathbf{U}_i^T (\mathbf{O} + \mathbf{S})^{-1} \left[\mathbf{y}_o - \mathbf{y}_s(\mathbf{x}_j) \right] \right) \end{aligned} \tag{3.26}$$

Notice that the derivatives with respect to the simulated observations only differ by a sign from those with respect to the observations.

Applying Eqn. (A.1) and making use of these derivatives, the (somewhat unsightly) uncertainty in a W_j is

$$\frac{\delta W_j}{W_j} = \frac{\sqrt{\sum_{i=1}^{N} \frac{1}{4} \left[\left[\mathbf{y}_o - \mathbf{y}_s(\mathbf{x}_j) \right]^T (\mathbf{O} + \mathbf{S})^{-1} \mathbf{U}_i + \mathbf{U}_i^T (\mathbf{O} + \mathbf{S})^{-1} \left[\mathbf{y}_o - \mathbf{y}_s(\mathbf{x}_j) \right] \right]^2 \times O_{ii}}}{+\sum_{i=1}^{N} \frac{1}{4} \left[\left[\mathbf{y}_o - \mathbf{y}_s(\mathbf{x}_j) \right]^T (\mathbf{O} + \mathbf{S})^{-1} \mathbf{U}_i + \mathbf{U}_i^T (\mathbf{O} + \mathbf{S})^{-1} \left[\mathbf{y}_o - \mathbf{y}_s(\mathbf{x}_j) \right] \right]^2 \times S_{ii}}$$

$$
\begin{aligned}
&+ \overline{\sum_{i=1}^{N-1}\sum_{k=i+1}^{N}\frac{1}{4}\left(\left[\mathbf{y}_o-\mathbf{y}_s(\mathbf{x}_j)\right]^T(\mathbf{O}+\mathbf{S})^{-1}\mathbf{U}_i+\mathbf{U}_i^T(\mathbf{O}+\mathbf{S})^{-1}\left[\mathbf{y}_o-\mathbf{y}_s(\mathbf{x}_j)\right]\right)} \\
&\times \overline{\left(\left[\mathbf{y}_o-\mathbf{y}_s(\mathbf{x}_j)\right]^T(\mathbf{O}+\mathbf{S})^{-1}\mathbf{U}_k+\mathbf{U}_k^T(\mathbf{O}+\mathbf{S})^{-1}\left[\mathbf{y}_o-\mathbf{y}_s(\mathbf{x}_j)\right]\right)\times O_{ik}} \\
&+ \overline{\sum_{i=1}^{N-1}\sum_{k=i+1}^{N}\frac{1}{4}\left(\left[\mathbf{y}_o-\mathbf{y}_s(\mathbf{x}_j)\right]^T(\mathbf{O}+\mathbf{S})^{-1}\mathbf{U}_i+\mathbf{U}_i^T(\mathbf{O}+\mathbf{S})^{-1}\left[\mathbf{y}_o-\mathbf{y}_s(\mathbf{x}_j)\right]\right)} \\
&\times \overline{\left(\left[\mathbf{y}_o-\mathbf{y}_s(\mathbf{x}_j)\right]^T(\mathbf{O}+\mathbf{S})^{-1}\mathbf{U}_k+\mathbf{U}_k^T(\mathbf{O}+\mathbf{S})^{-1}\left[\mathbf{y}_o-\mathbf{y}_s(\mathbf{x}_j)\right]\right)\times S_{ik}} \qquad (3.27)
\end{aligned}
$$

where N is the total number of measurements and O_{ik} and S_{ik} represent the elements of the O and S covariance matrices, respectively. Contributions from the uncertainties in the observed and simulated measurements are represented by the first two terms in Eqn. (3.27). The third and fourth terms account for the existence of correlations in the uncertainties between observations and simulations, respectively. We have made the assumption that there are no correlations between measured and simulated quantities. This is almost certain to be a good assumption since no measurements of any kind (eg. radiosonde data, sea surface temperature (SST), etc.) from the scenes observed by the satellite ever come to be used in the generation of the cloud profile database due to the fact that they are generated in advance based on simulations of conditions observed in past field studies (eg. TOGA COARE). If such correlations did exist, a fifth term representing the cross-correlations between the uncertainties in the measured and the simulated observations would be present. Recombining these terms, Eqn. (3.27) can be recast more simply as

$$
\frac{\delta W_j}{W_j} = \sqrt{\left[\vec{\mathbf{y}}_o-\vec{\mathbf{y}}_s(\vec{\mathbf{x}}_j)\right]^T(\mathbf{O}+\mathbf{S})^{-1}\left[\vec{\mathbf{y}}_o-\vec{\mathbf{y}}_s(\vec{\mathbf{x}}_j)\right]} \qquad (3.28)
$$

Allowing for completely arbitrary O and S matrices, Eqn. (3.28) is in its simplest possible form. A significant reduction in computation time can be realized, however, if correlations in the errors between measurements or between simulated observations of dif-

ferent channels are neglected. This represents the simplest case which is of any practical use but, in many cases, this may be the best we can do in making an uncertainty estimate since it can be extremely difficult in practice to determine the off-diagonal elements of the covariance matrices. Two dramatic simplifications arise if we set the off-diagonal elements of the covariance matrices to zero:

1. The third and fourth terms of Equation (3.27) completely vanish since O_{ik} and S_{ik} both vanish for $i \neq k$.

2. The matrix $(\mathbf{O} + \mathbf{S})^{-1}$ becomes diagonal eliminating all coupling of measurements or simulated observations for different channels.

It is easy to show that the second point allows the two terms in the derivatives of Eqns. (3.25) and (3.26) combine to yield

$$\frac{\partial W_j}{\partial y_{0_i}} = -W_j \times [y_{0_i} - y_{s_i}] \times OS_{ii}^{inv} \tag{3.29}$$

$$\frac{\partial W_j}{\partial y_{s_i}} = W_j \times [y_{0_i} - y_{s_i}] \times OS_{ii}^{inv} \tag{3.30}$$

where $OS_{ii}^{inv} = (O_{ii} + S_{ii})^{-1}$ is the (i,i) element of the matrix $(\mathbf{O} + \mathbf{S})^{-1}$. Substitution of these equations into Eqn. (A.1) yields:

$$\frac{\delta W_j}{W_j} = \sqrt{\sum_{i=1}^{N} \left(\frac{y_{0_i} - y_{s_i}}{(O_{ii} + S_{ii})} \right)^2 \times (O_{ii} + S_{ii})} = \sqrt{\sum_{i=1}^{N} \frac{d_i^2}{(O_{ii} + S_{ii})}} \tag{3.31}$$

where $d_i = y_{0_i} - y_{s_i}$. The uncertainty estimation has been reduced to the estimation of the diagonal elements of the covariance matrices and the calculation as a whole has been reduced to a single sum over the N channels in the system.

Due to its relative simplicity, Eqn. (3.31) is convenient for estimating weight uncertainties in situations where it is either too time-consuming to apply a more complete result

or simply impossible to estimate the off-diagonal elements of the covariance matrices with sufficient accuracy. For these reasons, the operational version of the GPROF algorithm ignores correlations between variables. The impact of this assumption on retrieved rainfall and its uncertainty will be investigated below.

3.5 Database Uncertainty

In this section a novel approach to estimating the uncertainty associated with the profiles, $\mathbf{x}_j$, is introduced. A considerable effort has been made to develop an approach that is mathematically consistent with the development that has been outlined so far.

Consider the physics of the retrieval process for a moment. We can think of each cloud in the database as a point in the multidimensional space defined by the variables in our observation system. Together the entire database forms a surface in this space. The algorithm proceeds by finding the point in this multidimensional space which most closely corresponds to the observations and assigns the largest weight to that profile. The weights then fall off exponentially in all directions around this point with the width of the resulting Gaussian defined by the model and observation uncertainties. All profiles are summed with the appropriate weights to produce the retrieved profile.

Figure 3.3 graphically represents this process for a hypothetical cloud parameter, x. The histogram represents a hypothetical cloud profile database and the dashed curves represent weights assigned to parameters based on a particular set of measurements. Two distinct cases emerge. Figure 3.3(a) corresponds to the case where the cloud profiles in the database can be distinguished from one another, i.e. they each yield a unique set of measurements. In this case, x varies only moderately over the range of measurements for which the weights are significant. As a result the measurements primarily drive the retrieval toward the correct result as opposed to the shape of the cloud database. Figure 3.3(b) displays a scenario where two profiles with significantly different values of x yield the same measurement profile.

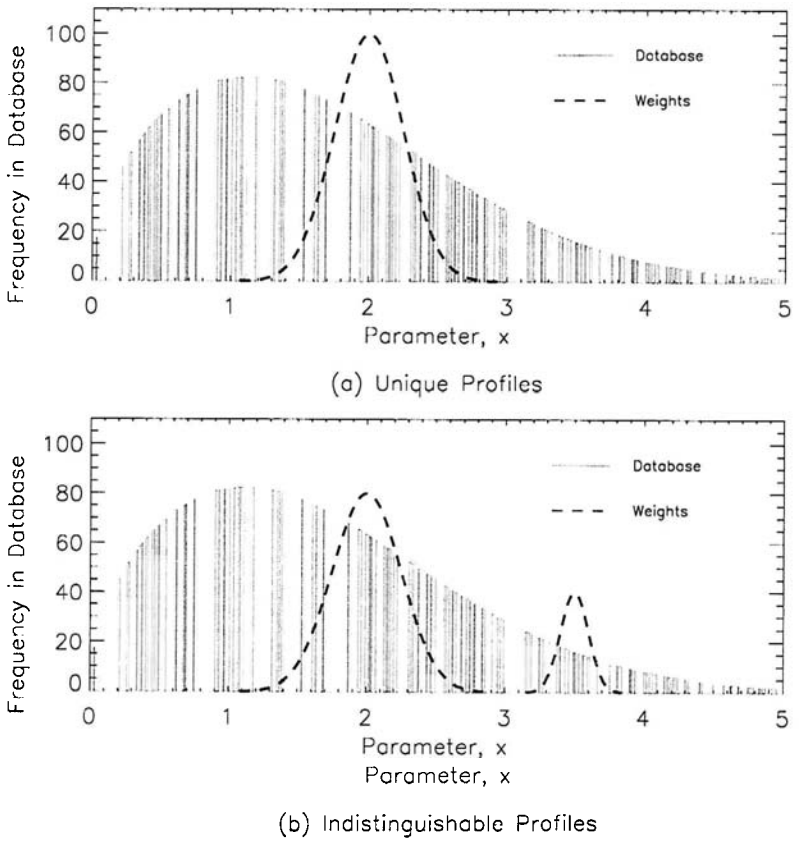

Figure 3.3: Graphical representation of retrieval process.

Under these circumstances, the shape of the cloud database is critical in determining the relative heights of the two weight curves which in turn drive the retrieval to the correct average profile.

The main issue regarding the "completeness" of the cloud database is, therefore, one of non-uniqueness. Do pairs of cloud profiles exist which, despite having significantly different hydrometeor and/or rainrate profiles, yield measurement vectors which cannot be distinguished from one another within the uncertainty limits of the observing system and mapping function? If no such pairs exist one can assume that the retrieval will weight the correct profile more strongly than the others by virtue of their dissimilar measurement

signatures and the resulting profile will indeed be the best estimate from the database. If, on the other hand, a number of different profiles yield similar measurement vectors, the relative frequency with which they occur in the database will be critical in determining how they are weighted to produce the retrieved profile. Finally, if the database does not contain a realization which matches the observations, many will be assigned very low but comparable weights and will, therefore, be indistinguishable from one another as far as the retrieval is concerned.

To address the question of non-uniqueness we must define a criterion for deciding whether or not any pair of cloud profiles can be distinguished by the retrieval system. There are four requirements we should impose on this criterion in advance that will ensure its effectiveness in the analysis which follows:

1. It should be as simple as possible so that the results of its application can be easily understood in terms of the fundamental properties of the retrieval algorithm.

2. It should naturally lead to a method for quantitatively estimating the uncertainty associated with the cloud profiles.

3. Its origins should be rooted in the analysis that has been carried out so far to facilitate direct comparison between the uncertainties associated with the cloud profile database and the other sources of error in the retrieval.

4. It should be flexible enough to allow modifications such as the addition or removal of channels to be useful when considering the information content of specific measurements.

Since the measurements enter into the retrieval through the exponential weights, a good candidate for a uniqueness criterion is the expression for the uncertainty in the weights. In particular Eqn. (3.31), which applies to the case where the uncertainties between different channels are uncorrelated, satisfies our requirements of simplicity and flexibility. Not only

does the expression lend itself well to the comparison of two profiles through the d_i, but it also provides a direct means of relating the difference in two cloud profiles to the combined uncertainty in the observation and computation systems. Replacing $d_i \rightarrow \delta_{y_i} = \left(y_i^X - y_i^Y\right)$ where y_i represents the i^{th} simulated measurement, the difference between any two cloud structures, X and Y, is defined as:

$$\Delta^{XY} = \sqrt{\frac{1}{2}\sum_{i=1}^{N} \frac{\delta_i^2}{(S_{ii}^X + S_{ii}^Y)}} \tag{3.32}$$

$\frac{\delta W_j}{W_j}$ is a natural threshold for determining the "likeness" of any two profiles as it represents the combined uncertainty from both model and observations. If Δ^{XY} is less than $\frac{\delta W_j}{W_j}$ then we must say that the resolution of the retrieval is not adequate to distinguish the cloud profiles X and Y. In that case their relative frequency in the cloud database becomes the sole factor determining their overall weight in the retrieval.

It is now possible to naturally extend this result to develop a straight-forward method for analyzing the uncertainty in the database resulting from the non-uniqueness of its constituent realizations. For a given database, $\frac{\delta W_j}{W_j}$ is computed for each realization using the observed $\mathbf{y}_o$ for the pixel being viewed. The threshold is defined to be the weighted-average of the $\frac{\delta W_j}{W_j}$,

$$\text{Threshold} = \frac{\sum_j W_j \left(\frac{\delta W_j}{W_j}\right)}{\sum_j W_j} \tag{3.33}$$

to prevent realizations whose simulated measurements differ significantly from the observations (and thereby don't impact the retrieval) from skewing the average threshold. Defined in this way, the thresholds provide information regarding how well the database represents the set of observations. If a scene is well-represented in the database, the threshold will be low. If, on the other hand, no realizations in the database resemble the scene being observed, a high threshold will result. In general the database will represent some scenes better than others so this calculation must be made for every retrieval independently

to accurately assess its uncertainty.

The difference between each pair of realizations within the database, evaluated using Eqn. (3.32), is then compared to the threshold to determine which pairs are unique. The uncertainty in any parameter is given by the square root of its variance over all realizations from which it cannot be distinguished. In this way $\delta \mathbf{x}_j$, the uncertainty in each realization, can be estimated.

The procedure for estimating the uncertainty in the GPROF retrieval product can be summarized as follows:

1. Determine threshold by estimating the average uncertainty $\overline{\frac{\delta W_j}{W_j}}$ for the database.
2. For every pair of profiles, evaluate the uniqueness criterion.
3. For each profile determine the set of profiles from which it cannot be distinguished.
4. Compute the uncertainty in each cloud profile vector.
5. Combine these with the values of δW_j already computed to yield an estimate in the overall uncertainty in the retrieved profile via Eqn. (3.16).

3.6 Special Cases

Before proceeding it is instructive to investigate some aspects of the error model. Consider its response to two special cases:

- Extremely large database which 'perfectly' represents the cloud probability density function observed in nature.
- Meager database consisting of only one cloud profile.

These special cases represent the perfect and most incomplete database limits, respectively.

In the first case the accuracy and volume of measurements determines the accuracy of the retrieval since all clouds are represented somewhere within the database but uncertainties associated with the instruments and the radiative transfer model still lead to errors in the weights assigned to each profile. Comparing Equations (3.32) and (3.33) we see that two profiles are indistinguishable within the accuracy limits of the retrieving system if

$$\Delta^{XY} < \frac{\sum_j W_j \frac{\delta W_j}{W_j}}{\sum_j W_j} \tag{3.34}$$

As the number of channels used in the retrieval increases, Equations (3.31) and (3.32) predict that both sides of this equation will increase. By virtue of the fact that the profiles which more closely resemble the observations are weighted more significantly in the summation performed to obtain the threshold, the left-hand side of the equation will increase more slowly than the right-hand side. Therefore as more channels are added to the retrieval, the number of indistinguishable profiles must either decrease or stay the same depending on the information content of each channel. Thus in the case where the database perfectly represents nature the retrieval is dominated by the observations.

Now suppose the database consists of only one cloud profile. According to Eqn. (3.7) the retrieval must choose this profile and assign it a weight of unity as a result of the normalization

$$\hat{E}\left(\mathbf{x}\right) \rightarrow \mathbf{x}_1 \tag{3.35}$$

Following the error model described above, the uncertainty associated with the cloud profile must vanish since there can be no indistinguishable profiles in the cloud database. The quality of the retrieval will be indicated through Eqn. (3.16) which reduces to

$$\frac{\delta \hat{E}(\mathbf{x})}{\hat{E}(\mathbf{x})} = \sqrt{2 \sum_i d_i^2 \beta_{ii}} \tag{3.36}$$

where i runs over all channels used in the retrieval. In most cases the differences between the observed T_Bs and those corresponding to the single profile in the database, d_i, are likely to be large resulting in a large uncertainty which indicates that the retrieval is weak. In this case, therefore, the cloud database itself dominates the retrieval.

In reality, we expect the actual cloud database to fall somewhere between these limits. The databases used in the GPROF retrieval consist of $\sim$10,000 cloud profiles but it is difficult to determine whether or not such databases, which are produced from a finite number of realizations of a cloud resolving model, accurately represent the probability distribution of clouds in nature. The method outlined in Section 3.5 provides a means of assigning an uncertainty to the cloud cloud database itself through the determination of the ranges of cloud parameters that give rise to indistinguishable T_B profiles.

3.7 Covariance Matrix Estimation

Contributions to the uncertainty in the radiative transfer calculations arise both from approximations used to simplify the radiative transfer equation as well as the effects of averaging profiles over the satellite field of view (see Kummerow (1998) for a detailed discussion of the latter). These uncertainties, of course, cannot be neglected since the retrieval relies on the fact that the T_B profiles provide an accurate representation of the cloud structures to determine the weight assigned to each in Eqn. (3.7). Here, a new method for estimating observation and simulation error covariance matrices for emission-based retrievals of cloud and rainfall is introduced. These matrices represent the most important aspect of any BMC retrieval scheme but are among the more difficult quantities to determine.

For the observations, we assume a diagonal error covariance matrix and estimate the diagonal elements directly from the TMI instrument specifications summarized in Kummerow et al. (1998). Thus the assumed error covariance assumed for the T_B basis is computed directly from the values presented there and the corresponding matrix in the emission

Table 3.1: "Observation" error covariance matrix for the emission and scattering basis. The first four diagonal elements are dimensionless while the last two are in K^2.

	P10	P19	P37	P85	S37	S85
P10	0.0034	0.0	0.0	0.0	0.0	0.0
P19	0.0	0.0024	0.0	0.0	0.0	0.0
P37	0.0	0.0	0.0011	0.0	0.0	0.0
P85	0.0	0.0	0.0	0.0057	0.0	0.0
S37	0.0	0.0	0.0	0.0	20.5	0.0
S85	0.0	0.0	0.0	0.0	0.0	103.8

and scattering index basis, obtained using Eqn. (A.1), is presented in Table 3.1.

Contributions to the uncertainty in simulated T_Bs arise from approximations used to simplify the radiative transfer equation, models of the external sources and sinks of radiation in the system, eg. the surface emissivity model, and microphysical assumptions regarding particle size, shape, and composition. These uncertainties cannot be neglected since the algorithm (BMC or otherwise) relies on the fact that the T_B profiles provide an accurate representation of the cloud structures. The method adopted here for estimating the simulation covariance matrix, **S**, combines direct comparisons with observations and a model intercomparison to address the issue of radiative transfer model uncertainty.

In general, the variance in any set of observations, $(X_1, X_2, X_3, ..., X_N)$, is defined as

$$\sigma = \frac{1}{N}\sum_{i=1}^{N}(\epsilon_i - \bar{\epsilon})^2 \tag{3.37}$$

where $\epsilon_i = X_i - X_{truth}$ and $\bar{\epsilon}$ is the average error or bias in the observational set. If the observations are vector quantities, this concept is easily extended to define an error covariance matrix with elements given by

$$S_{xy} = \frac{1}{N}\sum_{i=1}^{N}(\epsilon_i^x - \bar{\epsilon}^x)(\epsilon_i^y - \bar{\epsilon}^y) \tag{3.38}$$

where x and y run over all elements in the observation vector. We apply these definitions

in two distinct analyses of the error in the GPROF radiative transfer model. In both cases error statistics are compiled for T_Bs and are subsequently converted to the emission and scattering basis using Eqn. (A.1).

The first study consists of a direct comparison of modeled clear-sky T_Bs with observations from the TMI. Under clear-sky conditions, water vapor, SST, and surface wind speed dominate TMI T_Bs observed at the TOA so this comparison provides a direct estimate of the uncertainty associated with the surface emissivity model used in the algorithm. A cloud-screen based on both the VIRS and TMI instruments is used to isolate all clear-sky pixels in a TRMM orbit. For each clear pixel, the TOA T_Bs are simulated using a radiative transfer model initialized with SST, surface wind speed, and column water vapor estimates derived from the TMI observations[3]. These T_Bs are then compared with those observed by the TMI and an error covariance matrix for the surface emissivity model, $\mathbf{S_{SFC}}$, is computed via Eqn. (3.38).

To account for the uncertainty introduced by errors in the radiative transfer, including those associated with modeling the phase function, gaseous absorption, and depolarization of radiation as it interacts with rainfall and cloud particles, a model intercomparison is employed. T_Bs computed using the Eddington model are compared to those obtained using the more accurate polarized doubling and adding model of Evans and Stephens (1991) (hereafter referred to as the ES model) for more than 10,000 cloud profiles from the GCE CRM. Taking the output of the ES model to be "truth", Eqn. (3.38) is used to determine error covariance matrices for each of four rainrate bins, non-raining, $0 < R < 5$ mmh^{-1}, $5 < R < 20$ mmh^{-1}, and $R > 20$ mmh^{-1}, to account for the fact that the radiative transfer uncertainty varies with rainrate. The resulting covariance matrices are labeled $\mathbf{S^R_{RT}}$. Characterization of the uncertainties in radiative transfer due to microphysical assumptions is left for the future studies but could potentially lead to larger $\mathbf{S^R_{RT}}$.

[3]This data is obtained through the Remote Sensing Systems (RSS) website *www.ssmi.com.* For details of the algorithm see Wentz (1997) and Wentz et al. (2000).

Table 3.2: Simulation standard deviations, σ (in Kelvin), for each TMI channel.

Rainrate Bin	10 V	10 H	19 V	19 H	21 V	37 V	37 H	85 V	85 H
Non-raining	.919	0.887	1.413	1.532	1.380	2.210	1.482	4.309	7.691
R < 5 mmh^{-1}	.930	1.143	1.775	5.236	1.398	2.058	1.566	4.700	22.49
5 < R < 20	1.017	3.094	3.760	11.10	1.283	2.922	3.247	11.16	22.29
R > 20 mmh^{-1}	1.500	5.482	6.114	12.58	1.534	5.342	5.729	12.97	18.55

The complete simulation error covariance is formed by combining the surface emissivity and radiative transfer components. The method adopted in this work is to weight the surface emissivity model error deduced from the clear-sky comparisons according to the strength of influence of the surface emission on the observed radiances. At high rainrate, for instance, the TMI signal is dominated by emission from the rain column and is largely insensitive to the surface emission. Conversely, at low rainrate the TMI signal is dominated by surface emission. To account for this we define γ_j^R to be the ratio of the magnitude of the channel j weighting function at the surface to its maximum value and define the overall simulation error covariance matrix at a rainrate R by

$$\mathbf{S^R} = \mathbf{S_{RT}^R} + \mathbf{S_{SFC}^{\prime R}} \tag{3.39}$$

where

$$(S_{SFC}^{\prime R})_{ij} = \sqrt{\gamma_i^R \gamma_j^R}(S_{SFC})_{ij} \tag{3.40}$$

Finally, the observation and simulation error covariance matrices are combined to yield the overall error covariance matrix associated with the retrieval, **O+S**. Standard deviations, σ, derived from the diagonal elements of the resulting matrices are summarized in Tables 3.2 and 3.3 as a function of rainfall rate. The first of these tables provides results for each channel of the TMI instrument while the second highlights results applicable to the polarization and scattering index basis derived using the error combination formula in Eqn. (A.1). Correlations between the variables in each basis are presented in Figures 3.4 and 3.5

Table 3.3: Simulation standard deviations, σ (in Kelvin), for each variable in the emission and scattering index basis.

Channel/Rainrate Bin	P10	P19	P37	P85	S37	S85
Non-raining	0.059	0.049	0.034	0.083	4.578	12.57
R < 5 mmh^{-1}	0.059	0.049	0.039	0.139	6.299	24.77
5 < R < 20 mmh^{-1}	0.059	0.050	0.0376	0.154	12.13	24.20
R > 20 mmh^{-1}	0.059	0.049	0.040	0.160	14.04	20.81

in the form of correlation matrices defined as:

$$(C^R)_{ij} = \frac{(S^R)_{ij}}{\sigma_i \sigma_j} \tag{3.41}$$

These results illustrate some of the advantages of using the emission and scattering indices rather than the T_Bs themselves. First, the standard deviations for emission and scattering indices are considerably less sensitive to rainrate than those for the T_Bs themselves. In addition, the use of polarization and scattering indices significantly decorrelates the errors in different channels compared to the T_B basis. Since the operational version of the GPROF algorithm doesn't account for either the rainrate dependence or correlation effects in the error covariance matrices, this appears to be the best basis choice for that application. The results do, however, suggest that correlations can be significant particularly between the 37 and 85 GHz channels for both the emission and scattering indices. Correlations between S37 and S85, for example, reach approximately 50 percent for rainrates between 5 and 20 mmh^{-1}. The effects of neglecting these correlations in the retrieval are investigated in Section 3.9.3.

3.8 Procedure

The procedure outlined above is applied in a series of distinct steps yielding as many intermediate products as possible:

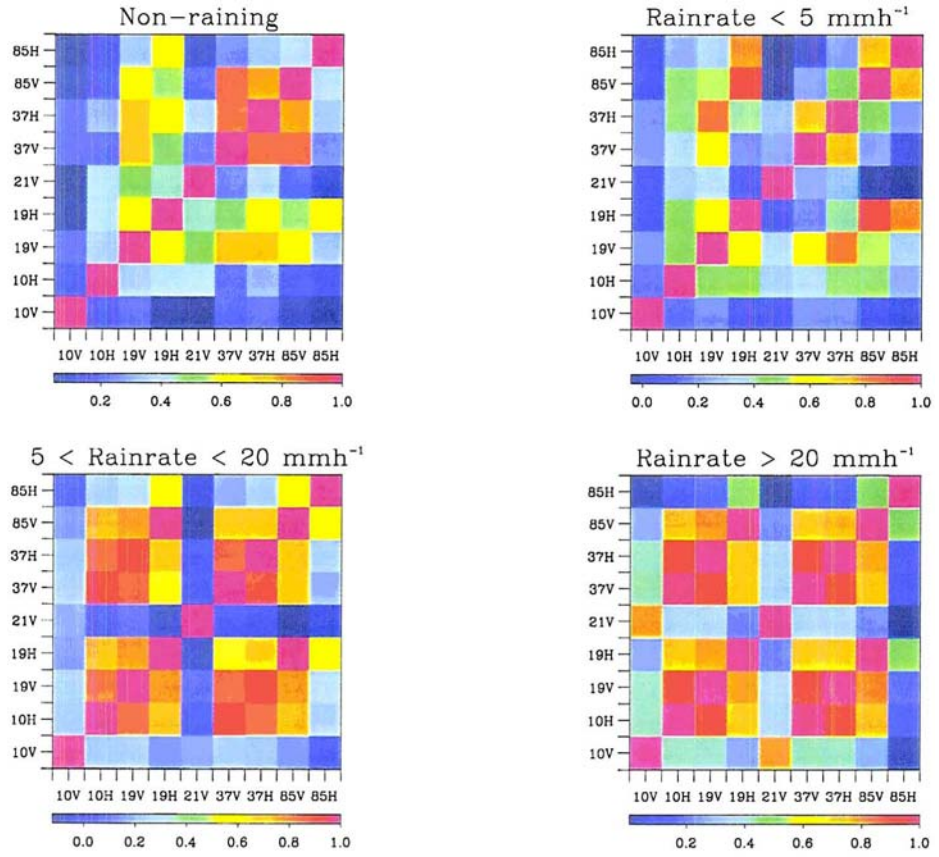

Figure 3.4: Correlation matrix for the 9 TMI channels.

1. First an error covariance matrix is estimated by combining the results from a model intercomparison with a direct clear-sky comparison of modeled and observed measurements.

2. Equation (3.32) is then evaluated for every pair of profiles. The resulting 'delta-matrix' is then written to a file for use in the following steps.

3. The threshold by which the differences in two profiles are judged to be statistically significant is determined by applying Eqn. (3.31) to a subset of cloud profiles in the database. At this step values of W_j and δW_j are also computed and stored for later use. Recall that the enormous variability possible in the observed scenes requires that a separate threshold be calculated for each pixel individually.

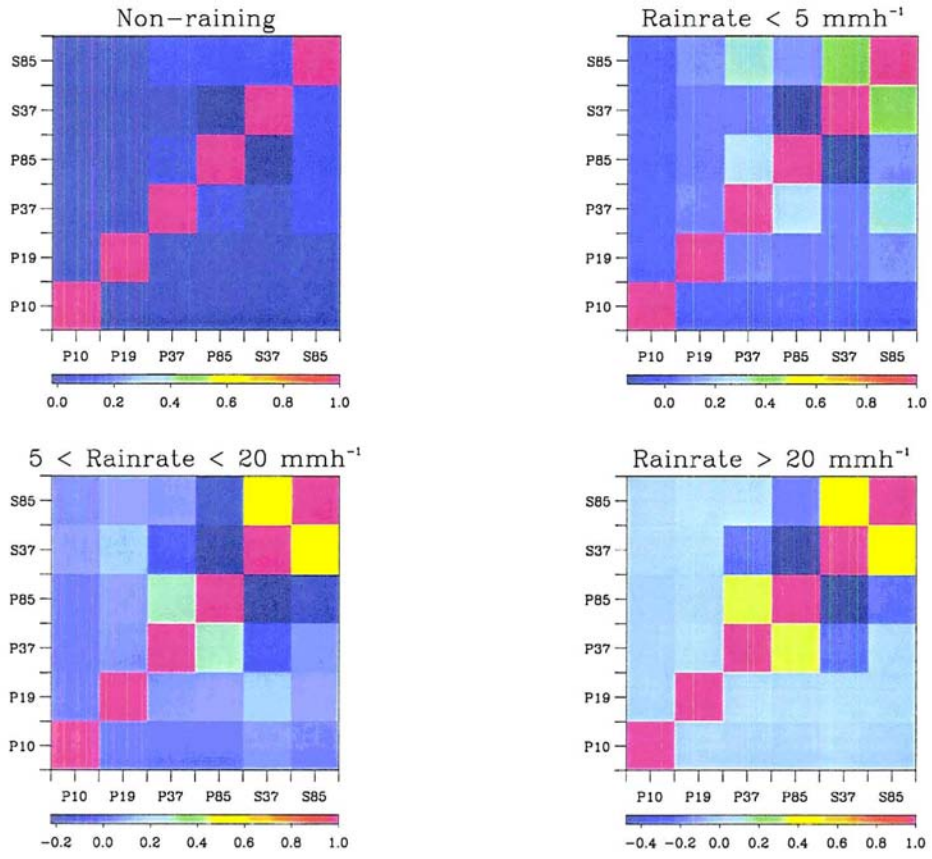

Figure 3.5: As in Figure 3.4 but for the P and S basis.

4. Each element of the delta-matrix is compared with the threshold and a 'flag-matrix' is created which consists of a '1' if X and Y are indistinguishable and '0' if they are unique with respect to the given threshold.

5. All pairs of non-unique profiles are gathered and a corresponding spread in all cloud parameters for each cloud profile is evaluated. This step, therefore, provides the $\delta \mathbf{x}_j$.

6. Finally, the W_j, δW_j, $\mathbf{x}_j$, and $\delta \mathbf{x}_j$ are combined using Eqn. (3.16) to determine the average fractional error in all of the retrieved cloud parameters.

Any combination of T_Bs, indices derived from them, or information from other instruments can be analyzed in this way. To change, add, or remove variables one only needs to

make an estimate of the appropriate error covariance matrix and modify the expressions for the weights and profile differences.

3.9 Results

3.9.1 A Single Pixel

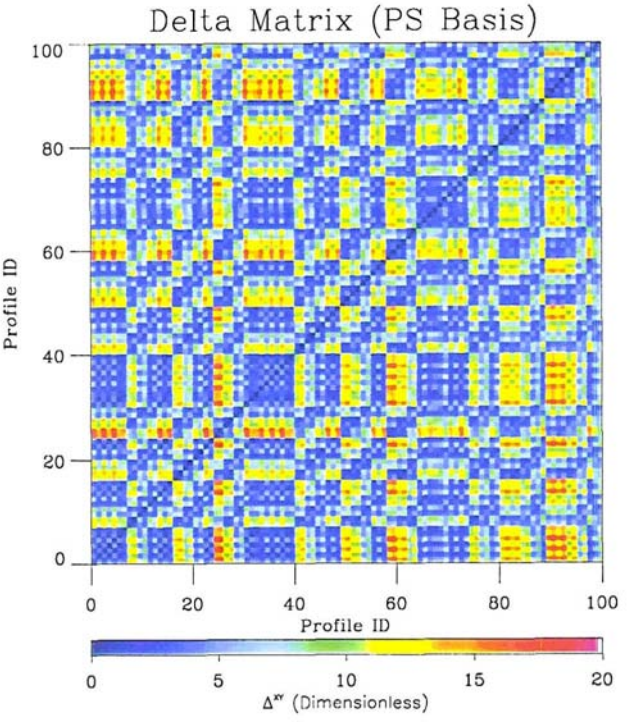

Figure 3.6: Example of a typical delta matrix. The intensity represents the combined emission and scattering index "difference" for any pair of cloud profiles.

A small section of the delta-matrix in the emission and scattering index basis is shown in Figure 3.6 and a corresponding flag matrix showing all non-unique pairs of profiles

at a threshold of 1.9843 (corresponding to a single TRMM pixel on October 5, 1999) is presented in Figure 3.7. It is clear that, while many profiles exhibit very different T_B signatures (characterized by high Δ^{XY}), a significant number of different cloud profiles have similar signatures and cannot be distinguished from one another given the present accuracy of the measurements and radiative transfer calculations.

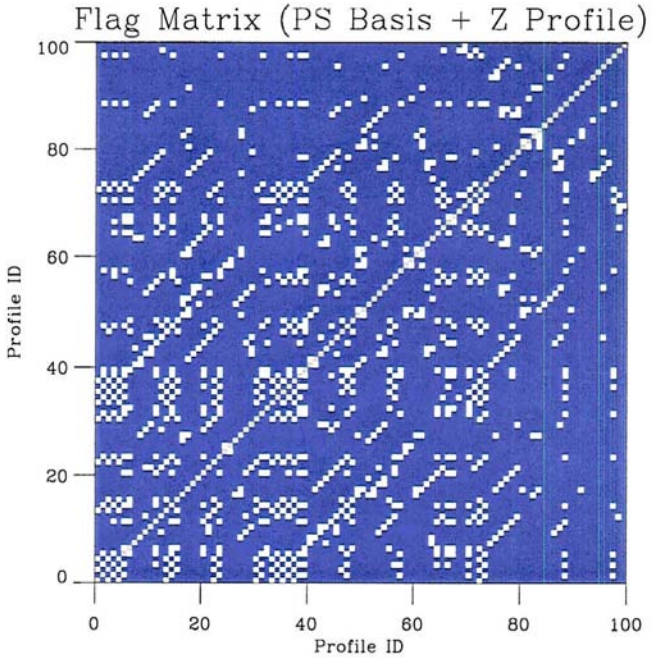

Figure 3.7: Example of a typical flag matrix illustrating all non-unique profiles using the emission and scattering indices (indicated in white) for a single pixel on one TRMM orbit.

Figure 3.8 illustrates how profile non-uniqueness translates into an uncertainty in the retrieval parameters. Shown are the spreads in T_Bs, surface rainrate, liquid and frozen precipitation for a single cloud profile from one evaluation of the error model using the

PS basis. A total of 87 profiles are found to be indistinguishable from the central profile (plotted in black) in this particular case. These profiles are assigned imperceptibly similar weights in the retrieval and their frequency in the cloud database determines their overall significance in the BMC algorithm. TMI observations alone, therefore, result in a significant database contribution to the retrieval uncertainty.

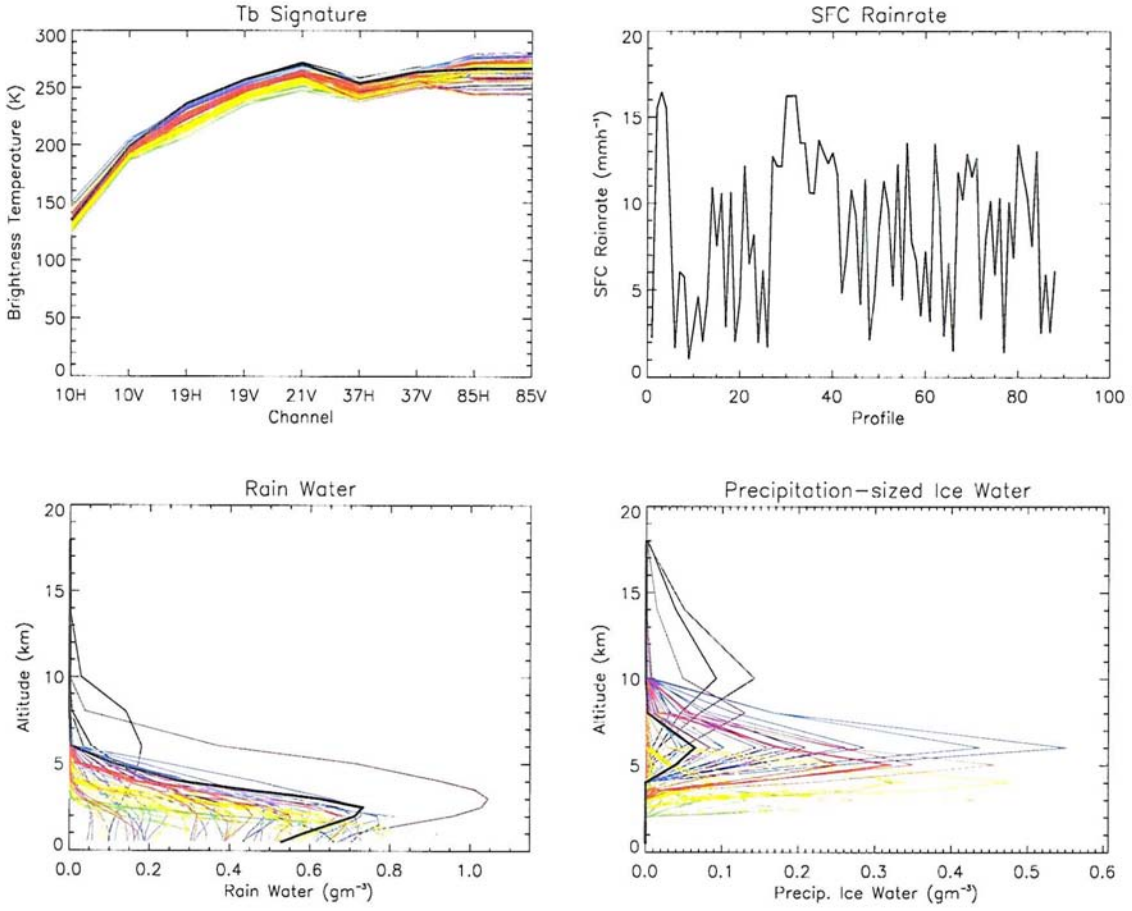

Figure 3.8: Spreads in (a) T_Bs, (b) surface rainrate, (c) rainrate profile, and (d) precipitation-sized ice particle profile, for a single profile (denoted by the heavy black line) contributing to the GPROF retrieval.

The utility of the error model is demonstrated in Fig. 3.9 in which retrieved profiles of rainfall and precipitating ice are presented along with associated profiles of uncertainty which account for both measurement errors and non-uniqueness. Immediately we are able

to determine that in this particular scene, liquid precipitation is retrieved very accurately (with uncertainties of approximately 20 %) between the surface and 4 km while frozen precipitation is retrieved with 40 percent accuracy between 4 and 8 km. Outside these regions the uncertainty rapidly increases in both estimates. These results demonstrate that the greatest accuracy is achieved where the cloud profile sensitivity of the TMI weighting functions for this rainrate, 5.15 mmh^{-1}, is the largest (see Chapter 2).

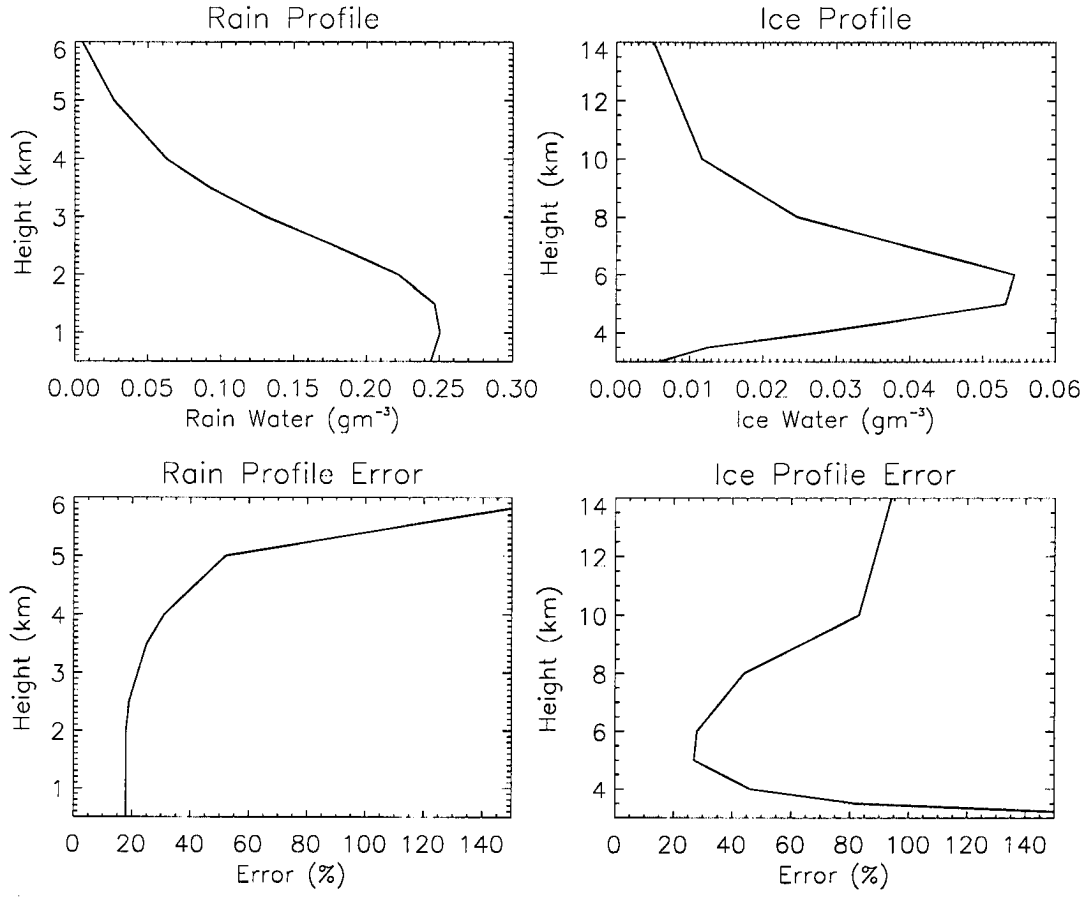

Figure 3.9: Example of retrieved rainfall and precipitation-sized ice hydrometeors and the resulting error profile estimated using our error model for a single pixel of a TRMM orbit.

3.9.2 Uncertainty Statistics

The preceding examples demonstrate the application of the model and results for a single pixel of one TRMM orbit. To determine the accuracy of the GPROF algorithm over the tropics as a whole, the model is applied to a more general sample of data from the TRMM mission.

Figure 3.10 shows surface rainrate estimates for a single TRMM orbit. The middle and lower panels highlight the retrieved surface rainrate and corresponding uncertainty for a rain system in the south Atlantic. The power of the method outlined here is that it allows explicit uncertainty estimates to be made for each pixel individually. In this way we account for the fact that some scenes are better represented by the cloud database than others, providing quantitative error bounds critical in climate change, data assimilation, and model validation studies.

Another powerful feature of this method is that it allows the overall uncertainty to be decomposed into separate cloud database and weight components. These components are plotted as a function of rainrate in Fig. 3.11 where statistics have been compiled for all raining pixels over ten TRMM orbits. Recall that the overall error is the sum of the squares of the individual components. The component associated with the database of cloud profiles dominates the uncertainty in retrieved surface rainrate below 4 mmh^{-1}. Between 4 and 10 mmh^{-1} both components are approximately equal while modeling and measurement uncertainties dominate the overall error in heavy rain. It must be noted, however, that neither component is negligible at any rainrate. This suggests that the database may be incomplete and cannot represent many of the cases being encountered by the satellite or, more likely, that a large number of profiles exist which are indistinguishable from one another through the TMI T_Bs alone.

Figure 3.11 also summarizes the overall rainfall uncertainty as a function of rainrate averaged over ten TRMM orbits. Uncertainties range from 40 to 60 % for rainrates up to

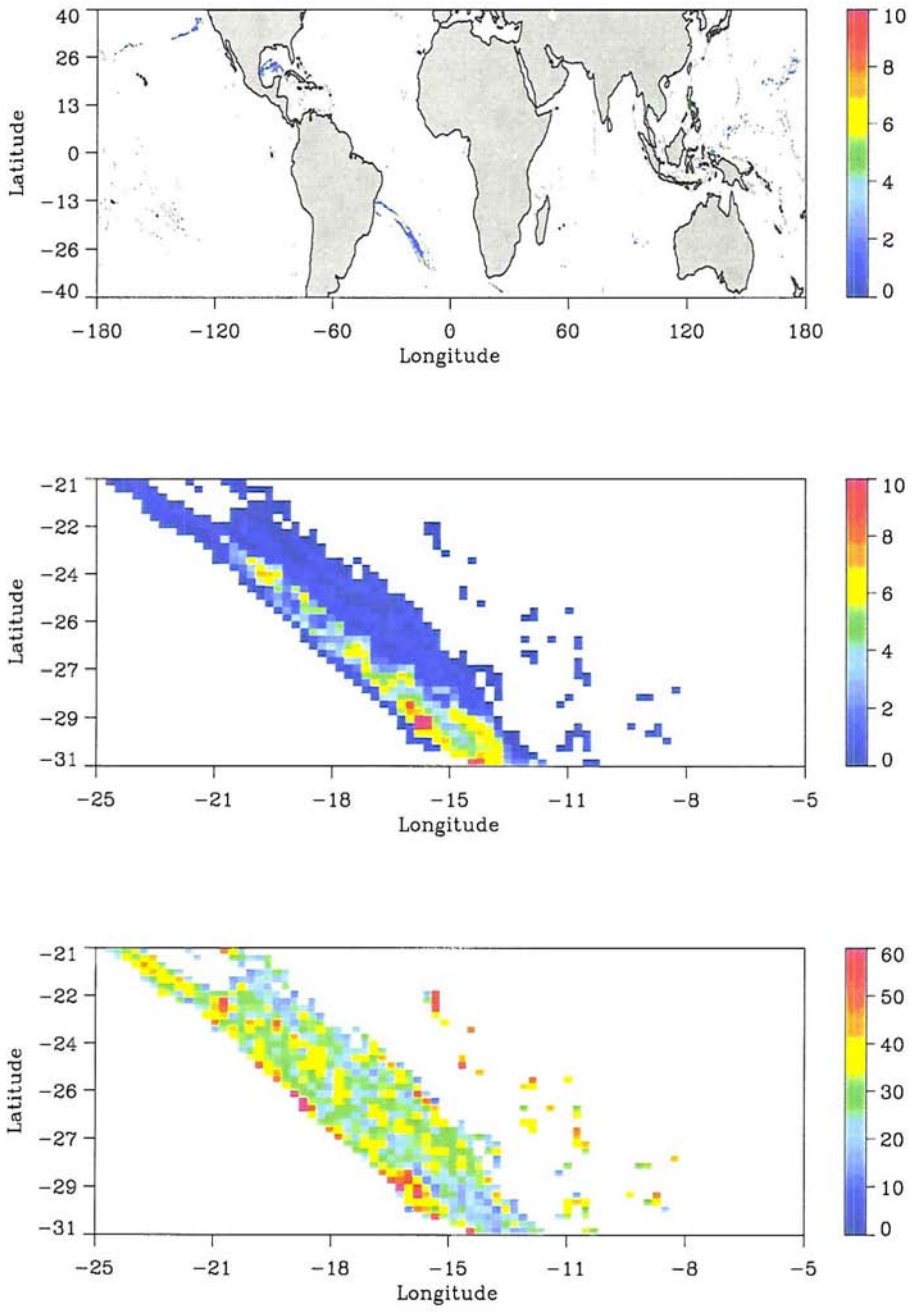

Figure 3.10: Surface rainrate for a single TRMM orbit (top), a small raining region (middle), and the corresponding uncertainty in the rainfall estimate for that region (bottom). Rainfall is presented in mmh^{-1} while errors are expressed in percent.

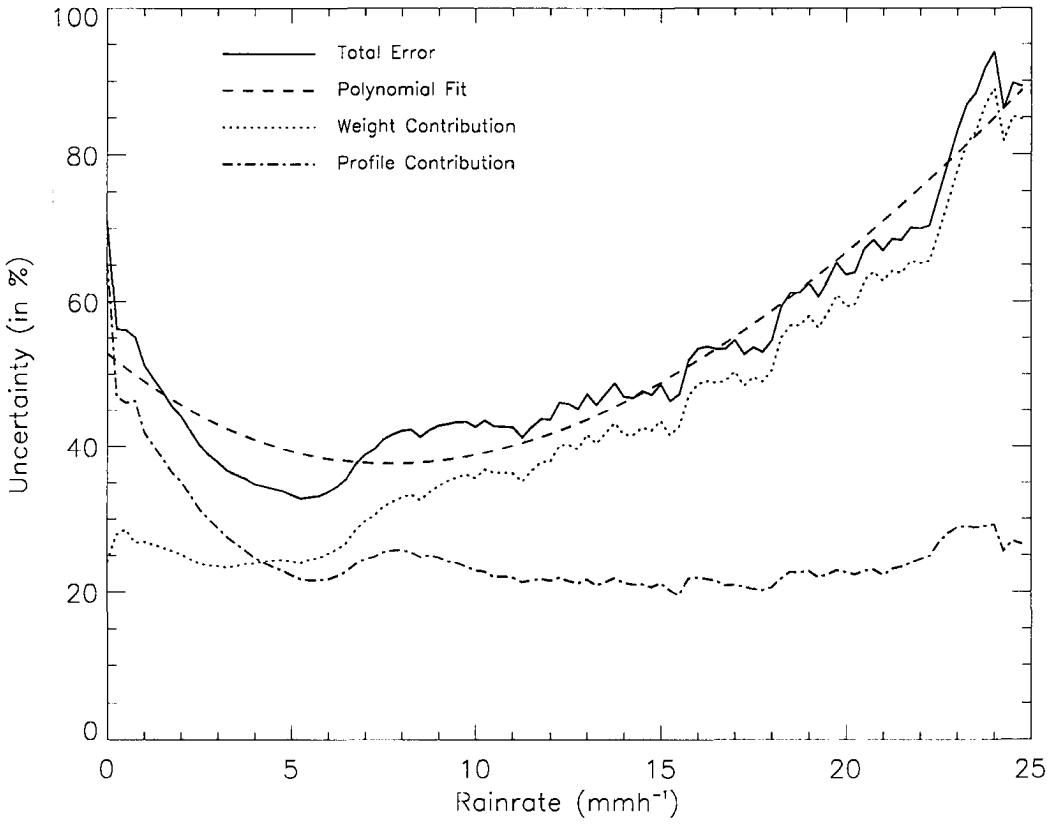

Figure 3.11: Cloud database and weight components to total uncertainty as a function of rainrate.

20 mmh^{-1} but increase rapidly in heavier rain consistent of the findings of Chapter 2 where it was shown that the TMI instrument does not directly sense the surface in heavy rainfall. In applications such as precipitation data assimilation experiments where rigorous pixel-by-pixel analyses of the TMI rainfall uncertainties are unavailable or too time-consuming, these results offer the potential for parameterizing uncertainty as a function of rainrate providing the most reliable estimates available to date. The third order polynomial

$$\frac{\delta R}{R} = 0.534 - 0.0423R + 0.0031R^2 - 0.000033R^3 \tag{3.42}$$

for example, provides a reasonable representation for the fractional uncertainty in surface rainrate in terms of its value. Analytical expressions of this type could significantly reduce computational effort in an operational assimilation while providing reasonable estimates of the required uncertainties. Assuming uncertainties are random, for example, the average uncertainty over a GCM grid box can be obtained through averaging via

$$\frac{\overline{\delta R}}{R} = \frac{\sum_j^{N_{raining}} \delta R_j / R_j}{< R > \sqrt{N_{raining}}} \tag{3.43}$$

where $N_{raining}$ is the total number of raining pixels in the grid box.

The GPROF algorithm provides considerably more information than just surface rainrate. Vertical profiles of hydrometeors in four classes, cloud liquid droplets, raindrops, cloud ice particles, and precipitating ice particles at 14 atmospheric levels are also retrieved. Uncertainty statistics for each class at all model levels along with the breakdown of these errors into database and weight components are presented in Figures 3.12-3.15.

Liquid precipitation is retrieved most accurately with uncertainties of 40-60 % over a wide range of water contents below 3.0km. This reflects the fact that the TMI exhibits good sensitivity to the strong emission signature of rainfall over the cold ocean background. Uncertainties in cloud liquid water are somewhat higher particularly at low water contents where they typically exceed 80 %. Uncertainties in both liquid hydrometeor classes increase rapidly at high water content values and above 3km. This can be partially explained by the fact that heavy rain is often accompanied by significant amounts of ice aloft which scatters radiation from below obscuring the emission signal from the rainfall. It may also be indicative of errors in the microphysical assumptions made in partitioning the liquid into cloud and precipitation categories in heavy rainfall. Under such conditions, large concentrations of hydrometeors collide, coalesce, and break-up and it is unclear how accurately microphysics schemes in current CRMs capture these rapidly varying size distributions. In addition, the assumption of spherical particles and particular DSDs in subsequent radiative

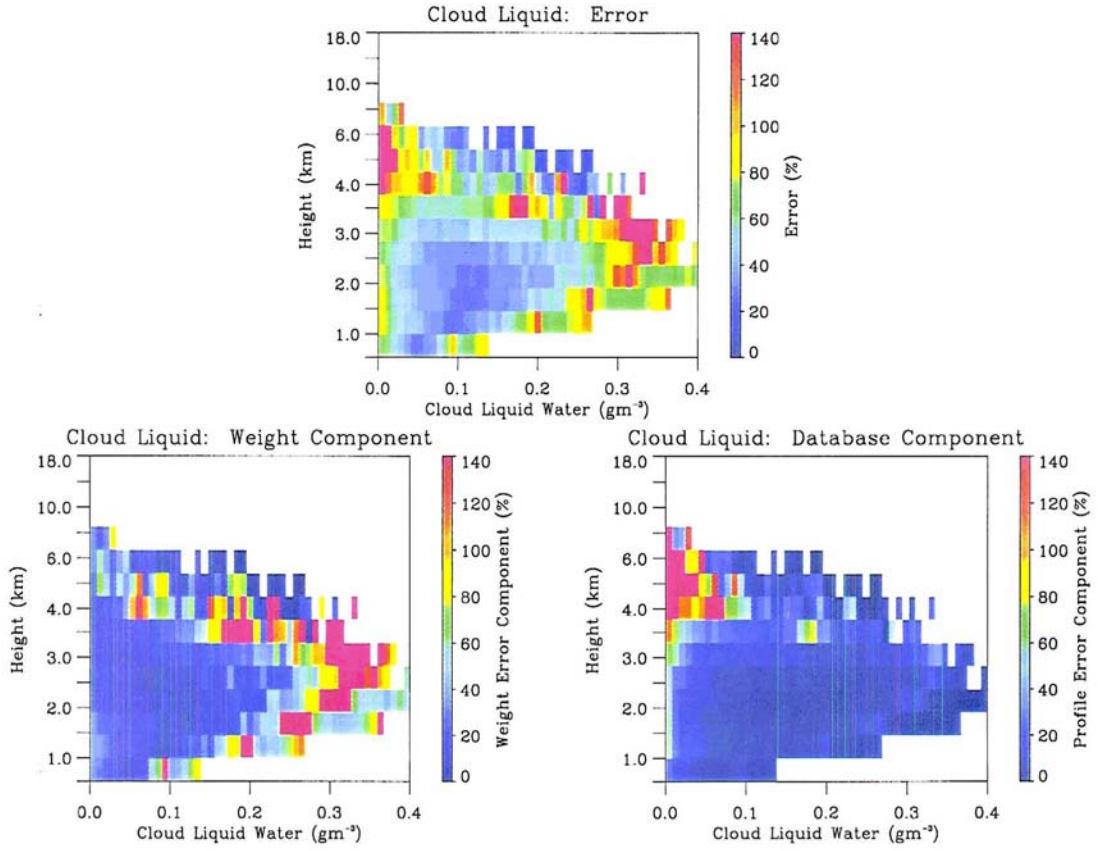

Figure 3.12: Uncertainties in cloud bin liquid water profile estimates and their corresponding weight and database components as a function of height and retrieved liquid water content. The irregular vertical axis accounts for the fact that cloud model levels are not equally spaced. See Table B.1 for model level heights.

transfer calculations can compound the problem. Evidence that either or both sets of microphysical assumptions may be in error is provided by the fact that the weight component of the uncertainty dominates in these conditions. Large weight errors result when the retrieval is unable to find T_B signatures in the database which match those observed by the TMI implying that some physics is missing from one of the two models that go into creating the *a priori* cloud profiles.

Frozen hydrometeors are not retrieved as accurately as their liquid counterparts due to a combination of poor TMI sensitivity to ice and strong similarity between the scattering

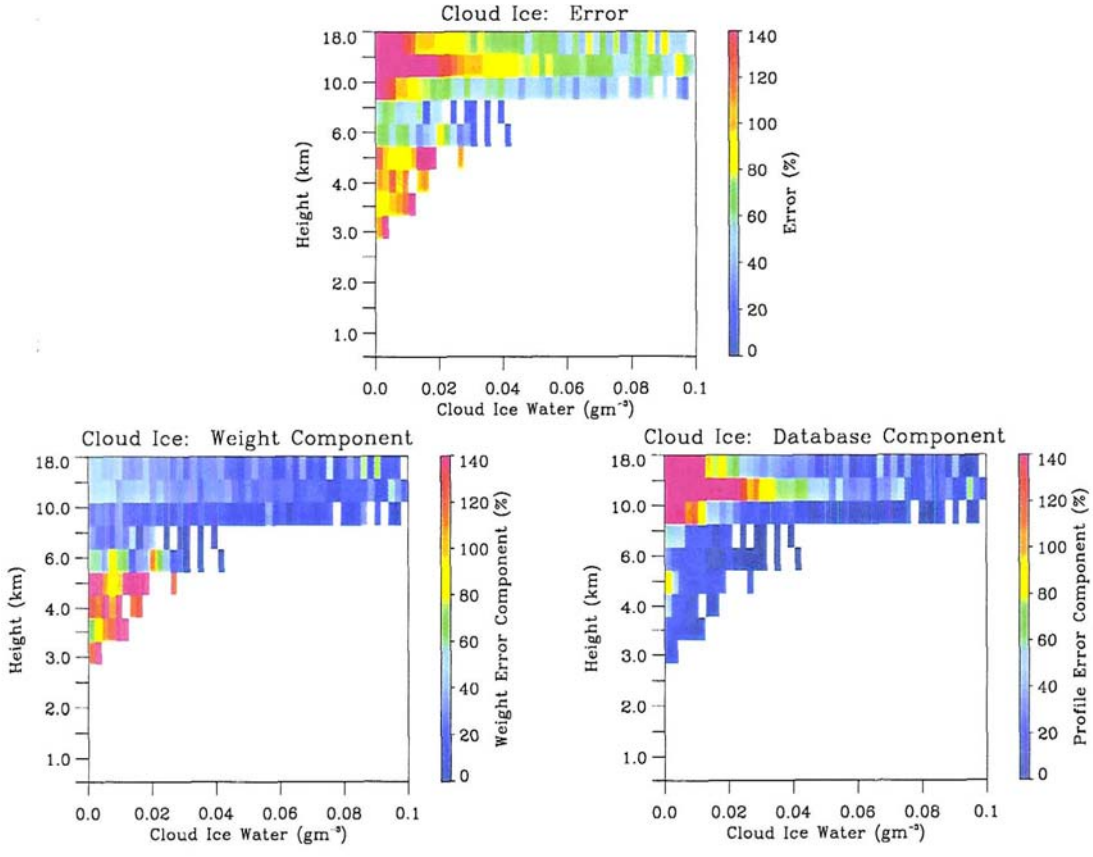

Figure 3.13: As in Figure 3.12 but for profiles of cloud ice.

signatures of the two ice hydrometeor classes which can lead to large uncertainties from microphysical assumptions in both the cloud resolving and radiative transfer models. The most accurate ice retrievals are for precipitating ice particles near the top of the precipitating portion of the cloud profiles ($\sim$ 6-8 km in most cases) in moderate to light rainfall. Under these conditions, 37 and 85 GHz radiation emitted from the surface is scattered by the large precipitating ice particles but penetrates through the optically thin cloud ice above it resulting in good TMI sensitivity to the former and very poor sensitivity to the latter. The result is a high degree of non-uniqueness in the nearly transparent cloud ice aloft. At lower levels, errors in the ice cloud microphysics, specifically in the distinction between cloud and precipitating hydrometeor classes in the CRM and in the shape and DSD assumptions

in the radiative transfer modeling, lead to a large degree of uncertainty in the scattering component of the simulated T_Bs which translates, through increased weight errors, to large uncertainties in cloud ice retrievals at low levels as well.

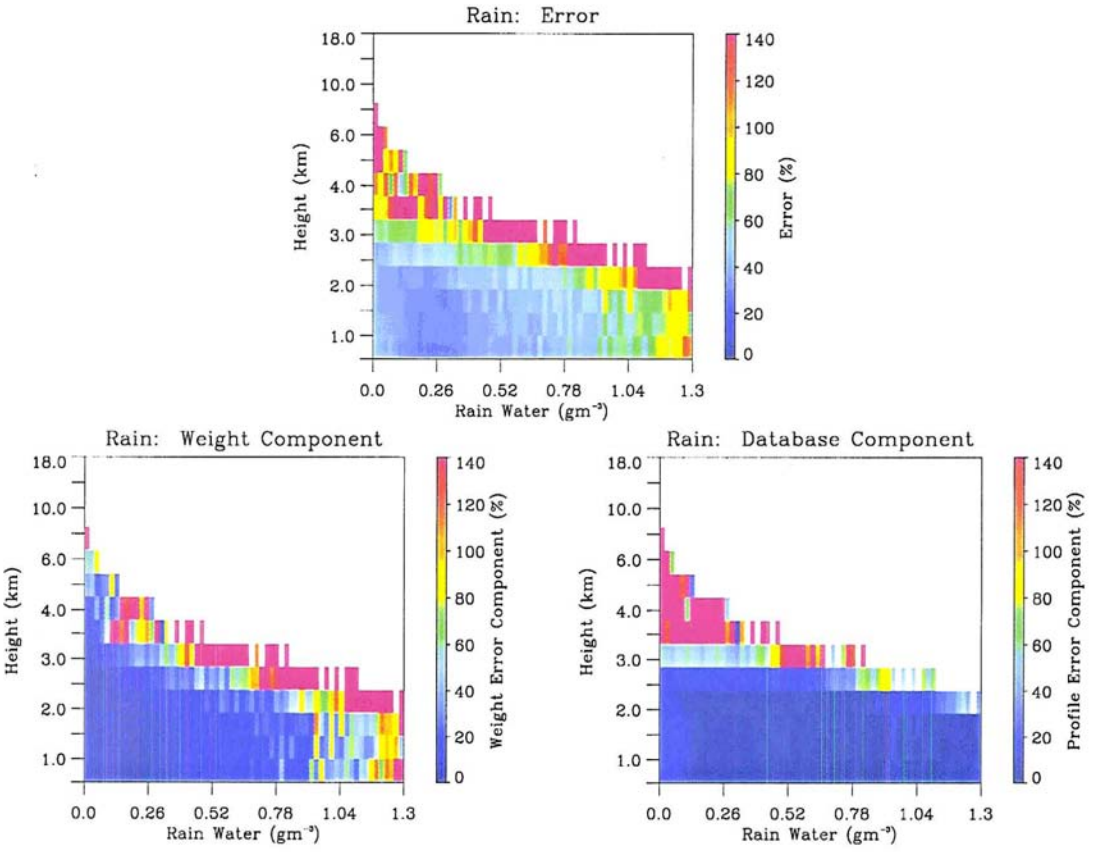

Figure 3.14: As in Figure 3.12 but for profiles of rainfall.

A special case and one which is extremely important both for research and for the inhabitants of Earth in general is that of strong convection, characterized by copious amounts of liquid precipitation at the surface, high concentrations of frozen precipitation and a significant amount of liquid cloud and precipitation at intermediate levels, and thick capping ice cloud anvil that reaches up to the tropopause. Under these conditions, scattering occurs near cloud top masking the scattering signal from the precipitating ice as well as the emission signal from the liquid hydrometeors at lower levels. This scattering results in narrow

weighting functions which all peak above 3km limiting the amount of information from below these levels. While some relationship exists between ice scattering aloft and precipitation below it, this relationship is poorly constrained and the relative contributions of emission and scattering must be deduced from the CRM results placing enormous pressure on its microphysical assumptions. As a result, uncertainties in the weights assigned to the cloud profiles in these conditions are large leading to poor retrievals in all but the cloud ice category which benefits from its strong scattering signal giving rise to uncertainties of ~50 percent.

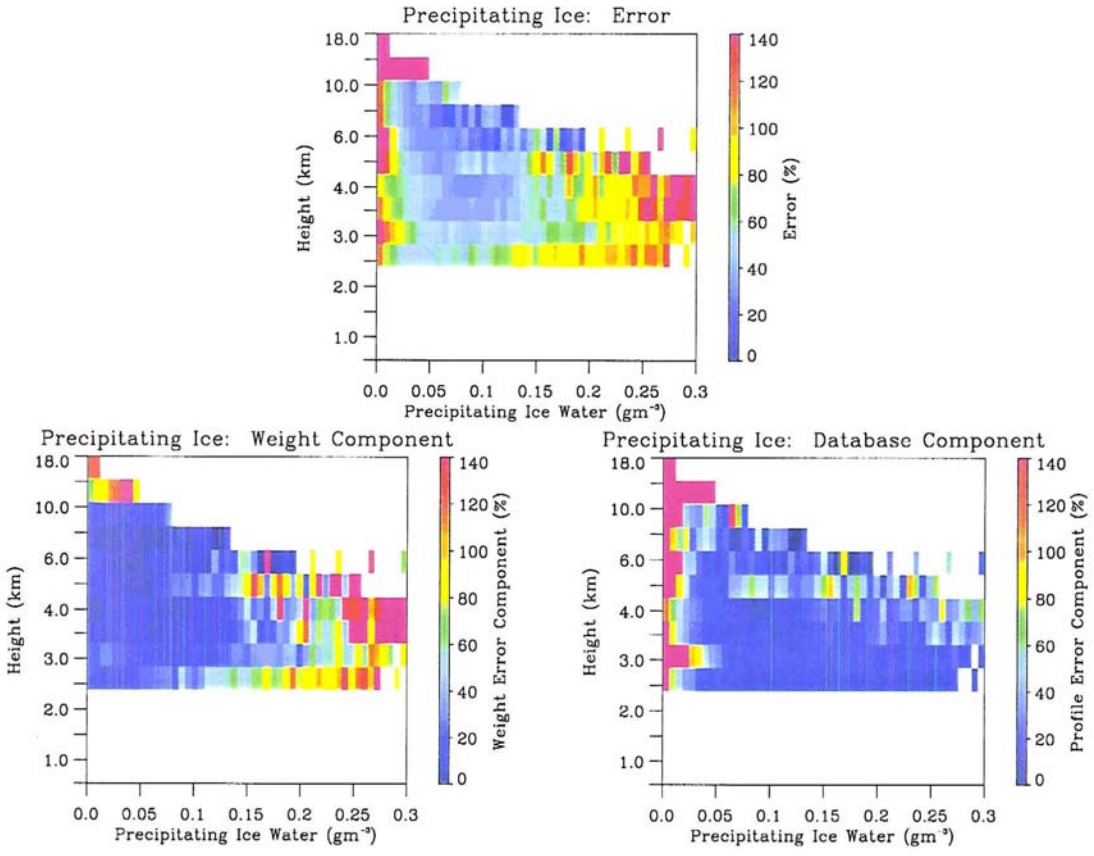

Figure 3.15: As in Figure 3.12 but for profiles of precipitating ice.

Following current trends toward the assimilation of satellite data in NWP models, it is logical to expect that numerical weather prediction will eventually seek to incorporate

cloud profile information as well as surface rainfall. Looking ahead to such applications, similar parameterizations for the uncertainties in retrieved water contents at each model level can also be made as demonstrated by the examples in Figure 3.16. Coefficients for

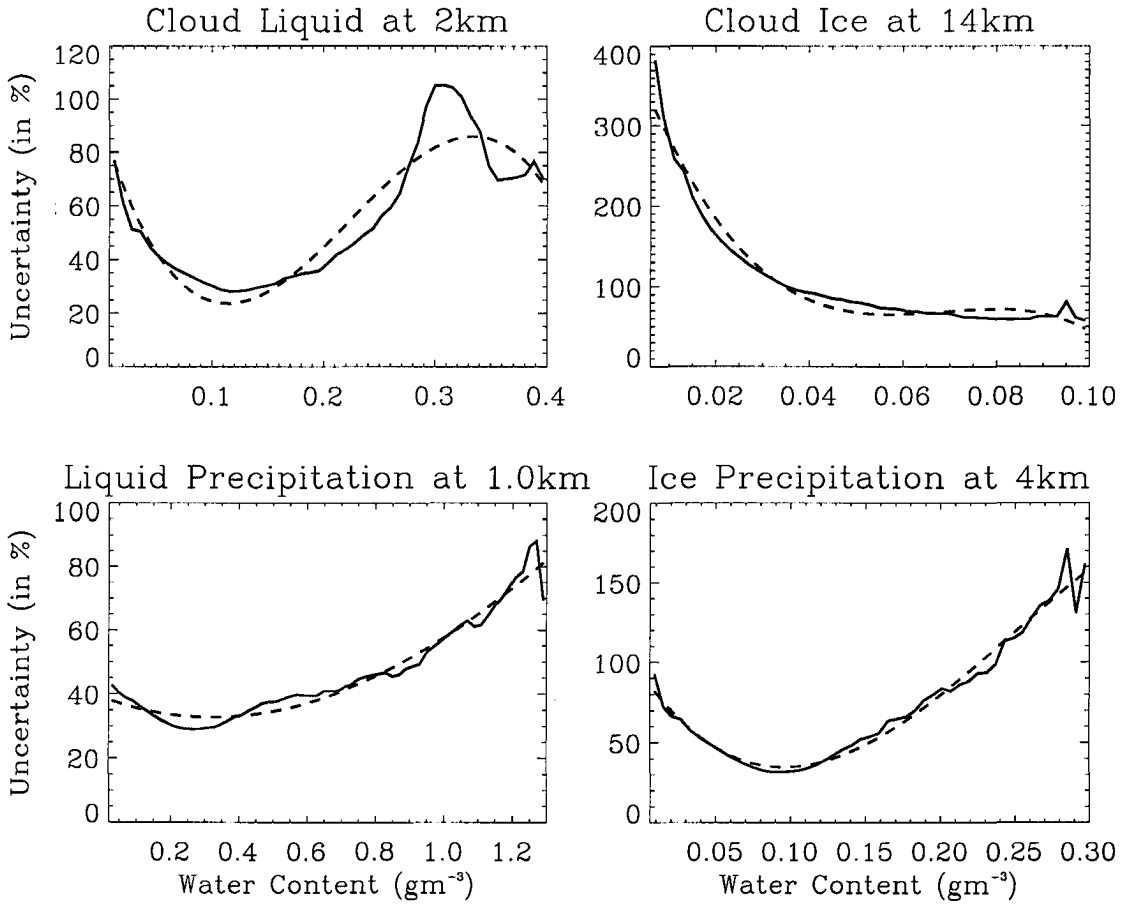

Figure 3.16: Sample third order polynomial fits to GPROF retrieval error for all four hydrometeor classes.

the fits of the form

$$\frac{\delta X}{X} = a_0 + a_1 X + a_2 X^2 + a_3 X^3 \tag{3.44}$$

where X is the water content in gm^{-3} are presented in Appendix B for all four hydrometeor classes at each model level.

3.9.3 The Effects of Correlations between Uncertainties

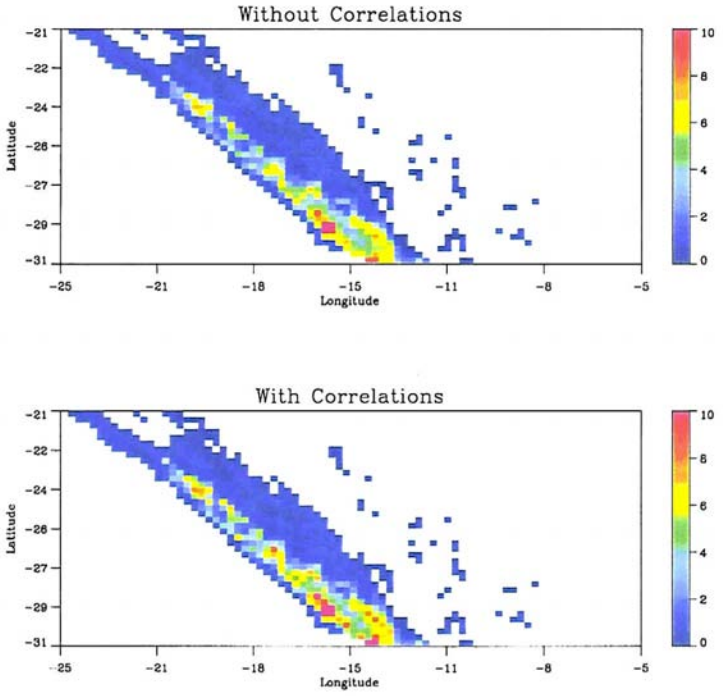

Figure 3.17: Uncertainty in retrieved rainrate using diagonal error covariance matrices (top) and a the full covariance matrices calculated in Section 3.7 (bottom).

It was shown in Section 3.7 that correlations among the uncertainties in the simulated emission and scattering indices do exist particularly between the two scattering channels at 37 and 85 GHz. Although the GPROF algorithm ignores these correlations in the interest of algorithm speed, it is instructive to investigate whether or not they significantly influence the retrieved rainfall and its uncertainty. Figure 3.17 shows that surface rainrate estimates change by less than 15 percent with the addition of correlations between the uncertainties and a comparison of error statistics from five TRMM orbits (Fig. 3.18) demonstrates that including these correlations does not significantly impact the overall uncertainty in the retrieved rainrates. It appears, therefore, that the emission and scattering indices are sufficiently decoupled that neglecting correlations between their errors does not appreciably alter the rainfall information they bring into the retrieval. The only exception

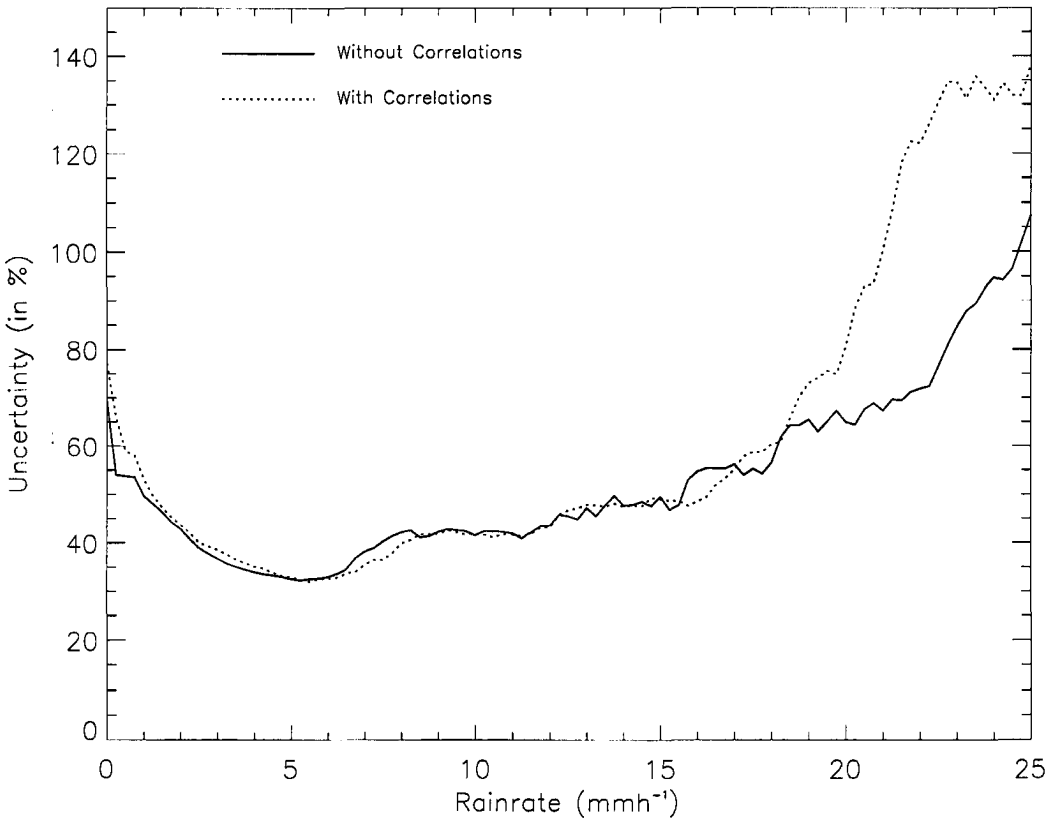

Figure 3.18: Retrieval errors assuming a diagonal covariance matrix (solid) and those using the full covariance matrix (dotted).

is in very heavy rainfall where the retrieval is dominated by scattering at 37 and 85 GHz. Under these conditions the strong coupling between these channels leads to larger model and measurement errors increasing the overall uncertainty in the retrieved rainrate. While this study focuses on retrievals over ocean, this result may have implications in TMI rainfall retrievals over land which are based entirely on scattering by ice.

3.9.4 Comparison of Measurement Bases

The BMC formulation is not restricted to any particular choice of measurement basis. In this section we compare the overall uncertainty in the estimated surface rainrate using three

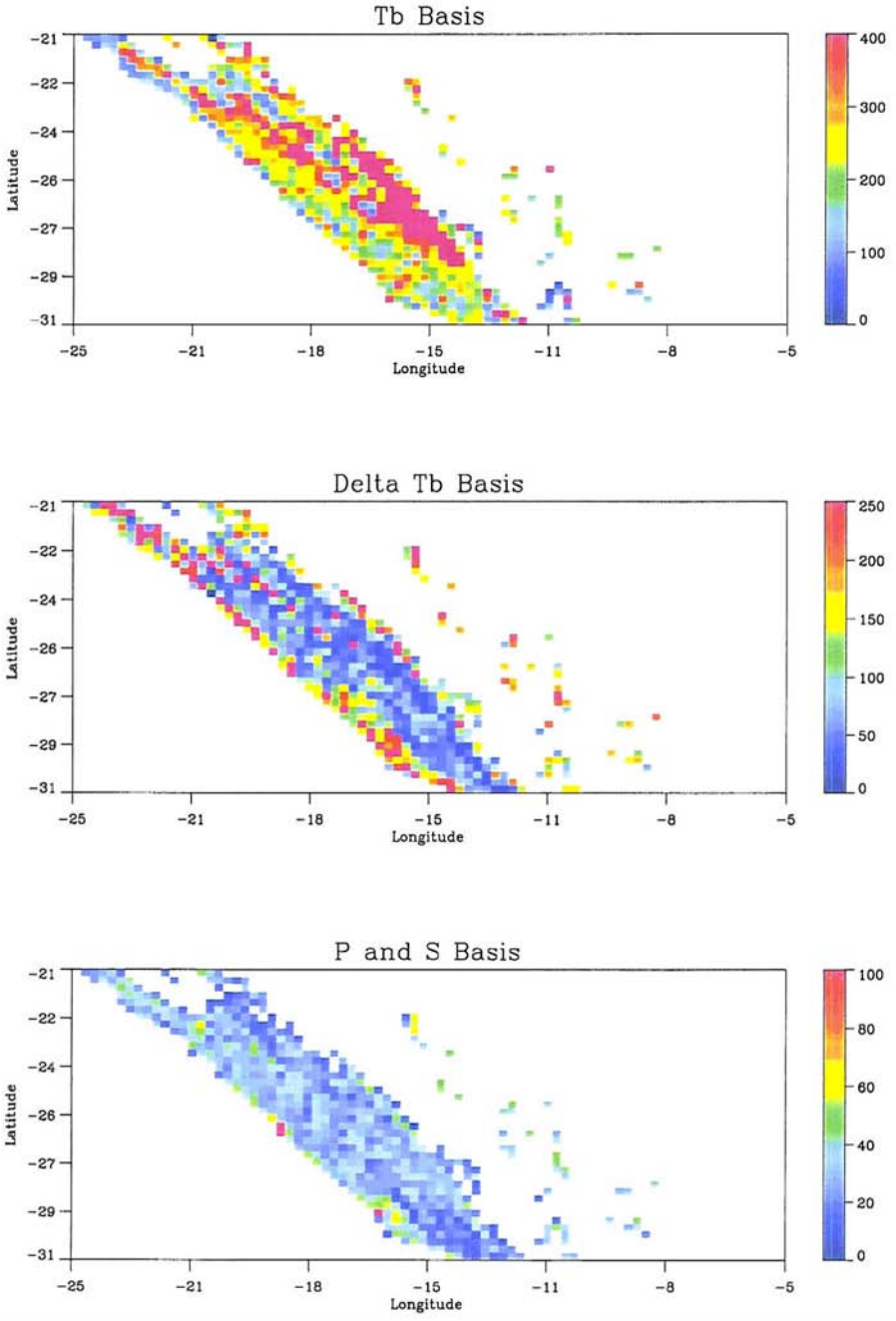

Figure 3.19: Uncertainty in retrieved rainrate using raw T_Bs (top), vertical minus horizontal T_B differences (middle), and emission and scattering indices (bottom).

different bases: one based on emission and scattering indices (PS basis), another on raw brightness temperatures (T_B basis), and the third on polarization differences, $T_{B_V} - T_{B_H}$ (ΔT_B basis) to quantify the differences in accuracy in using each method. Uncertainties in surface rainrate estimates using these three measurement bases are presented in Figures 3.19 and 3.20. Generally the polarization and scattering indices lead to a factor of three

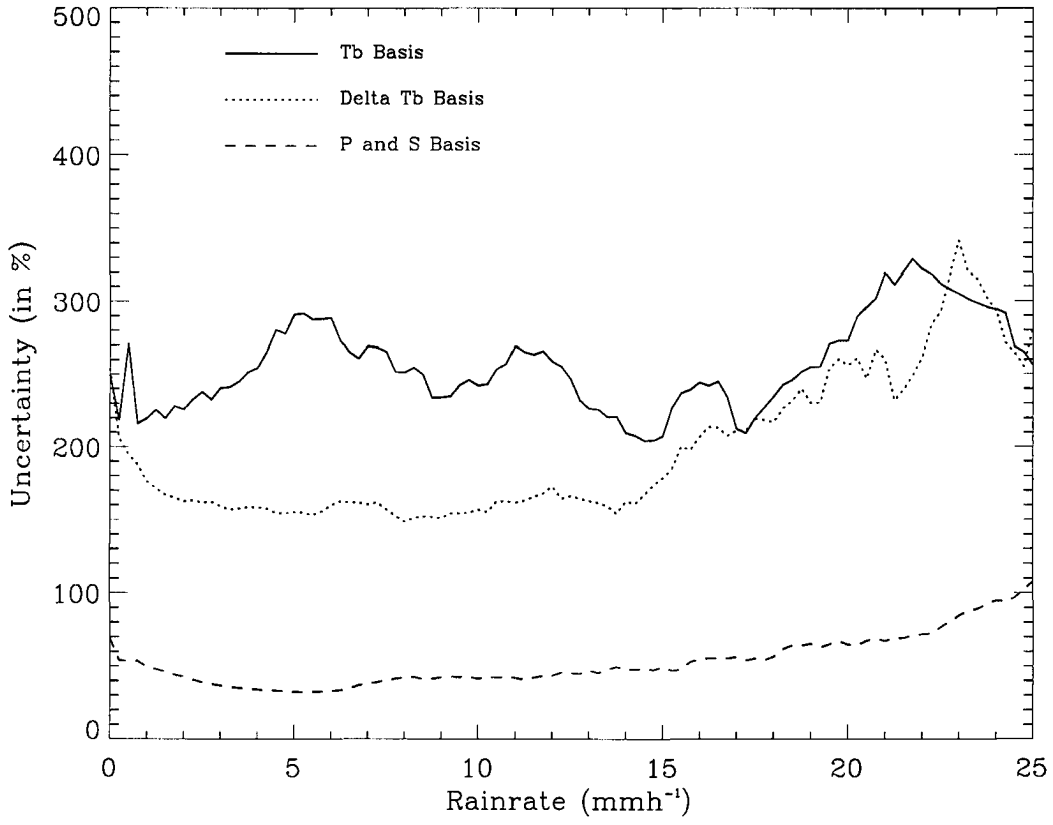

Figure 3.20: Comparison of retrieval uncertainty as a function of rainrate using raw T_Bs (solid), vertical minus horizontal T_B differences (dotted), and emission and scattering indices (dashed).

decrease in retrieved rainrate uncertainties relative to the other two measurement bases although the increase in accuracy can exceed a factor of 10 for individual pixels. These results are indicative of the fact that the T_Bs themselves are sensitive to errors in SST, sur-

face wind speed, and column water vapor. While the ΔT_B basis reduces this sensitivity by computing T_B differences, the reduction to only four variables leads to a high degree of indistinguishability within the cloud database and demonstrates only slight improvement relative to the T_B basis. The polarization and scattering indices, on the other hand, remove much of the sensitivity to errors in surface emission parameters by virtue of their definition as ratios while maintaining the majority of the information contained in the T_B measurements. As a result, the retrieval uncertainties are significantly suppressed in the PS basis. Fortunately, for reasons listed in Section 4a and in the appendix, the GPROF algorithm is currently cast in terms of these indices.

3.10 Including Other TRMM Measurements in the GPROF Algorithm

In principle any new information that may help to further distinguish between cloud profiles can be added to the retrieval provided a root-mean-square difference between observations and model simulated results can be defined. For the TRMM satellite information may be gleaned from the addition of VIRS T_Bs, PR reflectivities from different range gates, and even lightening information from the Lightening Imaging System (LIS). To incorporate the VIRS, PR and LIS information, one must respectively model the visible and infrared radiances, radar reflectivities as a function of range gate, and the lightening production associated with each profile and include rms differences between observed and modeled values of these quantities for each profile in Eqn. (3.7).

Immediately one can envision similar modifications to the uncertainty equations derived above to include new information in the error model as well. One merely modifies Eqn. (3.31) such that the sum runs over all data used in the retrieval making an appropriate modification to the definitions of the relevant d_i. This is the principle upon which we base our method of estimating the information content of measurements. Adding (or removing) information from estimates of the $\frac{\delta W_j}{W_j}$ and the cloud structure differences, Δ^{XY},

results in changes in the spreads in the cloud profile parameters. Detailed examination of these changes provides a means of determining which cloud profile parameters depend most strongly on any particular measurement. In this way the information content of each measurement as well as the information content of various combinations of measurements may be estimated. In the event that the removed measurement contains no information whatsoever identical flag-matrices and spreads will result. If, however, information is lost as a result of removing these channels, a larger fraction of indistinguishable profile pairs will emerge from the database.

Since radars are more sensitive to vertical profiles of precipitation than radiometers, the addition of PR data offers the potential for reducing the cloud database spread relative to the TMI alone. Of the TRMM instrument complement, therefore, we anticipate PR reflectivities to offer the greatest potential for improving the GPROF rainfall estimates. Figures 3.21 and 3.22 present similar delta- and flag-matrices to those depicted in Figs. 3.6 and 3.7 but with the addition of reflectivity profiles from the PR. Clearly the addition of reflectivity data helps to distinguish between similar profiles. The values in the delta-matrix increase by approximately a factor of four while the number of non-unique pairs of profiles evident in the flag-matrix is significantly reduced.

Further evidence for the reduction in non-uniqueness through the use of radar data is presented in Figure 3.23 which shows the spread in cloud profile parameters for the pixel illustrated in Figure 3.8 when the information from the PS basis is combined with a simple column-integrated PR reflectivity in the retrieval. Only 6 profiles remain indistinguishable from the original and the values of the various parameters spanned by these profiles has been dramatically reduced. As one might expect, when the full reflectivity profile is used in conjunction with the PS basis, the spread is reduced even further as shown in Figure 3.24.

Figure 3.25 illustrates the impact of including both a column-integrated reflectivity and

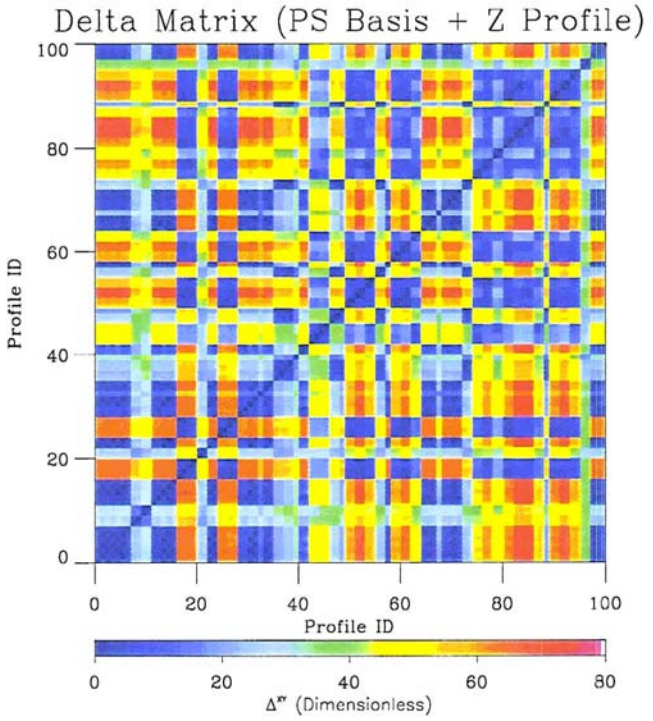

Figure 3.21: As in Figure 3.6 but using both emission and scattering indices and a PR reflectivity profile to distinguish each profile.

a full reflectivity profile on the overall retrieval error. The addition of a full radar reflectivity profile results in a reduction of $\sim$15 % in the overall uncertainty while the column-integrated reflectivity has a minimal effect. Figure 3.27 shows that, while the database component of the total error is reduced substantially in the presence of PR reflectivity data (Fig. 3.26), the weight component is significantly increased, suggesting that the algorithm is unable to find profiles which simultaneously reproduce the observed TMI T_Bs and PR reflectivity profile. This conclusion is supported by the fact that to make use of TMI and PR data simultaneously requires the assumption of extremely large variances ($\sim$ 20 dB) in

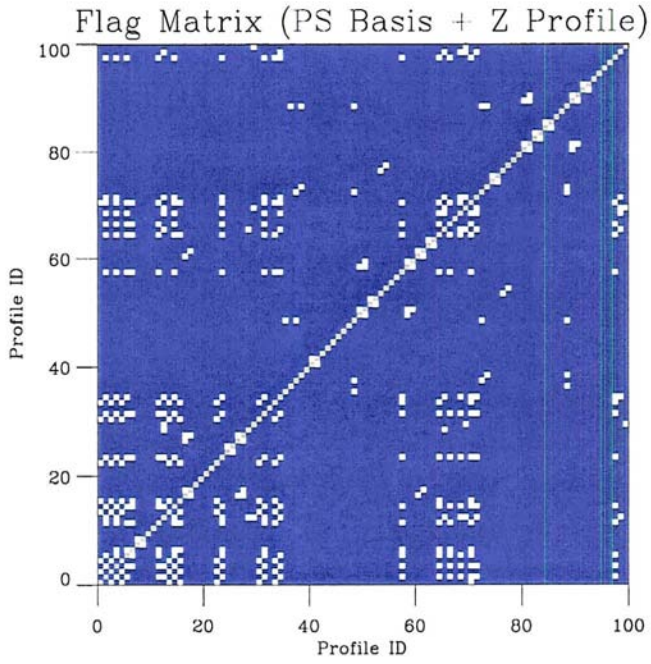

Figure 3.22: As in Figure 3.7 but for the case where both the emission and scattering indices and a PR reflectivity profile are used.

the radar reflectivity data to avoid increasing the overall uncertainty in the retrieval. These enormous uncertainties are not physically reasonable but are necessary to artificially overcome inconsistencies between the mappings of the active and passive data sets into the cloud and rainfall basis. Such mapping inconsistencies are caused by a magnification of any systematic errors in the cloud database, either from poor representation of microphysics in CRM simulations, incorrect assumptions in the radiative transfer or radar reflectivity calculations such as DSD or beamfilling effects, or missing cloud types. Viltard et al. (2000), for example, show that better consistency is obtained between TMI and PR observations if

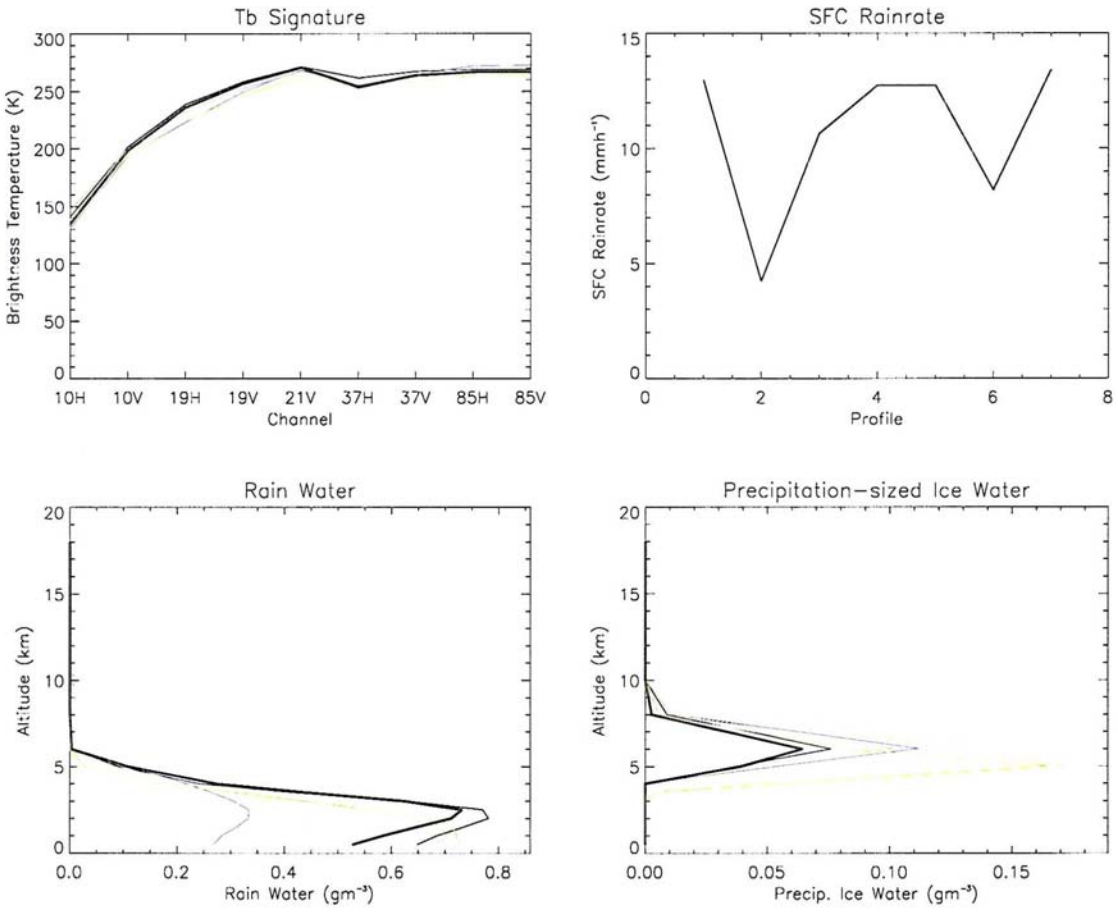

Figure 3.23: As in Figure 3.8 after including a column-integrated PR reflectivity profile.

somewhat different DSDs are assumed in modeling each.

At this time, under the assumption of unrealistically large variances in the radar data, we find that the addition of a reflectivity profile reduces the retrieval uncertainty at all rainrates as indicated by Fig. 3.25 but the assumed variance in the radar reflectivities must be "tuned" to optimize the compensating weight error increase and profile error decrease. With further investigation into the source of the differences in mapping reflectivities and radiances into rainrates (eg. studies like that conducted by Viltard et al., 2000), this procedure offers the potential for significantly reducing the overall retrieval uncertainty in the future.

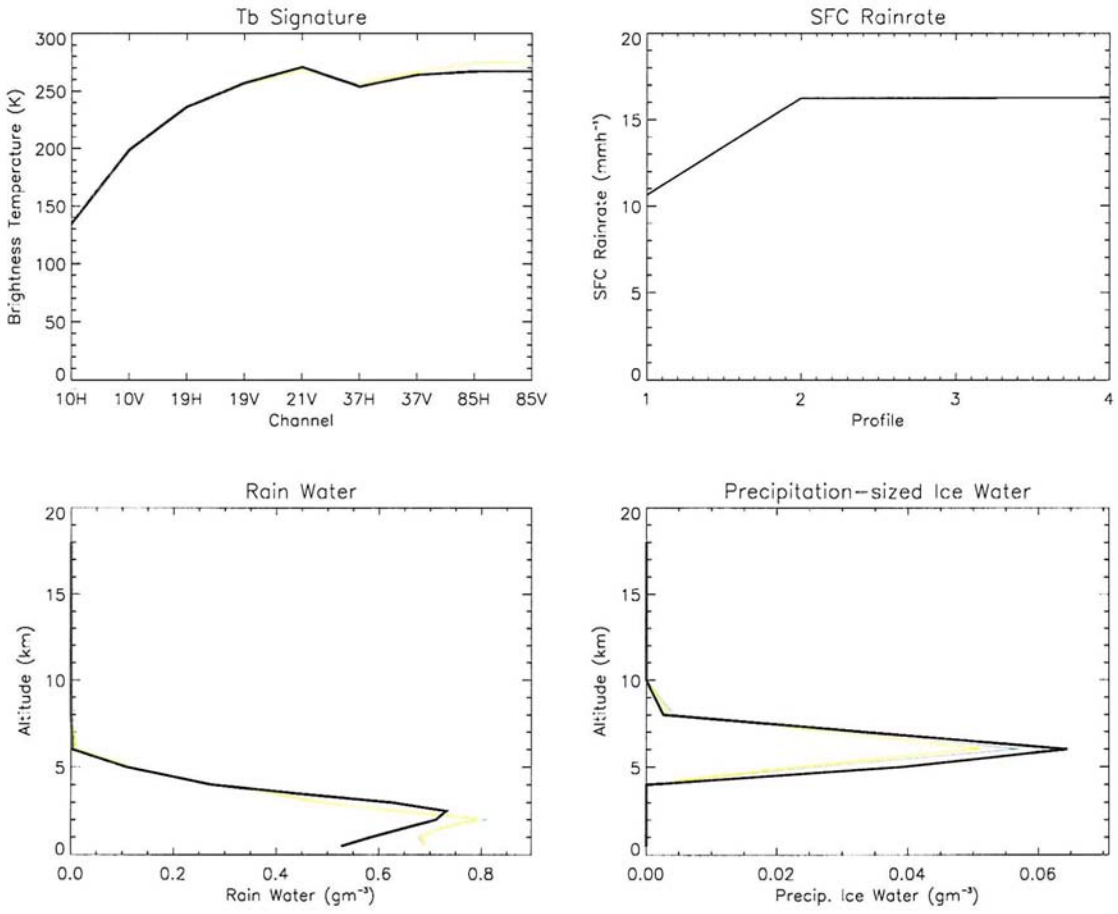

Figure 3.24: As in Figure 3.8 after including the corresponding PR reflectivity profile.

3.11 The Issue of Database Completeness

A question of significant interest to this type of retrieval concerns the completeness of the database. As was noted earlier, the shape of the probability density function of cloud profiles within the database is extremely important in the case where cloud profiles spanning a wide range of characteristics have non-negligible weights in the retrieval. From the preceding sensitivity studies we see that such a situation is indeed a possibility. The question arises, therefore, as to how sensitive the spreads in cloud profile parameters and their representation of nature are to the database itself. Again, the error model outlined in previous sections can be readily applied to obtain at least a qualitative answer to this question.

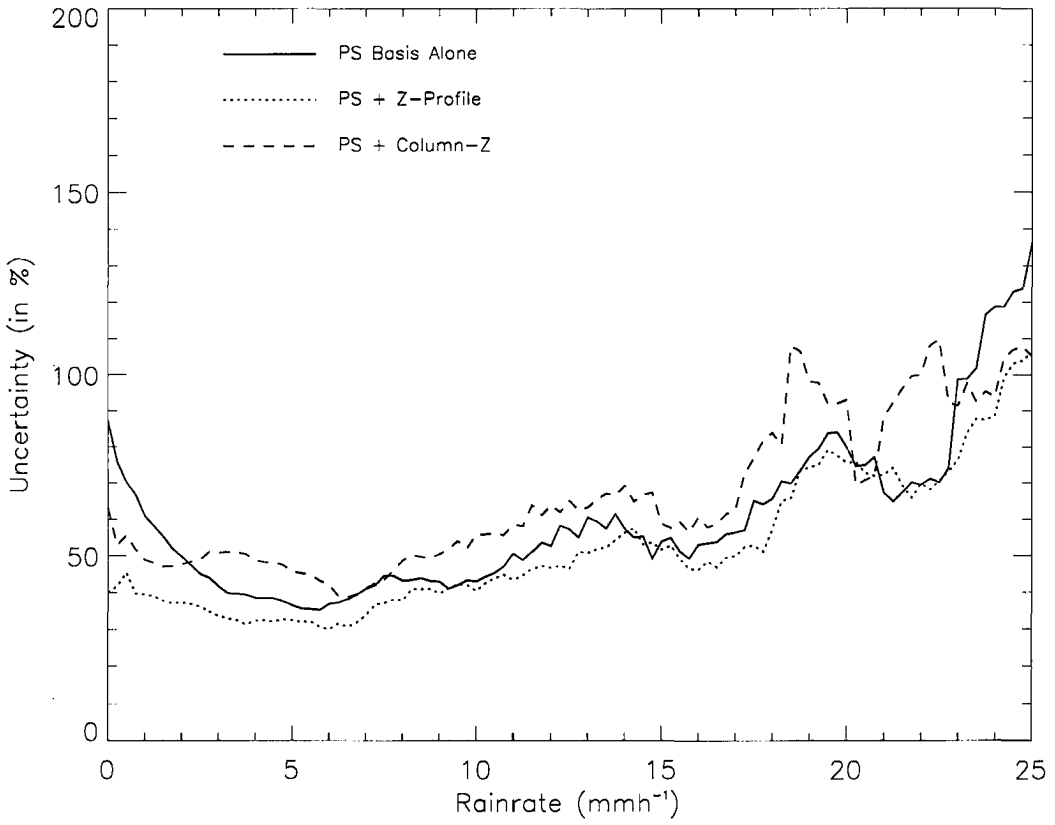

Figure 3.25: Total error in retrieved surface rainrate without PR data (solid), with the addition of a full PR reflectivity profile (dotted), and with the addition of a column-integrated reflectivity (dashed).

We are interested in determining how the uncertainty and its components vary with database size, $\frac{\partial(\text{error})}{\partial(\text{dbase})}$. By definition

$$\frac{\partial(\text{error})}{\partial(\text{dbase})} = \lim_{\delta(\text{dbase})\to 0} \left(\frac{\text{error}(\text{dbase} + \delta(\text{dbase})) - \text{error}(\text{dbase})}{\delta(\text{dbase})} \right) \tag{3.45}$$

which can be approximated as

$$\frac{\partial(\text{error})}{\partial(\text{dbase})} \approx \frac{\text{error}(\text{dbase} + \delta(\text{dbase})) - \text{error}(\text{dbase})}{\delta(\text{dbase})} \tag{3.46}$$

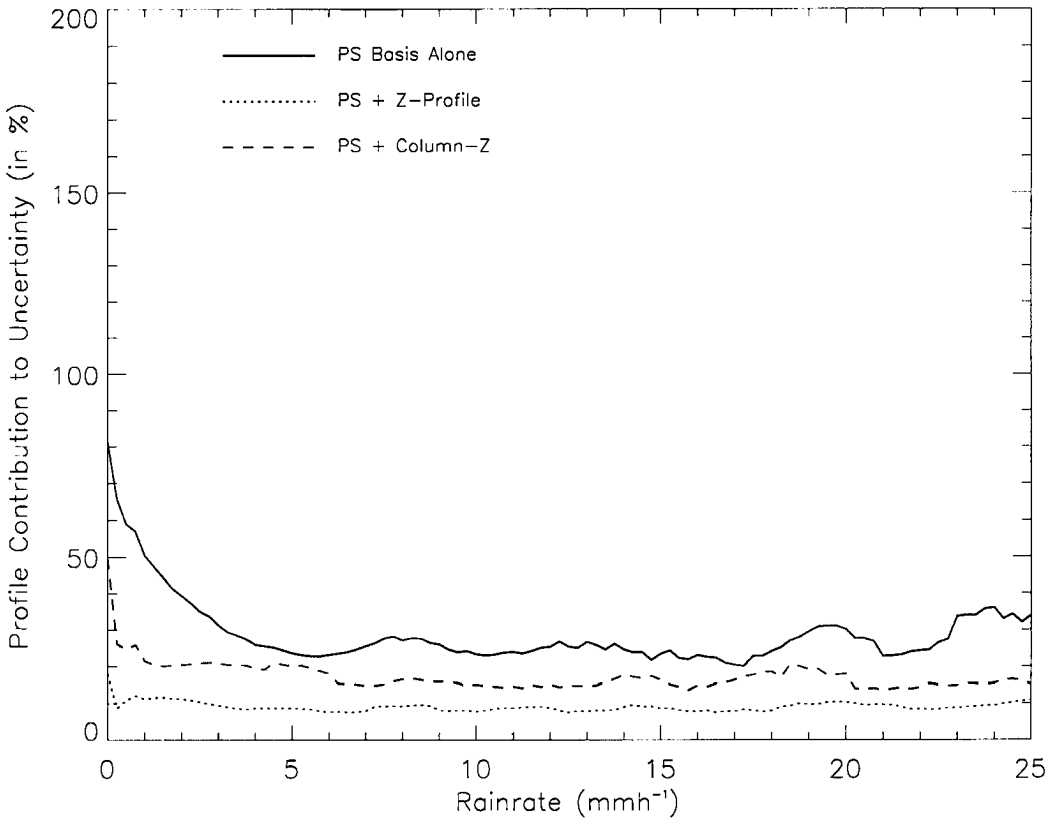

Figure 3.26: As in Figure 3.25 but for the profile database component to the uncertainty.

If the database were indeed complete or saturated, i.e. if it contained all possible scenes observed in nature, the uncertainties should be invariant with respect to the addition or removal of a small number of cloud profiles.

Figure 3.28 shows that the uncertainty in GPROF surface rainfall estimates depends very strongly on the fraction of the database used. As profiles are removed from the estimation process, the database becomes less representative of nature and errors increase accordingly. In addition, while the uncertainties are least when the full database is used, the rate of change of uncertainty remains non-negligible suggesting that additional, more diverse cloud profiles, may reduce errors further.

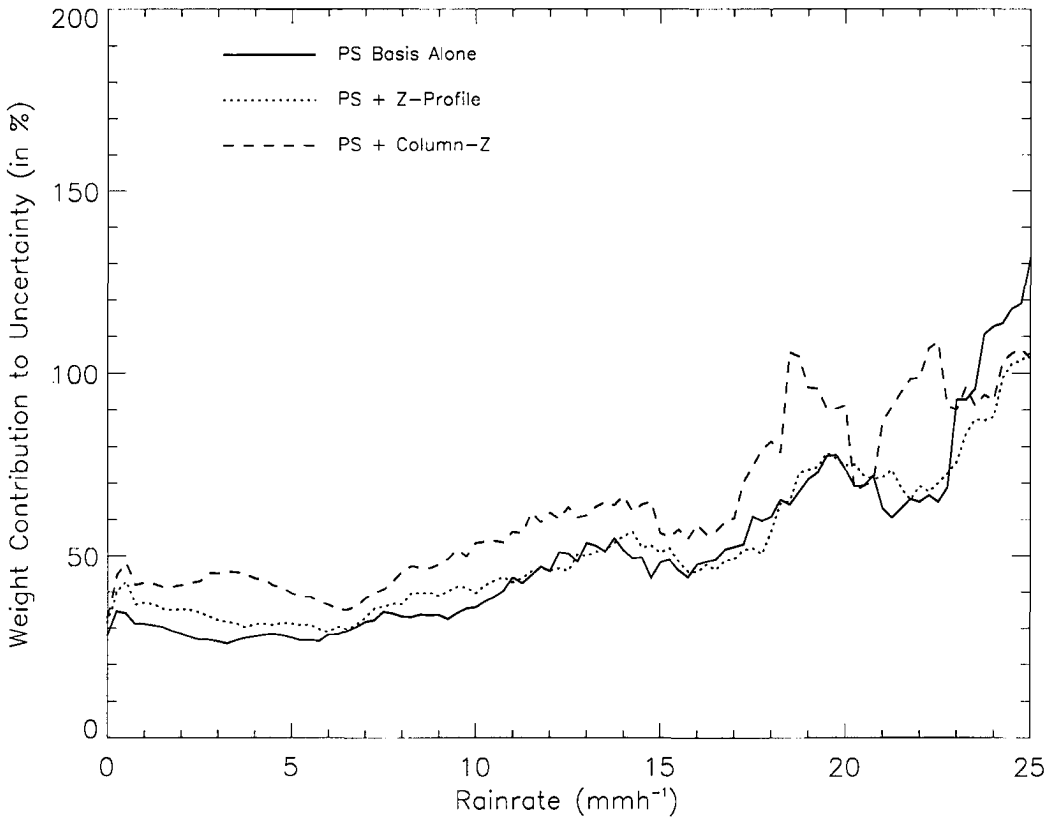

Figure 3.27: As in Figure 3.25 but for the weight component to the uncertainty.

Furthermore, weight and database contributions to the uncertainty, presented in Figures 3.29 and 3.30, suggest that the database is not saturated as far as either component is concerned. Recall that both the weight component, which is most representative of the uncertainties in the measurements and the radiative transfer modeling, and the database component, which can be loosely attributed to the non-uniqueness of profiles within the database, are minimized by the database that most accurately represents the scene being observed. Figures 3.29 and 3.30 show that, when profiles are removed from the database, its representation of nature is compromised leading to increases in both error components. While the rate of change of both components decreases as more profiles are added, it does

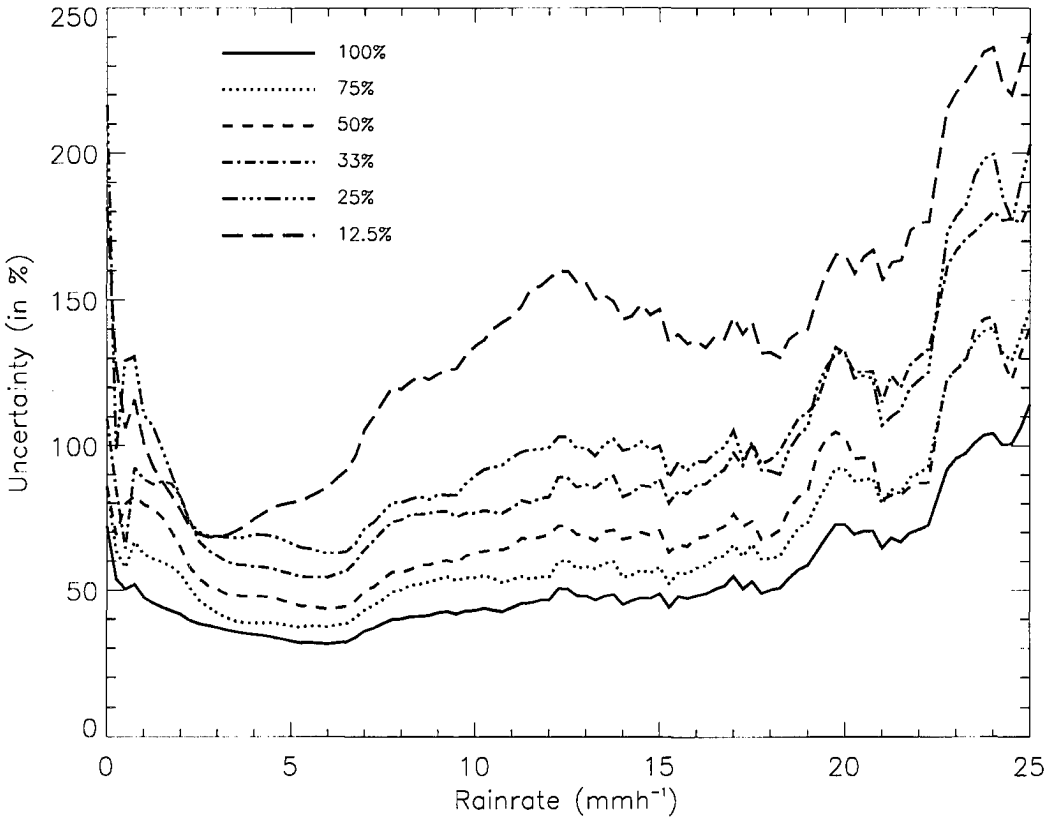

Figure 3.28: Uncertainty in retrieved surface rainrate as a function of database fraction used in the retrieval. The legend provides the percentage of the cloud database which gives rise to each curve.

not vanish indicating that the database may be incomplete and will improve through the addition of other cloud profiles from CRM studies under more diverse conditions.

3.12 Summary

A rigorous method has been introduced to estimate the uncertainty in the GPROF stochastic BMC retrieval of cloud and precipitation profiles from TMI observations. The model provides uncertainty estimates on a pixel-by-pixel basis accounting for the fact that the *a priori* database of realizations represents some scenes better than others. In addition, the

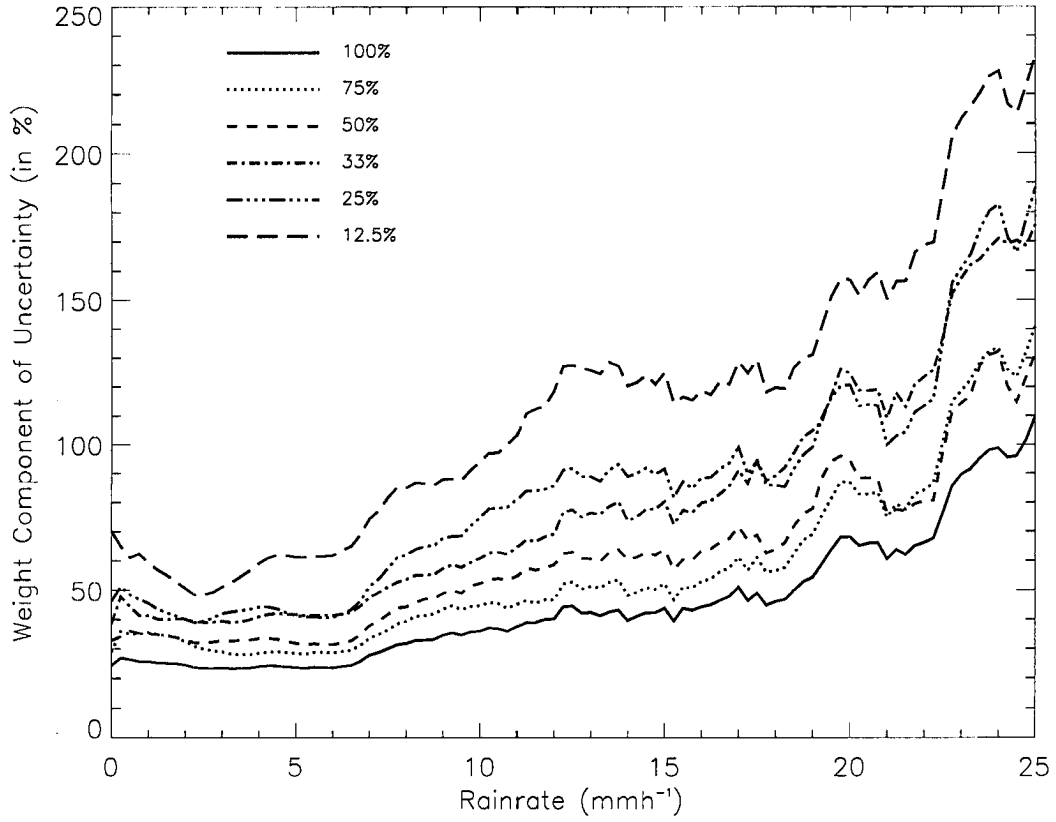

Figure 3.29: The component of the uncertainties plotted in Figure 3.28 owing to errors in measurement and radiative transfer modeling.

uncertainty can be broken down into components which can be identified with errors in the estimation of the weights and those incurred as a result of uncertainties in the database. In this way, the uncertainties can be easily understood in terms of the fundamental properties of the retrieval algorithm. In principle this method can be adapted to any combination of observables to test the impact of adding or removing information on the accuracy of the retrieval. Application of this model in operational satellite retrieval algorithms offers the potential to supply much needed uncertainty estimates for model validation and data assimilation applications.

We find that GPROF instantaneous surface rainrate estimates are typically accurate to

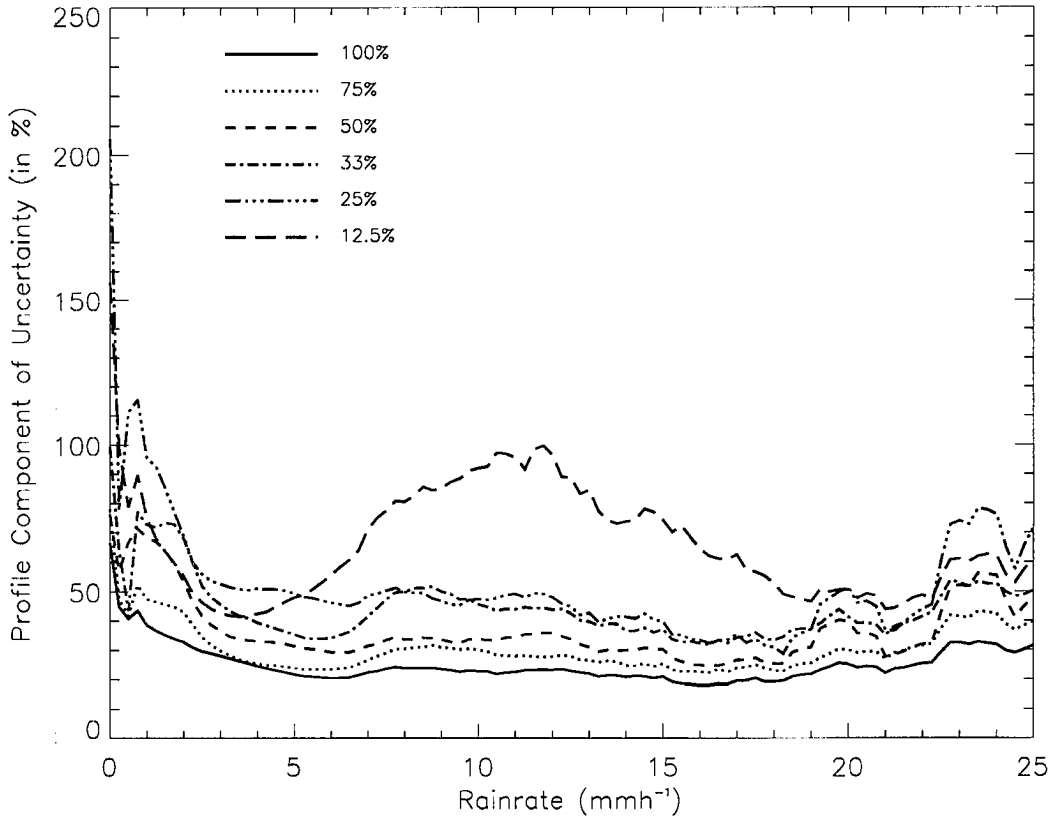

Figure 3.30: The component of the uncertainties plotted in Figure 3.28 owing to profile non-uniqueness and database bias errors.

fifty percent for rainrates below 19 mmh^{-1} but rapidly increase at higher rainrates. Corresponding profiles of precipitation have uncertainties ranging from 40 to 60 % below 3 km increasing rapidly at higher levels where ice scattering obscures the emission signal of the rainfall. As a consequence of its weaker signal, cloud liquid water is retrieved less accurately with uncertainties exceeding 80 % at low water contents. Precipitating ice is retrieved with similar accuracy as rainfall except at very low and very high ice water contents and at high altitude where its signal is overwhelmed by that of cloud ice. GPROF estimates of cloud ice, on the other hand, are very poor resulting from their weak scattering signal and possible uncertainties in the partitioning between ice hydrometeor categories in

the CRM. Cloud ice retrievals improve below the 100 % error level solely in instances of strong convection where significant concentrations exist near cloud top. Scattering by cloud ice, however, obscures the emission and scattering signals from the liquid and ice at lower levels resulting in less accurate retrievals of those quantities in such cases. These results provide baseline error estimates necessary in current efforts to assimilate surface rainfall data in NWP models and for attempts to assimilate profiles of cloud and precipitation in the future.

We have shown that TMI-based retrievals of cloud ice particles suffer primarily from the fact that the their signal is weak and that they are difficult to distinguish from larger precipitating ice hydrometeors. The radiative impact of rain systems on the Earth's radiation budget is, however, dominated by the particles near the cloud top since such systems are optically thick in the visible (solar) and infrared (terrestrial) regions of the spectrum. Uncertainties in the ice cloud information from the TMI, particularly at low ice water contents, hinders our ability to determine the cloud radiative forcing and heating rates in rain complexes from the TRMM observations. On the other hand, rainfall dominates the latent heating impact of a rain complex. Since liquid precipitation is retrieved much more accurately, TRMM is better suited to estimating latent heating than radiative heating. Accurate estimates of latent heating, however, require the additional information regarding local vertical air motions which may be extremely difficult to obtain given the current array of TRMM sensors. In subsequent chapters, it will be our goal to make use of this uncertainty information to determine how accurately the radiative and latent heating impacts of rain systems can be estimated using the GPROF cloud and rainfall information and to estimate the relative importance of each in the tropical energy budget.

Chapter 4

Three-Dimensional Cloud Structures from TRMM

4.1 Precipitating Pixels

With rigorous error estimates in hand, it is now possible to construct a three-dimensional picture of cloud and rainfall in the tropics with associated uncertainties using the GPROF product. The results will then serve as input to a broadband radiative transfer model to infer the cloudy-atmosphere components of the ERB complementing latent heating estimates derived from GPROF. For illustration purposes we focus on February of 1998 to facilitate comparison with the latent heating study of Tao et al. (2001) and all data will be mapped onto an even 0.25°x0.25° grid to aid in processing. Surface rainrates for February 1, 1998 are presented in Figure 4.1. There are a number of wide-spread areas of precipitation which are well-suited for illustrating the GPROF data and its uncertainty. One such region in the southeastern Pacific, demarcated by the gray box in Figure 4.1, is highlighted in Figure 4.2. The domain contains numerous areas of moderate to intense rainfall surrounded by widespread light rain and a substantial number of rain-free pixels which will be used in subsequent sections to illustrate the importance of cloud information in estimating radiative heating.

Figures 4.3 and 4.4 show longitude-height cross-sections of each GPROF hydrometeor species and their uncertainties for the segment of 8°S latitude between the two gray diamonds on Figure 4.2. The value of the TRMM data and the preceding uncertainty analyses in computing radiative and latent heating profiles is evident. For each pixel vertical profiles of four hydrometeor classes covering cloud and precipitating distributions of liquid and frozen hydrometeors are retrieved providing a rich source of information for radiative

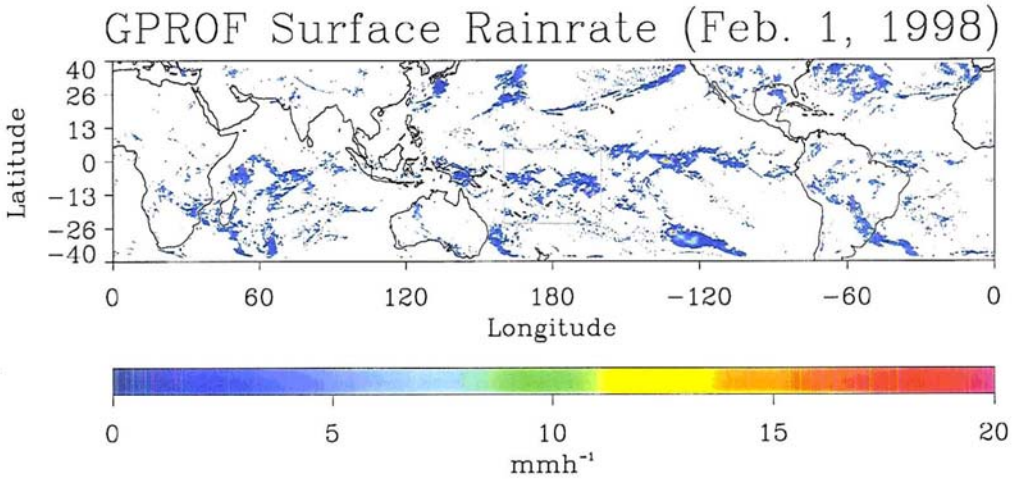

Figure 4.1: GPROF surface rainrate estimates from February 1, 1998. Results from the remainder of this chapter will focus on the region indicated by the gray box.

heating calculations to follow. In addition, perturbations of these profiles according to their uncertainties can be used to establish error bounds on the results.

It follows from the information content and error analysis studies that the TMI instrument is not well suited for retrieving ice cloud information. This is clearly demonstrated in Figure 4.4 where the uncertainties in cloud ice water exceed 100 % in most cases. In addition, the GPROF retrieval provides no information regarding the presence of ice clouds in non-precipitating regions. The radiative effects of these clouds could be significant considering their large spatial extent and long lifetimes relative to precipitation events (Liou, 1986) so we anticipate that the GPROF ice water content estimates will pose a significant source of uncertainty in the radiative transfer calculations that follow. Liquid cloud and

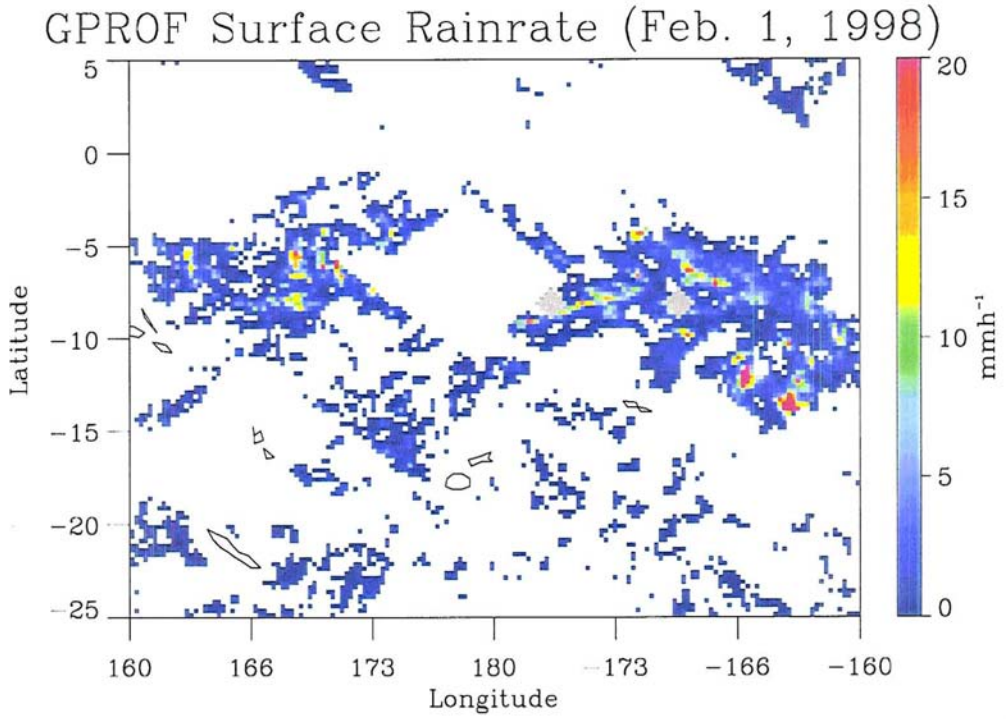

Figure 4.2: GPROF rainrates within the sample region indicated in Figure 4.1. Gray diamonds on the figure indicate the transect across which hydrometeor cross-sections and their errors are illustrated below.

rainfall estimates, on the other hand, are accurate along this segment relative to those of ice, so estimates of latent heating and downwelling radiative fluxes are expected to be more accurately characterized by the GPROF data.

4.2 Ice Cloud Properties from VIRS

Among the primary objectives of this study, is the desire to obtain as complete a view of tropical radiative and latent heating as possible. To this end, information on cloud distributions outside the precipitating regions sampled by the GPROF algorithm is required. In this section, an algorithm based on visible and infrared radiances will be applied to data from

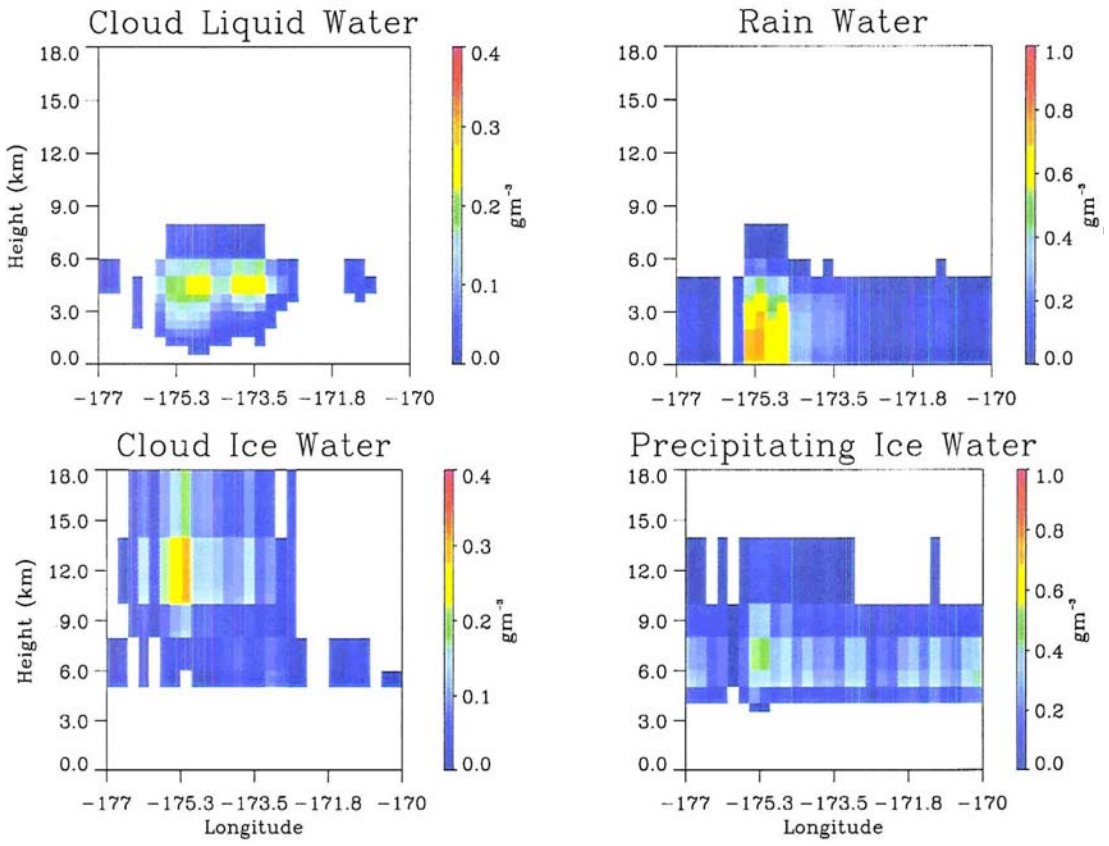

Figure 4.3: Longitude-height cross-sections of cloud liquid, cloud ice, precipitating liquid, and precipitating ice at 8°S from the GPROF algorithm.

the VIRS instrument to detect ice clouds and provide a rough estimate of their optical properties. Such measurements are essential to accurately quantify both the outgoing longwave and reflected shortwave components of the radiation budget. In addition, they will provide a means for studying the relationship between the hydrological cycle and ERB through careful examination of the balance between latent heating and cloud radiative forcing.

4.2.1 Retrieving Cirrus Optical Depth and Effective Radius in the VIS/IR

The importance of cirrus clouds in modulating atmospheric infrared (IR) heating (Roewe and Liou (1978), Stephens (1980), and Liou (1986)) has lead to the development of numerous diverse methods for the retrieval of their optical properties. As early as the 1960's

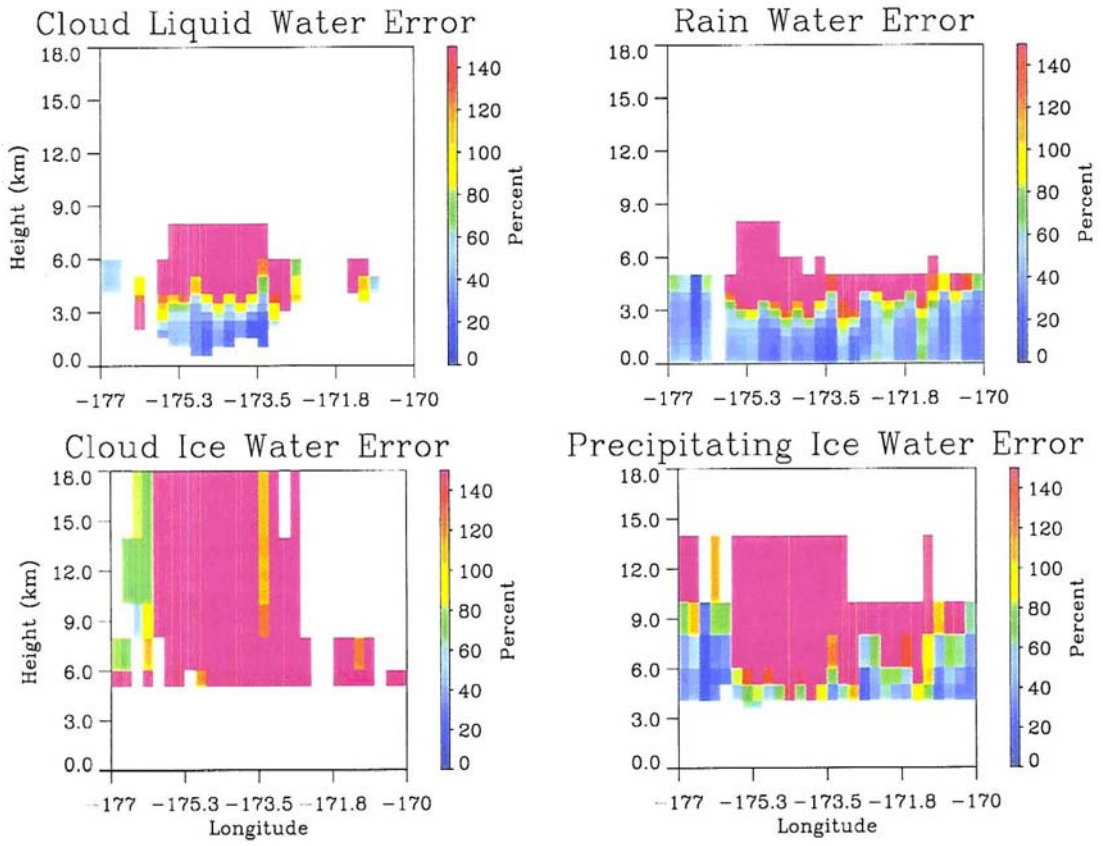

Figure 4.4: Uncertainties in the hydrometeor cross-sections presented in Figure 4.3.

aircraft measurements of cirrus IR emissivities were presented by Kuhn and Weikmann (1969) and Platt (1973) while Blau et al. (1966) introduced observations of ice cloud reflectance at visible and near-infrared (NIR) wavelengths. These observations prompted a number of theoretical investigations into the optical properties of cirrus clouds which form the foundation of many retrieval techniques still in use today. Hansen and Pollack (1970), for example, were among the first to employ theoretical calculations of the reflectance of ice clouds in an effort to describe the spectral variation observed by Blau et al. (1966) while Liou (1974) used radiative transfer calculations to illustrate the variation in cirrus cloud optical properties between 11 and 12 μm. Liou (1977) went on to develop an algorithm for the retrieval of the optical thickness, transmissivity and fractional cover of cirrus clouds

using multispectral observations at 8.7, 9.1, 10.5, and 11.1 μm.

These early studies paved the way for satellite observations of cirrus clouds which continue today. One of the first studies aimed at deriving the optical properties of cirrus from space was that of Platt et al. (1980) who developed a technique to infer visible albedo, infrared emittance and visible optical depth using visible and infrared radiances from geostationary satellites in combination with ground-based lidar measurements. In a study based entirely on measurements in the IR window region, Inoue (1985) noted high variability in the optical properties of cirrus clouds through the 10 μm atmospheric window. A method for inferring cirrus optical depth and effective radius based on this observation was later developed by Prabhakara et al. (1988) and applied to study global distributions of thin cirrus using the Nimbus-4 Infrared Interferometer Spectrometer (IRIS). Parol et al. (1991) present a similar technique applied to channels 4 and 5 (11 and 12 μm) of the Advanced Very High Resolution Radiometer (AVHRR) flown on NOAA polar orbiting satellites while Arking and Childs (1985) develop a method for retrieving cirrus optical depth, cloud fraction, and a parameter related to the size, shape, and phase of its constituent particles from the AVHRR 3.7 and 11 μm channels. Since then numerous other cirrus studies have been conducted using AVHRR observations or GOES radiances of which Minnis et al. (1990), Stone et al. (1990), Nakajima and King (1990), Minnis et al. (1993), Ou et al. (1993), and Nakajima and Nakajima (1995) are examples.

Current EOS satellite platforms carry the very modern Moderate-Resolution Imaging Spectroradiometer (MODIS) designed to measure cloud aerosol and water vapor using information from 36 spectral bands in the visible (VIS) and IR regions of the electromagnetic spectrum. King et al. (1992) provides an overview of the methods used in MODIS ice cloud retrievals each of which derive from those outlined above. Reflection of solar radiation at 0.66, 1.65, and 2.13 μm along with the combined reflection/emission channel at 3.75 μm are used in determining optical properties of thick cirrus while a method based on a com-

bination of radiances at 8.55, 11, and 12 μm is employed to detect optically thin cirrus[1].

While techniques based on passive observations have improved over the years, it is important to note that significant shortcomings remain. Of primary significance is the lack of information regarding cloud vertical structure in visible and infrared radiances alone. As a result, passive algorithms cannot account for the effects of multiple cloud layers and often have difficulty in determining cloud vertical placement, particularly when the clouds are optically thin. In addition, the resulting retrievals seldom resolve vertical variations in cloud microphysical structure. Research is ongoing to improve upon these methods both through the use of more diverse multispectral passive observations (Rolland et al., 2000) as well as active measurements such as measurements of lidar backscatter and reflectivity measurements from cloud radars. Miller et al. (2000), for example, demonstrate that lidar- and radar-derived cloud boundaries improve nighttime retrievals of thin cirrus by 30 % relative to methods which employ only passive observations. The present study, however, is constructed around the TRMM platform in the hopes of making simultaneous observations of latent and radiative heating so, while we acknowledge its potential deficiencies, a passive method based on IR radiances from VIRS will be adopted to infer ice cloud information.

4.2.2 VIRS-based Retrieval of τ and r_e

The VIRS radiometer on TRMM consists of five channels at VIS and IR wavelengths. The method introduced by Prabhakara et al. (1988) based on radiances at 10.8 and 12 μm, both channels on the VIRS instrument, is well-suited for the purpose of identifying cirrus and obtaining the rough estimates of their optical properties under both daytime and nighttime conditions as are required for this study.

At the root of the method is the fact that particles on the order of 25 μm or smaller more efficiently scatter 12 μm radiation relative to that at 10.8 μm. As a result, small ice particles

[1]The addition of the 8.55 μm channel, available from the MODIS instrument is viewed as an extension of the method of Prabhakara et al. (1988).

exhibit stronger extinction resulting in cirrus which appear "colder" at 12 μm than at 10.8 μm. This is illustrated in terms of mass scattering and extinction coefficients in Figure

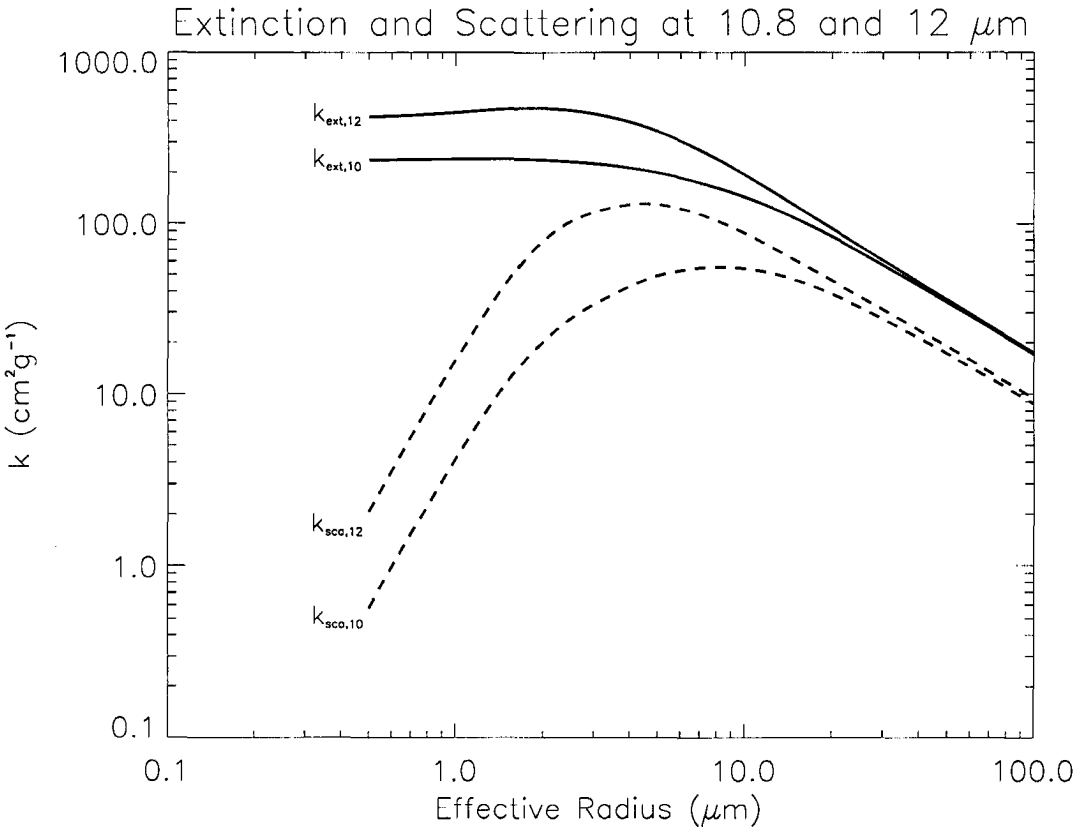

Figure 4.5: Mass extinction (solid curves) and scattering coefficients (dashed curves) at 10.8 and 12 μm plotted as a function of radius for monodispersed spherical ice particles.

4.5. For larger particles, the combination of radiation removed through diffraction around its edges with that blocked by its geometrical area results in a mass extinction coefficient proportional to twice the cross-sectional area of the particle, $k_{ext} = 2\pi r^2/m$, independent of the wavelength of radiation incident on the particle.

Aircraft spectra shown in Figure 4.6 demonstrate the impact of the differences in extinction at IR wavelengths on radiances transmitted through three cirrus clouds of varying thickness. In the absence of cloud, T_Bs are approximately constant over the entire atmo-

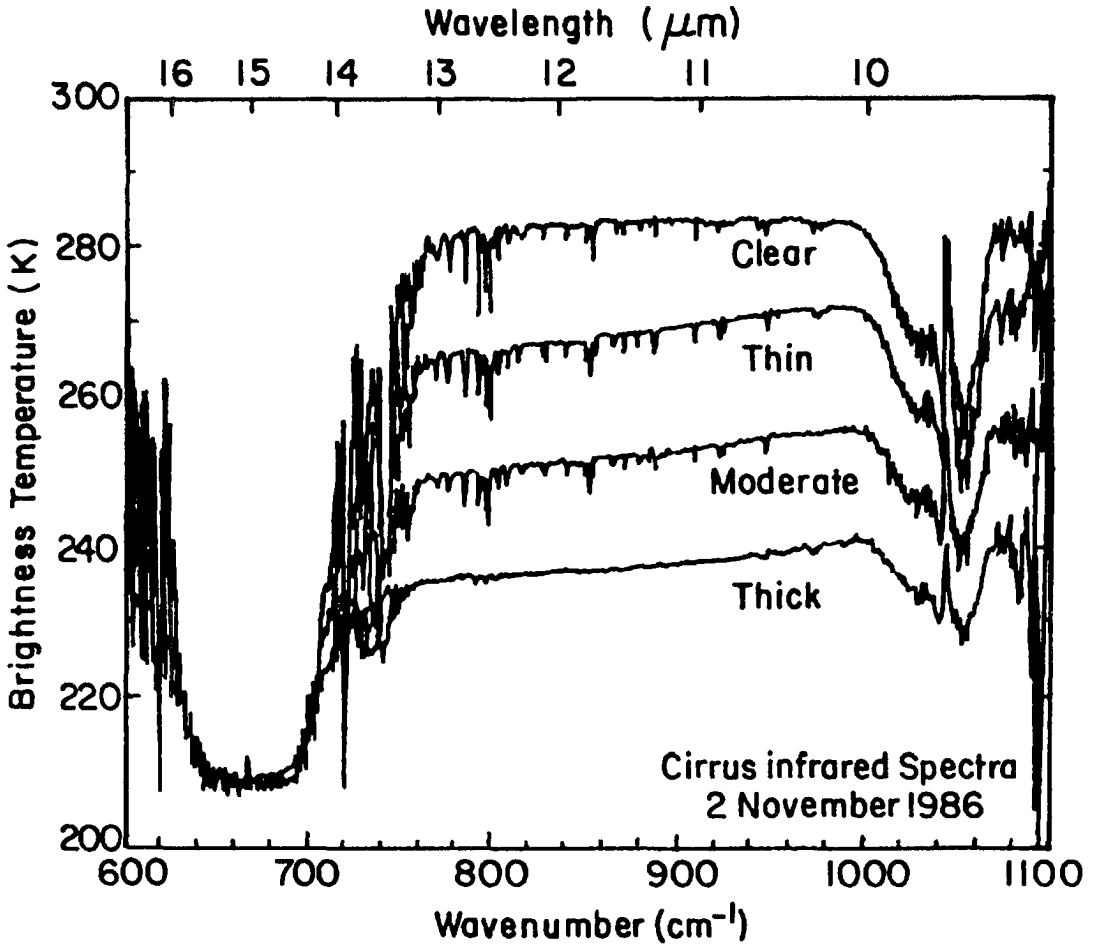

Figure 4.6: Emission spectra in the 8-12 μm atmospheric window due to clear-sky, thin, moderate, and thick cirrus scenes (from Stephens (1994)).

spheric window between 10 and 12.5 μm resulting in a very small $\Delta T_B = T_{10.8} - T_{12}$ due to absorption in the wings of nearby water vapor bands. In the presence of cirrus, the radiation observed at the aircraft arises from a combination of emission from the atmosphere below the cloud and emission at from the cloud itself. The thicker the cloud, the more closely the observed brightness temperature to the cloud emitting temperature, T_c. The effect of the extinction difference between 10.8 and 12 μm is also evident since the T_Bs in the window region decrease with increasing wavelength. ΔT_B is the greatest for thin clouds where the extinction is sufficient to have an impact on the radiation emitted from below the cloud but

not so great as to mask it entirely. As cloud optical depth increases decreasing the visibility of the signal from lower atmosphere, ΔT_B correspondingly decreases until, for extremely thick clouds (not shown) it vanishes completely as $T_{10.8} = T_{12} = T_c$.

In order to quantify this effect for use in a retrieval, radiances observed by a satellite flying over over the cirrus must be modeled as a function of effective radius and optical depth. The model adopted here is based on a simplified two-layer atmosphere described in Stephens (1994) which has been recently implemented by Cooper (2001). Neglecting scattering which is generally small for cloud particles at IR frequencies[2], the radiation received by the VIRS instrument is the sum of radiation emitted and reflected by the Earth's surface which is transmitted through the atmosphere and the integral of emission from the atmospheric column. In terms of optical depth, defined as $d\tau = -\sigma_{ext} dz$, the upwelling radiance at TOA, $I(0, \mu)$ is given by

$$I(0, \mu) = I(\tau^*, \mu) e^{-\tau^*/\mu} + \int_0^{\tau^*} B(t) e^{-t/\mu} \frac{dt}{\mu} \tag{4.1}$$

where τ^* is the optical depth of the atmospheric column as a whole, or, equivalently, the coordinate of the surface in optical depth space. $B(\tau)$ is the Planck function accounting for thermal radiation emitted at a level τ in the atmosphere and μ is the cosine of the satellite viewing angle. For simplicity, the atmosphere will be thought of as consisting of two layers, one representing the clear atmosphere below the cloud and the other containing a isothermal, homogeneous cloud. The errors introduced by such an approximation are likely to be less significant than those incurred as a result of a lack of information regarding cloud boundaries both in the retrieval and in modeling radiative heating in the next chapter.

[2]This assumption requires some justification. Ice particles of radii 10-50 μm which may be found in cirrus clouds scatter approximately as much IR radiation as they absorb. When an ensemble of these particles are modeled in a typical cirrus cloud, however, Stephens (1980) showed that they lead to a total IR reflectance of only about 5 % or 10 Wm^{-1}. While this may be significant in some applications, it will be shown that errors introduced by a lack of information regarding vertical cloud placement will be far greater in the present study.

Following Stephens (1994), Equation (4.1) reduces to

$$T_{obs} = T_a e^{-\tau_c/\mu} + T_c[1 - e^{-\tau_c/\mu}] \tag{4.2}$$

where T_a is the effective blackbody temperature of the atmosphere beneath the cloud, τ_c is the optical depth of the cloud which emits at a temperature T_c, and $e^{-\tau_c/\mu}$ is the transmission through the cloud layer. Cast in this form it is easy to see that the observed T_B is simply a weighted sum of the emitting temperatures of the atmosphere and cloud.

The dependence on effective radius enters through the cloud optical depth, τ_c, which can be estimated provided one makes some assumption regarding particle shape. For simplicity, we will assume spherical particles since we have no *a priori* reason to adopt any other particular shape. If we further assume the cloud consists of a monodispersed size distribution the cloud optical depth can be written as

$$\tau_c = \pi N_0 r_e^2 Q_{abs} \Delta z \tag{4.3}$$

where N_0 is the number of particles per unit volume and Δz is the geometric thickness of the cloud. In this study Q_{abs} is approximated using the anomalous diffraction theory (ADT) first introduced by Van de Hulst (1982). While not exact, the method provides a close approximation to the overall structure of the extinction derived from Lorenz-Mie theory provided particles are large with respect to the incident radiation and have real refractive indices close to that of the ambient atmosphere (see, for example, Figure 32 of Van de Hulst (1982)). From Stephens (1994), the absorption efficiency in the ADT approximation is given by

$$Q_{abs} \approx 2\left[\frac{1}{2} + \frac{e^{8\chi\kappa}}{8\chi\kappa} + \frac{e^{8\chi\kappa} - 1}{(8\chi\kappa)^2}\right] \tag{4.4}$$

where κ is the imaginary part of the refractive index and $\chi = \frac{2\pi r_e}{\lambda}$ is the size parameter. Equations (4.2), (4.3), and (4.4) constitute a simple, complete model governing the

transmission of radiation through a cirrus cloud from which 10.8 and 12 μm brightness temperatures can be evaluated for any combination of r_e and τ_c.

Figure 4.7 illustrates the relationship between $\Delta T_B = T_{10.8} - T_{12}$ and $T_{10.8}$ derived using this simple approximation to the radiative transfer equation assuming three different cloud emitting temperatures. The resulting curves resemble arches. The right foot of the arch corresponds to the limit of an optically transparent cloud which is transparent to the radiation emitted from the atmosphere below it. In this case ΔT_B arises solely from differences in the height at which the clear-sky weighting functions at 10.8 and 12 μm peak. The

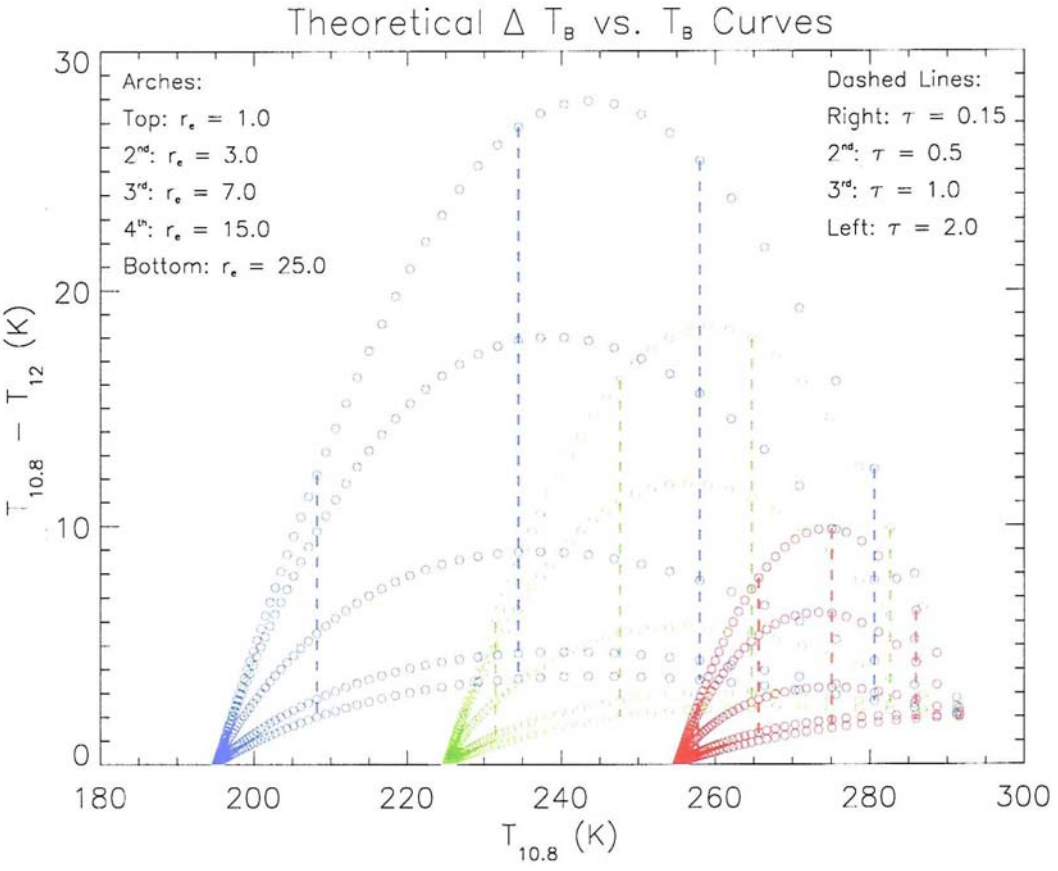

Figure 4.7: 10.8 - 12 μm brightness temperature differences as a function of 10.8 μm T_B for cirrus clouds containing spherical ice particles at 255 K (red), 225 K (green), and 195 K (blue). Radii assumed for each arch are indicated in the left-hand legend while optical depths corresponding to the vertical lines on the figure appear on the right.

left foot occurs in the presence of optically thick cloud where all radiation from below the cloud is obscured at both wavelengths providing an estimate of the emitting temperature of the optically thick cloud. Between these points the extinction difference gives rise to larger ΔT_Bs which are greatest for small particles and optical depths of ≈ 1.

These results are in good agreement with those presented in Prabhakara et al. (1988) and demonstrate the strong sensitivity of ΔT_B to the assumption of cloud emitting temperature. One can conceive of a method to estimate this temperature based, for example, on T_Bs of nearby thick cloud pixels but the added benefits of such an approach are questionable considering the enormous uncertainties which would still be present. Instead, we will adopt the approach of merely assigning a cloud emitting temperature to all retrievals and attempt to establish bounds on the uncertainty this introduces by perturbing its value over a range one might reasonably expect to find in the tropics. The resulting optical property estimates will be rough, at best, and it is anticipated that their uncertainties will dominate the uncertainties in estimates of the radiative component of the diabatic heating. In addition the algorithm is not sensitive to particle size or optical depth in thick clouds ($\tau > 3$) where both channels saturate and T_{12} and $T_{10.8}$ converge to the cloud emitting temperature. In such cases a simple cloud identification is all that will be possible. Even so, it is important to reiterate the significance of even a crude identification of cirrus when attempting to estimate atmospheric components of the ERB. This section may, therefore, be more aptly named "VIRS-based Retrieval of Thin Cirrus Optical Properties and Detection of Thick High Cloud" but that is simply too long for a section heading.

It should be noted that methods making use of the VIRS 0.6 μm visible and 3.75 μm near IR channels such as that proposed by Nakajima and King (1990) would allow one to estimate the optical properties of thicker clouds during daylight hours. In this way improvements could be made to the ice cloud estimates from GPROF which would otherwise be impossible using the IR-only method we adopt since the cloud above rainfall is optically

extremely thick. Perhaps more importantly as far as radiative heating is concerned is the

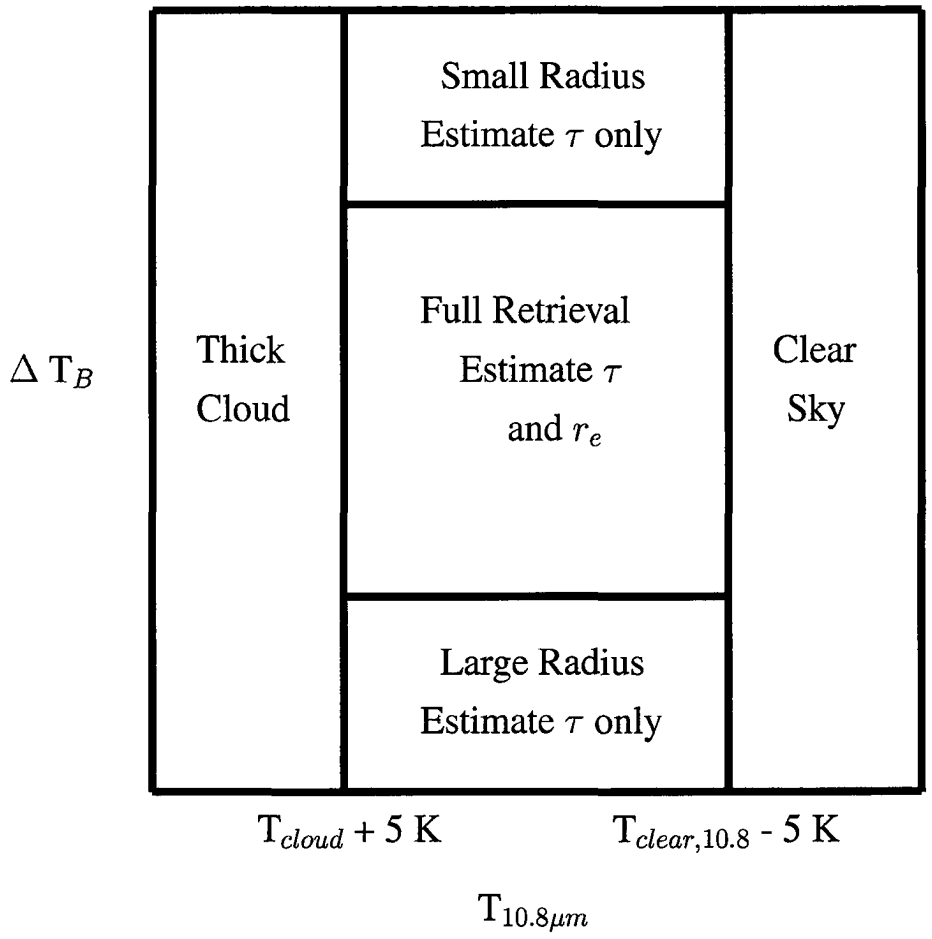

Figure 4.8: Cloud classification scheme used in VIRS-based retrievals of ice cloud optical properties. In the standard retrieval, pixels with $T_{10.8} > T_{clear,10.8} - 5$ K are designated as clear-sky and those with $T_{10.8} > T_{cloud} + 5$ K as thick cloud.

potential of screening out potential contamination from low altitude stratocumuli which can be mistaken for thin high cirrus in the IR-only algorithm but would appear much brighter in the visible channel allowing them to be flagged as unphysical. In the present study, however, we will take the position that the benefits of an algorithm applicable at any time of

day (eg. for studying diurnal variability) exceed the information lost by neglecting the 0.6 μm channel and its addition will be left as another exercise for the future. To summarize, then, the algorithm proceeds as follows:

- To be consistent with the lower resolution TMI data and products, VIRS data is gridded to 0.25°x0.25° resolution also.

- The algorithm proceeds by computing Δ T_B vs. $T_{10.8}$ relationships for a variety of optical depths and effective radii using the simple radiative transfer model outlined above and assumptions of clear-sky 10.8 and 12 μm T_Bs and a cloud emitting temperature.

- The retrieval consists of looking up the observed values of $T_{10.8}$ and Δ T_B and interpolating to provide an estimate of τ and r_e.

- Data points which fall outside the domain of the arches are classified as thick cloud if $T_{10.8}$ falls below a certain threshold, clear-sky if $T_{10.8}$ greater than a second threshold, and as containing small or large particles otherwise. This classification is illustrated in Figure 4.8 along with definitions of the clear-sky and thick cloud cutoffs.

4.2.3 Results

Observed 10.8 and 12 μm brightness temperatures and ΔT_B for the sample region selected earlier are presented on the left hand side of Figure 4.9. High cloud tops associated with the raining pixels shown in Figure 4.2 appear cold ($T_B \sim 200K$) at both 10.8 and 12 μm while clear-sky pixels are characterized by brightness temperatures on the order of 290 K and $\Delta T_B \sim 2$ K. Based on these observations, values of clear-sky emitting temperatures are set to $T_{clr,10.8} = 292K$ and $T_{clr,12} = 290K$ in the retrieval. In addition, the cloud emitting temperature, T_c, is taken to be 225 K corresponding to a mean cloud height of 12 km in a

McClatchey standard tropical atmosphere (McClatchey et al., 1972). The sensitivity of the retrieval to each of these assumptions will be investigated in detail below.

Of primary importance to this study is the region of intermediate T_Bs in the transition from clear to raining conditions. Unlike the clear pixels identified above and raining pixels for which $\Delta T_B \sim 0$, brightness temperature differences in this intermediate region range from 5 to 8 K suggesting the presence of thin ice clouds by the arguments presented above. Estimates of r_e, τ, and ice water path (IWP) for these pixels are shown in the plots on the right hand side of Figure 4.9. The IWP is derived from r_e and τ by assuming a modified gamma distribution

$$N(D) = \frac{N_t}{D_n \Gamma(\nu)} \left(\frac{D}{D_n}\right)^{\nu-1} e^{-D/D_n} \tag{4.5}$$

where $D_n = r_e/2$ is the characteristic diameter and $\nu = 2$ defines the width of the distribution (after Stephens et al. (1990)). Recall that effective radius retrievals are possible only in those pixels which fall in the central block of Figure 4.8 while optical depths are estimated for all classifications except clear and thick cloud so estimates of the latter are not always accompanied by the former. Substantial regions of thin cirrus exist on the periphery of the rainfall particularly in regions between raining pixels. Generally the optical thickness and liquid water path of the ice clouds decreases with increasing distance from rainfall. The region between 175E and 175W longitude north of 5S, however, is an exception. Here the algorithm has detected a fairly substantial region of thin cirrus which is far removed from any rainfall. Clearly, the absence of such information would severely hinder attempts to characterize radiative heating in this region, emphasizing the rationale behind developing the ice cloud retrieval presented here.

4.2.4 Sensitivity Studies

Earlier it was noted that estimates of r_e and IWP are extremely sensitive to assumed clear-sky and cloud emitting temperatures which define the anchor points in the arch-shaped

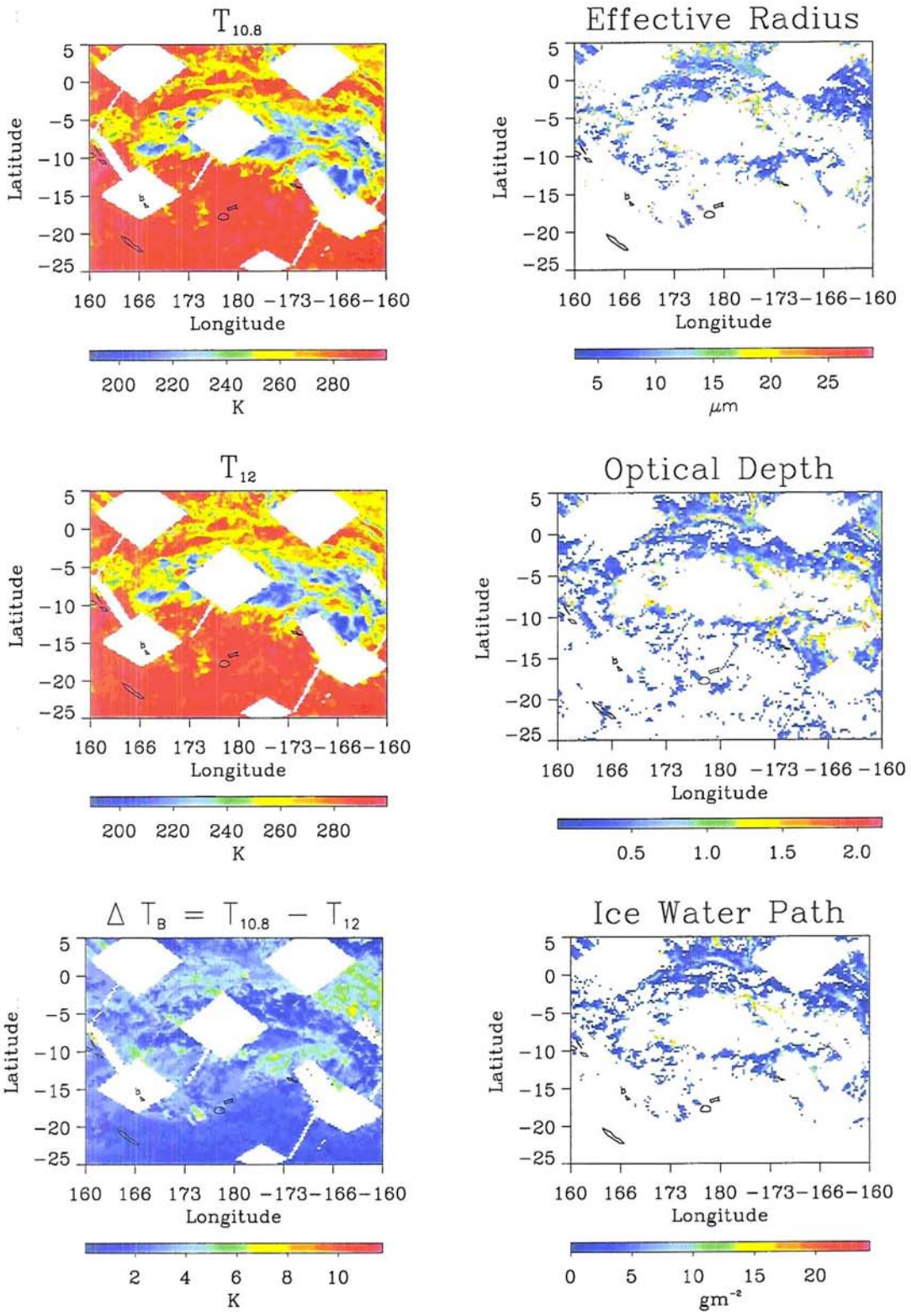

Figure 4.9: VIRS channel 4 and 5 input and resulting effective radius and IWP estimates from the sample region on February 1, 1998.

relationship between ΔT_B and $T_{10.8}$. In order to establish error bounds on the results, the retrieval has been repeated using a large number of different sets of T_c, $T_{clr,10.8}$ and $T_{clr,12}$. Figure 4.10 presents the fraction of pixels which fall into each of the retrieval classifica-

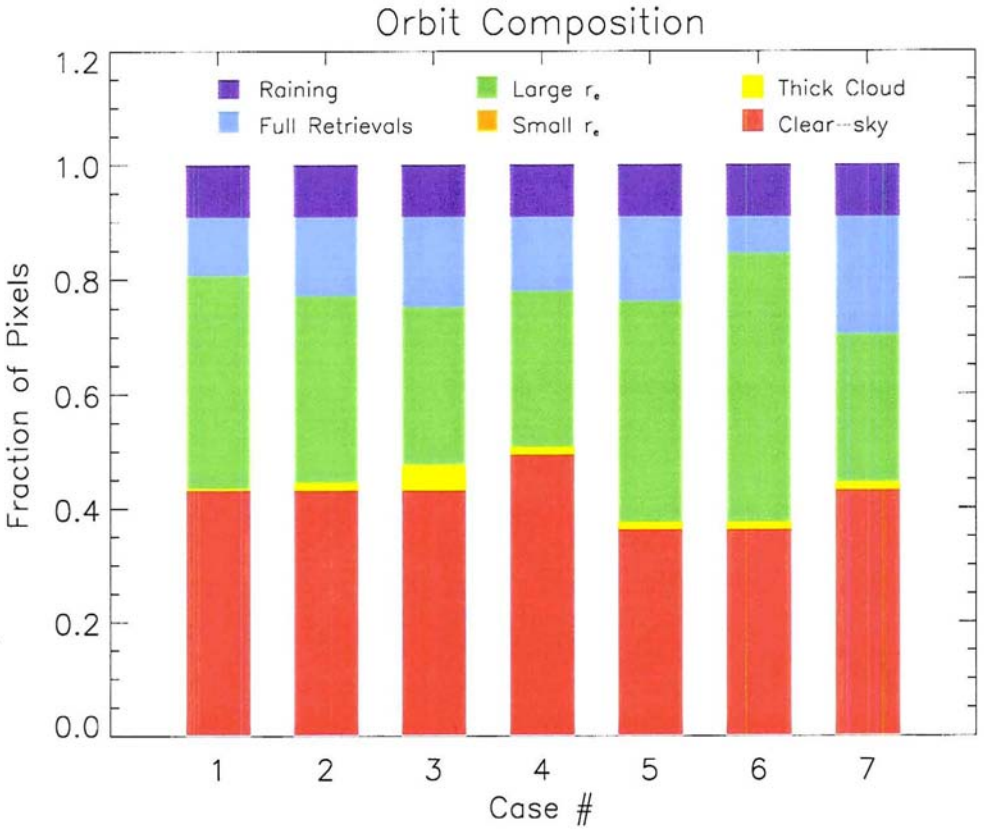

Figure 4.10: Approximate composition of output pixels from ice cloud retrievals with different cloud and clear-sky emitting temperatures. Assumptions used in each case are summarized in Table 4.1.

tions defined in Figure 4.8 for each of the seven sets of assumptions listed in Table 4.1. The statistics were accumulated over 16 orbits from February 1, 2001, representing some 670,000 pixels in all. Cases 1-3 examine the sensitivity of the retrieval to cloud emitting temperature holding clear-sky brightness temperatures constant. The number of clear-sky pixels is the same for all three cases since it is solely a function of $T_{clr,10.8}$ and the number

Table 4.1: Clear-sky and cloud emitting temperature characteristics (in K) for each sensitivity study case presented in Figure 4.10.

Case	T_c	$T_{clr,10.8}$	$T_{clr,12}$	ΔT_{clr}
1	210.0	292.0	290.0	2.0
2	225.0	292.0	290.0	2.0
3	240.0	292.0	290.0	2.0
4	225.0	290.0	288.0	2.0
5	225.0	294.0	292.0	2.0
6	225.0	294.0	290.0	4.0
7	225.0	292.0	291.0	1.0

of raining pixels is, likewise, invariant as they are designated using the GPROF rainfall product. Partitioning of the remaining pixels between the four intermediate classifications varies as a function of the cloud emitting temperature. Assuming $T_c = 210$ K, almost forty percent of the pixels are classified as having large particles allowing only optical depth to be retrieved. As T_c increases, however, the number of pixels for which ΔT_B falls within the boundaries of the lowest arch increases resulting in a greater number of full retrievals. When T_c is taken to be 255 K, the fraction of pixels for which retrievals of both r_e and T_c are possible is sixty percent greater than that for $T_c = 210$ K amounting to a difference of more than 6,000 pixels per orbit. At the same time the number of pixels classified only as containing thick cloud increases by approximately 4,000 over the same range of T_c.

The remaining cases investigate the impact of different assumptions regarding clear-sky emitting temperatures at 10.8 and 12 μm. Generally, reducing $T_{10.8}$ while holding $\Delta T_{B,clr}$ fixed increases the number of pixels which are classified as clear-sky at the expense of the four cloud categories. Furthermore, increasing (decreasing) $\Delta T_{B,clr}$ results in a significant increase (decrease) in the relative fraction of large radius to full-retrieval pixels, by increasing (decreasing) the ΔT_Bs along the lowest retrieval arch.

Quantitative assessment of the sensitivity of r_e and IWP to the emitting temperatures is more challenging since pixels often completely change classification when T_c and T_{clr} are modified. It is, however, possible to gain some insight into the general dependencies

by focusing on the subset of pixels for which full r_e and IWP retrievals were possible in all cases. This unavoidably restricts the values for which valid sensitivities can be determined but serves to illustrate some general features of the retrieval nonetheless. Figure

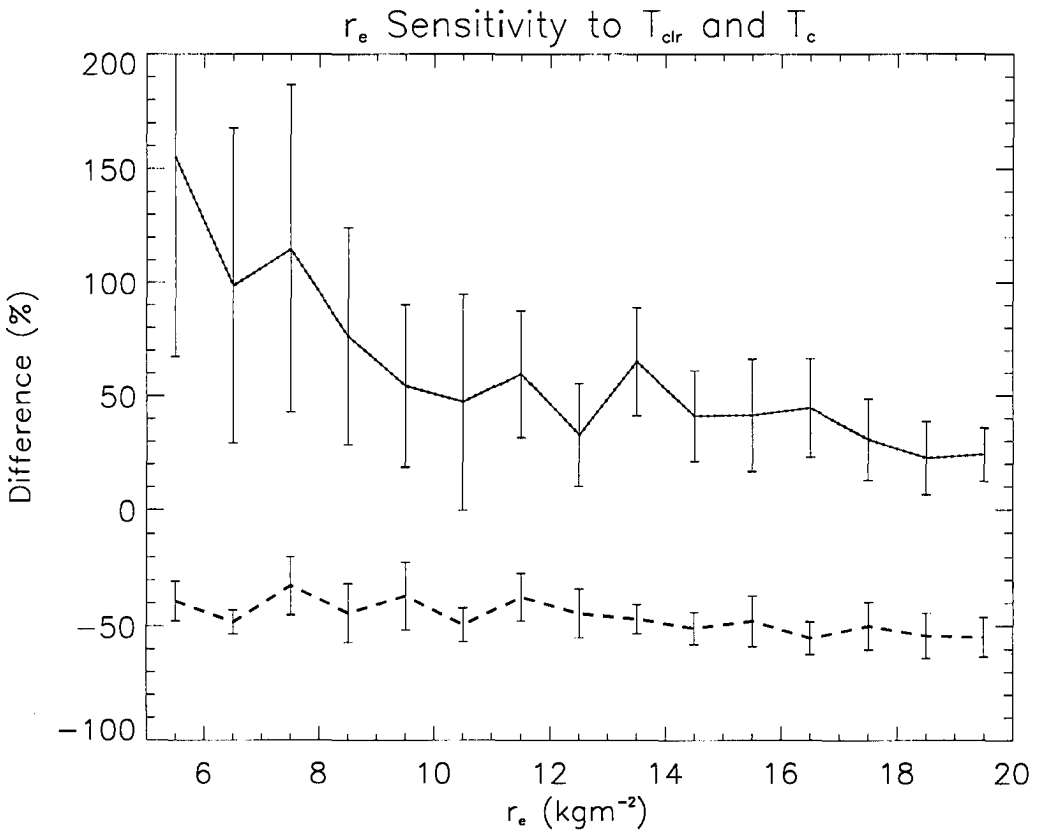

Figure 4.11: Expected range of uncertainty in r_e estimates resulting from required assumptions on T_{clr} and T_c.

4.11 illustrates the range of uncertainty introduced in retrievals of effective radius due to the arbitrary assumptions made regarding cloud and clear-sky emitting temperatures. The solid and dashed lines represent the mean departure from the baseline retrieval or r_e (case 2 in Table 4.1) while the bars denote the variance in these departures over all sets of assumptions tested.

The sensitivity of retrievals of small particles exceeds 150 % but decreases with in-

creasing particle size leveling off at 50 % for particles with radii greater than 10 μm. It is important to note that the decreasing trend of upper bound with increasing radius for $r_e > 15\mu$m is an artifact of the fact that as the upper retrieval limit (25 μm) is approached, a corresponding limit is placed on the maximum perturbation which can be realized through any adjustment of the emitting temperatures. The upper error bound above 15 μm should, therefore, be regarded with caution. The lower bound established by the range of emitting temperatures tested is approximately 50 % apparently independent of the particle size. Once again, however, it is important to note that a limit of 4 μm is imposed as a minimum in the retrievals, thereby limiting the range of perturbations below the retrieved value which can occur as a result of changing the emitting temperatures. Extrapolating the results to the less trustworthy regions, then, we conclude that uncertainties in r_e range from $\pm$150 % at small effective radius to $\pm$50 % for particles larger than 10 μm.

Similar results demonstrating the spread in retrieved IWP over the range of emitting temperatures tested are shown in Figure 4.12. The estimates of IWP shown are less sensitive to the initial assumptions than effective radius, ranging from $+80/-50$ % at the lowest retrievable IWP to a minimum of $\pm$ 20 % above 0.01 gm^{-2}. This result is primarily due to the fact that full retrievals are only possible for thin clouds for which the range in retrieved τ is very small. Again, these results do not account for pixels which are reclassified as thick cloud or small/large effective radius retrievals as a result of changes to the emitting temperatures. The sensitivities indicated in Figure 4.12, therefore, represent only perturbations to IWP in cases where full retrievals were possible for all T_c, $T_{clr,10.8}$, and $T_{clr,12}$. When employed in the radiative transfer calculations, each case study will be input in full allowing for both the sensitivity of r_e and τ to the emitting temperature assumptions highlighted above as well as the potential for pixel reclassification. The results should provide a complete characterization of the impact of T_c and T_{clr} on derived cirrus radiative properties.

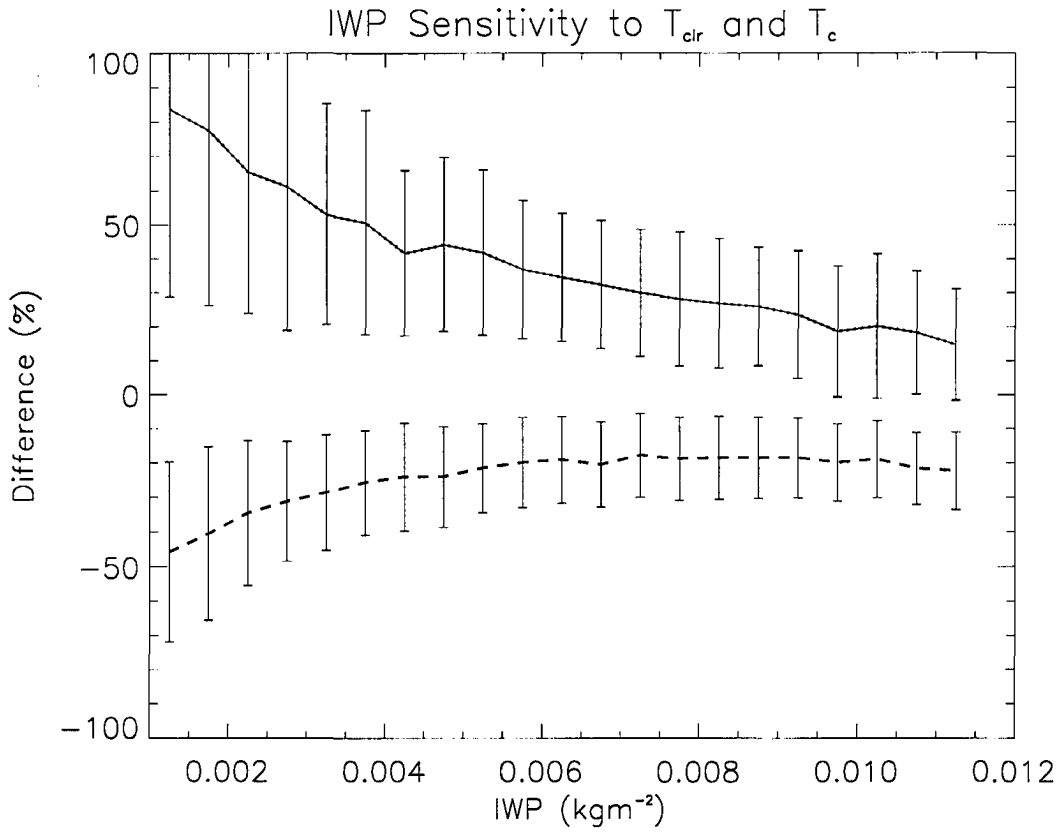

Figure 4.12: As in Figure 4.11 but for IWP.

Finally, since IWP and r_e are not quantitatively estimated for "thick cloud" pixels, their uncertainties are on the order of hundreds of percent. Note, however, that the radiative impact of thick clouds is not likely as sensitive to the specific values of IWP and r_e as that of thin cirrus for which retrievals are possible. In such cases a threshold value of IWP must be assigned and a representative r_e assumed in the radiative transfer calculations but, since the cloud is optically thick, its vertical boundaries will dominate its impact in the ERB, as opposed to these parameters.

4.3 Liquid Clouds

In addition to the well-documented impact of ice clouds on the ERB, there have been a number of studies which suggest that water clouds have a significant impact on the global climate through strong radiative interactions (eg. Paltridge (1980) and Somerville and Remer (1984)). Furthermore, using data from the Nimbus-7 and ERBE satellites, Stephens and Greenwald (1991) demonstrated that the response of the ERB to changes in cloud liquid water can vary substantially from region to region resulting from "gross macrophysical differences" between the clouds in disparate locales. In light of these observations, some estimate of the location and magnitude of cloud liquid water is advantageous to this study.

The impact of liquid clouds on the TOA IR is generally small (but not negligible) since they reside in the lowest levels of the atmosphere at warm temperatures relative to ice clouds and, therefore, have emission characteristics similar to the Earth's surface. These clouds are, however, highly reflective and strongly influence the SW components of the radiation budget, particularly in the absence of high cloud. To account for this, a method will be adopted to estimate cloud liquid water path from the passive microwave measurements available from the TMI. The resulting LWP estimates and a climatologically based estimate of effective radius will be then be employed in concert with the precipitation and ice cloud information determined above, to deduce the radiative component of the tropical energy budget.

4.3.1 Passive Microwave Techniques for Retrieving Liquid Water Path

Up to now, the absence of spaceborne radars sensitive enough to detect cloud-sized particles coupled with the strong attenuation suffered by spaceborne lidars has lead researchers to develop methods for the retrieval of liquid cloud parameters which are based on passive sensors. Besides their application for retrieving ice clouds, visible and infrared radiances have also been used to infer liquid cloud properties. Han et al. (1998), for example, made

use of ISCCP and AVHRR data to study the relationship between cloud liquid water path, effective radius, and albedo in low-level clouds. Greenwald et al. (1999) detail and evaluate a LWP algorithm based on reflectance measurements at 0.6 and 3.9 μm from the GOES-9 imager and Kuji et al. (2000) present an algorithm for retrieving effective radius and liquid water path (LWP) in low-level marine clouds using AVHRR channels 1, 3, and 4.

For this study, however, we look to the well-established array of microwave-based retrievals which apply over a greater range of liquid water contents[3] and allow greater sensitivity to the liquid column as a whole rather than the regions near cloud top as is often the case with VIS/IR methods. Algorithms making use of passive microwave observations to simultaneously retrieve water vapor, liquid water and/or surface properties such as wind speed and SST have been applied with some success for 30 years. Pioneering studies by Basharinov et al. (1969) and Akvilonova et al. (1973) introduced the idea of retrieving liquid cloud information from measurements made by the Russian Cosmos satellites. In the years which followed, numerous techniques and variations thereof have been proposed to estimate atmospheric water vapor based on microwave instruments aboard a variety of satellites. Grody (1976), for example, used radiances at 22 and 31 GHz from the Nimbus-E Microwave Spectrometer (NEMS) on the Nimbus-5 satellite to retrieve atmospheric liquid water contents while Chang and Wilheit (1979) employed a similar technique with the addition of the 19 GHz channel to simultaneously retrieve surface wind speed and column-integrated water vapor and liquid water. Later, Grody et al. (1980) extended these studies to the observations from the Scanning Microwave Spectrometer (SCAMS) flown on the Nimbus-6 satellite.

Further developments in microwave liquid water retrievals accompanied the introduction of the Special Multichannel Microwave Radiometer (SMMR) in the mid-1980's. Those of Njoku and Swanson (1983) and Prabhakara et al. (1986), for example, used improved

[3]Methods based on visible and infrared data often fail in regions of high liquid water content such as those containing drizzle.

empirical relationships to derive a variety of physical parameters such as SST, liquid water and surface wind speed from the Seasat and Nimbus-7 satellites, respectively.

Since 1987, a series of DMSP spacecraft have carried the SSM/I instrument, the predecessor to the TMI, leading to the refinement of algorithms in existence at that time as well as spawning the development of new approaches which now make up the current generation of liquid water retrievals. These include the statistical methods of Alishouse et al. (1990) and Karstens et al. (1994) and semi-physical algorithms of Petty (1990), Greenwald et al. (1993), Liu and Curry (1993), and Lin et al. (1998a,b). In addition, Jung et al. (1998) have developed a technique to derive liquid water paths from three different combinations of the SSM/I radiances using the comparatively new technique of neural networks.

While the foundations upon which these algorithms are based are similar, namely physical differences in the emission and polarization signatures of liquid water droplets and the ocean background, we favor an approach rooted in a physical model to those based entirely on empirical or statistical relationships. Both techniques have their advantages, but the physical approach facilitates the process of uncovering and understanding the primary sources of uncertainty in the results, an important requirement in this work.

4.3.2 TMI-based LWP Retrieval

The method adopted for retrieving non-precipitating liquid clouds parallels that of Greenwald et al. (1993) which is based on both horizontally and vertically polarized brightness temperatures at 19 and 37 GHz. While originally applied to retrievals from the SSM/I, this technique is readily adapted to the TMI as both instruments possess channels at the required frequencies. Since scattering by liquid clouds is negligible at microwave frequencies, Equation (4.1) applies equally to the radiation observed by the TMI instrument at 19 and 37 GHz[4]. The component of the radiation received at the satellite owing to the Earth's

[4]Recall that our focus in this section is on liquid clouds, not precipitation for which scattering may be important. The GPROF algorithm supplies all profile information used in precipitating pixels.

surface is given by

$$I(\tau^*, \mu)e^{-\tau^*/\mu} = \left[\epsilon^P B(\tau^*) + R^P I(\tau^*, -|\mu|)\right] e^{-\tau^*/\mu} \tag{4.6}$$

The first term accounts for radiation emitted from the surface while the second accounts for the reflection of downwelling radiation emitted from the atmosphere. The superscript P is used to denote the polarization dependence of the emissivity, ϵ, and the surface reflection coefficient, R. Substituting Equation (4.6) into Equation (4.1) and re-casting the result in terms of brightness temperature, T_B, we obtain

$$T_B^P = \epsilon^P T_s e^{-\tau^*/\mu} + R^P \int_0^{\tau^*} T(t) e^{-(\tau^* - t)/|\mu|} \frac{dt}{|\mu|} e^{-\tau^*/\mu} + \int_0^{\tau^*} T(t) e^{-t/\mu} \frac{dt}{\mu} \tag{4.7}$$

Assuming that a majority of the emission at 19 and 37 GHz is due to water (liquid and vapor) in the lowest few kilometers of the atmosphere, we replace $T(t) \rightarrow T_s$ so that Equation (4.7) reduces to

$$T_B^P = T_s \left[1 - R^P Tr^2\right] \tag{4.8}$$

where $Tr = e^{-\tau^*/\mu}$ is the transmissivity of the atmosphere and we have used the fact that, for an opaque medium, $\epsilon^P = 1 - R^P$. Thus, under the assumptions made above regarding scattering and emission, the radiation observed at a satellite depends only on surface temperature and wind speed through the surface reflection coefficient and the amount of water, liquid and vapor, in the atmospheric column through the transmissivity.

Figure 4.13 illustrates the polarization dependence of emission and reflection of microwave radiation by an oceanic surface neglecting the effects of salinity, surface sloping, and surface roughening. Based on the solid curves, the reflection of horizontally polarized radiation always exceeds that of vertically polarized light. At the TMI view angle, $R^H - R^V$ are .28 and .19 at 19 and 37 GHz, respectively. While wind-induced sloping and roughening of the ocean's surface somewhat reduces this difference, it remains appreciable for all

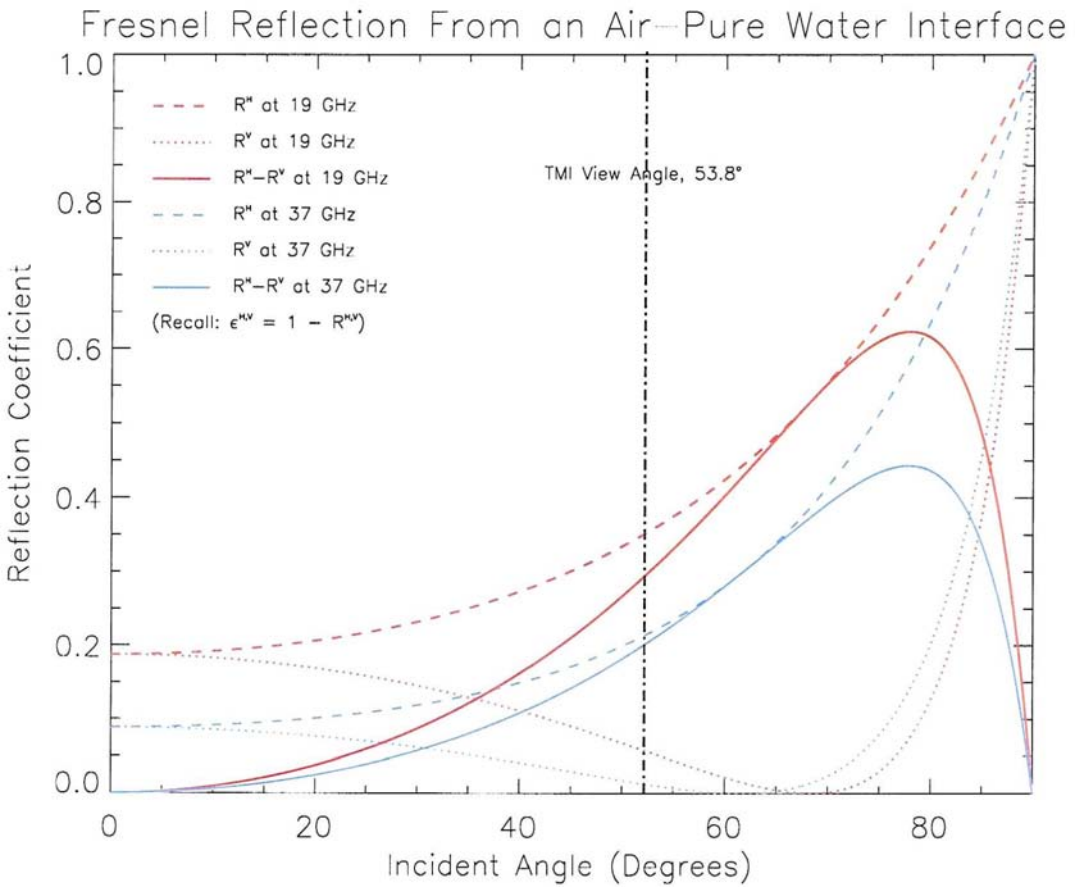

Figure 4.13: Reflection coefficients, $R^{V,H}$, at 19 and 37 GHz for reflection from a horizontal, smooth air-pure water interface at 295 K.

meteorological conditions under which we expect to find non-precipitating liquid clouds. The precept upon which the method is based is that absorption and emission by small water molecules and quasi-spherical cloud droplets in the atmosphere reduces the degree of polarization of the surface radiation. In principle, given a reasonably accurate estimate of the surface reflection (eg. from Figure 4.13 corrected for the effects of surface sloping and roughening resulting from wind), one can estimate the amount of water vapor and liquid water present in the atmospheric column provided measurements of two independent polarizations at two different frequencies are available. Taking the transmissivity to be the product of the transmission through water vapor, liquid water, and molecular Oxygen, the

difference in Equation (4.8) evaluated at vertical and horizontal polarizations is

$$\Delta T_B = T_B^V - T_B^H = T_s \left[R^H - R^V\right] Tr_{O_2}^2 e^{-2(k_l L + k_w W)/\mu} \tag{4.9}$$

where L and W are the LWP and column water vapor (CWV), respectively, and the $e^{-k_X X}$ represent the transmission through each. Tr_{O_2} denotes the transmission through molecular Oxygen which is assumed to obey

$$Tr_{O_2} = a + bT_s + cT_s^2 + dT_s^3 \tag{4.10}$$

following Greenwald et al. (1993). Note that, according to Figure 4.13, ΔT_B will always be positive. Measurements of T_B^H and T_B^V at 19 and 37 GHz, therefore, provide two equations for the two unknowns, L and W, which can be solved yielding

$$W = \frac{C_{19} k_{l,37} - C_{37} k_{l,19}}{k_{l,37} k_{w,19} - k_{w,37} k_{l,19}} \tag{4.11a}$$

$$L = \frac{C_{37} k_{w,19} - C_{19} k_{w,37}}{k_{l,37} k_{w,19} - k_{w,37} k_{l,19}} \tag{4.11b}$$

where

$$C_i = -\frac{\mu}{2} ln \left[\frac{\Delta T_B^i}{T_s (R_i^H - R_i^V) Tr_{O_2}}\right] \tag{4.12}$$

Greenwald et al. (1993) note that the assumption $T(t) \sim T_s$ breaks down when TPW exceeds 25 kg m^{-2} as is often the case in the tropics. To account for the dependence of the effective level of emission on water vapor when $W > 25$ kg m^{-2}, they introduce the following correction to Equation (4.12)

$$R_{19}^V - R_{19}^H = R_{19}^V \left(1 - \frac{R_{19}^H}{R_{19}^V}\right) \approx \frac{T_{B,19}^H - \bar{T}}{T_{B,19}^V - \bar{T}} \tag{4.13}$$

where $\bar{T} = T_s + \Gamma H_w(1 - T_{B,19}^V)Tr_{O_2,19}$ and the factor $e^{50k_{W,19}/\mu}$ is included to prevent discontinuities in the vicinity of 25 kgm^{-1}. $H_w = 2.2$ km is the water vapor scale height and $\Gamma = -5.8$ K km^{-1} is an assumed lapse rate. Greenwald et al. (1993) also employ a correction to the 37 GHz channel to correct a constant offset observed in water vapor optical depth comparisons in that study. No such correction will be employed here since considerable effort has been made by the TRMM science team to ensure that the TMI radiances are well-calibrated.

In order to determine the reflection coefficients $R^{H,V}$ some estimate of surface wind speed needs to be made. The algorithm of Goodberlet et al. (1989), used in Greenwald et al. (1993) is based on an empirical relation using the 22.235 GHz channel of the SSM/I instrument. Since the corresponding channel on the TMI has been shifted off the center of the water vapor band to 21.3 GHz, the corresponding fit parameters are likely to be different. Rather than re-parameterize this relationship using co-located TMI and buoy data, we choose to revert back to the RSS product introduced in the previous chapter. This data provides high resolution (0.25°x0.25°) estimates of surface wind speeds derived from the TMI observations as well as an independent estimate of column water vapor which we will use to test the performance of the present algorithm. The emissivity, and hence the reflection coefficient, of the wind-roughened surface is then calculated based on the model developed by Petty (1990). Finally, cubic polynomial parameterizations of liquid water mass absorption coefficients at 19 and 37 GHz are adopted directly from Greenwald et al. (1993) based on their observation that, in a climatological sense, cloud temperature roughly follows SST as $T_c \approx T_s - 6K$. Table 4.2 summarizes the cubic polynomial coefficients for both Oxygen transmission from Equation (4.10) and liquid water absorption.

Table 4.2: Replica of Table 1 from Greenwald et al. (1993) which provides cubic fit parameters for Oxygen transmission and liquid water absorption coefficients at 19 and 37 GHz.

	a	b	c	d
$Tr_{O_2,19}$	0.978	-6.31x10^{-5}	7.75x10^{-6}	-1.00x10^{-7}
$Tr_{O_2,37}$	0.927	-8.53x10^{-5}	1.81x10^{-5}	-2.01x10^{-7}
$k_{L,19}$	0.0786	-2.30x10^{-3}	4.48x10^{-5}	-4.64x10^{-7}
$k_{L,37}$	0.267	-6.73x10^{-3}	9.75x10^{-5}	-7.24x10^{-7}

4.3.3 Results

Horizontally and vertically polarized brightness temperatures at 19 and 37 GHz are presented in Figure 4.14 for the sample region discussed above. The warm emission signature of the rainfall is clearly evident in all four channels. These data, in conjunction with estimates of SST and surface wind speed from RSS, were used to retrieve the CWV and LWP shown in Figure 4.15. The panels on the left side display the RSS input data while those on the right summarize resulting CWV and LWP estimates. The upper right plot indicates regions where the retrieval failed either due to the presence of a land or coastal region within the pixel (flagged with a 1) or a risk of contamination by precipitation (flagged with a 2). Neither CWV or LWP is plotted for these pixels.

In general the retrieved column-integrated water vapor (CWV) agrees well both in structure and magnitude with those from RSS. With the exception of the northern most regions, differences in the two products range from 10-15 %. Areas of high LWP are evident adjacent to most precipitation pixels indicating either light rain or drizzle missed by GPROF or areas of thick non-precipitating stratocumulus clouds surrounding convective rainfall. In either case, the radiative implications of such clouds cannot be neglected particularly at solar wavelengths. In addition, there are numerous more expansive regions with LWP on the order of 0.06-0.08 kgm^{-2} throughout the domain. The significance of these regions as far as the tropical energy budget is concerned will be investigated in the next chapter.

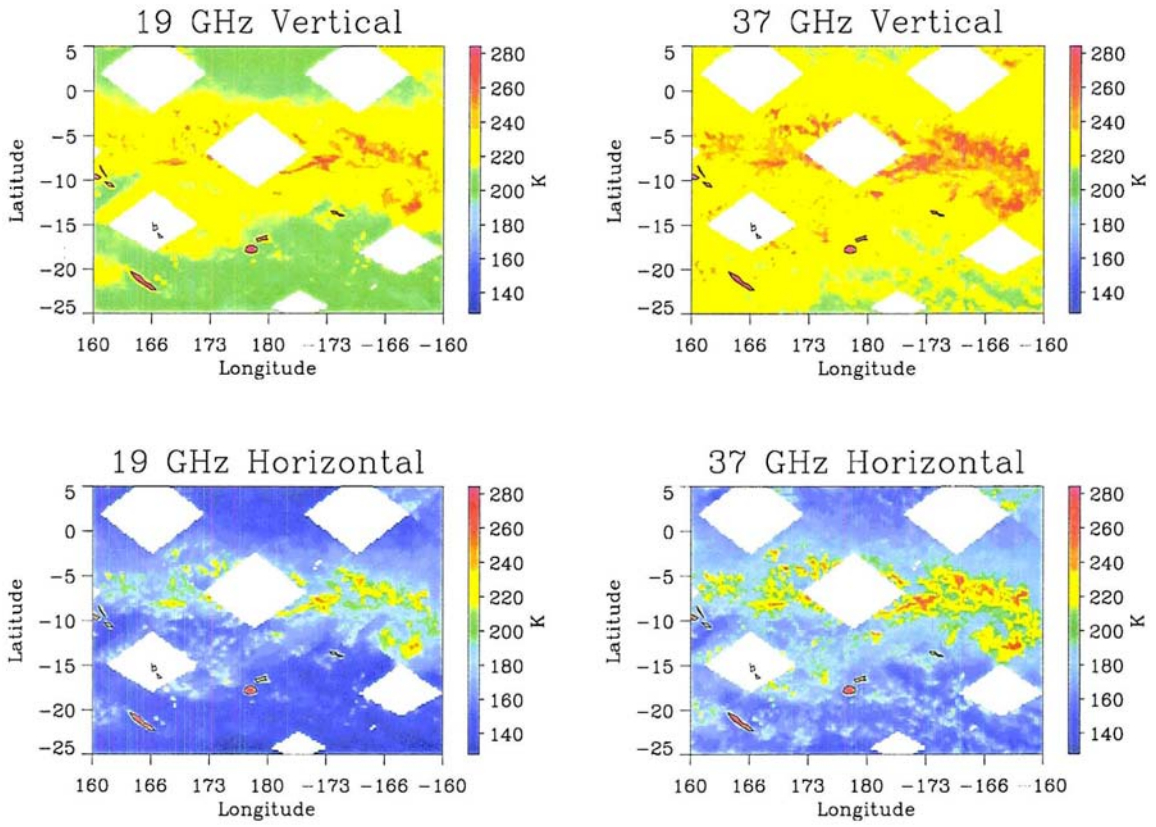

Figure 4.14: TMI T_Bs at 19 and 35 GHz on February 1, 1998 used as input to the LWP retrieval.

4.3.4 Sensitivity Studies

Before characterizing uncertainties in the LWP estimates themselves, it is interesting to determine how well retrieved precipitable water from the present study compares with that made independently at RSS. As noted in the previous section, both CWV products exhibit similar patterns over the illustrated region and provide comparable magnitudes throughout the domain. Employing statistics from many TRMM orbits, Figure 4.16 directly compares the two estimates on a 0.25°x0.25° pixel-by-pixel basis. The correlation between the products is quite good although a significant degree of scatter exists in the points which is to be expected given the lack of refinement to the Greenwald et al. (1993) method for the

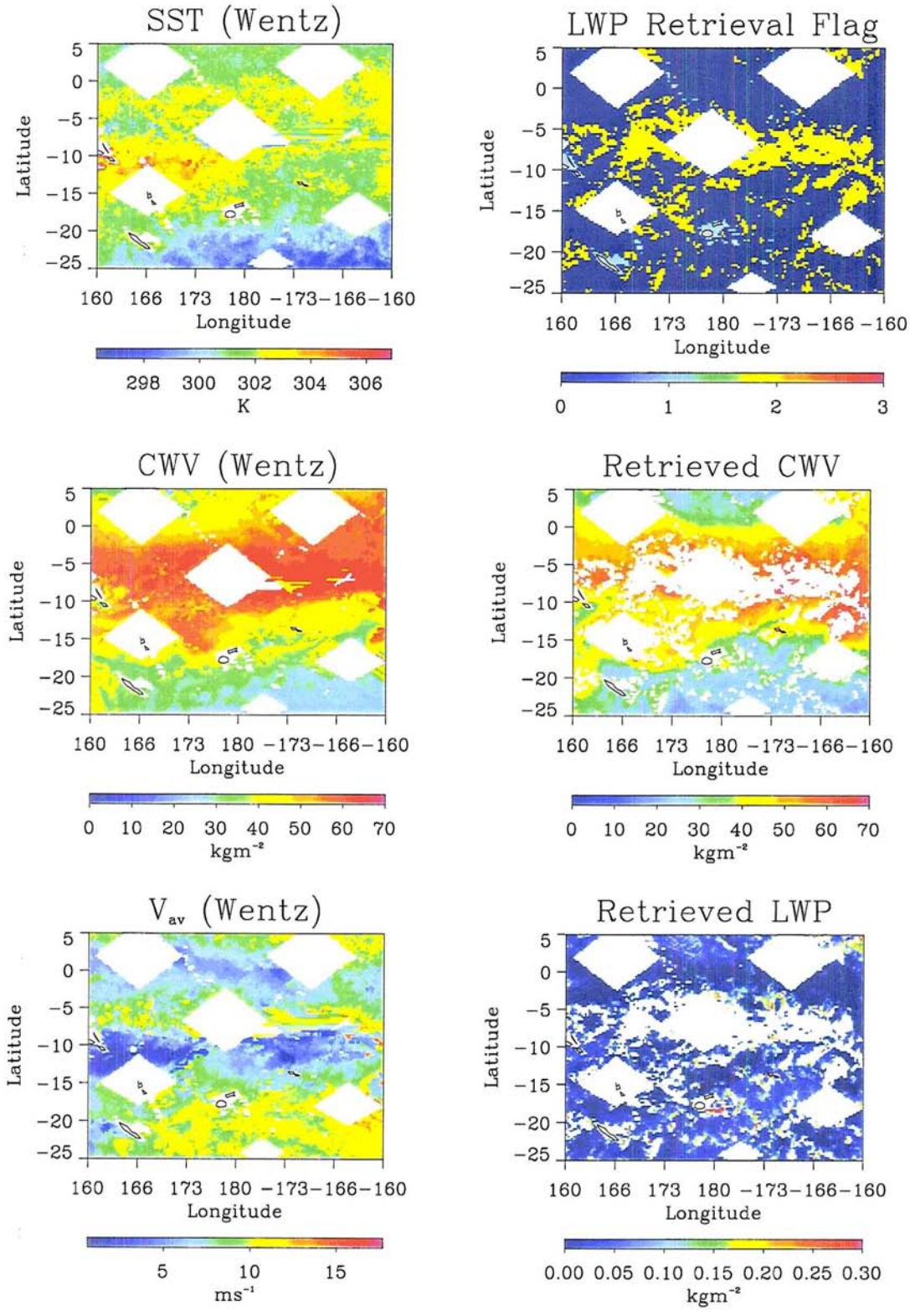

Figure 4.15: LWP retrievals from the sample region on February 1, 1998.

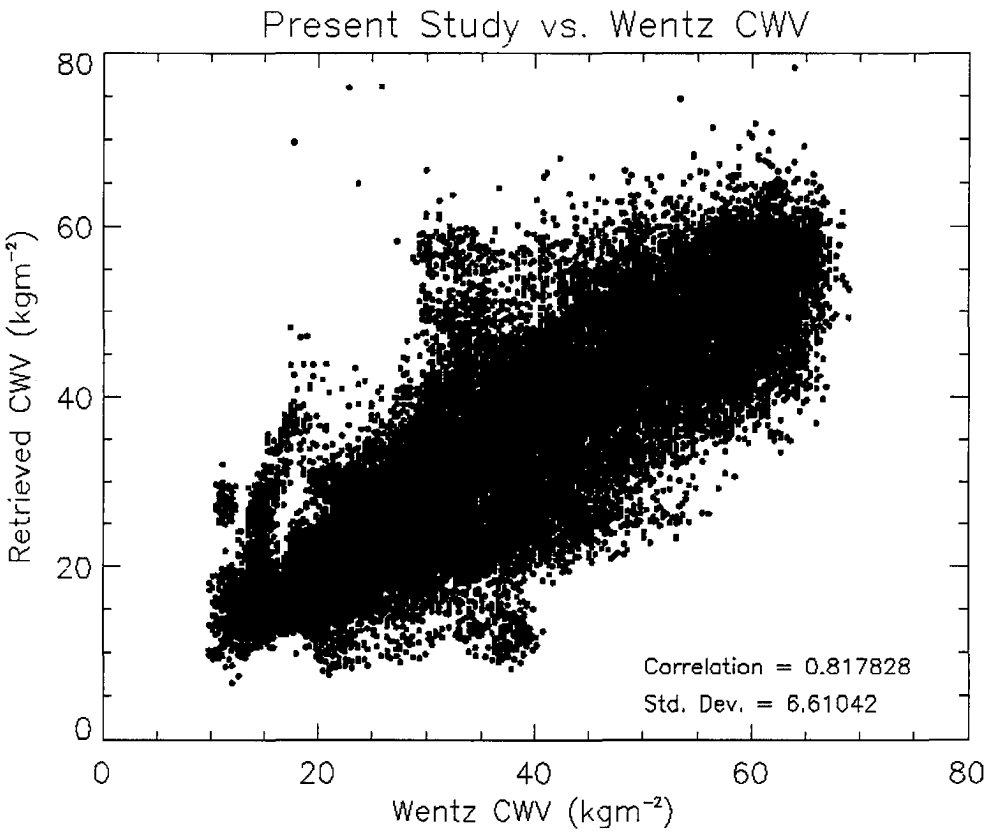

Figure 4.16: Comparison of precipitable water estimates from the present study with those from Wentz et al at RSS.

present study. In fact, the results are remarkably good given the the fact that the parameterization used in this study hasn't been significantly adjusted since its publication in 1993 and considering the lack of any additional calibration employed here to account for differences between the TMI and SSM/I instruments. Furthermore the small spatial scale over which the correlations hold as well as the lack of temporal averaging represents the most rigorous scale at which the data can be compared. These results are in no way intended to serve as a validation of the approach, for that the interested reader is referred to Greenwald et al. (1993). Instead they are presented here to suggest that the algorithm is behaving in a manner consistent with that used at RSS.

Establishing the sensitivity of the LWP estimates to the principal inputs is not nearly as difficult as it was in the ice cloud retrievals. First, the retrieval either works, yielding a physically acceptable estimate of liquid water path, or it fails. Furthermore, the relationship between LWP and the model inputs is more straight-forward than those between IWP/r_e and the emitting temperatures assumed in the ice cloud retrieval. For a given set of brightness temperatures, increasing either SST or surface wind speed generally increases the estimated LWP while decreasing these quantities leads to a corresponding decrease in LWP. Retrievals were repeated perturbing SST and surface wind speed estimates by

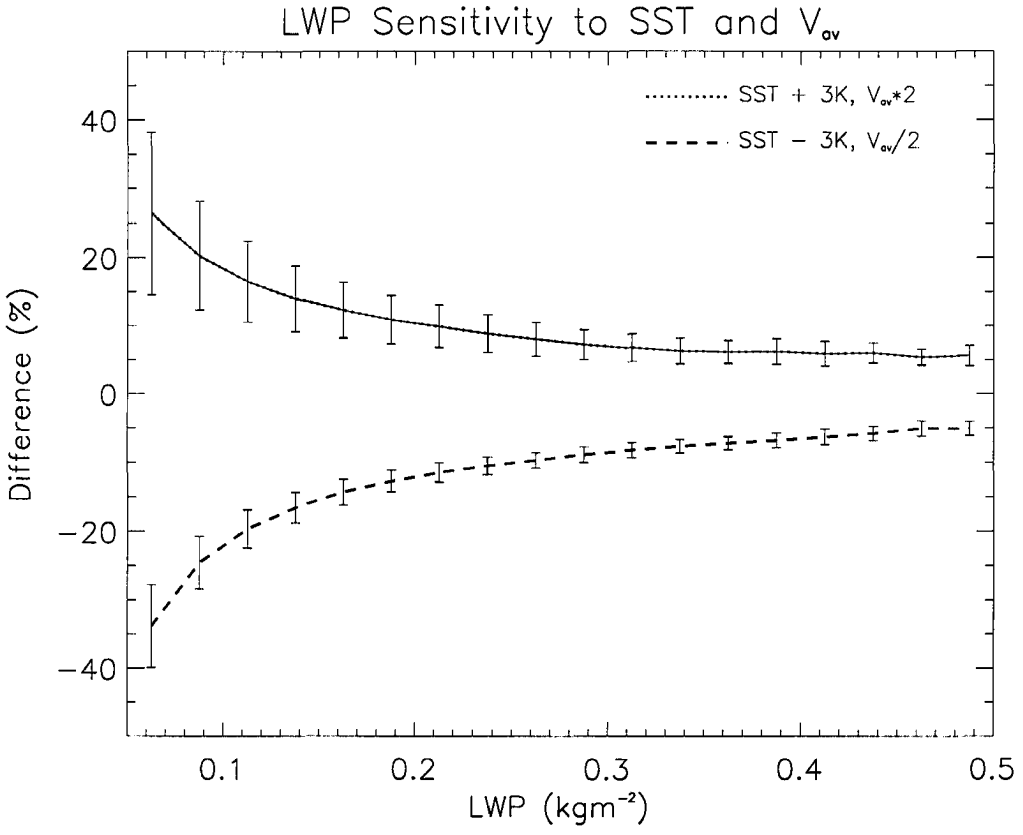

Figure 4.17: Expected range of uncertainty in LWP estimates resulting from errors in assumed SST and surface wind speed, V_{av}.

amounts consistent with reasonable values for the uncertainties in the RSS data. Aver-

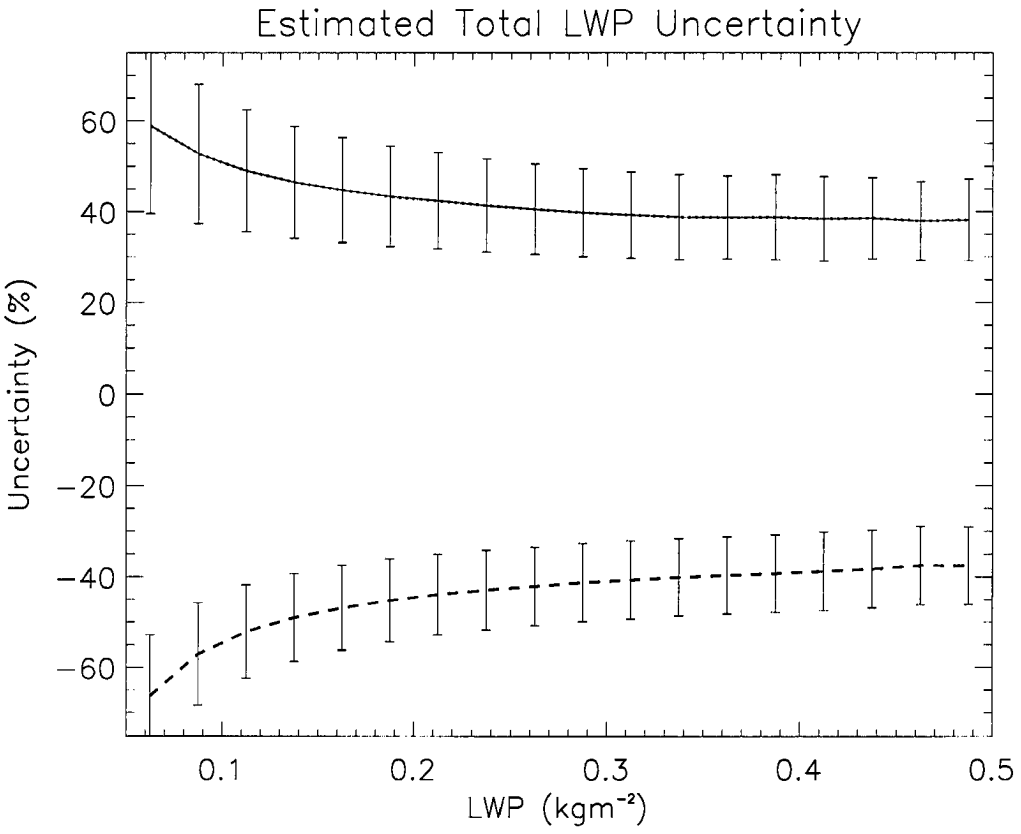

Figure 4.18: Total uncertainty in LWP estimates as a function of LWP.

age differences between original retrievals and LWP retrieved augmenting SST by 3K and doubling V_{av} (solid curve) and decreasing SST by 3K and halving V_{av} (dashed curves) are presented in Figure 4.17 establishing both upper and lower bounds under the assumption that the retrieval model itself is perfect. The bars represent the variance of the errors about their mean. The results suggest that the retrieved LWP is most sensitive to the external input at low LWP. Physically this seems reasonable since one expects the TMI brightness temperatures to be most sensitive to the atmosphere, and therefore least sensitive to the properties of the ocean surface, when large amounts of cloud liquid are present. Thus at high LWP, the contribution of surface emission to the radiation observed by the TMI is

much less than that due to the liquid water column itself reducing the impact of the SST and surface wind speed.

Ultimately the uncertainty in retrieved LWP is a combination of sensitivity to SST and wind speed errors and some inherent model error. To account for the latter while maintaining the trend observed in Figure 4.17, the mean of the uncertainty quoted in Greenwald et al. (1993) will be added to the component owing to uncertainties in SST and V_{av} determined above. This approach, while somewhat arbitrary, ensures that uncertainty estimates employed in the radiative transfer calculations are pessimistic and provide a maximum error bound on the results. Resulting uncertainties in LWP are presented in Figure 4.18. The solid and dotted lines represent the uncertainty in the LWP estimates which will be assumed in the radiative transfer calculations to follow while the error bars indicate the values one would obtain using the minimum and maximum uncertainty quoted in Greenwald et al. (1993), 25 and 40 %, respectively.

When employed in the ERB analysis, assumptions of both cloud height (base and top) as well as an effective particle size will need made since the retrieval presented above provides only a column-integrated LWP estimate. A detailed discussion of the radiative implications of these assumptions will be left for the next chapter.

4.4 Summary

Through the use of the GPROF algorithm and two semi-physical cloud property retrievals, the three-dimensional structure of clouds and precipitation between 40N and 40S have been determined. Clear-sky pixels can now be identified within the uncertainties imposed by the assumptions in the liquid and ice cloud retrievals. For the purposes of estimating radiative heating rates, a pixel will be considered clear if it is both classified as being devoid of high cloud in the VIRS retrieval and has a LWP of less than 0.05 kgm^{-2} according to the TMI retrieval. While this value may seem arbitrary, it represents the minimum uncertainty in

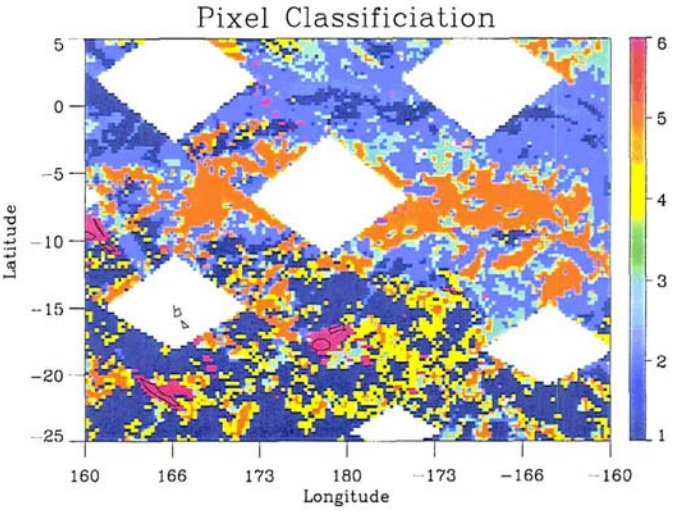

Figure 4.19: Pixel classification used to specify the locations of cloud and rainfall for future radiative transfer modeling. Flags are defined in Table 4.3.

the retrieved LWP and is consistent with the lower limit of observed LWC in thin stratus (Cotton and Anthes, 1989).

Collecting results from each retrieval, Figure 4.19 illustrates the composition of all pixels observed by TRMM in terms of the presence of precipitation, ice cloud, liquid cloud,

Table 4.3: Description of flags used to identify the constituents in each pixel for future radiative transfer modeling. The last two columns indicate the fraction of pixels which fall into each category for the sample region and globally, respectively.

Flag	Type	Comments	Region	Global
1	Clear-sky	$T_{10.8} > T_{clr} - 5$ K; LWP < 0.05 kgm^{-2}	0.255	0.167
2	Ice cloud	$T_{10.8} < T_{clr} - 5$ K; LWP < 0.05 kgm^{-2}	0.212	0.209
		(a) - thick cirrus		
		(b) - r_e less than minimum in look-up table		
		(c) - r_e exceeds maximum in look-up table		
		(d) - full r_e and τ retrieval		
3	Both clouds	$T_{10.8} < T_{clr} - 5$ K; LWP > 0.05 kgm^{-2}	0.091	0.159
4	Liquid cloud	$T_{10.8} > T_{clr} - 5$ K; LWP > 0.05 kgm^{-2}	0.060	0.035
5	Raining pixel	Pixels containing precipitation	0.163	0.110
6	Land pixel	Pixels containing land or coastal regions	0.018	0.320

and land. Each flag is defined in Table 4.3 and the fraction of pixels in the sample region which fall into each category are presented. The importance of cloudy pixels is, again, evident as more than 30 % of the pixels in this region are classified as having one or both types of cloud with no precipitation while precipitating pixels account for less than 17 % of the cases. Furthermore, since this particular region was selected for its high density of precipitating pixels, its ratio of precipitating to non-precipitating cloudy pixels is significantly enhanced relative to the global average which we find to be $1 : 4$, approximately half the $17 : 30$ ratio observed in the highlighted region. The significance of these findings for the ERB will be addressed in the next chapter where radiative and latent heating profiles will be derived accounting for all cloud and precipitation information furnished by the methods outlined thus far.

Chapter 5

Toward A Tropical Energy Budget from TRMM Rainfall Observations

The preceding chapters have laid the groundwork necessary to address the primary objective of this dissertation: to derive tropic-wide estimates of radiative and latent heating. This chapter takes an in-depth look at the impact of TRMMs cloud and precipitation information on the exchange of radiant energy in the tropics. Monthly-mean maps of long- and shortwave fluxes, heating rates, and cloud radiative forcing are derived for the month of February 1998. Uncertainties in the results are determined through an extensive set of sensitivity studies and some validation is attempted through the use of outgoing longwave radiation derived from the CERES and AVHRR instruments. In general, derived OLR estimates agree with these products within the uncertainties associated with the cloud data used in this study. The chapter concludes by revisiting the concept of a complete, observation-based energy budget derived from TRMM observations. Fluxes derived using the technique described here are averaged over the region observed by TRMM to evaluate the principal components in the short-term tropical energy budget. Due to as yet unresolved problems with the GPROF database, recent latent heating estimates made using the GPROF algorithm for the same period are left as future work. The interested reader is directed to Appendix C which presents recent latent heating estimates made using the GPROF algorithm for the same period and discusses the results in the context of previous studies. Instead, surface rainfall estimates are used to provide an estimate of the column-integrated latent heating to fill in some estimate of this form of energy exchange in the energy budget estimates.

5.1 Methodology

Given an estimate of the three-dimensional structure of a tropical cloud system, it is a relatively simple matter to deduce a corresponding three-dimensional view of radiative heating (RH) within it. For this purpose the independent pixel approximation (IPA) is invoked in which each 0.25°x0.25° pixel will be treated as radiatively isolated from its neighbors. This approximation neglects the the effects of horizontal inhomogeneity within the clouds but such information has already been lost as a result of the footprint size of the instruments and the retrieval methods employed in the previous chapter. Up- and downwelling broadband radiative fluxes are computed for each pixel within the cloud system making use of an implementation of the δ-two-stream approximation to the radiative transfer equation[1] over six shortwave and twelve longwave spectral bands. The model, known as BUGSRAD[2], explicitly accounts for the effects of scattering, absorption and emission from the four hydrometeor classes retrieved by GPROF using the parameterization of cloud optical properties introduced in Stephens et al. (1990), and includes gaseous absorption through the correlated k-distribution method of Fu and Liou (1992).

5.2 Clear-sky Pixels

Of the six pixel classifications identified in Section 4.4, clear-sky pixels provide the simplest set of radiative transfer calculations (excluding land pixels for which calculations are

[1] In the interest of space the reader is referred to Stephens and Webster (1979), Ritter and Geleyn (1992), and Stephens et al. (2001) for an overview of the δ-two-stream model equations and details of their derivation.

[2] A version of the BUGSRAD model is currently implemented in the CSU GCM. In the present study, however, some significant modifications have been made to facilitate its application to the GPROF output. First, two additional hydrometeor classes, corresponding to liquid and frozen precipitation, were added to allow the model to account for scattering and absorption in rainfall. To account for the large size of precipitating hydrometeors relative to the cloud particles for which the model was originally designed, a new parameterization of the asymmetry parameter was also required. For this purpose exponential fits were made to theoretical relationships between asymmetry parameter and effective radius assuming MP distributions of spherical particles. To improve accuracy, separate fits were made for r_e below and above 40 μm. Finally, size distributions assumed in the model were modified to reflect the assumptions used in the GCE CRM simulations used as input to the GPROF algorithm.

not made). Fluxes depend only on the reflection and emission properties of the underlying surface and profiles of temperature and humidity since all other atmospheric constituents are assumed invariant for simplicity. The albedo of the ocean surface is assumed to be 0.12, consistent with the ERBE-derived mean cited in Harrison et al. (1990). Atmospheric temperature and humidity profiles are determined by scaling the mean tropical atmosphere of McClatchey et al. (1972) so that the SST and column-integrated water vapor match corresponding estimates from RSS data. Although BUGSRAD is capapble of modeling aerosols, their effects will be neglected in the present study as a result of a lack of accurate observations.

5.2.1 Radiative Heating Profiles and Column Heating Rates

Radiation provides an important mechanism for the exchange of energy between the components of the Earth-atmosphere system through its interaction with molecules and small particles. Through the absorption of radiation impinging on it from above and below and emission of radiation towards the Earth's surface and to space, an atmospheric layer often experiences a net flux difference which results either in a heating, if positive, or cooling, if negative, within it. The heating rate of a volume of air is related to the vertical gradient of the net flux through the volume via

$$\frac{dT}{dt} = -\frac{1}{c_p \rho} \frac{\partial F_{NET}}{\partial z} \tag{5.1}$$

where c_p is the specific heat at constant pressure and ρ is density. The net flux is defined as the difference between the upwelling and downwelling flux through a level, $F^{NET} = F^{\uparrow} - F^{\downarrow}$.

SW and LW fluxes and heating rates derived from them are shown in Figure 5.1 for a cloud-free tropical pixel. The pixel, 15.125° S and 179.875° W, was viewed by TRMM at approximately noon, local time on February 1, 1998. With the solar insolation at TOA

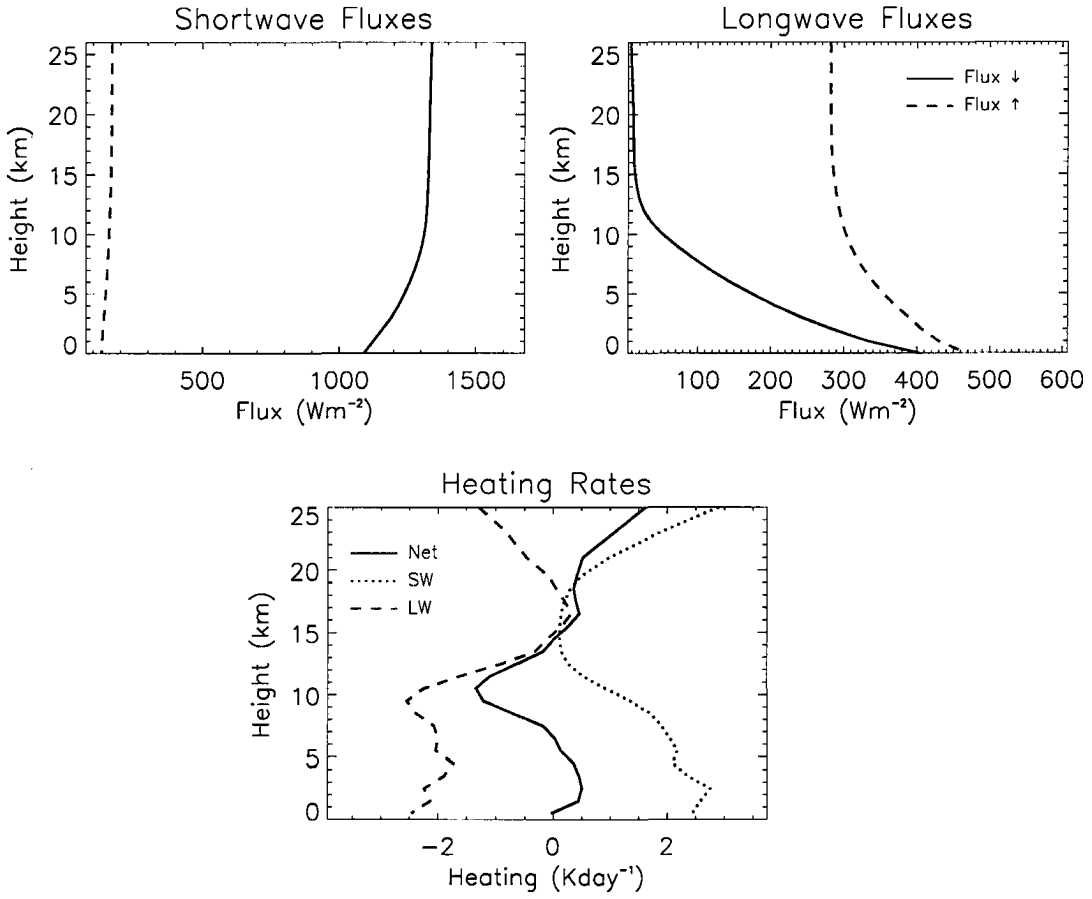

Figure 5.1: Radiative fluxes and heating rates for a tropical clear-sky pixel. The symbols ↑ and ↓ refer to upwelling and downwelling fluxes, respectively.

at a peak, the shortwave and longwave components of the total heating are approximately equal, leading to a slight net heating[3] of 0.13 $Kday^{-1}$ when integrated over the column. The net heating profile exhibits moderate cooling in the middle and upper troposphere due to absorption and re-emission in the rotational bands of the water vapor spectrum and a heating in the stratosphere due to absorption of solar radiation by Ozone. At night, in the absence of solar radiation, this pixel cools at a rate of about 2 $Kday^{-1}$ due to strong water vapor emission in the lower atmosphere coupled with emission from CO_2 in the

[3]Note that net heating rate and net cloud radiative forcing (below) are defined as the sum of the LW and SW components and should not be confused with the definition of net flux earlier.

stratosphere, typical of the moist tropical atmosphere.

5.2.2 Sensitivity Studies

Although relatively few assumptions are required to model the tropical atmosphere, uncertainties in these parameters can have a significant impact in the clear-sky components of the radiation budget. It is, therefore, important to quantify the sensitivity of the cloud-free fluxes and heating rates to errors in surface albedo, SST, CWV, and its vertical distribution as these, potentially variable, quantities primarily control the magnitude and vertical distribution of heating under cloud-free conditions.

Figure 5.2 presents flux and heating rate profiles corresponding to ocean surface albedos of 0.09 and 0.15, characteristic of the range of variability observed in ERBE data (Harrison et al., 1990). Despite a small increasing in the upwelling shortwave flux, small perturbations to the reflection from the ocean surface have little impact on the clear-sky fluxes and heating rates in the tropical atmosphere. Still small, but perhaps not negligible, is the sensitivity of the heating rates in this pixel to CWV and SST. Figure 5.3 displays heating rates derived assuming two extremes based on expected uncertainties in the RSS data product. The "Max." case corresponds to SST and CWV increased by 3 K and 30 %, respectively, while the "Min." case derives from each decreased by an equivalent amount. It should be noted that the low sensitivity to CWV is likely a result of the fact that the pixel chosen for illustration is nearly saturated. Small perturbations in CWV have a more substantial impact in drier regions.

In addition to the column-integrated water vapor and temperature at the surface, we are required to specify a standard vertical distribution of relative humidity and temperature. While the McClatchey tropical atmosphere is almost certainly the most suitable choice given its foundations as the mean of years of soundings spanning the variety of conditions expected in the tropical atmosphere, it is instructive to determine the sensitivity of

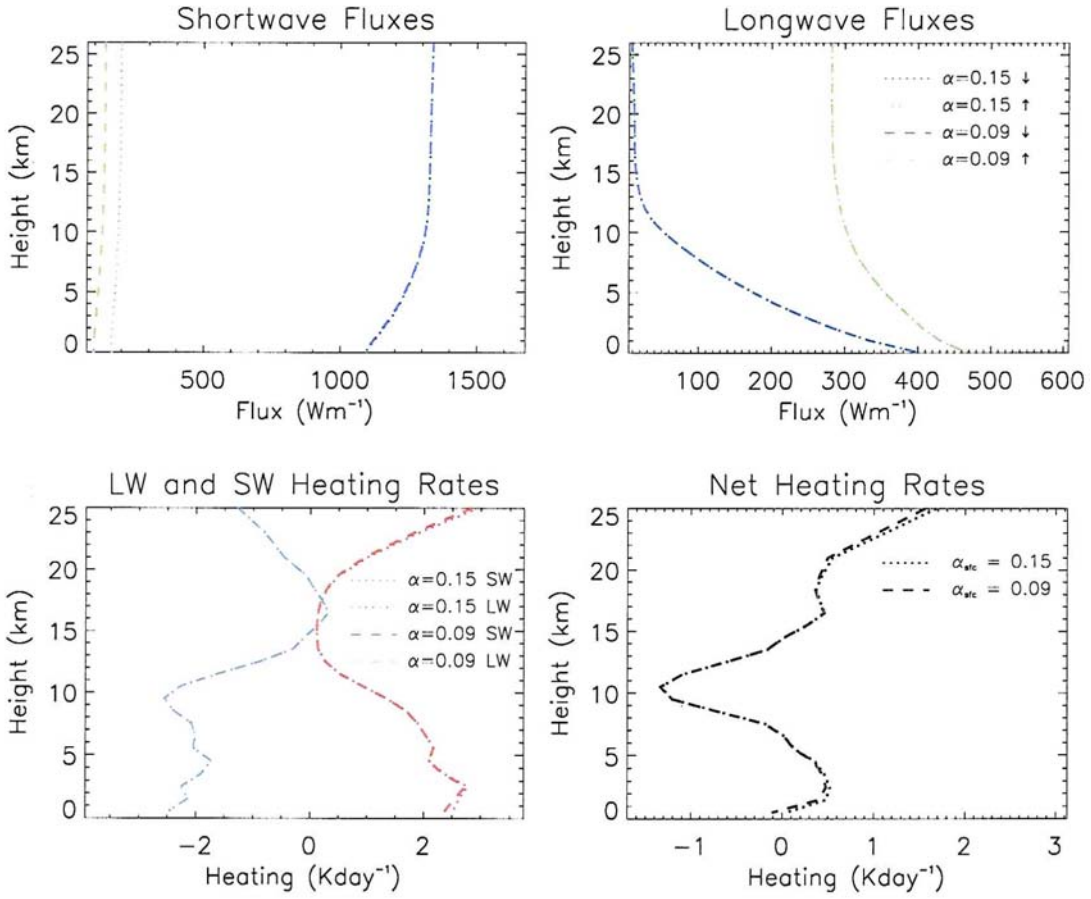

Figure 5.2: Sensitivity of clear-sky radiative fluxes and heating rates to ocean albedo.

the derived heating rate profiles to modifications in the vertical distribution of humidity and temperature. Figure 5.4 provides an extreme case where a humidity and temperature profile characteristic of midlatitude winter conditions is employed in the radiative transfer calculations. Even though both are scaled to yield the same CWV, the vertical structure of the relative humidity and temperature profile has a profound impact on the resulting heating rate profile. Both the heating and cooling by water vapor at lower levels are reduced. The largest difference in the net cooling results from the reduction in LW cooling by water vapor in the middle and upper troposphere leading to an overall heating in the column of 0.5 Kday^{-1}.

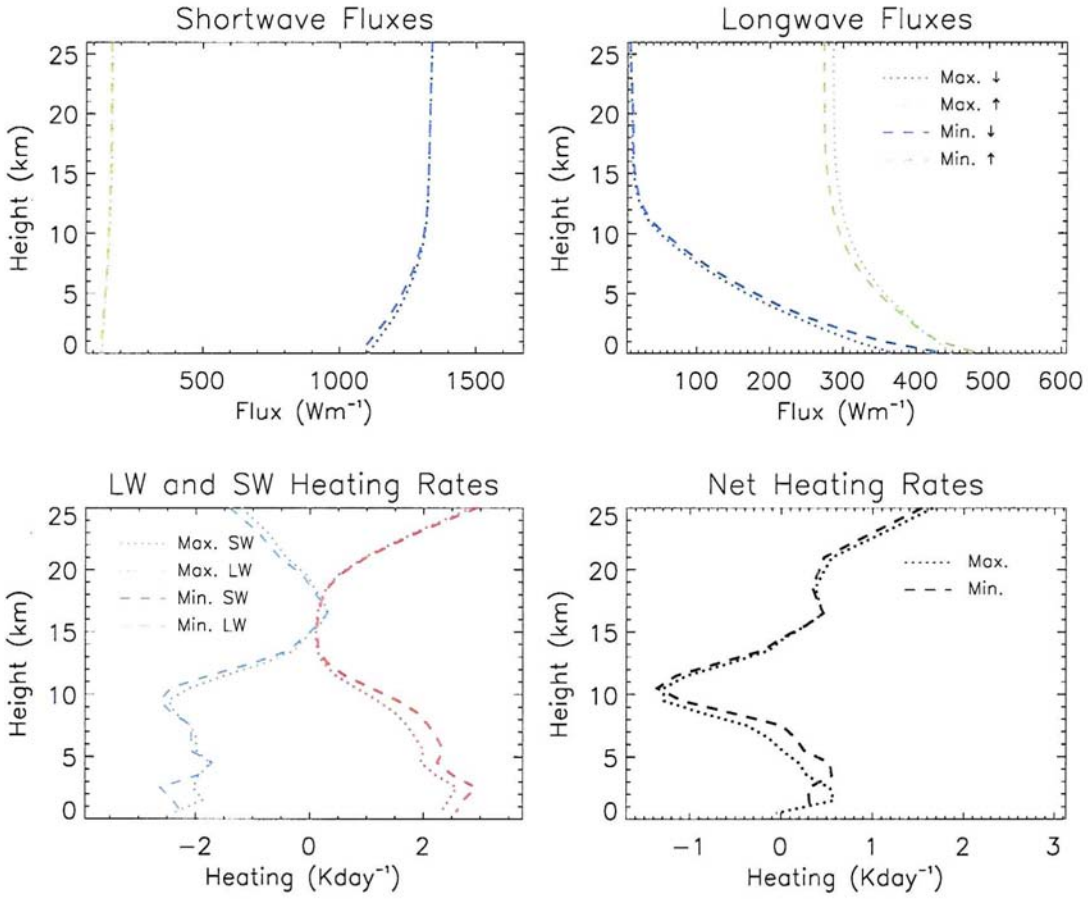

Figure 5.3: Sensitivity of radiative flux and heating rate profiles to errors in CWV and SST under cloud-free conditions.

Column-integrated heating rates for each of the cases presented above are presented in Table 5.1. With the exception of the assumed vertical profiles of temperature and humidity, the column heating rates exhibit very weak sensitivities over the range of uncertainties expected in the RSS and ERBE-derived input. Furthermore, these error bounds likely represent a maximum as we anticipate the presence of clouds and precipitation to reduce the impact of these assumptions. As a result, cloud-free conditions will be used to establish the error bounds resulting from CWV, SST, and albedo in the analyses which follow.

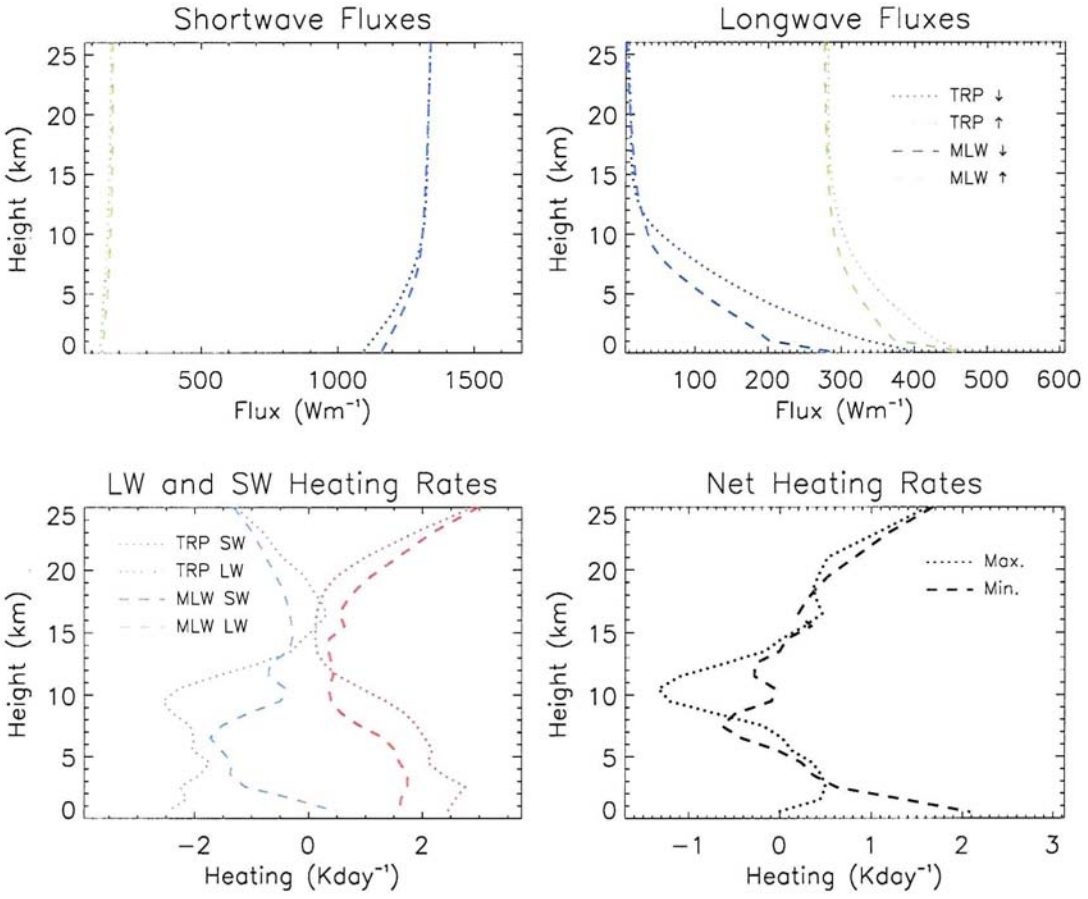

Figure 5.4: Clear-sky radiative flux and heating rate profiles for a standard tropical (TRP) and midlatitude winter (MLW) profiles of temperature and relative humidity.

5.3 Non-precipitating Cloudy Pixels

Clouds modify the exchange of radiation between the surface, atmosphere, and space through reflection of solar and absorption and re-emission of LW radiation. It is through these processes that clouds, both precipitating and non-precipitating, impact the ERB establishing an intimate connection between the Earth's radiative equilibrium and the global hydrological cycle. We now seek to quantify the effects of clouds on radiative transfer in the tropical atmosphere and the accuracy with which the TRMM observations can provide such information.

Table 5.1: Sensitivities of clear-sky column heating to humidity, SST, and surface albedo. Heating is expressed in Kday^{-1}.

Case	Modifications to Base Case	SW Heating	LW Heating	Net Heating
1	Baseline case (see text)	1.96	-1.83	0.13
2	Albedo decreased by 25 % (to 0.09)	1.94	-1.83	0.11
3	Albedo increased by 25 % (to 0.15)	1.98	-1.83	0.15
4	MLW RH and T profile	1.39	-0.83	0.55
5	SST and CWV decreased by 3 K and 33 %	1.83	-1.74	0.09
6	SST and CWV increased by 3 K and 33 %	2.09	-1.90	0.19

In addition to assuming surface and clear-sky atmospheric parameters, modeling clouds requires a number of additional quantities as input. The BUGSRAD model requires effective radius and cloud water content to be specified for all cloud layers. For thin cirrus, r_e and IWC information is supplied by the retrieval, provided the observed IR brightness temperatures fall within the boundaries of the outer arches in Figure 4.7. For those retrievals falling outside these limits, an assumption on particle size is required. According to the theory, pixels with large ΔT_B are predominantly composed of small particles. Effective radii for pixels which lie above the upper-most arch are, therefore, set equal to the minimum effective radius in the retrieval, $r_e = 5\mu$m. All other failed r_e retrievals can be classified as either thick cirrus or containing larger particles than the maximum assumed in generating the ΔT_B-T_B relations. In such cases the effective radii are set based on climatological data from McFarquhar and Heymsfield (1998) and Francis et al. (1999) who present a variety of *in situ* observations of r_e in cirrus clouds.

The primary drawback to passive-only approaches for deriving cirrus cloud optical properties is a lack of information regarding their vertical boundaries. As a result, a representative geometry must be assumed for all cases deemed to have cloud. Based loosely on the observational evidence from McFarquhar and Heymsfield (1998) and Francis et al. (1999), cirrus clouds will be taken to be 1.5 km or three model layers thick. To be radiatively consistent with the IR-based retrieval, the cloud is placed at the model level associated with the assumed emitting temperature, T_c. A combination of the various retrieval

cases discussed in the previous chapter and various assumptions of cloud geometry will be used to assess the sensitivity of the broadband fluxes to these assumptions and to establish error bounds on the results.

A disadvantage to using passive microwave data to infer LWP, is that cloud droplets are typically much smaller than the wavelength of the radiation used, so the measurements provide little information regarding particle size. As a result, a characteristic particle size must be assumed based on observations. In the present study, an effective radius of 11 μm will be adopted consistent with the mean value presented in Table 1 of Miles et al. (2000), who compile a database of *in situ* observations of low-level stratiform clouds made between 1972 and 1995. These values are also consistent with those quoted in Han et al. (1998). Liquid cloud vertical boundaries will be assumed to be 0.5 and 1.5 km, also based on Miles et al. (2000). A rough estimate of the uncertainty owing to these assumptions may be derived from the standard deviation of the observations in the study since they represent a wide variety of cases, studied in different regions and at different times of the year. Based on the maximum and minimum values presented in the table, two extreme scenarios will be tested in addition to the mean conditions, one representing an extremely thin cloud between 0.5 and 1.0 km and the other a thick cloud between 1.0 km and 2.5 km. Similarly, the sensitivity to particle size will be examined by performing calculations assuming radii of 6 μm and 17 μm, spanning the range of data presented in Miles et al. (2000).

5.3.1 Radiative Heating Profiles

Radiative fluxes and heating rate profiles at noon for a pixel containing a thin cirrus cloud are presented in Figure 5.5. The cloud, located between 11.5 and 13 km, introduces moderate increases in both SW and LW heating rates near its base accompanied by a smaller increase in LW cooling at its top. Since these effects are localized in the vertical, the cloud

results in a column-integrated net heating of only 0.5 $Kday^{-1}$.

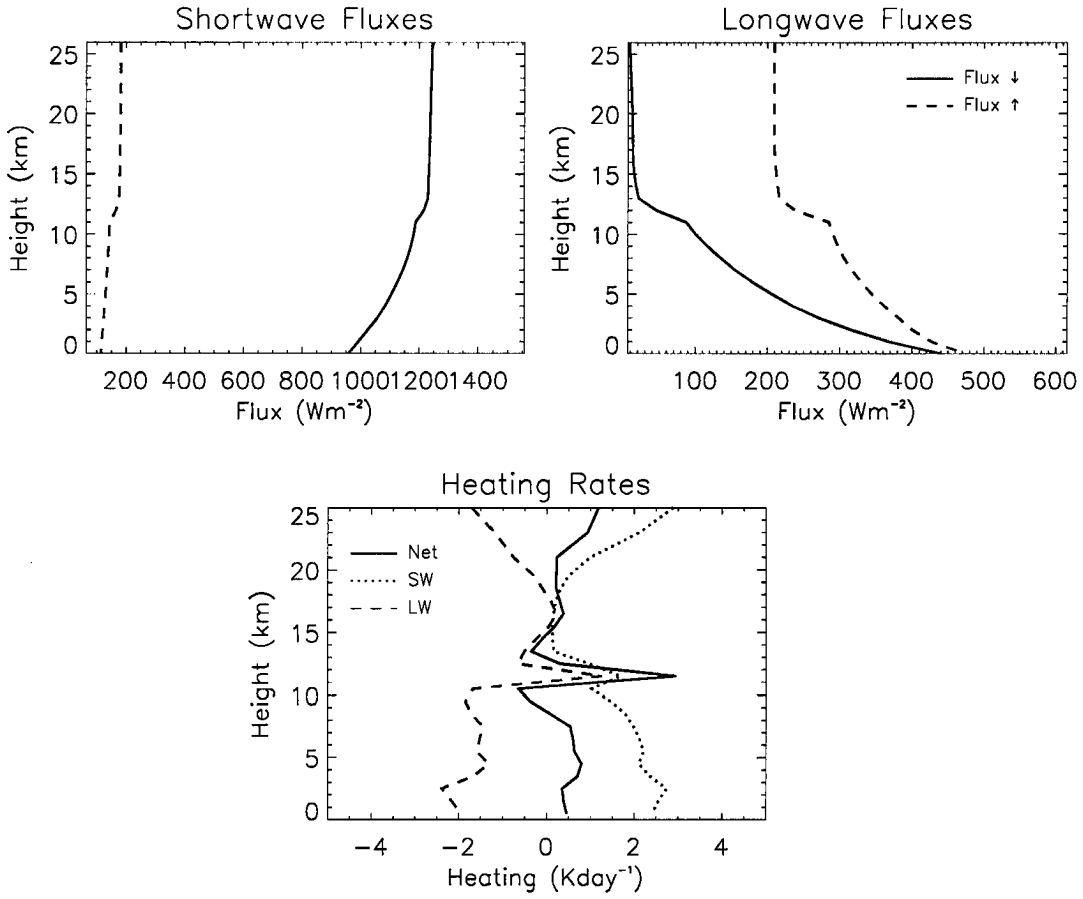

Figure 5.5: As in Figure 5.1 but for a pixel containing a cirrus cloud with an IR optical depth of 0.4, located between 11.5 and 13 km.

For the comparison purposes, RH profiles from a nearby pixel containing a cloud with an IR optical depth approximately three times as great, are presented in Figure 5.6. The enhancement of SW radiative heating in the presence of the thicker cloud is pronounced and leads to a column-integrated heating of more than 1 $Kday^{-1}$. From the flux profiles, we see that the cloud enhances SW reflection to space as well as trapping a large fraction of the LW radiation emitted from below it. Thus, even the crude cirrus information provided by the VIRS-based ice cloud retrieval presents a substantial addition to the GPROF rainfall information and is critical for making quantitative estimates of the ERB.

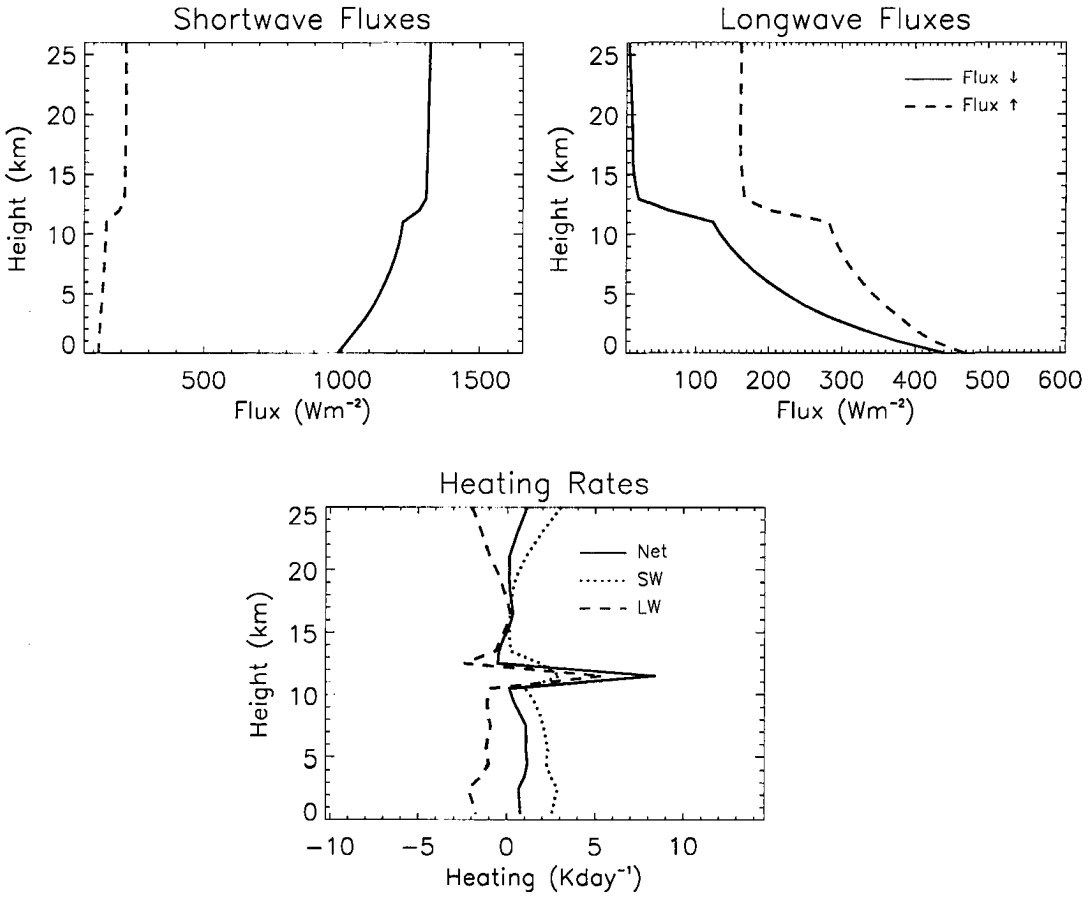

Figure 5.6: As in Figure 5.5 for a cirrus cloud with an IR optical depth of 1.2.

The effect of stratus clouds on atmospheric fluxes and heating rates is demonstrated through another example presented in Figure 5.7. The cloud, located between 1 and 2 km with an IR optical depth of approximately 15, impacts the exchange of both LW and SW radiation between the surface, atmosphere, and space. The enhancement of SW reflection to space, and corresponding reduction in that which reaches the surface is evident from the upper left plot. At the same time the cloud enhances downwelling LW radiation at the Earth's surface through increased atmospheric emission. Integrating over the atmospheric column, the competing effects of shortwave heating and longwave cooling result in a modest column net heating of 0.31 $Kday^{-1}$.

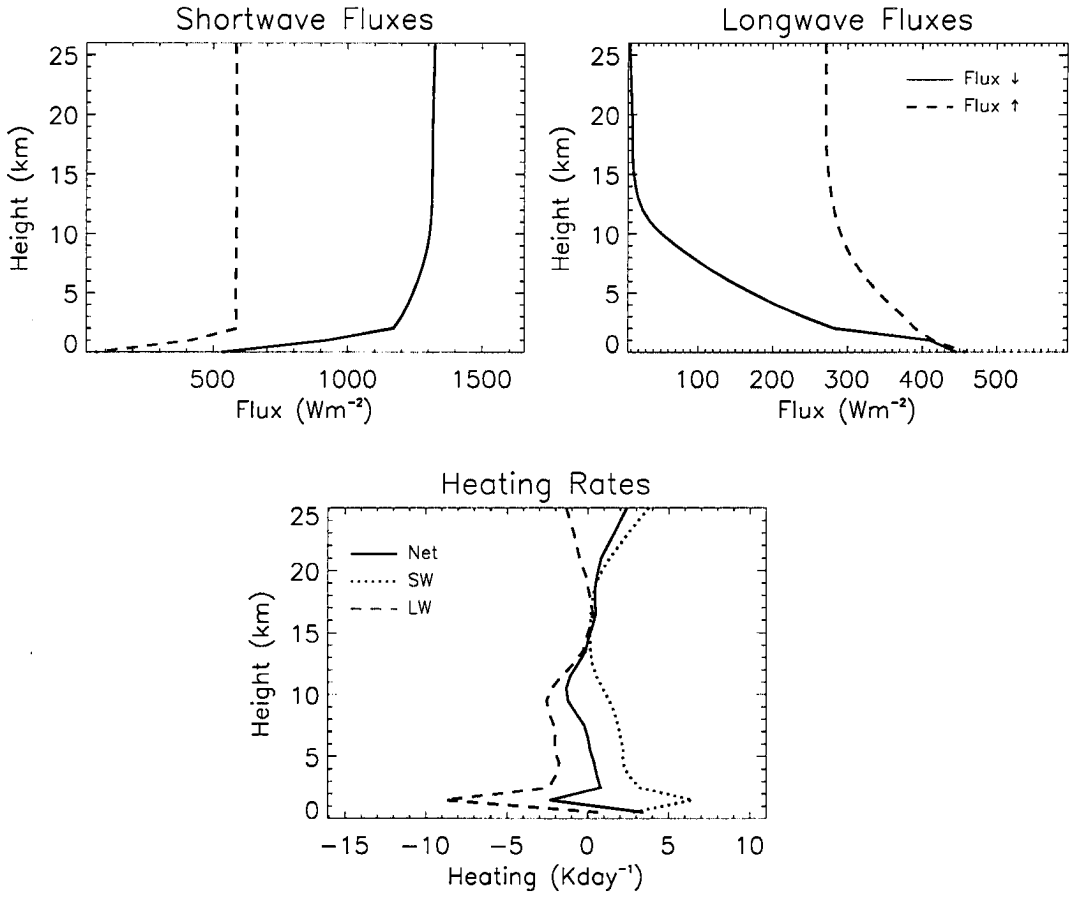

Figure 5.7: As in Figure 5.1 but for a pixel containing a 1 km stratus cloud with IR optical depth of 15 centered at 1.5 km.

5.3.2 Cloud Forcing

A useful quantity for quantifying the impact of clouds on the radiation budget is the cloud radiative forcing (CRF) defined as the difference in net flux (upwelling minus downwelling) between the clear-sky atmosphere and that which contains clouds, precipitating or otherwise,

$$C = F^{NET}_{clear} - F^{NET}_{all-sky} \tag{5.2}$$

The subscript *all-sky* refers to the cloudy atmosphere while *clear* denotes that from which all clouds and precipitation have been removed. In the shortwave, clouds tend to re-

duce the amount of radiation incident at the Earth's surface through the reflection of solar radiation back to space. This increases $F^{NET}_{all-sky}$ resulting in a negative CRF at the top of the atmosphere. Shortwave CRF at the surface is also negative. At the surface $F^{NET} = F^{\uparrow} - F^{\downarrow} = F^{\downarrow}(\alpha - 1)$, a negative quantity. Assuming that the presence of cloud doesn't modify the surface albedo, reducing $F^{\downarrow}$ correspondingly reduces the CRF.

In the longwave, clouds absorb radiation emitted from the surface and re-radiate it both to space and back towards the surface. Since the radiating temperature of a cloud is generally colder than that of the surface, clouds reduce the amount of radiation emitted to space resulting in a positive TOA CRF. Similarly, the increased emission of longwave radiation back to the Earth's surface reduces F^{NET} relative to cloud-free conditions providing a positive SFC CRF.

The relative magnitudes of the competing SW and LW effects and their spatial and temporal variability is a crucial component modulating global atmospheric circulations. The strengths of these forcings, in turn, depend strongly on the optical properties of the cloud and its height in the atmosphere. A high, thin, cirrus cloud, for example, emits radiation at a much colder temperature than the Earth's surface while reflecting only a small fraction of the solar radiation incident upon it. Such clouds, therefore, heat the atmosphere. Conversely, bright stratus clouds, which reside at much warmer temperatures, reflect considerably more solar radiation than they trap at IR wavelengths, thereby serving to cool the planet. At noon, the thin and moderate cirrus cases presented in the preceding section, for example, result in TOA net (SW + LW) CRFs of 35 and 50 Wm^{-2}, respectively, whereas the highly reflective stratus cloud results in a net CRF of -403. Wm^{-2}.

Figure 5.8 presents TOA cloud radiative forcing for all pixels designated as precipitation-free by GPROF over small section of a TRMM orbit on February 1, 1998. Apart from the clear-sky regions for which CRF is, by definition, zero, there are a substantial number of radiatively significant, non-precipitating cloudy pixels. The presence of many pixels with

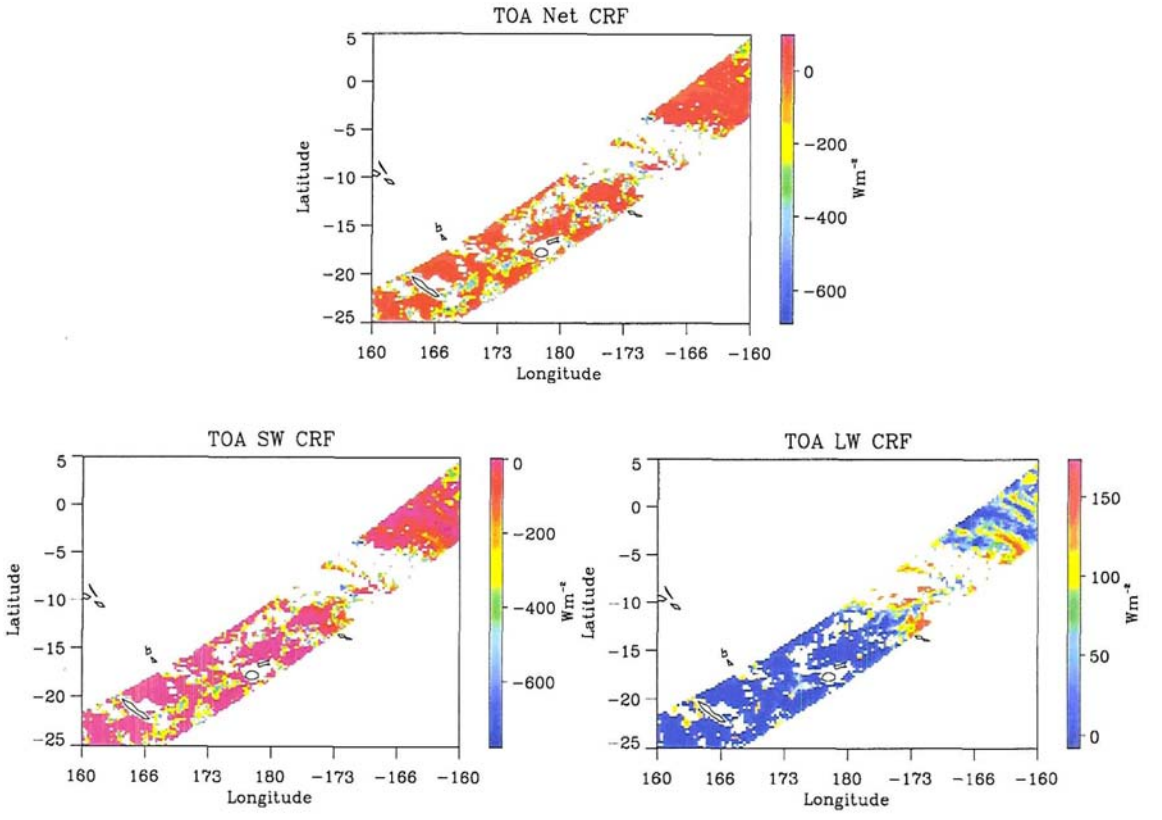

Figure 5.8: LW, SW, and net cloud radiative forcing at the TOA for a small section of orbit.

high SW CRF and comparatively low LW CRF in the southwestern corner of the orbit, suggests the presence of highly reflective liquid clouds at low-levels in the atmosphere. Conversely the signature of cold-topped thin cirrus is clearly evident over a substantial fraction of the northeastern part, most likely associated with convective precipitation centered at 8° S and 170 ° W. CRF at the Earth's surface for the same period is displayed in Figure 5.9. At the surface, the impact of thin cirrus is minimal due to a combination of water vapor which masks their small enhancement to the downwelling LW radiation and their low albedos relative to low clouds. On the other hand, more reflective thicker cirrus and stratus clouds surrounding the large precipitating regions give rise to shortwave forcings on the order of -400 Wm^{-2}. Finally, warm stratus clouds have the additional effect of increas-

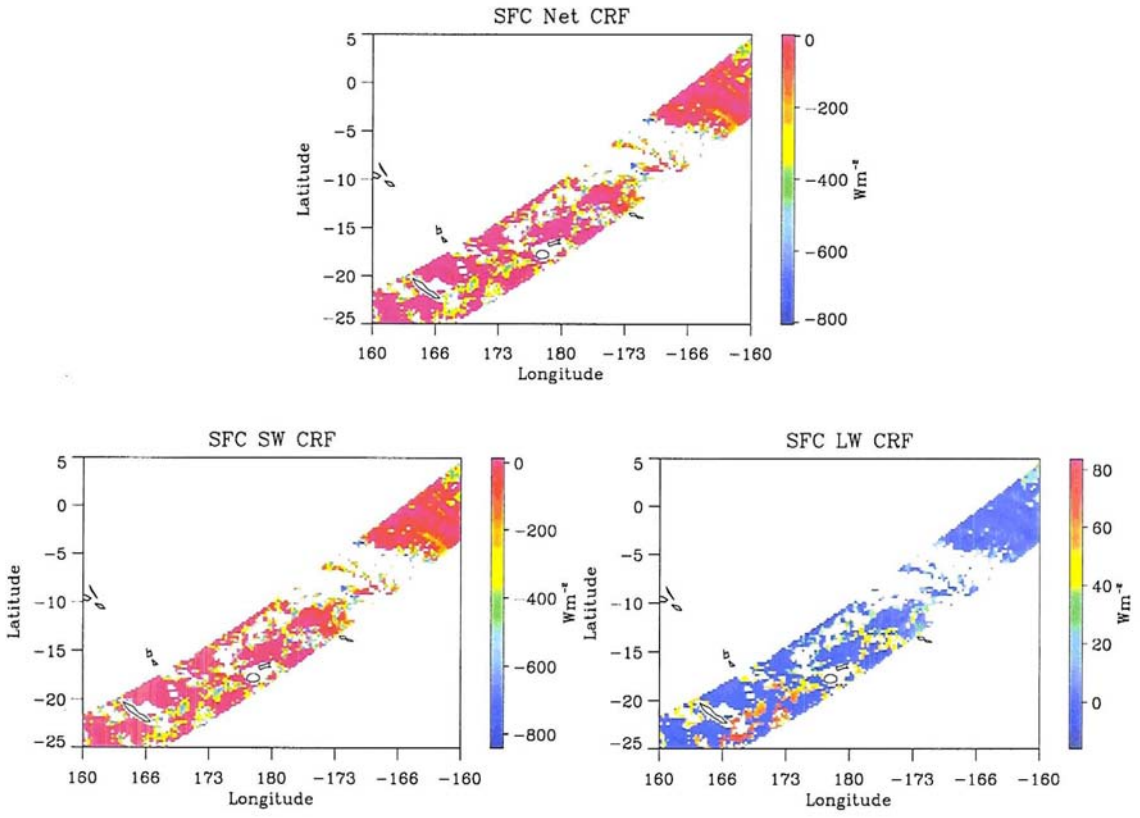

Figure 5.9: As in Figure 5.8 but for SFC cloud radiative forcing.

ing atmospheric emission to the surface, resulting in a surface LW forcing of between 60 and 80 Wm^{-2} in the southwestern corner of the orbit.

5.3.3 Column Heating

By modifying the net flux change through the atmosphere, clouds also influence the rate at which it heats or cools through the absorption or emission of radiation. By reducing the amount of radiation emitted to space, for example, cirrus clouds reduce LW cooling while slightly increasing SW heating by absorbing a small amount of solar radiation. The presence of liquid clouds, on the other hand, increases LW cooling through enhanced emission but also increases SW heating through a combination of absorption and enhanced reflection

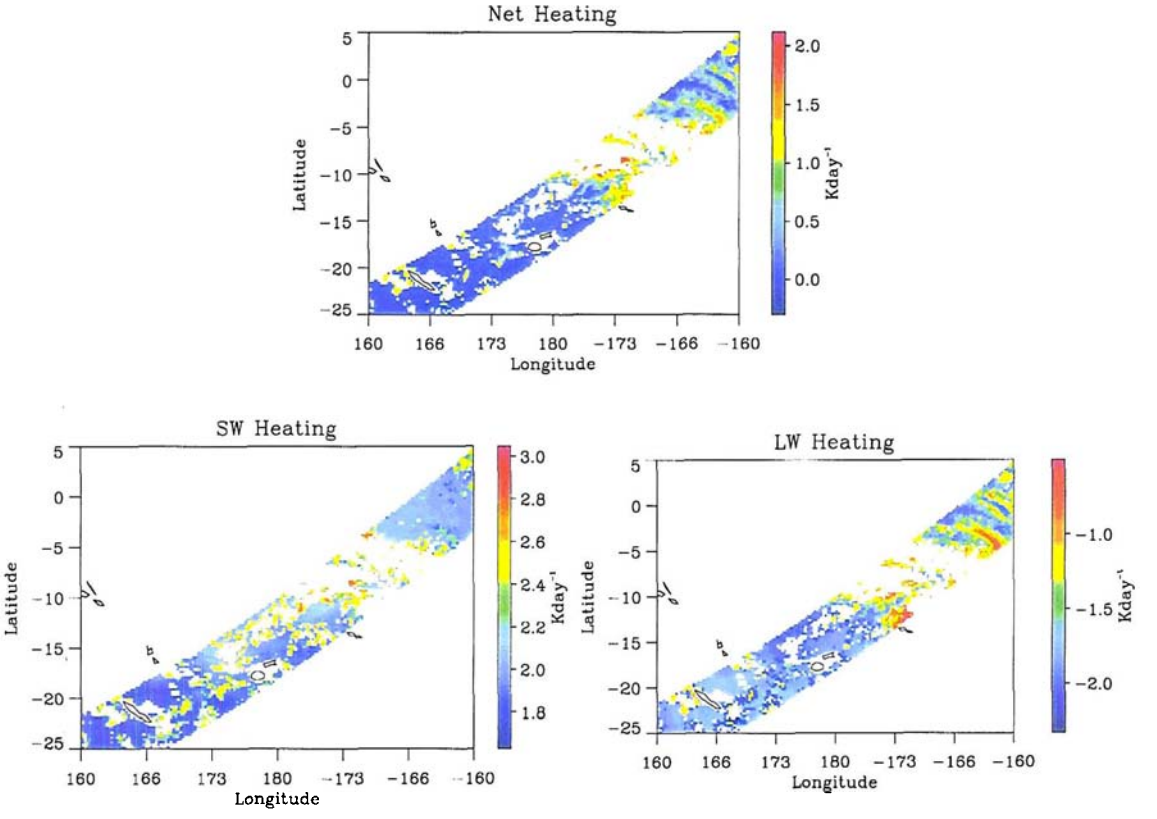

Figure 5.10: As in Figure 5.8 but for column-integrated SW, LW, and Net radiative heating.

of SW radiation back to space effectively doubling the path length through the water vapor above them. These effects are highlighted in Figure 5.10 which shows maps of column heating. Recall that, at this time of day, a typical clear-sky pixel exhibits a SW heating of 1.96 Kday^{-1} while cooling at a rate of 1.83 Kday^{-1} through thermal emission, resulting in a net heating of a tenth of a degree per day (Table 5.1). Regions of reduced LW cooling associated with cirrus dominate the central and northeastern sections of the swath surrounding the precipitation producing stronger net heating within the atmospheric column. Evidence of liquid clouds is less conclusive but regions of enhanced LW cooling and SW heating (relative to the clear-sky values) are evident surrounding precipitation between 10° and 16° S. When summed, however, these effects cancel for the most part resulting in

no appreciable net heating or cooling.

5.3.4 Sensitivity Studies

In order to establish error bounds on these estimates of CRF and radiative heating, it is important to investigate their sensitivities to the required assumptions. Even though they are designed primarily as error analyses, these sensitivity studies also provide valuable information toward determining the sensitivity of the ERB to both natural and anthropogenic climate perturbations. For example, the impact of decreasing particle radii while holding LWP fixed is akin to modeling the indirect radiative forcing of increased aerosol concentrations. It has been speculated that such increases may increase available cloud condensation nuclei (CCN) thereby increasing their particle concentration while decreasing their mean particle size (see, for example, Seinfeld and Pandis (1998)). Alternatively, the effects of variable cloud height illustrate the response of our model to variations such as those proposed by Cess et al. (2001) to explain the observed increase in the ratio of SW to LW CRF during the 1998 El Niño. It is easy to see how the distribution and optical properties of ice cloud, liquid cloud, and precipitation and coincident radiative flux data provided here might be used to provide observational evidence to test these and other atmospheric phenomena in the future.

Figures 5.11 and 5.12 demonstrate the impact of cirrus cloud height on flux profiles and heating rates derived using the BUGSRAD model. Each of the cirrus clouds described in Section 5.3.1 have been modeled and the results derive from varying the assumed emitting temperature in the ice cloud retrieval between 210 and 240 K. The height of a cirrus cloud has little impact on its SW reflective and absorptive properties so the vertical placement of the cloud changes the altitude at which SW heating occurs but does not substantially affect its magnitude. LW fluxes and heating rates, however, are extremely sensitive to the temperature difference between the cloud and the underlying surface. As a result, both

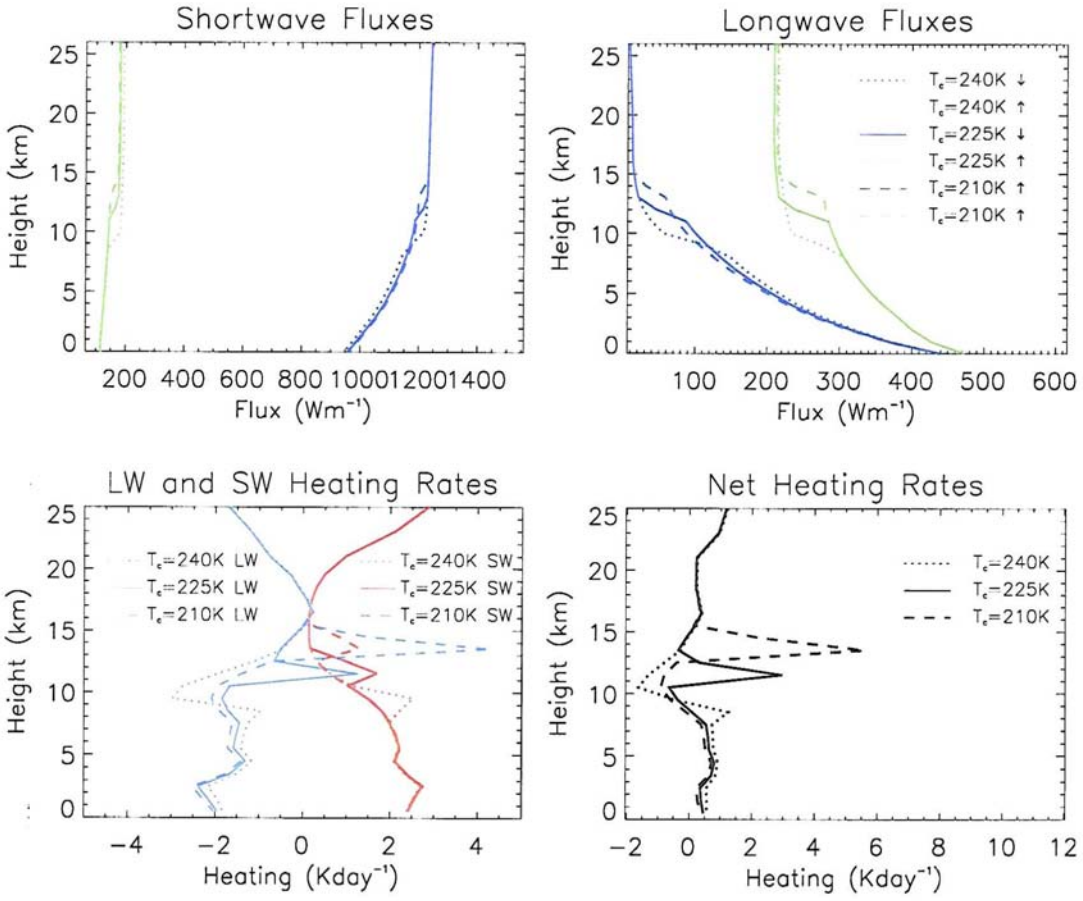

Figure 5.11: Sensitivity of radiative fluxes and heating rates to assumed cloud emitting temperature for thin cirrus case.

the magnitude and the vertical distribution of LW heating vary substantially as a function of the assumed cirrus cloud emitting temperature. The higher the cloud, the stronger the heating at cloud base. Peak LW heating in a thin cirrus cloud at 240 K is -1 Kday^{-1} while the same cloud placed at 210 K gives rise to a peak heating of 4 Kday^{-1}. The thicker ice clouds depicted in Figure 5.12 exhibit similar sensitivity to height but at larger magnitudes. In addition, the lower two clouds exhibit some LW cooling at cloud top which decreases with decreasing cloud temperature.

Unlike high clouds for whom vertical placement largely governs their impact on atmospheric heating profiles, low liquid clouds are most sensitive to assumptions which affect

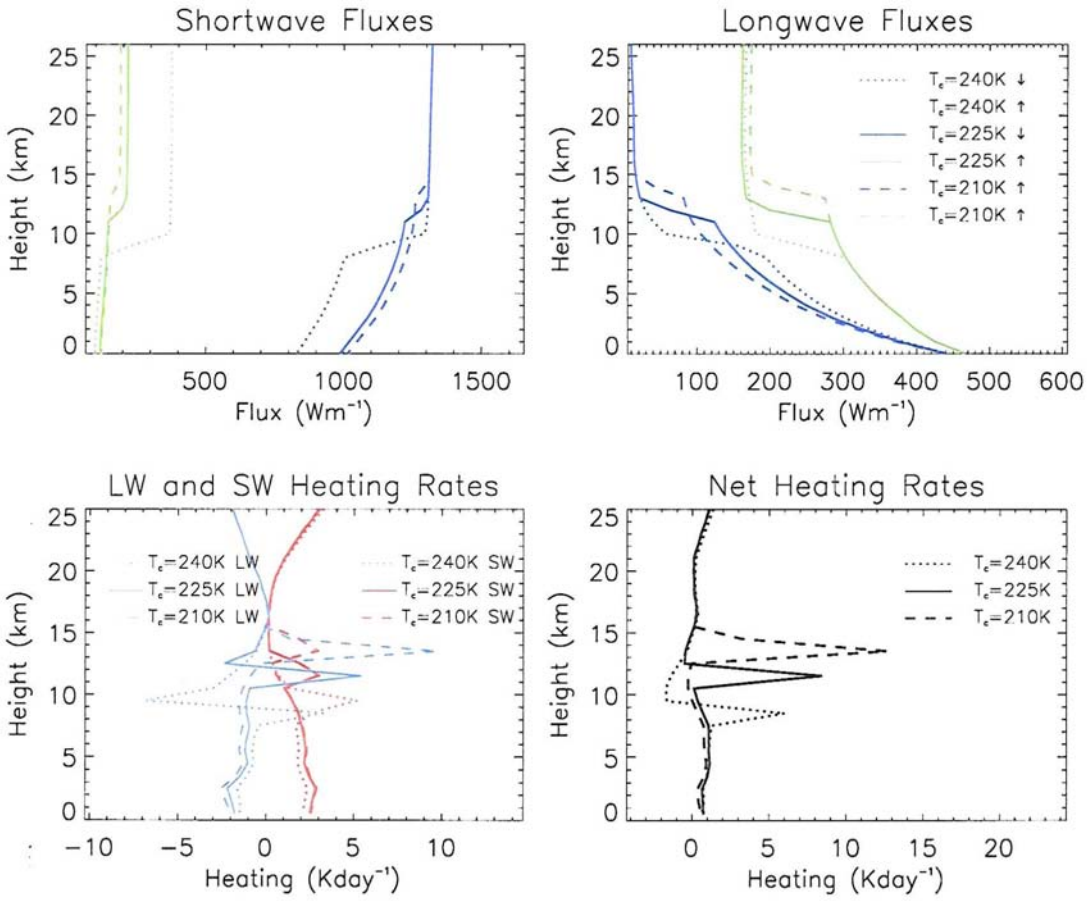

Figure 5.12: As in Figure 5.11 but for a cloud with an IR optical depth three times greater.

their SW properties, such as the effective radius of their constituent particles. Figure 5.13 presents the range of fluxes and heating rates which can be expected by varying the effective radius of a sample stratus cloud between 6 and 17 μm, consistent with the range in observations presented in Miles et al. (2000). Reflection of incoming solar radiation increases substantially with decreasing effective radius, evidence of an overall increase in the number of scattering events which occur within the cloud at a given LWP. This effect manifests itself as a substantial decrease in net cooling through the cloud layer with decreasing r_e. At a radius of 17 μm, for example, peak cooling reaches approximately 3 Kday^{-1} while a similar cloud composed of 6 μm droplets cools at only 1 Kday^{-1} at the same atmospheric

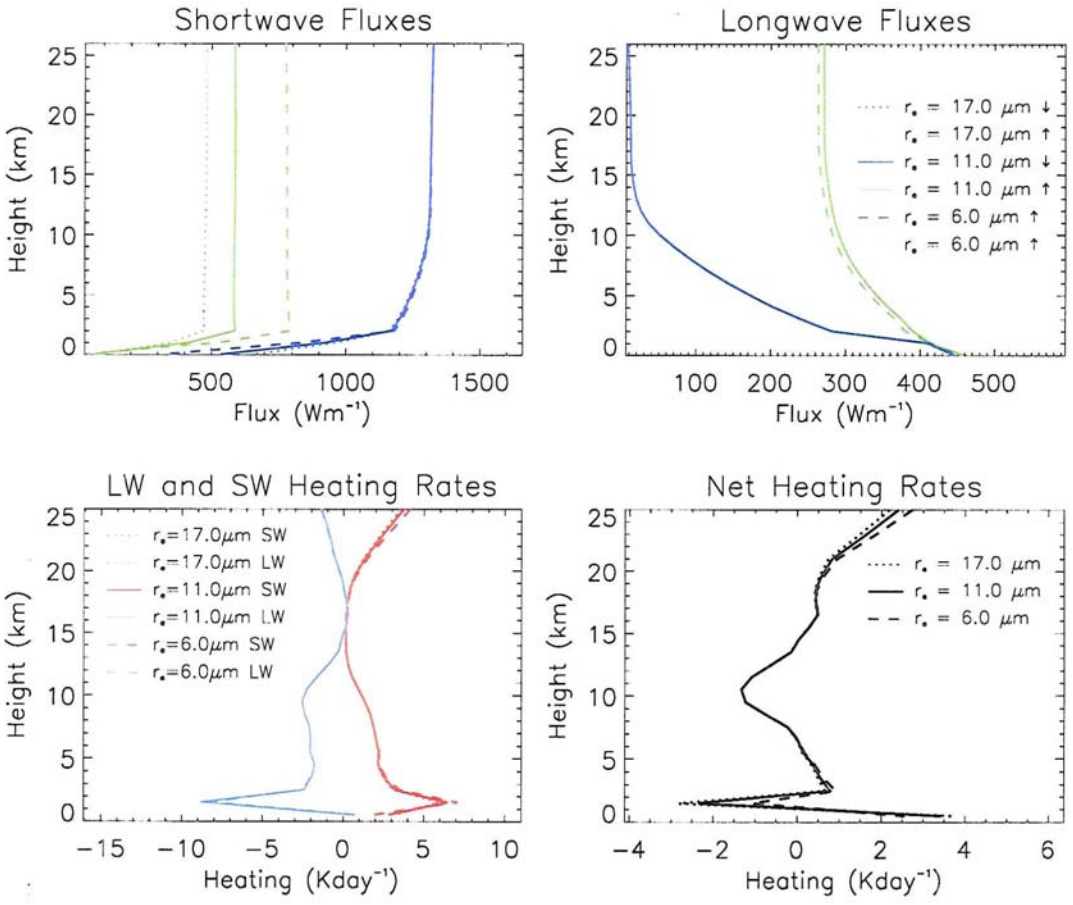

Figure 5.13: Sensitivity of radiative flux and heating rate profiles for liquid clouds with different r_e.

level.

A short description of other selected case studies used to investigate the sensitivity of the BUGSRAD model to the assumed parameters is given in Table 5.2. This is not a comprehensive list of all studies that have been conducted but these cases, in particular, represent the dominant contributions to the overall uncertainties in the derived fluxes and heating rates. CRF and column-integrated heating rates for each of these cases are summarized in Table 5.3.

The impact of cirrus cloud vertical placement on the column-integrated quantities is represented by cases 4-7 in which cirrus clouds are placed at each of the two bounding tem-

Table 5.2: Description of non-precipitating cloud case studies. Only those parameters explicitly listed are modified from the base case described in the text.

Case	Modifications to Base Case
1	Baseline: liquid clouds at 0.5-1.5 km and ice clouds at 11.5-13 km
2	SST and CWV decreased by 3 K and 33 %, respectively
3	SST and CWV increased by 3 K and 33 %, respectively
4	High-geometrically thick ice cloud (13-15.5 km)
5	High-geometrically thin ice cloud (14-14.5 km)
6	Low-geometrically thick ice cloud (8.5-11 km)
7	Low-geometrically thin ice cloud (9.5-10 km)
8	High-geometrically thick liquid cloud (1-2.5 km)
9	Low-geometrically thin liquid cloud (0.5-1 km)
10	Liquid cloud $r_e \rightarrow 6.0\mu$m
11	Liquid cloud $r_e \rightarrow 17.0\mu$m

peratures, 210 and 240 K, and with geometrical thicknesses ranging from an upper bound of 2.5 km to a lower bound of 0.5 km. For both clouds, the effect of cloud height on column heating rates is surprisingly low given the strong sensitivities exhibited by the vertical profiles of heating. Recall that these estimates derive from a combination of modifications to the retrieval and to the assumptions made in the radiative transfer code. Changing cloud emitting temperature results in corresponding changes to its retrieved optical properties such that the cloud yields 10.8 and 12 μm brightness temperatures consistent with those observed by the VIRS instrument. When these optical properties are subsequently used in radiative transfer calculations they produce similar radiances to the VIRS observations used as input. While this does not necessarily hold over the entire range of IR wavelengths which go into the flux calculations, it is reasonable to speculate that some degree of consistency between the observations and the derived fluxes should result.

Comparing column heating from the two clouds, it is clear that the optically thicker cloud results in approximately twice as much net heating as the optically thin cloud. This is primarily a result of an increased greenhouse effect whereby the cloud traps emission from the Earth's surface. A more significant difference between the two clouds is the

Table 5.3: Sensitivity of CRF and column radiative heating to retrieval and modeling assumptions in representative non-precipitating liquid and ice clouds. Refer to table 5.2 for a description of each case.

Thin Cirrus									
Case	Shortwave			Longwave			Net		
	Heating	TOA F	SFC F	Heating	TOA F	SFC F	Heating	TOA F	SFC F
1	2.04	-24.1	-25.0	-1.49	59.1	2.26	0.55	35.0	-22.7
2	1.91	-26.1	-12.4	-1.42	54.3	-10.1	0.49	28.2	-22.5
3	2.16	-22.0	-38.1	-1.51	65.0	11.4	0.65	43.0	-26.7
4	2.03	-20.9	-21.5	-1.51	55.9	1.71	0.53	35.0	-19.8
5	2.03	-21.2	-21.7	-1.51	55.5	1.69	0.52	34.3	-20.1
6	2.04	-35.0	-35.9	-1.55	52.6	3.17	0.49	17.6	-32.7
7	2.04	-34.6	-35.4	-1.56	50.7	3.06	0.47	16.1	-32.3
Thicker Cirrus									
Case	Shortwave			Longwave			Net		
	Heating	TOA F	SFC F	Heating	TOA F	SFC F	Heating	TOA F	SFC F
1	2.17	-53.1	-55.6	-1.15	103.	3.08	1.02	50.1	-52.5
2	2.04	-55.3	-42.3	-1.09	101.	-6.76	0.95	45.7	-49.2
3	2.30	-51.0	-69.2	-1.19	106.	9.94	1.11	55.4	-59.3
4	2.19	-27.6	-32.1	-1.22	93.8	1.67	0.96	66.2	-30.4
5	2.19	-27.9	-32.4	-1.23	92.8	1.62	0.96	64.9	-30.7
6	2.01	-208.	-192.	-1.19	101.	4.97	0.82	-107.	-187.
7	2.02	-202.	-186.	-1.23	95.9	4.77	0.79	-106.	-181.
Stratus									
Case	Shortwave			Longwave			Net		
	Heating	TOA F	SFC F	Heating	TOA F	SFC F	Heating	TOA F	SFC F
1	2.48	-414.	-482.	-2.18	10.9	53.1	0.31	-403.	-429.
2	2.37	-422.	-476.	-2.09	6.31	59.8	0.09	-415.	-416.
3	2.60	-406.	-488.	-2.12	16.0	47.9	0.51	-390.	-440.
8	2.50	-417.	-486.	-2.21	7.46	53.6	0.29	-409.	-433.
9	2.42	-503.	-564.	-2.04	22.4	48.3	0.38	-481.	-515.
10	2.50	-603.	-673.	-2.13	18.4	54.5	0.38	-584.	-618.
11	2.43	-309.	-371.	-2.18	10.4	53.8	0.26	-299.	-318.

sensitivities of their CRF to changing cloud height. The thin cloud LW and SW forcings behave similar to its column heating, exhibiting very slight sensitivity to cloud height. While the sensitivity of the LW forcing from the thicker cloud to its height is also weak, this is not true of its SW and Net forcings. In moving the cloud from 210 K to 240 K, SW forcing at TOA goes from a modest -28 Wm^{-2} to more than -200 Wm^{-2}. This feature is evident in Figure 5.12 where the upwelling SW flux at TOA varies by nearly 200 Wm^{-2} between the two cloud cases, implying significantly more reflection from the lower cloud. At first this result is unexpected. As noted previously, the emitting temperature of a cirrus cloud primarily impacts its LW properties. We have found the opposite to be true, the LW properties are approximately invariant while the SW properties are sensitive to cloud height. The explanation once again lies in the fact that these results simultaneously reflect the sensitivities of both the radiative transfer and original cirrus cloud retrieval models to the assumed emitting temperature. In this case, the assumption of a 240 K cloud emitting temperature in the retrieval resulted in a retrieved effective radius of only 3.5 μm compared to approximately 10 μm at 225 K. The "anomalous reflection" from the 240 K cloud is, therefore, not a result of the flux calculations but the effect of varying the assumptions used in the retrieval. This finding illustrates the importance of accounting for the sensitivities of both the retrieval and the radiative transfer calculations to the assumptions.

Finally, provided total IWP remains constant, varying the cloud geometric thickness from 0.5 to 2.5 km has a negligible impact on both the column heating rates and CRF. The radiative transfer equation for the simple two-layer atmosphere presented in Equation (4.2) predicts this result since changing the cloud geometric thickness has very little impact on its optical depth if all other properties are held fixed.

The lowest panel of Table 5.3 demonstrates the sensitivity of the fluxes and heating rates to stratus cloud parameters. First, note that the stratus cloud impacts the SW components of the ERB much more significantly than those in the LW while the opposite was true of

the cirrus clouds. In this case only assumptions regarding SST and CWV impact both the retrieval and the radiative transfer calculations. SW and LW heating rates vary by 5-10 % over the a $\pm$ 3 K range in SST and $\pm$ 30 % change in CWV. Corresponding SW and LW CRFs vary by less than 10 Wm^{-2} over the same range of initial conditions.

Assumptions regarding the vertical placement liquid clouds and the size of their constituent particles are required only in deriving fluxes and heating rates, not in the retrieval, so the results from cases 8-11 reflect solely the sensitivity of the BUGSRAD model to these parameters. As with the profiles flux and heating rates discussed above, SW radiative transfer in the presence of stratus clouds is extremely sensitive to assumed effective radius. Assuming an effective radius of 6 μm results in a factor of two greater cloud SW forcing than a r_e of 17 μm. As a result, this assumption dominates uncertainties in results associated with stratus clouds.

5.4 Precipitating Pixels

All remaining pixels are classified as either containing precipitation or residing over a land background. Due to the complications associated with modeling a land surface, the present study focuses on oceanic pixels only. All that remains to completely characterize the radiative properties of the tropical atmosphere is to derive radiative flux profiles corresponding to the GPROF hydrometeor content estimates.

5.4.1 Radiative Heating Profiles

Employing the modified version of the BUGSRAD broadband radiation scheme, LW and SW flux profiles were derived on a pixel-by-pixel basis for all precipitating pixels. A longitude-height cross-section of radiative heating rates at noon local time is presented in Figure 5.14. These profiles correspond to the hydrometeor profiles shown in Figure 4.3. In many ways this figure represents the culmination of the research conducted in the previous

three chapters. Here, finally, we obtain a glimpse at the three-dimensional structure of radiative heating in tropical rainfall. There is a sharp contrast in heating profiles east and

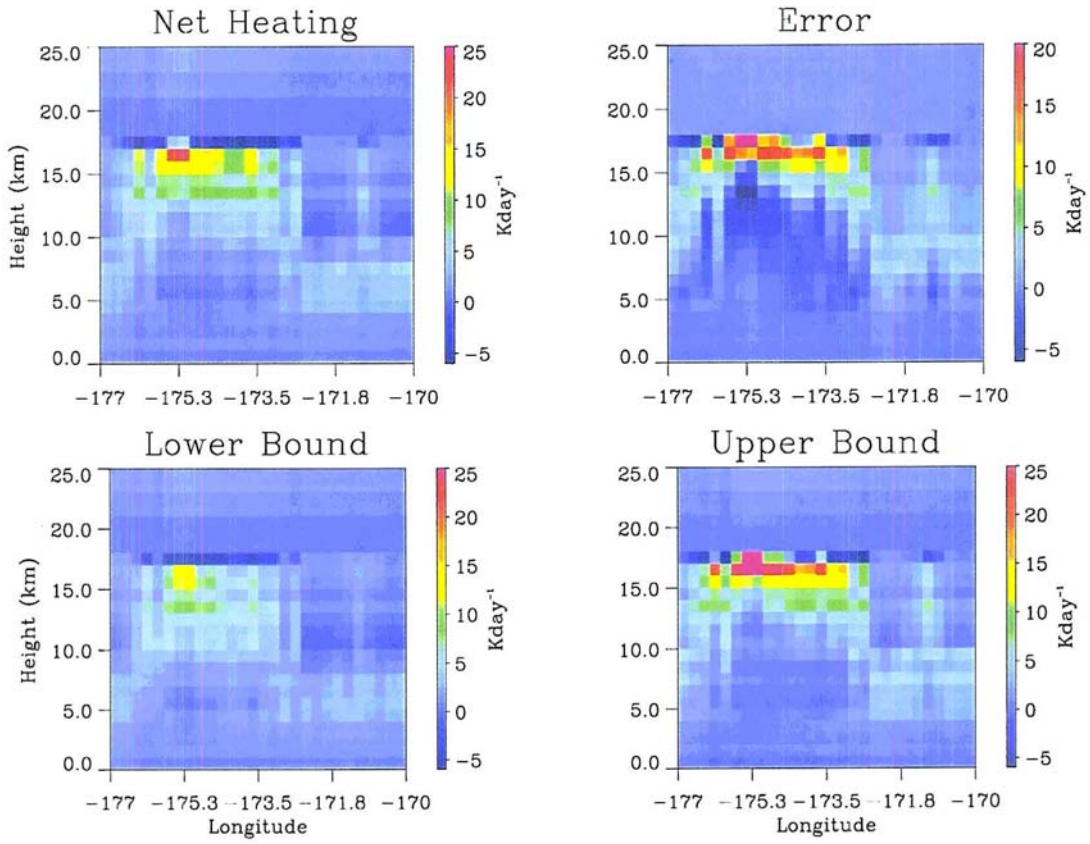

Figure 5.14: Longitude-height cross-sections of net radiative heating and associated errors using the cloud and precipitation shown in Figure 4.3.

west of -174° W. To the east, where rainrates are low and ice water contents are negligible above 9 km (see Figure 4.3), heating does not exceed 5 Kday^{-1} and peaks between 5 and 10 km. To the west, in regions of heavier convective rainfall, peak heating occurs near the GPROF model top of 18 km. Furthermore, many profiles show peak heating in excess of 15 Kday^{-1} approximately 1 km below cloud top and a cooling of 5 Kday^{-1} in the uppermost cloud layer. In both cases a majority of the heating occurs near cloud top in regions primarily consisting of ice particles.

Since estimates of IWC from GPROF have high uncertainties, errors in derived heating

rates are also very large. In fact, uncertainties in vertically-resolved heating rates are on the same order of magnitude as the estimates themselves, a point that will be discussed in more detail below.

Two of the flux and heating rate profiles from Figure 5.14 will be discussed in more detail here. Figure 5.15 presents profiles of temperature, water vapor, ozone, and the four GPROF hydrometeor classes for a light rain pixel at 172.375 ° W. This profile is repre-

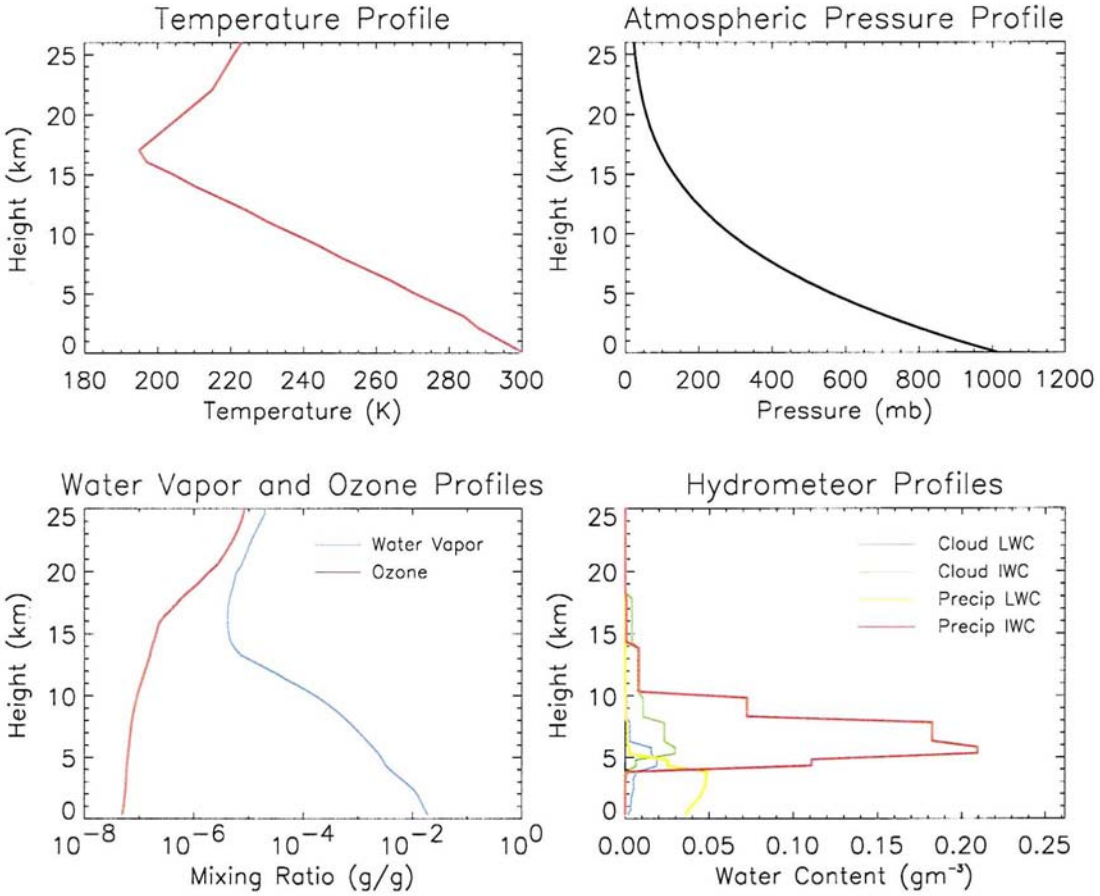

Figure 5.15: Inputs to the radiative transfer model for the light rain case.

sentative of stratiform rainfall and is characterized by light precipitation at the surface, a well-defined melting layer consisting of precipitating ice particles and very low cloud liquid and ice water contents. Fluxes and heating rate profiles for this pixel are presented

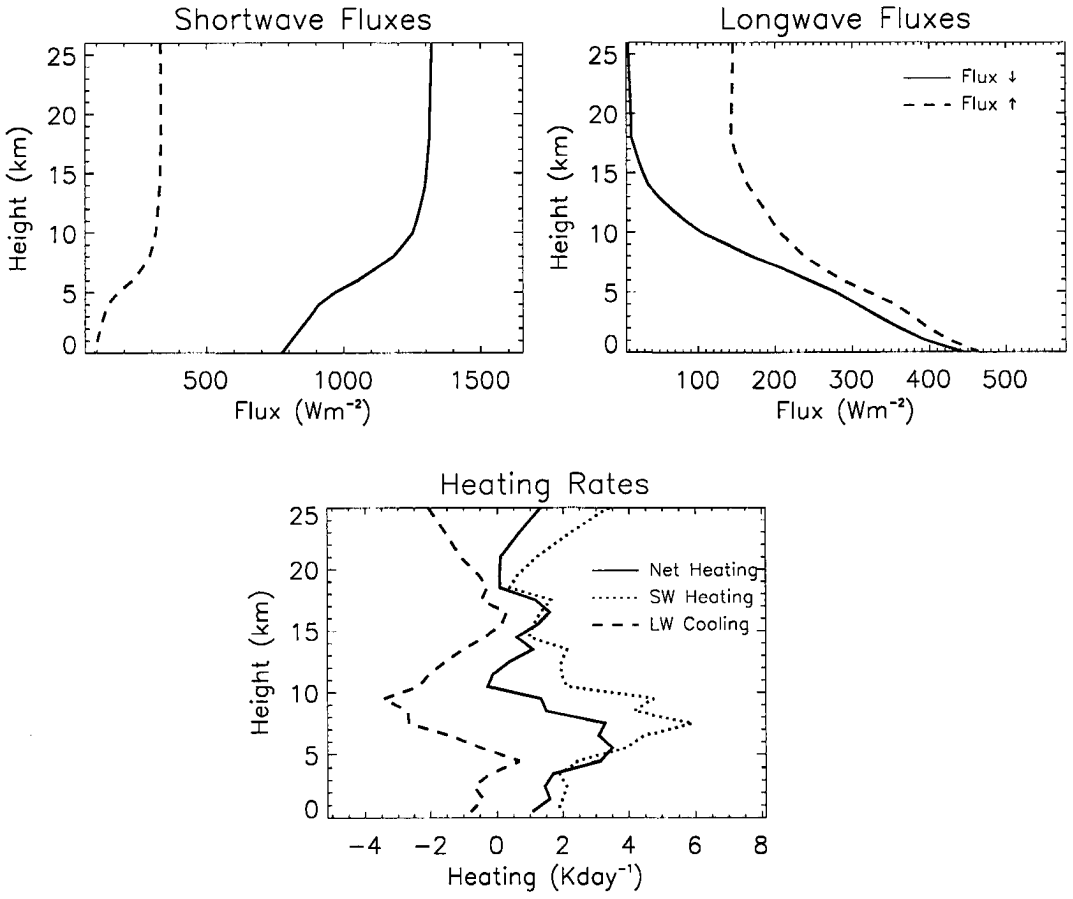

Figure 5.16: Flux and radiative heating rate profiles derived from the input shown in Figure 5.15.

in Figure 5.16. The cloud and precipitation increases reflection of SW radiation while decreasing emission of LW radiation at the TOA. At the same time the amount of SW radiation reaching the surface is reduced while atmospheric emission to the surface is increased. In this way the precipitating cloud exhibits some of the characteristics of both ice and liquid clouds. The resulting heating rate profiles reflect this, showing an enhanced LW cooling through the upper ice regions of the cloud and an enhanced SW heating at slightly lower levels. Since the calculations were made at noon local time, the net heating is biased towards the SW impact of the cloud, resulting in an average heating of 1.7 degree per day through the atmospheric column.

Hydrometeor profiles for a convective rain pixel at 174.875 ° W are presented in Figure 5.17. This pixel is characterized by moderate rainfall of 12 mmh^{-1} at the surface and a substantial amount of cloud ice extending through to the model boundary at 18 km.

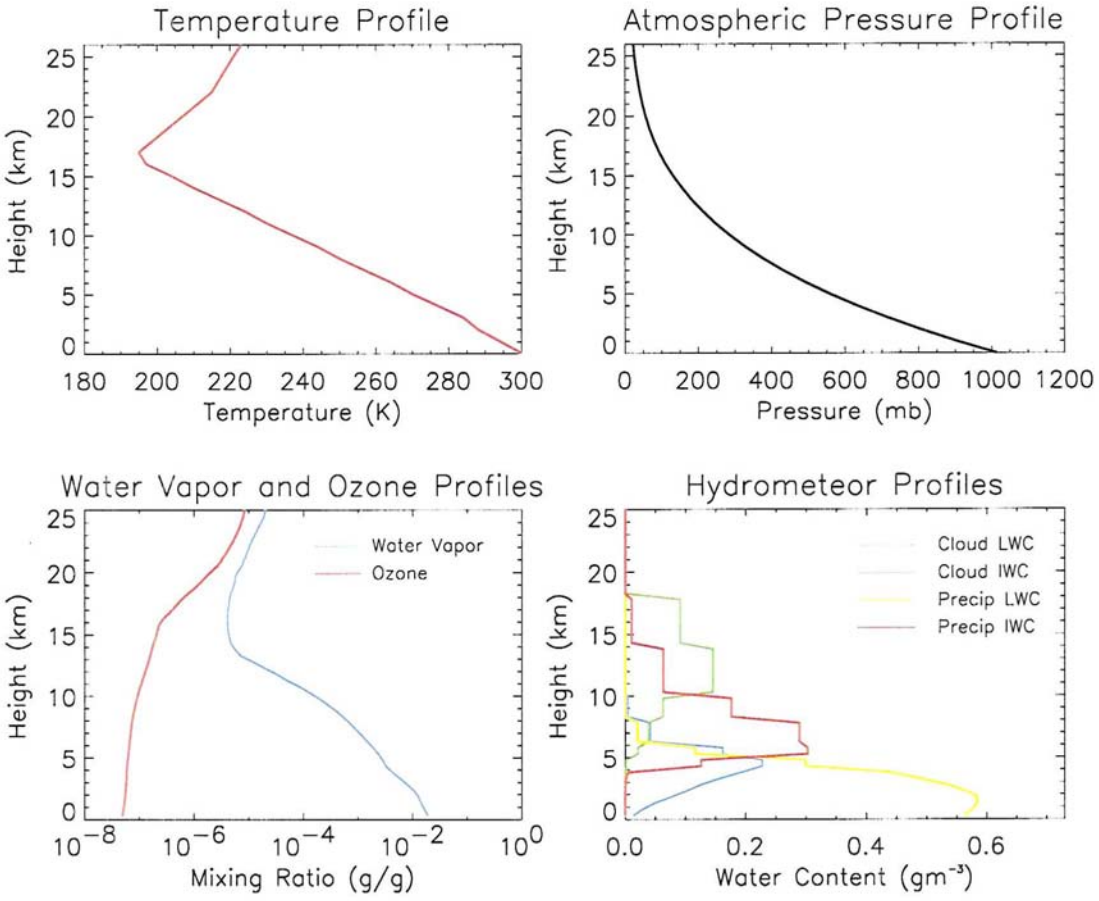

Figure 5.17: Inputs to the radiative transfer model for the moderate rain case.

Fluxes and heating rates for this case, shown in Figure 5.18, are considerably different. The reduction of LW emission to space and enhanced reflection are more pronounced and the enhanced emission back to the surface results in a net flux (upwelling minus downwelling) of nearly zero. Atmospheric heating and cooling are more tightly confined near cloud top, particularly in the longwave, and their magnitudes are five times larger than in the light precipitation case. Furthermore, the cloud and precipitation in the convective case

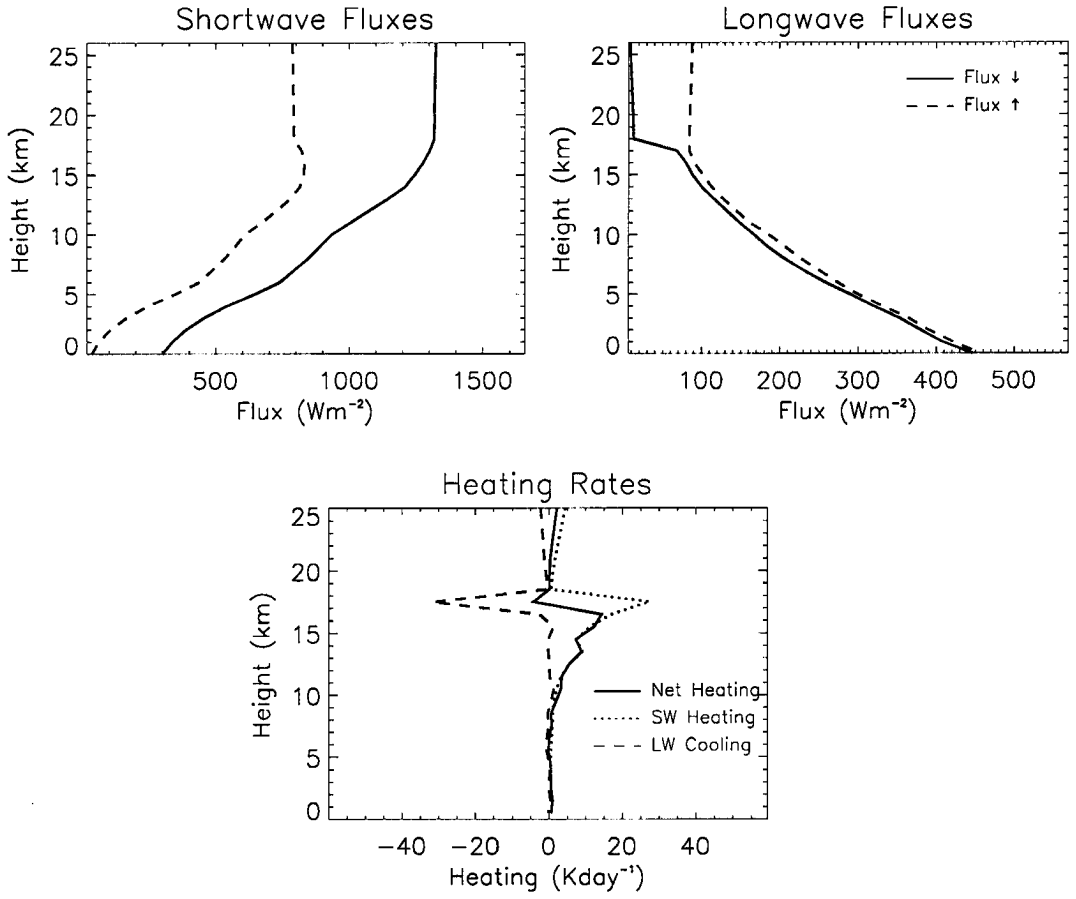

Figure 5.18: Flux and radiative heating rate profiles derived from the input shown in Figure 5.17.

give rise to -618 Wm^{-2} of SW and 180 Wm^{-2} of LW CRF compared to -167 and 123 Wm^{-2} in the light rain case.

5.4.2 Cloud Forcing

Figure 5.19 provides a look at TOA CRF due to precipitating cloud. In the large areas of deep convection, LW TOA CRF is 180 Wm^{-2} and is constant across much of the cloud system implying a uniform cloud top height associated with the capping effect of the tropopause. Making use of the Stefan-Boltzmann law, $F = \sigma T^4$ where $\sigma = 5.67\text{x}10^{-8}$ $Wm^{-2}K^{-4}$, we find that this forcing corresponds to the difference in emission from black-

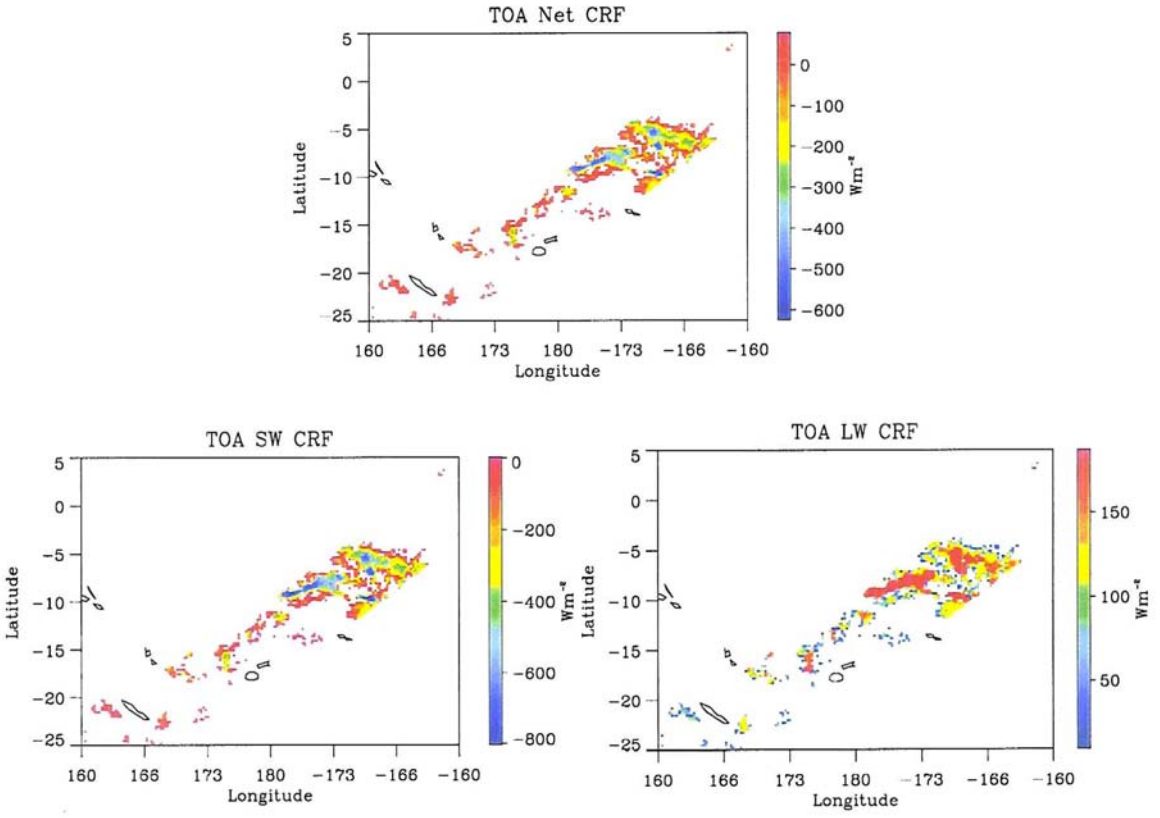

Figure 5.19: Cloud radiative forcing at TOA for precipitating pixels in a section of orbit.

bodies radiating at 265 and 205 K, respectively. Since 265 K, roughly corresponds to the clear-sky emitting temperature of the moist tropical atmosphere and 205 K is consistent with the temperature of the upper most model layer, this demonstrates the fact that the thick clouds associated with convective precipitation effectively mask all emission from below, providing 180 Wm^{-2} of longwave energy to heat both the atmosphere and surface.

The shortwave CRF is substantially larger owing to the greater source of radiation provided by the sun at noon. In the heaviest precipitation, clouds reflect 800 Wm^{-2} of solar energy back to space dominating the LW heating in similar regions. On the periphery of these regions lower cloud top heights associated with lighter rainfall are evidenced by the somewhat lower LW forcings they produce. SW forcing is also substantially reduced in the

surrounding light precipitation areas resulting in a net forcing near 0.

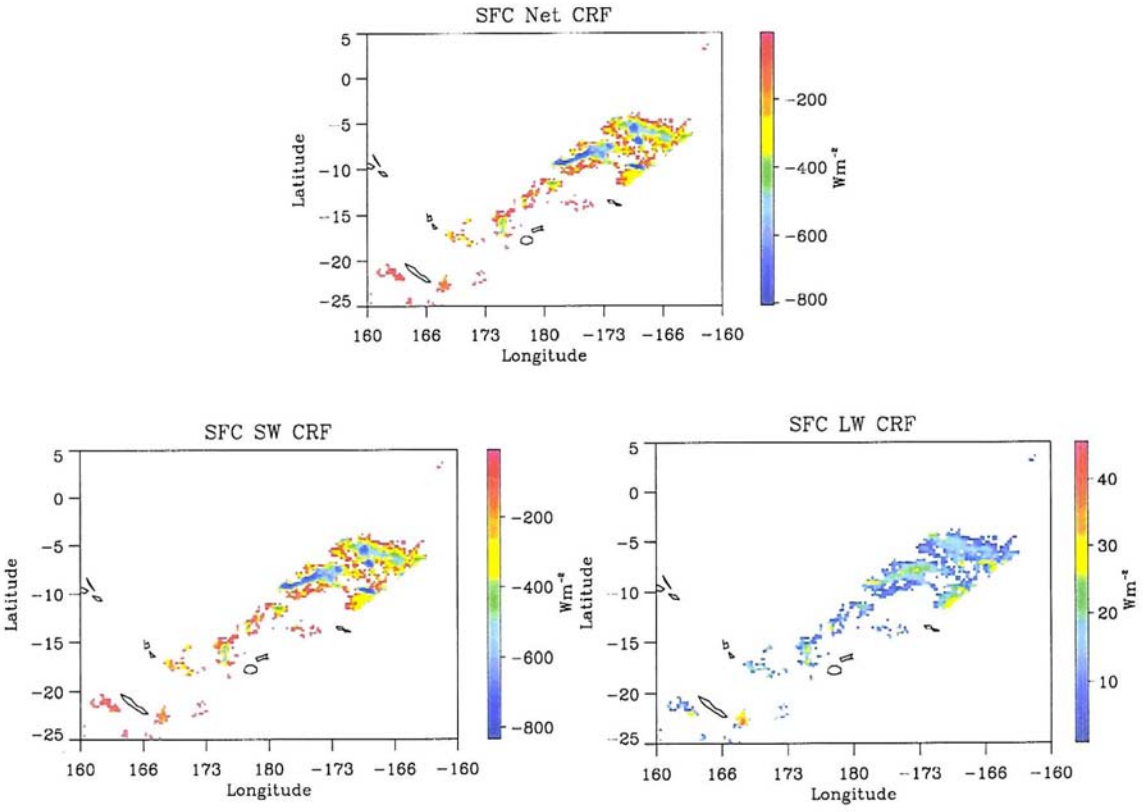

Figure 5.20: As in Figure 5.19 but illustrating CRF at the Earth's surface.

SW surface CRF, depicted in Figure 5.20, resembles that at TOA since the magnitude of an increase in reflection to space induces a corresponding reduction in the radiation reaching the surface. LW CRF at the surface, on the other hand, derives from additional emission of radiation to the surface by liquid droplets in the atmosphere. Its magnitude depends not only on the amount of liquid water present but also on its temperature. Heavy convective rainfall, deriving from recently melted ice particles, results in less surface LW forcing than low clouds and stratiform precipitation which emit at a temperature closer to that of the ambient atmosphere. This is particularly evident when the values in the lower right panel of Figure 5.20 are compared with those for non-precipitating liquid cloud

regions in Figure 5.9. Despite the fact that the non-precipitating clouds contain an order of magnitude less liquid mass, they produce between 70 and 80 Wm^{-2} of LW CRF at the surface, three times more than the heavy precipitation.

5.4.3 Column Heating

The influence of precipitating clouds on the column-integrated radiative heating is presented in Figure 5.21 for the same section of orbit. The deep cold clouds associated with

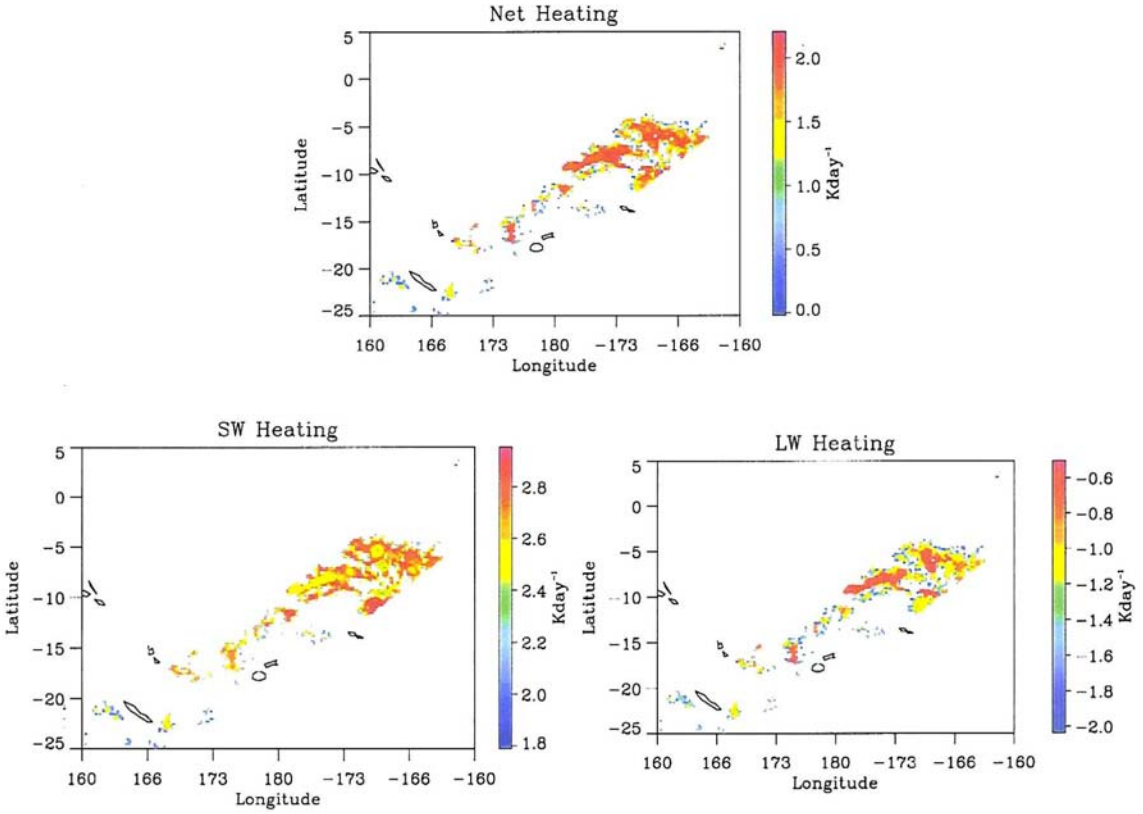

Figure 5.21: Column-integrated radiative heating rates for in precipitating pixels corresponding to a TRMM overpass at local noon.

the large regions of convection substantially reduce the exchange of longwave radiation between the atmosphere and space. At the same time the absorption of SW radiation is

slightly enhanced resulting in a substantial increase in net heating relative to clear sky conditions. Over much of the precipitating region, the net heating is greater than 2 Kday^{-1} and shows little spatial variability. The SW and LW heating fields, on the other hand, can vary by half a degree per day or more but both increase at approximately the same rate with decreasing rainrate leading to a canceling of this variability in the net heating field.

The storms in the focus area were long-lived and, as a result, TRMM provided a second overpass of these regions 13 hours later, at 1:00 am local time. Column heating rates derived from this return visit are displayed in Figure 5.22. The effects of the diurnal vari-

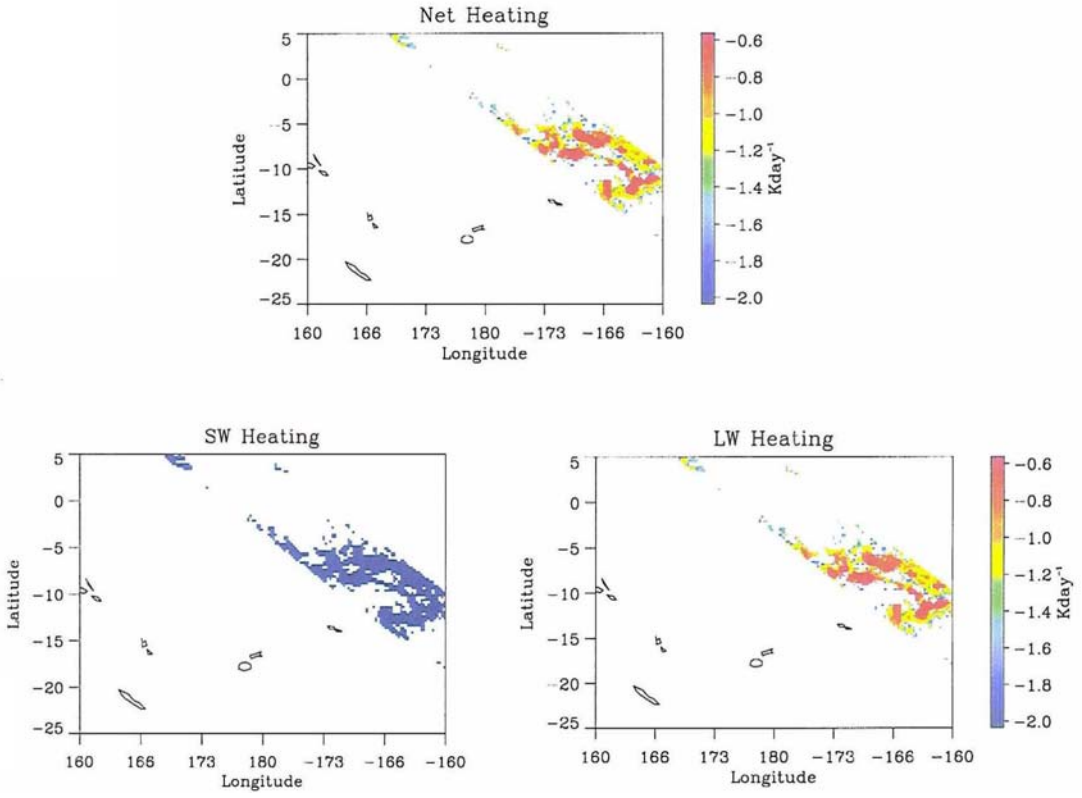

Figure 5.22: As in figure 5.21 but for an overpass at 1:00 am local time.

ability in solar insolation are clear. As opposed to a heating of approximately 2 Kday^{-1} at noon, the atmosphere is cooled by -1.0 Kday^{-1} at night. This emphasizes both the obvious

importance of making estimates of cloud and precipitation at night for deriving a complete picture of the tropical ERB and the more subtle observation that the methods presented here are well-suited to study diurnal variability in the ERB. With the concept of a constellation of satellites to provide better temporal resolution being introduced in preliminary discussions regarding a follow-up to TRMM, these techniques could be used to analyze the diurnal cycle of cloud- and precipitation-induced radiative heating and CRF.

5.4.4 Sensitivity Studies

Estimates of the sensitivities of CRF and column heating to errors in the hydrometeor contents are straightforward given the uncertainty analyses presented in Chapter 3. Upper and lower error bounds on the fluxes and heating rate profiles can be established by perturbing the water contents retrieved by GPROF by an amount consistent with their estimated uncertainties. Figure 5.23 illustrates the resulting sensitivities for the light rain case presented above. The reflection and emission properties of this precipitating cloud are very sensitive to the large uncertainties in the prescribed profiles of LWC and IWC. In particular the downwelling shortwave radiation at the surface varies by 250 Wm^{-2} over the range of values tested. This translates into substantially greater net heating throughout the cloud when water contents are set to their maximum value.

In the case of heavier rainfall, sensitivities appear to be greater as can be seen from Figure 5.24. This is, however, primarily an artifact of the fact that the majority of the SW heating and LW cooling occurs over a region confined to near the cloud top. Within this layer, SW heating varies by as much as a factor of three while LW cooling varies by a factor of 2. This produces a net heating of 25 $Kday^{-1}$ when water contents are at their maxima compared to 5 $Kday^{-1}$ at their minima. When integrated over the atmospheric column, however, this difference amounts to less than 0.3 $Kday^{-1}$. By virtue of its distribution over a broader range of height, the column-integrated net heating difference is 0.6 $Kday^{-1}$ in

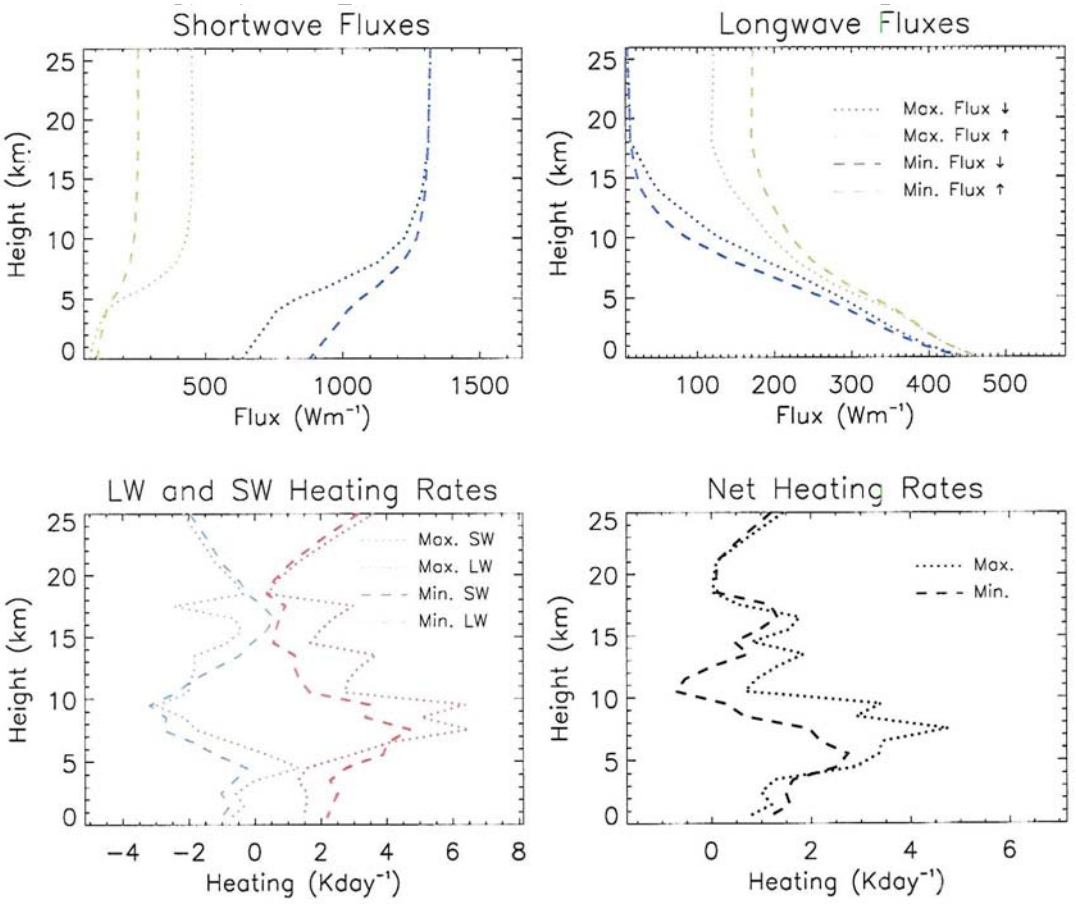

Figure 5.23: Sensitivity of flux and heating rate profiles in light rain to errors in retrieved water contents.

light rain.

Column-integrated heating and CRF from these and a number of other sensitivity studies based on the GPROF error analyses are presented in Table 5.4. A summary of the perturbations made in each case is presented in Table 5.5. The effects of perturbing water contents, vary between the two cloud and rainfall profiles as well as between the SW and LW. LW cloud forcing and column heating are insensitive to errors in LWC in the light rain case, but differ substantially over the range of IWCs tested. When IWC is halved, for example, the LW CRF is 50 Wm^{-2} less than when it is doubled. Differences in the SW are even larger. The SW TOA CRF can be as low as -90 Wm^{-2} or as high as 284 Wm^{-2} while

Table 5.4: Sensitivities of column heating and CRFs in light and moderate rainfall to errors in retrieved liquid and ice water content. Column heating is expressed in $Kday^{-1}$ while cloud radiative forcing estimates are in Wm^{-2}. See Table 5.5 for a brief account of the perturbations made in each case.

Light Rain									
Case	Shortwave			Longwave			Net		
	Heating	TOA F	SFC F	Heating	TOA F	SFC F	Heating	TOA F	SFC F
1	2.78	-167.	-249.	-1.07	123.	15.6	1.71	-43.7	-233.
2	2.80	-184.	-269.	-1.08	124.	16.9	1.72	-60.7	-252.
3	2.76	-155.	-235.	-1.07	123.	14.5	1.70	-31.7	-220.
4	2.83	-270.	-358.	-0.88	147.	16.0	1.95	-123.	-342.
5	2.68	-103.	-173.	-1.28	97.6	15.1	1.39	-5.66	-158.
6	2.83	-284.	-372.	-0.89	147.	17.1	1.94	-137.	-355.
7	2.64	-90.3	-126.	-1.28	96.7	13.8	1.36	6.37	-142.
Moderate Rain									
1	2.53	-618.	-669.	-0.69	180.	24.1	1.84	-438.	-645.
2	2.51	-653.	-702.	-0.70	180.	25.3	1.81	-473.	-677.
3	2.54	-587.	-641.	-0.68	180.	22.9	1.87	-407.	-618.
4	2.42	-705.	-745.	-0.70	179.	24.1	1.73	-526.	-720.
5	2.64	-535.	-600.	-0.70	178.	24.1	1.94	-357.	-576.
6	2.42	-724.	-762.	-0.70	179.	25.3	1.71	-545.	-737.
7	2.67	-486.	-554.	-0.69	178.	22.9	1.98	-308.	-531.

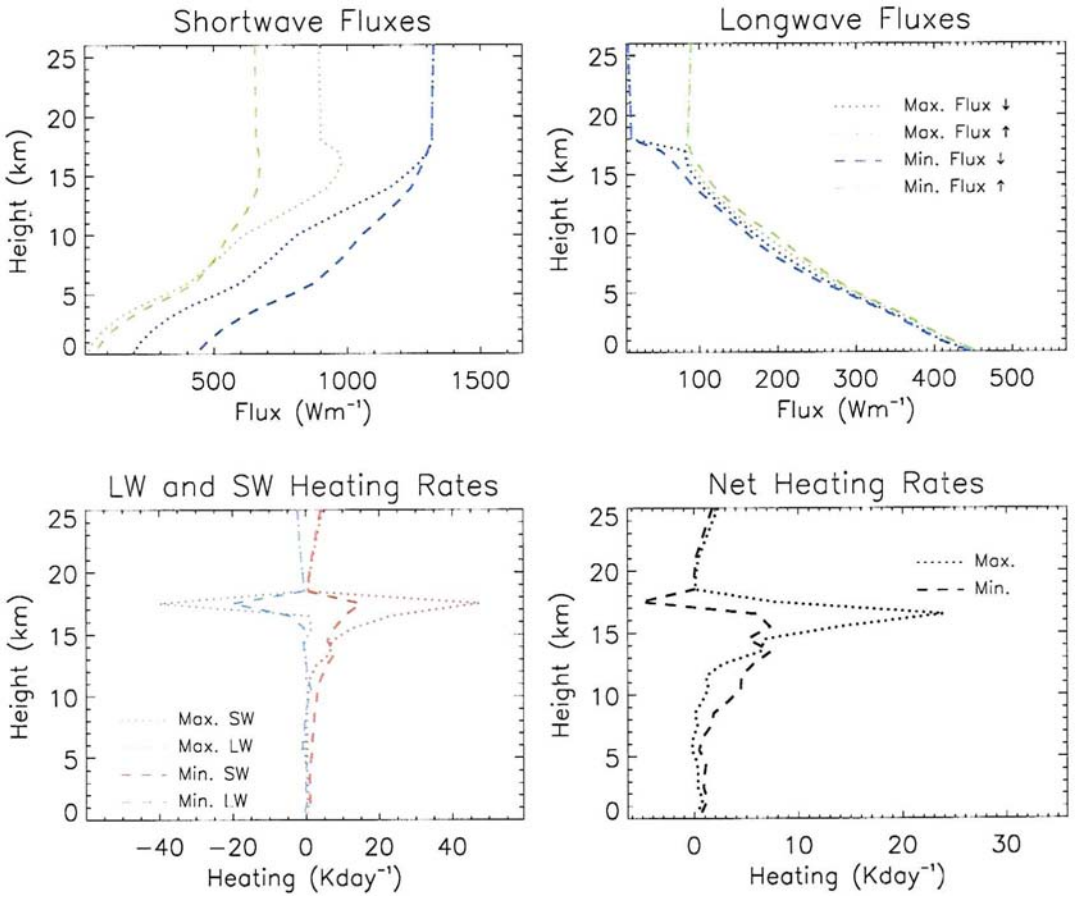

Figure 5.24: As in Figure 5.23 but in moderate rainfall.

surface CRF estimates range from -126 to -372 Wm^{-2}.

In heavier rain, the LW CRF and column heating exhibit no sensitivity to perturbations in the amounts of either liquid or ice since the cloud already blocks all emitted radiation from below. Its reflective properties, on the other hand, exhibit substantial sensitivity, particularly to perturbations in IWC. SW TOA and surface CRF vary by as much as 238 and 208 Wm^{-2}, respectively, over the range of perturbations implied by the GPROF uncertainties.

For both cases, the results show that errors in retrieved IWCs dominate expected uncertainties in the derived radiative heating rates and cloud forcing. This is easily explained

Table 5.5: Summary of precipitation case studies. Only those parameters explicitly listed are modified from the base case described in the text.

Case	Modifications to Base Case
1	Baseline: as retrieved by GPROF
2	LWCs magnified by 50 %
3	LWCs reduced by 50 %
4	IWCs doubled
5	IWCs halved
6	LWCs magnified by 50 % and IWCs doubled
7	LWCs reduced by 50 % and IWCs halved

since ice resides at upper levels within the cloud and therefore dominates its emitted radiation and cloud IWC is the most uncertain quantity retrieved by GPROF.

To provide additional statistics, Figure 5.25 illustrates maximum (case 6) and minimum (case 7) column heating rates for the orbit cross section highlighted earlier. The results emphasize the important difference between the heavy and light rain regions. In heavy rainfall, column heating decreases with increasing liquid and ice water contents while the opposite is true in lighter rain. It is also clear that atmospheric heating is most sensitive to errors in the water content estimates when they are low to begin with. An estimate of the uncertainty in column heating rates for light raining pixels from this figure is 0.6 $Kday^{-1}$, as opposed to 0.3 $Kday^{-1}$ in heavy rainfall.

Similar results for LW, SW, and net CRF are presented in Figure 5.26 illustrating a number of interesting differences between them. The results emphasize the fact that, at noon, SW cloud effects dominate those in the LW. It is also clear that the LW CRF is truly at a maximum in the deep convective region as it does not vary when the water contents are varied between their error bounds. SW forcings at both the surface and TOA, however, are sensitive to errors in the water contents varying by as much as 300 Wm^{-2} in heavy precipitation and 150 Wm^{-2} in lighter precipitation. As a result, we anticipate uncertainties in the net TOA and surface cloud forcing estimates to be on the order of 200 Wm^{-2} during the daytime due to the SW contribution but to be significantly reduced at night. At best,

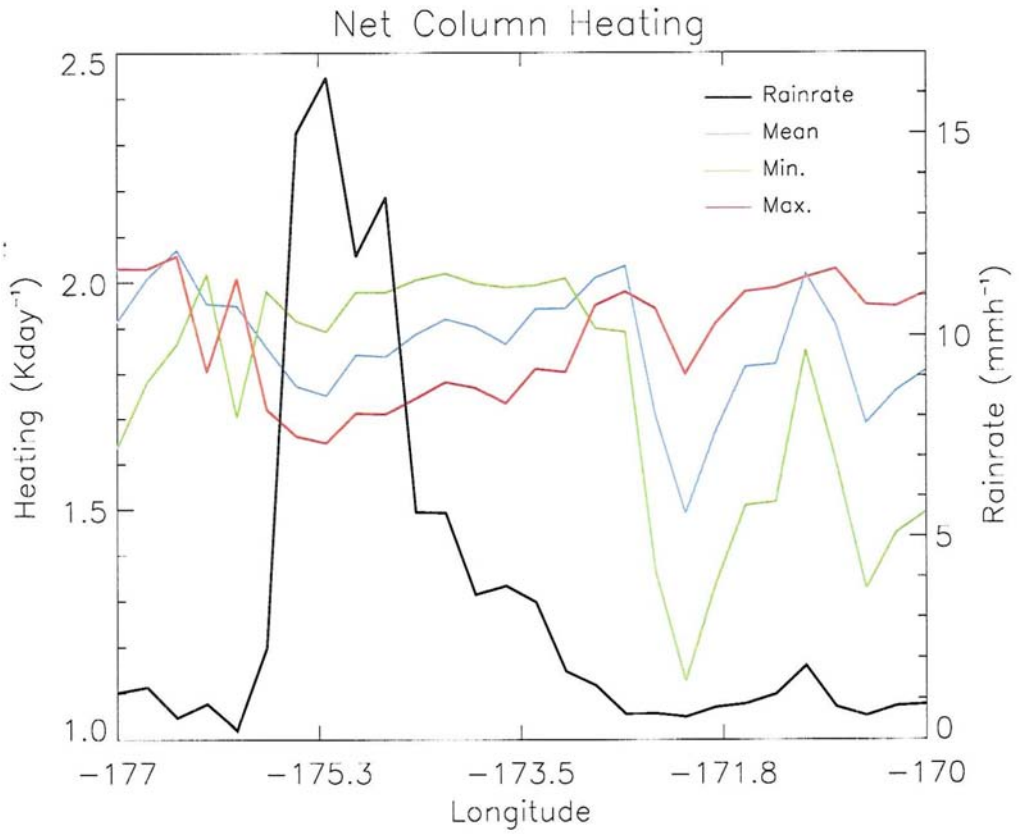

Figure 5.25: Range in estimates of column heating induced by GPROF retrieval uncertainties. Max. and Min. refer to the maximum and minimum perturbations in liquid and ice water contents, respectively.

however, we can probably expect accuracies on the order of about 50 % since the forcing at night is considerably smaller than that during the daytime. These estimates will be quantified further below.

5.5 Composite View

It is now possible to combine these results to produce tropic-wide maps of TOA and surface radiative fluxes, cloud forcing, and column heating rates, the first step towards determining a tropical radiation budget. The following pages present maps covering all of the primary

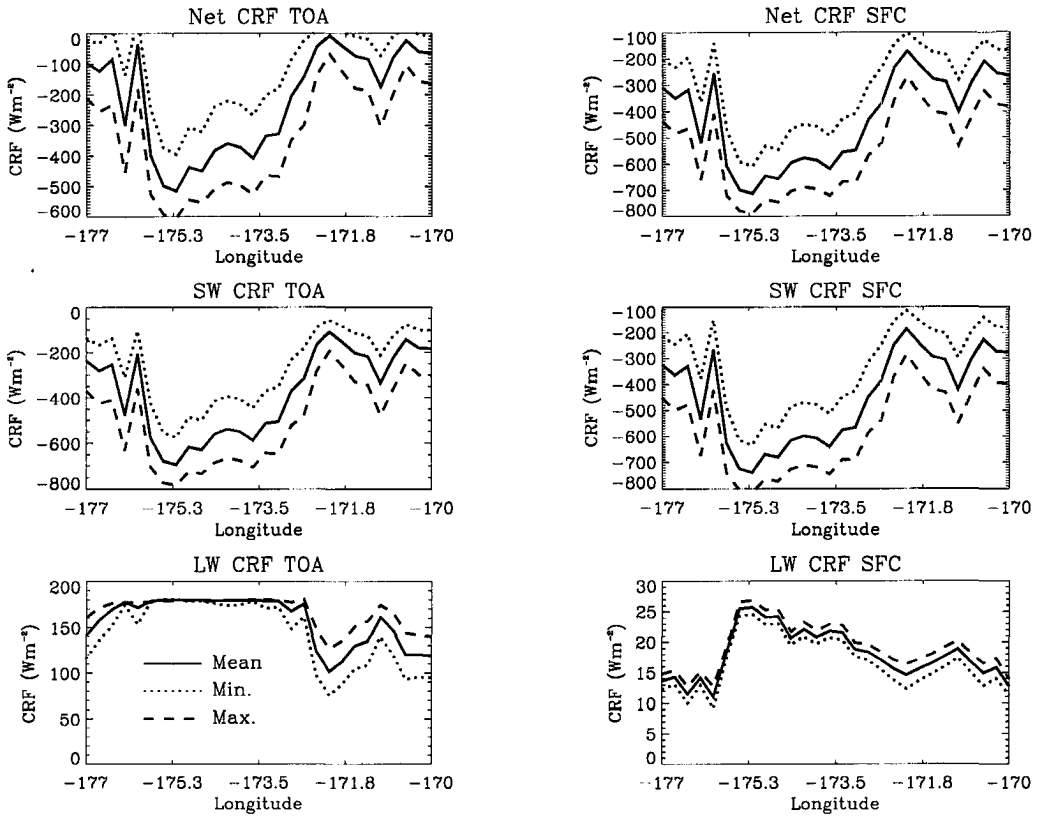

Figure 5.26: As in Figure 5.25 but corresponding to CRF estimates.

interactions that govern radiative exchanges in the atmosphere to portray the full range of quantities that can be deduced using the model.

Quantities relating to the exchange of LW radiation in the Earth-atmosphere system are displayed in Figures 5.27-5.30. The first of these illustrates LW fluxes at the atmospheric boundaries. Downwelling LW radiation emitted from the cold space background is negligible. Surface emission follows the monthly-mean SST, and is greatest in tropical regions just south of the equator and least over the cool winter-time oceans at northern midlatitudes. This emission is largely balanced by emission from atmospheric water vapor back to the surface demonstrating the strong atmospheric greenhouse effect in the tropics. The lowest

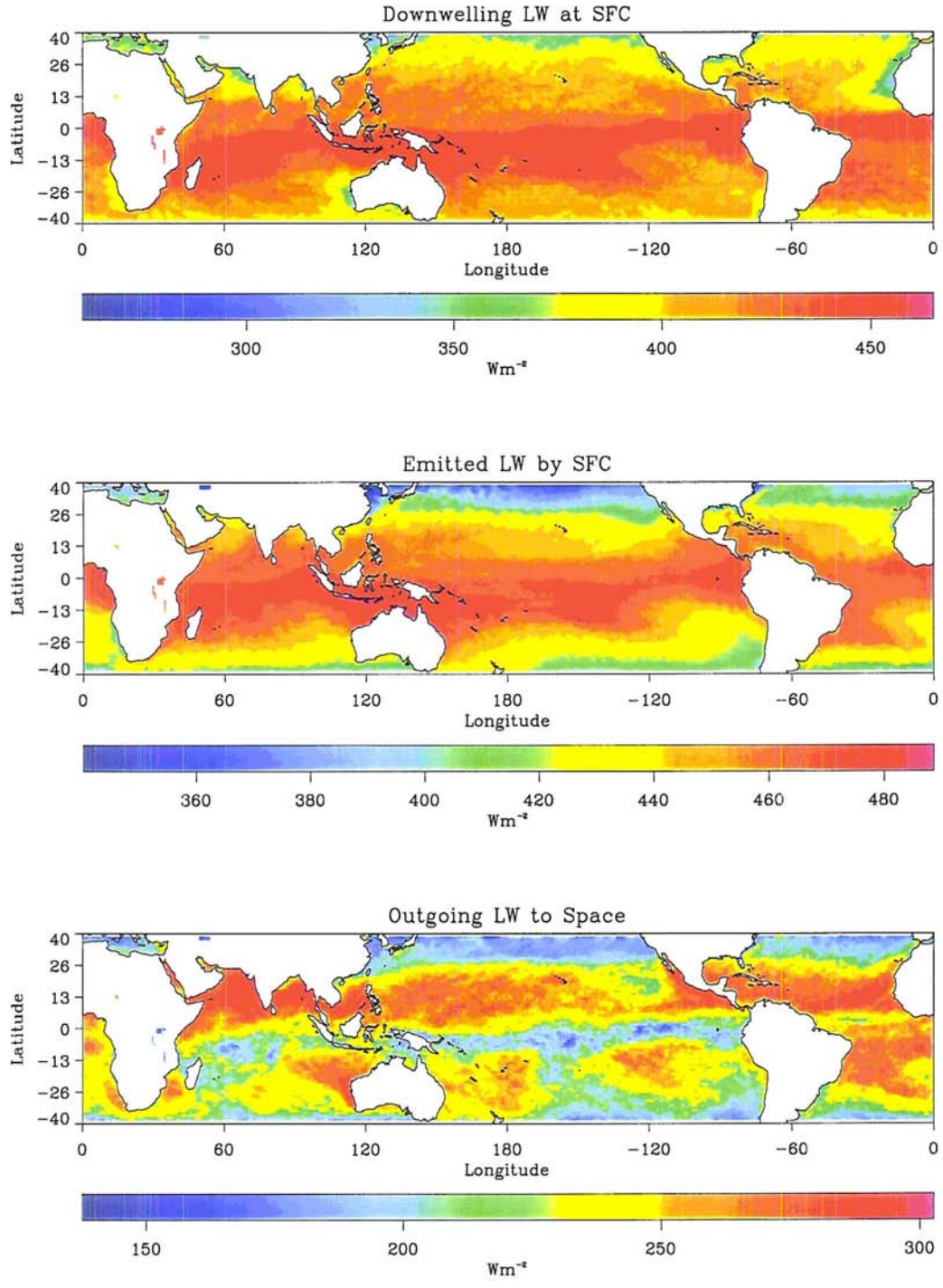

Figure 5.27: Monthly-mean LW fluxes for February 1998.

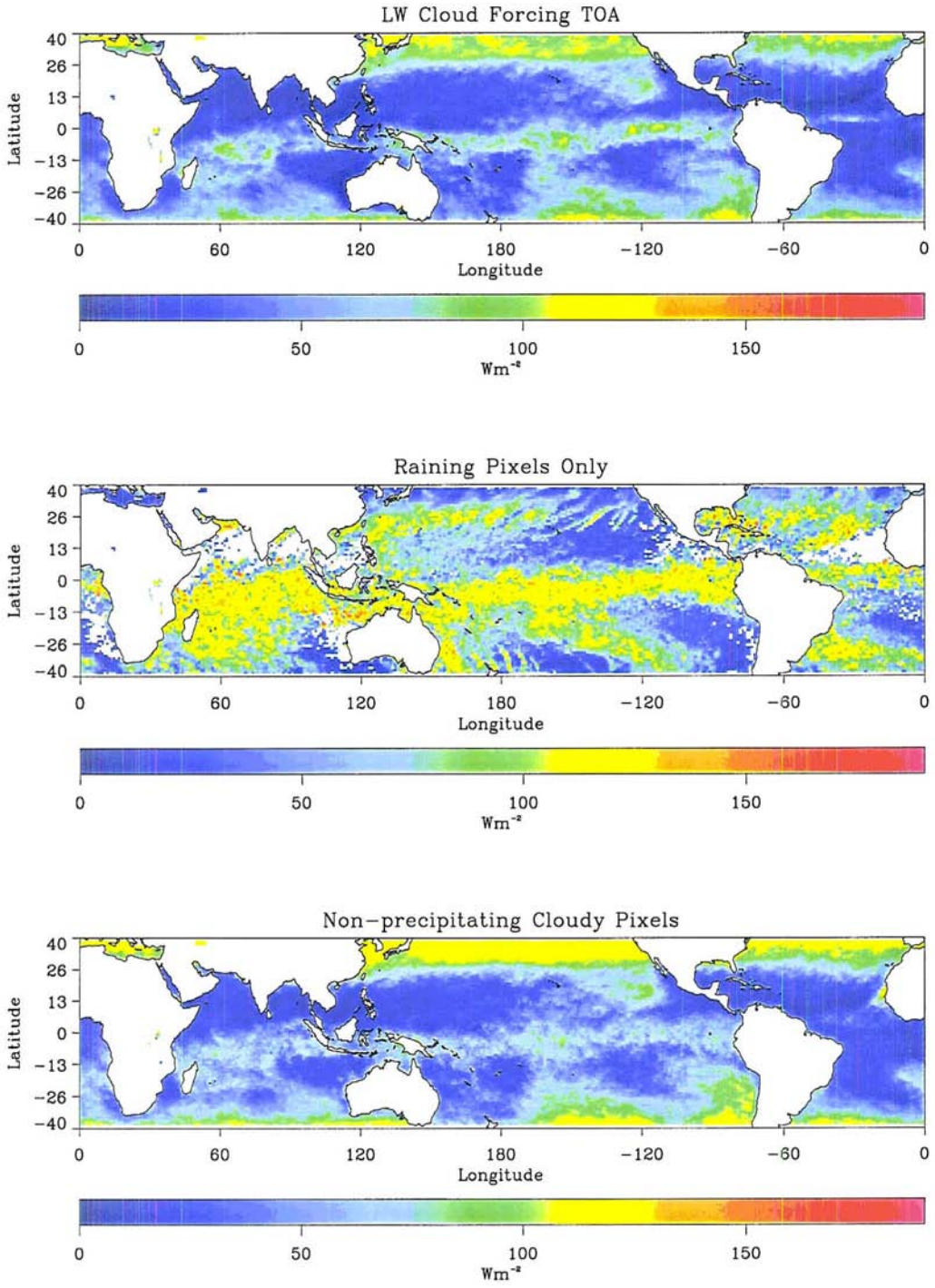

Figure 5.28: Monthly-mean longwave cloud forcing at the top of the atmosphere for February 1998.

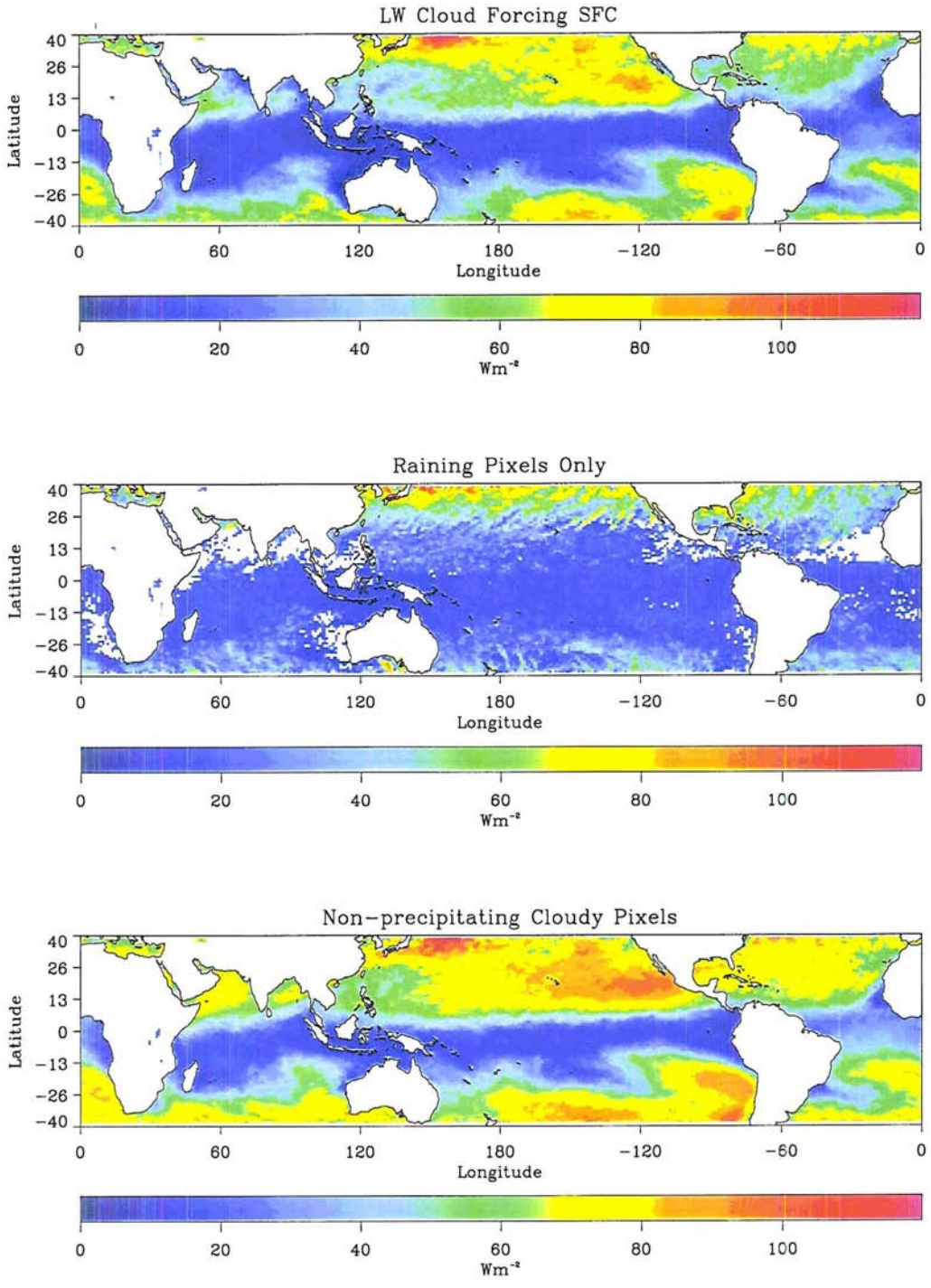

Figure 5.29: As in Figure 5.28 but for surface longwave cloud forcing.

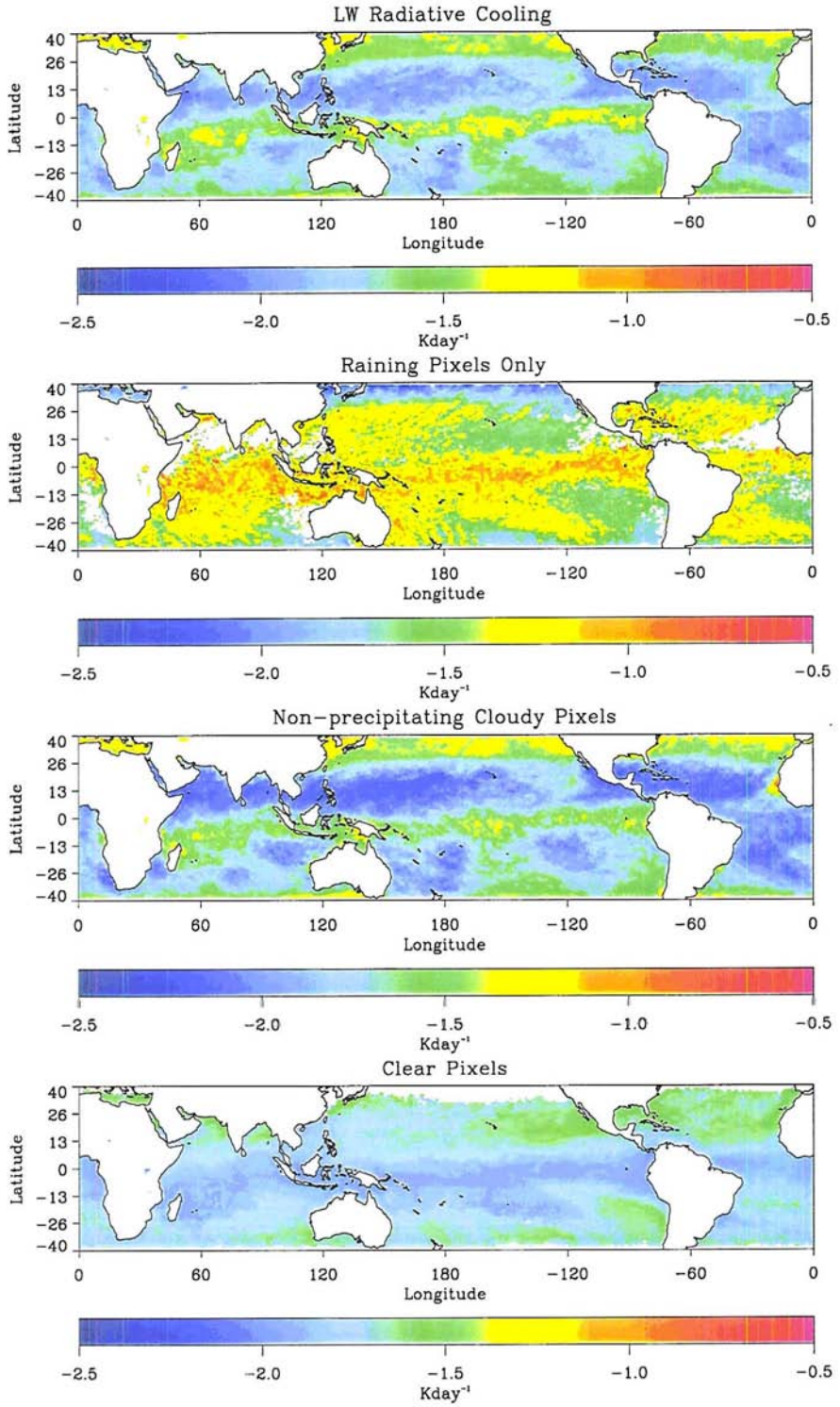

Figure 5.30: Monthly mean column-integrated longwave cooling for February 1998.

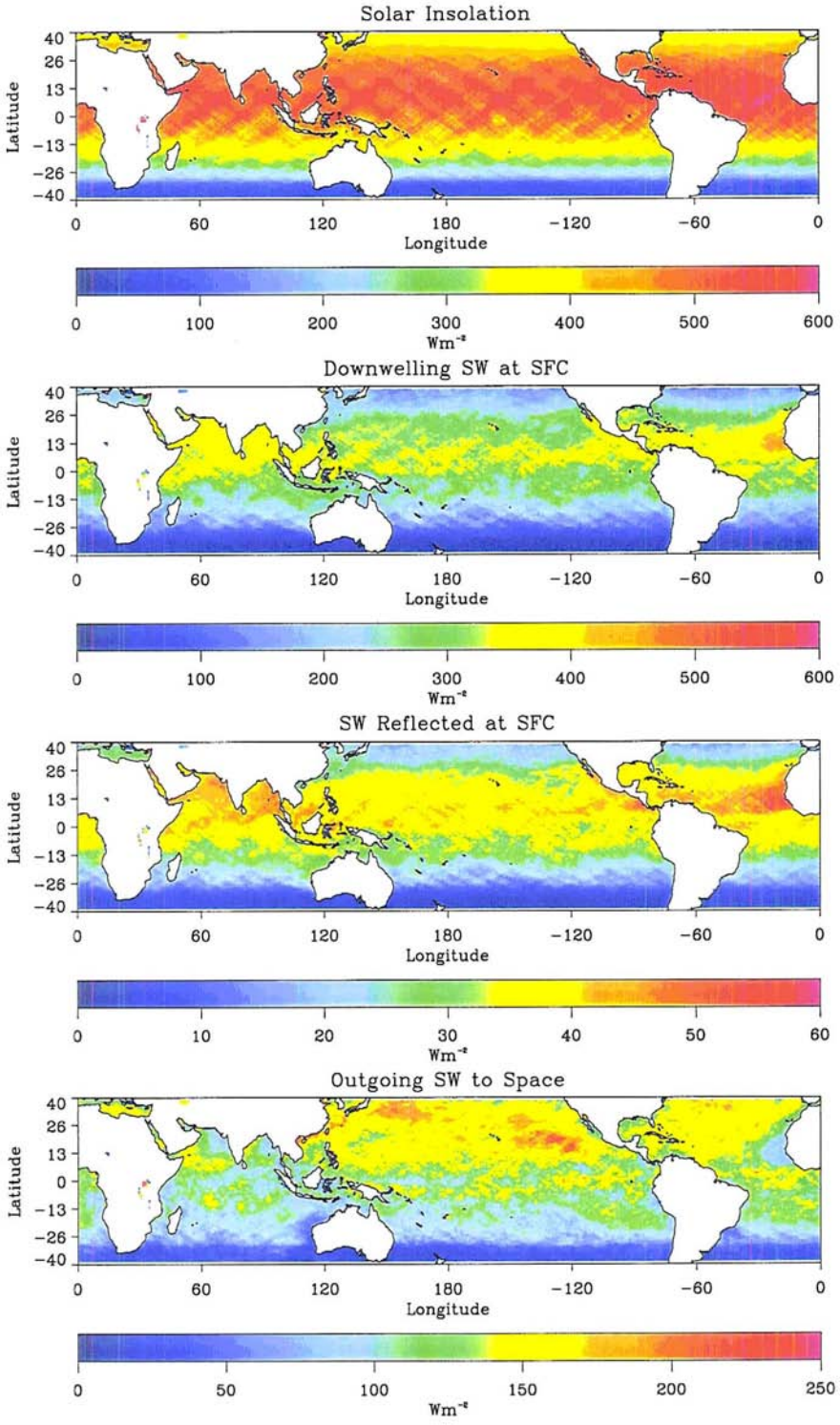

Figure 5.31: Monthly-mean SW fluxes for February 1998.

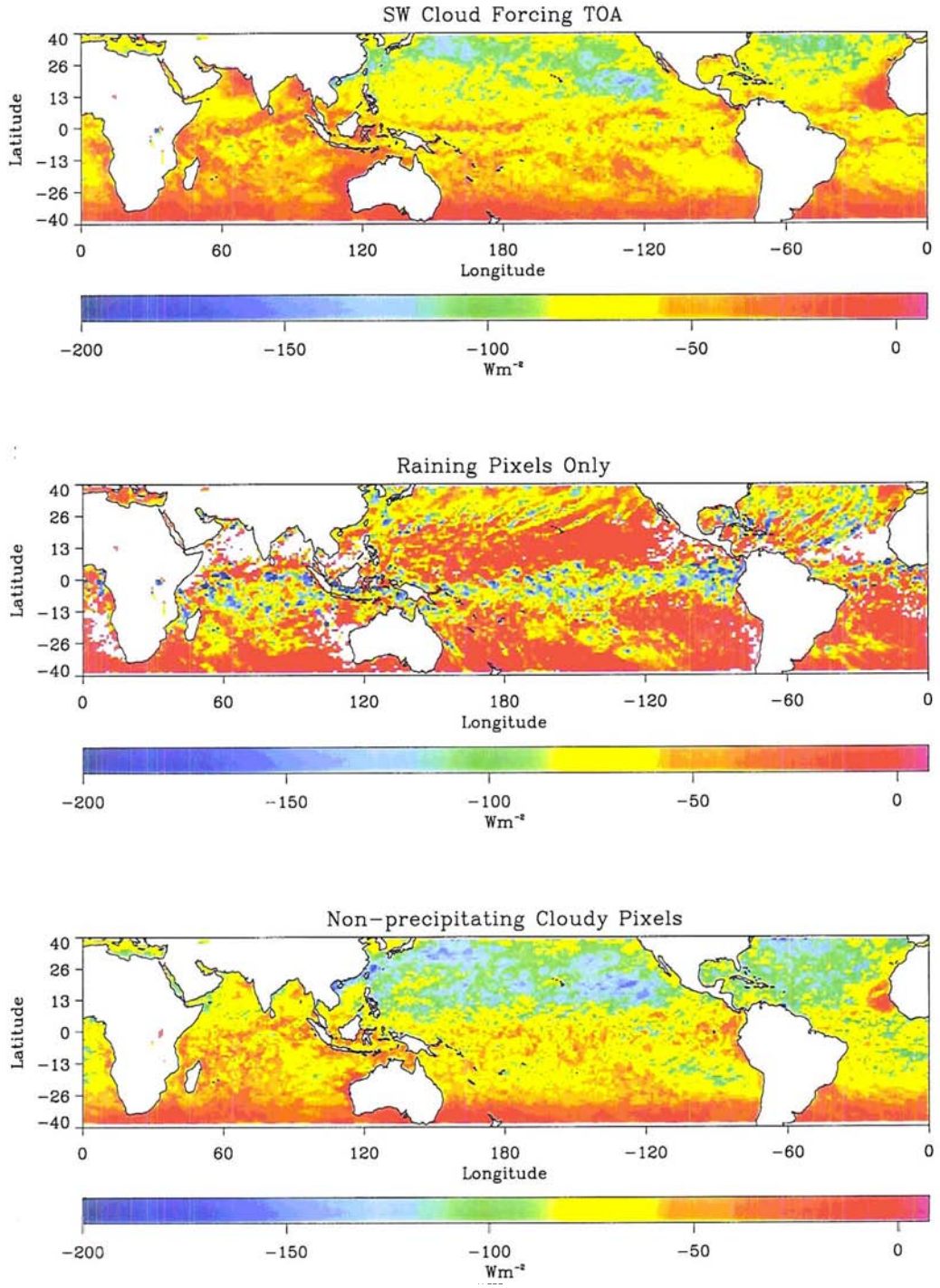

Figure 5.32: Monthly-mean shortwave cloud forcing at the top of the atmosphere for February 1998.

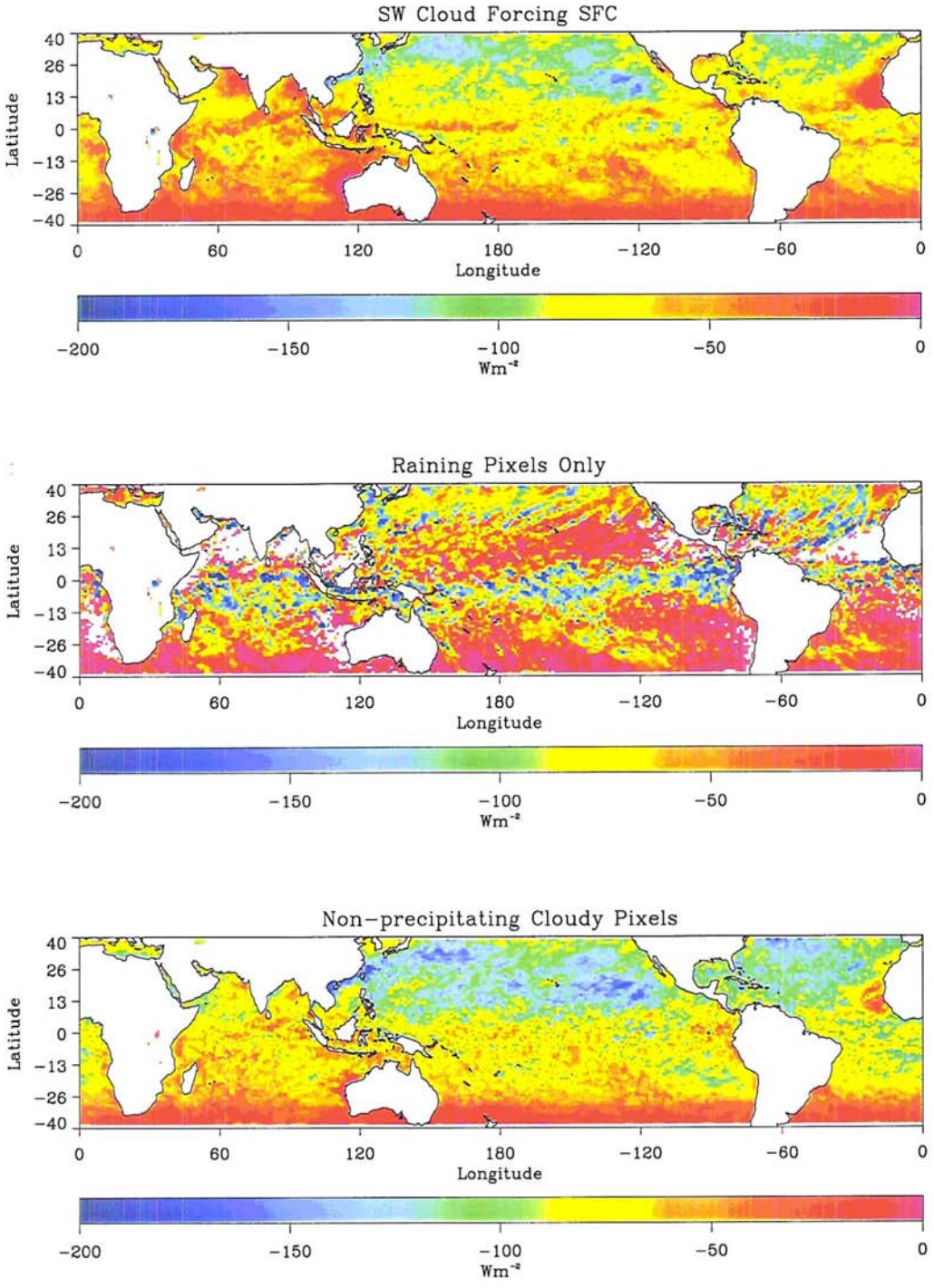

Figure 5.33: As in Figure 5.32 but for surface shortwave cloud forcing.

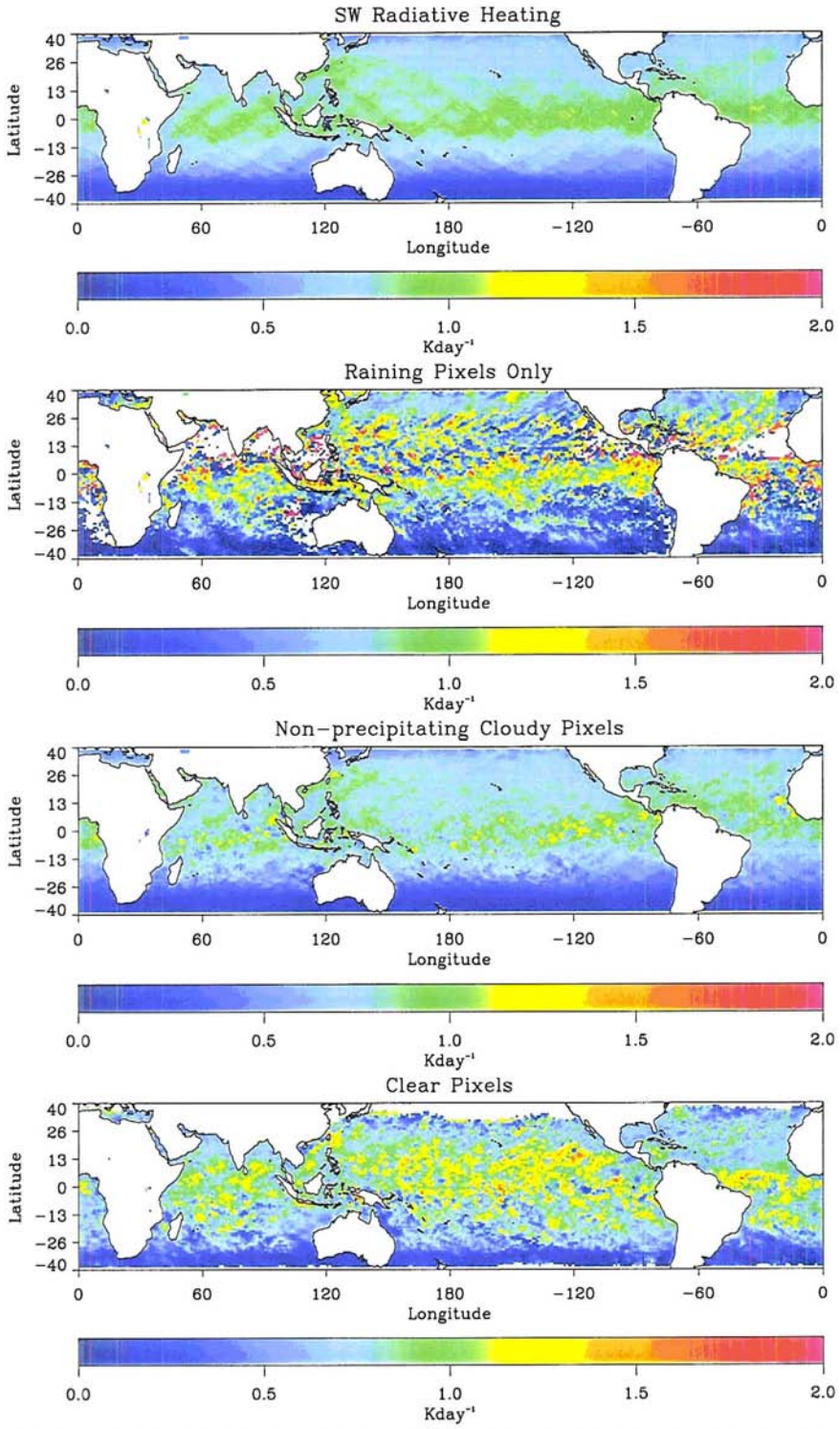

Figure 5.34: As in Figure 5.30 but for shortwave heating.

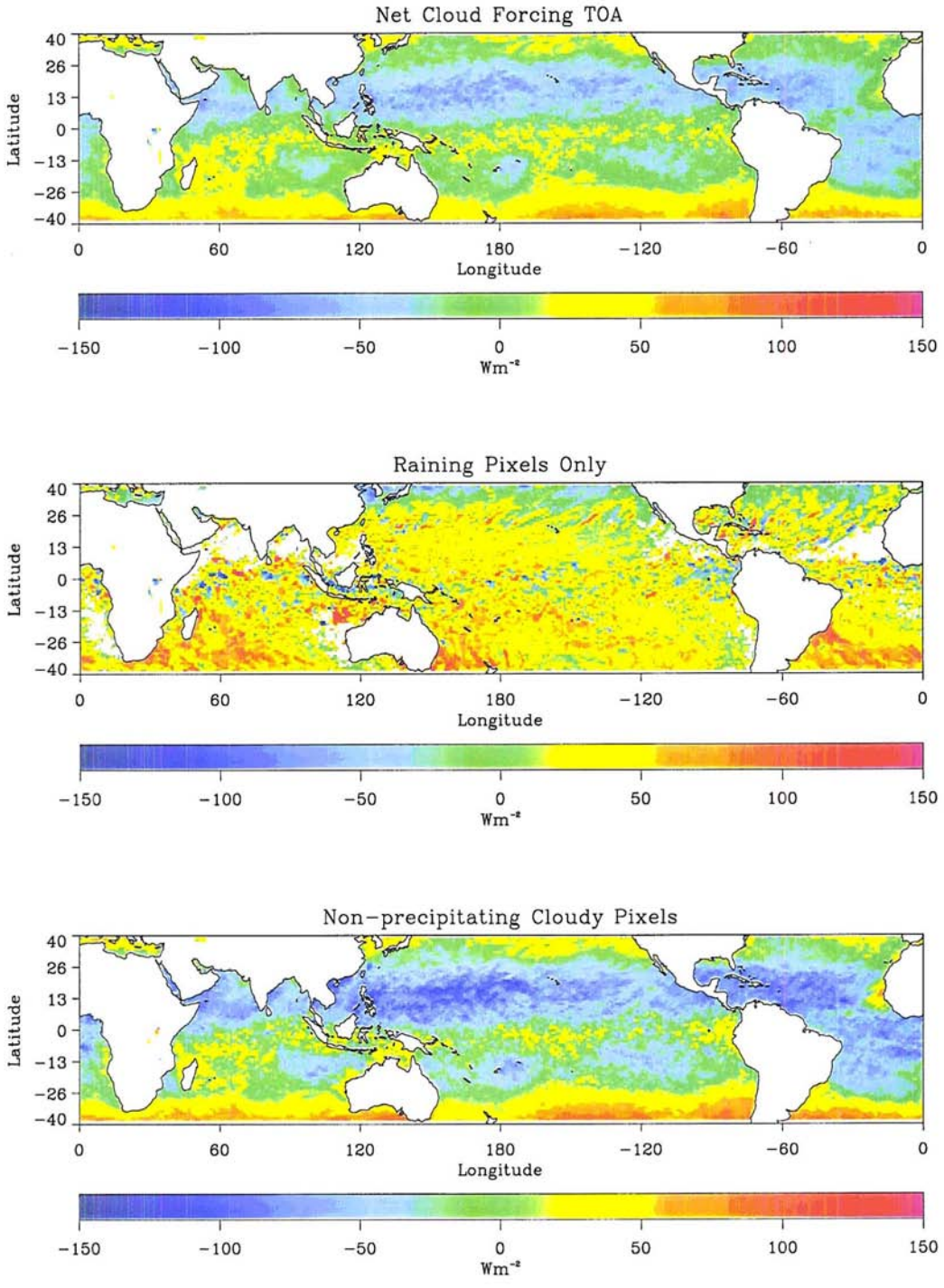

Figure 5.35: Monthly-mean net cloud forcing at the top of the atmosphere for February 1998.

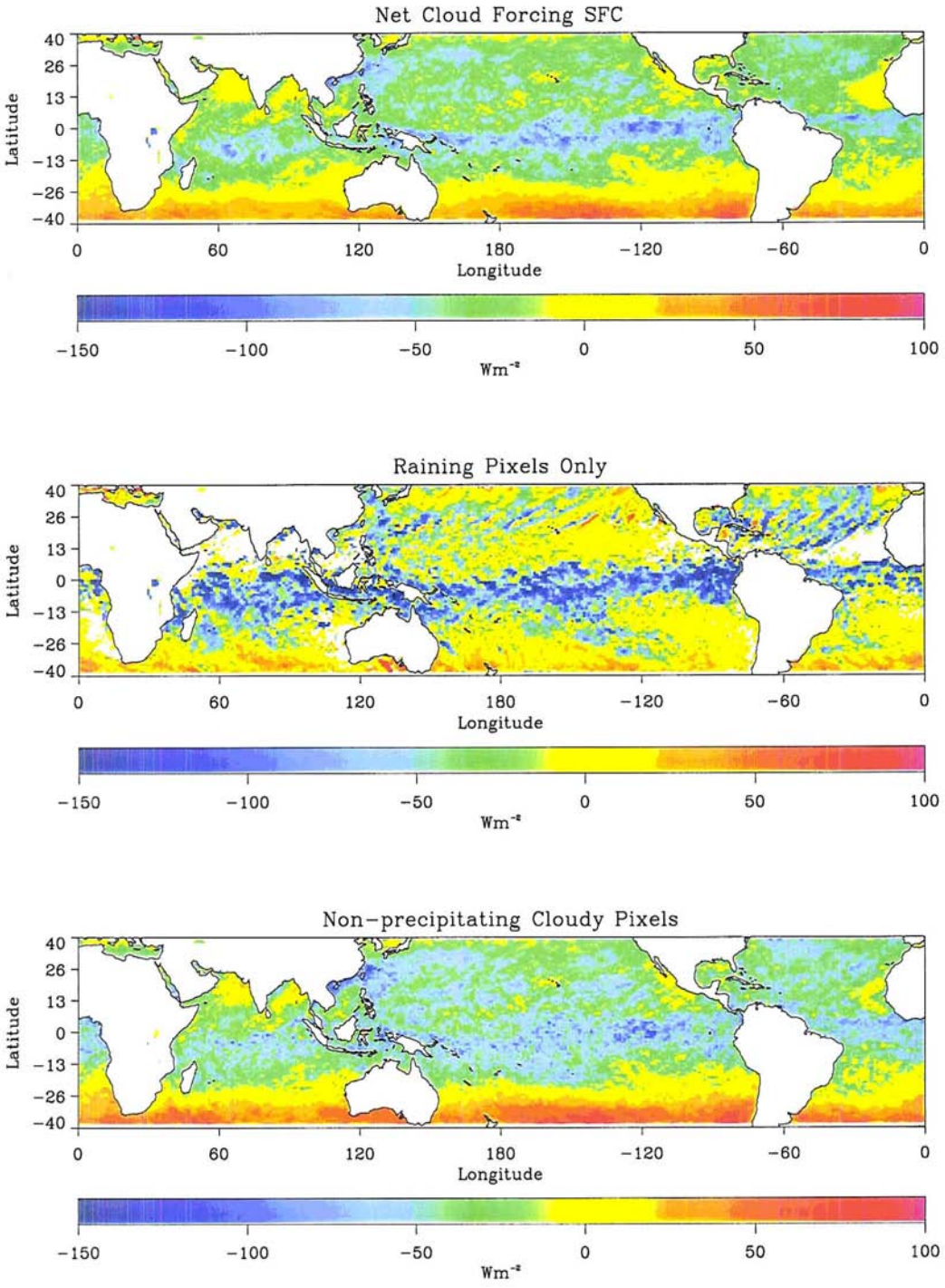

Figure 5.36: As in Figure 5.35 but for net cloud forcing at the surface.

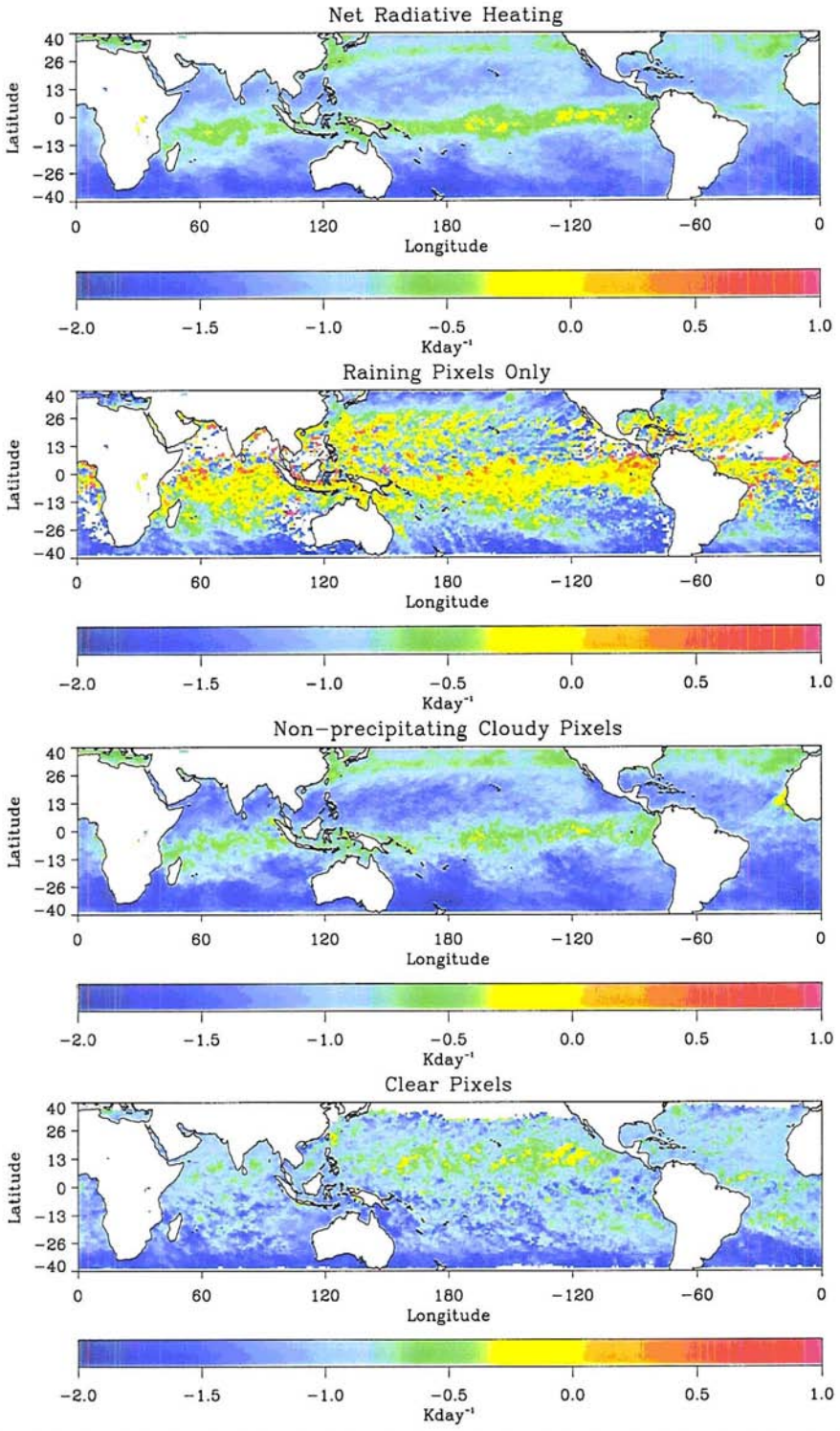

Figure 5.37: As in Figure 5.30 but for net heating.

panel presents the total outgoing longwave radiation to space. Cold cloud tops associated with the ITCZ and SPCZ reduce OLR to less than 200 Wm^{-2} while a comparable effect is realized as a result of the reduced surface emission and the presence of clouds at higher latitude in the northern hemisphere.

Many of these features are highlighted in Figure 5.28 which presents LW cloud radiative forcing at TOA as well as a breakdown of this forcing into components owing to precipitating and non-precipitating clouds, individually. The strong greenhouse effect due to precipitating clouds is evident by comparing with monthly-mean surface rainfall estimates from GPROF, presented in Figure 5.38. In all regions where precipitation is significant on a monthly-mean timescale, the corresponding raining-pixel only cloud forcing exceeds 100 Wm^{-2}. At the surface, on the other hand, the forcing by precipitation is much weaker than that due to liquid clouds. As a result, clouds in the ITCZ and SPCZ provide minimal surface CRF while warm low clouds above 15 N substantially increase atmospheric emission to the surface.

The exchange of thermal energy between the atmosphere and space is represented by the LW cooling presented in Figure 5.30. Longwave emission from the water vapor in the tropical atmosphere acts to cool it by more than 2 $Kday^{-1}$ in clear regions. The presence of clouds, particularly deep, precipitating clouds in the ITCZ, traps a significant fraction of this emitted radiation and reduces cooling by a factor of two. When all three pixel-types are combined, cooling in the ITCZ is approximately 1.3 $Kday^{-1}$ and approximately 1.5 $Kday^{-1}$ in the SPCZ. At higher latitudes in the northern hemisphere, lower amounts of water vapor combined with persistent high cloudiness result in an equivalent reduction in LW cooling.

It should be noted that the magnitudes presented in the component plots isolate those pixels which fall into the category considered. The upper panel, on the other hand, represents a true monthly mean derived by averaging all TRMM observations in each pixel,

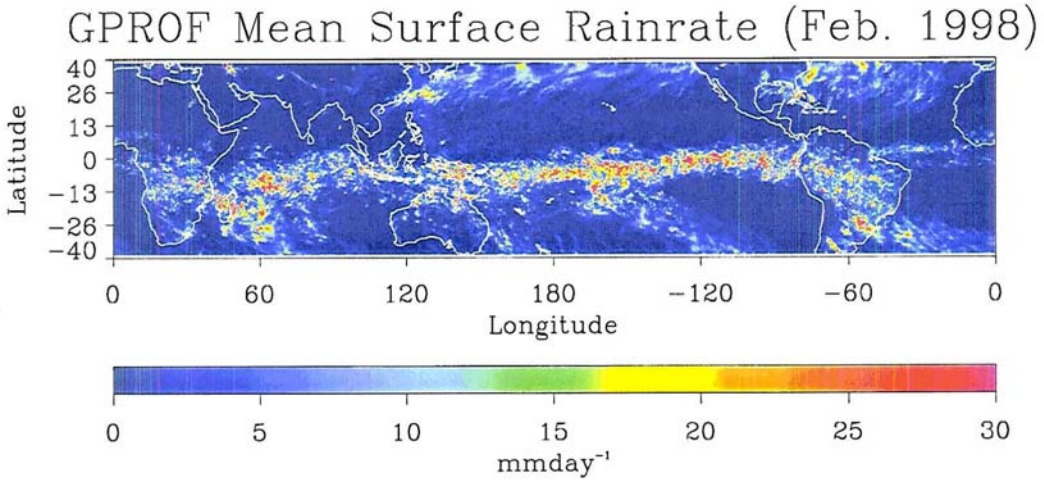

Figure 5.38: GPROF monthly-mean rainfall for February 1998.

including both clear and cloudy skies. Thus the top panel does not necessarily resemble a mean of the other panels, particularly as far as cloud forcing is concerned.

Figures 5.31-5.34 present the factors governing the exchange of shortwave energy in the atmosphere. The first, presents SW fluxes at the atmospheric boundaries and highlights an important drawback to using TRMM measurements in deriving short-term products such as these. By virtue of its axial tilt, the Earth's northern and southern hemispheres receive different amounts of radiation at different times of year. In February, the southern hemisphere receives more than the northern hemisphere since the latter is tilted away from the sun. The top panel of Figure 5.31, however, implies precisely the opposite showing three times as much solar insolation at 40° N than 40° S. The explanation for this lies in the

time of day each region is sampled by the TRMM satellite. From a combination of its precession rate and the fact that it observes the southern latitudes at approximately 6 am on February 1, 1998, a majority of the observations made of the region south of -20° take place at night when solar insolation is 0. Conversely, a majority of the observations above 40° N take place during the daytime biasing the shortwave fields presented here to the northern hemisphere. This will be avoided when longer term maps[4] are produced but for now it is important to keep it in mind when considering the SW figures.

Figures 5.32 and 5.33 present SW cloud forcing at the TOA and surface, respectively. The effects of clouds on the net (upwelling minus downwelling) radiation at the top of the atmosphere and the surface are very similar for the reasons discussed earlier. In general, bright convective clouds associated with precipitation in the ITCZ reflect a majority of the solar radiation incident upon them, resulting in SW forcing of less than -200 Wm^{-2}. Non-precipitating clouds reflect slightly less radiation but are more widespread resulting in SW forcing on the order of -100 to -150 Wm^{-2} but over a larger region. In both cases, subsequent averaging with clear-sky pixels reduces the magnitude of this forcing but the impact of clouds on the SW components of the ERB remains evident. Figure 5.34 illustrates how clouds impact the heating of the tropical atmosphere. In most cases, the presence of non-precipitating clouds reduces the amount of solar radiation available to be absorbed by water vapor below them, resulting in a decrease in SW column heating. Precipitation has the opposite effect, most likely due to enhanced absorption of solar radiation by ice at upper levels in precipitating systems.

Combining these LW and SW components, maps of net cloud radiative forcing and column heating are presented in 5.35-5.37. These figures illustrate the competing effects of LW and SW cloud forcing and column heating. The result is that, on average for the month of February 1998, the tropical atmosphere cools at -1 $Kday^{-1}$ and experiences a net cloud

[4]The TRMM satellite samples the complete diurnal cycle once every 46 days at its orbittal extremities. As a result a 46 day increments provide a more representative time increment than monthly time-scales.

Table 5.6: Average uncertainties in monthly mean estimates of fluxes (Wm^{-2}), column heating rates ($Kday^{-1}$), and cloud radiative forcing (Wm^{-2}) attributed to retrieval uncertainties and radiative transfer model assumptions.

Category	Quantity	Clear-sky	Non-precip. Clouds	Precipitation
Flux ↑	LW TOA	6	114	42
	LW SFC	~ 0	~ 0	~ 0
	SW TOA	15	89	39
	SW SFC	3	13	6
Flux ↓	LW TOA	~ 0	~ 0	~ 0
	LW SFC	56	74	12
	SW TOA	< 3	< 3	< 3
	SW SFC	25	108	52
Column Heating	SW	0.1	0.2	0.1
	LW	0.2	0.7	0.3
	Net	0.1	0.6	0.3
TOA CRF	SW	N/A	83	60
	LW	N/A	54	38
	Net	N/A	120	61
SFC CRF	SW	N/A	85	66
	LW	N/A	34	5
	Net	N/A	71	66

forcing of -10 Wm^{-2} at TOA and -22 Wm^{-2} at the surface.

The sensitivity studies introduced in the preceding sections have been used to estimate average uncertainties in fluxes, heating rates, and CRF estimates. Table 5.6 summarizes these uncertainties in terms of pixel composition. "~ 0" is used to denote uncertainties in parameters which are not sensitive to the atmospheric properties studied here and whose errors cannot be predicted as a result. When considered as an ensemble, we expect uncertainties in these quantities to be negligible compared to those introduced by components which strongly depend on the assumed cloud properties.

Clear-sky fluxes and heating rates are the most accurate by virtue of the limited number of assumptions required for their estimation. Since quantities such as SST and CWV are known accurately, particularly on a monthly timescale, the uncertainties they induce in the flux calculations are small. The clear-sky uncertainties presented in Table 5.6 are likely

somewhat low since both longwave and shortwave fluxes in cloud-free conditions are very sensitive to the reflective and emissive properties of the surface which have not been perturbed. Even so, the basic properties of an oceanic surface are reasonably well understood so it is reasonable to assume that the clear-sky pixels are determined most accurately.

With the exception of LW emission to the surface which strongly depends on the amount and distribution of water vapor in the atmosphere, uncertainties in cloudy pixels are substantially larger than those characteristic of clear-sky regions. Potential errors in outgoing longwave and reflected shortwave radiation, for example, are at least five times larger in the presence of clouds and precipitation. In addition, the uncertainties in non-precipitating cloudy pixels are generally a factor of two or more larger than their raining counterparts. This reflects the crude retrievals employed in establishing cloud information compared with the more refined GPROF precipitation algorithm. Errors in cloud forcing are also significantly larger in the shortwave than in the longwave. While this may seem counter-intuitive given the strong sensitivity of a cloud's emitting properties to its, highly uncertain, vertical placement in the atmosphere, it is important to recall that cirrus optical properties have been prescribed based on IR observations from the VIRS instrument. Thus the optical properties of the cloud are constrained in the retrieval while its SW properties are largely unconstrained.

Overall, we find that, in the absence of additional information, the procedure described in the present work provides monthly-mean estimates of column radiative heating accurate to $\sim$ 30 % and cloud radiative forcing with accuracies ranging from approximately 40 % for raining pixels to 75 % in non-precipitating clouds. It is important to note that a number of sources of uncertainty related to the flux calculations have not been investigated in depth. The surface emissivity model, for example, which dominates uncertainties in the amount of LW radiation emitted by the Earth's surface, has been assumed to be perfect thus far. When considering the cloud and precipitation components of the results, however, these

additional sources of uncertainty are anticipated to be small compared to those associated with the vertical structure and optical properties of the clouds and precipitation.

5.6 CERES Observations and NOAA Interpolated OLR

The month of February 1998 was primarily chosen for the purpose of providing some validation for the results since it corresponds to a time when the CERES instrument on TRMM was fully operational. LW fluxes measured by CERES provide an appropriate source of information with which to test the present approach since its observations are necessarily co-located with those from which the cloud and precipitation information derive. Figure 5.39 displays the CERES monthly-mean outgoing longwave and shortwave flux product (ES-9)[5] for February 1998. These results are qualitatively similar to those derived above (Figure 5.27). A distinct reduction in OLR accompanying regions of intense precipitation in the ITCZ and SPCZ are clearly evident in both plots[6]. The present study also captures the decrease in OLR associated with storm tracks through the northern portion of the TRMM domain as well as a large region of reduced OLR induced by the clouds trailing away from the heavy rainfall located in central South America.

Significant differences in the OLR estimates are evident, however, particularly outside the ITCZ and SPCZ. OLR derived in the present study shows large regions of reduced emission off the Pacific coast of Mexico and to the east of South America. Taking OLR less than 235 K as an indicator of precipitation (Arkin and Meisner, 1987), the OLR estimates in the present study imply a substantial amount of rainfall in these regions but neither the CERES OLR data nor the monthly-mean GPROF surface rainfall map confirm this. Such anomalies are most likely due to incorrect ice cloud retrievals in these areas, perhaps relating to the assumptions regarding vertical cloud placement, for instance, but this needs

[5]These data were obtained from the NASA Langley Research Center Atmospheric Sciences Data Center.

[6]Arkin (1979) and Arkin and Meisner (1987) have suggested that a mean OLR of less than 235 K over the spatial scales characteristic of the results presented here provides a strong indicator of rainfall in tropical regions.

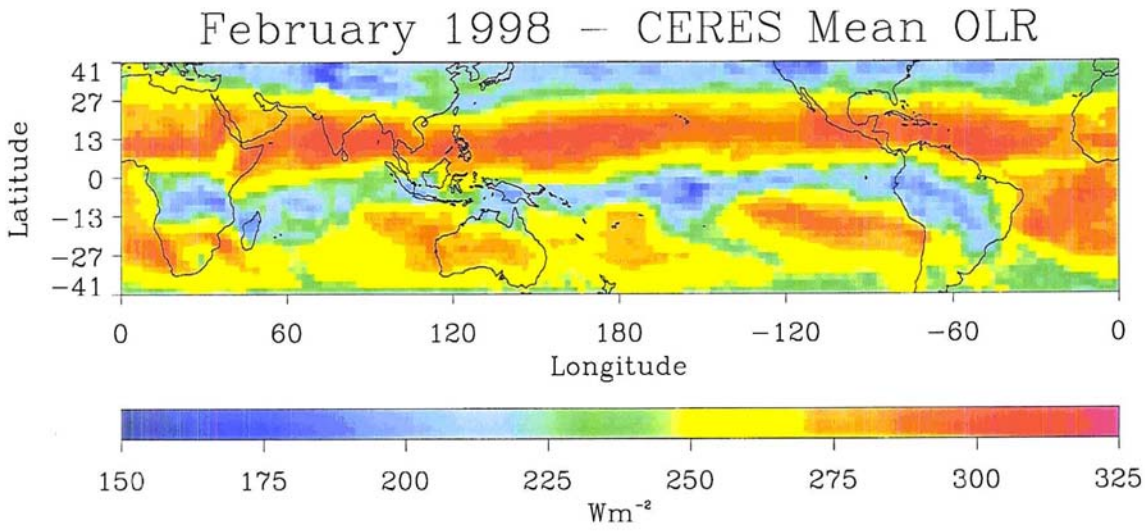

Figure 5.39: CERES monthly-mean outgoing LW and reflected SW fluxes for February 1998.

to be verified.

The NOAA Interpolated OLR[7], depicted in Figure 5.40, provides a similar product derived from AVHRR radiances. There are notable differences between the NOAA and CERES OLR estimates. Most notably, the NOAA product exhibits a substantially stronger precipitation signature over the SPCZ and along coastal regions of South Africa. In addition, the CERES data imply substantially larger emission in the large-scale subsidence region between 10° and 25° N.

Direct comparison of monthly-mean OLR estimates from the present study with those

[7]Interpolated OLR data provided by the NOAA-CIRES Climate Diagnostics Center, Boulder, Colorado, from their Web site at http://www.cdc.noaa.gov/.

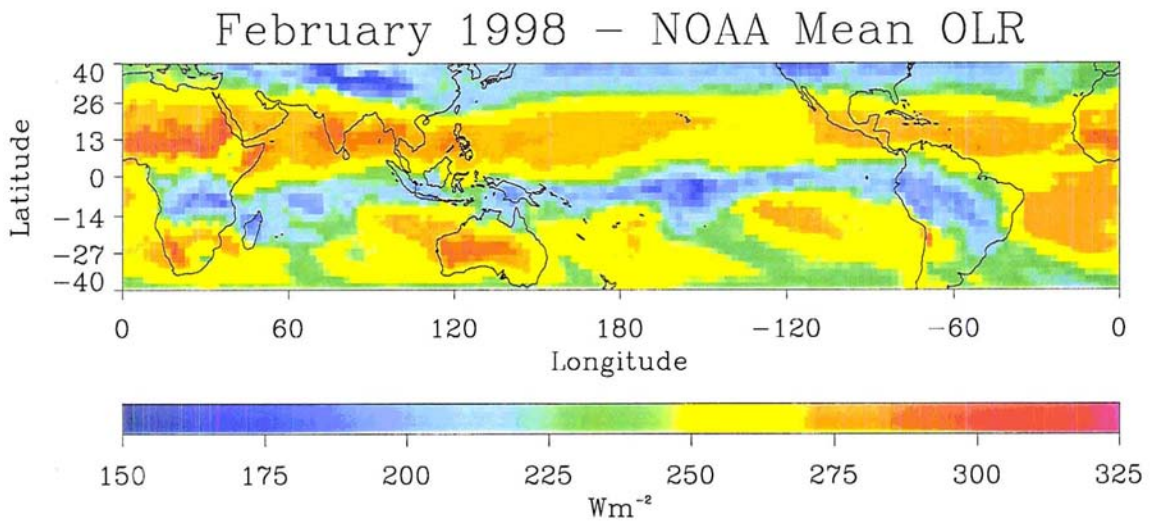

Figure 5.40: NOAA monthly mean OLR for February 1998.

from both the CERES and NOAA products is presented in Figure 5.41. The figure demonstrates that a reasonably strong correlation exists between the results of the present study and both the NOAA and CERES OLR products but that a substantial spread is present in the results. It is interesting to note that the present estimates correlate better with the NOAA OLR (0.83) than those from CERES (0.82) despite the fact that the latter is flown on TRMM. Another important result from this comparison is that the results of the present study appear to be biased about 20 Wm^{-2} lower than those from CERES. A direct comparison of the CERES and NOAA products indicates a similar, although less slightly less pronounced bias of 10 Wm^{-2} between those estimates, and a correlation of only 0.82. As a result, the bias between the results presented here and those from NOAA is less than

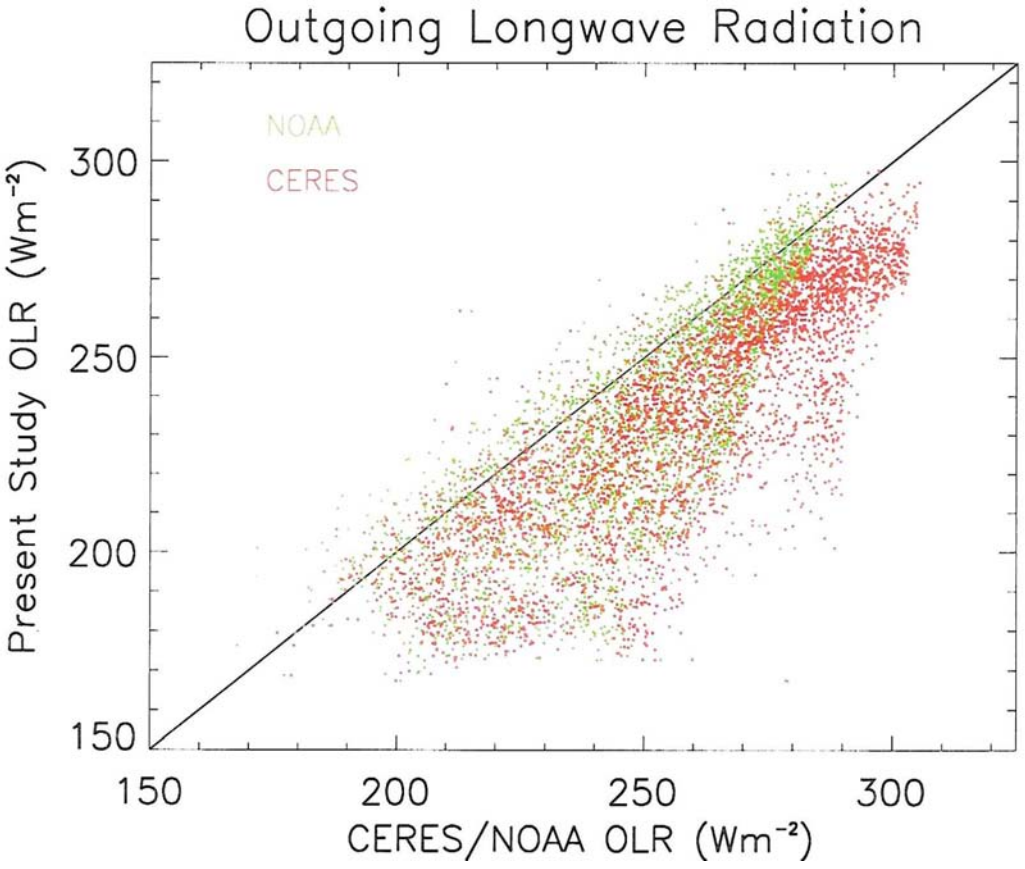

Figure 5.41: Scatter plot of derived monthly-mean OLR versus equivalent NOAA and CERES products.

10 Wm^{-2}. Considering the fact that the present model has not been tuned in any way and taking into account the large uncertainties introduced through a number of its assumptions, correlations greater than 0.8 are encouraging. The large errors associated with the non-precipitating cloud pixels are sufficient to account for the discrepancies in the results. Furthermore, the CERES product is corrected for the diurnal sampling of the TRMM satellite while the NOAA product samples at all times of day.

Three conclusions can be drawn from these comparisons:

1. As an initial attempt at using the technique introduced here with no external con-

straint or advance calibration, these results are promising. Beyond exhibiting qualitative agreement with the corresponding precipitation fields, the results correlate well with similar products derived from the AVHRR and CERES instruments.

2. There is a significant potential for biases to enter into the results through the physical assumptions required in both the retrieval and the broadband flux calculations. While the negative implications of this result are clear, these biases also provide insight into an alternative source of information which may prove useful in constraining future versions of the model. In principle, the strong sensitivity of the results to assumptions regarding cloud height provide a means for constraining the retrieval using broadband flux observations such as those made by CERES.

3. The OLR field represents only one of many produced by the methods here. More exhaustive testing of some of the other fields, particularly those pertaining to surface fluxes, are required to establish adequate confidence in the method. To this end, intercomparison exercises using downwelling flux measurements at the surface observed during the Joint Air-Sea Monsoon Interaction Experiment (JASMINE) cruises are planned to provide an independent validation of the SFC flux predictions.

5.7 A Short-term Tropical Energy Budget

In Section 1.1 it was noted that observations of the temporal and spatial variability of the principal components of Earth's energy budget in response to both natural and anthropogenic forcings on the hydrologic cycle represents a significant challenge facing the climate community. One of the primary motivations for this research was to establish a technique for making such estimates based on presently available data. The results of this endeavor are presented in Figure 5.42 which illustrates a short-term tropical oceanic energy budget derived from TRMM observations in February 1998. This illustration provides

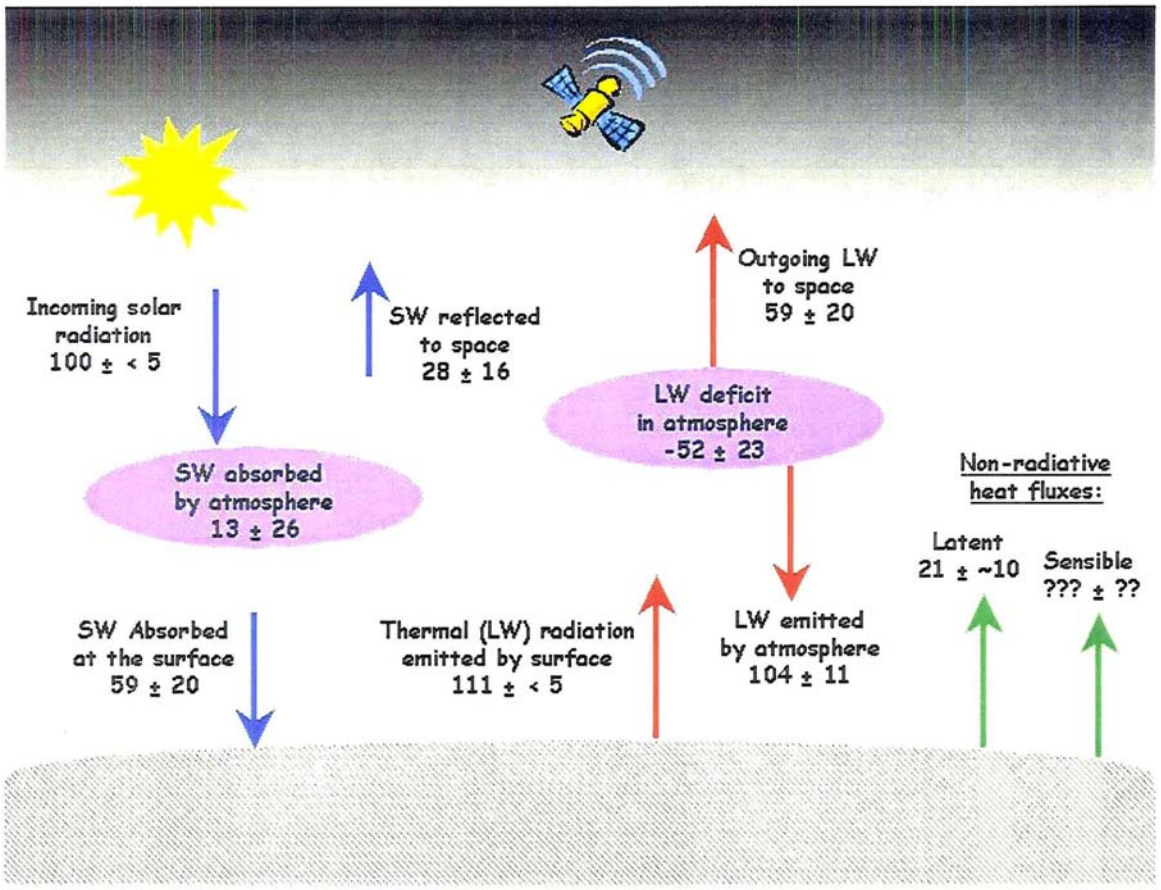

Figure 5.42: February 1998 tropical energy budget from TRMM. All quantities are expressed as a percentage of the total incoming solar radiation at the top of the atmosphere, 393.6 Wm^{-2}.

a near-complete breakdown of the major processes governing the exchange of energy between the sun, the atmosphere, and the ocean over the TRMM region, which extends from 40 S to 40 N covering approximately 64 % of the globe. In addition, rigorous uncertainty estimates which are rooted in the physical assumptions governing both the retrieval and the radiative transfer models have been assigned to each quantity based on the sensitivity studies conducted above.

In February 1998, an average of 28 % of the incoming solar radiation to this region is reflected to space while the atmosphere absorbs only 13 %. The remaining 59 % is absorbed by the ocean. At the same time, the ocean emits 111 units of thermal energy

which is nearly balanced by a corresponding atmospheric emission of 104 units back to the Earth's surface. The moist tropical atmosphere further emits 59 units of energy to space resulting in a net deficit of 39 units or approximately 150 Wm^{-2} in the atmosphere. Based on a surface rainrate-derived estimate of latent heating[8], latent heat release accounts for 81 Wm^{-2} leaving an overall atmospheric energy deficit of $\sim$ 70 Wm^{-2}. At the TOA and surface boundaries we find a deficit of 51 Wm^{-2} and a surplus of 121 Wm^{-2}, respectively. Thus this region is not in energetic balance on a monthly timescale.

Absent from the processes depicted in Figure 5.42 are the meridional transport of energy to midlatitudes as well as the magnitude of the sensible heat flux at the ocean surface. These processes, as well as oceanic energy transport, must account for the observed differences when averaged globally and on annual timescales.

The radiation budget presented is only representative of a small fraction of the lifetime of the TRMM satellite, never-mind the history of climate change on Earth, but it furnishes a foundation onto which future extensions can be built. With the addition of successive months and years of data, a climatology can start to be developed from which analyses of short-term climate variability and preliminary observations of long-term climate change can begin to be realized.

[8]Provided a spatial and temporal domain large enough to encompass the geographic evolution and lifecycle of the cloud complex is considered, the LH terms can be vertically integrated from the surface to the top of the cloud to yield

$$LH_{col} = \int_0^{z_{top}} \bar{\rho} \left[L_v(\bar{c} - \bar{e}) + L_f(\bar{f} - \bar{m}) + L_s(\bar{d} - \bar{s}) \right] dz \approx \rho_l L_v R \tag{5.3}$$

where R is the surface precipitation rate. Thus the column-integrated LH is, in a space-time average sense, related to the total condensate removed from the system by precipitation processes. For further discussion of latent heating and results for the month of February 1998 obtained using the GPROF algorithm, see Appendix C.

5.8 Discussion

Together, Chapters 4 and 5 constitute a complete method for determining the principal components of the tropical energy budget using solely passive observations from the TRMM satellite. The method makes use of a crude representation of liquid and ice clouds and more detailed information regarding profiles of liquid and ice in precipitating regions to derive SW and LW fluxes throughout the atmosphere. From these profiles, column heating, cloud forcing, and the vertical structure of heating in the atmosphere can be diagnosed and broken down into components owing to clear-sky, low cloud, high cloud, and precipitation, affording us the opportunity to quantify important relationships between the hydrologic cycle and the Earth's energy budget. This data can, in principle, be applied to study short term climate variability through investigations of perturbations to the radiation balance induced by changes in the distributions of water vapor, cloud, and precipitation on short to moderate timescales. The spatial coverage of the TRMM satellite is well-suited to study the tropical region as a whole and the duration of the mission should provide a continuous three and a half year data set with which one can begin constructing climatologies of the key components of the tropical radiation budget. The resulting data can then be used to study climatic cycles on diurnal, intraseasonal, seasonal, and annual timescales.

Beyond extending the results to cover a longer time period, improved spatial coverage and temporal resolution also offer the potential to significantly enhance the results presented here. Extension of the TRMM mission to $\pm$ 70° and the constellation of satellites being proposed for GPM will certainly improve upon this aspect of the present work. A continuous data set spanning the lifetime of the TRMM mission followed by the application of the technique to the GPM constellation will provide a means for studying global and regional weather phenomena such as the El Niño Southern Oscillation (ENSO) as well as providing a mechanism for observing climate change. In addition, increased temporal resolution provides an opportunity to assimilate ERB information to constrain cloud

information in NWP models in the future.

At present there are a number of drawbacks to the approach which still need to be addressed. The method has been restricted to oceanic regions by the passive microwave and VIS/IR methods employed in cloud retrievals. To fulfill our need for cloud information, alternate approaches will be needed over land surfaces. In addition, further refinements are necessary to better constrain cloud and precipitation vertical structure and optical properties in the model. Looking to the future, a solution to both of these deficiencies may be realized through the use of active sensors such as the PR and CPR. This possibility is explored in more detail in Appendix D which presents a novel approach to rainfall profiling from attenuating radars formulated in such a way as to facilitate the combination of information from multiple sensors. Results suggest that explicit cloud vertical profile information from active sensors and bulk estimates of precipitation water path from passive observations provide complementary information to rainfall retrievals. The combination of the Aqua and CloudSat satellites flying in formation in the near future will provide an opportunity to develop and study such methods in greater detail in the future. In light of the sensitivities presented above, we anticipate significant improvements in the energy budget components as a result.

Chapter 6

Conclusions

Today's satellite platforms provide a unique global perspective of the Earth's climate system. Recent technological advances have made it possible to operate combinations of instruments, which have traditionally been restricted to ground-based applications, in space. This has made possible a new generation of multi-sensor techniques for inferring the properties of the Earth-atmosphere system on a global scale. This dissertation has sought to make use of information regarding the distribution of cloud and precipitation from the Tropical Rainfall Measuring Mission to develop a new method for estimating the principal components of the tropical energy budget. The method, which simultaneously exploits information from both the TMI and VIRS instruments aboard TRMM, furnishes estimates of short- and longwave radiative fluxes throughout the atmosphere which are then used to determine atmospheric heating rates and cloud radiative forcing. In so doing we are able to quantitatively assess the mechanisms by which clouds and precipitation impact energy exchange in the tropics.

A concerted effort has been made to characterize uncertainties in all results to satisfy requirements for pursuing studies of global climate change, model validation, and data assimilation exercises. It has been well established that GCMs are sensitive to profiles of radiative and latent heating arising from clouds and precipitation, yet current representations of their development are crude, at best. Simultaneous assimilation of cloud, precipitation, and associated profiles of radiative and latent heating offers the potential for substantially improving the characterization of these processes and, in turn, lead to improved forecasts. In addition, a breakdown of the uncertainties into their principal components highlights the

primary areas of deficiency in the method. From this information, a number of modifications to improve the technique are suggested.

6.1 Information and Uncertainties in TMI-based Rainfall Retrievals

Chapter 2 presents a new application of the PCA approach to determining the information content of an observing system to establish a basic understanding of the precipitation profiling information contained in the TMI observations. The results, based on a simplified model relating profiles of both liquid and ice to the rainrate at the surface, show that the information content of the TMI can be broken down into three distinct rainfall ranges. At rainrates less than ~ 6 mmh^{-1}, the weighting functions of the TMI peak near or at the surface providing sensitivity to surface rainfall but limited information from the layers above it. Conversely, in rainfall exceeding ~ 25 mmh^{-1}, none of the TMI channels directly sense rainfall below 3 km. The optimal range for rainfall profiling by algorithms which explicitly incorporate vertical structure information was found to lie at rainrates between these two thresholds. At this rain intensity, the high frequency 37 and 85 GHz channels are sensitive to scattering by large ice particles near cloud top while the low frequency 10 and 19 GHz channels are sensitive to liquid water emission near and slightly above the surface, respectively. By virtue of its proximity to the water vapor absorption band, weighting functions for the 21 GHz channel peak higher still providing a direct observation relating to the liquid water in the middle of the cloud.

In a perfect remote sensing application there exists a one-to-one relationship between the observations and the quantity or quantities being retrieved. Measurements can then be used to uniquely determine an appropriate solution to the inversion problem. In satellite-based passive microwave rainfall retrievals, however, similar observed brightness temperature signatures can arise from a multitude of different combinations of liquid and ice hydrometeors in the atmosphere resulting in a non-uniqueness problem (recall Figure 2.27).

In this case it is impossible to unambiguously assign a single set of hydrometeor profiles to a given set of measurements. To quantify the effects of this non-uniqueness and provide a useful estimate of the uncertainty in passive microwave rainfall retrievals from the TMI instrument, a quantitative analysis of the uncertainties in the TMI-based GPROF cloud and precipitation profile retrieval algorithm are presented in Chapter 3. A rigorous new uncertainty model for general Bayesian Monte Carlo retrieval algorithms is constructed and applied to GPROF which is responsible for the TMI instantaneous rainfall product (2a12). The method not only accounts for uncertainties in the observations and radiative transfer modeling, but also those which occur as a result of the use of a finite representation of the distribution of cloud and precipitation profiles in nature. The method provides uncertainty estimates for all retrieved parameters on a pixel-by-pixel basis and decomposes these uncertainties into components which can be identified with errors in deriving the weights assigned to each profile and the *a priori* cloud database.

GPROF instantaneous surface rainrate estimates are accurate to fifty percent for rainrates below 20 mmh^{-1} but rapidly increase at higher rainrates where TMI weighting functions fail to directly sense the lowest levels of the atmosphere. In addition, a parameterization of the fractional uncertainty in the GPROF instantaneous surface rainfall product as a function of the magnitude of the estimate is proposed. The resulting third order polynomial accurately represents the uncertainties in surface rainfall estimates over the range $0 - 25$ mmh^{-1} providing an alternative to performing pixel-by-pixel calculations in applications where computational cost must be kept at a minimum. The example offered here is variational data assimilation of surface rainfall data which, before now, have relied on off-the-cuff error estimates to weight the observations. Similar uncertainty statistics and polynomial fits are derived for all hydrometeor classes at all levels in the GCE model atmosphere.

Another feature of the uncertainty model is that it can be used to quantitatively assess

the impact of different combinations of observations on the retrieval. Making use of this property, it was shown that the polarization and scattering indices of Petty (1994a) constitute a substantial improvement over unprocessed TMI brightness temperatures or polarization differences. In addition, preliminary attempts to incorporate radar reflectivity data to reduce profile database uncertainties show promise but can lead to a compensating increase in the modeling and measurement error component. These results highlight the need for studying sources of systematic error in the cloud database such as errors in cloud microphysical assumptions, beamfilling errors, or biases in the radiative transfer calculations used to simulate brightness temperatures for each profile.

6.2 The Tropical Energy Budget

Chapters 4 and 5 present a new "algorithm" for determining the principal components of the tropical oceanic energy budget using passive microwave and infrared observations from the TRMM satellite. The technique proceeds as follows:

1. Passive microwave radiances from the TMI instrument are used to retrieve column liquid water paths for all non-precipitating pixels (as determined by the GPROF algorithm).

2. For the same subset of pixels, VIRS radiances at 10.8 and 12 μm are employed to detect cirrus clouds and estimate their optical properties, when possible.

3. Crude representations of liquid and ice clouds derived from these estimates are used, along with the more detailed cloud and precipitation profiles from the GPROF algorithm in precipitating regions, to derive SW and LW fluxes throughout the atmosphere. A pixel is assumed clear if the 10.8 μm brightness temperature is within 5 K of an assumed clear-sky emitting temperature and the retrieved LWP is less than 0.05 kgm^{-2}.

4. From these profiles, column heating, cloud forcing, and the vertical structure of radiative heating in the atmosphere is diagnosed and decomposed into components owing to clear-sky, low cloud, high cloud, and precipitation.

5. At the same time, profiles of latent heating are estimated as part of the GPROF retrieval package, providing information regarding non-radiative energy transfer in the tropics.

6. Finally, these instantaneous products are gridded to lower spatial resolution and temporally averaged over daily and monthly timescales to produce maps of the principal components governing the exchange of energy between the ocean, atmosphere, and space. Tropic-wide monthly-mean estimates of the fluxes at atmospheric boundaries are also derived which, when combined with a corresponding monthly mean estimate of latent heating, comprise a short-term estimate of the tropical energy budget over oceans.

Results have been compiled for the month of February 1998 to illustrate the utility of the technique and derive a preliminary short-term tropical energy budget. On average, over this period, the tropical atmosphere absorbs 13 % of the solar radiation incident at the top of the atmosphere. A further 28 % is reflected by atmospheric particles, clouds, and the surface leaving 59 % to be absorbed by the ocean. At thermal wavelengths, it is found that the ocean emits 111 units of energy to the atmosphere while the atmosphere emits a total of 163 units, 104 downward toward the surface and 59 to space. Accounting for latent heat release which amounts to an exchange of 21 units of energy between the surface and atmosphere, the results imply a deficit of 70 Wm^{-2} of energy in the atmosphere and a surplus of 121 Wm^{-2} at the Earth's surface. The implied net gain of 51 Wm^{-2} in the Earth-atmosphere system is consistent with the difference between the incoming solar radiation and emitted thermal radiation at the top of the atmosphere. It is speculated that these

imbalances are largely accounted for by sensible heating, meridional energy transport, and absorption and transport of energy in the ocean.

Limited validation for the method, through a comparison of monthly-mean OLR estimates at 2.5 degree resolution with similar products from CERES and NOAA, provide an indication that the method captures general trends in tropical OLR. Large-scale features such as the ITCZ and SPCZ qualitatively agree between the three products but the present results indicate spurious high cloud in some regions a direct result of the lack of cloud height information in both the cloud retrievals and radiative transfer modeling. Correlations of 0.82 and 0.83 are obtained between the present estimates and those from CERES and NOAA, respectively. Uncertainty estimates deriving from detailed sensitivity studies provide information regarding the validity of the results as well as highlighting areas where more appropriate measurements or more accurate algorithms are required in the future.

This approach represents a preliminary attempt to make tropic-wide (and ultimately global) estimates of the components of the energy budget using explicit cloud and precipitation information from spaceborne observations. The results can, in principle, be applied to study short term climate variability through investigations of perturbations to the radiation balance induced by changes in the distributions of water vapor, cloud, and precipitation on short to moderate timescales affording us the opportunity to quantify important relationships between the hydrologic cycle and the Earth's energy budget.

6.3 Rainfall Profile Information from Spaceborne Radars

The final chapter introduces a novel approach for estimating profiles of rainfall from spaceborne radars, particularly those which ordinarily suffer from copious amounts of attenuation. The Constrained Optimal estimation Rainfall Retrieval ALgorithm, or CORRAL, makes use of an optimal estimation technique to deduce the profile of rainfall which best fits the observed reflectivity profile. The method is constrained by attenuation information

from estimates of surface return-derived PIA or passive microwave-derived PWP. Salient features of the algorithm include:

- This technique, while purely mathematical in nature, provides a framework well-suited for explicitly incorporating information regarding the accuracy of the measurements, forward model, and any *a priori* information used to derive the results. In addition, a suite of retrieval diagnostics are available to determine the quality and accuracy of the resulting rainfall profiles.

- It is straightforward to include external information, such as an estimate of PIA, through a constraint whose strength can be varied to account for its accuracy. In principle, any addition information related to some aspect of the rainfall can be added in this way and its impact on the retrieval will be directly proportional the sensitivity of the precipitation profile to the information and the accuracy with which it can be estimated.

- Since the results derive from the minimization of a general cost function, it is also possible to include measurements from alternative instruments directly in the estimation process. In this way the model is not exclusively limited to either active or passive information and can incorporate the complementary information offered by each in a coherent manner. Furthermore, the error diagnostic analyses are readily modified to provide a breakdown of the total uncertainty into components owing to each piece of information used in the retrieval.

- The flexibility afforded by the optimal estimation approach allows the algorithm to be re-cast in terms of a variable DSD by changing the forward model used to map rainfall to the observations. Such changes substantially increase the utility of the algorithm for global rainfall estimation which is often complicated by the variety of different microphysical processes leading to rain formation.

Through the use of synthetic retrievals using the GPROF cloud and precipitation database and simplifying assumptions regarding DSD, it was shown that, at 14 GHz (the frequency of the TRMM PR), retrievals of rainfall up to 40 mmh^{-1} were accurate to better than 20 %. The presence of a constraint allows this rainfall range to be extended to over 40 mmh^{-1} and generally reduces uncertainties by 25 % when attenuation is important. At 94 GHz (the frequency of the CloudSat CPR), an accurate constraint is a necessity to overcome strong attenuation suffered by the radar beam at this frequency. While the CloudSat radar detects rainfall throughout the atmospheric column for surface rainrates up to 5 mmh^{-1} or more, quantitative retrievals are exceedingly uncertain in the absence of a constraint. A moderately certain estimate of PIA or PWP, however, markedly improves the results allowing accurate retrievals to be made in rainfall up to 8-10 mmh^{-1} provided a the signal is not attenuated by the rainfall in the column. In heavier precipitation, the reflectivities from layers near the surface may be completely attenuated but, provided a PWP estimate is available, rainfall profiles can still be inferred in upper layers and may be crudely projected to the surface using a representative rainfall profile. Furthermore, the CPR is sensitive to cloud-sized liquid droplets, cloud ice, and frozen precipitation. Thus cloud and light precipitation profile information from the CPR, coupled with precipitation and corresponding PWP estimates from the AMSR instrument on Aqua will provide an opportunity to test improved techniques for estimating global diabatic heating.

6.4 Ongoing and Future Work

The analyses presented here are intended to provide a series of starting points from which, it is hoped, future research projects will evolve. The challenges posed by the problem of establishing observational evidence for climate change are many and will, no doubt, occupy the community for many years into the future. This work has sought to provide the underpinnings of a method for deriving observation-based estimates of the Earth's energy

budget and its relationship to the global hydrologic cycle, an important aspect of this problem. While preliminary results are promising, the techniques presented require substantial refinements before their full potential can be realized.

Of immediate importance is to extend the time period over which ERB estimates have been examined in the present work to cover the duration of the TRMM mission. This TRMM-derived climatology can then be used to study a variety of problems such as those summarized in the Introduction. The spatial coverage and time period encompassed by the TRMM data set make it well-suited to study energy balance in the tropical atmosphere and the role played by clouds and precipitation in establishing and modifying this balance. Another problem readily addressed in the future is to examine the role of cloud radiative effects in driving regional atmospheric circulations and vice versa, particularly on timescales characteristic of short term climate variability, such as the $30 - 60$ day intraseasonal oscillation (MJO).

Concurrent research is underway to implement more sophisticated cloud retrieval algorithms to improve vertical placement and microphysical assumptions in the broadband flux calculations. In the short term, this requires additional calibration of the TMI-based LWP retrieval and extension of the VIRS-based ice cloud retrieval to incorporate supplemental information to constrain cloud emitting temperature. The outgoing SW and LW fluxes measured by CERES, for example, could be used to pre-condition cloud retrievals reducing potential misclassification of ice cloud pixels. In the more distant future, methods combining active and passive observations, such as those from the AMSR, MODIS and CPR instruments on the Aqua and CloudSat satellites, to simultaneously retrieve cloud boundaries and ensure consistency between a wide variety of observations will be developed. In light of the sensitivity studies conducted in Chapter 5, such improvements, while requiring a substantial amount of future development, should appreciably reduce uncertainties in derived profiles of radiative heating and TOA and surface fluxes.

A related area of future work concerns the optimal estimation-based radar retrieval algorithm introduced in Appendix D. While the CORRAL algorithm was not directly applied in the radiation budget analysis, it is clear how vertically resolved cloud and precipitation profiles can improve them. Before it can be applied in such applications, however, the algorithm needs to be tested using a combination of real-world reflectivity and in situ microphysical observations. Furthermore, to realize its full potential, the algorithm should be re-cast to retrieve a variable DSD from reflectivity measurements at multiple radar wavelengths, or, alternatively coincident active and passive observations. Until this is accomplished, the algorithm is susceptible to non-uniqueness as a result of the different drop size distributions found in nature. Once developed and tested, the CORRAL data can be implemented in concert with that deriving from methods already discussed, to further improve estimates of radiative and latent heating and the ERB.

Finally, with the ongoing development of new, more sophisticated, instruments and improvements to those already in existence, we anticipate the necessity for continuous updates to the technique in an effort to maintain contact with the state-of-the art in cloud and precipitation profile remote sensing. In this regard there are no well-defined beginning and end to the problem. This work represents an extension of those published previously and will hopefully find its place as a building block for those to come.

Bibliography

Adler, R. F., Y. H.-Y. M. Yeh, N. Prasad, W.-K. Tao, and J. Simpson: 1991, Microwave simulations of a tropical rainfall system with a three-dimensional cloud model. *J. Appl. Meteor.*, **30**, 924–653.

Akvilonova, A. B., A. Y. Basharinov, A. K. Gorodetskiy, A. S. Gurvich, M. S. Krylova, B. G. Kutuza, D. T. Matveyev, and A. P. Orlov: 1973, Cloud parameters measured from the cosmos-384 satellite. *Atmos. Oceanic Phys.*, **9**, 187–189.

Alishouse, J. C., S. A. Snyder, J. Vongsathorn, and R. R. Ferraro: 1990, Determination of oceanic total precipitable water from the SSM/I. *IEEE Trans. Geosci. Remote Sens.*, **28**, 811–816.

Amayenc, P., J. P. Diguet, M. Marzoug, and T. Tani: 1996, A class of single- and dual-frequency algorithms for rain-rate profiling from a spaceborne radar. part II: Tests from airborne radar measurements. *J. Atmos. Oceanic Technol.*, **13**, 142–164.

Aonashi, K., A. Shibata, and G. Liu: 1996, An over-ocean precipitation retrieval using SSM/I multichannel brightness temperatures. *J. Meteor. Soc. Japan*, **74**, 617–637.

Arkin, P. A.: 1979, The relationship between fractional coverage of high cloud and rainfall accumulations during GATE over the B-Scale array. *Monthly Weather Review*, **107**, 1382–1387.

Arkin, P. A. and B. N. Meisner: 1987, The relationship between large-scale convective rainfall and cold cloud over the western hemisphere during 1982-84. *Monthly Weather Review*, **115**, 51–74.

Arking, A.: 1991, The radiative effects of clouds and their impact on climate. *Bull. Amer. Meteor. Soc.*, **72**, 795–813.

Arking, A. and J. D. Childs: 1985, Retrieval of cloud cover parameters from multispectral satellite images. *J. Climate and Appl. Meteor.*, **24**, 322–333.

Basharinov, A. Y., A. S. Gurvich, and S. T. Yegorov: 1969, Determination of geophysical parameters from data on thermally-induced radioemission obtained with the cosmos 243 satellite. *Dokl. Akad. Nauk SSSR*, **188**, 1273–1276.

Battan, L. J.: 1973, *Radar Observations of the Atmosphere*. University of Chicago Press, Chicago, IL.

Blau, H. H., R. P. Espinola, and E. C. Reifenstein: 1966, Near infrared scattering by sunlit terrestrial clouds. *Applied Optics*, **5**, 555–564.

Cess, R. D., M. Zhang, B. A. W. nd D. F. Young, X.-L. Zhou, and Y. Nikitenko: 2001, The influence of the 1998 El Niño upon cloud-radiative forcing over the Pacific Warm Pool. *Climate Dynamics*, **14**, in Press.

Cess, R. D., M.-H. Zhang, G. L. Potter, V. Alekseev, H. W. Barker, S. Bony, R. A. Colman, D. A. Dazlich, A. D. D. Genio, M. Déqué, M. R. Dix, V. Dymnikov, M. Esch, L. D. Fowler, J. R. Fraser, V. Galin, W. L. Gates, J. J. Hack, W. J. Ingram, J. T. Kiehl, Y. Kim, H. L. Treut, X.-Z. Liang, B. J. McAvaney, V. P. Meleshko, J. J. Morcrette, D. A. Randall, E. Roeckner, M. E. Schlesinger, P. V. Sporyshev, K. E. Taylor, V. Timbal, E. M. Volodin, W. Wang, W. C. Wang, and R. T. Wetherald: 1997, Comparison of the seasonal change in cloud-radiative forcing from atmospheric general circulation models and satellite observations. *J. Geophys. Res.*, **102**, 16593–16603.

Chang, A. T. C. and T. T. Wilheit: 1979, Remote sensing of atmospheric water vapor, liquid water, and wind speed at the ocean surface by passive microwave techniques from the Nimbus 5 satellite. *Radio Science*, **14**, 793–802.

Chen, T.-C. and M.-C. Yen: 1991, A study of the diabatic heating associated with the Madden-Julian Oscillation. *J. Geophys. Res.*, **96**, 13163–13177.

Chou, C. and J. D. Neelin: 1999, Cirrus detrainment-temperature feedback. *Geophys. Res. Letters*, **26**, 1295–1298.

Chou, M.-D., W. Zhao, and S.-H. Chou: 1998, Radiation budgets and cloud radiative forcing in the Pacific warm pool during TOGA COARE. *J. Geophys. Res.*, **103**, 16967–16977.

Clement, A. C., R. Seager, M. A. Cane, and S. E. Zebiak: 1996, An ocean dynamical thermostat. *Climate Dynamics*, **9**, 2190–2196.

Cooper, S. J.: 2001, personal communication.

Cotton, W. R. and R. A. Anthes: 1989, *Storm and Cloud Dynamics*. Academic Press, Inc., New York, NY.

Daley, R.: 1991, *Atmospheric Data Analysis*. Cambridge University Press, New York, NY.

Engelen, R. J. and G. L. Stephens: 1999, Characterization of water vapour retrievals from TOVS/HIRS and SSM/T-2 measurements. *Quart. J. Roy. Meteorol. Soc.*, **125**, 331–351.

— 2000, On the information content of the infrared water vapor absorption spectrum: retrievals and climate change signal, submitted to Bulletin of the American Meteorological Society.

Evans, K. F. and G. L. Stephens: 1991, A new polarized atmospheric radiative transfer model. *J. Quant. Spectrosc. Radiat. Transfer*, **46**, 413–423.

Ferriday, J. G. and S. K. Avery: 1994, Passive microwave remote sensing of rainfall with SSM/I: Algorithm development and implementation. *J. Appl. Meteor.*, **33**, 1587–1596.

Francis, R. N., J. S. Foot, and A. J. Baran: 1999, Aircraft measurements of the solar and infrared radiative properties of cirrus and their dependence on ice crystal shape. *J. Geophys. Res.*, **104**, 31685–31695.

Frank, W. H., H. Wang, and J. L. McBride: 1996, Rawinsonde budget analyses during the TOGA COARE IOP. *J. Atmos. Sci*, **53**, 1761–1780.

Fu, Q. and K.-N. Liou: 1992, On the correlated k-distribution for radiative transfer in nonhomogeneous atmospheres. *J. Atmos. Sci*, **49**, 2139–2156.

Fujita, M., K. Okamoto, H. Masuko, T. Ojima, and N. Fugono: 1985, Quantitative measurements of path-integrated rain rate by an airborne microwave radiometer over the ocean. *J. Atmos. Oceanic Technol.*, **2**, 285–292.

Fujita, M. and M. Satake: 1997, Rainfall rate profiling with attenuating-frequency radar using nonlinear LMS technique under a constraint on path-integrated rainfall rate. *Int. J. Remote Sensing*, **18**, 1137–1147.

Gill, A. E.: 1980, Some simple solutions for heat-induced tropical circulation. *Quart. J. Roy. Meteorol. Soc.*, **106**, 447–462.

Goodberlet, M. A., C. T. Swift, and J. C. Wilkerson: 1989, Remote sensing of ocean surface winds with the Special Sensor Microwave/Imager. *J. Geophys. Res.*, **94**, 14547–14555.

Green, A. W.: 1975, An approximation for the shapes of large raindrops. *J. Appl. Meteor.*, **14**, 1578–1583.

Greenwald, T. J., S. A. Christopher, J. Chou, and J. C. Liljegren: 1999, Intercomparison of cloud liquid water path derived from the GOES 9 imager and ground based microwave radiometers for continental stratocumulus. *J. Geophys. Res.*, **104**, 9251–9260.

Greenwald, T. J., G. L. Stephens, T. H. Vonder Haar, and D. L. Jackson: 1993, A physical retrieval of cloud liquid water over the global oceans using special sensor microwave/imager (SSM/I) observations. *J. Geophys. Res.*, **98**, 18471–18488.

Grody, N. C.: 1976, Remote sensing of atmospheric water content from satellites using microwave radiometry. *IEEE Trans. Antennas Propag.*, **24**, 155–162.

— 1991, Classification of snow cover and precipitation using the Special Sensor Microwave Imager. *J. Geophys. Res.*, **96**, 7423–7435.

Grody, N. C., A. Gruber, and W. C. Shen: 1980, Atmospheric water content over the tropical Pacific derived from the Nimbus-6 scanning microwave spectrometer. *J. Appl. Meteor.*, **19**, 986–996.

Grove, J. M.: 1988, *Little Ice Age*. Methuen and Co. Ltd., London, UK.

Gunn, L. S. and T. W. R. East: 1954, The microwave properties of precipitation particles. *Quart. J. Roy. Meteorol. Soc.*, **80**, 522–545.

Gupta, S. K., W. F. Staylor, W. L. Darnell, A. C. Wilber, and N. A. Ritchey: 1993, Seasonal variation of surface and atmospheric cloud radiative forcing over the globe derived from satellite data. *J. Geophys. Res.*, **98**, 20761–20778.

Haddad, Z., E. A. Smith, C. D. Kummerow, T. Iguchi, M. R. Farrar, S. L. Durden, M. Alves, and W. S. Olson: 1997, The TRMM "Day-1" radar/radiometer combined rain-profiling algorithm. *J. Meteor. Soc. Japan*, **75**, 799–809.

Han, Q., W. B. Rossow, J. Chou, and R. M. Welch: 1998, Global survey of the relationships of cloud albedo and liquid water path with droplet size using ISCCP. *Climate Dynamics*, **11**, 1516–1528.

Hansen, J. E. and J. B. Pollack: 1970, Near-infrared light scattering by terrestrial clouds. *J. Atmos. Sci*, **27**, 265–281.

Harrison, E. F., P. Minnis, B. R. Barkstrom, V. Ramanathan, R. D. Cess, and G. G. Gibson: 1990, Seasonal variation of cloud radiative forcing derived from the Earth Radiation Budget Experiment. *J. Geophys. Res.*, **95**, 18687–18703.

Hartmann, D. L., H. H. Hendon, and J. R. A. Houze: 1984, Some implications of the mesoscale circulation in tropical cloud clusters for large-scale dynamics and climate. *J. Atmos. Sci*, **41**, 113–121.

Hartmann, D. L. and M. L. Michelsen: 1993, Large-scale effects on the regulation of tropical sea surface temperature. *Climate Dynamics*, **6**, 2049–2062.

Hartmann, D. L., M. E. Ockert-Bell, and M. L. Michelsen: 1992, The effect of cloud type on Earth's energy balance: global analysis. *Climate Dynamics*, **5**, 1281–1304.

Hartmann, D. L. and D. A. Short: 1980, On the use of earth radiation budget statistics for studies of clouds and climate. *J. Atmos. Sci*, **37**, 1233–1250.

Heckley, W. A., G. Kelly, and M. Tiedke: 1990, On the use of satellite-derived heting rates for data assimilation within the tropics. *Monthly Weather Review*, **118**, 1743–1757.

Hitschfeld, W. and J. Borden: 1954, Errors inherent in the radar measurement of rainfall at attenuating wavelengths. *J. Appl. Meteor.*, **11**, 58–67.

Hou, A. Y., D. Levina, A. M. da Silva, S. Zhang, J. Joiner, R. Atlas, G. Huffman, and C. Kummerow: 2000a, Assimilation of SSM/I-derived surface and total precipitable water for improving the GEOS analysis for climate studies. *Monthly Weather Review*, **128**, 509–537.

Hou, A. Y., S. Q. Zhang, A. M. da Silva, and W. S. Olson: 2000b, Improving assimilated global datasets using TMI rainfall and columnar moisture observations. *Climate Dynamics*, **13**, 4180–4195.

Houze, R. A.: 1982, Cloud clusters and large-scale vertical motions in the tropics. *J. Meteor. Soc. Japan*, **60**, 396–409.

Iguchi, T., T. Kozu, R. Meneghini, J. Awaka, and K. Okamoto: 2000, Rain-profiling algorithm for the TRMM Precipitation Radar. *J. Appl. Meteor.*, **39**, 2038–2052.

Iguchi, T. and R. Meneghini: 1994, Intercomparison of single-frequency methods for retrieving a vertical rain profile from airborne or spareborne radar data. *J. Atmos. Oceanic Technol.*, **11**, 1507–1516.

Inoue, T.: 1985, On the temperature and effective emissivity determination of semitransparent cirrus clouds by bispectral measurements in the 10 μm window region. *J. Meteor. Soc. Japan*, **63**, 88–98.

Jaynes, E. T.: 2001, Probability theory: The logic of science, while still in preparation, an incomplete version of this outstanding book can be accessed via the World Wide Web from ftp://bayes.wustl.edu/Jaynes.book.

Johnson, R. H. and P. E. Ciesielski: 2000, Rainfall and radiative heating rates from TOGA COARE atmospheric budgets. *J. Atmos. Sci*, **57**, 1497–1514.

Jung, T., E. Ruprecht, and F. Wagner: 1998, Determination of cloud liquid water path over the oceans from Special Sensor Microwave/Imager (SSM/I) data using neural networks. *J. Appl. Meteor.*, **37**, 832–844.

Karstens, U., C. Simmer, and E. Ruprecht: 1994, Remote sensing of cloud liquid water. *Meteorol. Atmos. Phys.*, **54**, 157–171.

Kasahara, A. and A. P. Mizzi: 1996, Use of precipitation data for diabatic initialization to improve the tropical analysis of divergence and moisture. *Meteorol. Atmos. Phys.*, **60**, 143–156.

Kedem, B., H. Pavlopoulos, X. Guan, and D. A. Short: 1994, A probability distribution model for rain rate. *J. Appl. Meteor.*, **33**, 1486–1493.

Kidd, C.: 1998, On rainfall retrieval using polarization-corrected temperatures. *Int. J. Remote Sensing*, **19**, 981–996.

King, M. D., Y. J. Kaufman, W. P. Menzel, and D. Tanré: 1992, Remote sensing of cloud, aerosol, and water vapor properties from the Moderate Resolution Imaging Spectrometer (MODIS). *IEEE Trans. Geosci. Remote Sens.*, **30**, 2–27.

Knutson, T. R., K. M. Weickmann, and J. E. Kutzbach: 1986, Global scale intraseasonal oscillations of outgoing longwave radiation and 250 mb zonal wind during the Northern Hemisphere summer. *Monthly Weather Review*, **114**, 605–623.

Kuhn, P. M. and H. K. Weikmann: 1969, High altitude radiometric measurements of cirrus. *J. Appl. Meteor.*, **8**, 147–154.

Kuji, M., T. Hayasaka, N. Kikuchi, T. Nakajima, and M. Tanaka: 2000, The retrieval of effective particle radius and liquid water path of low-level marine clouds from NOAA AVHRR data. *J. Appl. Meteor.*, **39**, 999–1016.

Kummerow, C.: 1993, On the accuracy of the eddington approximation for radiative transfer in the microwave frequencies. *J. Geophys. Res.*, **98**, 2757–2765.

— 1998, Beamfilling errors in passive microwave rainfall retrievals. *J. Appl. Meteor.*, **37**, 356–370.

Kummerow, C., W. Barnes, T. Kozu, J. Shiue, and J. Simpson: 1998, The Tropical Rainfall Measuring Mission TRMM sensor package. *J. Atmos. Oceanic Technol.*, **15**, 809–817.

Kummerow, C. and L. Giglio: 1994a, A passive microwave technique for estimating rainfall and vertical structure information from space. part I: Algorithm description. *J. Appl. Meteor.*, **33**, 3–18.

— 1994b, A passive microwave technique for estimating rainfall and vertical structure information from space. part II: Applications to SSM/I data. *J. Appl. Meteor.*, **33**, 19–34.

Kummerow, C., W. S. Olson, and L. Giglio: 1996, A simplified scheme for obtaining precipitation and vertical hydrometeor profiles from passive microwave sensors. *IEEE Trans. Geosci. Remote Sensing*, **34**, 1213–1232.

Lagerloef, G. S. E., R. Lukas, R. A. Weller, and S. P. Anderson: 1998, Pacific Warm Pool temperature regulation during TOGA COARE: upper ocean feedback. *Climate Dynamics*, **11**, 2297–2309.

Lau, K.-M. and L. Peng: 1987, Origin of low-frequency (intraseasonal) oscillations in the tropical atmosphere Part I: Basic theory. *J. Atmos. Sci*, **44**, 950–972.

Lau, K.-M. and C.-H. Sui: 1997, Mechanisms of short-term sea surface temperature regulation: Observations during TOGA COARE. *Climate Dynamics*, **10**, 465–472.

Li, Q., R. L. Bras, and D. Veneziano: 1996, Passive microwave remote sensing of rainfall considering the effects of wind and nonprecipitating clouds. *J. Geophys. Res.*, **101**, 26503–26515.

Liebmann, B. and D. L. Hartmann: 1982, Interannual variations of outgoing IR associated with tropical circulation changes during 1974-1978. *J. Atmos. Sci*, **39**, 1153–1162.

Lin, B., P. Minnis, B. Wielicki, D. R. Doelling, R. Palikonda, D. F. Young, and T. Uttal: 1998a, Estimation of water cloud properties from satellite microwave, infrared and visible measurements in oceanic environments 2. results. *J. Geophys. Res.*, **103**, 3887–3905.

Lin, B., B. Wielicki, P. Minnis, and W. Rossow: 1998b, Estimation of water cloud properties from satellite microwave, infrared and visible measurements in oceanic environments 1. Microwave brightness temperature simulations. *J. Geophys. Res.*, **103**, 3873–3886.

Lindzen, R. S., M.-D. Chou, and A. Hou: 2001, Does the earth have an adaptive infrared iris?, not yet submitted.

Liou, K.-N.: 1974, On the radiative properties of cirrus in the window region and their influence on remote sensing of the atmosphere. *J. Atmos. Sci*, **31**, 522–532.

— 1977, Remote sensing of the thickness and composition of cirrus clouds from satellites. *J. Appl. Meteor.*, **16**, 91–99.

— 1986, Influence of cirrus clouds on weather and climate processes: A global perspective. *Monthly Weather Review*, **114**, 1167–1199.

Liu, G. and J. A. Curry: 1992, Retrieval of precipitation from satellite microwave measurement using both emission and scattering. *J. Geophys. Res.*, **97**, 9959–9974.

— 1993, Determination of characteristic features of cloud liquid water from satellite microwave measurements. *J. Geophys. Res.*, **98**, 5069–5092.

Madden, R. A. and P. R. Julian: 1972, Description of global-scale circulation cells in the tropics with a 40-50 day period. *J. Atmos. Sci*, **29**, 1109–1123.

Marécal, V. and J.-F. Mahfouf: 2000, Variational retrieval of temperature and humidity profiles from TRMM precipitation data. *Monthly Weather Review*, **128**, 3853–3866.

Marks, C. J. and C. D. Rodgers: 1993, A retrieval method for atmospheric composition from limb emission measurements. *J. Geophys. Res.*, **98**, 14939–14953.

Marshall, J. S. and W. H. Palmer: 1948, The distribution of raindrops with size. *J. Meteor.*, **5**, 165–166.

Marzoug, M. and P. Amayenc: 1994, A class of single- and dual-frequency algorithms for rain-rate profiling from a spaceborne radar. part I: Principle and tests from numerical simulations. *J. Atmos. Oceanic Technol.*, **11**, 1480–1506.

Mather, J. H., T. P. Ackerman, M. P. Jensen, and W. E. Clements: 1998, Characteristics of the atmospheric state and the surface radiation budget at the Tropical Western Pacific ARM site. *Geophys. Res. Letters*, **25**, 4513–4516.

McClatchey, F. A., R. W. Fenn, J. E. Selby, F. E. Volz, and J. S. Goring: 1972, *Optical Properties of the Atmosphere, 3rd ed.*. AFCRL-72-0497, 102 pp., Air Force Cambridge Res. Lab., L. G. Hanscom Field, Mass.

McFarquhar, G. M. and A. J. Heymsfield: 1998, The definition and significance of an effective radius for ice clouds. *J. Atmos. Sci*, **55**, 2039–2052.

Meneghini, R. and T. Kozu: 1990, *Spaceborne Weather Radar*. Artech House, Inc., Norwood, MA.

Miles, N. L., J. Verlinde, and E. E. Clothiaux: 2000, Cloud droplet size distributions in low-level stratiform clouds. *J. Atmos. Sci*, **57**, 295–311.

Miller, B. I.: 1962, *On the momentum and energy balance of hurricane Helene (1958)*. National Hurricane Research Project, Rep. 53, U.S. Weather Bureau, Washington, D.C.

Miller, S. D. and G. L. Stephens: 2001, CloudSat instrument requirements as determined from ECMWF forecasts of global cloudiness, to appear in JGR.

Miller, S. D., G. L. Stephens, C. K. Drummond, A. K. Heidinger, and P. T. Partain: 2000, A multisensor diagnostic satellite cloud property retrieval scheme. *J. Geophys. Res.*, **105**, 19955–19971.

Minnis, P., K.-N. Liou, and Y. Takano: 1993, Inference of cirrus cloud properties using satellite-observed visible and infrared radiances, part I, Parameterization of radiance fields. *J. Atmos. Sci*, **50**, 1279–1304.

Minnis, P., D. F. Young, K. Sassen, J. M. Alvarez, and C. J. Grund: 1990, The 27-28 October 1986 FIRE IFO cirrus case study: cirrus parameter relationships derived from satellite and lidar data. *Monthly Weather Review*, **118**, 2402–2425.

Miyahara, S.: 1987, A simple model of the tropical intraseasonal oscillation. *J. Meteor. Soc. Japan*, **65**, 341–351.

Mizzi, A. P. and A. Kasahara: 1989, Intercomparison of daily values of atmospheric variables, including diabatic heating rates, from the ECMWF, GFDL, and Goddard Laboratory for Atmospheres FGGE Level IIIb analyses. *J. Geophys. Res.*, **94**, 14717–14748.

Moore, R. W. and T. H. Vonder Haar: 2001, Interannual variability of cloud forcing and meridional energy transport for the northern hemisphere winter from 1984-1990. *Climate Dynamics*, **14**, in press.

Nakajima, T. and M. D. King: 1990, Determination of the optical thickness and effective particle radius of clouds from reflected solar radiation measurements. part I: Theory. *J. Atmos. Sci*, **47**, 1878–1893.

Nakajima, T. Y. and T. Nakajima: 1995, Wide-area determination of cloud microphysical properties from NOAA AVHRR measurements for FIRE and ASTEX regions. *J. Atmos. Sci*, **52**, 4043–4059.

NIST: 1994, The NIST reference on constants, units, and uncertainty.

Njoku, E. G. and L. Swanson: 1983, Global measurements of sea surface temperature, wind speed, and atmospheric water content from satellite microwave radiometry. *Monthly Weather Review*, **111**, 1977–1987.

Olson, W. S., C. D. Kummerow, G. M. Heymsfield, and L. Giglio: 1996, A method for combined passive-active microwave retrievals of cloud and precipitation profiles. *J. Appl. Meteor.*, **35**, 1763–1789.

Olson, W. S., C. D. Kummerow, Y. Hong, and W.-K. Tao: 1999, Atmosperic latent heating distributions in the tropics derived from satellite passive microwave radiometer measurements. *J. Appl. Meteor.*, **38**, 633–664.

Ou, S. C., K. N. Liou, W. M. Gooch, and Y. Takano: 1993, Remote sensing of cirrus cloud parameters using advanced very-high-resolution radiometer 3.7- and 10.9-μm channels. *Applied Optics*, **32**, 2171–2180.

Palmén, E. and H. Riehl: 1957, Budget of angular momentum and energy in tropical cyclones. *J. Meteor.*, **14**, 150–159.

Paltridge, G. W.: 1980, Cloud-radiation feedback to climate. *Quart. J. Roy. Meteorol. Soc.*, **106**, 895–899.

Parol, F., J. C. Buriez, G. Brogniez, and Y. Fouquart: 1991, Information content of AVHRR channels 4 and 5 with respect to the effective radius of cirrus cloud particles. *J. Appl. Meteor.*, **30**, 973–984.

Petty, G. W.: 1990, *On the response of the Special Sensor Microwave/Imager to the marine environment - Implications for atmospheric parameter retrievals*. Ph.D. thesis, University of Washington.

— 1994a, Physical retrievals of over-ocean rain rate from multichannel microwave imagery. part I: Theoretical characteristics of normalized polarization and scattering indices. *Meteorol. Atmos. Phys.*, **54**, 79–99.

— 1994b, Physical retrievals of over-ocean rain rate from multichannel microwave imagery. part II: Algorithm implementation. *Meteorol. Atmos. Phys.*, **54**, 101–121.

Petty, G. W. and K. B. Katsaros: 1990, Precipitation observed over the south china sea by the Nimbus-7 scanning multichannel microwave radiometer during winter MONEX. *J. Appl. Meteor.*, **29**, 273–287.

Pierrehumbert, R. T.: 1995, Thermostats, radiator fins, and the local runaway greenhouse. *J. Atmos. Sci*, **52**, 1784–1806.

Platt, C. M. R.: 1973, Lidar and radiometric observations of cirrus clouds. *J. Atmos. Sci*, **30**, 1191–1204.

Platt, C. M. R., D. W. Reynolds, and N. L. Abshire: 1980, Satellite and lidar observations of the albedo, emittance and optical depth of cirrus compared to model calculations. *Monthly Weather Review*, **108**, 195–204.

Prabhakara, C., G. Dalu, R. Suhasini, J. J. Nucciarone, and G. L. Liberti: 1992, Rainfall over oceans: Remote sensing from satellite microwave radiometers. *Meteorol. Atmos. Phys.*, **47**, 177–199.

Prabhakara, C., R. S. Fraser, G. Dalu, M.-L. C. Wu, and R. J. Curran: 1988, Thin cirrus clouds: seasonal distribution over oceans deduced from Nimbus-4 IRIS. *J. Appl. Meteor.*, **27**, 379–399.

Prabhakara, C., R. Meneghini, D. A. Short, J. A. Weinman, R. I. Jr., R. Oki, and M. Cadeddu: 1998, A TRMM microwave radiometer rain retrieval method based on fractional rain area. *J. Meteor. Soc. Japan*, **76**, 765–781.

Prabhakara, C., D. A. Short, W. Wiscombe, and R. S. Fraser: 1986, Rainfall over oceans inferred from Nimbus 7 SMMR: Application to 1982-83 El Niño. *J. Climate and Appl. Meteor.*, **25**, 1464–1474.

Puri, K. and N. E. Davidson: 1992, The use of infrared satellite cloud imagery data as proxy data for moisture and diabatic heating in data assimilation. *Monthly Weather Review*, **120**, 2329–2341.

Ramanathan, V. and W. Collins: 1991, Thermodynamic regulation of ocean warming by cirrus clouds deduced from observations of the 1987 El Niño. *Nature*, **351**, 27–32.

Randel, D. and T. H. Vonder Haar: 1990, On the interannual variation of the earth radiation balance. *Nature*, **342**, 1168–1173.

Rao, P. K., S. J. Holmes, R. K. Anderson, J. S. Winston, and P. E. Lehr, eds.: 1990, *Weather Satellites: Systems, Data, and Environmental Applications*. Lancaster Press, Lancaster, PA.

Reynolds, R. W. and T. M. Smith: 1994, Improved global sea surface temperature analyses. *Climate Dynamics*, **7**, 929–948.

Riehl, H. and J. S. Malkus: 1958, On the heat balance in the equatorial trough zone. *Geophysica*, **6**, 503–538.

— 1961, Some aspects of hurricane Daisy. *Tellus*, **13**, 181–213.

Ringer, M. A. and K. P. Shine: 1997, Sensitivity of the Earth's radiation budget to interannual variations in cloud amount. *Climate Dynamics*, **13**, 213–222.

Ritter, B. and J.-F. Geleyn: 1992, A comprehensive radiation scheme for numerical weather prediction models with potential applications in climate simulations. *Monthly Weather Review*, **120**, 303–325.

Rodgers, C. D.: 1976, Retrieval of atmospheric temperature and composition from remote measurements of thermal radiation. *Rev. Geophys. and Space Phys.*, **14**, 609–624.

— 1990, Characterization and error analysis of profiles retrieved from remote sounding measurements. *J. Geophys. Res.*, **95**, 5587–5595.

Roewe, D. and K.-N. Liou: 1978, Influence of cirrus clouds on the infrared cooling rate in the troposphere and lower stratosphere. *J. Appl. Meteor.*, **17**, 99–106.

Rolland, P., K.-N. Liou, M. D. King, S.-C. Tsay, and G. M. McFarquhar: 2000, Remote sensing of optical and microphysical properties of cirrus clouds using Moderate-Resolution Imaging Spectrometer channels: Methodology and sensitivity to physical assumptions. *J. Geophys. Res.*, **105**, 11721–11738.

Schneider, S. H.: 1992, *In: Climate System Modeling (pp. 3-26)*. Cambridge University Press, New York, NY.

Seager, R. and R. Murtugudde: 1997, Ocean dynamics, thermocline adjustment, and regulation of Tropical SST. *Climate Dynamics*, **10**, 521–534.

Seinfeld, J. H. and S. N. Pandis: 1998, *Atmospheric Chemistry and Physics: From Air Pollution to Climate Change*. John Wiley & Sons, New York, NY.

Sheu, R.-S., J. A. Curry, and G. Liu: 1996, Satellite retrieval of tropical precipitation using combined International Satellite Cloud Climatology Project DX and SSM/I data. *J. Geophys. Res.*, **101**, 21291–21301.

Simpson, J., R. F. Adler, and G. R. North: 1988, A proposed Tropical Rainfall Measuring Mission (TRMM) satellite. *Bull. Amer. Meteor. Soc.*, **69**, 278–295.

Simpson, J., C. Kummerow, W.-K. Tao, and R. F. Adler: 1996, On the Tropical Rainfall Measuring Mission (TRMM). *Meteorol. Atmos. Phys.*, **60**, 19–36.

Simpson, J. and W.-K. Tao: 1993, Goddard Cumulus Ensemble Model. Part II: Applications for studying cloud precipitating processes and for NASA TRMM. *TAO*, **4**, 73–116.

Slingo, A. and J. M. Slingo: 1988, The response of a general circulation model to cloud longwave radiative forcing. I: Introduction and initial experiments. *Quart. J. Roy. Meteorol. Soc.*, **114**, 1027–1062.

Slingo, J. M. and A. Slingo: 1991, The response of a general circulation model to cloud longwave radiative forcing. II: Further studies. *Quart. J. Roy. Meteorol. Soc.*, **117**, 333–364.

Smith, E. A., X. Xiang, A. Mugnai, R. E. Hood, and R. W. Spencer: 1994a, Behavior of an inversion-based precipitation algorithm with high-resolution AMPR measurements including a low-frequency 10.7-GHz channel. *J. Atmos. Oceanic Technol.*, **11**, 858–873.

Smith, E. A., X. Xiang, A. Mugnai, and G. J. Tripoli: 1994b, Design of an inversion-based precipitation profile retrieval algorithm using an explicit cloud model for initial guess microphysics. *Meteorol. Atmos. Phys.*, **54**, 53–78.

Soden, B. J.: 2000, The sensitivity of the tropical hydrological cycle to ENSO. *Climate Dynamics*, **13**, 538–549.

Sohn, B.-J. and E. A. Smith: 1992a, Global energy transports and the influence of clouds on transport requirements: a satellite analysis. *Climate Dynamics*, **5**, 717–734.

— 1992b, The modulation of the low-latitude radiation budget by cloud and surface forcing on interannual time scales. *Climate Dynamics*, **5**, 831–846.

— 1992c, The significance of cloud-radiative forcing to the general circulation on climate time scales: a satellite interpretation. *J. Atmos. Sci*, **49**, 845–860.

Somerville, R. C. J. and L. A. Remer: 1984, Cloud optical thickness feedbacks in the CO_2 retrieval problem. *J. Geophys. Res.*, **89**, 9668–9672.

Spencer, R. W.: 1986, A satellite passive 37-GHz scattering-based method for measuring oceanic rain rates. *J. Climate and Appl. Meteor.*, **25**, 754–766.

Spencer, R. W., H. M. Goodman, and R. E. Hood: 1989, Precipitation retrieval over land and ocean with the SSM/I: Identification and characteristics of the scattering signal. *J. Atmos. Oceanic Technol.*, **6**, 254–273.

Spencer, R. W., D. W. Martin, B. B. Hinton, and J. A. Weinman: 1983, Satellite microwave radiances correlated with radar rain rates over land. *Nature*, **304**, 141–143.

Stephens, G. L.: 1980, Radiative properties of cirrus clouds in the infrared region. *J. Atmos. Sci*, **37**, 435–446.

— 1994, *Remote Sensing of the Lower Atmosphere*. Oxford University Press, New York, NY.

Stephens, G. L., G. G. Campbell, and T. H. Vonder Haar: 1981, Earth radiation budgets. *J. Geophys. Res.*, **86**, 9739–9760.

Stephens, G. L., P. M. Gabriel, and P. T. Partain: 2001, Parameterization of atmospheric radiative transfer I: Validity of simple models, *J. Atmos. Sci* in press.

Stephens, G. L. and T. J. Greenwald: 1991, The Earth's radiation budget and its relation to atmospheric hydrology 2. observations of cloud effects. *J. Geophys. Res.*, **96**, 15325–15340.

Stephens, G. L., S.-C. Tsay, J. P. W. Stackhouse, and P. J. Flatau: 1990, The relevance of the microphysical and radiative properties of cirrus clouds to climate and climatic feedback. *J. Atmos. Sci*, **47**, 1742–1753.

Stephens, G. L., D. G. Vane, and S. J. Walter: 2000, The CloudSat mission: A new dimension to space-based observations of cloud in the coming millenium. *Bull. Amer. Meteor. Soc.*, **81**, in Press.

Stephens, G. L. and P. J. Webster: 1979, Sensitivity of radiative forcing to variable cloud and moisture. *J. Atmos. Sci*, **36**, 1542–1556.

Stone, R. S., G. L. Stephens, C. M. R. Platt, and S. Banks: 1990, The remote sensing of thin cirrus cloud using satellites, lidar and radiative transfer theory. *J. Appl. Meteor.*, **29**, 353–366.

Takahashi, M.: 1987, A theory of the slow phase speed of the intraseasonal oscillation using the Wave-CISK. *J. Meteor. Soc. Japan*, **65**, 43–49.

Tao, W.-K., S. Lang, W. S. Olson, R. Meneghini, S. Yang, J. Simpson, C. Kummerow, E. Smith, and J. Halverson: 2001, Retrieved vertical profiles of latent heat release using TRMM rainfall products for February 1998. *J. Appl. Meteor.*, **40**, 957–982.

Tao, W.-K., S. Lang, J. Simpson, and R. Adler: 1993, Retrieval algorithms for estimating the vertical profiles of latent heat release: Their applications for TRMM. *J. Meteor. Soc. Japan*, **71**, 685–700.

Tao, W.-K. and J. Simpson: 1993, Goddard Cumulus Ensemble Model. Part I: Model description. *TAO*, **4**, 35–72.

Thacker, W. C.: 1989, The role of the Hessian matrix in fitting models to measurements. *J. Geophys. Res.*, **94**, 6177–6196.

Tiedke, M.: 1993, Representation of clouds in large-scale models. *Monthly Weather Review*, **121**, 3040–3061.

Trenberth, K. E., ed.: 1992, *Climate System Modeling*. Cambridge University Press, New York, NY.

Twomey, S.: 1977, *Introduction to the Mathematics of Inversion in Remote Sensing and Indirect Measurements*. Elsevier Scientific Publishing Company, New York, NY.

Ulaby, F. T., R. K. Moore, and A. K. Fung: 1981, *Microwave Remote Sensing Active and Passive, Vol I: Microwave Remote Sensing Fundamentals and Radiometry*. Addison-Wesley Publishing Co., Reading, MA.

— 1986, *Microwave Remote Sensing Active and Passive, Vol III: From Theory to Applications*. Addison-Wesley Publishing Co., Reading, MA.

Van de Hulst, H. C.: 1982, *Light Scattering by Small Particles*. Dover Press, New York, NY.

Viltard, N., C. Kummerow, W. S. Olson, and Y. Hong: 2000, Combined use of the radar and radiometer of TRMM to estimate the influence of drop size distribution on rain retrievals. *J. Appl. Meteor.*, **39**, 2103–2114.

Weickmann, K. M., G. R. Lussky, and J. E. Kutzbach: 1985, Intraseasonal (30-60 day) fluctuations of outgoing longwave radiation and 250 mb streamfunction during northern winter. *Monthly Weather Review*, **113**, 941–961.

Wentz, F.: 1997, A well-calibrated ocean algorithm for special sensor microwave/imager. *J. Geophys. Res.*, **102**, 8703–8718.

Wentz, F., C. Gentemann, D. Smith, and D. Chelton: 2000, Satellite measurements of sea surface temperature through clouds. *Science*, **288**, 847–850.

Wexler, R.: 1948, Rain intensities by radar. *J. Meteor.*, **5**, 171–173.

Wilheit, T. T.: 1986, Some comments on passive microwave measurement of rain. *Bull. Amer. Meteor. Soc.*, **67**, 1226–1232.

Wilheit, T. T. and A. T. C. Chang: 1980, An algorithm for retrieval of ocean surface and atmospheric parameters from the observations of the Scanning Multichannel Microwave Radiometer. *Radio Science*, **15**, 525–544.

Wilheit, T. T., A. T. C. Chang, M. S. V. Rao, E. B. Rodgers, and J. S. Theon: 1977, A satellite technique for quantitatively mapping rainfall rates over the oceans. *J. Appl. Meteor.*, **16**, 551–560.

Yanai, M.: 1961, Dynamical aspects of typhoon formation. *J. Meteor. Soc. Japan*, **39**, 283–309.

Yanai, M., S. Esbensen, and J.-H. Chu: 1973, Determination of bulk properties of tropical cloud clusters from large-scale heat and moisture budgets. *J. Atmos. Sci*, **30**, 611–627.

Yang, S. and E. A. Smith: 1999a, Four-dimensional structure of monthly latent heating derived from SSM/I satellite measurements. *Climate Dynamics*, **12**, 1016–1037.

— 1999b, Moisture budget analysis of TOGA COARE area using SSM/I-retrieved latent heating and large-scale Q_2 estimates. *J. Atmos. Oceanic Technol.*, **16**, 633–655.

— 2000, Vertical structure and transient behavior of convective-stratiform heating in TOGA COARE from combined satellite-sounding analysis. *J. Appl. Meteor.*, **39**, 1491–1513.

Appendix A

General Uncertainty Formulae

To aid in characterizing the uncertainty in a quantity which results from the combination of a number of measurements a few key formulas which are commonly used in the calculation of a "combined standard uncertainty" (see the NIST Reference (1994)) will be summarized in this appendix. Let δx_i represent the uncertainty in the measurement x_i and let $y = f(x_1, x_2, x_3, \ldots, x_n)$ be a function of n measurements. In general, the uncertainty in y is given by:

$$\delta y = + \sqrt{\sum_{i=1}^{n} \left(\frac{\partial f}{\partial x_i} \right)^2 (\delta x_i)^2 + 2 \sum_{i=1}^{n-1} \sum_{j=i+1}^{n} \left(\frac{\partial f}{\partial x_i} \right) \left(\frac{\partial f}{\partial x_j} \right) \delta x_{ij}} \qquad \text{(A.1)}$$

where δx_i is the estimated standard deviation (equal to the square root of the variance) in the measurement x_i and δx_{ij} is the estimated covariance of the measurements x_i and x_j.

The first term in Eqn. (A.1) represents the contributions of the individual uncertainties in the x_i to the overall uncertainty in y while the second term accounts for the fact that the uncertainties in the measurments may not be completely independent of one another. In the subsections below, we will look at a few examples to illustrate the use of Eqn. (A.1) that will be of use in trying to estimate the uncertainties associated with more complex combinations of measurements.

A.1 Example 1: Sum of 2 measurements

Consider the function $y(x_1, x_2) = ax_1 + bx_2$. Differentiating y with respect to x_1 and x_2 yeilds

$$\frac{\partial y}{\partial x_1} = a$$

$$\frac{\partial y}{\partial x_2} = b \tag{A.2}$$

Using Eqn. (A.1) the uncertainty in y is

$$\delta y = \sqrt{a^2 (\delta x_1)^2 + b^2 (\delta x_2)^2 + ab\delta x_{12}} \tag{A.3}$$

If we can show that the uncertainties in the two measurements are uncorrelated, then the second term vanishes and the uncertainty in y reduces to the well-known Pythagorean theorem, $\delta y^2 = a^2(\delta x_1)^2 + b^2(\delta x_2)^2$.

A.2 Example 2: Product of 2 measurements

Now consider the function $y(x_1, x_2) = ax_1x_2$.

$$\frac{\partial y}{\partial x_1} = ax_2$$

$$\frac{\partial y}{\partial x_2} = ax_1 \tag{A.4}$$

In this case the estimated uncertainty in y is:

$$\delta y = \sqrt{a^2 \left(x_2^2 (\delta x_1)^2 + x_1^2 (\delta x_2)^2 + x_1 x_2 \delta x_{12}\right)} \tag{A.5}$$

With some rearrangement, the fractional uncertainty in y is given by

$$\frac{\delta y}{y} = \sqrt{\left(\frac{\delta x_1}{x_1}\right)^2 + \left(\frac{\delta x_2}{x_2}\right)^2 + \frac{\delta x_{12}}{x_1 x_2}} \tag{A.6}$$

A.3 Example 3: Quotient of 2 measurements

Now consider the function $y(x_1, x_2) = a\frac{x_1}{x_2}$.

$$\begin{aligned} \frac{\partial y}{\partial x_1} &= \frac{a}{x_2} \\ \frac{\partial y}{\partial x_2} &= -\frac{a x_1}{x_2} \end{aligned} \tag{A.7}$$

The estimated uncertainty in y is

$$\delta y = \sqrt{\left(\frac{a}{x_2}\right)^2 (\delta x_1)^2 + \left(\frac{a x_1}{x_2^2}\right)^2 (\delta x_2)^2 - \left(\frac{a^2 x_1}{x_2^3}\right) \delta x_{12}} \tag{A.8}$$

In this case the fractional uncertainty in y is given by:

$$\frac{\delta y}{y} = \sqrt{\left(\frac{\delta x_1}{x_1}\right)^2 + \left(\frac{\delta x_2}{x_2}\right)^2 - \frac{\delta x_{12}}{x_1 x_2}} \tag{A.9}$$

Notice that Eqn. (A.6) and Eqn. (A.9) differ only by the sign of the covariance term. The covariance term increases the overall uncertainty in a product while decreasing it in a quotient.

A.4 Example 4: Exponential of a measurement

Finally consider the function $y(x) = be^{ax}$. Here the uncertainty is given by

$$\delta y = \left(\frac{\partial y}{\partial x}\right)\delta x$$

$$\delta y = abe^{ax}\delta x \tag{A.10}$$

In this case we find the interesting property that as a becomes large, the uncertainty in y can actually exceed the value of y since:

$$\frac{\delta y}{y} = a\delta x \tag{A.11}$$

So, if $a > \frac{1}{\delta x}$, the uncertainty in y exceeds the value the value of y itself! This is due to the fact that the exponential is a very rapidly increasing function.

Appendix B

GPROF Uncertainty Parameterizations

Table B.1: Parameters for third order polynomial fits to the uncertainties in GPROF cloud and precipitation profile estimates. Levels with no data indicate that a fit was not possible due to too few (or no) data points for a meaningful result.

Hydro. Class	Model Level	a_0	a_1	a_2	a_3
Cloud Liquid Water	0.5 km	1.06	-30.9	408	-1430
	1.0 km	1.05	-18.3	132	-244
	1.5 km	0.937	-13.5	81.7	-124
	2.0 km	0.920	-13.7	80.4	-120
	2.5 km	0.876	-11.7	64.2	-83.6
	3.0 km	1.01	-13.4	77.0	-100
	3.5 km	0.775	-3.32	28.3	-41.9
	4.0 km	1.33	-6.62	8.11	25.2
	5.0 km	2.51	-39.7	245	-492
Cloud Ice	4.0 km	1.12	-22.6	-2510	70500
	5.0 km	3.40	-508	32400	-5.93×10^5
	6.0 km	0.748	-9.74	69.5	-4160
	8.0 km	0.587	8.85	-1120	15500
	10.0 km	1.89	-73.3	1220	-6530
	14.0 km	4.25	-167	2550	-12600
	18.0 km	2.79	-110	1760	-9070
Rain	0.5 km	0.358	0.0713	-0.507	-0.670
	1.0 km	0.391	-0.403	0.663	-0.076
	1.5 km	0.335	0.0717	-0.281	0.488
	2.0 km	0.233	1.488	-4.07	3.45
	2.5 km	0.705	-3.25	8.38	-3.64
	3.0 km	0.806	-3.67	16.4	-11.6
	3.5 km	0.216	21.1	-98.1	131
	4.0 km	2.01	-33.1	262	-545
	5.0 km	2.58	-48.8	559	-2120
Precipitating Ice	2.5 km	0.925	-11.4	101	-209
	3.0 km	1.44	-21.5	136	-234
	3.5 km	1.09	-16.8	109	-166
	4.0 km	0.950	-14.1	93.4	-134
	5.0 km	1.65	-32.0	228	-415
	6.0 km	1.97	-40.4	268	-487
	8.0 km	1.38	-44.5	541	-2060
	10.0 km	1.80	-86.0	1616	-9325

Appendix C

Latent Heating from TRMM

C.1 Background

The cooling of the atmosphere through radiative processes is largely balanced by the release of latent heat by precipitation. This is particularly true in the tropics which accounts for two thirds of global precipitation (Simpson et al., 1996). In this appendix, profiles of latent heating derived using the GPROF algorithm are presented to complement the radiative heating calculations of Chapter 5.

When averaged over a suitably large horizontal domain, small-scale eddies in the horizontal wind components can be neglected, and the "apparent" atmospheric heat source can be written as the sum of vertical eddy flux convergence of heat, latent heating from condensation, evaporation, and sublimation, and radiative cooling (Yanai et al. (1973), Tao et al. (1993), and Olson et al. (1999)). Letting c, e, f, m, d, and s represent the rates of condensation, evaporation, freezing, melting, deposition, and sublimation per unit mass of air, and denoting the latent heats of vaporization, fusion, and sublimation by L_v, L_f and L_s, we have

$$Q_1 = -c_p\bar{\pi}\frac{1}{\bar{\rho}}\frac{\partial\bar{\rho}\overline{w'\theta'}}{\partial z} + L_v(\bar{c}-\bar{e}) + L_f(\bar{f}-\bar{m}) + L_s(\bar{d}-\bar{s}) + \bar{Q}_R \qquad \text{(C.1)}$$

where $\pi = (p/1000mb)^{R/c_p}$ with R the dry gas constant and c_p the specific heat of air at constant pressure. θ is the potential temperature, w the vertical velocity, and p is pressure. The overbar denotes horizontal averages while the primes denote deviations from these means. The first term accounts for the eddy flux contribution to the total heating and $\bar{Q}_R$

denotes the radiative heating component. The remaining terms constitute the latent heating due to all relevant hydrometeor phase changes and will be the focus of this section.

Provided a spatial and temporal domain large enough to encompass the geographic evolution and life-cycle of the cloud complex is considered, the LH terms can be vertically integrated from the surface to the top of the cloud to yield

$$LH_{col} = \int_0^{z_{top}} \bar{\rho} \left[L_v(\bar{c} - \bar{e}) + L_f(\bar{f} - \bar{m}) + L_s(\bar{d} - \bar{s}) \right] dz \approx \rho_l L_v R \qquad \text{(C.2)}$$

where R is the surface precipitation rate. Thus the column-integrated LH is, in a space-time average sense, related to the total condensate removed from the system by precipitation processes.

Profiles of LH not only depend on profiles of condensate and water vapor but also on the dynamics of the local environment and are considerably more challenging to estimate as a result (Olson et al., 1999). Such information is not readily available from the TRMM measurements alone and must, therefore, be introduced from an external source. In the absence of observations, cloud resolving models provide the most complete source of cloud dynamics information. Yang and Smith (1999a,b, 2000) (the last of which will hereafter be referred to as YS3), for instance, incorporate CRM dynamical information by parameterizing local vertical motion in terms of the constituent hydrometeor water contents viz

$$W_i = A_i + B_i Cloud_i + C_i Rain_i + D_i Graupel_i + E_i Ice_i + F_i Snow_i \qquad \text{(C.3)}$$

where $Cloud_i$, $Rain_i$, $Graupel_i$, Ice_i, and $Snow_i$ are the water contents of the various species in the University of Wisconsin-Numerical Modeling System (UW-NMS) CRM. Following YS3, LH due to hydrometeor species, X, is given by the vertical derivative of its mass flux, R_X^*, which depends on vertical fluxes of condensation or deposition. The total

LH at any level, z, in the atmosphere is determined by

$$Q_{LH}(z) = \frac{g}{c_p}\left[L_v\left(\frac{\partial R^*_{rd}(z)}{\partial p} + \frac{\partial R^*_{cd}(z)}{\partial p}\right) + (L_v + L_f)\left(\frac{\partial R^*_{pi}(z)}{\partial p} + \frac{\partial R^*_{id}(z)}{\partial p}\right)\right] \quad \text{(C.4)}$$

where c_p is the specific heat at constant pressure, g is the acceleration due to gravity, and L_v and L_h are the latent heats of vaporization and fusion, respectively. The crux of the model lies in the assumptions for computing the vertical mass fluxes for rain, liquid cloud droplets, precipitating ice, and ice cloud droplets, denoted with subscripts rp, cd, pi, and id, respectively.The mass fluxes depend on the terminal velocity of the precipitating particles, W_X, and the local vertical velocity W through

$$R^*_X(z) = -\left[W_X(z) + W(z)\right] LWC_X(z) \quad \text{(C.5)}$$

Required terminal velocities can be derived from gravitational fallout equations based on aerodynamical considerations and appropriate assumptions regarding particle size and shape (eg. a MP distribution of spherical particles), while the liquid water contents, LWC_X, are retrieved by the algorithm. The local vertical velocity in model level i is then determined using Eqn. (C.3) providing all supplemental information needed to compute LH via Eqn. (C.4). This approach, while relatively straight-forward, adds the element of uncertainty associated with parameterizing the highly variable wind speed to the already difficult task of retrieving profiles of multiple hydrometeor classes from passive microwave observations.

Tao et al. (1993, 2001) have suggested a different approach involving CRM results in a more direct way. Their approach, the convective-stratiform heating (CSH) algorithm, is to select an appropriate mean region- and cloud type-specific LH rate profile derived based on GCE CRM simulations. A convective/stratiform classification is used as a criterion for selecting a particular profile and the result is then scaled according to a retrieved near-surface

rainfall rate. While this method is conceptually simple and avoids some of the uncertainties incurred in passive microwave cloud profile retrievals, it incurs a potentially substantial and difficult to quantify uncertainty owing to its strong dependence on the CRM-derived LH estimates.

While each of these methods has its merits, the estimates presented here derive from the GPROF algorithm itself. The method, described in detail by Olson et al. (1999), retrieves cloud, precipitation and LH simultaneously through the BMC techniques described earlier. LH estimates associated with each cloud profile in the *a priori* cloud database are computed directly using the CRM. The retrieved LH profile is composed of a weighted-average of all profiles in the database whose simulated multi-spectral microwave T_B signature matches that observed by the TMI in the same way as the hydrometeor water contents themselves. This method, too, relies heavily on CRM-derived estimates of LH but averages only those profiles whose spectral signatures match those observed removing some, but not all, of the non-uniqueness inherent in the CSH approach.

C.2 GPROF Latent Heating Rates

Figure C.1 presents a profile of latent heating superimposed on profiles of daytime and nighttime heating rates for the 12 mmh^{-1} rain case presented earlier. As noted earlier, LW cooling is confined to a thin layer near cloud top but SW heating due to absorption by cloud ice persists through the top 5 km of the cloud. Surprisingly, the latent heat release by precipitation at lower levels in the cloud is rather weak by comparison. Despite being spread over a greater vertical range, the column-integrated latent heating resulting from this profile is only 200 Wm^{-2} or 1.66 $Kday^{-1}$ compared to a column radiative heating of 1.84 $Kday^{-1}$. This result is contrary to many typical latent heating profiles in the literature. Tao et al. (2001), for example, present a collection of profiles from a variety of prior studies. The minimum convective latent heating profile from the set predicts a maximum heating of

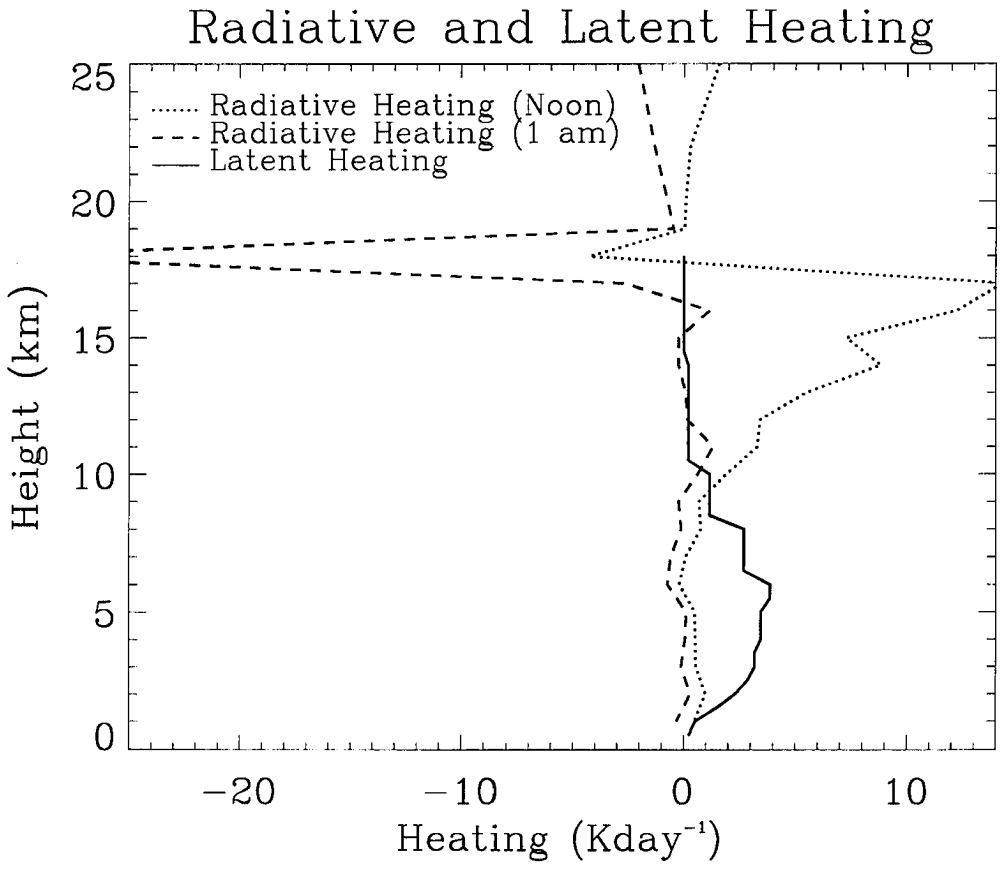

Figure C.1: Profiles of radiative and latent heating for a single precipitating pixel (R = 11 mmh^{-1}).

approximately 40 Kday^{-1} for a rainrate of 12 mmh^{-1}.

With this concern in mind, we will proceed to examine a more substantial data set in the hopes that the previous example was an isolated anomaly. When integrated in the vertical and spatially and temporally averaged, the GPROF estimates should provide a reasonable measure of the large-scale latent heat release in the tropics. Figure C.2 presents column-integrated latent heating averaged over the month of February 1998 as well as monthly-mean cross-sections of latent heating at 2, 5, and 8 km. The maps show that latent heating generally tracks the heavy precipitation expected in the Intertropical Convergence Zone (ITCZ) and South Pacific Convergence Zone (SPCZ). Isolated regions of strong latent

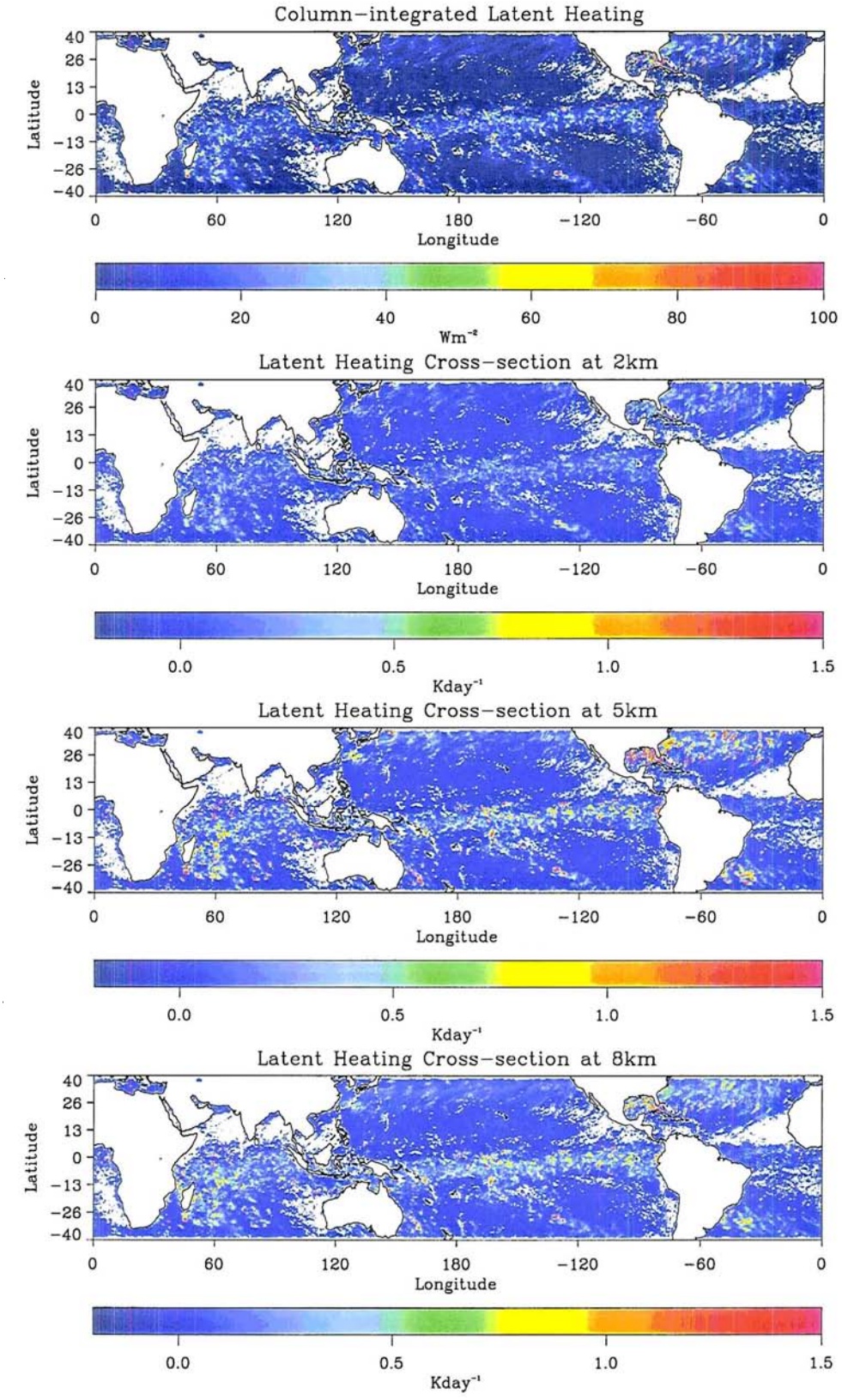

Figure C.2: Monthly mean column latent heating and cross-sections at 2.0, 5.0, and 8.0 km as retrieved by GPROF.

heat release are also present in the Gulf of Mexico and along the Atlantic coast of the United States. The monthly mean cross-sections of latent heating illustrate the height in the vertical where the majority of latent heating occurs. Latent heating is extremely weak at 2 km reflecting the fact that most precipitation formation occurs higher in the atmosphere. Latent heat release at 5 and 8 km are comparable in magnitude and much larger than at 2 km indicating that the condensation and deposition processes leading to precipitation formation occur between these levels. The present results agree qualitatively with similar figures from Tao et al. (2001) but significantly underestimate the magnitude of latent heating by a factor of 10.

Monthly mean surface rainfall and a corresponding estimate column-integrated latent heat release is presented in Figure C.3. On a tropic-wide and monthly mean sense, these estimates, derived using Equation (C.2), provide a reasonable estimate of the column latent heating in the tropics for February 1998. The fact that these estimates, while exhibiting similar a spatial distribution, are more than an order of magnitude larger than those obtained through direct vertical integration of the latent heat profiles retrieved using GPROF confirms that there is a problem with the latter.

While there is clearly a need for further refinement to the latent heating estimates presented here, the results demonstrate that it is feasible to simultaneously infer both radiative and latent heating using the TRMM platform. It is likely that either the latent heating assigned to each cloud and precipitation database by the CRM is in error or that information is being lost in the generation of the FOV-averaged database used as input to the version of the GPROF algorithm used here. It should be noted that alternative versions of the algorithm have been used by other investigators to derive more reasonable results (see, for example, the afore mentioned Olson et al. (1999) and Tao et al. (2001)). It is, therefore, likely that the error will be fixed in the very near future.

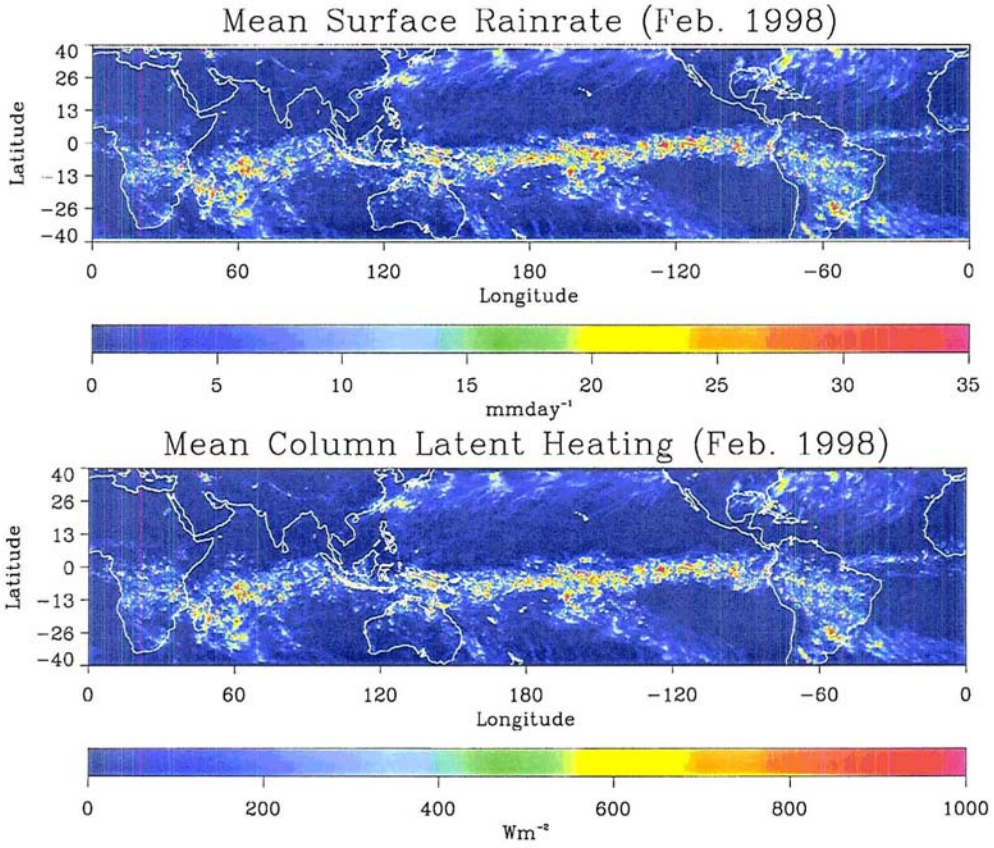

Figure C.3: GPROF monthly mean rainfall and associated column-integrated latent heat release for February 1998.

C.3 Uncertainties

In light of these observations, uncertainty estimates for the latent heating rate estimates derived in the present study are somewhat pointless. It is still useful, however to present the latent heating component of the GPROF uncertainty derived in Chapter 3 as they will apply when the model is corrected. Error statistics compiled over a number of TRMM orbits are presented in Figure C.4. It is interesting to note that the uncertainties are largest in and around the climatological melting layer at 5-6 km. This reinforces the notion that numerous distributions of liquid and ice give rise to very similar passive microwave brightness temperatures. Thus the precise distribution of latent heat release, which depends strongly

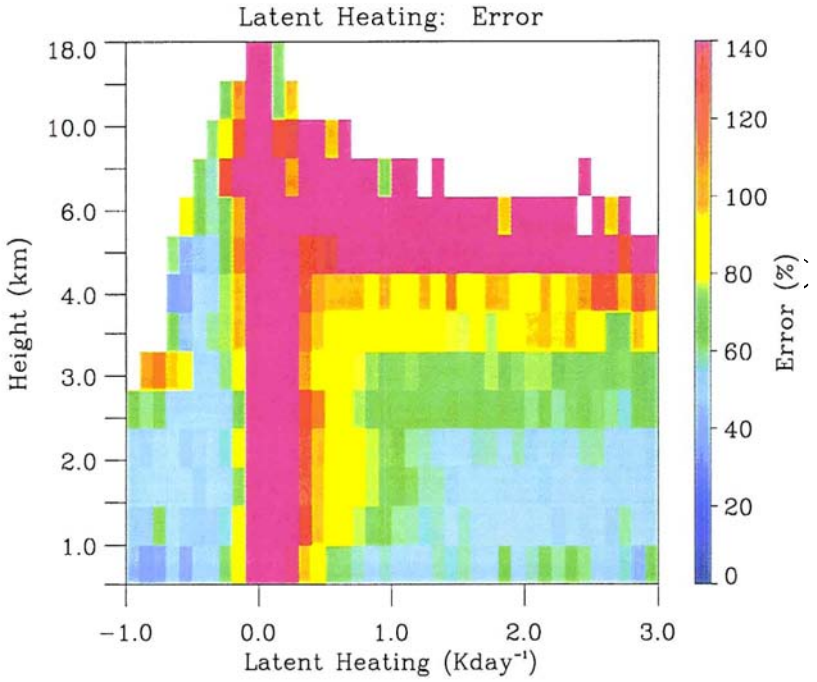

Figure C.4: Uncertainties in GPROF latent heating estimates assuming the latent heating assigned to each profile by the CRM is perfect.

on the specific distribution and phase of the particles forming the rainfall, is difficult to determine uniquely given the TMI observations alone.

These estimates assume that the latent heating estimates assigned to each cloud profile are not biased. Since latent heating does not influence the retrieval in any way once the cloud database is generated, it relies on the fact that the CRM generated latent heating profiles are, in a mean sense, representative of nature. Provided this is true, Figure C.4 provides an appropriate estimate of uncertainty since the model predicts that the more scatter there is in the relationship between TMI T_Bs and latent heating, the more uncertain the estimate of latent heat release is for a given set of hydrometeor water contents.

There is debate as to the amount of temporal and spatial averaging required to satisfy

the assumptions governing the use of Equation (C.2). It seems reasonable, however, that on a monthly timescale and over a region of a few tens of degrees, total precipitation should provide a reasonable proxy for total latent heating. In that case the uncertainty in surface rainfall estimates and latent heating should be identical. Thus the uncertainty in total latent heat release derived using monthly-mean GPROF surface rainrates will be on the order of 50 %, considerably more accurate than that anticipated for retrievals of instantaneous profiles of latent heating.

Appendix D

Complementary Information from Spaceborne Radars

Satellite observations are not restricted to passive microwave radiometers. Alternative passive sensors such as those operating at visible and infrared wavelengths, those which measure broadband fluxes, and lightening detectors as well as active instruments which include radars and lidars are either currently in operation or planned for the near future. Each system has spawned its own unique approaches to the retrieval problem which employ distinct forward models to estimate unique sets of retrievables. While it is beyond the scope of this dissertation to study all such instruments, the profiling capabilities of spaceborne radars, their recent use in global precipitation observations from TRMM, and the fact that they too operate at microwave frequencies, justifies exploring them in greater depth.

Since each reflectivity measurement from a range-resolved radar system can be attributed to the hydrometeors in a distinct volume of the atmosphere, radar observations are well-suited to cloud and rainfall profiling applications. Making use of this information is complicated by microphysical assumptions such as DSD and the shape and phase of the hydrometeors in the scattering volume, all of which add a degree of non-uniqueness to radar retrievals. The problem of characterizing the information contained in radar observations and its implications for uncertainties in rainfall retrievals is, therefore, of considerable interest to the search for alternatives to the passive microwave techniques described above. In this appendix we begin to address this problem through the development and preliminary analysis of an algorithm for retrieving rainfall profiles from attenuating spaceborne radars.

D.1 Introduction

The profiling capabilities of spaceborne radars have the potential to add vertical structure information to complement techniques based exclusively on passive measurements. As a result, the TRMM carried the first radar designed for precipitation measurements flown in space. Given the success of the PR, which has been operational for more than three years, future spaceborne radar missions are being discussed. The potential for extensive spatial coverage offered by satellite-based radars has also been recognized by the CloudSat science team (Stephens et al., 2000) and a 94 GHz Cloud CPR will be flown on that satellite which may be capable of measuring light rainfall as well as clouds. As a result of the logistics of flying a radar in space, most notably size, weight, and power restrictions, only frequencies greater than 10 GHz are practical for a spaceborne radar system (Fujita and Satake, 1997). Consequently, all spaceborne radars are subject to significant attenuation caused by the rain and clouds they are measuring necessitating new radar-rainfall retrieval algorithms which explicitly account for attenuation effects. Hitschfeld and Borden (1954) were the first to propose a method for directly correcting measured reflectivities for the attenuation. Since then numerous retrieval schemes have been developed which incorporate aspects of this early work along with the more recent technique of constraining retrievals using path-integrated attenuation (PIA) derived from surface return echoes. Iguchi and Meneghini (1994), Marzoug and Amayenc (1994), and Amayenc et al. (1996) describe many such algorithms and evaluate them in the context of airborne and spaceborne operation.

Many ground-based radar retrieval algorithms are based on the Rayleigh approximation where raindrops are assumed to be small compared to the radar wavelength and some assumed DSD providing simple relationships between radar reflectivity and rainrate. From an operational standpoint these algorithms are computationally efficient, simple to implement, and produce useful results but they incur uncertainties which are difficult to estimate as a result of their underlying assumptions. Errors associated with the assumption of an

idealized size distribution were pointed out as early as 1948 by Wexler (1948) while Gunn and East (1954) showed that the Rayleigh approximation is not valid for wavelengths less than 3 cm (or frequencies greater than 10 GHz) emphasizing the need for an algorithm which isn't restricted by such assumptions in spaceborne applications. This has been recognized by the designers of the TRMM PR algorithm who select a DSD based on rain type and the presence or absence of a bright band and correct the DSD based on a PIA estimate (Iguchi et al., 2000). Another shortcoming of many algorithms their inability to adapt measurements from other instruments except in a limited capacity. With the growing trend towards multi-sensor platforms, exemplified by the TRMM satellite, it is important to develop algorithms better suited to combining information from a variety of different sources simultaneously in rainfall retrievals. Again, this has been recognized by the TRMM science team and a first-generation combined PR-TMI algorithm has been developed which employs a Bayesian approach to retrieve DSD parameters from PR reflectivities with a PIA estimate derived from the 10.6 GHz channel of the TMI (Haddad et al., 1997).

For model validation and data assimilation applications, rigorous estimates of the uncertainty in the retrieved rainfall profiles are required but many algorithms are limited to a rough estimate of their accuracy at best. For this reason, all operational TRMM algorithms, including the two PR algorithms described above, are required to provide estimates of their accuracy and considerable emphasis will be placed on error diagnostics for the algorithm presented below.

This appendix presents a complete algorithm for retrieving profiles of rainfall from spaceborne radar measurements which seeks to address these issues and provide an alternate method of inversion to either of those currently employed in the TRMM algorithms. This new algorithm, the Constrained Optimal estimation Rainfall Retrieval ALgorithm (CORRAL)[1], differs from those of many previous works in that it can be adapted

[1]This acronym was adopted at the expense of the more humorous alternative: Constrained Optimal estimation Rain Profiling SystEm (CORPSE) which runs the risk of foreshadowing a somewhat dubious fate.

to use any DSD, requires no simplifying assumptions regarding particle shape provided backscatter information can be computed, and is readily modified to include any additional measurements that are available. Furthermore, the CORRAL algorithm is accompanied by a suite of error diagnostics which facilitate sensitivity studies and uncertainty analyses of the resulting rainfall estimates for the purposes of comparison with the passive microwave technique described earlier. As opposed to presenting radar as an alternative to radiometer observations, a concerted effort will be made to highlight the complementary nature of information from active and passive instruments. With this frame of mind, the methodology herein provides the groundwork necessary for the simultaneous use of active and passive information in future rainfall retrievals. The CORRAL retrieval method and some synthetic retrieval examples are summarized in "An Estimation-based Precipitation Retrieval Algorithm for Attenuating Radars", to appear in *The Journal of Applied Meteorology*.

D.2 Attenuating Radar Forward Model

In general, the return power, P_r, received by a radar which transmits a power P_t at wavelength λ is given by

$$P_r = \left(\frac{P_t G^2 \lambda^2 \theta \phi h}{512(2ln2)\pi r^2} \right) exp[-2 \int_0^r k_{ext}(s) ds] \, \eta \tag{D.1}$$

where G is the antenna gain, θ and ϕ characterize the half-power beamwidth of the pulse, h is the length of the emitted pulse, and r is the range to the target. With k_{ext} defined as the attenuation coefficient, the exponential factor accounts for the two-way attenuation due to all atmospheric constituents along the slant path, s, of the radar beam. Finally, η is the radar reflectivity per unit volume, V, given by

$$\eta = \int_V \sigma_b dV \tag{D.2}$$

where the σ_b are the backscatter cross sections (per unit volume) of the particles in the target volume.

Ground-based radar models assume that the particles in the target volume are much smaller than the wavelength of the incident radiation, $\frac{\pi D}{\lambda} << 1$, and use the Rayleigh approximation for the backscatter cross-section yielding

$$\eta = \frac{\pi^5}{\lambda^4}|K|^2 Z \tag{D.3}$$

where $Z = \int D^6 N(D) dD$ is the Rayleigh reflectivity factor. Here $N(D)dD$ is used to denote the number of particles with diameters between D and $D + dD$ in the target volume. $K = \frac{m^2-1}{m^2+2}$ is the dielectric factor of a scattering particle where $m = n - ik$ is the wavelength and temperature dependent complex refractive index of the scatterers. At the frequencies used in most spaceborne applications, the Rayleigh approximation breaks down in rain. Figure D.1a illustrates the ratio of Mie to Rayleigh reflectivity factors at 14, 35, and 94 GHz as a function of size parameter, $\chi = \frac{\pi D}{\lambda}$, assuming spherical liquid raindrops distributed according to the MP DSD. Plotted in this way, the frequency dependence of the ratio can be attributed solely to differences in the real part of the refractive index which is greatest at 14 GHz and lowest for 94 GHz. The results show that using the Rayleigh approximation leads to large errors for size parameters greater than about 0.15 when integrating over a size distribution. Cast as a function of rainfall rate in Figure D.1b, we deduce that the Rayleigh approximation is only suitable for rainrates less than 2.5 mmh^{-1} at 14 GHz, and is not applicable in any appreciable rainfall at 35 or 94 GHz.

Based on Figure D.1, we adopt a more general form for the reflectivity, η,

$$\eta = \int_V \sigma_b dV = \frac{1}{4} \int Q_{sca} P(\Theta = 180) \pi D^2 N(D) dD \tag{D.4}$$

where $P(\Theta = 180)$ is the scattering phase function evaluated in the backscatter direction,

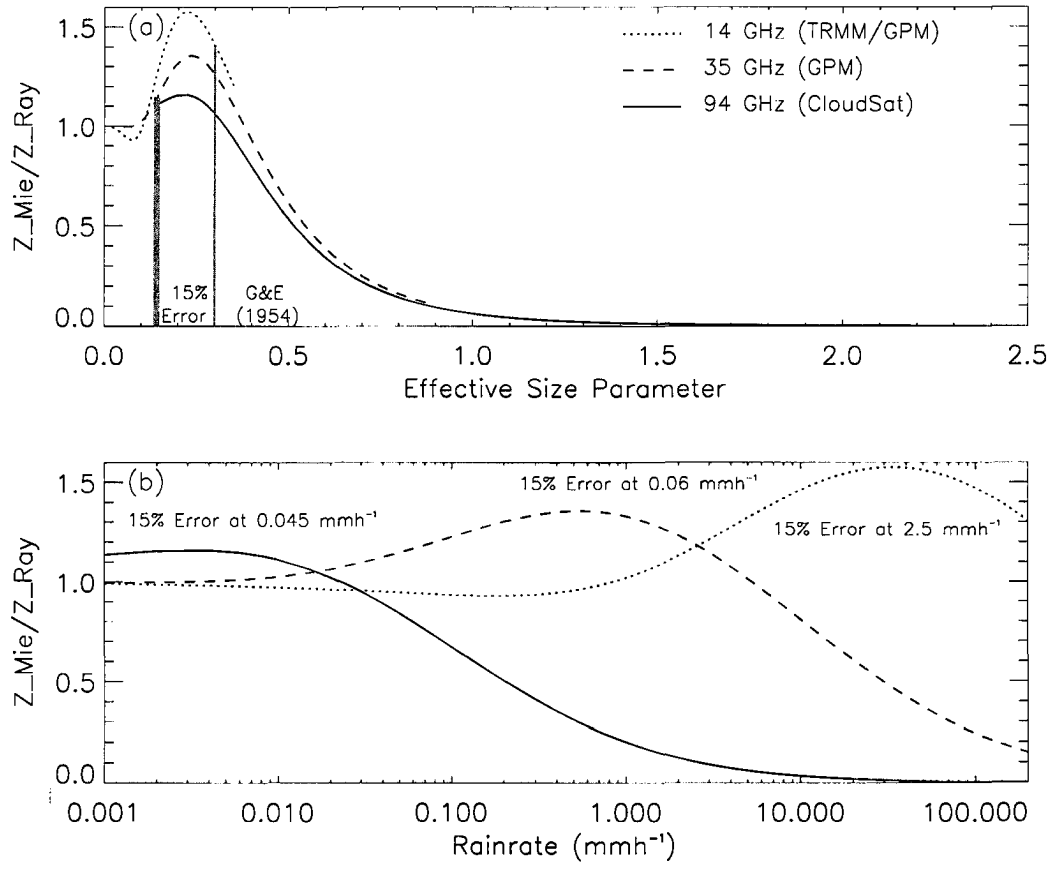

Figure D.1: Ratio of effective reflectivity computed using Mie theory to Rayleigh reflectivity as a function of: (a) effective size parameter, and (b) rainrate.

Q_{sca} is the scattering efficiency equal to the ratio of the particle's scattering cross section to it's geometric cross section, and $N(D)$ is an arbitrary number distribution of particles as a function of their effective diameter, D. A series of tables of $P(\Theta = 180)$ and Q_{sca} are created as a function of particle size using Mie theory for spherical particles or some alternate computational method for more complicated particle shapes. This allows flexibility with regard to particle size, shape, and number concentration, all of which can be adapted to any given problem as needed.

Combining Equations (D.1), (D.3), and (D.4), we now construct a model to simulate an

effective reflectivity factor for any atmospheric profile

$$Z_{eff} = exp[-2\int_0^r k_{ext}(s)ds]\ \frac{\lambda^4}{4\pi^5|K|^2}\ \int Q_{sca}P(\Theta = 180)\pi D^2 N(D)dD \qquad \text{(D.5)}$$

Unattenuated reflectivities are computed at each level along with an attenuation correction due to the hydrometeors in that level. Each reflectivity is then corrected in turn for the attenuation through the levels above it.

D.3 Sensitivity of Spaceborne Radars to Rainfall

Prior to inverting this radar equation to estimate rainfall from observations of radar reflectivity, it is instructive to review the pertinent physical mechanisms which give rise to these measurements at frequencies typical of spaceborne radars and briefly investigate the sensing capabilities of a few such radars.

D.3.1 Scattering and Absorption of Radar Beams

Figure D.2 presents effective reflectivity factor as a function of rainrate for spaceborne radars operating at 14, 35, and 94 GHz. MP distributions of spherical liquid and ice particles are assumed and attenuation is neglected. Frequencies are chosen to be representative of the currently operational TRMM PR (14 GHz), the CloudSat CPR to be flown in the near future (94 GHz), and a second frequency proposed for the next generation PR (35 GHz) and axes have been set to facilitate later comparison with a similar figure in which attenuation has been included.

In the Rayleigh regime, characterized by particles which are small with respect to the radar wavelength, Z_{eff} increases linearly with the logarithm of rainrate, consistent with power-law relationships of the form $Z = aR^b$, commonly employed in ground-based radar retrievals. As rainrate increases and particles become larger, the backscatter cross-section

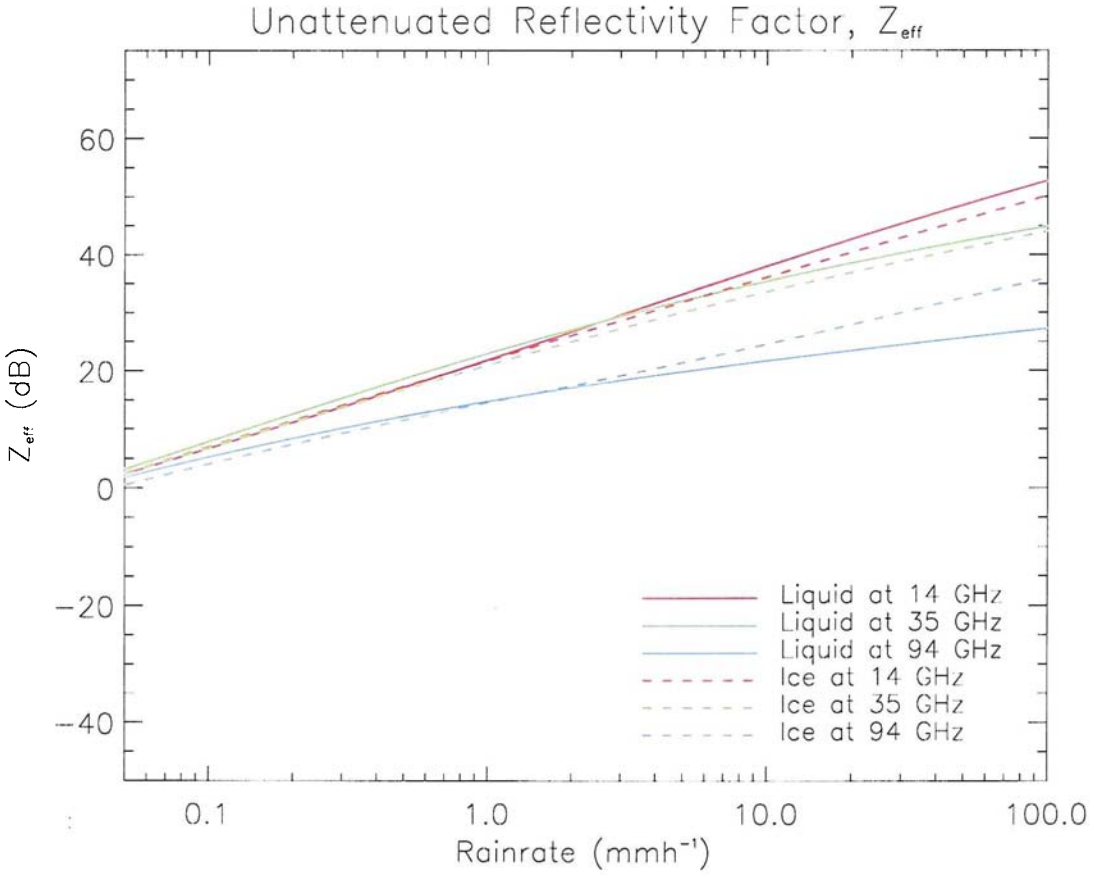

Figure D.2: Effective reflectivity factors as a function of rainrate at 14, 35, and 94 GHz in the absence of attenuation.

transitions from dependence on particle size to the sixth power under the Rayleigh approximation to a dependence on the square of particle size in the large particle limit. At the same time, the rate of change of effective particle size with rainrate decreases as rainrate increases[2] further reducing the sensitivity of Z_{eff} to changes in rainrate in heavy rain. These effects are particularly evident at 94 GHz where the relationship between Z_{eff} and the logarithm of rainrate deviates substantially from linear even in light rain.

In liquid precipitation, non-Rayleigh effects are compounded by absorption within the particles which reduces the amount of radiation they scatter relative to non-absorbing ice

[2]For a MP distribution, effective radius goes as rainrate to the 0.21 power. $\frac{\partial r_e}{\partial R}$, therefore, goes as $R^{-0.79}$.

particles. When particles are small compared to wavelength, this effect is minimal relative to the factor of five difference in the value of $|K|^2$ for liquid and ice so liquid droplets appear "brighter" than their frozen counterparts. At size parameters approaching unity, however, absorption in liquid droplets exceeds this factor of five and backscatter from ice exceeds that from liquid droplets. This results in a fundamental difference between low and high frequency radars when observing precipitating particles. At 14 GHz, effective size parameters are less than 1 for all rainfall thus liquid raindrops have greater reflectivities than equivalent sized ice particles. At 94 GHz, however, most appreciable rainfall contains enough large particles for absorption effects to dominate and ice particles appear brighter than liquid raindrops to the radar. Reflectivities at the intermediate frequency primarily reflect the difference in $|K|^2$ but as rainrate increases the reflectivities of liquid and ice particles converge, evidence of the fact that the effective size parameter approaches unity in heavy rain at 35 GHz.

Backscattered radiation from a particular atmospheric volume suffers from attenuation due to interactions with molecules and other particles along the path from the radar to and from the target volume. Following Battan (1973), the loss of intensity in a radar beam due to attenuation can be expressed (in decibels, dB) as

$$10log\frac{P_r}{P_{r0}} = -2\int_0^R (\kappa_g + \kappa_c + \kappa_p)\, dr \tag{D.6}$$

where the κ are attenuation coefficients in dBkm^{-1} for gas, cloud, and precipitation and R represents the range of the target from the radar. At frequencies characteristic of ground-based weather radars, attenuation by cloud and gases is negligible by virtue of their extremely small size relative to the wavelength of the incident radiation. At the higher frequencies characteristic of spaceborne radars, however, absorption by molecular Oxygen and water vapor as well as liquid cloud droplets can contribute a significant fraction of the total attenuation suffered by the radar signal.

Table D.1: Two-way attenuation (in dB) through a number of standard cloud-free atmospheres between TRMM PR (14 GHz) and CloudSat CPR (94 GHz) and three representative atmospheric levels (10km, 5km, and 0.5km).

McClatchey Profile	14 GHz			94 GHz		
	10km	5km	0.5km	10km	5km	0.5km
Tropical	0.0149	0.0471	0.2923	0.1211	0.5499	5.4541
Midlatitude Summer	0.0140	0.0433	0.2313	0.1144	0.4760	4.0841
Midlatitude Winter	0.0124	0.0385	0.1366	0.0994	0.3520	1.8200
Subarctic Winter	0.0114	0.0373	0.1178	0.0908	0.3214	1.3121

Examples of gaseous attenuation over the two-way path between two spaceborne radars and various depths in the atmosphere are presented in Table D.1. Four McClatchey standard atmospheres (McClatchey et al., 1972), spanning the range of water vapor concentrations observed globally, are examined and results are presented in dB, (defined as $10\log(e^{[} - 2\int_0^r k_{ext}(s)ds]))$. Attenuation by gases is clearly negligible at the lower frequency TRMM PR reaching a maximum of 0.3 dB through the entire moist, tropical atmosphere, well within the instrument's uncertainty. The cloud radar, on the other hand, experiences significant attenuation in the lowest 5 km of the atmosphere which strongly depends on the amount of moisture present. Gaseous attenuation at 94 GHz, therefore, ranges from 1.5 and 6 dB and must be accounted for in the retrieval.

At microwave frequencies, attenuation by small cloud particles is dominated by absorption since, in the Rayleigh approximation, the absorption efficiency, Q_{abs}, is proportional to the ratio of the particle radius to the wavelength of the incident radiation while the scattering efficiency, Q_{sca}, is related to the fourth power of this ratio. Specifically, $Q_{ext} \approx Q_{abs} = 4\chi\mathrm{Im}\{-K\}$, so the attenuation in dBkm^{-1} due to cloud particles can be written

$$\kappa_c = k_c w = 0.4343\frac{6\pi}{\rho\lambda}\mathrm{Im}\{-K\}w \tag{D.7}$$

where k_c is a coefficient expressed in dB km^{-1} (g m^{-3})$^{-1}$, w and ρ are the water content and density of particles of the species under consideration, and λ is the wavelength of

Table D.2: Parameters describing attenuation due to liquid and ice cloud particles at 14 and 94 GHz.

Parameter	Liquid						Ice	
	14 GHz			94 GHz			14 GHz	94 GHz
	-8°C	10°C	20°C	-8°C	10°C	20°C	-20°C	-20°C
n	5.39	6.89	7.44	2.53	3.04	3.34	1.78	1.78
k	3.03	2.78	2.41	1.23	1.75	2.04	.0007	0.003
Im{-K}	0.063	0.035	0.027	0.217	0.117	0.153	.0003	0.001
k_c	0.239	0.135	0.102	5.72	4.68	4.05	.0011	0.029

the incident radiation. Table D.2 summarizes real and imaginary parts of the refractive index, $\mathrm{Im}\{-K\}$, and k_c for liquid and ice particles at selected temperatures. Due to their rigid lattice structure, ice particles have very small imaginary refractive indices and do not absorb radiation. As a result, attenuation by cloud ice is negligible at all microwave frequencies. Since typical cloud liquid water contents range from 0.1 kgm^{-3} in stratus to, at most, 2.0 kgm^{-3} in towering cumulus, attenuation by liquid cloud particles is also negligible at 14 GHz. At 94 GHz a 1km thick stratus cloud with a LWC of 0.1 kgm^{-3} gives rise to approximately 1 dB of attenuation, already significant. Attenuation from thick cumuli may exceed 50 dB at 94 GHz, in some cases.

The effects of attenuation by rainfall can seldom be neglected at the frequencies characteristic of spaceborne radars. Figures D.3 and D.4 show the total attenuation, κ_p^{ext}, and its components due to scattering, κ_p^{sca} and absorption, κ_p^{abs}, as a function of rainrate for MP distributions of liquid and ice spheres, respectively. Unlike cloud-sized droplets, attenuation from liquid precipitation derives from a combination of both radiation absorbed and scattered away from the radar beam while scattering dominates attenuation from frozen precipitation. Regardless of phase, attenuation by precipitation increases by orders of magnitude with increasing frequency. Neglecting cloud and atmospheric gases, a 4km thick column of rainfall at 15.0 mmh^{-1} results in 3 dB of attenuation at 14 GHz compared to 43 dB at 94 GHz. This will play a critical role in the detection capabilities of each radar and will ultimately determine the range of rainfall intensities one might expect to retrieve with

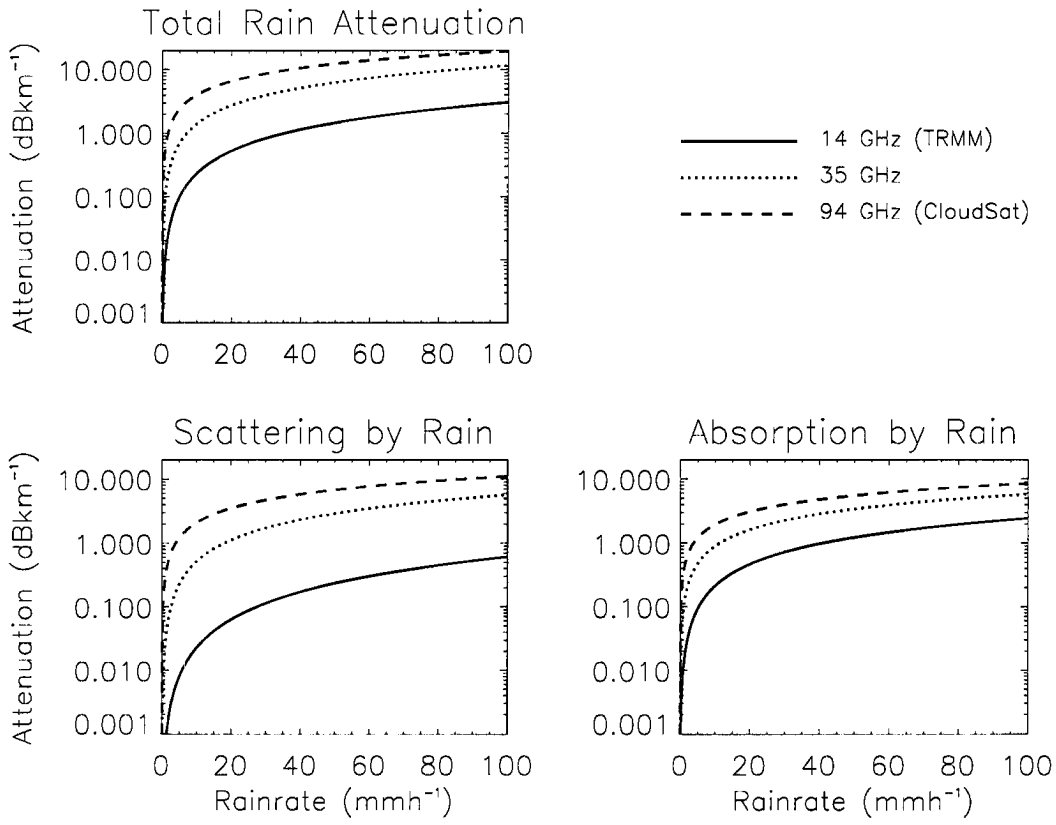

Figure D.3: Attenuation and its scattering and absorption components in dBkm^{-1} for liquid rain assuming a Marshall-Palmer DSD at 14, 35, and 94 GHz.

each system.

D.3.2 Rainfall Detection Capabilities of Spaceborne Radars

Equipped with a basic understanding of the fundamental principles governing the interaction of a radar beam with the atmosphere we can proceed to apply the forward model outlined in Section D.2 to simulate spaceborne radar observations of realistic cloud and precipitation structures. It is once again useful utilize the GPROF database of cloud and precipitation profiles for a number of reasons. The database provides a large collection of physically-based, CRM-generated cloud and precipitation profiles which span a wide

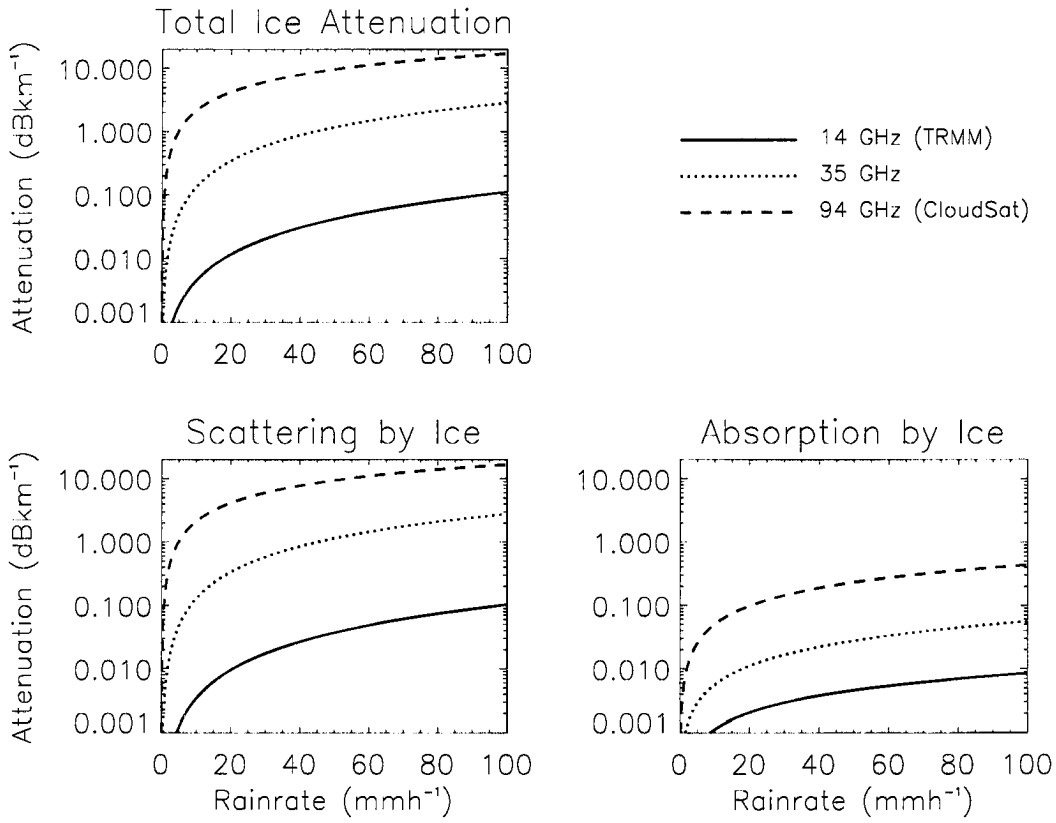

Figure D.4: As in Figure D.3 but for frozen hydrometeors.

range of rainfall intensities and generation mechanisms and its use furnishes some degree of continuity with the remainder of the dissertation. Also the hydrometeor contents in the database have been averaged over the field of view (FOV) of the 85.5 GHz channel of the TMI instrument which is approximately the same size as that of the TRMM PR[3]. This FOV is, however, much larger than ~1km footprint of the CloudSat CPR but no attempt is made to account for this since this study is primarily of a qualitative nature.

Using Equation (D.5) profiles of Z_{eff} have been modeled for all cloud structures in the database accounting for backscatter and attenuation from the four hydrometeor classes

[3]The PR scans between ±17° cross-track so its footprint varies from a circle of diameter 4.3km at nadir to an ellipse with a major axis of approximately 5km at the limbs.

as well as attenuation due to gases. The effective reflectivity in the range gate nearest the surface was then compared with an appropriate minimum detectable signal (MDS) for each radar to determine the range of profiles for which a surface rainfall signature can be detected with each. Following the instrument specifications summarized in Kummerow et al. (1998), the TRMM PR MDS is set to 18 dBZ while that of the CloudSat CPR is set to -30 dBZ after Miller and Stephens (2001). Preliminary discussions regarding the proposed 35 GHz frequency for GPM place its MDS at 8 dBZ.

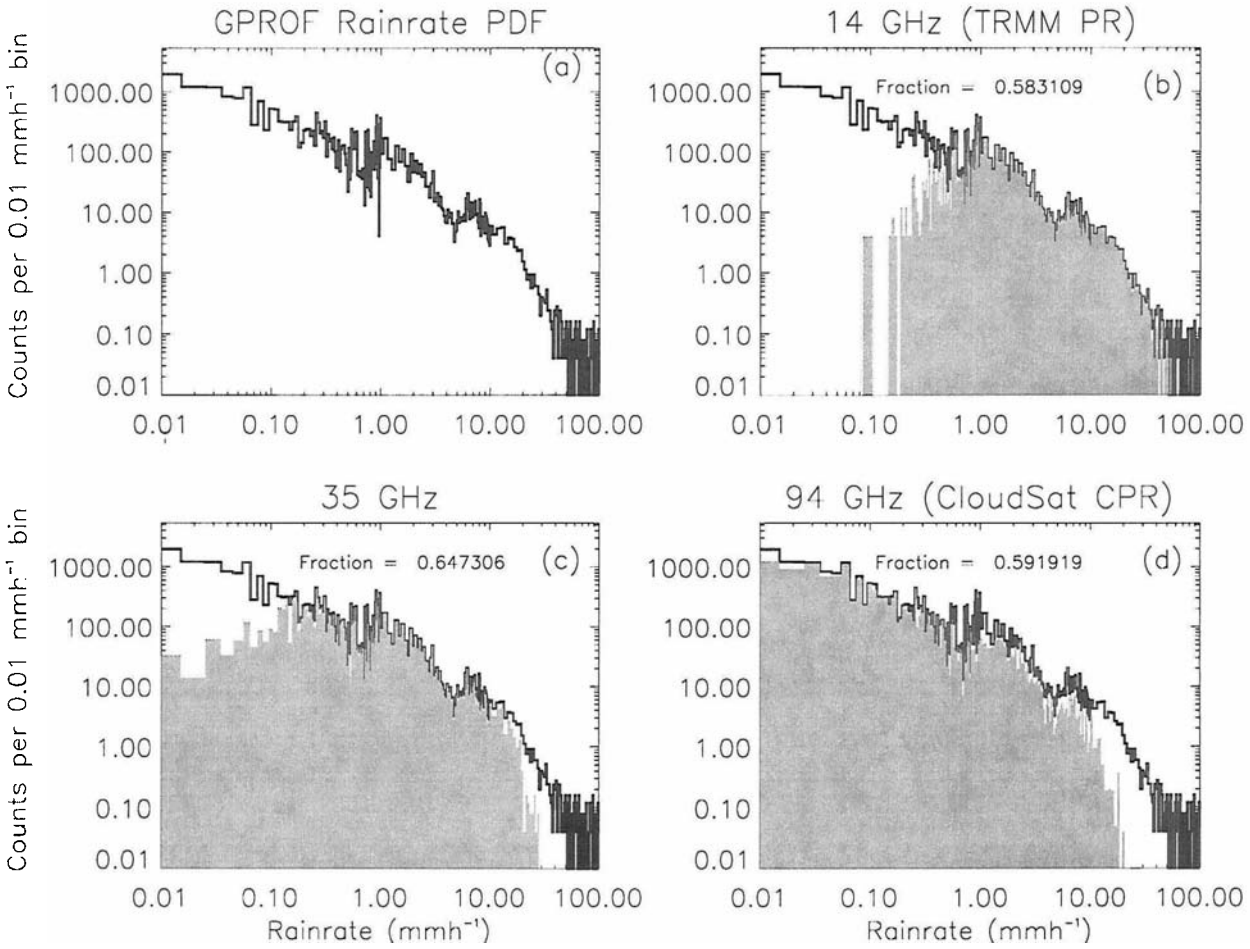

Figure D.5: (a) PDF of near-surface rainrate for the entire GPROF algorithm. (b)-(d) Fraction of profiles for which the reflectivity return from near-surface rainfall exceeds the radar minimum detectable signal for the TRMM PR, a hypothetical second frequency (35 GHz) on GPM, and the CloudSat CPR.

A PDF of near-surface rainrates from the GPROF algorithm is presented in Figure D.5a. The remaining plots illustrate the fraction of profiles (indicated by the shaded region) for which surface rainfall is detectable using each of the three radars. The different character of each radar is clearly evident. The TRMM PR is well-suited for observing rainfall between 1 and 35 mmh^{-1} but is unable to detect extremely light rain. The CPR, on the other hand, is capable of detecting cloud and all light rain up to approximately 4 mmh^{-1} but suffers from attenuation in heavier rainfall. The 35 GHz frequency provides an intermediate range of detection capable of observing a small fraction of very light rain scenes as well as moderate rainfall up to 11 mmh^{-1} before succumbing to the effects of attenuation.

A notable characteristic of the database is that its rainrate PDF heavily favors light rain. Since the database derives from realistic CRM simulations of tropical rainfall events which employ detailed treatments of microphysical and dynamical processes, we expect the resulting distribution of rainfall to be somewhat representative of nature, that is, after all, the basis for its use in GPROF. When comparing individual events, considerably more precipitation results from strong rain systems than their light rain counterparts but if the frequency of occurrence of each rain type resembles that in the database, light rain may account for a significant fraction of total tropical precipitation[4].

Figure D.6 displays the results in Figure D.5 in terms of the normalized cumulative probability distribution (CDF) of near-surface rainfall rate in the GPROF algorithm. Note that 55 % of the profiles in the database correspond to rain lighter than 1 mmh^{-1}. As a result, while the range of rainrates detectable at 14 GHz far exceeds that at 94 GHz, both the PR and CPR detect roughly the same percentage of total scenes in the database. It must be noted, however, that in terms of total precipitation, which is proportional to the integral under the curves, the PR detects a far greater fraction of the total rainfall at the surface than either of the other two radars.

[4]Extension to midlatitudes, as is proposed for the GPM, will likely result in a greater frequency of light rain events suggesting that the fraction of global rainfall which falls as light rain may be even more substantial.

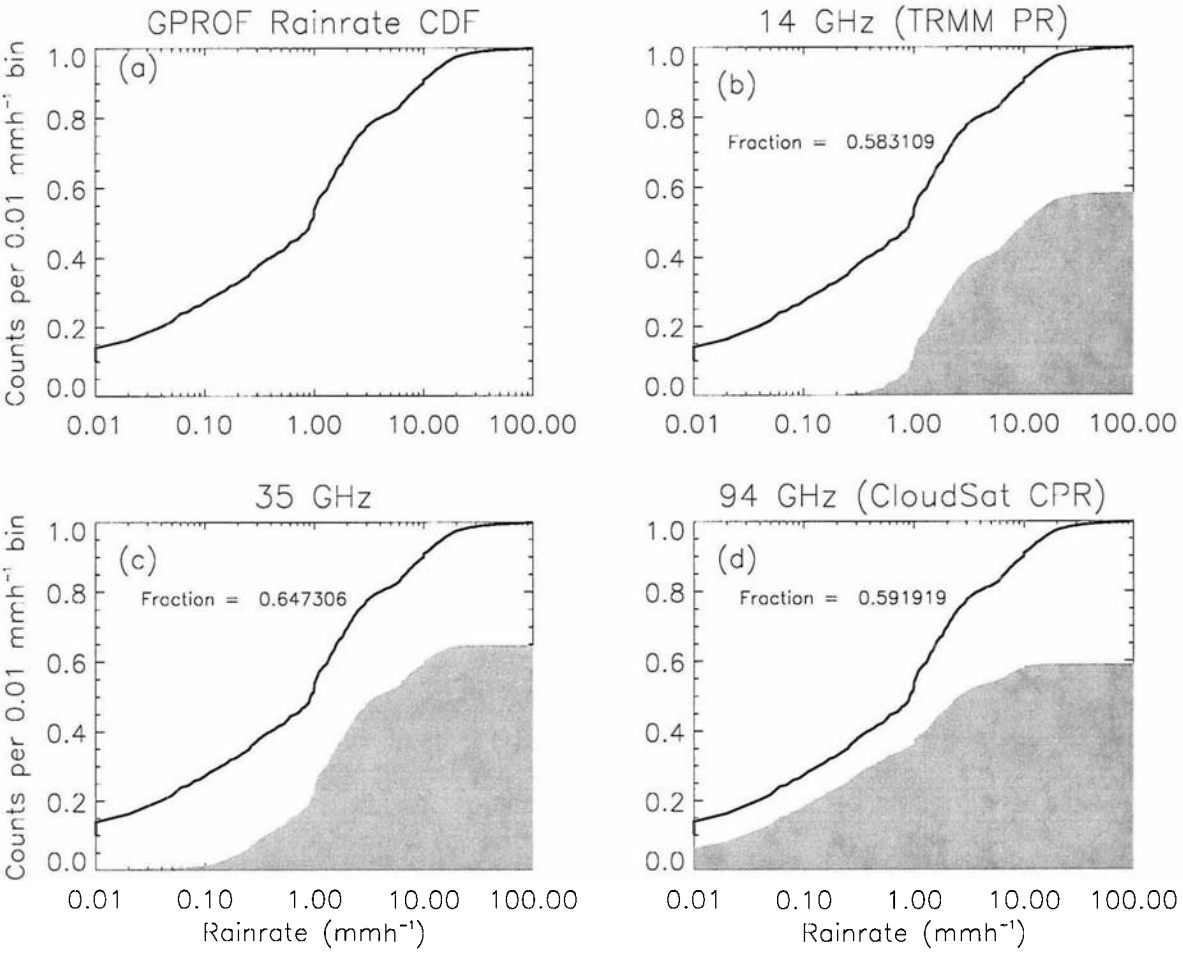

Figure D.6: The results displayed in Figure D.5 expressed in terms of normalized CDFs.

At the root of these results are the competing effects of backscatter and attenuation. Average two-way attenuation over the total atmospheric column and attenuation-corrected reflectivities from the rainfall layers nearest the surface are plotted as a function of near-surface rainrate in Figure D.7. By comparing average reflectivities with the MDS of each radar, an approximate range of detectable rainrates can be deduced which agrees quite well with the results presented above. At 94 GHz, for example, the average reflectivity drops below -30 dBZ for near-surface rainrates in excess 4 mmh^{-1} implying that, in an average sense, the CPR is capable of detecting surface rainfall in scenes characterized by rainrates below this threshold. At 14 GHz, on the other hand, average reflectivities

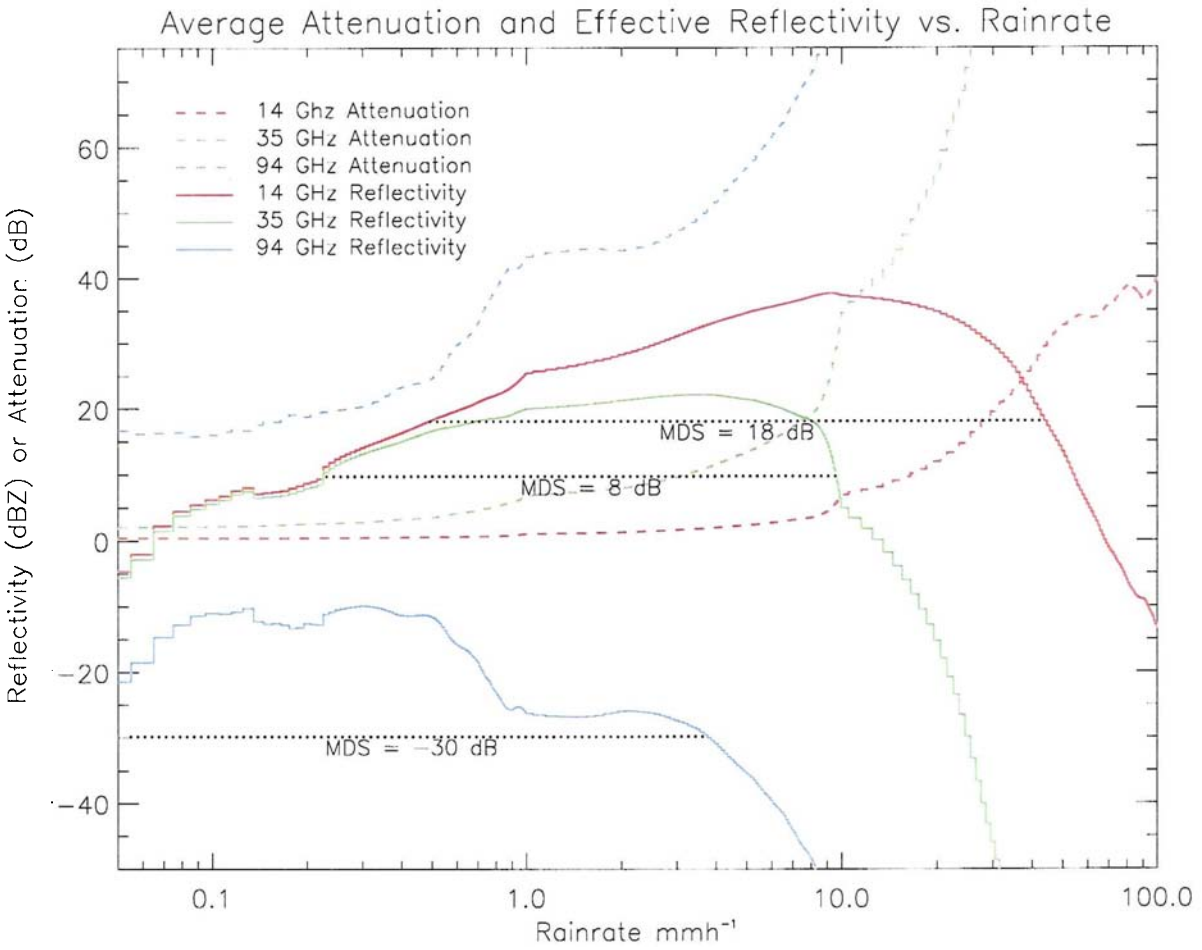

Figure D.7: Average attenuation and attenuation-corrected reflectivity from near surface rainfall plotted as a function of rainrate at 14, 35, and 94 GHz. Black dotted lines indicate the minimum detectable signals of each radar.

exceed 18 dBZ in rainfall between 0.6 and 45 mmh^{-1} indicative of the utility of the PR for measuring tropical rainfall. In addition, the figure clearly demonstrates the physical mechanism limiting the higher frequency radars to low rainrates, namely the overwhelming effects of attenuation, and that which limits the utility of the lower frequency TRMM PR in the extremely light rainfall regime, the relative transparency of the atmosphere to 14 GHz radiation. It is interesting to note the differences between Figure D.7 and the idealized unattenuated reflectivities shown in Figure D.2. The impact of attenuation from realistic cloud profiles is clearly a critical factor in determining the detection capabilities of any

radar.

It is also important to recall that these results apply only to the range gate nearest the surface which, in effect, maximizes the effects of attenuation. In profiles for which attenuation at 94 GHz precludes the detection of surface rainfall, the CPR may still offer rainfall and cloud information from higher levels in the atmosphere. The inability of the 14 GHz radar to detect light rain, however, is due to its relative transparency to the incident radar beam so very little information, if any, is expected from other atmospheric levels. This point is illustrated in Figures D.8-D.10 which present profiles of all reflectivities which lie above each radar's MDS for three different rainfall intensity ranges. All profiles with surface rainrates within $\pm$ 5 % of the value listed in the plot titles are presented.

The upper panel of Figure D.8 shows that in very light rain the TRMM PR provides limited information restricted to levels in and around the melting layer in some profiles while receiving no discernible signal in others. Rainfall in the lowest 2km of the atmosphere is largely missed at 35 GHz also. The CloudSat CPR, on the other hand, is designed to measure cloud and receives strong backscatter signals from all profiles including a significant fraction of the ice clouds region above the rainfall.

At 3 mmh^{-1} (middle panel) all three radars detect a majority of the near-surface rainfall. The PR receives a near-surface signal from all profiles while the 35 GHz radar misses only a few profiles characterized by geometrically thick cloud and precipitation profiles with appreciable signals extending through the top model layer at 18km. At 94 GHz the more severe attenuation results in a greater fraction of cases where the signal at the surface is completely blocked by the cloud and precipitation above it but in all but a few cases, the radar receives a discernible signal down to the 3km level. The bottom panel, which illustrates profiles with surface rainrates of 20 mmh^{-1}, is the antithesis of the top panel. The surface rain signal is blocked for only a single profile at the frequency of the PR, reflecting its design for tropical rainfall measurements. Both the 35 and 94 GHz radars suffer from

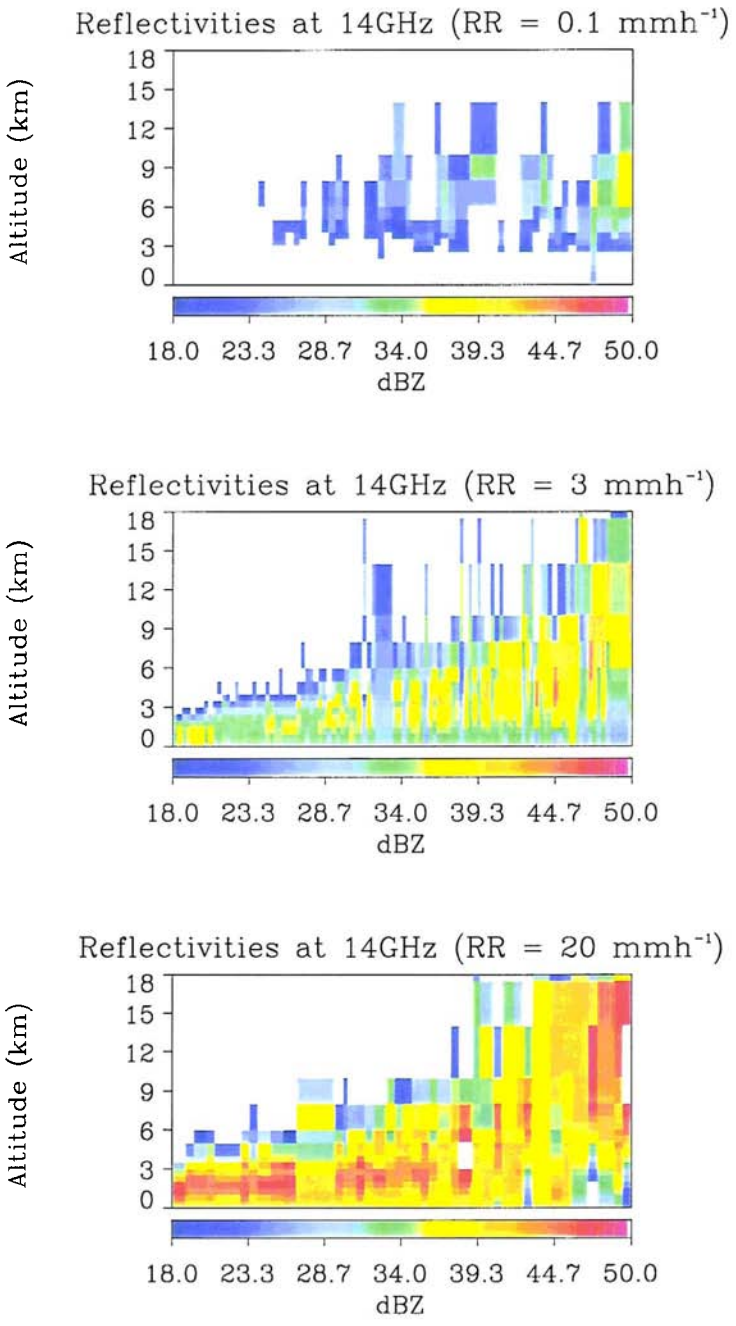

Figure D.8: Profiles of radar reflectivity at 14 GHz for GPROF cloud structures corresponding to extremely light rain (top), light rain (middle), and moderate to heavy rain (bottom).

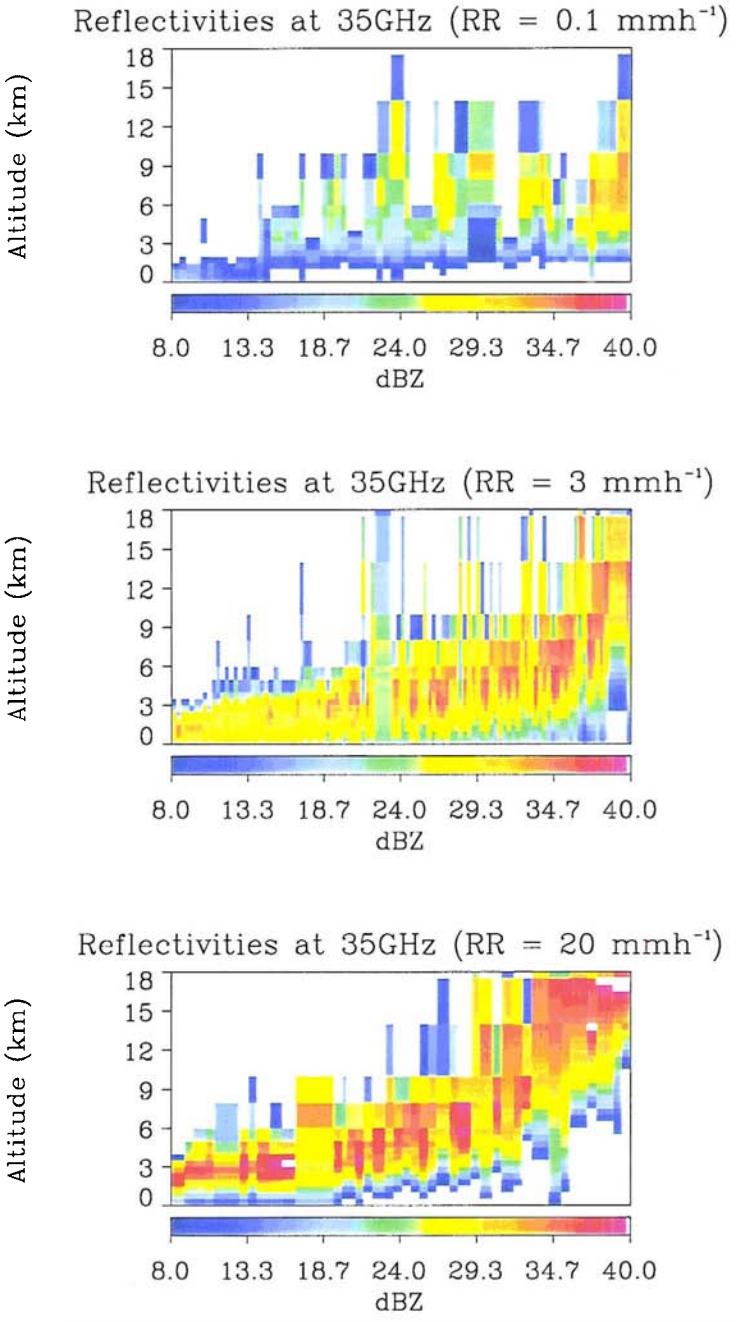

Figure D.9: As in Figure D.8 but at 35 GHz.

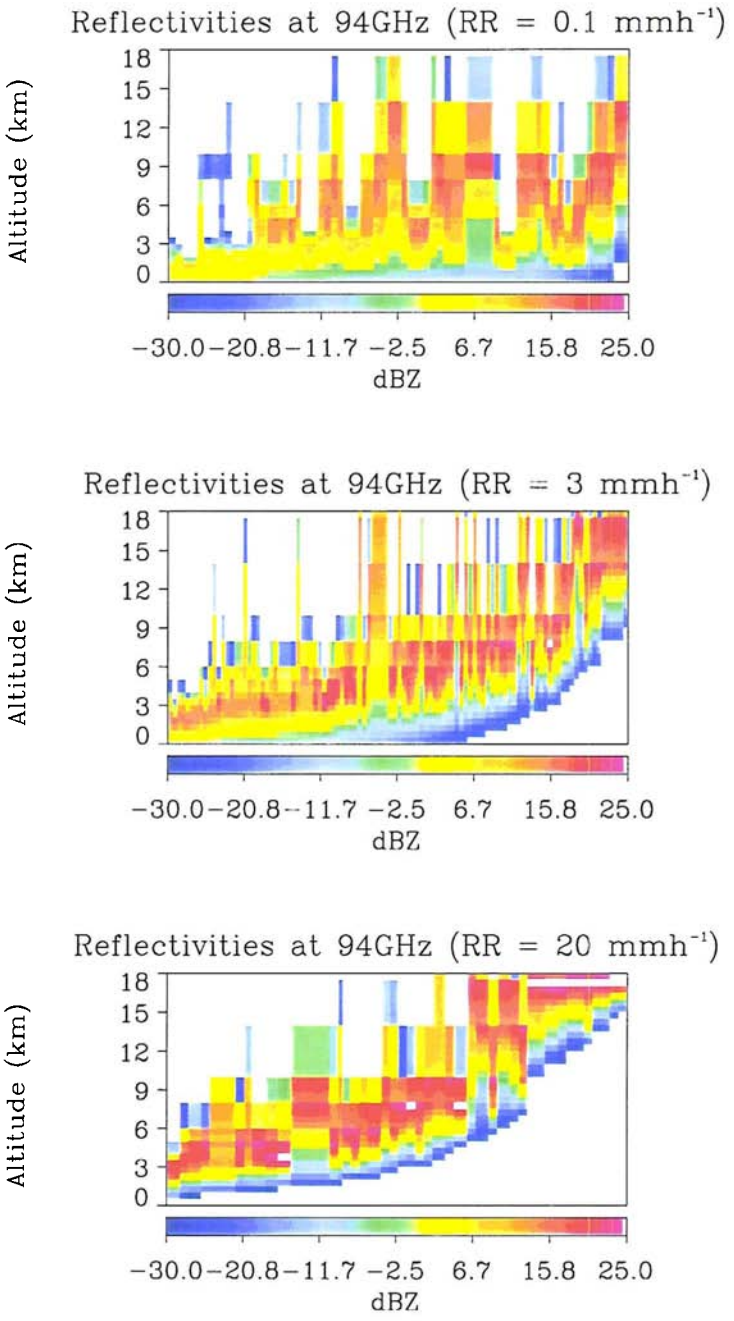

Figure D.10: As in Figure D.10 but at 94 GHz.

attenuation effects at this rainrate. At 35 GHz, the surface rainfall signal is completely attenuated in more than half of the cases but information is obtained down to 1.5 km for 75 % of the profiles. Remarkably, despite the strong attenuation, the CloudSat CPR is able to detect rainfall down to at least 3 km in 50 % of the cases. Even so, the CPR does not detect rainfall in the lowest range gate for any of the profiles at this rainfall intensity. Nevertheless, one could envision making some simplifying assumptions regarding the vertical distribution of precipitation between the lowest detectable level and the surface in order to obtain an, albeit crude, estimate of the near-surface rainrate even in high attenuation. With the recent confirmation of the CloudSat mission, this idea warrants further study at least in an experimental capacity.

Figure D.11 illustrates the individual components which comprise the attenuation at each frequency for two different cloud and rainfall profiles each of which results in a surface rainrate of approximately 5 mmh^{-1}. Both the effects of attenuation from each hydrometeor class as well as the principal contributions to the total attenuation as a function of height are highlighted at each frequency. The importance of the vertical distribution of cloud and precipitation, in particular, the depth of the liquid precipitation column, in determining the signal received at the radar is evident. The relatively shallow precipitation in the upper three plots results in less than half the attenuation of the deeper precipitation column in the lower three. At 94 GHz this amounts to a difference of almost 60 dB and wholly determines whether or not the radar can detect the near-surface rainfall. This strong influence of cloud and precipitation vertical structure preclude us from assigning rigid quantitative limits on the range of detectable rainrates, requiring, instead, that we draw only the general qualitative conclusions noted above regarding the capabilities of each radar. Furthermore, there is an important distinction between merely detecting rainfall and accurately determining its intensity. The remainder of this appendix is dedicated to the design and implementation of a new inversion algorithm for estimating rainrate profiles from spaceborne radars in gen-

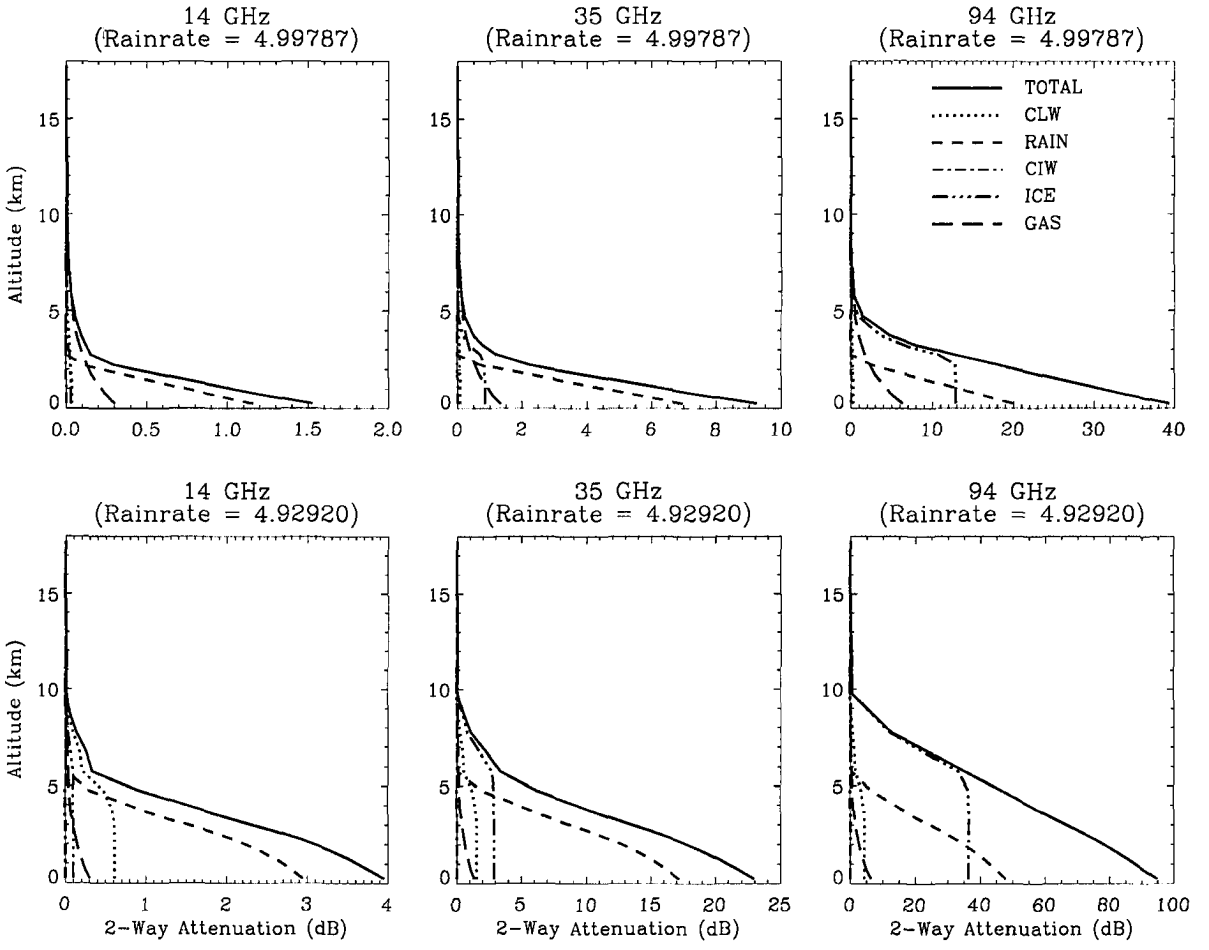

Figure D.11: Profiles of attenuation at 14, 35, and 94 GHz from each of the GPROF hydrometeor classes for two distinct profiles of rainfall both characterized by the same surface rainrate (5 mmh^{-1}).

eral. Through synthetic retrievals, discussed below, we hope to gain insight into the rainfall measurement capabilities of each radar.

D.4 Optimal Estimation Approach to Inversion

Many radar algorithms assume a size distribution and Rayleigh scattering to obtain relations of the form $Z = aR^b$ and $k = \alpha R^\beta$ which are directly invertible to obtain rainrate given radar reflectivity measurements. These methods have the advantage that they cast the problem into a simple analytical form, which results in a computationally quick and

relatively simple retrieval algorithm. These assumptions also lead to two potential sources of uncertainty: (1) the assumption of a DSD strongly influences the values of a, b, α, and β and (2) the Rayleigh assumption is not valid for radars with frequencies in excess of 10 GHz, a characteristic of both the TRMM PR and CloudSat CPR. In addition, the use of such functions precludes the addition of information from alternative sources such as passive microwave sensors and makes estimates of retrieval uncertainty difficult. Here we apply a significantly different technique to invert Equation (D.5) based on the works of Rodgers (1976, 1990) and Marks and Rodgers (1993) and applications of their work by Engelen and Stephens (1999) and Miller et al. (2000). Within the constructs of this approach we are able to maintain a high degree of generality in the problem which allows one to vary assumed particle size and shape and facilitates the addition of complementary information from different sensors if so desired.

D.4.1 Basic Theory

Denoting the forward model in Equation. (D.5) by F, a general profile of radar reflectivities, $\mathbf{Z}$, can be expressed as

$$\mathbf{Z} = F(\mathbf{R}, \mathbf{b}) + \epsilon_Z \tag{D.8}$$

where ϵ_Z is a vector of measurement uncertainties. For the purpose of illustrating the method, we cast the retrieval in terms of the vertical profile of rainrate $\mathbf{R}$ (in mmh^{-1}), representing all other parameters in the radar forward model by $\mathbf{b}$. This choice is purely arbitrary and the algorithm could, equivalently, be developed in terms of any other set of parameters which completely describe the DSD. An alternate formulation may be particularly useful when other observations are available to supplement the reflectivities to constrain the shape of the size distribution. In either case, an appropriate F to be used in the retrieval can be selected from criteria such as rain type, freezing level, or the presence of a bright band and uncertainties in the parameter vector, $\mathbf{b}$, must be explicitly accounted for in the

inversion approach.

Our problem is to estimate the rainrate profile which most likely produced a given observed profile of reflectivity. Following Olson et al. (1996), the optimal rainrate profile is given by

$$E(\mathbf{R}) = \int \mathbf{R}\, pdf(\mathbf{R}) d\mathbf{R} \tag{D.9}$$

where $pdf(\mathbf{R})$ is a probability density function proportional to the conditional probability that $\mathbf{R}$ is the true atmospheric rainrate profile given the observed reflectivity profile, $P(\mathbf{R} = \mathbf{R}_{true} | \mathbf{Z}_{true} = \mathbf{Z})$. Invoking Bayes' theorem, the probability density function can be recast as a product of the probability of observing a reflectivity profile, $\mathbf{Z}$, given a simulated reflectivity profile, $F(\mathbf{R})$, and the *a priori* probability that $\mathbf{R}$ is the true rainrate profile

$$pdf(\mathbf{R}) \propto P(\mathbf{Z}|F(\mathbf{R}))P_a(\mathbf{R}) \tag{D.10}$$

Some assumption is now required regarding the shape of the probability distributions $P(\mathbf{Z}|F(\mathbf{R}))$ and $P_a(\mathbf{R})$. Jaynes (2001) argues that, according to the Principle of Maximum Entropy, the Gaussian distribution is the "most honest" representation of errors if only the mean and variance of a probability distribution are known. Alternate distributions, unless rigorously justifiable, add spurious information to the retrieval therefore biasing the results. Since we have no compelling reason to assume any particular shape for the error distributions, Gaussian statistics will be adopted so that only distribution mean and variance information are introduced in the retrieval. Under this assumption,

$$P(\mathbf{Z}|F(\mathbf{R})) \propto exp[-\frac{1}{2}(F(\mathbf{R}) - \mathbf{Z})^T \mathbf{S}_Z^{-1}(F(\mathbf{R}) - \mathbf{Z})] \tag{D.11}$$

where $\mathbf{S}_Z$ is the total error covariance matrix representing the sum of the measurement and model errors. Similarly, if $\mathbf{R}_a$ represents some *a priori* guess at a rainrate profile, the

probability of finding the true atmospheric rainrate profile $\mathbf{R}$ will be expressed as

$$P_a(\mathbf{R}|\mathbf{R}_a) \propto exp[-\frac{1}{2}(\mathbf{R}-\mathbf{R}_a)^T\mathbf{S}_a^{-1}(\mathbf{R}-\mathbf{R}_a)] \tag{D.12}$$

where $\mathbf{S}_a$ is the error covariance matrix associated with the *a priori* guess. The "best" estimate of a rainfall profile given these two probabilities is that which maximizes the joint probability

$$\begin{aligned} P(\mathbf{Z}|F(\mathbf{R}))P_a(\mathbf{R}|\mathbf{R}_a) \quad &\propto \quad exp\Big[-\frac{1}{2}[(F(\mathbf{R})-\mathbf{Z})^T\mathbf{S}_Z^{-1}(F(\mathbf{R})-\mathbf{Z}) \\ &+ \quad (\mathbf{R}-\mathbf{R}_a)^T\mathbf{S}_a^{-1}(\mathbf{R}-\mathbf{R}_a)]\Big] \end{aligned} \tag{D.13}$$

or, alternatively, minimizes the scalar cost function

$$\Phi(\mathbf{R},\mathbf{R}_a,\mathbf{Z}) = (F(\mathbf{R})-\mathbf{Z})^T\mathbf{S}_Z^{-1}(F(\mathbf{R})-\mathbf{Z}) + (\mathbf{R}-\mathbf{R}_a)^T\mathbf{S}_a^{-1}(\mathbf{R}-\mathbf{R}_a) \tag{D.14}$$

with respect to the rainrate profile $\mathbf{R}$. The resulting rainrate profile is

$$\hat{\mathbf{R}} = \mathbf{R}_a + \mathbf{S}_a\mathbf{K}^T\mathbf{S}_Z^{-1}(\mathbf{Z}-F(\hat{\mathbf{R}})) \tag{D.15}$$

Here $\mathbf{K} = \partial F/\partial\mathbf{R}$ is the Kernel or weighting function representing the sensitivity of the model to the parameter being retrieved. From Equation (D.15) it is clear that a model which is very sensitive to the rainfall rate profile is desirable since the Kernel functions weight the measurement portion of the retrieval. It is worth noting that under the assumptions of uncorrelated, unbiased, Gaussian error statistics, the maximum-likelihood estimate computed here is identical to the minimum variance solution (Daley, 1991) which guarantees that $\mathbf{R}$ estimated using Equation (D.15) will be the best possible fit to the observations given our uncertainty estimates.

Equation (D.15) is implemented numerically through a Newtonian iteration scheme

$$\hat{\mathbf{R}}_{i+1} - \hat{\mathbf{R}}_i = \mathbf{S}_{\hat{R}} \left[\mathbf{K}_i^T \mathbf{S}_Z^{-1} (\mathbf{Z} - F(\hat{\mathbf{R}}_i)) + \mathbf{S}_a^{-1} (\mathbf{R}_a - \hat{\mathbf{R}}_i) \right] \tag{D.16}$$

where $\mathbf{S}_{\hat{R}} = (\mathbf{S}_a^{-1} + \mathbf{K}_i^T \mathbf{S}_Z^{-1} \mathbf{K}_i)^{-1}$ is the covariance matrix of the retrieved rainfall profile. The iteration proceeds until such time as the covariance-weighted square difference between successive estimates is much less than the total number of independent variables being retrieved, in this case the number of layers in the atmosphere, N_l

$$(\hat{\mathbf{R}}_{i+1} - \hat{\mathbf{R}}_i)^T \mathbf{S}_{\hat{R}}^{-1} (\hat{\mathbf{R}}_{i+1} - \hat{\mathbf{R}}_i) << N_l \tag{D.17}$$

D.4.2 Error Diagnostics

The preceding optimal estimation formulation of the inversion problem furnishes a number of useful diagnostics to measure the quality of the results. The most important of these is the covariance matrix of the retrieved parameters

$$\mathbf{S}_{\hat{R}} = (\mathbf{S}_a^{-1} + \mathbf{K}_i^T \mathbf{S}_Z^{-1} \mathbf{K}_i)^{-1} \tag{D.18}$$

Equation (D.18) provides a direct estimate of the uncertainty in the retrieved rainrate profile due to uncertainties associated with the *a priori* profile, forward model, and measurements themselves. The diagonal elements of $\mathbf{S}_{\hat{R}}$ give the variance for the retrieved rainrate at each level while the off-diagonal elements indicate correlations between the uncertainties in retrieved rainrate at different levels. Returning to the details of the forward model, F, for example, uncertainties in the parameter vector $\mathbf{b}$, such as those associated with assumptions regarding the highly variable DSD, must be accounted for in the measurement and model covariance matrix, $\mathbf{S}_Z$. An appropriate $\mathbf{S}_Z$ dictates the reliability of the observations and forward model in the retrieval and ensures a reliable estimate of retrieval accuracy through

Equation (D.18).

Defining the matrix

$$\mathbf{A} = \mathbf{S}_{\hat{R}}\mathbf{K}_i^T\mathbf{S}_Z^{-1}\mathbf{K}_i \tag{D.19}$$

Equation (D.16) can be written

$$\hat{\mathbf{R}}_{i+1} - \hat{\mathbf{R}}_i = \mathbf{A}\mathbf{K}_i^{-1}(\mathbf{Z} - F(\hat{\mathbf{R}}_i)) + (\mathbf{I} - \mathbf{A})(\mathbf{R}_a - \hat{\mathbf{R}}_i) \tag{D.20}$$

In this way, the contributions to the retrieved profile from the measurements and from the *a priori* profile are isolated. In an ideal retrieval, the so-called "*a priori* matrix", $\mathbf{A}$, will be an identity indicating that the retrieval is based exclusively on the measurements. Departures from the identity represent a combination of influences from the *a priori* data and reflectivity measurements from different atmospheric levels on the rainrate retrieved at a given level.

Finally, one can investigate the validity of the assumption of Gaussian error statistics using the χ^2-test. If the assumption is valid,

$$\chi^2 = (F(\hat{\mathbf{R}}) - \mathbf{Z})^T\mathbf{S}_Z^{-1}(F(\hat{\mathbf{R}}) - \mathbf{Z}) + (\hat{\mathbf{R}} - \mathbf{R}_a)^T\mathbf{S}_a^{-1}(\hat{\mathbf{R}} - \mathbf{R}_a) \tag{D.21}$$

will be approximately equal to the number of independent parameters in the retrieval, in this case N_l. In cases where our physical assumptions, particularly those relating to the DSD, are grossly different from those being observed or in the event that the Gaussian distribution and assumed variances do not properly characterize uncertainties in the measurements and model, χ^2 will be much greater than N_l. In global applications, a significant number of retrievals characterized large χ^2 is indicative of over-optimistic error covariance assumptions in the algorithm, such as a misrepresentation of the DSD variability encountered by the satellite. On the other hand, if χ^2 is much less than N_l, the measurement, model, and/or *a priori* covariances may have been over estimated and $\mathbf{S}_{\hat{R}}$ will correspondingly overestimate

Table D.3: Z-R and k-R parameters used to initialize rainfall retrieval. The distinction between the "high" and "low" fits occurs at 17.8 mmh^{-1} at 14 GHz and 11.0 mmh^{-1} at 94 GHz.

Parameter	14 GHz (low)	14 GHz (high)	94 GHz (low)	94 GHz (high)
a	155.1	243.4	29.2	42.2
b	1.61	1.45	0.71	0.55
α	0.014	0.020	0.68	0.88
β	1.23	1.10	0.78	0.67

the retrieval uncertainty.

D.4.3 Algorithm Initialization

There is generally no "average" climatological profile of rainfall available to use as an *a priori* guess. As a result, we resort to the more traditional relationships

$$Z = aR^b \quad ; \qquad k_{ext} = \alpha R^\beta \tag{D.22}$$

to obtain $\mathbf{R}_a$ and we use this rainfall profile to initialize the iteration. Table D.3 summarizes parameters determined assuming a MP size distribution of spherical raindrops and Mie theory for the backscatter cross-sections at 14 and 94 GHz. Due to the departure from the linear relationship as Mie effects become important, the fit was divided into two regions to improve results. The fits at 94 GHz are illustrated in Figures D.12 and D.13.

The CORRAL retrieval procedure is illustrated in Figure D.14 and can be summarized as follows:

1. Infer an initial rainrate and extinction coefficient for the upper-most rain layer using the appropriate Z-R and k-R relations.

2. Correct the measured reflectivity in the next layer for the attenuation due to the one above it and determine an initial rainrate and extinction coefficient for that layer.

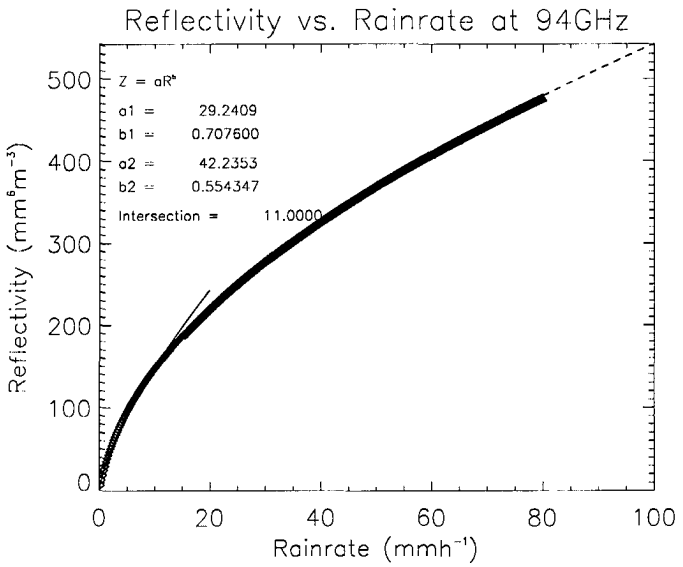

Figure D.12: Reflectivity vs. rainrate for a MP distribution of spherical raindrops.

3. Repeat for all layers, correcting the measured reflectivity of each layer for the attenuation due to all layers above it. In the event of a negative or unreasonably large rainrate which can result from the instability of the HB method, rainrates are artifically set either to 0.01 or to a maximum value assigned based on the detection capabilities of the radar.

4. Using this initial profile of rainrate, simulate reflectivities using the radar forward model (Equation (D.5)).

5. Compute a new rainrate profile using Equation (D.16).

6. Iterate until Equation (D.17) is satisfied.

D.5 Synthetic Retrievals

In order to illustrate the utility of the model, reflectivity profiles with 0.5 km vertical resolution were computed for all cloud and rainrate profiles in the GPROF database assuming

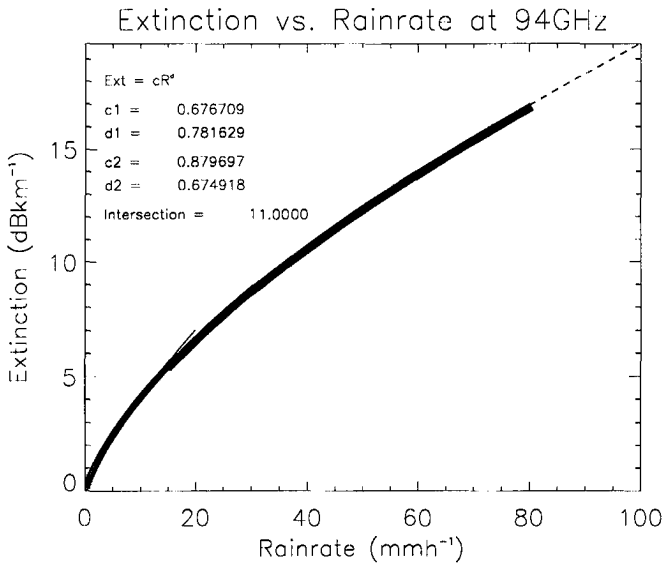

Figure D.13: Extinction vs. rainrate for a MP distribution of spherical raindrops.

a MP distribution of spherical raindrops and cloud droplets[5]. These reflectivity profiles were then perturbed by adding a randomly distributed noise component and run through the CORRAL algorithm to recover the original profile. The noise was set to 1 dB (or 23 %) for profiles with surface rainrates less than 20 mmh^{-1} and 2 dB (or 46 %) for higher rainrates to reflect the fact that errors due to particle shape are more significant for larger raindrops than smaller ones (Green, 1975). In the retrieval, the measurement covariance matrix is assumed to be diagonal with elements equal to 1.0 dB^2 (or 4.0, where applicable). In light of the concerns discussed earlier regarding the use of such relationships, we assume a variance of 25.0 mm^2h^{-2} in all *a priori* rainrates and all correlations between errors at different levels are neglected. In this way, the retrieval is based far more heavily on the measurements and the *a priori* merely serves as an initial guess and an extremely weak positivity constraint on the retrieval. In addition, the assumption of high *a priori* variances minimizes errors incurred as a result of neglecting correlations between uncertainties at

[5]As noted previously, the database consists of approximately ten thousand cloud and rainfall profiles varying from non-precipitating cirrus and stratus clouds to heavily precipitating cumulonimbus cloud complexes and represents a wide range of conditions with which to test the CORRAL algorithm.

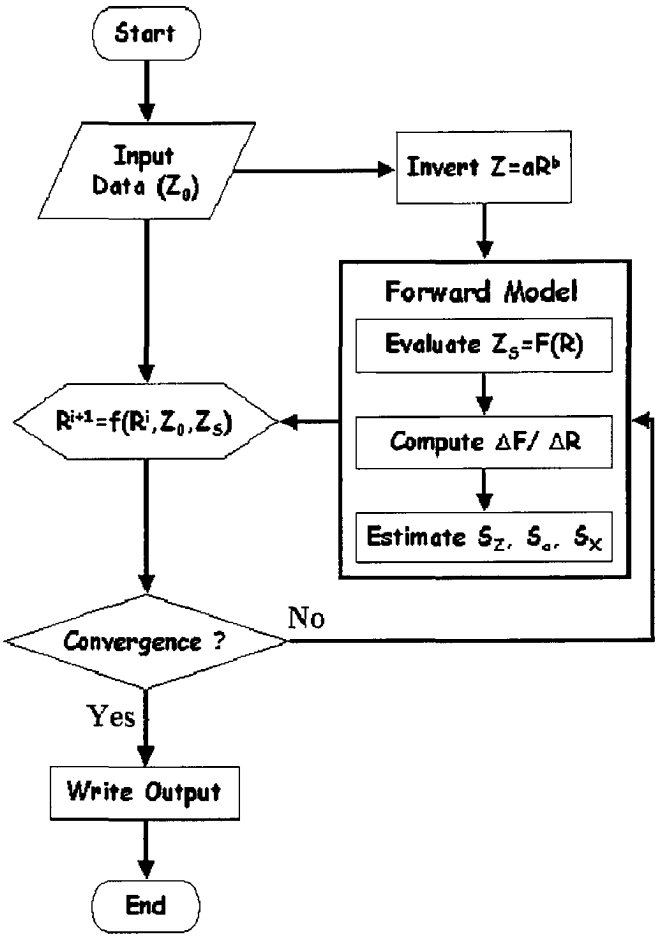

Figure D.14: The CORRAL retrieval algorithm.

different levels which are, in practice, extremely difficult to determine. In this appendix, results will focus on the 14 GHz TRMM PR and the 94 GHz CloudSat CPR. Readers interested in the performance of the CORRAL algorithm at the intermediate 35 GHz frequency proposed for GPM are directed to Appendix E.

A scatter plot of retrieved surface rainrate against the GPROF input at 14 GHz is presented in the Figure D.15. The results show excellent agreement for all rainrates below 40 mmh^{-1}. Significant attenuation by large raindrops at higher rainrates, however, degrades the quality of the retrievals. Figure D.16 shows similar results obtained from a retrieval

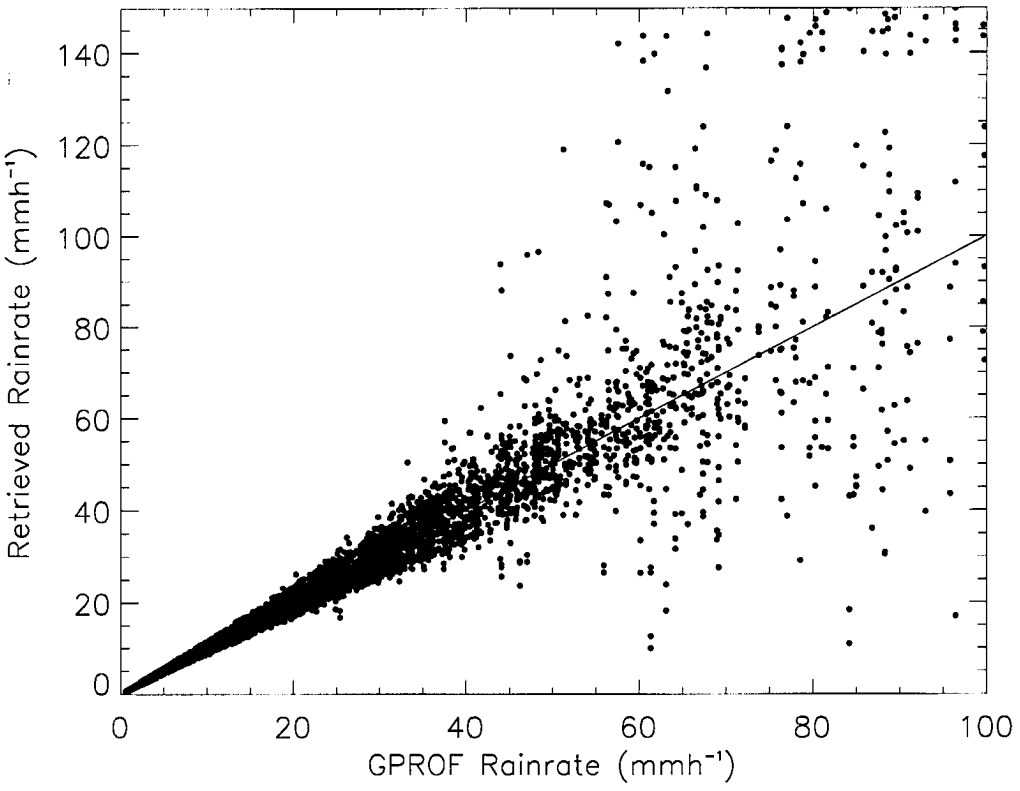

Figure D.15: Synthetic near-surface rainfall retrievals at 14 GHz.

using reflectivities at 94 GHz. Attenuation is severe for all rainfall at 94 GHz and only rainrates less than 1.5 mmh^{-1} are retrieved accurately at this frequency in the absence of additional information.

Figures D.17 and D.18 present the estimated error in the retrieved surface rainfall rate and the corresponding component of the *a priori* matrix at 14 GHz. Together, the two figures demonstrate that, under the present assumptions, the uncertainty in retrieved rainfall is below 30 percent for all profiles with surface rainrates between 0 and 40 mmh^{-1}. In heavier rain, the retrieval relies heavily on the *a priori* guess so, although the retrieval errors appear to be acceptable, the results do not reflect the information contained in the

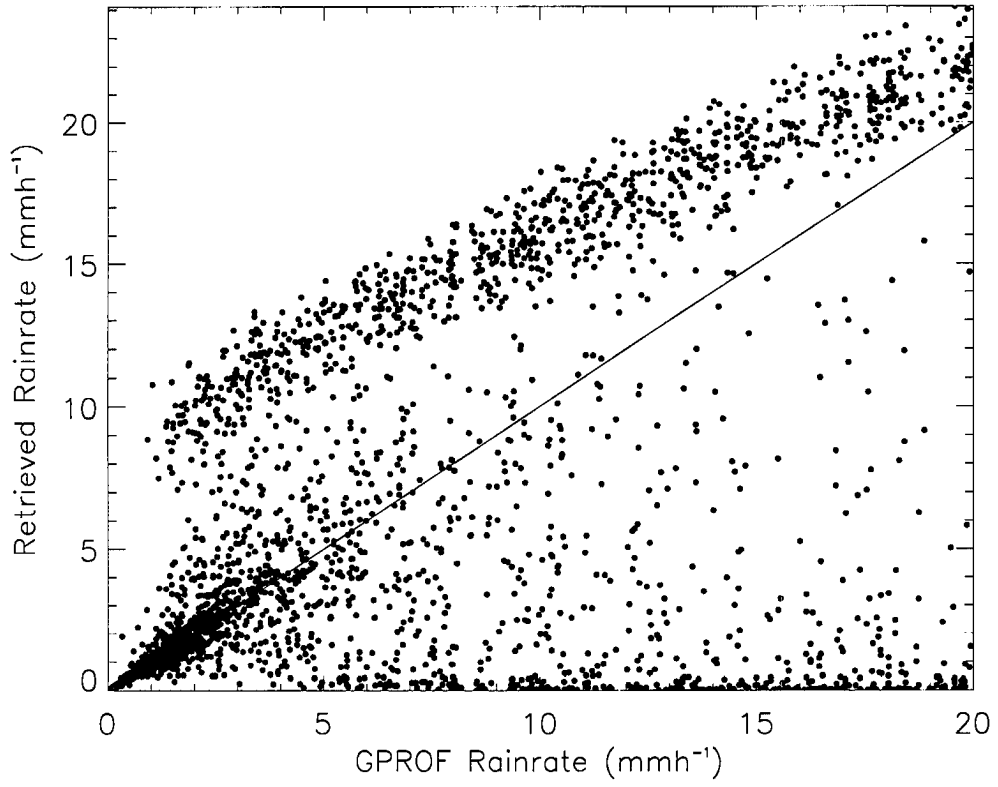

Figure D.16: As in Figure D.15 but for retrievals at 94 GHz.

measurements and must be discarded.

At 94 GHz, the enormous retrieval uncertainties illustrated in Figure D.19 demonstrate the fact that reflectivity measurements do not provide sufficient information to accurately determine surface rainfall rate. The fractional error only remains within tolerable limits up to about 1.0 mmh^{-1}. In heavier rain, uncertainties become large and differences in the vertical distribution of rainfall above the surface give rise to scatter in the results. Many of the 94 GHz retrievals also yield extremely high values of χ^2 (not shown) indicating that the retrieved profile of rainfall seldom attains satisfactory agreement with the observations.

These results may be attributed to the method adopted for applying the attenuation cor-

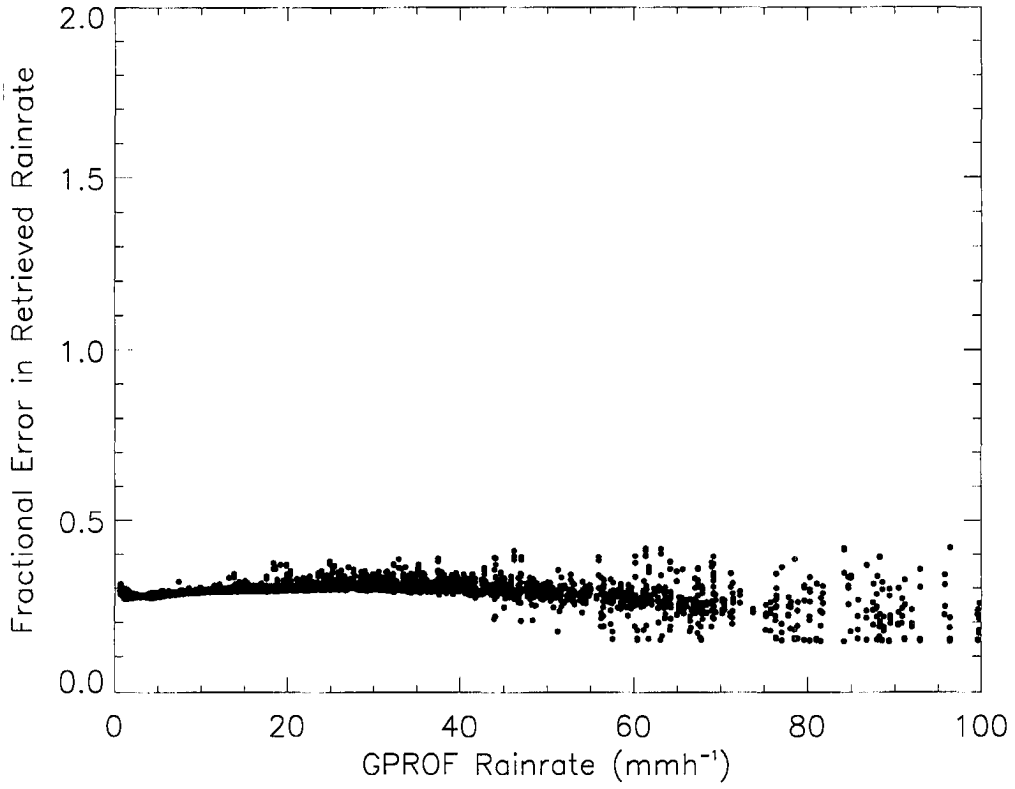

Figure D.17: Error in retrieved rainrate as a function of rainrate for the 14 GHz synthetic retrievals.

rection. Since the procedure, which is analogous to the HB method, first corrects the layers closest to the radar and then adjusts lower layers according to rainrates derived from these corrections, it leads to the propagation and magnification of errors as the algorithm proceeds to lower levels within the cloud. Figure D.21 supports this hypothesis. The figure shows rainrates retrieved at 94 GHz at 4.0 km, near the top of the liquid rain column. Although the retrievals exhibit some deviation from the input at high rainrate, the agreement is clearly far superior than that at the surface. Figures D.22 and D.23 show that the uncertainties in the retrieved rainrates are much smaller at 4.0 km and that the retrieval relies less heavily on the initial guess near the top of the cloud.

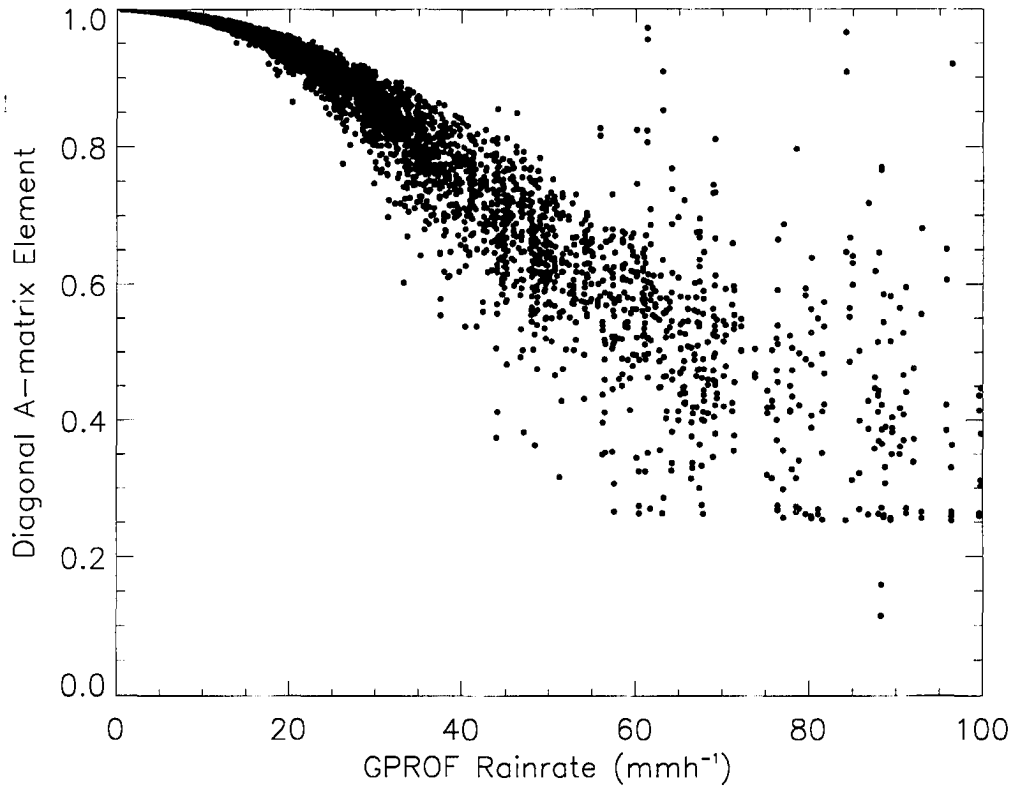

Figure D.18: Diagonal element of the *a priori* matrix corresponding to the surface rainrate bin as a function of rainrate for the 14 GHz retrievals.

D.6 Constraining the Retrieval

Due to the severity of attenuation by rainfall at high frequencies, it is not sufficient to rely exclusively on a profile of radar reflectivity to make estimates of rainfall profiles. Fortunately, many spaceborne platforms such as TRMM offer additional sources of information either from the radar itself or from other instruments. Most notable among these are the column-integrated precipitation water path (PWP) which can be estimated using microwave radiometers (see, for example, Fujita et al. (1985) and Alishouse et al. (1990)) and the PIA which can be determined from surface radar returns. Both the PWP and PIA complement

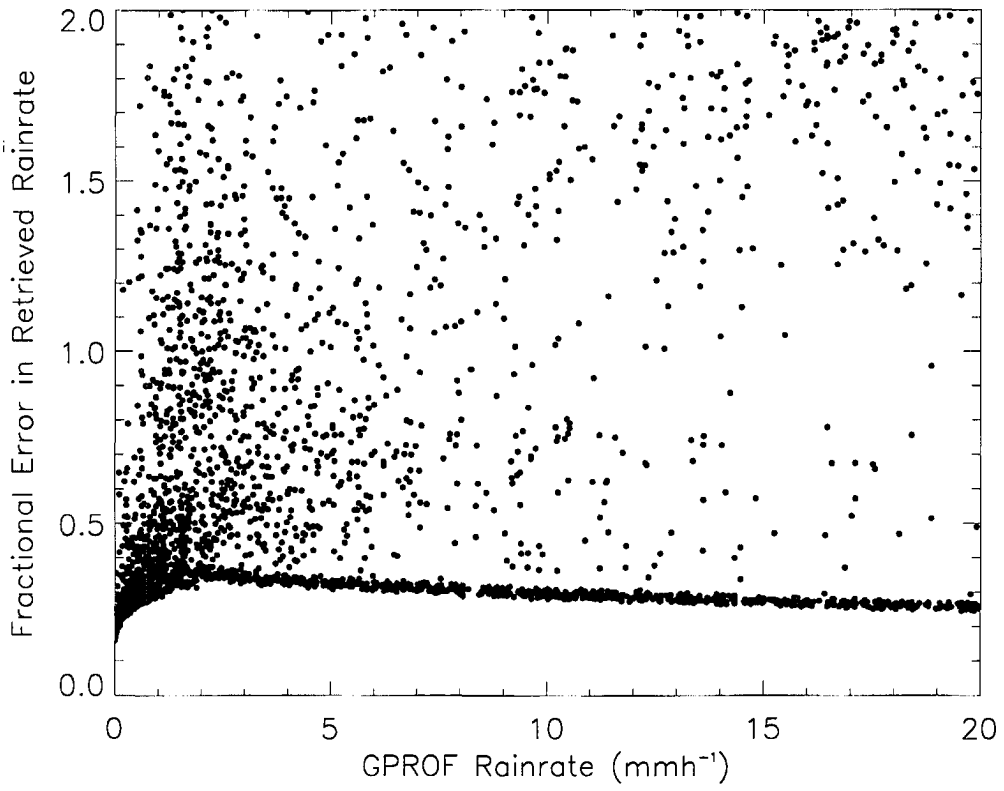

Figure D.19: As in Figure D.17 but at 94 GHz.

the radar reflectivity measurements in that they impose a constraint on the total attenuation through the rain column.

D.6.1 Theory

In the presence of either constraint, the cost function can be expressed as

$$\begin{aligned}\Phi(\mathbf{R},\mathbf{R}_a,\mathbf{Z}) &= (F(\mathbf{R})-\mathbf{Z})^T\mathbf{S}_R^{-1}(F(\mathbf{R})-\mathbf{Z}) \\ &+ (\mathbf{R}-\mathbf{R}_a)^T\mathbf{S}_a^{-1}(\mathbf{R}-\mathbf{R}_a)+\frac{(X_{sim}-X_{obs})^2}{\sigma_X^2} \end{aligned} \quad \text{(D.23)}$$

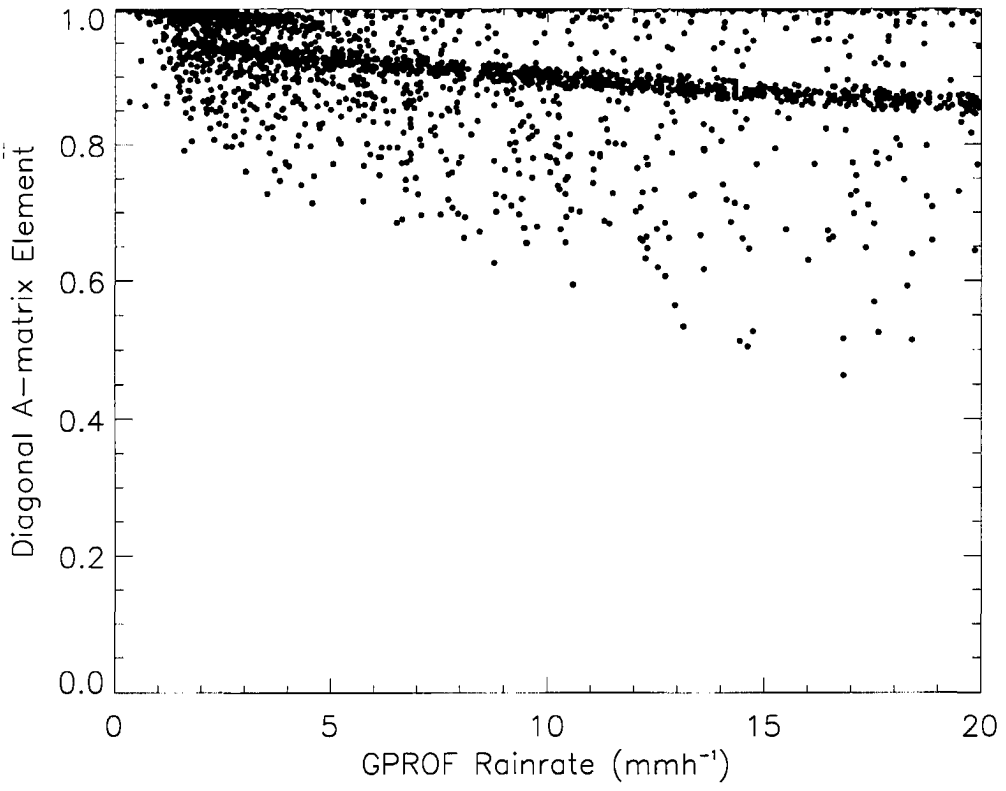

Figure D.20: As in Figure D.18 but at 94 GHz.

where X_{obs} represents the observed PWP or PIA with standard deviation σ_X. X_{sim} is the simulated PWP or PIA obtained by integrating the rainrate profile or its resulting attenuation, in height. Minimizing with respect to $\mathbf{R}$, we obtain

$$\hat{\mathbf{R}}_{i+1} = \mathbf{S}_{\hat{R}} \left[\mathbf{S}_a^{-1}\mathbf{R}_a + \mathbf{K}_i^T \mathbf{S}_Z^{-1}(\mathbf{Z} - F(\hat{\mathbf{R}}_i)) + \frac{1}{\sigma_X^2}\mathbf{L}_i \Delta z (X_{obs} - X_{sim} + \mathbf{L}_i^T \Delta z \hat{\mathbf{R}}_i) \right] \tag{D.24}$$

with $\mathbf{S}_{\hat{R}} = \left(\mathbf{S}_a^{-1} + \mathbf{K}_i^T \mathbf{S}_Z^{-1} \mathbf{K}_i + \frac{\Delta z^2}{\sigma_X^2} \mathbf{L}_i \mathbf{L}_i^T \right)^{-1}$. The vector, $\Delta z \mathbf{L}$, consists of the derivatives of X with respect to the rainrate at each level.

One measure of the strength of the constraint is to determine the relative contributions

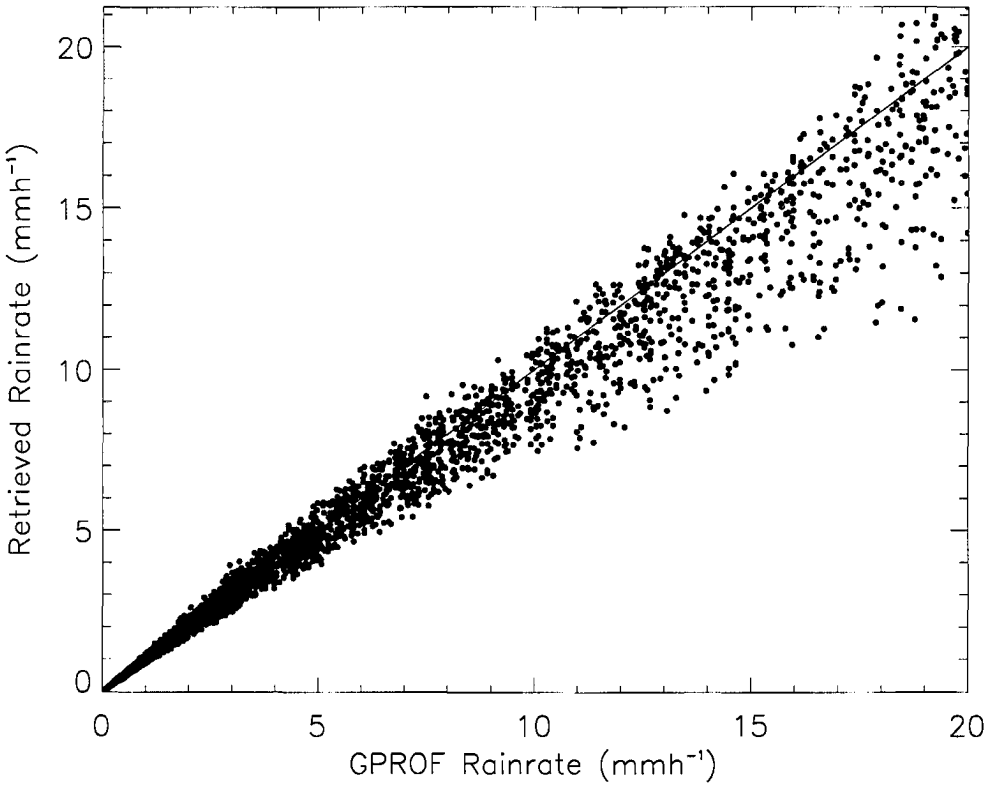

Figure D.21: As in Figure D.16 but at an altitude of 4.0 km.

of the measurements, *a priori* guess, and the constraint to the retrieval error covariance matrix, $\mathbf{S}_{\hat{R}}$. Defining

$$\mathbf{D}_Z = \mathbf{S}_{\hat{R}}\mathbf{K}^T\mathbf{S}_Z^{-1} \tag{D.25a}$$

$$\mathbf{D}_a = \mathbf{S}_{\hat{R}}\mathbf{S}_a^{-1} \tag{D.25b}$$

$$\mathbf{D}_X = \frac{\mathbf{S}_{\hat{R}}\mathbf{L}\Delta z}{\sigma_X^2} \tag{D.25c}$$

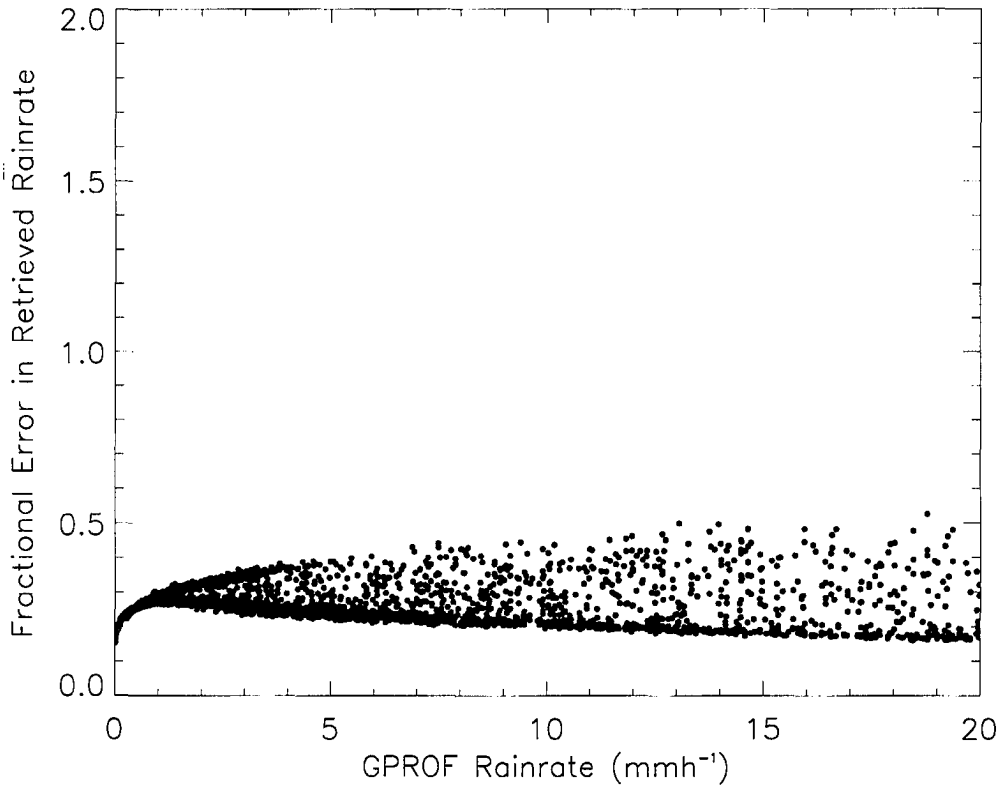

Figure D.22: As in Figure D.19 but at an altitude of 4.0 km.

the total retrieval error covariance matrix can be expressed as

$$\mathbf{S}_{\hat{R}} = \mathbf{D}_Z \mathbf{S}_Z \mathbf{D}_Z^T + \mathbf{D}_a \mathbf{S}_a \mathbf{D}_a^T + \mathbf{D}_X \mathbf{S}_X \mathbf{D}_X^T \tag{D.26}$$

where $\mathbf{S}_X$ is a diagonal matrix with σ_X^2 on the diagonal. Diagonal elements of each term represent the contributions of the measurements, *a priori* guess, and the constraint to the retrieval uncertainty making it possible to assess the relative strengths of the three components in determining the rainrate profile. In addition, the χ^2 test can, again, be employed to

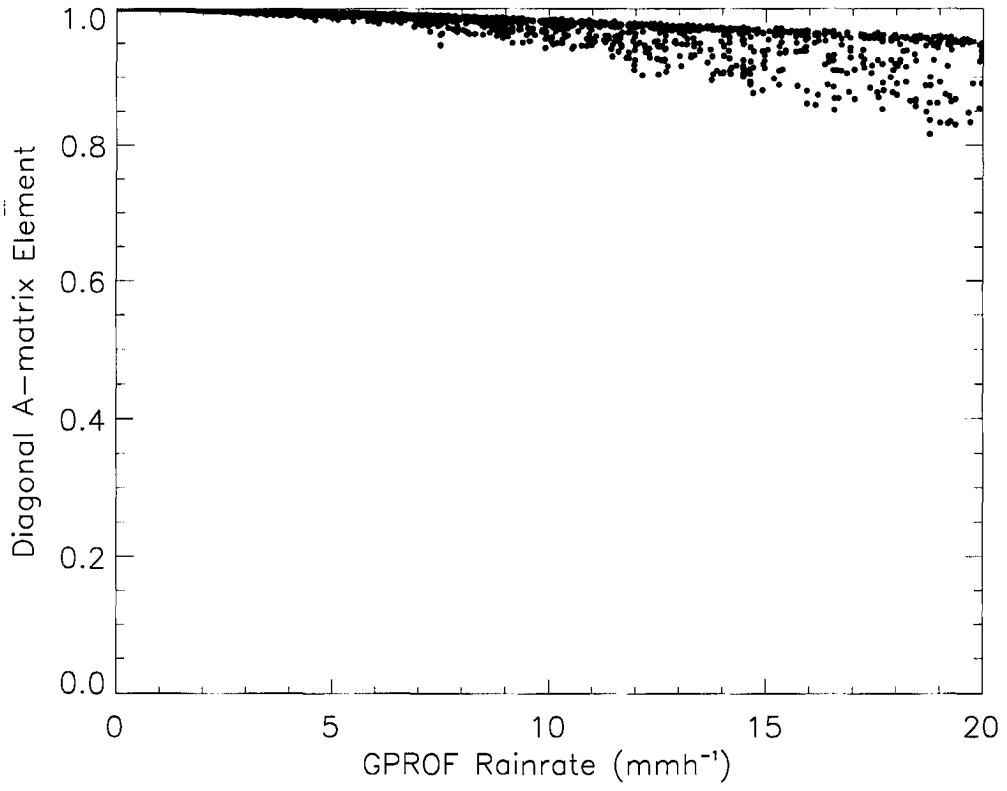

Figure D.23: As in Figure D.20 but at an altitude of 4.0 km.

test the assumption of Gaussian statistics and the values assumed for the variances

$$\chi^2 = (F(\hat{\mathbf{R}}) - \mathbf{Z})^T \mathbf{S}_Z^{-1} (F(\hat{\mathbf{R}}) - \mathbf{Z}) + (\hat{\mathbf{R}} - \mathbf{R}_a)^T \mathbf{S}_a^{-1} (\hat{\mathbf{R}} - \mathbf{R}_a) + \frac{(X_{obs} - X_{sim})^2}{\sigma_X^2} \approx N_l \tag{D.27}$$

D.6.2 Results

Precipitation Water Path

Surface rainrate retrievals at 94 GHz with a precipitation water path constraint are presented in Figure D.24. The constraint variance was taken to be 10 percent and no other

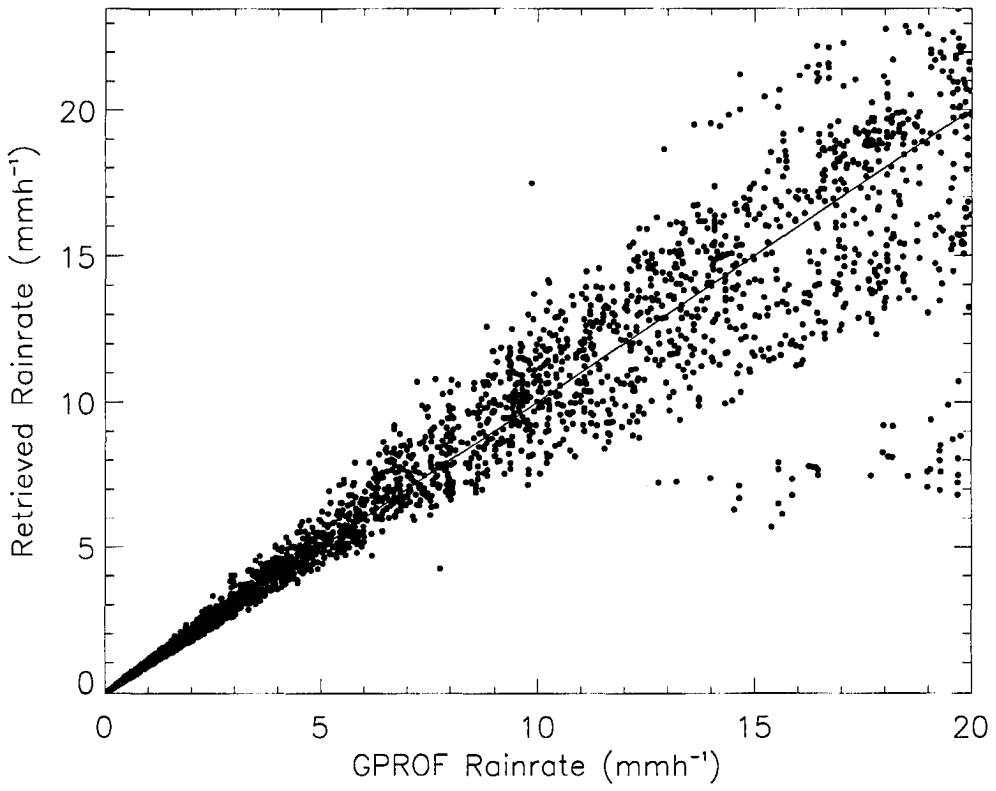

Figure D.24: Constrained synthetic near-surface rainfall retrievals at 14 GHz.

retrieval parameters were changed. An accurate estimate of PWP forces CORRAL to put the correct water mass in the atmosphere while the radar reflectivities determine how this mass is distributed in the vertical. This emphasizes the compatibility of active and passive microwave data in rainfall retrievals. The value of an accurate PWP estimate is further evidenced by Tables D.4 and D.5, which compare the correlation coefficients and their standard deviations for unconstrained and constrained retrievals at 14 and 94 GHz, respectively. The constraint reduces the retrieval standard deviation in all rainrate bins at both frequencies. At 14 GHz, errors are reduced by between 20 and 30 percent over the entire range of rainrates tested and rainrates up to 80 mmh^{-1} exhibit standard deviations of less

Table D.4: Correlation coefficients and standard deviation (in mmh^{-1}) for unconstrained and constrained synthetic surface rainrate retrievals at 14 GHz.

Rainrate Range	Unconstrained		σ_{PWP} = 10 %	
	Correlation	Std. Dev.	Correlation	Std. Dev.
0 - 20 mmh^{-1}	0.991	0.834	0.993	0.739
20 - 40 mmh^{-1}	0.869	3.267	0.918	2.434
40 - 60 mmh^{-1}	0.521	9.989	0.604	7.646
60 - 80 mmh^{-1}	0.305	24.407	0.394	16.500
80 - 100 mmh^{-1}	0.166	37.805	0.063	31.366
0 - 100 mmh^{-1}	0.932	8.375	0.958	6.346

Table D.5: As in Table D.4 but for retrievals at 94 GHz.

Rainrate Range	Unconstrained		σ_{PWP} = 10 %	
	Correlation	Std. Dev.	Correlation	Std. Dev.
0 - 5 mmh^{-1}	0.718	2.050	0.992	0.170
5 - 10 mmh^{-1}	0.153	5.578	0.837	1.046
10 - 15 mmh^{-1}	0.126	7.538	0.547	1.923
15 - 20 mmh^{-1}	0.105	9.774	0.245	3.530
0 - 20 mmh^{-1}	0.651	5.184	0.968	1.477

than 25 percent when constrained. At 94 GHz, standard deviations in the absence of a constraint are on the order of 50 percent over the range of rainrates presented but are reduced by a factor of five when it is introduced. Biases introduced by attenuation affects are also substantially reduced when the PWP constraint is enforced.

Figure D.25 shows retrievals of selected rainfall profiles from the GPROF database at the frequency of the TRMM PR with constraints of varying strength. The constraint has little impact on the PR retrievals below 30 mmh^{-1} regardless of its accuracy. At a near-surface rainrate of over 45 mmh^{-1}, however, the surface rainrate is underestimated by 25 % in the absence of a constraint but improves significantly with a strong one. In extremely heavy rain, where the attenuation effects are severe, an accurate PWP estimate improves retrieved surface rainrate errors from 40 percent to less than 10 percent. Similar results are presented in Figure D.26 for the CloudSat CPR. Due to the different range of rainfall rates detectable by the CPR, the two heaviest rain profiles have been replaced by light rain

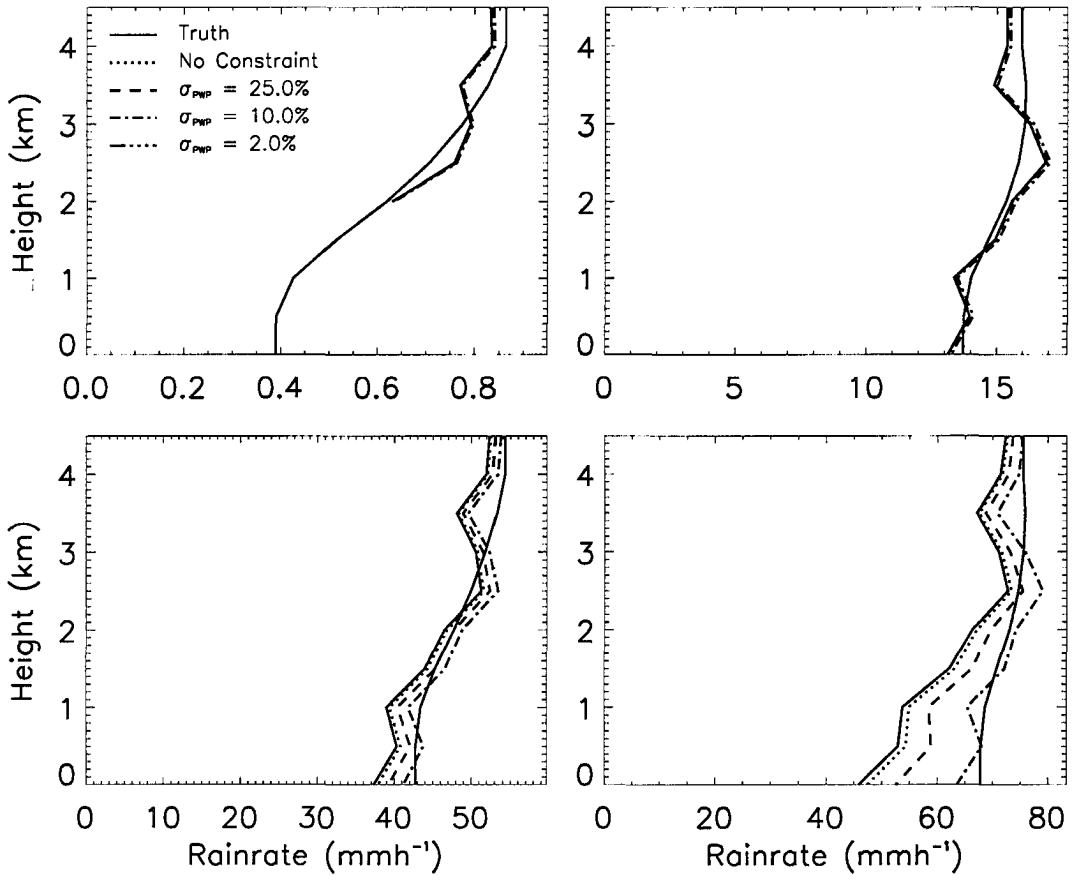

Figure D.25: Sample rainfall retrievals at 14 GHz.

cases in this figure. In extremely light rain the retrieved rainfall profile varies little with the addition of a constraint. For all other rainfall, the constraint has a marked impact. Note that the accuracy in the PWP estimate required to obtain an accurate retrieval increases with rainrate following the increasing trend of the attenuation.

Figures D.25 and D.26 also illustrate a very important, yet heretofore overlooked, benefit to using coincident cloud and precipitation radar measurements. The 14 GHz radar cannot detect rainfall lighter than 0.7 mmh^{-1} as is evidenced by the upper left plot. The cloud radar, on the other hand, is perfectly suited to retrieve light rain as well as cloud but is incapable of quantitatively measuring heavy rainfall. Despite their low rainfall rates,

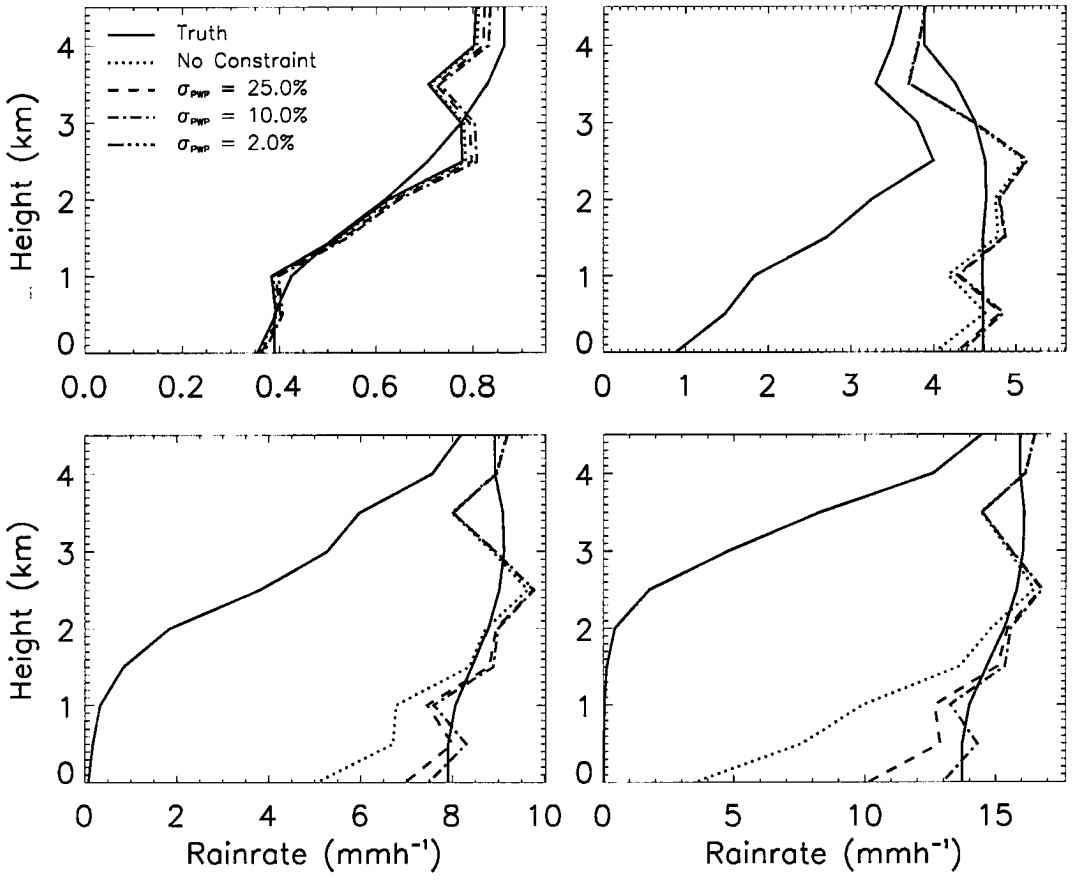

Figure D.26: As in Figure D.25 but for retrievals of lighter rain at 94 GHz.

light rain systems typically occur over large areas and are long-lived relative to heavy rain. They may, therefore, account for a significant fraction of the total precipitation globally and cannot be ignored when studying the impacts of the hydrological cycle on the Earth's climate system. In addition, given the radiative impact of clouds in driving global circulations (see Stephens et al. (2000) and references therein and recall the results of Chapter 5), they represent a significant omission from the information provided by a lower frequency radar. The synergy offered by these two instruments makes them well-suited to be operated simultaneously in future studies.

A cursory glance at the retrieval covariance matrices for the same four CPR retrievals

further emphasizes the dramatic improvement realized in the presence of an accurate PWP constraint. The covariance matrices, $\mathbf{S}_{\hat{R}}$, shown in Figure D.27 illustrate the difficulties

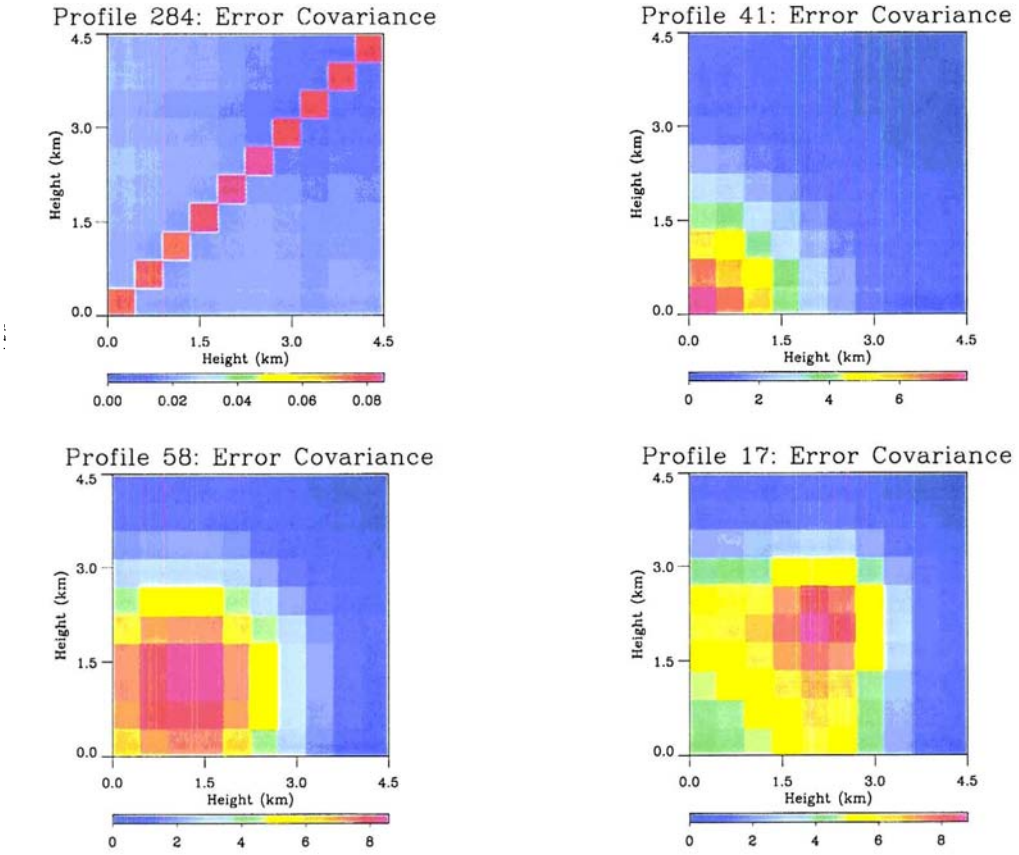

Figure D.27: Retrieval covariance matrices for synthetic retrievals at 94 GHz. All elements have been normalized by the appropriate retrieved rainrate and therefore represent fractional uncertainties.

encountered at high frequency due to strong attenuation by rainfall. In the absence of an attenuation constraint, variances for some levels exceed 100 % in all cases except the lightest rainfall. These high uncertainties can be directly attributed to attenuation effects which are implied by the large off-diagonal elements in the $\mathbf{S}_{\hat{R}}$. In an attenuation-free retrieval, reflectivities in each range bin are completely uncorrelated with those at other levels since they arise solely from scattering within the volume at that range. In rainfall at 94GHz, however, radiation reflected at lower levels in the column is scattered and absorbed

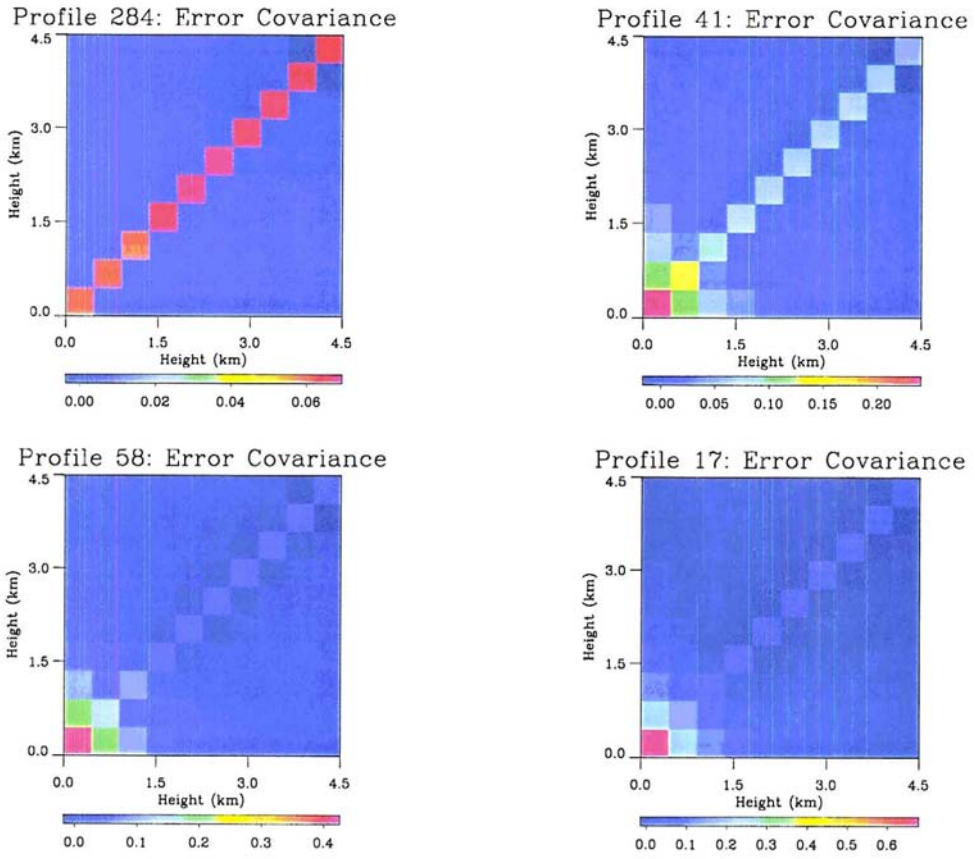

Figure D.28: As in Figure D.27 but for retrievals with a PWP constraint accurate to 10 %.

by the hydrometeors in upper levels introducing significant correlations between them. These correlations manifest themselves as non-zero off-diagonal elements in the covariance matrices and, the stronger the rainfall, the higher in the atmosphere such correlations occur. Similar covariance matrices illustrated in Figure D.28 characterize retrievals with a PWP estimate uncertainty of 10 %. Not only are uncertainties reduced to less than 50 % for all cases, the strong attenuation-induced correlations evident in the unconstrained cases have been removed except in the lowest levels of the atmosphere.

Contributions from the measurements, *a priori* guess, and constraint to the overall retrieval uncertainty at 94 GHz are illustrated in Figure D.29 for a moderate ($\sigma_{PWP} = 10\%$) constraint. In the absence of attenuation in extremely light rain, the retrieval is dominated

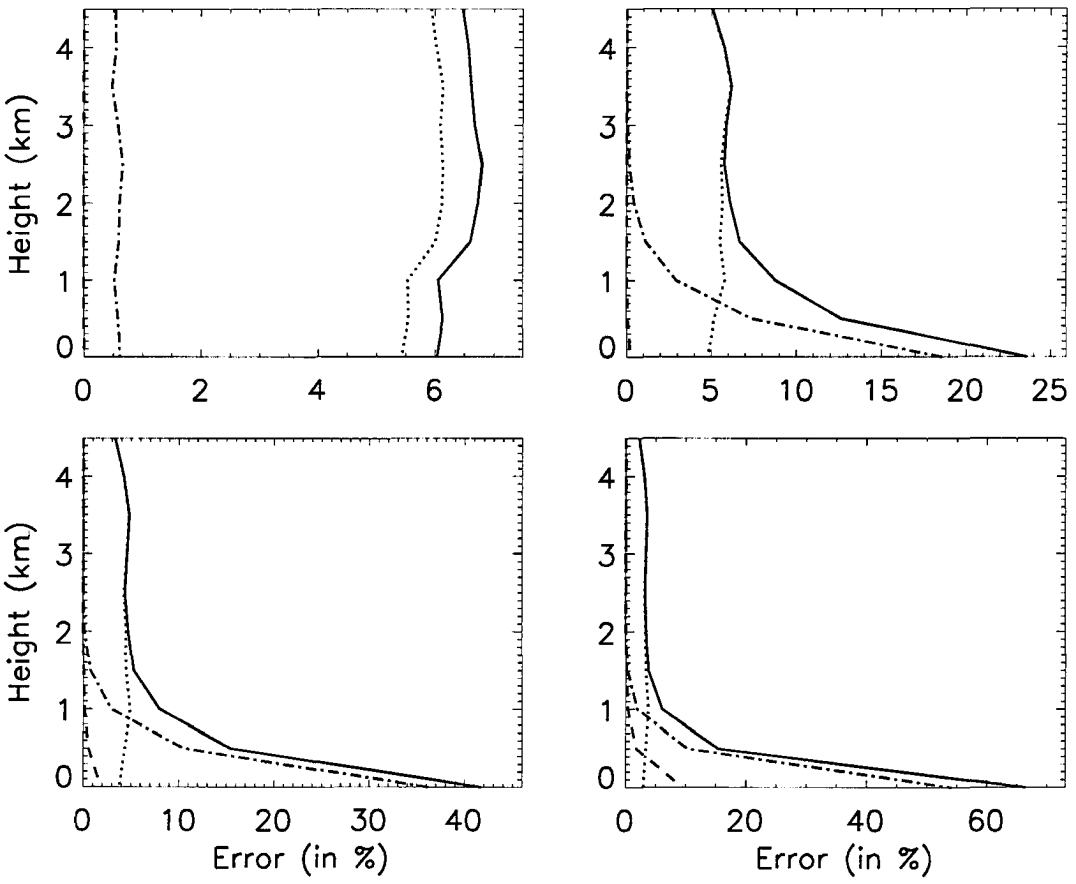

Figure D.29: The measurement (dotted line), *a priori* (dashed line), and PWP constraint (dot-dashed line) contributions to the total error (solid line) in the retrievals from Figure D.26 assuming a constraint accuracy of 10%.

by the reflectivity measurements. In each of the other cases, the retrieval is dominated by measurements at upper levels and by the constraint at lower levels. Once again this supports the hypothesis that the constraint adds important attenuation information in the algorithm. Finally, it is somewhat disturbing to note that CORRAL relies heavily on the *a priori* guess in the highest rainfall shown. Given the concerns raised earlier as to the accuracy of the initial guess, this serves as a warning to restrict application of this algorithm to rainrates of 10 mmh^{-1} or less when using the high frequency radar unless an extremely accurate PWP estimate is available. Figures D.27-D.29 also serve to highlight the powerful uncertainty

analyses that are possible within the constructs of an optimal estimation based retrieval. We are able to deduce the specific information driving the retrieval in addition to obtaining the rainrate and an associated uncertainty.

The ratio of the constraint contribution to the 94 GHz retrieval uncertainty to those of the *a priori* guess and measurements is displayed in Figure D.30 as a function of constraint accuracy. The peak in these curves can be taken as an optimal σ_{PWP} for the retrieval. If the

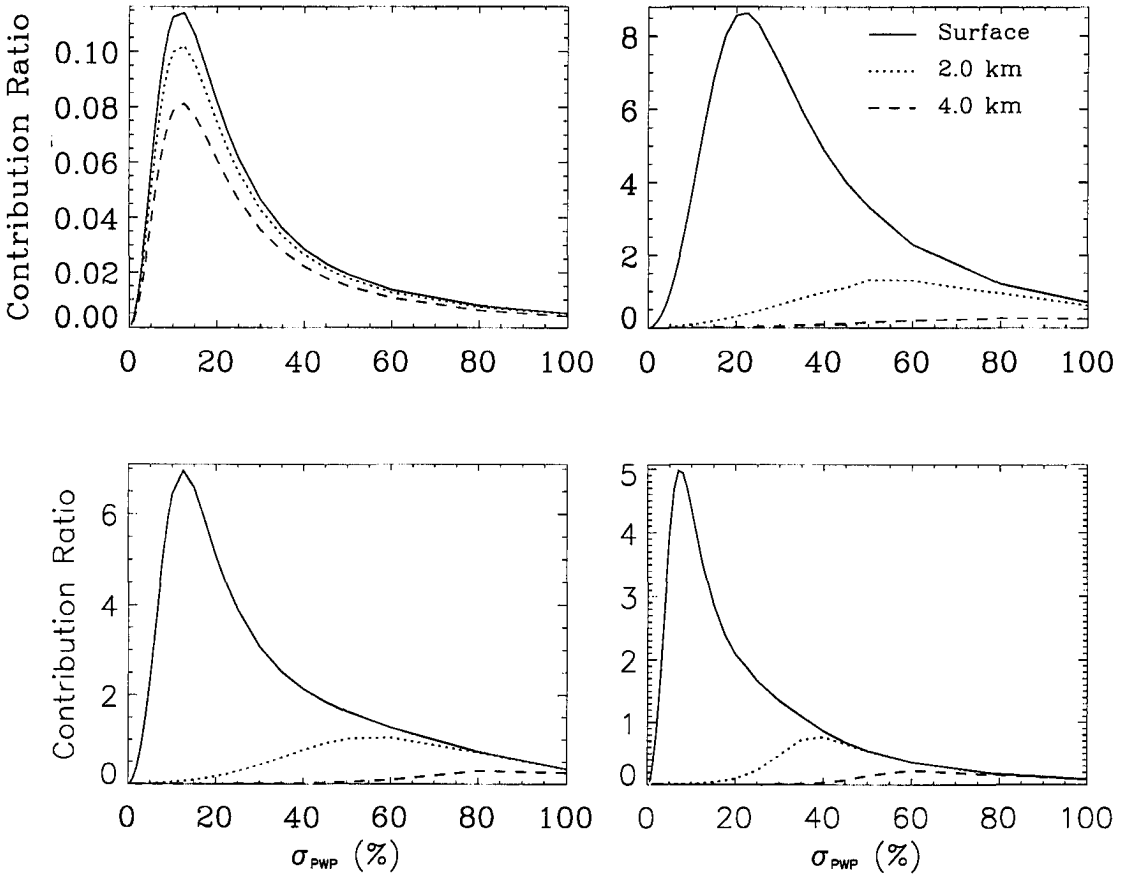

Figure D.30: Ratio of the constraint contribution to the total error to the sum of the corresponding measurement and *a priori* contributions as a function of constraint strength for the rainfall retrievals in Figure D.26.

constraint is significantly less accurate, it's impact on the retrieval will be minimal while the benefits of increasing its accuracy beyond the peak aren't likely to be significant enough to

Table D.6: Similar to Tables D.4 and D.5 but for retrievals at both 14 and 94 GHz with the addition of a PIA constraint.

14 GHz (σ_{PIA} = 10 %)			94 GHz (σ_{PIA} = 10 %)		
Rainrate Range	Correlation	Std. Dev.	Rainrate Range	Correlation	Std. Dev.
0 - 20 mmh^{-1}	0.993	0.727	0 - 5 mmh^{-1}	0.960	0.4207
20 - 40 mmh^{-1}	0.922	2.277	5 - 10 mmh^{-1}	0.525	2.577
40 - 60 mmh^{-1}	0.620	7.878	10 - 15 mmh^{-1}	0.216	3.964
60 - 80 mmh^{-1}	0.373	17.74	15 - 20 mmh^{-1}	0.143	6.038
80 - 100 mmh^{-1}	0.200	30.06			
0 - 100 mmh^{-1}	0.957	6.417	0 - 20 mmh^{-1}	0.898	2.801

warrant the extra effort required to obtain such accuracy. From the magnitudes of the peaks it is clear that the constraint has little impact on the retrieval in extremely light rain but very significant, and comparable, impact for the three remaining rain profiles. It is also apparent that the optimal constraint accuracy increases with increasing rainrate and with decreasing altitude. The greater the attenuation, the more accurate the PWP estimate must be to correct for it. Depending on the specific goals for the application of the CORRAL algorithm, an estimate of PWP with only moderate accuracy might be all that is required to constrain the retrieval. In applications involving the use of a high frequency radar to supplement rainfall information obtained at lower frequency, for example, retrievals in rainfall lighter than 4 or 5 mmh^{-1} may be of primary importance in which case a PWP estimate accurate to 20 percent is sufficient.

Path Integrated Attenuation

Similar results are obtained constraining the retrieval using an estimate of path integrated attenuation. Table D.6 provides correlation coefficients and their standard deviations for retrievals constrained using PIA estimates with uncertainties of 10 % at 14 and 94 GHz. Significant improvement is obtained with respect to the unconstrained results although higher standard deviations generally result when using a PIA constraint instead of a PWP constraint, particularly at 94 GHz where attenuation effects are the most pronounced. This

is likely a result of the fact that an imperfect physical model is still required to convert between attenuation and precipitation while the PWP is directly related to the integral of precipitation in the vertical.

Figure D.31 displays a collection of synthetic rainrate profile retrievals at 94 GHz using PIA constraints with the same accuracies as in Figure D.26. Qualitatively the results

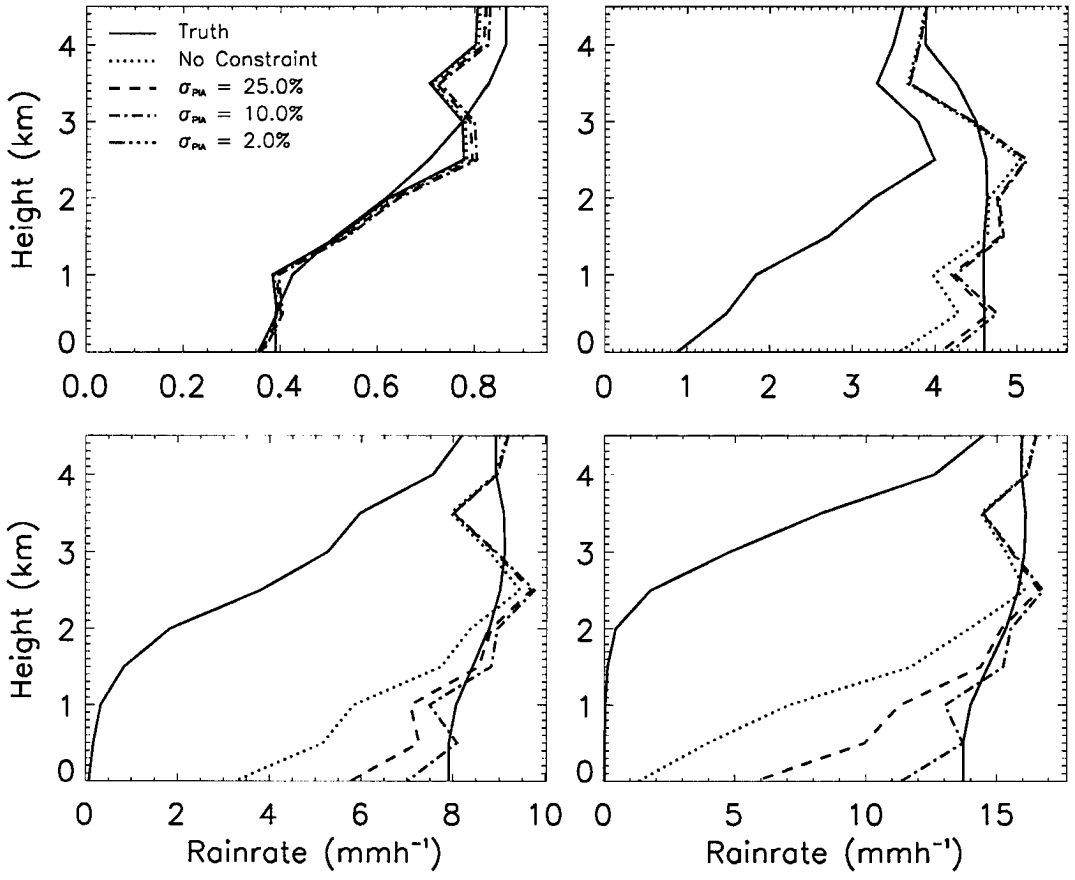

Figure D.31: As in Figure D.26 but with PIA constraints.

are very similar but subtle differences can be discerned particularly at low levels. Most notably, when the constraints are weak the PIA constraint is less effective at lower levels than the PWP. Analysis of the optimal PIA constraint strength provided by Figure D.32 confirms that the PWP provides a stronger constraint on the retrieval. Regardless of rain-

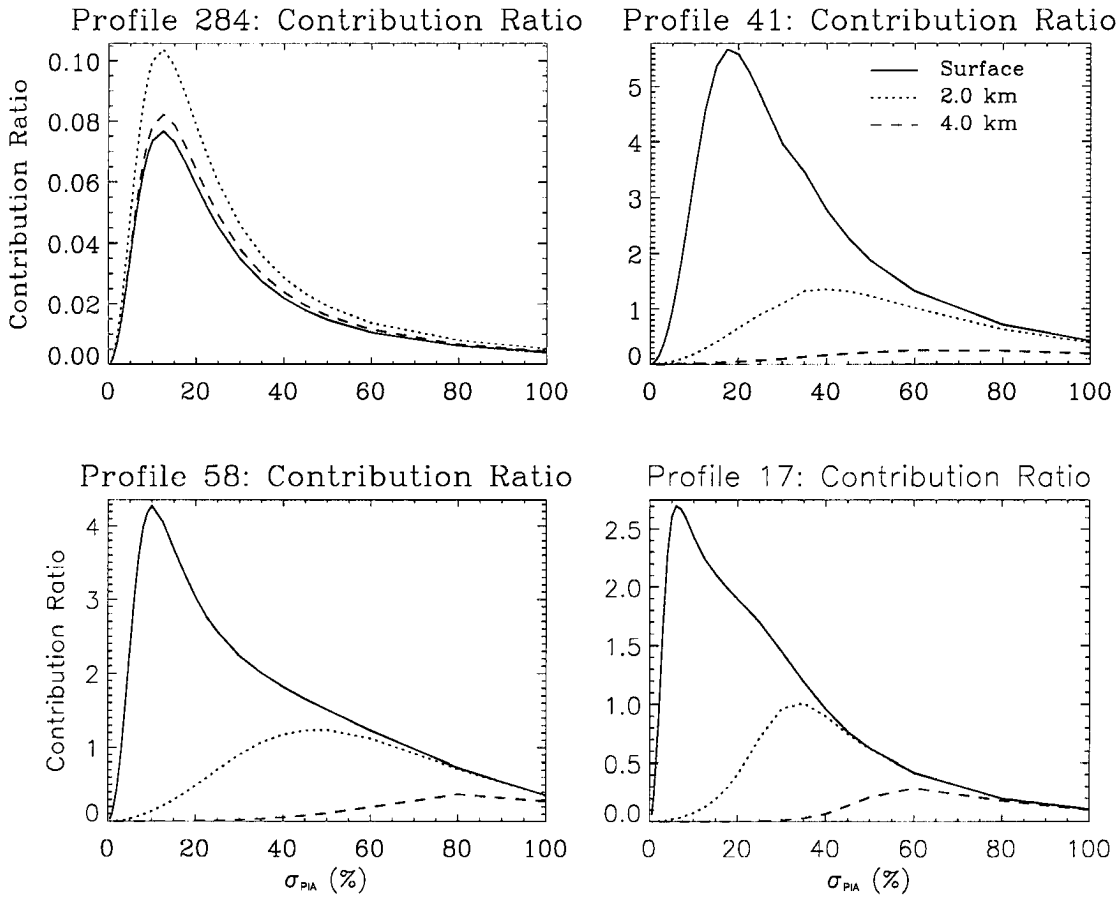

Figure D.32: As in Figure D.30 but for varying strengths of PIA constraint.

rate, the magnitudes of the maximum contribution of the PIA estimates are smaller than corresponding values from PWP estimates. Furthermore the peak occurs at lower σ_{PIA} suggesting that a more accurate PIA estimate is required to maximally impact the retrieval.

Physical Interpretation

Figure D.33 illustrates the physics introduced in the retrieval process from both the active and passive measurements. Shown are rainrate profiles at each step of the iteration process for a single retrieval from the database with constraints at four different accuracies. The upper left plot illustrates the propagation of errors due to attenuation in the absence of a

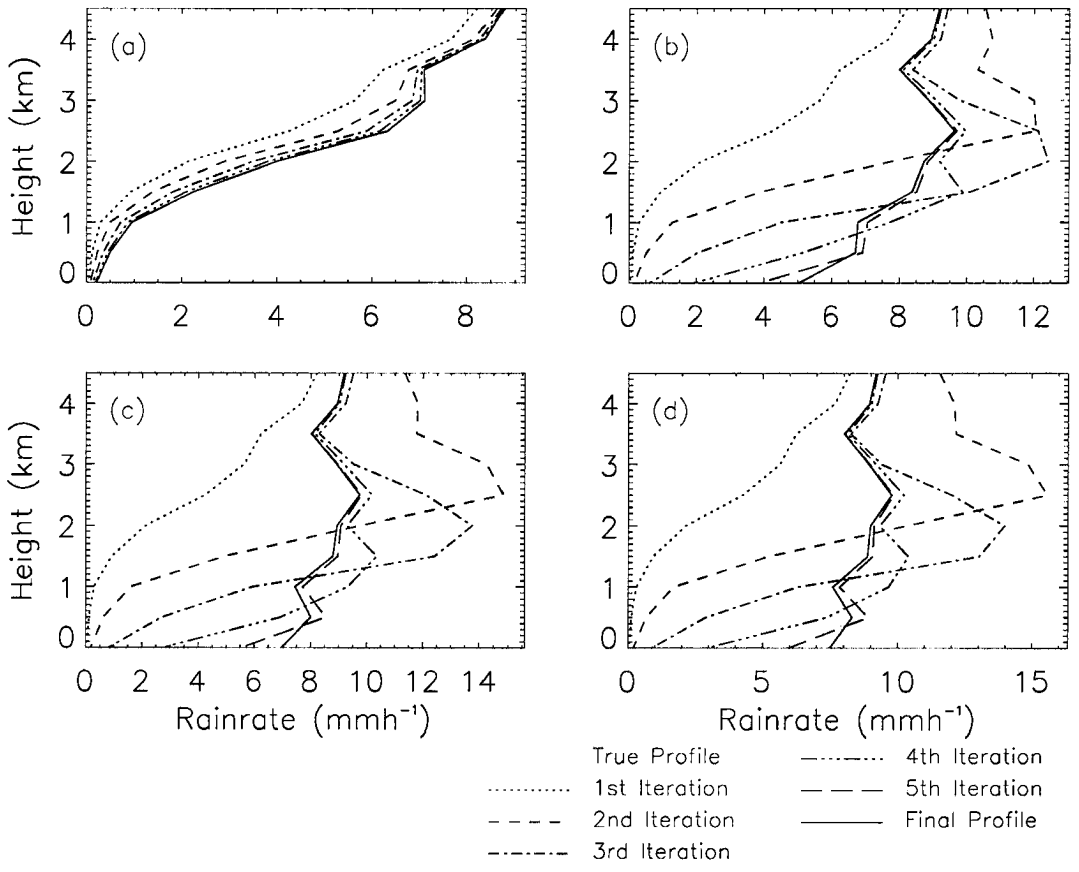

Figure D.33: Iterations in a synthetic retrieval at 94 GHz with (a) no constraint, (b) a constraint with $\sigma_{PWP} = 25.0$, (c) a constraint with $\sigma_{PWP} = 10.0$, and (d) a constraint with $\sigma_{PWP} = 2.0$.

constraint. In this case, the CORRAL algorithm suffers from the inability to distinguish between unattenuated light rain and attenuated heavier rain, retrieving the former when, in fact, viewing the latter. A modest PWP constraint ($\sigma_{PWP} = 25\%$) results in significantly improved agreement with the true profile particularly above 1.5 km. When stricter constraints are imposed, as in the lower two plots, CORRAL increases the rainrate at all levels in subsequent iterations eventually attaining good agreement with the true profile. Note that in every case the same initial guess, based on the Z-R and k-R relations, is made. The presence of a PWP constraint, however, forces CORRAL to "pump" more water into

the column in the three cases involving a constraint. We see, therefore, that the constraint determines the PWP in the atmospheric column during the first few iterations and the reflectivity measurements establish its vertical distribution in the remaining iterations. By virtue of Equations (D.17) and (D.24), the process cannot stop until agreement is obtained with both measurements.

Similar results using a PIA constraint are presented in Figure D.34 providing similar results. The PIA constraint also forces CORRAL to augment the initially underestimated

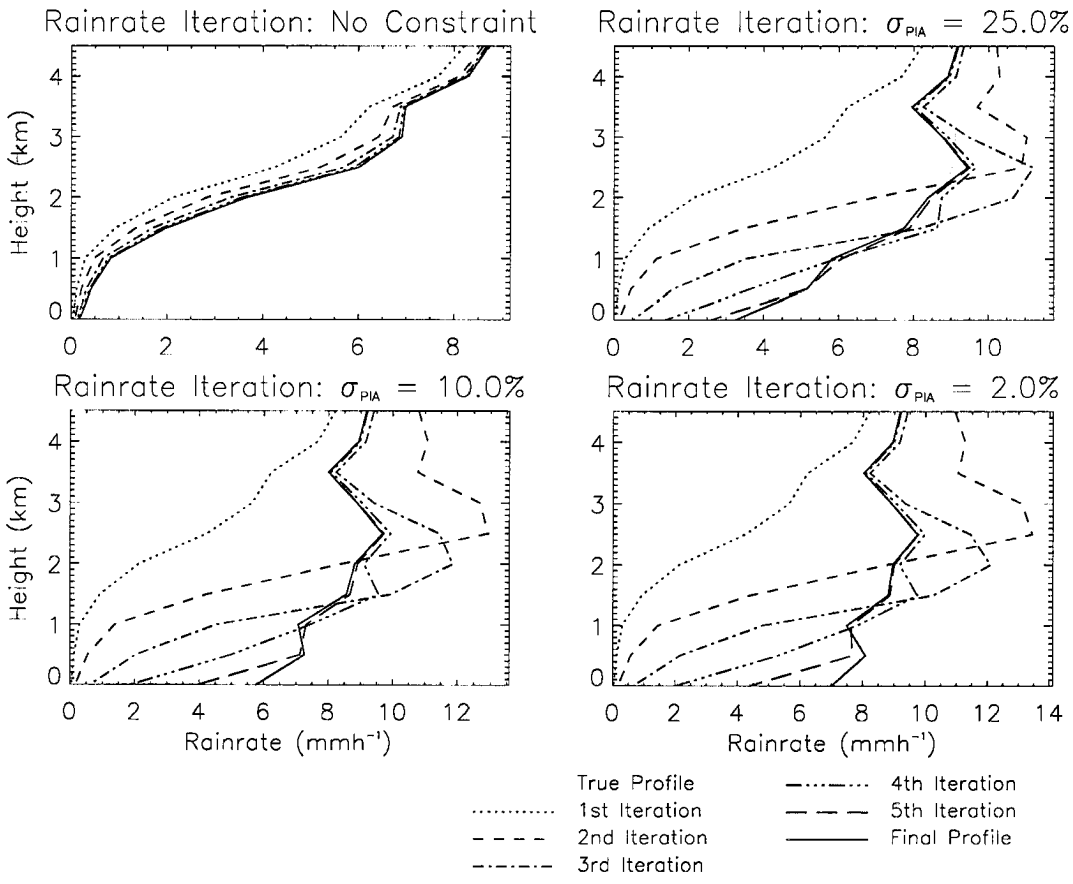

Figure D.34: As in Figure D.33 but using a PIA constraint as opposed to a PWP constraint.

column integrated precipitation in the first two iterations while the radar reflectivities determine its vertical distribution. Careful comparison of Figures D.33 and D.34 reveals that the

principal difference between the two constraints is the magnitude of the initial correction to the integrated precipitation. When the constraints are equally accurate, the PWP estimate introduces slightly more water to the column during the first iteration resulting in slightly better retrievals, particularly at lower levels. These results likely reflect the more indirect relationship between precipitation and PIA relative to the direct integrated water content provided by the PWP estimate.

To recapitulate, both constraints have very similar impact on the retrievals, improving them significantly in the presence of strong attenuation. This is an important result since passive observations are not always available or may be inaccurate due to water vapor and cloud liquid water effects, their large footprints with respect to those of active systems, and difficulties in co-locating them with radar observations resulting from the need to either orient the instruments with different view angles as on TRMM or to fly them on different satellites as will be the case with the CloudSat CPR and AMSR-E radiometer. Conversely, the PIA is a well-calibrated quantity which is guaranteed to be co-located with the other radar measurements and is always available provided a surface return is detectable. Even though the more direct measure of water content provided by the PWP provides a slightly stronger constraint for a given accuracy, we expect estimated PIA values to be at least two or three times more accurate in present observing systems so the PIA may ultimately be the best candidate to constrain the retrieval. Finally, in the event that both estimates are available, the formalism outlined here can use them simultaneously by merely adding a second constraint term to Eqn. D.24.

D.7 Sensitivity to Model Errors

A necessary but regrettable consequence of synthetic retrievals is the arbitrary assumption of a number of important parameters with little or no justification from observations. Through human nature we are often predisposed to tune these parameters in such a way as

to generate the best possible results. In our case, the variances used above may be optimistic particularly given the strong dependence of radar reflectivities on the highly variable real-world DSDs. In this section, assumed variances are augmented in order to supply a more thorough assessment of the expected range in algorithm performance over the variety of rainfall scenarios provided by the GPROF database.

Figures D.35 illustrates surface rainrate retrievals at 14 GHz assuming 6 dB of random noise while Figure D.35 presents similar results with the addition of an accurate PIA constraint. Comparing Figures D.15 and D.35 we find that model and measurement accuracy

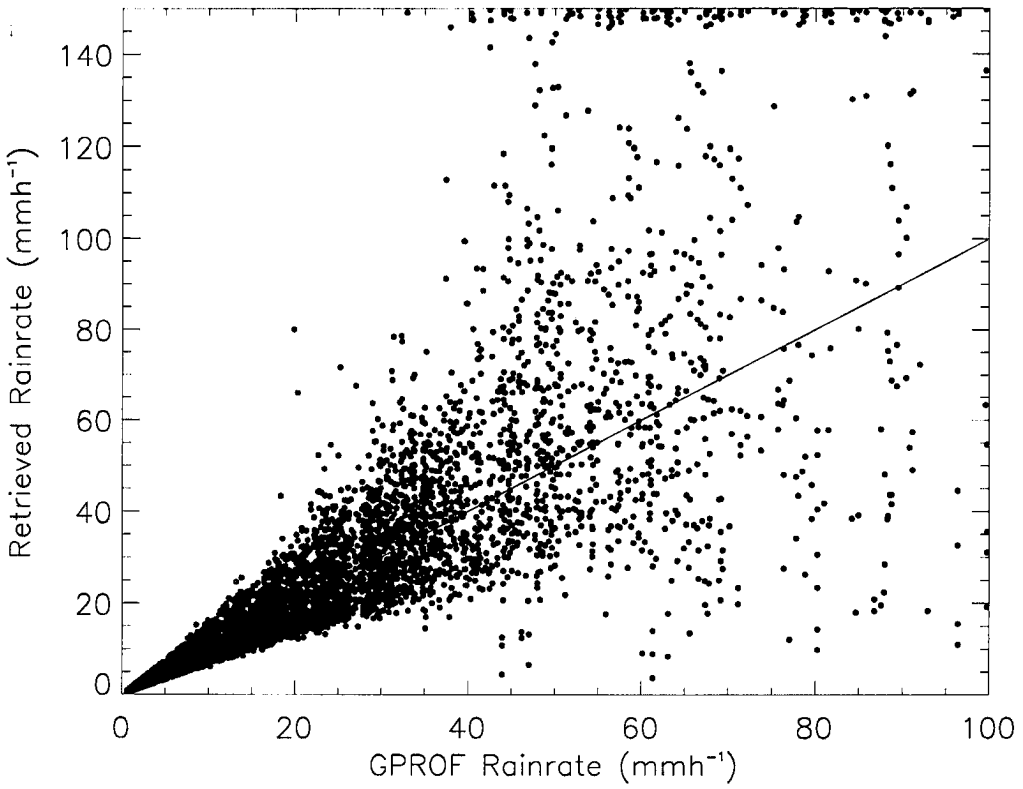

Figure D.35: Synthetic retrievals at 14 GHz as in Figure D.15 but assuming 6 dB errors.

is of paramount importance to the success of the retrieval. If errors are large, the range of

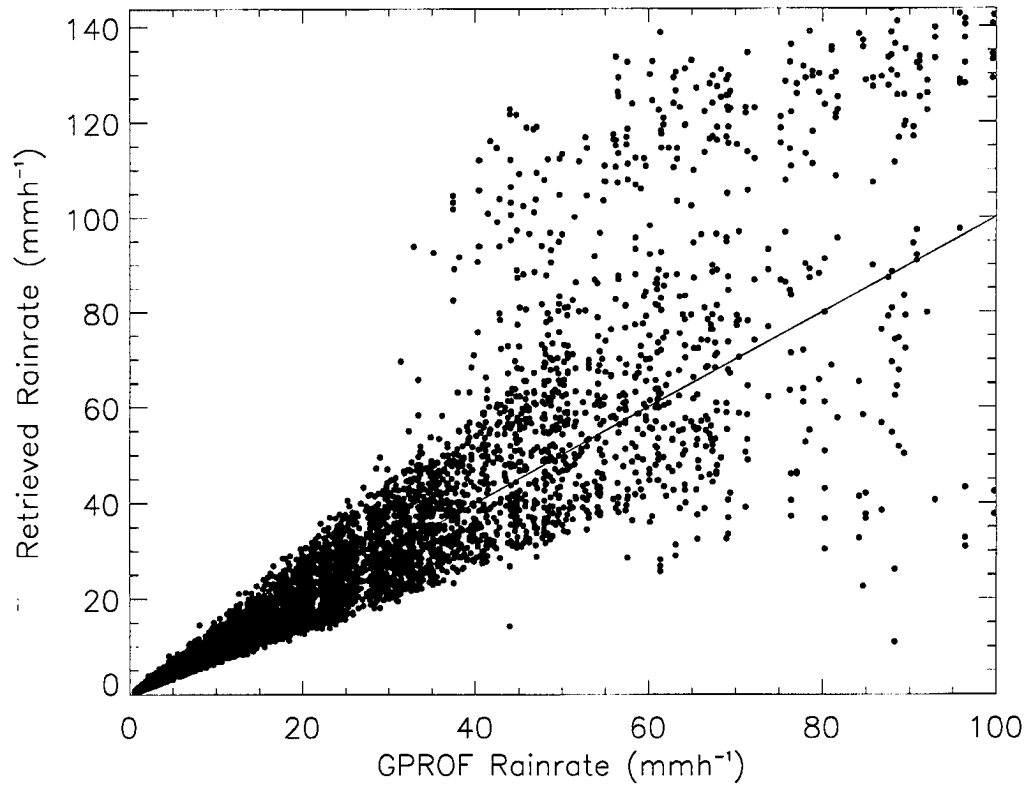

Figure D.36: As in Figure D.35 but with a PIA estimate accurate to 10 %.

accurately retrievable rainrates is reduced significantly. Furthermore, Figure D.36 shows that the impact of the constraint is more pronounced when model and measurement errors are large, highlighting the fact that the severity of the instability one encounters in the HB method of correcting for attenuation increases with increasing forward model error.

In the interest of space, results from all remaining synthetic retrievals at 14 GHz assuming random noise levels of 1.5, 3.0, and 6.0 dB are summarized in Table D.7 while corresponding results at 94 GHz can be found in Table D.8. At both frequencies, standard deviations from the unconstrained synthetic retrievals increase significantly when more noise is added, particularly at rainrates where the retrievals work the best. Uncertainties

in PR retrievals between 1 and 40 mmh^{-1}, for example, double when noise is augmented from 1.5 to 3 dB and again when it is further increased to 6 dB. At 94 GHz the effects of increasing noise are not quite as severe since the unconstrained retrievals are poor even with very little noise. Even so, uncertainties in retrievals between 5 and 10 mmh^{-1} increase by approximately 50 % each time noise is incremented.

Table D.7: Correlation statistics for synthetic surface rainrate retrievals at 14 GHz assuming 1.5 dB (top), 3.0 dB (middle), and 6.0 dB, random noise.

Rainrate Range	Unconstrained		σ_{PWP} = 10 %		σ_{PIA} = 10 %	
	Correlation	Std. Dev.	Correlation	Std. Dev.	Correlation	Std. Dev.
1.5 dB Noise						
0 - 20 mmh^{-1}	0.994	0.64	0.995	0.57	0.996	0.56
20 - 40 mmh^{-1}	0.918	2.41	0.947	1.89	0.956	1.69
40 - 60 mmh^{-1}	0.617	7.72	0.745	5.18	0.742	5.12
60 - 80 mmh^{-1}	0.226	19.9	0.435	15.5	0.294	14.9
90 - 100 mmh^{-1}	0.108	33.1	0.169	26.9	0.186	27.0
0 - 100 mmh^{-1}	0.949	6.94	0.968	5.43	0.970	5.34
3.0 dB Noise						
0 - 20 mmh^{-1}	0.979	1.28	0.983	1.11	0.985	1.06
20 - 40 mmh^{-1}	0.719	5.76	0.804	4.07	0.855	3.45
40 - 60 mmh^{-1}	0.388	15.8	0.498	11.1	0.484	10.1
60 - 80 mmh^{-1}	0.163	32.7	0.218	25.8	0.259	22.7
90 - 100 mmh^{-1}	0.003	46.6	0.155	34.2	0.269	32.7
0 - 100 mmh^{-1}	0.892	11.5	0.933	8.62	0.943	7.82
6.0 dB Noise						
0 - 20 mmh^{-1}	0.914	2.83	0.936	2.27	0.941	2.17
20 - 40 mmh^{-1}	0.517	11.0	0.601	8.37	0.609	7.96
40 - 60 mmh^{-1}	0.223	31.8	0.354	22.6	0.289	21.7
60 - 80 mmh^{-1}	0.153	43.8	0.208	31.7	0.270	29.3
90 - 100 mmh^{-1}	0.026	51.5	0.118	39.6	0.211	37.7
0 - 100 mmh^{-1}	0.827	17.3	0.888	12.7	0.895	12.0

A major distinction between the two radars is their response to increasing measurement noise in the presence of a constraint. Uncertainties in TRMM PR constrained retrievals also rapidly increase with increasing measurement noise although the impact of the constraint is notably stronger in the presence of a high level of noise. Errors in constrained retrievals at the CPR frequency, however, show little sensitivity to measurement noise with the exception of estimates of very light rainfall. This result is easily explained if we note that the constraint accuracy remains constant in all cases. In all but the lightest rainfall,

Table D.8: As in Figure D.7 but for retrievals at 94 GHz.

Rainrate Range	Unconstrained		σ_{PWP} = 10 %		σ_{PIA} = 10 %	
	Correlation	Std. Dev.	Correlation	Std. Dev.	Correlation	Std. Dev.
1.5 dB Noise						
0 - 5 mmh^{-1}	0.671	2.64	0.968	0.38	0.882	0.94
5 - 10 mmh^{-1}	0.112	6.36	0.610	1.94	0.381	3.49
10 - 15 mmh^{-1}	0.063	8.15	0.291	3.34	0.176	5.24
15 - 20 mmh^{-1}	0.073	10.2	0.116	5.33	0.151	7.54
0 - 20 mmh^{-1}	0.618	5.75	0.921	2.36	0.823	3.68
3.0 dB Noise						
0 - 5 mmh^{-1}	0.589	4.19	0.934	0.59	0.873	1.02
5 - 10 mmh^{-1}	0.132	8.29	0.553	2.36	0.316	3.86
10 - 15 mmh^{-1}	0.034	9.63	0.301	3.68	0.180	5.45
15 - 20 mmh^{-1}	0.071	10.8	0.150	5.49	0.096	7.82
0 - 20 mmh^{-1}	0.550	7.09	0.910	2.56	0.809	3.88
6.0 dB Noise						
0 - 5 mmh^{-1}	0.536	6.80	0.801	1.25	0.769	1.79
5 - 10 mmh^{-1}	0.003	9.96	0.476	2.90	0.218	2.91
10 - 15 mmh^{-1}	-0.009	10.8	0.236	3.95	0.055	5.53
15 - 20 mmh^{-1}	0.054	11.44	0.053	5.19	0.049	7.38
0 - 20 mmh^{-1}	0.409	9.11	0.893	2.83	0.796	4.08

CPR retrievals always rely most heavily on the information introduced by the constraint while the reflectivities themselves are used primarily to determine the vertical distribution of the rainfall. As a result, increasing noise in the reflectivity measurements induces smaller errors in the surface rainfall retrievals than reducing the accuracy of the constraint. PR retrievals, on the other hand, are dominated by the reflectivity measurements themselves over the range of noise levels tested and the retrieval uncertainties reflect this. Finally it should be noted that in some cases increasing the noise actually appears to slightly decrease the retrieval standard deviation at 94 GHz. This serves to point out the statistical nature of the results and the fact that they can fluctuate slightly from trial to trial. These fluctuations, however, are not statistically significant and it is important to restrict our attention to large differences.

In practice, the performance of the algorithm will depend on a number of factors including the sensitivity of each radar to particle shape, size distribution, and composition (eg. mixed-phase particles) as well as the amplitude of spatial and temporal fluctuations in these

factors over the scenes being observed. Estimation of S_y is, therefore, radar and application dependent and is left as a topic for further study. It is expected that the resulting S_y and corresponding algorithm performance will lie somewhere within the cases presented here.

D.8 Discussion

With the growing trend towards space-based observation platforms which carry high frequency cloud and rain profiling radars, the need for accurate, flexible algorithms for retrieving rainfall at attenuating frequencies is paramount. In this paper, we have presented an algorithm which is not, in principle, restricted by assumptions of size distribution or particle shape and accounts for attenuation through direct integration of two-way extinction due to all rain along the path to each target layer. The algorithm maximizes a posterior probability density function derived from an assumption of uncorrelated, unbiased errors following a Gaussian distribution. The Gaussian distribution, by virtue of its symmetry, adds the least bias of any assumed error distribution in the absence of additional information and ensures equivalence between the locations of its maximum and its mean, a necessary condition for the solution to be optimal.

Preliminary results, using simplifying assumptions, illustrate the utility of the CORRAL algorithm, particularly at low frequencies. At 14 GHz, synthetic retrievals of rainfall profiles using the GPROF cloud database accurately reproduce the input for rainrates as high as 40 mmh^{-1}. At 94 GHz, however, the CORRAL algorithm grossly over- or underestimates surface rainfall at all rainrates above 1.5 mmh^{-1} due to instability inherent in the method employed to correct for attenuation. The PIA approach to correct for attenuation, which makes use of the surface return echo to estimate the total attenuation through the rain column, is stable and yields much more accurate results when attenuation is severe (Iguchi and Meneghini, 1994). This is confirmed by the remarkable improvement in the retrieval when precipitation water path or path-integrated attenuation constraints are imposed on the

retrieval. Since the PIA derives from the precipitation water path, both constraints perform essentially the same function. Either method (or both) can be used in the present algorithm with very little modification. It is also worth noting that the application of this algorithm to the CloudSat radar is explicitly for the purpose of retrieving very light rain which may not be detectable at lower frequencies. In this light, the results presented here are encouraging.

It is interesting to briefly compare these results with those obtained in the studies of the passive microwave GPROF algorithm discussed earlier. Recall that the major drawback of the TMI-based GPROF retrieval was a lack of explicit vertical profile information in the measurements. Spaceborne radars, in effect, suffer from the opposite problem, requiring some measure of the attenuation due to the bulk PWP. This suggests a synergy between active and passive instruments which to date has not been fully exploited. Radars offer the potential to enhance the limited profile information in passive microwave cloud and rainfall retrievals while the sensitivity of passive microwave observations to bulk liquid water contents can provide much-needed information to constrain DSD by requiring consistency between observed reflectivities and liquid water path estimates. As a result, these two sensors complement each another and an algorithm which combines both types of information can begin to resolve some of the problems suffered by each independently. While the analyses presented above have not directly addressed the performance of a combined TMI-PR algorithm (or a multi-parameter radar algorithm which offers equally intriguing possibilities), the utility of the optimal estimation approach for such applications has been strongly emphasized and this research will proceed in that direction in the future.

The assumption of an exponential DSD and spherical particles greatly over simplifies the problem. It is worth pursuing extensions of the model to include more direct estimation of size distribution parameters making more complete use of the other observations available to both the TRMM and CloudSat missions. In a slightly more general form, Equation

(D.14) can be written as

$$\Phi(\mathbf{x}, \mathbf{x}_a, \mathbf{y}) = (F(\mathbf{x}) - \mathbf{y})^T \mathbf{S}_y^{-1} (F(\mathbf{x}) - \mathbf{y}) + (\mathbf{x} - \mathbf{x}_a)^T \mathbf{S}_a^{-1} (\mathbf{x} - \mathbf{x}_a) \qquad \text{(D.28)}$$

where $\mathbf{x}$ is a more general vector of retrieval parameters, perhaps consisting of DSD parameters at each level, $\mathbf{y}$ is a general vector of satellite measurements, and F is an appropriate combination of forward models which map the retrieval parameters into the basis of these measurements. This equation can be solved in exactly the same manner as above yielding an iterative solution to determine the best estimate of rainrate based on all available observations simultaneously. As the TRMM PR algorithms have demonstrated, directly accounting for DSD variability is of paramount importance for the next generation of satellite radar retrievals. Studies are currently underway to re-cast the CORRAL algorithm in terms of a more general DSD and a parallel effort is being undertaken to directly incorporate radiances from the TMI to provide the more rigorous constraint required to estimate a more flexible DSD.

Finally, it is important to note that this appendix relies heavily on synthetic retrievals which provide useful comparison studies but are in no way presented as validation of the merits of such an approach in an operational context. The fact that the same assumptions are made in both the forward and inverse models undoubtedly masks the impact of variable DSD and particle shape on the results but synthetic retrievals of this type are not necessarily meant to provide a rigorous test of the algorithm. This study merely demonstrates the feasibility of applying the optimal estimation at attenuating frequencies and has supplied us with crude estimates of the uncertainties we might expect when such an approach is applied to single-frequency radars. Complete validation of a new approach such as this requires application to real-world data and detailed comparison with other algorithms and sensors including *in situ* observations. Time did not permit such studies for this work but a number are planned for the near future which will focus on rainfall retrievals from the

CloudSat CPR (possibly using the AMSR-E as a constraint although a significant effort will be required to overcome uncertainties resulting from the mismatch in footprints between these instruments), the proposed dual-frequency radar for GPM, and simultaneous radar/passive microwave observations, employing airborne and spaceborne radar data with aircraft and ground validation. In many of these studies the algorithm can be cast in such a way that the DSD itself can be modified to give the best overall fit to all data available including passive microwave radiances. Furthermore, the skill of these variants in deriving profiles of radiative and latent heating needs to be addressed.

Appendix E

Synthetic Radar Retrievals at 35 GHz

Current proposals for a follow-up to the TRMM mission include a 35 GHz radar flown in conjunction with the 14 GHz TRMM PR to determine DSD through differential attenuation techniques[1]. The algorithm presented in Chapter D is well-suited for simultaneously using data from a variety of instruments but such an application must be left as an exercise for the future. Instead some results regarding the use of radar reflectivity measurements from a single spaceborne 35 GHz in profiling rainfall will be examined in this appendix. These results are not meant to be a critique of the combined 14-35 GHz system, but to compare the rainfall retrieval capabilities of a single 35 GHz radar to those at 14 and 94 GHz.

Synthetic retrievals of near-surface rainrate and their corresponding uncertainties are displayed in Figures E.1 and E.2. As expected based on the radar sensitivity study in Section D.3 (and a little intuition), the results at 35 GHz lie between those at 14 and 94 GHz. Suitable agreement is obtained rainfall estimates are made up to 8 mmh^{-1} in the absence of any constraint, an improvement over the negligible range retrievable at 94 GHz but much lower than the range of the TRMM PR. Retrieval uncertainties over this range vary from 25 % to 75 %. Beyond 8 mmh^{-1}, both figures exhibit extreme scatter indicative of pronounced attenuation effects similar to those encountered at 94 GHz.

Statistics for near-surface rainfall retrievals from 35 GHz with both PWP and PIA constraints accurate to 10 % are summarized in Table E.1. Correlation coefficients and standard deviations suggest that acceptable rainfall retrievals are possible in moderate rainfall exceeding 20 mmh^{-1} in the presence of either constraint with the prescribed accuracy.

[1]See (Meneghini and Kozu (1990)) for an overview of the method of differential attenuation from spaceborne dual-frequency radars.

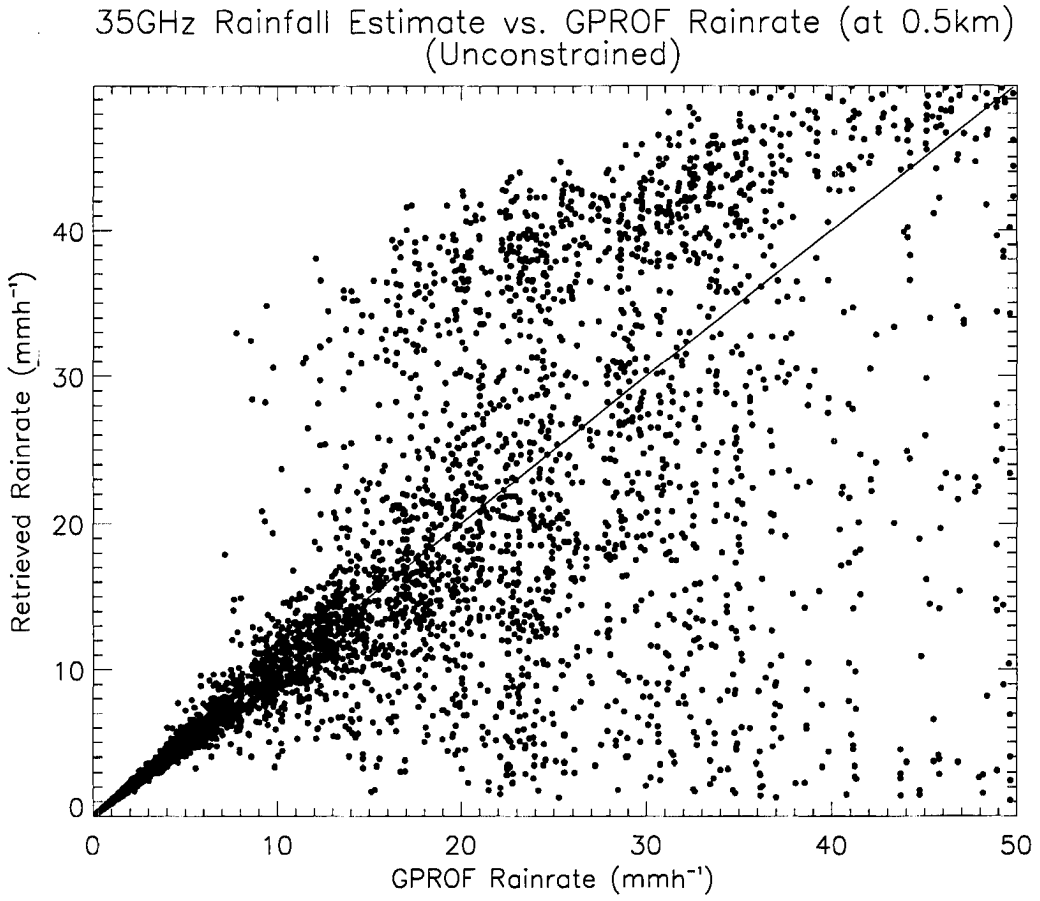

Figure E.1: Comparison of near-surface rainfall estimates using reflectivities at 35 GHz with truth.

Both forms of constraint yield at least a factor of two improvement in retrieval accuracy in rainfall up to 30 mmh^{-1}.

Comparison of sample rainfall retrievals over a range of rainrates (shown in Figure E.3) with those obtained at 14 and 94 GHz, highlights the fact that the attenuation at 35 GHz is significant but somewhat less so than at 94 GHz. Attenuation errors below 8 mmh^{-1} are minimal, but a moderate constraint is required up to 15 mmh^{-1}, and retrievals are not possible in rainfall exceeding 20 mmh^{-1} without an unrealistically accurate constraint.

An error breakdown for the retrievals in Figure E.3 similar to that in Figure D.29 is presented in Figure E.4. The results demonstrate that the measurements dominate the 35

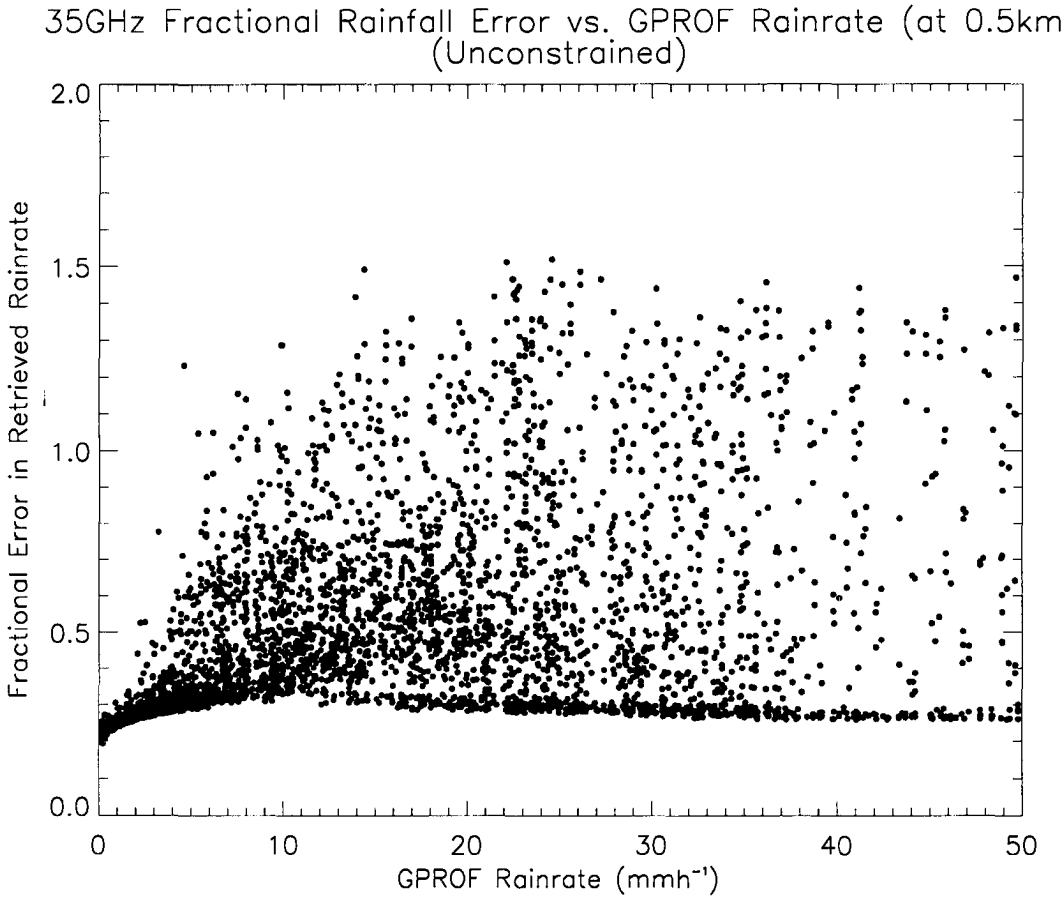

Figure E.2: Error in retrieved rainrate as a function of rainrate for the 35 GHz synthetic retrievals.

Table E.1: Correlation coefficients and standard deviation (in mmh^{-1}) for unconstrained and constrained synthetic surface rainrate retrievals at 35 GHz.

Rainrate Range	Unconstrained		σ_{PWP} = 10 %		σ_{PIA} = 10 %	
	Correlation	Std. Dev.	Correlation	Std. Dev.	Correlation	Std. Dev.
0 - 10 mmh^{-1}	1.0557	1.244	0.99856	0.298	0.99942	0.297
10 - 20 mmh^{-1}	1.1705	7.175	1.02926	1.531	1.10050	2.395
20 - 30 mmh^{-1}	0.8380	12.14	0.91747	3.675	0.88189	5.338
30 - 40 mmh^{-1}	0.4222	14.83	0.86811	5.541	0.64125	8.040
40 - 50 mmh^{-1}	0.2354	16.78	0.57466	7.795	0.52337	10.57
0 - 50 mmh^{-1}	0.9060	8.421	0.96068	3.001	0.96256	4.265

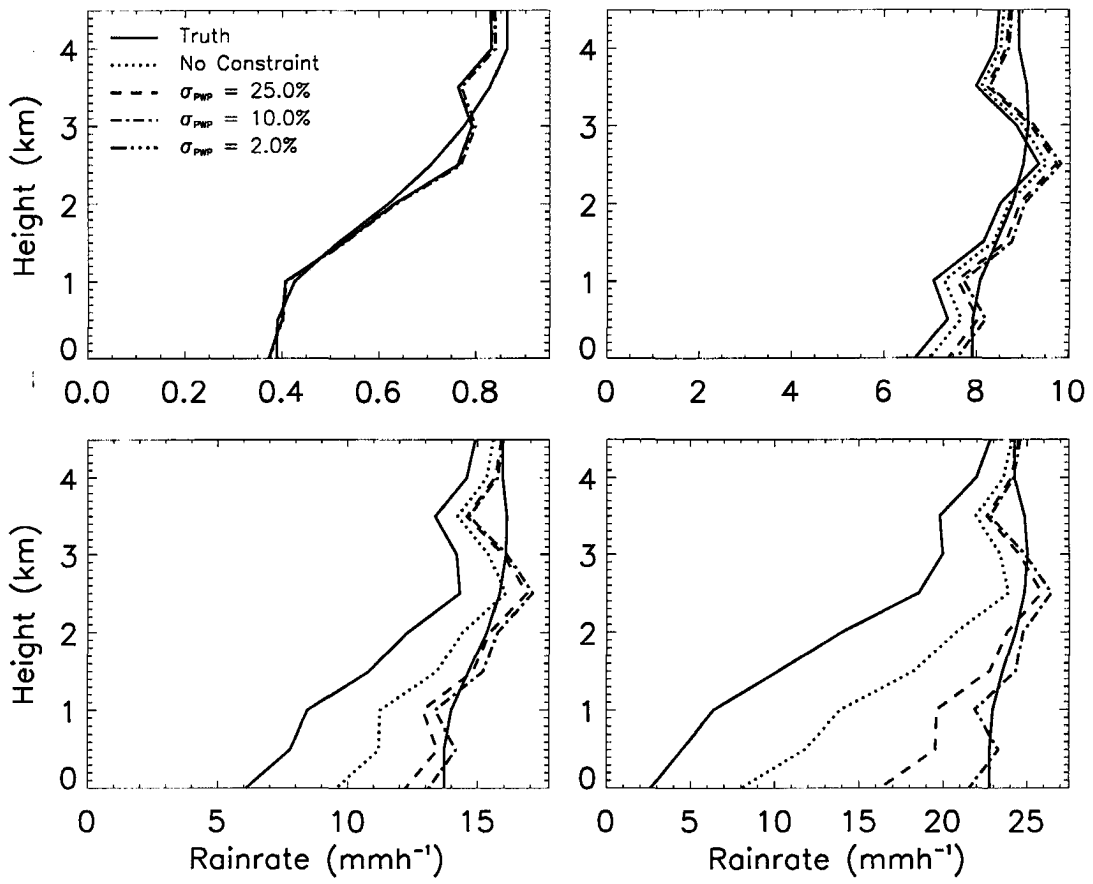

Figure E.3: Sample rainfall retrievals at 35 GHz. Profiles are chosen to reflect the range of rainfall retrievable at 35 GHz and therefore include some of those shown to represent 14 GHz retrievals in Figure D.25 at some shown in Figure D.26 illustrating 94 GHz retrievals.

GHz retrievals at upper levels while the constraint dominates at lower levels where the effects of attenuation are more pronounced. Also evident when comparing the figures is the fact that errors incurred as a result of attenuation are significantly stronger at 94 GHz since the constraint dominates more absolutely at that frequency. This fact is even more apparent in Figure E.5 which presents the ratio of the constraint contribution to the retrieval error to those due to *a priori* and measurement errors. Comparing with similar results at 94 GHz (Figure D.30) we see that, in general, the impact of the constraint is less pronounced at 35 GHz. It is also worth noting that the location of optimal constraint is shifted to higher

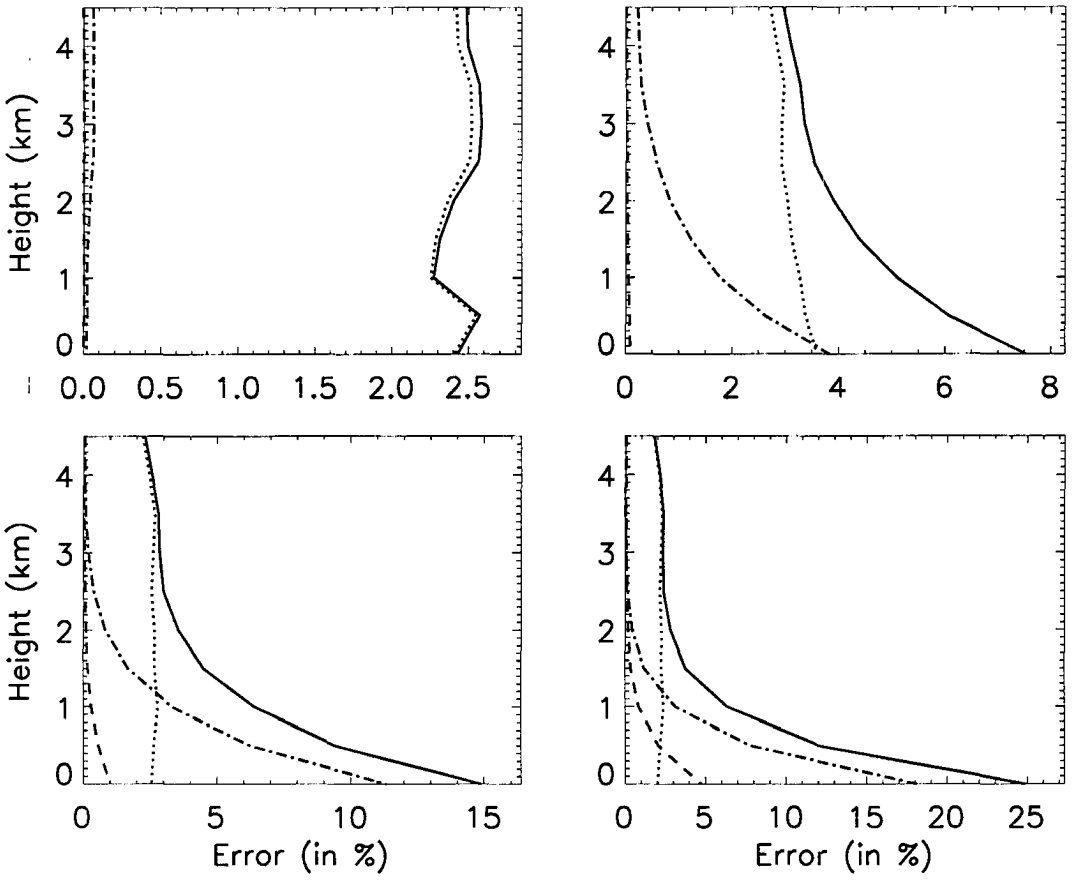

Figure E.4: The measurement (dotted line), *a priori* (dashed line), and PWP constraint (dot-dashed line) contributions to the total error (solid line) in the retrievals from Figure E.3 assuming a constraint accuracy of 10%.

accuracy at 35 GHz but the inverse dependence on rainrate and proportionality to height is evident, emphasizing that the same physical mechanism is responsible for the improvement in both cases. Considering the 35 GHz radar as a separate entity, we find its ability to detect and measure rainfall falls somewhere between that of the 14 GHz TRMM PR and the 94 GHz CloudSat CPR both in terms of the detectable rainfall (Section D.3) and the range of quantatitively retrievable rainfall profiles.

For comparison purposes, Figure E.6 illustrates the fraction of rainfall scenes from the GPROF database that can be detected by two hypothetical combinations of the 14, 35, and

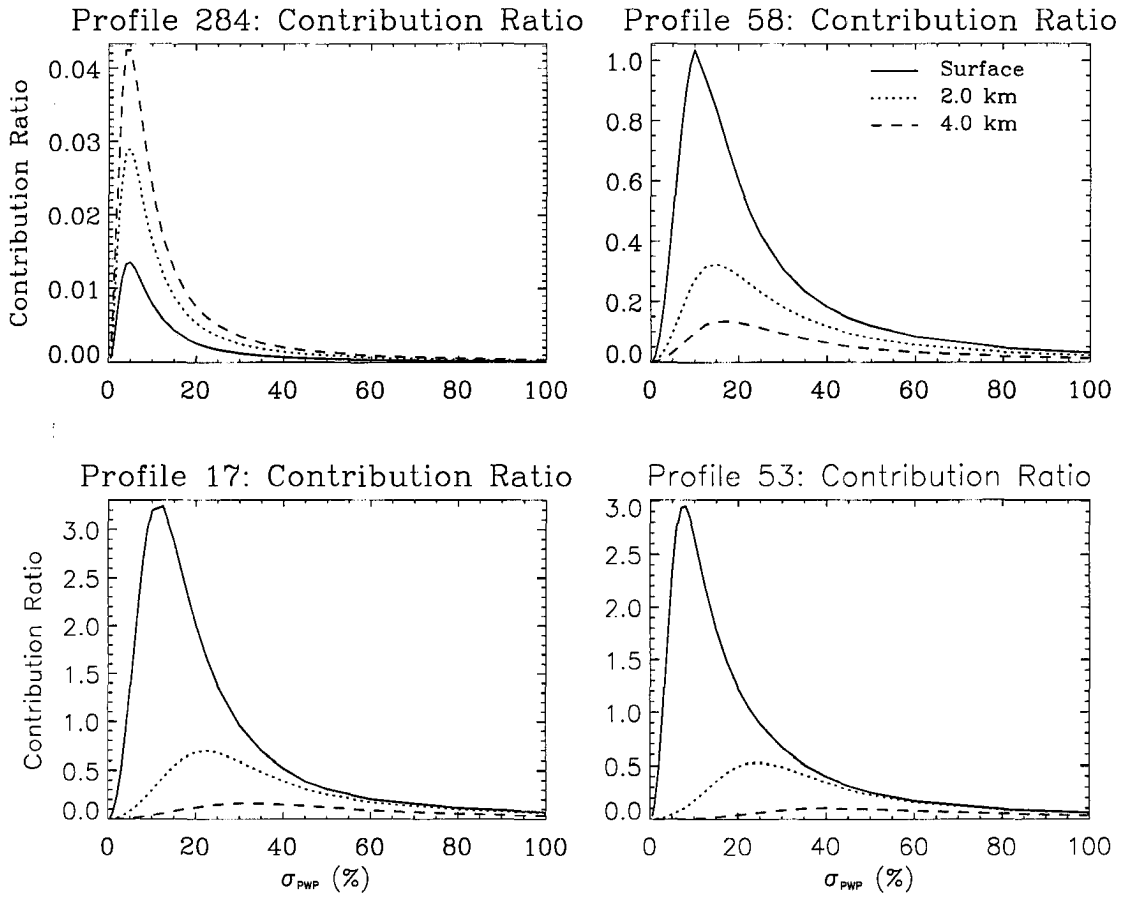

Figure E.5: Ratio of the constraint contribution to the total error to the sum of the corresponding measurement and *a priori* constributions as a function of constraint strength for the rainfall retrievals in Figure E.3.

94 GHz radars investigated above. The results assume that the radars operate independently and a successful detection requires that either of the two radars sense the near-surface rainfall. While algorithms to retrieve rainfall from dual-frequency radar systems will never be restricted to merely combining results from independent applications of single frequency algorithms in this way, it is interesting to note the complementary nature of the 14 and 94 GHz radars. While the significance of the contribution from extremely light rain to global precipitation and latent heat budgets is uncertain and may be small, their radiative impact is considerable and the prospect of coincident cloud and precipitation radar measurements

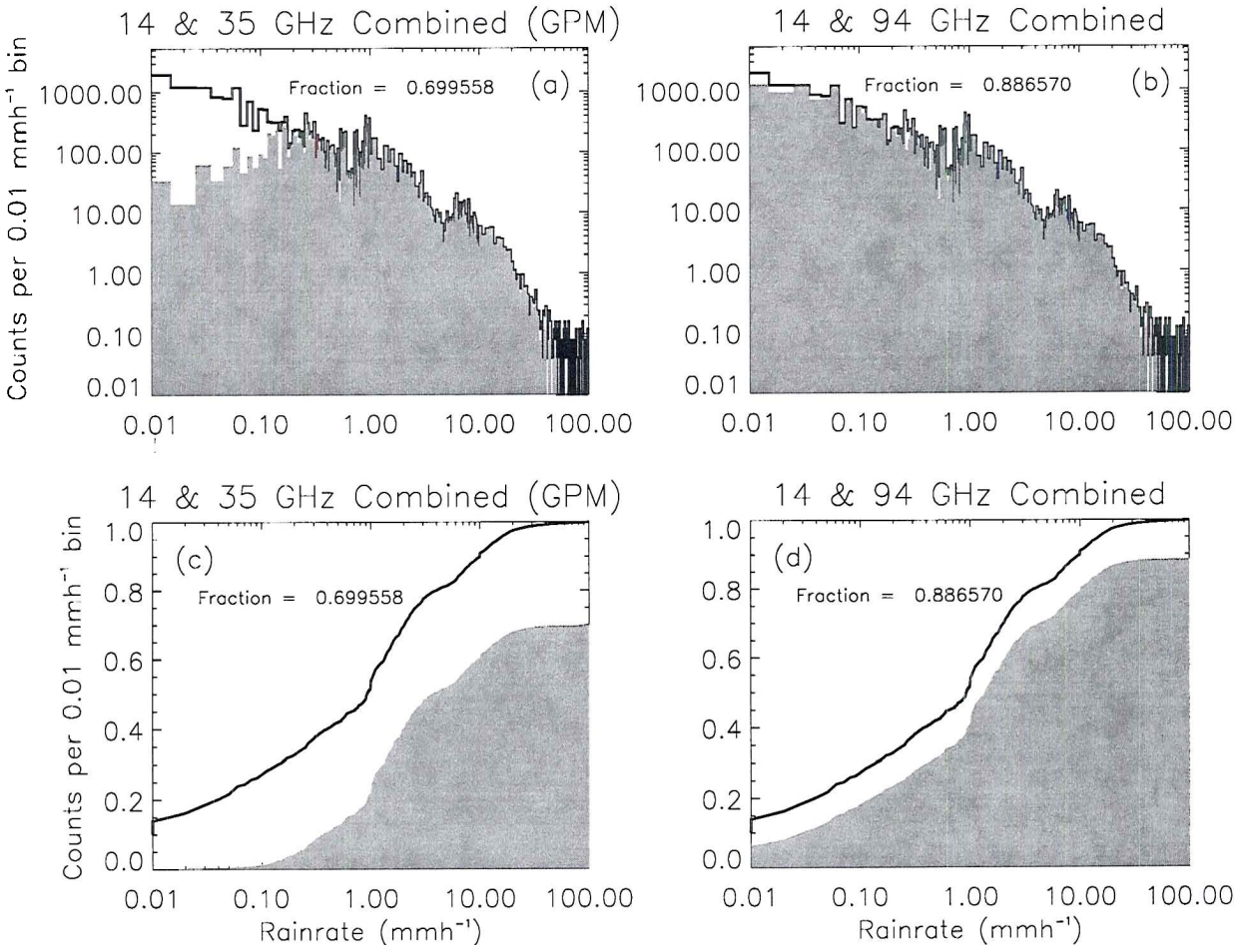

Figure E.6: As in Figures D.5 and D.6 but for hypothetical combinations of radars.

to simultaneously infer radiative and latent heating should not be overlooked.

The utility of either a 35 or a 94 GHz radar in conjunction with the TRMM PR depends on the application. For GPM, where the focus is on rainfall, it may be important to have a combination of radars that will provide measurements of differential attenuation in moderate to heavy rainfall. In that case the 35 GHz radar may be better suited than a higher frequency radar by virtue of the enormous attenuation suffered by the latter. For light rain and cloud applications, such as the estimation of radiative heating, on the other hand, the addition of a 35 GHz radar does little to improve undersampling at 14 GHz. In such applications a 94 GHz cloud radar presents a greater addition system as a whole. Quantitative

assessment of the properties of combinations of these radars and passive microwave radiometers clearly warrants further study in light of the complementary information they contain.

Appendix F

Symbol Definitions and Common Units

a, b - coefficients in Z-R relation

α, β - coefficients in k_{ext}-R relation

A - *a priori* matrix

$B(\tau)$ - Planck function ($Wm^{-2}sr^{-1}$)

χ - size parameter

C - a general error covariance matrix

D_n - characteristic diameter in gamma distribution (μm)

δ - a random error

ΔT_B - (Sec. 4.2) 10.8 - 12 μm brightness temperature difference

ΔT_B - (elsewhere) vertical minus horizontal T_B polarization difference

Δ^{XY} - difference in T_B signatures for cloud profiles X and Y

ϵ - a random error

ϵ^P - surface emissivity at polarization, P

F - a general forward model or mapping function

f - a known function

f_m - mean value of the function f

G - radar antenna gain

γ^R - ratio of a measurement's sensitivity to the surface to that at the weighting function peak (at rainrate R)

$\Gamma(x)$ - the gamma function

h - radar pulse length (m)

I - radiance ($\mathrm{Wm^{-2}sr^{-1}}$)

I - identity matrix

K - sensitivity or weighting function

$|K|^2$ - dielectric factor

k_{ext} - mass extinction coefficient ($\mathrm{m^2\ kg^{-1}}$)

k_L - liquid water mass extinction coefficient ($\mathrm{m^2\ kg^{-1}}$)

k_W - water vapor mass extinction coefficient ($\mathrm{m^2\ kg^{-1}}$)

κ_g - gas attenuation coefficient ($\mathrm{dBkm^{-1}}$)

κ_c - cloud attenuation coefficient ($\mathrm{dBkm^{-1}}$)

κ_p - precipitation attenuation coefficient ($\mathrm{dBkm^{-1}}$)

L - liquid water path ($\mathrm{kgm^{-2}}$)

λ - Lagrange multiplier (chapter 2) or wavelength (μm)

μ - cosine of the solar zenith or satellite view angle

N_0 - number density ($\mathrm{m^{-4}}$)

$N(D)$ - a drop size distribution

$m = n + i\kappa$ - complex index of refraction

η - radar reflectivity per unit volume

O - a general observation covariance matrix

P - polarization index (Petty (1994a))

$P(\alpha)$ - probability of criterion α

$P(\Theta)$ - scattering phase function

P_r - return power recieved by a radar

P_t - power transmitted by a radar

Q_{abs} - absorption efficiency

Q_{sca} - scattering efficiency

Q_{ext} - extinction efficiency

R - rainfall rate (mmh^{-1})

R^P - surface reflection at polarization P

$\mathbf{R}$ - a profile of rainfall rate (mmh^{-1})

r - radius (μm)

r_e - effective radius (μm)

ρ - density (gm^{-3})

ρ_l - liquid density (gm^{-3})

ρ_i - ice density (gm^{-3})

ρ_a - air density (gm^{-3})

s - path length

S - scattering index (Petty (1994a))

$\mathbf{S}$ - a general model covariance matrix

$\mathbf{S}_a$ - *a priori* error covariance matrix

$\mathbf{S}_{\hat{R}}$ - retrieved rainrate error covariance matrix

$\mathbf{S}_Z$ - reflectivity measurement error covariance matrix

σ_b - backscatter cross-section per unit volume

T - temperature (K)

T_B - brightness temperature (K)

T_f - freezing temperature (K)

T_m - melting temperature (K)

T_s - surface temperature (K)

$Tr(a, b)$ - transmission between points a and b

τ - optical depth

τ^* - total atmospheric column optical depth

V - volume

W - column water vapor or total precipitable water (kgm^{-2})

$\mathbf{x}$ - a general state vector

$\mathbf{x}_a$ - *a priori* value of the state vector $\mathbf{x}$

$\hat{E}(\mathbf{x})$ - expectation value of the state vector $\mathbf{x}$

$\mathbf{y}_o$ - vector of observations

$\mathbf{y}_s$ - vector of modeled or simulated measurements

Z - radar reflectivity

Z_{eff} - effective radar reflectivity

$\mathbf{Z}$ - radar reflectivity profile (mm^6m^{-3} or dBZ, as specified in the text)

Appendix G

Acronymns and Abbreviations

ADT - anomalous diffraction theory

AMSR-E - Advanced Microwave Scanning Radiometer

AMIP - Atmospheric Modeling Intercomparison Project

AVHRR - Advanced Very High Resolution Radiometer

BMC - Bayesian Monte Carlo

CCM1 - NCAR Community Climate Model

CDF - cumulative distribution function

CERES - Clouds and the Earth's Radiant Energy System

CIMSS - Cooperative Institute for Meterological Satellite Studies

CORRAL - Constrained Optimal estimation Rainfall Retrieval ALgorithm

CPR - Cloud Profiling Radar

CRAS - CIMSS Regional Assimilation System

CRF - cloud radiative forcing

CRM - cloud resolving model

CWV - column water vapor

DMSP - Defense Meteorological Satellite Program

DSD - drop size distribution

ECMWF - European Centre for Medium-Range Weather Forecasts

EFOV - effective field of view

ENSO - El Niño Southern Oscillation

EOS - Earth Observing System

ERB - Earth's radiation budget

ERBE - Earth Radiation Budget Experiment

ESSA - Environmental Science Services Administration

FGGE - First GARP Global Experiment

FOV - field of view

GARP - Global Atmospheric Research Program

GCE - Goddard Cumulus Ensemble (model)

GCM - General Circulation Model

GFDL - Geophysical Fluid Dynamics Laboratory

GLA - Goddard Laboratory for Atmospheres

GMS - Geostationary Meteorological Satellite (Japanese)

GOES - Geostationary Operational Environmental Satellites

GOMS - Geosynchronous Meteorological Satellite (Russian)

GPCC - Global Precipitation Climatology Centre

GPM - Global Precipitation Mission

GPROF - Goddard Profiling Algorithm

IR - infrared portion of the electromagnetic spectrum (λ = 0.7 μm - 1 mm)

IRIS - Infrared Interferometer Spectrometer

ISCCP - International Satellite Cloud Climatology Project

ITCZ - intertropical convergence zone

IWC - ice water content

IWP - ice water path

JASMINE - Joint Air-Sea Monsoon Interaction Experiment

LIS - Lightening Imaging System

LH - latent heating

LW - radiation with wavelenths in the range 4.0 - 100.0 μm (dominated by terrestrial emis-

sion)

LWC - liquid water content

LWP - liquid water path

MDS - minimum detectable signal

MJO - Madden-Julian Oscillation

MLW - McClatchey standard mid-latitude winter atmosphere

MODIS - Moderate-Resolution Imaging Spectroradiometer

MP - Marshall-Palmer

MW - microwave portion of the electromagnetic spectrum (λ = 1 mm - 1 m)

NASA - National Aeronautics and Space Administration

NCAR - National Center for Atmospheric Research

NCEP - National Center for Environmental Prediction

NEMS - Nimbus-E microwave spectrometer

NIR - near-infrared portion of the electromagnetic spectrum (λ = 0.7 - 3 μm)

NIST - National Institute of Standards and Technology

NOAA - National Oceanic and Atmospheric Administration

NUBF - non-uniform beamfilling

NWP - numerical weather prediction

OLR - outgoing longwave radiation

PCA - principal component analysis

PDF - probability density function

PIA - path-integrated attenuation

POES - Polar Orbitting Environmental Satellites

PR - Precipitation Radar

PWP - precipitation water path

RH - radiative heating

RSS - Remote Sensing Systems (*www.ssmi.com*)

SCAMS - Scanning Microwave Spectrometer

SFC - surface

SSM/I - Special Sensor Microwave/Imager

SMMR - Special Multichannel Microwave Radiometer

SPCZ - South Pacific convergence zone

SST - sea surface temperature

SW - radiation with wavelenths in the range 0.1 - 4.0 μm (dominated by solar radiation)

TMI - TRMM Microwave Imager

TOA - top of the atmosphere

TOGA COARE - Tropical Ocean Global Atmospheres Coupled Ocean-Atmosphere Response Experiment

TRMM - Tropical Rainfall Measuring Mission

TRP - McClatchey standard tropical atmosphere

VIRS - Visible Infrared Sounder

VIS - visible portion of the electromagnetic spectrum (λ = 0.4 - 0.7 μm)